Transactions of the ASME

EDITORIAL STAFF
Editor, J. J. JAKLITSCH, JR.
Production Editor, STELLA ROBINSON
Editorial Prod. Asst., BETH DARCHI

HEAT TRANSFER DIVISION
Chairman, R. L. WEBB
Secretary, C. J. CREMERS
Senior Technical Editor, E. M. SPARROW
Technical Editor, B. T. CHAO
Technical Editor, D. K. EDWARDS
Technical Editor, M. EPSTEIN
Technical Editor, J. S. LEE
Technical Editor, V. E. SCHROCK
Technical Editor, R. SIEGEL
Technical Editor, K. T. YANG

POLICY BOARD, COMMUNICATIONS
Chairman and Vice-President
I. BERMAN

Members-at-Large
J. W. LOCKE
J. E. ORTLOFF
M. J. RABINS
W. J. WARREN

Policy Board Representatives
Basic Engineering, F. LANDIS
General Engineering, C. F. PHILLIPS
Industry, R. K. HAMPTON
Power, R. E. REDER
Research, G. P. COOPER
Codes and Stds., L. L. ELDER

Nom. Com. Rep., J. W. LOCKE

Business Staff
345 E. 47th St.
New York, N. Y. 10017
(212) 644-7789
Mng. Dir., Publ., C. O. SANDERSON

OFFICERS OF THE ASME
President, CHARLES E. JONES
Exec. Dir. & Sec'y., ROGERS B. FINCH
Treasurer, ROBERT A. BENNETT

Journal of Heat Transfer (ISSN 0022-1481) is edited and published quarterly at the offices of The American Society of Mechanical Engineers, United Engineering Center, 345 E. 47th St., New York, N. Y. 10017. ASME-TWX No. 710-581-5267, New York. Second-class postage paid at New York, N. Y., and at additional mailing offices.

CHANGES OF ADDRESS must be received at Society headquarters seven weeks before they are to be effective. Please send old label and new address.

PRICES: To members, $25.00, annually; to nonmembers, $50.00. Single copies, $15.00 each. Add $1.50 for postage to countries outside the United States and Canada.

INDEXED by the Engineering Index, Inc.

Journal of Heat Transfer

Published Quarterly by The American Society of Mechanical Engineers
VOLUME 102 • NUMBER 3 • AUGUST 1980

ANNOUNCEMENTS

TECHNICAL PAPERS

(*Continued on page 444*)

TECHNICAL NOTES

DISCUSSIONS

ERRATUM

Experimental Study of Laminar Heat Transfer to In-Tube Flow of Non-Newtonian Fluids

S. D. Joshi
A. E. Bergles

Department of Mechanical Engineering and Engineering Research Institute, Iowa State University, Ames, Iowa 50011

An experimental study is reported of heat transfer to laminar flow of two water-methocel pseudoplastic (power law) solutions in a circular tube subjected to a uniform wall heat flux. The object of this study was to evaluate the effects of non-Newtonian behavior and temperature-dependent consistency on heat transfer. The experimental Nusselt numbers are compared with numerical predictions and experimental data. Two correlations are recommended according to the temperature-dependence of the rheological characteristics.

Introduction

Non-Newtonian fluids exhibit a nonlinear shear stress-shear rate dependence. Commonly encountered non-Newtonian fluids, such as polymer solutions or melts, greases, starch suspensions, mayonnaise, soap and detergent slurries, and paper pulp, are pseudoplastic. The shear stress-shear rate relation for these pseudoplastic fluids is described as

$$\tau = K\left(\frac{du}{dy}\right)^n \tag{1}$$

where K, the consistency index, is normally a strong function of temperature, while n, the flow behavior index, is generally a weak function of temperature. The limiting case of a Newtonian fluid is obtained with $n = 1$. The value of n determines the shape of the fully developed velocity profile. For $n = 1$, a parabolic profile exists, and for $n = 0$, a slug profile exists. Since most pseudoplastic fluids are highly viscous in nature, laminar flow is of greatest practical interest.

Each year, a large number of heat exchangers are designed and manufactured for the food and chemical process industries to heat or cool pseudoplastic fluids. Even today, there is a general lack of experimental data for heat transfer coefficients which are required for the design of these heat exchangers. Many of the gaps in understanding relate to circular tubes with constant heat flux at the wall, and, therefore, this boundary condition is considered here. Relative to the complex geometries often found in industry, such as agitated vessels, the present experimental configuration is idealized. It is felt, however, that the rheological behavior can best be investigated with a well-defined geometry. Furthermore, the results provide an appropriate basis for evaluating the effects of heat transfer augmentation by stirring, surface scraping, etc.

Comprehensive reviews of literature for heat transfer to various non-Newtonian fluids have been published by Skelland [1], Metzner [2], and others [3, 4]. For the uniform wall heat flux boundary condition, only a few experimental studies are reported [5–8].

Mizushina, et al. [5] conducted an experimental study with methocel solutions. The data were compared with their analytical solution. Their two-step correlation was[1]

$$\mathrm{Nu} = 1.41\left(\frac{\pi\Delta}{2X^+}\right)^{1/3}\left(\frac{K}{K_w}\right)^{0.1/n^{0.7}} \qquad \text{for } X^+ < 0.05 \tag{2}$$

and

$$\mathrm{Nu} = 4.36\Delta^{1/3}\left(\frac{K}{K_w}\right)^{0.14/n^{0.7}} \qquad \text{for } X^+ \geq 0.05 \tag{3}$$

Large deviations (as much as ± 50–60 percent) were found between these correlations and the data.

Bassett and Welty [6] obtained data with methocel and polyox solutions. The rheological model they used was

$$\frac{du}{dy} = E_1\tau + E_2\tau^2 + E_3\tau^3 \tag{4}$$

where E_1, E_2, and E_3 are constants. In the strict sense, this is not a pseudoplastic model. However, the shear stress-shear rate characteristics for their 5.4 percent methocel solution are pseudoplastic. These data were correlated by

$$\mathrm{Nu}_w = 1.85\left(\frac{\pi}{2X^+}\right)^{(1/3)-0.03(1/\Delta_w)^{nw}} \tag{5}$$

Mahalingam, et al. [7] obtained data with various methocel solutions having n vary from 0.34 to 0.75. The data reported (23 points) are restricted to the thermal entrance length. The authors correlated their data as follows.

$$\mathrm{Nu} = 1.46\left(\frac{K}{K_w}\right)^{0.14}\Delta_w^{1/3}\left[\left(\frac{\pi}{2X^+}\right) + 0.0083(\mathrm{GrPr})_w^{0.75}\right]^{1/3} \tag{6}$$

Bader, et al. [8] conducted a study involving uniform velocity at the onset of heating. No experimental correlation is suggested. However, most pseudoplastic fluids have $\mathrm{Pr} \gg 5$; therefore, this case of simultaneous development of velocity and temperature profile is of little practical interest.

The preceding discussion indicates that there are considerable differences in the form of correlation and in the manner in which temperature-dependent properties are correlated. In general, the number of available data points is limited and the emphasis is on the entrance region. The role of temperature-dependent density is not clear, as only one of the correlations includes a free-convection correction.

The objective of this study was to obtain heat transfer data for pseudoplastic fluids in fully developed as well as developing flow. Thermal conditions were varied so that various proposals for incorporation of temperature-dependent properties could be included. The data were compared with both correlations of experimental data and analytical predictions.

Experimental Apparatus and Test Procedure

Test Facility. The test facility utilized in this investigation was constructed in the Iowa State University Heat Transfer Laboratory. A schematic layout of the test loop is shown in Fig. 1. It is a closed-loop, low-pressure system with all piping made of copper tubes and brass fittings. The viscous working fluids were circulated with a gear pump. The energy supplied to the electrically heated test section was removed in a water cooled heat exchanger. A preheater, a tank to accommodate fluid expansion and facilitate degassing, and an accumulator to dampen pump disturbances were also provided. Precise

[1] All fluid properties are evaluated at the fluid bulk temperature, unless otherwise indicated.

Contributed by the Heat Transfer Division for publication in the JOURNAL OF HEAT TRANSFER. Manuscript received by the Heat Transfer Division November 15, 1979.

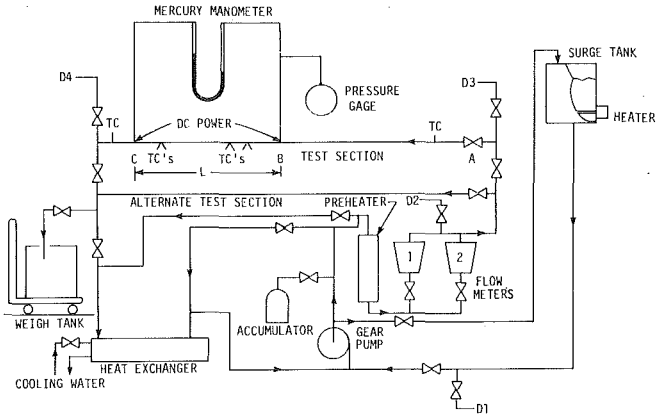

Fig. 1 Schematic diagram of test loop

fluid temperature control was accomplished by adjustment of the preheater, degassing tank, and secondary coolant.

Two rotameters were provided in the test section line. However, for the pseudoplastic fluids, shear stress is a nonlinear function of du/dy, K is highly sensitive to temperature, and the fluids undergo degradation with time. These factors made it impossible to obtain a consistent flowmeter calibration. Hence, a weigh tank was incorporated at the outlet of the test section to measure the flow rate, while the flometers were simply used as flow indicators. Many drains (D1, D2, D3, and D4) were provided in the loop to facilitate removal of entrapped air.

Two thin-walled, 304 stainless steel circular tubes were used as test sections. The wall thickness of the tubes was a compromise between minimum thickness required for maximum electrical resistance and sufficient mechanical strength. The tubes were heated by passing d-c current directly through the tube wall. An inlet calming section was provided to allow the velocity profile to be fully developed at the entrance of the heated section. The details of these test sections are given in Table 1.

At each axial measuring station, three copper-constantan thermocouples were attached circumferentially, 90 deg apart, and electrically insulated from the tube. Fluid temperatures were measured at the inlet and exit of the heated test section. The test tubes were heavily insulated with glass fiber insulation to minimize heat loss. The pressure drop along the heated length was measured with a mercury U-tube manometer.

Test Fluid Characteristics. Two pseudoplastic fluids, a 1 percent and an 0.9 percent by weight aqueous solution of HEMC,[2] were used as the working fluids. These two fluids have substantially different viscosities, and for a given temperature, they exhibit substantially different K and n values. These solutions were chosen because they form pseudoplastic fluids which are fairly stable, because no health or fire hazard is associated with them, and because they are relatively easy to obtain and prepare in large quantities. These fluids are quite viscous (about 0.1 Ns/m^2), yet they could be handled by the gear pump in the test loop.

[2] XD-7630.02, cellulose ether powder, Dow Chemical Company.

Table 1 Test section details

	Test Section I	Test Section II
Inner diameter (mm)	10.19	12.85
Outer diameter (mm)	11.20	14.27
Total length (m)	3.35	3.73
Heated length (m)	1.82	2.74
Calming length (m)	1.07	0.76
Number of axial temperature measuring stations on the heated test section	4	8

The solutions were prepared by dissolving the polymer powder in water and then raising the pH values of the solutions to increase viscosity. The details of solution preparation are given elsewhere [9, 10]. These solutions are very weak; therefore, all fluid properties, other than K and n, were assumed to be the same as the water solvent [11–13].

The constitutive equation for pseudoplastic fluids can be written as

$$\tau_w = K' \left(\frac{8\bar{u}}{D}\right)^n \tag{7}$$

where $(8\bar{u}/D)$ is the velocity gradient at the wall for Newtonian fluids in fully developed laminar flow. It is noted that

$$K' = K \left(\frac{3n+1}{4n}\right)^n \tag{8}$$

These log-linear equations were utilized to construct flow curves. On the plot of τ versus $(8\bar{u}/D)$, the intercept on the Y-axis at $(8\bar{u}/D) = 1$ gives the value of K', while n is the slope of the line. The parameter $(8\bar{u}/D)$ can be calculated from the specified fluid flow rate and tube geometry for hydrodynamically developed flow; τ_w is estimated by measuring the pressure drop and using the following equation

$$\tau_w = \frac{D\Delta P}{4L} \tag{9}$$

Test Section I was utilized as a straight-tube rheometer [14] by simply measuring the isothermal pressure drop as a function of flow rate and inlet temperature. These data points were reduced to desired flow curve parameters, as shown in Fig. 2.

The pseudoplastic fluids are basically polymer solutions that degrade with time because of breakage of polymer chains. The fluid degradation with time caused a noticeable change in the values of K' and n. In general, K' decreased and n increased. To account for this aging, the following procedure was developed.

Nineteen heat transfer runs were made for the 0.9 percent HEMC solution. The K' and n values for four different temperatures were estimated at

Time I: before the start of the heat transfer experiments
Time II: after 10 heat transfer runs (about 48 hr)
Time III: after 19 heat transfer runs (about 75 hr)

Nomenclature

A = tube surface area, m^2
C_p = isobaric specific heat, Ws/kgK
D = inside tube diameter, m
g = gravitational acceleration, m/s^2
h = heat transfer coefficient, W/m^2K
k = fluid thermal conductivity, W/mK
K = consistency index, Ns^n/m^2
K' = modified consistency index, Ns^n/m^2
L = length of the test section, m
n = flow behavior index
P = pressure, N/m^2
q'' = heat flux, W/m^2
r = radius, m
t = temperature, K or °C
u = axial velocity, m/s
$\bar{u}$ = average axial velocity, m/s
x = distance from the tube inlet, m/s
β = isobaric coefficient of thermal expansion, K^{-1}
γ = consistency parameter, $-1/K(dK/dt)$, K^{-1}
ρ = density, kg/m^3
μ = viscosity, Ns/m^2
μ_{eff} = effective viscosity, Ns/m^2
τ = shear stress, N/m^2
$\Delta = (3n+1)/4n$
ΔP = pressure drop, N/m^2
Δt = temperature difference, K
$\Delta T = q''_w D/2k$, K
Gr = Grashof number, $\rho^2 g\beta\Delta t D^3/\mu^2_{eff}$
Nu = Nusselt number, hD/k
Pr = effective Prandtl number, $\mu_{eff}C_p/k$
Re = effective Reynolds number, $\rho D\bar{u}/\mu_{eff}$
X^+ = dimensionless distance, $2(x/D)/RePr$

Subscripts

cp = constant property
e = thermal entrance length
vp = variable property
x = at distance x from the inlet
w = wall temperature
∞ = fully developed condition

As shown in Fig. 2, a significant effect of degradation was observed Linear curves were fitted to these data by a linear regression analysis. The correlation coefficients are of the order of 0.99 (at 95 percent confidence), thus confirming the pseudoplastic characteristics of these fluids. On semi-logarithmic paper, the n-t relation exhibited linear behavior. A linear regression analysis gave correlation coefficients of the order of 0.99 (at 95 percent confidence), thus confirming the first-order exponential n-t correlation.

The arithmetic averages of the K-t and n-t correlations for Times I and II for a given temperature were correlated and used to reduce data for Runs 1–10, and similar averages of correlations for Times II and III were taken to reduce data for Runs 10–19. A similar procedure was also followed for the 1 percent HEMC solutions. Nine heat transfer runs were made with this solution. Rheological flow curves were obtained before the heat transfer runs and after nine heat transfer runs (about 48 hr), and averages of these two (K-t and n-t) curves at given temperatures were correlated and used to reduce the data. For these two fluids, the K and n temperature dependences are

$$K = a \exp(-bt - ct^2) \tag{10}$$

$$n = a_1 \exp(b_1 t) \tag{11}$$

where t is in °C. The constants in these equations are recorded in Table 2. With the help of statistical analysis of variance, it can be shown that arithmetic time averaging gives the best representation of time-dependent rheological properties [9, 10].

Experimental Procedure and Data Reduction. The experiments generally proceeded by increasing power to the heated section (with flow rate and inlet temperature remaining constant). At each power setting, data were recorded for inlet and exit fluid temperatures, current, voltage drop, outer tube wall temperatures, pressure drop, and fluid flow rate. The experimental variables were

For the 0.9 percent HEMC solution

Flow rate: 16–140 kg/hr
Heat flux: $12.5 \times 10^6 - 62 \times 10^6$ W/m^2
Pr: 560–1344
Re: 2–26
n values (21 – 55°C): 0.55–0.76

And, for the 1 percent HEMC solution

Flow rate: 18–131 kg/hr
Heat flux: $8 \times 10^6 - 21 \times 10^6$ W/m^2
Pr: 940–1980

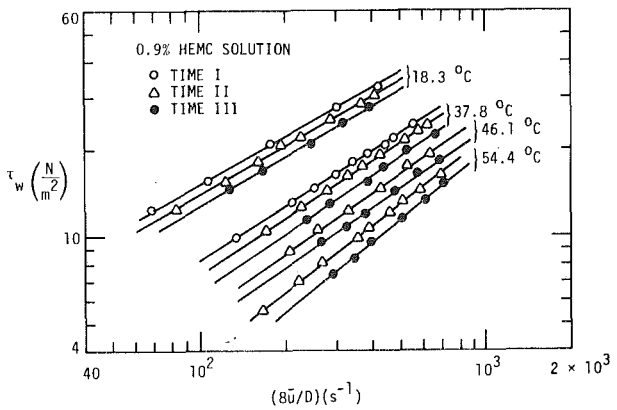

Fig. 2 Flow curve for 0.9 percent HEMC Solution

Re: 2–26
n values (21–55°C): 0.6–0.85

Heat input was determined from the measured electrical power input as corrected for heat loss through the outer wall (estimated to be 1.5 percent [9,10]). This value generally agreed with the value determined from the fluid enthalpy rise; however, the latter method was not reliable due to lack of a suitable mixing device at the tube outlet. The heat balance was improved up to 3 percent when a static mixer was installed upstream of the exit thermocouple.

The local bulk temperature at the measuring section was computed from the inlet temperature, flow rate, and heat input. A linear variation in bulk temperature from the inlet to the exit of the heated length was assumed. The tube wall temperature drop was calculated by employing the steady-state, one-dimensional heat conduction equation with uniform heat generation inside the cylindrical tubes. The correction (less than 0.5 K) was applied uniformly around the circumference of the tube. The circumferential average wall temperature was computed from the three inner-wall temperature readings by Simpson's rule of numerical integration. The wall temperature variation was very small, thus indicating absence of significant free convection. The wall temperature and bulk temperature were combined with the heat flux to evaluate the heat transfer coefficient and the Nusselt number. The error in the Nusselt number is estimated to be 5.5 percent by the propagation-of-error technique. The details of this analysis are given elsewhere [9, 10].

For pseudoplastic fluids, the effective viscosity is defined as

$$\mu_{\text{eff}} = \frac{\tau_w}{8(\bar{u}/D)} \tag{12}$$

This would be viscosity if the fluid were Newtonian. The shear stress is a time average, as indicated in the preceding section. This viscosity was utilized to calculate Prandtl and Reynolds numbers.

Further details of apparatus, procedure, and data reduction are given elsewhere [9, 10].

Heat Transfer Results and Discussion

A total of 144 data points were obtained for both HEMC solutions. Fig. 3 shows a plot of local Nusselt numbers against dimensionless distances. The abscissa is chosen so as to be consistent with most presentations of uniform heat flux results, even though this differs from the usual non-Newtonian presentations. Most of the Nusselt numbers are substantially higher than the constant property Newtonian predictions. The suitability of available correlations is now examined.

Figure 4 presents a comparison of the present data with the correlation of theoretical results by Mizushina, et al. [5]. The correlation fits the general characteristics of the data; however, the correlation is generally high in the entrance region and low in the fully developed region. The two-step correlation does not adequately represent the transition region between entrance and fully developed regions.

As shown in Fig. 5, the correlation of Bassett and Welty [6] also tends to overestimate the entrance region data. The correlation is limited to the entrance region. A similar trend, but more pronounced, is observed in Fig. 6 where the data are compared with the correlation of Mahalingham, et al. [7].

The final comparison with previous results involves a numerical solution for developing laminar flow completed earlier in this program [9, 15, 16]. The assumed K-t dependence was

$$K = a\, e^{-bt} \tag{13}$$

and n was assumed independent of temperature. The correlation of

Table 2 Fluid properties

HEMC Solution	Constants				
	$a \times 10^3$	$b \times 10^3$	$c \times 10^3$	$a_1 \times 10^3$	$b_1 \times 10^3$
0.9 percent (Average of Times I and II)	1860.882	24.777	0.504	493.556	7.577
0.9 percent (Average of Times II and III)	1499.287	22.995	0.521	509.245	7.625
1 percent (Average of Times I and II)	1939.023	33.343	0.434	525.636	8.650

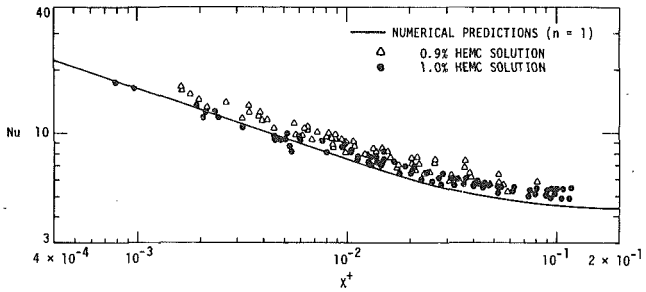

Fig. 3 Plot of experimental heat transfer data and constant property numerical prediction for Newtonian flow [9]

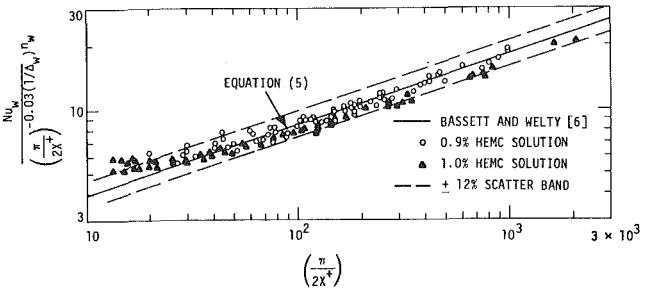

Fig. 5 Comparison of present data with correlation of Bassett and Welty [6]

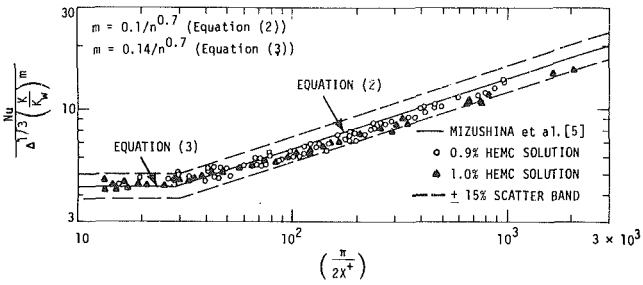

Fig. 4 Comparison of present data with correlation of Mizushina, et al. [5]

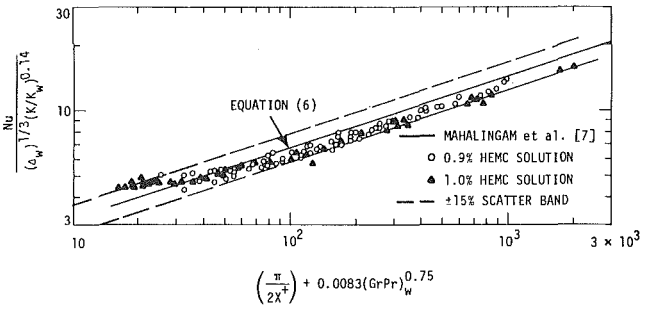

Fig. 6 Comparison of present data with correlation of Mahalingam, et al. [7]

the numerical results was based on two modifications of the standard constant property solution. The common basis non-Newtonian correction, $\Delta^{1/3}$, noted in equations (2, 3), and (6), was confirmed for both entrance and fully developed regions. The K-t effects were more complex, with separate correlations being required for entrance and fully developed regions. A single correlation was developed for the entire tube

$$\mathrm{Nu}_{vp,n} = \left(\frac{\mathrm{Nu}_{cp,n}}{\mathrm{Nu}_{cp,n=1}}\right)\left(\frac{\mathrm{Nu}_{vp,n}}{\mathrm{Nu}_{cp,n}}\right)\mathrm{Nu}_{cp,n=1} \qquad (n<1) \qquad (14)$$

where

Non-Newtonian Correction:

$$\left(\frac{\mathrm{Nu}_{cp,n}}{\mathrm{Nu}_{cp,n=1}}\right) = \Delta^{1/3}$$

Consistency Index Correction:

$$\left(\frac{\mathrm{Nu}_{vp,n}}{\mathrm{Nu}_{cp,n}}\right) = \frac{1}{\left(\frac{\mathrm{Nu}_{cp,n}}{\mathrm{Nu}_{vp,n}}\right)_\infty \left\{1 + \left[\frac{(\mathrm{Nu}_{vp,n}/\mathrm{Nu}_{cp,n})_\infty}{(Nu_{vp,n}/\mathrm{Nu}_{cp,n})_e}\right]^{30}\right\}^{1/30}}$$

$$\left(\frac{\mathrm{Nu}_{vp,n}}{\mathrm{Nu}_{cp,n}}\right)_e = \left(\frac{K}{K_w}\right)^{0.58-0.44n}$$

$$\left(\frac{\mathrm{Nu}_{vp,n}}{\mathrm{Nu}_{cp,n}}\right)_\infty = 1 + (0.1232 - 0.0542\,n)\,\gamma\Delta\tau - (0.0101 - 0.0068\,n)(\gamma\Delta\tau)^2$$

and

$$\mathrm{Nu}_{cp,n=1} = 4.36\,\{1 + [0.376(X^+)^{-0.33}]^6\}^{1/6}$$

To the experimental $\mathrm{Nu}_{vp,n}$, non-Newtonian and consistency index variation corrections were applied. The reduced data are compared with the analytical correlation in Fig. 7. Very good agreement is observed in the fully developed region; however, the data lie well below the correlation in the entrance region. This can be attributed to the simplified temperature-dependent property formulations used in the analysis. In particular, n was assumed constant, whereas the present working fluid exhibited variable n. Furthermore, in the numerical solution a first-order K-t relation was assumed (equation (13)), while the fluid actually has a second-order temperature dependence (equation (10)). An attempt was made to compensate for this by fitting piecewise first-order curves to the data over 6 °C intervals; however, it is doubtful whether this technique properly accounts for the actual K-t dependence. In any event, both n-t and K-t effects tend to overestimate the predicted Nusselt number, as reflected in Fig. 7.

Since the general framework of correlation represented by equation (14) seems to be reasonable, those coordinates are retained and the data are correlated using the method of Churchill and Ozoe [17] as follows

$$\frac{\mathrm{Nu}_{vp,n}}{\left(\frac{\mathrm{Nu}_{vp,n}}{\mathrm{Nu}_{cp,n}}\right)\left(\frac{\mathrm{Nu}_{cp,n}}{\mathrm{Nu}_{cp,n=1}}\right)} = 4.36\,\{1 + [0.381(X^+)^{-0.303}]^8\}^{1/8} \qquad (15)$$

From this correlation $\mathrm{Nu}_{vp,n}$ can be evaluated explicitly by evaluating non-Newtonian correction and consistency index variation correction as shown in equation (14). This equation is included in Fig. 7; 90 percent of the data show less than 5 percent deviation from the correlation. The correlation thus seems to be able to accommodate reasonable variations in n as well as second-order K-t effects.

Returning to the data of other investigators, it is seen from Fig. 8 that the present experimental correlation, equation (15), is in generally good agreement with the data of Bassett and Welty [6], whereas the analytical correlation given by equation (14) is in excellent agreement with the data of Mahalingam, et al. [7]. From the preceding discussion, this is expected, as the working fluid used by Bassett and Welty exhibited the same general characteristics as the present test fluid, i.e., temperature-dependent n and second-order K-t. On the other hand, the fluid used by Mahalingam, et al. had nearly constant n and a first-order K-t dependence. The data of Mizushina, et al. [5] could not be included in this comparison, as insufficient details are given in their paper.

It is noted that the data of Mahalingam, et al. are correlated very well by equation (14), which does not consider free convection effects. In fact, this equation gives somewhat better correlation of data of Mahalingam, et al. than does their own correlation. This suggests that free convection is probably not an important factor in laminar flow of high viscosity non-Newtonian fluids in horizontal tubes.

Conclusions

This study has provided new experimental information for heat transfer to laminar flow of pseudoplastic (power law) fluids in a circular tube subjected to uniform heat flux. The two aqueous solutions of cellulose ether powder exhibited temperature and time-dependent consistency index and flow behavior index. Averaging techniques were developed to cast the data in a form for comparison with available

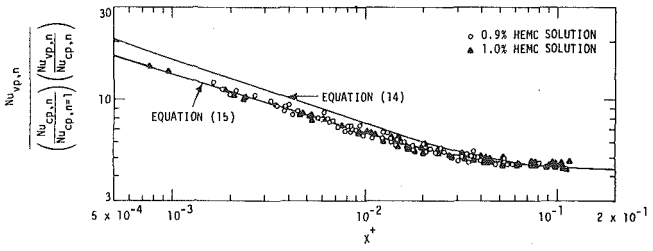

Fig. 7 Comparison of numerical and experimental results

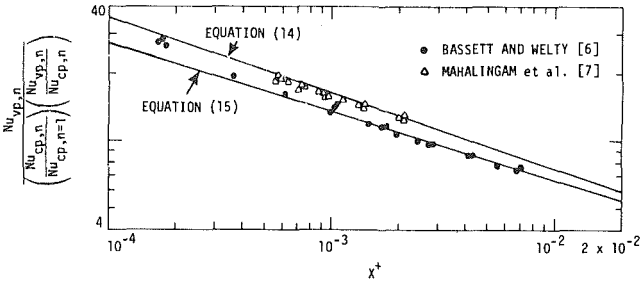

Fig. 8 Comparison of numerical and experimental results

numerical solutions and experimental results.

The best correlation of the data was given by a modification of the correlation of numerical results prepared earlier in this study. The experimental data of Basset and Welty [6] are well described by this correlation. On the other hand, the data of Mahalingam et al. [7] are well described by the original numerical correlation. These conclusions are explained by the difference in the temperature-dependent rheological characteristics of the test fluids and the fluid assumed for the numerical model. Two correlations are thus proposed to predict the behavior of two common types of power law behavior.

A more refined numerical model with n-t and second-order K-t would be required to fully verify the correlation of the present data. Further work in this general area is desirable to more accurately account for the substantial increases in heat transfer coefficients above Newtonian, constant property values.

Acknowledgments

This study was supported by the Engineering Research Institute of Iowa State University through funds provided by the Power Affiliates Program and the Department of Mechanical Engineering. Leon Girard and associates from the Engineering Research Institute Machine Shop and Hap Steed from the Mechanical Engineering Department helped in fabricating the test apparatus. Dr. J. L. Hall provided helpful suggestions for the statistical analysis of the data.

References

1 Skelland, A. H. P., *Non-Newtonian Flow and Heat Transfer,* John Wiley and Sons, New York, 1967.

2 Metzner, A. B., "Heat Transfer in Non-Newtonian Fluids," *Advances in Heat Transfer,* Vol. 2, Hartnett, J. P., and Irvene, Jr., T. F., eds., Academic Press, New York, 1965, pp. 357–397.

3 Porter, J. E., "Heat Transfer at Low Reynolds Number (Highly Viscous Liquids in Laminar Flow) Industrial Research Fellow Report," *Transactions of the Institution of Chemical Engineers,* Vol. 49, 1971, pp. 1–29.

4 Froishteter, G. B., and Smorodinskii, E. L., "Laminar Heat Transfer of Non-Newtonian Liquid in Tubes with Variable Physical Properties," translated from *Teoreticheskir Osnovy Khimicheskoi Tekhnologii,* Vol. 9, No. 3, 1975, pp. 392–405.

5 Mizushina, T., Ito, R., Kuriwake, Y., and Yahikazawa, K., "Boundary Layer Heat Transfer in a Circular Tube to Newtonian and Non-Newtonian Fluids," *Kagaku Kogaku,* Vol. 31, 1967, pp. 250–255.

6 Bassett, C. E., and Welty, J. R., "Non-Newtonian Heat Transfer in the Thermal Entrance Region of Uniformly Heated Horizontal Pipes," *American Institute of Chemical Engineers Journal,* Vol. 21, No. 4, 1975, pp. 691–706.

7 Mahalingam, R., Tilton, L. O., and Coulson, J. M., "Heat Transfer in Laminar Flow of Non-Newtonian Fluids," *Chemical Engineering Science,* Vol. 30, 1975, pp. 921–929.

8 Bader, H. J., McKillop, A. A., and Harper, J. C., "An experimental and Analytical Study of Entrance-Region Flow of Non-Newtonian Fluids," *International Heat Transfer Conference,* Vol. IV, Paris-Versailles, 1970.

9 Joshi, S. D., "Heat Transfer in In-Tube Flow of Non-Newtonian Fluids," PhD Thesis, Iowa State University, Ames, Iowa, 1978.

10 Joshi, S. D., and Bergles, A. E., "Heat Transfer in Laminar In-Tube Flow of Non-Newtonian Fluids, Part II, Experimental Study," Engineering Research Institute Report, Heat Transfer Laboratory, HTL-18, ISU-ERI-Ames-80034, Iowa State University, 1979.

11 Uhl, V. W., and Root, W. L., "Heat Transfer in Hollow Cut-Flight Jacketed Units to Viscous Fluids," *Chemical Engineering Progress Symposium Series 102,* Vol. 66, 1970, pp. 199–205.

12 Amato, W. S., and Tien, C., "Free Convection Heat Transfer from Isothermal Spheres in Polymer Solutions," *International Journal of Heat and Mass Transfer,* Vol. 19, 1976, pp. 1257–1266.

13 Oliver, D. R., and Asghar, S. M., "The Laminar Flow of Newtonian and Viscoelastic Liquids in Helical Coils," *Transactions of the Institution of Chemical Engineers,* Vol. 53, 1975, pp. 181–186.

14. Scheve, J. L., "A Simplified Process Viscometer for Non-Newtonian Fluids," MS Thesis, Iowa State University, 1971.

15 Joshi, S. D., and Bergles, A. E., "Heat Transfer in Laminar In-Tube Flow of Non-Newtonian Fluids, Part I, Analytical Study," Engineering Research Institute Report, Heat Transfer Laboratory, HTL-17, ISU-ERI-Ames-79088, Iowa State University, 1979.

16 Joshi, S. D., and Bergles, A. E., "Analytical Study of Heat Transfer to Laminar In-Tube Flow of Non-Newtonian Fluids," to be presented at the 19th National Heat Transfer Conference, Orlando, Florida, 1980.

17 Churchill, S. W., and Ozoe, H., "Correlations for Laminar Forced Convection with Uniform Heating in Flow over a Plate and in Developing and Fully Developed Flow in a Tube," ASME JOURNAL OF HEAT TRANSFER, Vol. 95, 1973, pp. 78–84.

Fluid-to-Fluid Conjugate Heat Transfer for a Vertical Pipe—Internal Forced Convection and External Natural Convection

E. M. Sparrow
Department of Mechanical Engineering,
University of Minnesota,
Minneapolis, Minn. 55455
Fellow ASME

M. Faghri[1]
Department of Mechanical Engineering,
Tehran University of Technology,
Tehran, Iran

An analysis is made of the interactive heat transfer problem involving forced convection flow in a vertical pipe and natural convection boundary layer flow external to the pipe. Both flows are laminar. Solutions of the conservation equations for mass, momentum, and energy were obtained numerically by an iterative scheme which deals successively with the internal and external flows. Remarkably rapid convergence was achieved by adopting a procedure whereby information is transferred between the two flows via heat transfer coefficients rather than via the wall or bulk temperatures or the heat flux. Results are presented for the axial distributions of the internal and external Nusselt numbers, of the wall temperature, and of the bulk temperature of the internal flow—all as a function of three parameters. It was found that at any (dimensionless) axial station, the pipe Nusselt number is insensitive to the parameters and is bounded between the values for uniform wall temperature and uniform wall heat flux. On the other hand, the external natural convection Nusselt number is highly sensitive to the parameters and departs substantially from the standard uniform wall temperature results.

Introduction

Analyses of duct-flow and external-flow (i.e., boundary layer) heat transfer have each generated a voluminous literature. In the main, these analyses have been based on models in which the thermal boundary conditions are specified at the surfaces which bound the flowing fluid. Such models avoid consideration of possible thermal interactions of the fluid flow with heat conduction processes in the bounding walls and with other fluid flows (e.g., flows adjacent to the back side of the bounding walls).

As documented in the exhaustive survey of [1], there has been limited analytical study of thermal interactions between duct-flow convection and wall heat conduction, and a similar state of affairs exists for boundary layers ([2, 3] are representative of the available literature). The treatment of fluid-to-fluid interactions has generally been confined to duct flows (e.g., double-pipe heat exchangers) and to situations where the participating heat transfer coefficients are assumed known and constant along the duct.

The present paper is concerned with a class of thermal interactions that has not yet been treated in the published literature. Attention will be focused on a forced convection flow in a vertical pipe which exchanges heat with a natural convection boundary layer flow external to the pipe. These thermally interacting flows are analyzed here from first principles (i.e., via solutions of the basic conservation equations) so that the heat transfer coefficients need not be assumed in advance; rather, the axial distributions of the internal and external transfer coefficients are determined among the results of the analysis.

The physical situation to be analyzed is diagrammatically depicted in Fig. 1. As shown there, a pipe flow with a uniform temperature T_1 at inlet exchanges heat in the region $x > 0$ with an external fluid environment whose temperature T_∞ is less than T_1. During the course of its flow, the bulk temperature of the internal fluid decreases monotonically with x owing to the external heat loss. The wall temperature also decreases with x, but always exceeds T_∞ so that there is a natural convection upflow as indicated in the diagram. Since both the wall temperature and wall heat flux vary with x and since both are unknown a priori, neither the internal nor the external heat transfer coefficients, both of which are x-dependent, can be taken from the literature. It can be expected, on the basis of prior experience, that the natural convection heat transfer coefficient will be especially sensitive to the variation of the pipe wall temperature.

The solution of the just-described fluid-to-fluid conjugate heat transfer problem requires that the relevant conservation equations for the internal and external flows be satisfied simultaneously. Solutions will be obtained here for laminar flow both internal and external to the pipe. For the internal flow, the solution method can deal equally well with simultaneously developing velocity and temperature

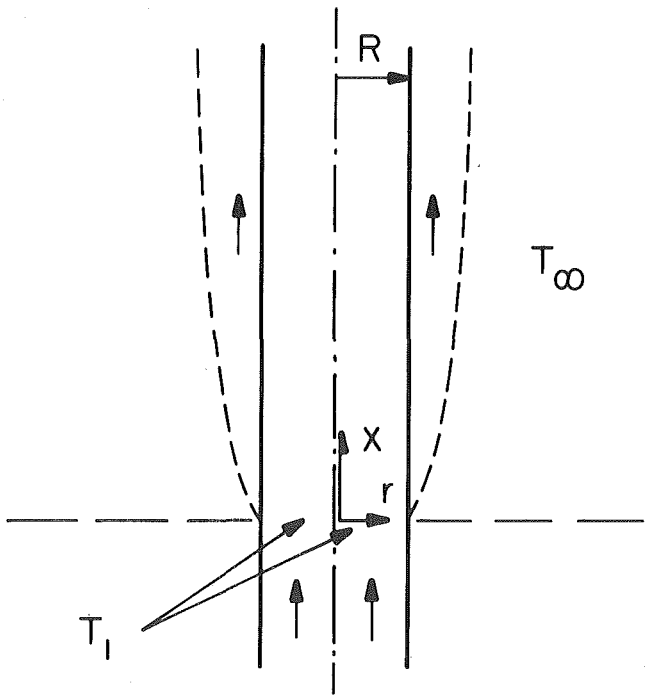

Fig. 1 Schematic of the fluid-to-fluid conjugate heat transfer problem

[1] Work performed when the author was an adjunct associate professor at the University of Minnesota.

Contributed by the Heat Transfer Division for publication in the JOURNAL OF HEAT TRANSFER. Received by the Heat Transfer Division October 1, 1979.

fields or with a developing temperature field in the presence of a hydrodynamically developed velocity field. Since the former situation involves the specification of an additional prescribable parameter (the Prandtl number of the internal flow), over and above the basic set of three parameters, the present solutions will be carried out for a hydrodynamically developed internal flow. For the external flow which is buoyancy driven, it is, of course, necessary to deal simultaneously with the velocity and temperature fields.

Another feature that can be readily accommodated in the analysis is the thermal resistance of the pipe wall. This would, however, require the specification of an additional prescribable parameter and, because of this, the wall resistance has been neglected.

The numerical solutions of the conjugate pipe flow—boundary layer flow problem were carried out by adapting the Patankar-Spalding method. The solutions and results depend on prescribed values of the following parameters

$$\text{Ra/Pe}, \qquad \text{Pr}_o, \qquad k_o/k_i \tag{1}$$

where the Rayleigh number pertains to the external flow and is based on the pipe outside diameter D and on $T_1 - T_\infty$; the Peclet number pertains to the internal flow. With regard to the other parameters, the subscripts o and i refer to fluid properties of the outside and inside fluids, respectively. The external Prandtl number Pr_o was given values of 0.7 and 5, with air and water in mind. Correspondingly, values of $k_o/k_i \leq 1$ were assigned for $\text{Pr}_o = 0.7$, while $k_o/k_i \geq 1$ for $\text{Pr}_o = 5$. For each assigned value of Pr_o and k_o/k_i, Ra/Pe was varied over a range appropriate to potential applications. The presentation of results will provide axial distributions for four quantities of engineering interest: (1) the local Nusselt number for the pipe flow, (2) the local Nusselt number for the external natural convection flow, (3) the local wall temperature, and (4) the local bulk temperature of the pipe flow.

Analysis and Solution

Formulation of the Problem. To initiate the formulation of the problem, dimensionless variables are introduced as follows
(a) for both the internal and external flows

$$X = (x/R)/\text{Pe}, \quad \eta = r/R, \quad \theta = (T - T_\infty)/(T_1 - T_\infty) \tag{2}$$

(b) for the external flow

$$U = (uR/\nu_0)/\text{Pe}, \qquad V = vR/\nu_0 \tag{3}$$

Note that to avoid the emergence of the pipe wall radius ratio as an additional parameter, the wall is assumed to be thin. Consequently, $\eta \leq 1$ corresponds to the pipe flow and $\eta \geq 1$ corresponds to the external boundary layer flow.

For the pipe flow with a hydrodynamic developed velocity profile $u = 2\bar{u}(1 - \eta^2)$, only the dimensionless form of the energy conservation equation need be written

$$(1 - \eta^2)\frac{\partial\theta}{\partial X} = \frac{1}{\eta}\frac{\partial}{\partial\eta}\left(\eta\frac{\partial\theta}{\partial\eta}\right) \tag{4}$$

On the other hand, for the external flow, the full slate of conservation equations is required

$$\partial(\eta U)/\partial X + \partial(\eta V)/\partial\eta = 0 \tag{5}$$

$$U\frac{\partial U}{\partial X} + V\frac{\partial U}{\partial\eta} = \frac{(\text{Ra/Pe})\theta}{8\,\text{Pr}_o} + \frac{1}{\eta}\frac{\partial}{\partial\eta}\left(\eta\frac{\partial U}{\partial\eta}\right) \tag{6}$$

$$U\frac{\partial\theta}{\partial X} + V\frac{\partial\theta}{\partial\eta} = \frac{1}{\text{Pr}_o}\frac{1}{\eta}\frac{\partial}{\partial\eta}\left(\eta\frac{\partial\theta}{\partial\eta}\right) \tag{7}$$

The internal and external problems are coupled by temperature and heat flux continuity at the pipe wall. Therefore, at each X and at $\eta = 1$

$$\theta_i = \theta_o \tag{8a}$$

$$(\partial\theta/\partial\eta)_i = (k_o/k_i)(\partial\theta/\partial\eta)_o \tag{8b}$$

Additionally, for the pipe flow

$$\theta = 1 \text{ at } X = 0, \qquad \partial\theta/\partial\eta = 0 \text{ at } \eta = 0 \tag{9}$$

while for the external flow

$$\theta,\ U \to 0 \text{ as } \eta \to \infty \text{ and as } X \to 0 \tag{10}$$

Inspection of equations (4 − 10) confirms the presence of the three parameters that were cited in equation (1) and also reveals the tight interconnection between the internal and external problems. Although these equations are a precise mathematical statement of the physical problem, certain of them will be reinterpreted as the solution methodology is developed.

Solution Methodology. The primary tool to be used in solving the foregoing governing equations is the Patankar-Spalding method [4]. This is a fully implicit finite difference scheme designed for duct flow and boundary layer problems where streamwise second derivatives ($\partial^2/\partial X^2$) can be neglected. The absence of such derivatives enables solutions to be obtained by starting with known values at $X = 0$ and marching downstream in the direction of increasing X. For conventional duct or boundary layer problems, the Patankar-Spalding method is noniterative; that is, the solution always marches forward and, once an axial station has been visited, it is never revisited.

In the present instance, owing to the fact that mutually consistent solutions of two problems (i.e., the inner and outer problems) have to be obtained, the Patankar-Spalding method is employed iteratively. The present solution scheme will now be described, first in broad outline and then with the finer details that are essential to its success.

In its overall pattern, the solution scheme begins by solving the external (natural convection) problem for the boundary condition of

Nomenclature

D = pipe diameter
c_{pi} = specific heat of internal flow
h_i = local internal heat transfer coefficient, $q/(T_{bx} - T_{wx})$
h_o = local external heat transfer coefficient, $q/(T_{wx} - T_\infty)$
k_i = thermal conductivity of internal flow
k_o = thermal conductivity of external flow
$\dot{m}$ = internal mass flow rate
Nu_i = local internal Nusselt number, h_iD/k_i
Nu_o = local external Nusselt number, h_oD/k_o
Pe = Peclet number of internal flow, $\bar{u}D/\alpha_i$
Pr_o = Prandtl number of external flow
q = local heat flux at pipe wall
r = radial coordinate
R = pipe radius
Ra = Rayleigh number of external flow, $g\beta_0(T_1 - T_\infty)D^3\text{Pr}_o/\nu_o^2$
T = temperature
T_{bx} = local bulk temperature of internal flow
T_{wx} = local wall temperature
T_1 = inlet temperature of internal flow
T_∞ = free stream temperature of external flow
X = dimensionless axial coordinate, $(x/R)/\text{Pe}$
x = axial coordinate
U,V = dimensionless velocities, equation (3)
u,v = velocity components
$\bar{u}$ = mean velocity of internal flow
α_i = thermal diffusivity of internal flow
β_0 = thermal expansion coefficient of external flow
η = dimensionless radial coordinate, r/R
θ = dimensionless temperature, $(T - T_\infty)/(T_1 - T_\infty)$
ν_0 = kinematic viscosity of external flow

Subscripts

i = inner flow (i.e., pipe flow)
o = outer flow (i.e., natural convection flow)

uniform wall temperature. Results from this solution are then employed as input to the thermal boundary conditions for the pipe flow problem and, with this, the pipe flow problem is solved. That solution furnishes inputs for the thermal boundary conditions for the external flow problem, which is then solved. This procedure of alternately solving the inner and outer problems is continued until the wall temperature and heat flux distributions converge. By using the particular boundary condition formulations to be described shortly, convergence to five significant figures was attained within three to five iterations.

In deciding on the most effective means of transferring information from the outer to the inner solution and vice versa, cognizance was taken of prior experience with the sensitivity of the heat transfer coefficient to various distributions of wall temperature or wall heat flux. For laminar duct flows, the heat transfer coefficient responds rather passively to a variety of thermal boundary conditions [1, 5]. Thus, at any stage during the iteration procedure, the heat transfer coefficient may be much closer to the final converged result than either the wall temperature or the wall heat flux. This characteristic suggests the heat transfer coefficient as an effective vehicle for transmitting information from the inner solution to the outer solution during the iteration process. In the case of natural convection, the heat transfer coefficient is expected to be more responsive to the thermal boundary conditions than for forced convection. Even with this, it is believed to be advantageous to convey information from the outer to the inner solution via the heat transfer coefficient. The implementation of these ideas will now be described.

Let a cycle of the iteration process be defined as including a set of consecutive solutions of the outer and inner flows. Suppose that a cycle has just been completed and the local heat transfer coefficients $h_i(x)$ for the inner flow have been evaluated as part of the inner solution. The next cycle begins with the solution for the outer flow. The governing equations to be solved include the conservation equations (5–7) along with boundary conditions (10). However, in view of the availability of $h_i(x)$, the thermal continuity equations (8a) and (8b) are replaced by

$$-k_o(\partial T/\partial r)_o = h_i(T_{bx} - T_{wx}) \tag{11}$$

at $r = R$ and all x; the quantity T_{bx} is the local bulk temperature of the internal flow.

To actually employ equation (11) as a boundary condition for the outer problem, the distribution of T_{bx} must either be known or be calculable. It is a temptation to take T_{bx} from the just-completed solution for the inner problem, but doing so would tend to propagate errors inherent in the nonconverged nature of the solution. Instead, a procedure for computing T_{bx} as part of the marching procedure for the outer flow can be devised.

To develop the equation for T_{bx}, the starting point is the pipe-flow energy balance

$$\dot{m}c_{pi}dT_{bx} = -q2\pi Rdx, \qquad q = h_i(T_{bx} - T_{wx}) \tag{12}$$

Let x_j and x_{j-1} be two adjacent cross sections in the finite difference grid and $\Delta x^j = x_j - x_{j-1}$. To be consistent with the fully implicit format of the Patankar-Spalding method, equation (12) may be put into implicit finite-difference form and then solved for $T_{bx}{}^j$ at x_j

$$T_{bx}{}^j = (T_{bx}{}^{j-1} + \Omega^j T_{wx}{}^j)/(1 + \Omega^j) \tag{13}$$

$$\Omega^j = 2\pi R\Delta x^j h_i{}^j/\dot{m}c_{pi} = 2\Delta X^j Nu_i{}^j \tag{13a}$$

Then, returning to the boundary condition (11), applying it at $x = x_j$, and introducing equation (13) along with dimensionless variables, there follows

$$(-\partial\theta/\partial\eta)_0{}^j = [Nu_i{}^j(k_i/k_o)/2(1 + \Omega^j)](\theta_{bx}{}^{j-1} - \theta_{wx}{}^j) \tag{14}$$

It may be noted that because of the marching nature of the solution method, $\theta_{bx}{}^{j-1}$ would already be known when computations are being made at X_j. Therefore, equation (14) serves to interrelate $(\partial\theta/\partial\eta)_0$ and θ_{wx} at X^j. As such, it mates excellently with the implicit format of the Patankar-Spalding method.

Therefore, equation (14) is used along with equations (5–7) and (10) to solve the outer problem, with the $\mathrm{Nu}_i{}^j$ from the most recent inner solution serving as input. When the outer solution is found at any axial station X_j, $\theta_{wx}{}^j$ is also determined, and $\theta_{bx}{}^j$ is then evaluated from equation (13) (with all T's replaced by θ's). In addition, the local natural convection heat transfer coefficient $h_o{}^j$ is evaluated from the outer solution at every station X_j.

Attention may now be turned to the second part of the iteration cycle, namely, the solution for the duct flow. The energy equation (4) is to be solved subject to boundary conditions (9), with the continuity equations (8a) and (8b) replaced by

$$-k_i(\partial T/\partial r)_i = h_o(T_{wx} - T_\infty) \tag{15}$$

or, in dimensionless terms,

$$-(\partial\theta/\partial\eta)_i = (\mathrm{Nu}_o/2)(k_o/k_i)\theta_{wx}, \qquad \mathrm{Nu}_o = h_oD/k_o \tag{15a}$$

Since numerical values of $\mathrm{Nu}_o(X)$ are available from the just-completed outer solution, equation (15a) is a conventional convective boundary condition which is accommodated without modification by the Patankar-Spalding method. The pipe flow solution is thus carried out, and numerical values of $h_i(X)$ are evaluated in preparation for the next cycle of iteration.

To monitor the progress of the solutions, values of Nu_i, θ_{wx}, and θ_{bx} are printed out for the inner solution, and Nu_o and θ_{wx} are printed out for the outer solution. As noted earlier, convergence to five significant figures was attained within three to five iterations, depending on the values of the parameters. This rapid convergence is believed due primarily to the use of the boundary condition (14) along with the input values of $\mathrm{Nu}_i(X)$.

The inner solutions were carried out with 200 grid points in the region $0 \le \eta \le 1$, with the points being more closely spaced near $\eta = 1$. Two hundred grid points were also deployed across the thickness of the external boundary layer, with a higher concentration of points near the wall ($\eta = 1$). In the X-direction,[2] the grid encompassed about 2000 axial stations, with a step size ΔX which increased with X. Thus, about 400,000 grid points participated in the inner and outer solutions, respectively.

A number of accuracy checks were made to establish the validity of the present solutions and to guide the selection of the number and depolyment of the grid points. Local Nusselt numbers computed for natural convection adjacent to an isothermal vertical plate agreed with the well-known similarity solution to within 0.03 percent. For natural convection on an isothermal vertical cylinder, the present computational scheme gives local Nusselt numbers within 0.1–0.2 percent of those obtained in [6] by the so-called local nonsimilarity method, which contains some approximations. To check the pipe flow program, local Nusselt numbers were computed for the case of surface heat exchange with an external fluid having a uniform, prescribed heat transfer coefficient. These results were compared with those from the eigenvalue-eigenfunction solution of [7], the series nature of which limits the zone of high accuracy to the downstream portion of the thermal entrance region. In that zone, agreement to within 0.01 percent was observed.

Results and Discussion

The presentation of results will begin with the Nusselt number distributions for the inner and outer flows, to be followed by the distributions of the wall temperature and of the bulk temperature for the inner flow.

Nusselt Numbers. The local pipe-flow Nusselt number at any axial station was evaluated from the defining equations

$$h_i = q/(T_{bx} - T_{wx}), \qquad \mathrm{Nu}_i = h_iD/k_i \tag{16}$$

[2] For the outer solution, the calculations were initiated at $X = 10^{-8}$ using profiles from the integral momentum-energy solution.

which becomes

$$\mathrm{Nu}_i = -2(\partial\theta/\partial\eta)_i/(\theta_{bx} - \theta_{wx}) \tag{17}$$

when rephrased in terms of the variables of the analysis. The derivative $(\partial\theta/\partial\eta)_i$ and the temperatures θ_{bx} and θ_{wx} are all from the inner solution.

When equation (17) was evaluated from the solutions as a function of X for each of the cases investigated and working graphs were prepared, it was discovered that at any given X there was remarkably little variation of Nu_i from case to case. In view of this, the presentation format shown in Fig. 2 was adopted.

In this figure, Nu_i is plotted as a function of $(x/R)/\mathrm{Pe}$ $(= X)$. The solid lines respectively represent results for uniform wall temperature and uniform wall heat flux obtained using the present computer program. Results for a selection of cases for the conjugate fluid-to-fluid heat transfer problem are depicted by means of data symbols. This format was adopted because the data symbols enable the individual cases to be identified; in contrast, hopeless confusion would have resulted had curves been plotted. To illustrate the course of the data, a dashed curve corresponding to one of the cases is shown. The cases depicted in Fig. 2 encompass all of the k_o/k_i and Pr_o values that were investigated, while the Ra/Pe values correspond to the maximum and minimum among those investigated.

Examination of the figure shows that the Nu_i values for the conjugate problem are bounded between those for uniform wall temperature and uniform wall heat flux. Near the tube inlet (i.e., small X), the conjugate Nu_i values tend to be closer to those for uniform wall temperature, whereas at larger downstream distances the conjugate Nu_i are closer to the values for uniform heat flux.

These trends are related to the fact that the external heat transfer coefficient h_o is relatively large at small X and relatively small at large X, and similarly for a local Biot number Bi defined as h_oD/k_i. In [5], which dealt with fully developed heat transfer characteristics, it was shown that large Bi yield Nu_i values close to that for uniform wall temperature while small Bi yield Nu_i values close to the uniform wall heat flux value. Figure 2 indicates that these relationships also hold for flows experiencing complex thermal development.

The figure affirms the expectation that Nu_i takes on large values in the thermal entrance region and decreases with increasing downstream distance. Whereas the Nu_i for the uniform wall temperature and uniform heat flux cases ultimately level off to respective constant fully developed values, the Nu_i distributions for the conjugate problem tend to attain a shallow minimum and then rise very gradually. This characteristic is illustrated by the dashed curve in Fig. 2. Therefore, the interaction between internal and external convection appears to preclude the attainment of a conventional thermally developed regime characterized by Nu_i = constant. However, the departures from strict constancy are not large.

The main message of Fig. 2 is the relative insensitivity of Nu_i to the details of the thermal boundary conditions. This insensitivity is, in fact, the major cause of the rapid convergence of the iterative scheme employed in the present solution method.

Attention will now be turned to the Nusselt number results for the external (natural convection) flow. The numerical values of Nu_o were evaluated from

$$\mathrm{Nu}_o = h_oD/k_o = -2(\partial\theta/\partial\eta)_0/\theta_{wx} \tag{18}$$

For the presentation of results, the local Nusselt numbers for the conjugate problem will be compared with those for the standard case of natural convection about an *isothermal* vertical cylinder. Thus, for each case characterized by k_o/k_i, Pr_o, and Ra/Pe, the ratio $\mathrm{Nu}_o/(\mathrm{Nu}_o)_{uwt}$ has been evaluated as a function of $(x/R)/\mathrm{Pe}$ $(= X)$, where uwt denotes uniform wall temperature.[3] Numerical values of $(\mathrm{Nu}_o)_{uwt}$ are available in [6, 8] and [9] and are not reproduced here because of space limitations.

[3] Note that the UWT boundary condition uncouples the inner and outer problems.

The Nu_o results are presented in Figs. 3 and 4 respectively for Pr_o = 0.7 and 5, with $\mathrm{Nu}_o/(\mathrm{Nu}_o)_{uwt}$ plotted against $(x/R)/\mathrm{Pe}$. In each figure, curves are presented for values of k_o/k_i and Ra/Pe which encompass the total range investigated here.

Inspection of Figs. 3 and 4 shows that the natural convection Nusselt numbers for the conjugate problem are smaller than those for the isothermal-walled cylinder. Furthermore, the margin of difference between Nu_o and $(\mathrm{Nu}_o)_{uwt}$ increases with increasing downstream distance, so that ultimately Nu_o is only a small fraction of its isothermal wall counterpart.

The aforementioned relationship between Nu_o and $(\mathrm{Nu}_o)_{uwt}$ reflects the fact that the pipe wall temperature in the conjugate problem decreases with x, as does $(T_{wx} - T_\infty)$. The latter is proportional to the buoyancy force which drives the natural convection. Its decrease, relative to the constant value of $(T_{wx} - T_\infty) = (T_1 - T_\infty)$ in the uniform wall temperature problem, is responsible for both the fact that $\mathrm{Nu}_o < (\mathrm{Nu}_o)_{uwt}$ and that $\mathrm{Nu}_o/(\mathrm{Nu}_o)_{uwt}$ decreases with x.

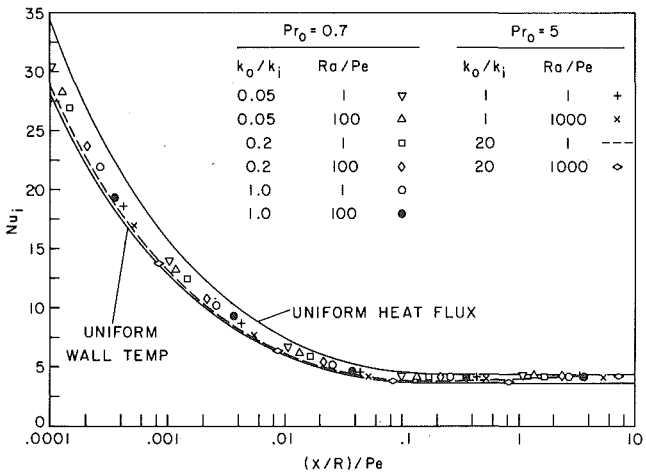

Fig. 2 Nusselt number distributions for the forced convection pipe flow

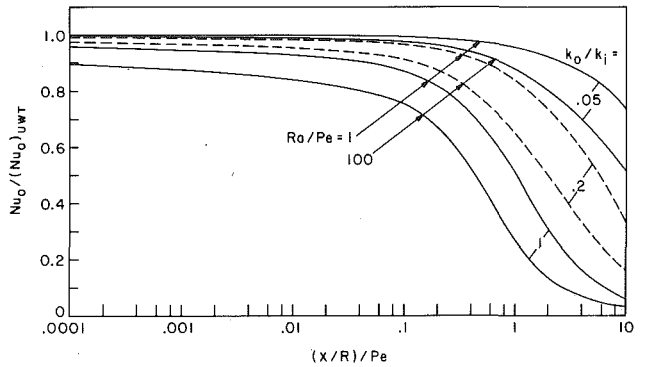

Fig. 3 Nusselt number distributions for the external natural convection flow, Pr_o = 0.7

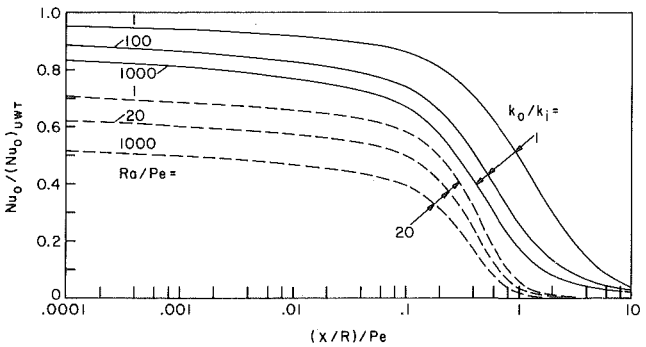

Fig. 4 Nusselt number distributions for the external natural convection flow, Pr_o = 5

In light of the foregoing, the influence of the parameter values on $Nu_o/(Nu_o)_{uwt}$ can be readily identified. In particular, those parameter values which accentuate the decrease of $(T_{wx} - T_\infty)$ with X will bring about lower values of $Nu_o/(Nu_o)_{uwt}$. As will be demonstrated shortly, increasing parametric values of both k_o/k_i and Ra/Pe give rise to more rapid decreases of $(T_{wx} - T_\infty)$. These influences are physically plausible, since increases of both parameters tend to decrease the thermal resistance of the outer flow relative to a fixed thermal resistance of the inner flow. At fixed values of k_o/k_i and Ra/Pe, variations of Pr_o in the range between 0.7 and 5 do not have a marked effect on the results, as can be witnessed by comparing the curves for $k_o/k_i = 1$ in the two figures. It is quite likely, however, that k_o/k_i will respond to changes in Pr_o.

From the foregoing presentation, it appears that while the internal Nusselt number Nu_i can be adequately represented by a simple model (i.e., uniform wall temperature or uniform heat flux), the external Nusselt number defies such a simplified representation.

Wall and Bulk Temperature Distributions. The wall temperature distributions are common to both the inner and outer solutions and, in fact, the attainment of identical distributions from the two solutions is an indication of the convergence of the iterative procedure. The wall temperature results are presented in Figs. 5, 6, and 7, where the dimensionless wall temperature $(T_{wx} - T_\infty)/(T_1 - T_\infty)$ is plotted as a function of $(x/R)/Pe$. Figures 5 and 6 respectively correspond to $Pr_o = 0.7$ and 5; in each of these figures, the curves are parameterized by k_o/k_i and Ra/Pe. The case $k_o/k_i = 1$ is somewhat special because it corresponds to the same inner and outer fluids. Results for this case have been brought together and compared in Fig. 7.

These figures verify the expected decrease of the wall temperature with increasing downstream distance along the pipe. The decrease of the wall temperature is significantly accentuated at larger values of both k_o/k_i and of Ra/Pe. In connection with the influence of k_o/k_i, it may be noted that k_o/k_i values ≤ 1 were selected for the case of $Pr_o = 0.7$ to reflect the relatively low conductivity of air. On the other hand, for $Pr_o = 5$, k_o/k_i values ≥ 1 were chosen in response to the high conductivity of water. These choices of k_o/k_i are responsible for the relatively low wall temperatures that are in evidence in Fig. 6, relative to those of Fig. 5.

As a case in point, note may be taken of the results for $k_o/k_i = 20$ in Fig. 6. This case may be regarded as corresponding to internal air flow and external water flow. For such a situation, it is readily understood that the external thermal resistance is very small compared with the internal thermal resistance, and this gives rise to a precipitous drop in wall temperature at very small x values (upstream of those exhibited in Fig. 6).

The $k_o/k_i = 1$ case is the only k_o/k_i ratio among those investigated that is common to both $Pr_o = 0.7$ and $Pr_o = 5$. In Fig. 7, the $k_o/k_i = 1$ results are brought together in order to focus attention on the effects of Pr_o, that is, to examine the sufficiency of Ra as a correlating parameter. To aid in this examination, selected points from the $Pr_o = 0.7$ curves for Ra/Pe = 1 and 100 are replotted as discrete data points amongst the $Pr_o = 5$ curves. This transference of information is illustrated in the figure for the leftmost pair of points.

A comparison of the $Pr_o = 0.7$ and 5 results (e.g., by using the aforementioned discrete data) indicates that Pr_o does not play a decisive role in the range investigated. Thus, for a fixed k_o/k_i, the Rayleigh number (which appears in the Ra/Pe grouping) appears to be an adequate correlating parameter.

Results for the axial distribution of the bulk temperature of the pipe flow will now be presented, and Figs. 8, 9, and 10 have been prepared for this purpose. The format of these figures is similar to that employed in Figs. 5, 6, and 7 for the presentation of the wall temperature results. Figures 8 and 9 respectively convey the bulk temperature distributions for $Pr_o = 0.7$ and 5, with k_o/k_i and Ra/Pe as curve parameters. The bulk temperature results for $k_o/k_i = 1$ are brought together in Fig. 10.

The bulk temperature ratio $(T_{bx} - T_\infty)/(T_1 - T_\infty)$ plotted in these figures can be related to the heat transfer effectiveness ϵ. The effectiveness compares the heat transfer rate Q_x for a length of pipe between $x = 0$ to $x = x$ to the heat transfer rate Q^* for an infinitely long pipe, with both Q_x and Q^* corresponding to the same mass flow. Since

$$Q_x = \dot{m}c_p(T_1 - T_{bx}), \qquad Q^* = \dot{m}c_p(T_1 - T_\infty) \tag{19}$$

and $\epsilon = Q_x/Q^*$, it follows that

$$(T_{bx} - T_\infty)/(T_1 - T_\infty) = 1 - \epsilon \tag{20}$$

Thus, the ordinate of Figs. 8, 9, and 10 can also be regarded as $1 - \epsilon$.

Examination of Figs. 8, 9, and 10 shows that the bulk temperature decreases with x as heat is transferred from the pipe flow to the external flow.[4] The rapidity of the decrease is governed by those factors which control the rate of heat transfer. Higher values of both k_o/k_i and Ra/Pe increase the heat transfer rate and thereby give rise to more rapid decreases in T_{bx}. The effect of these parameters can be rationalized by thinking in terms of a parameter-independent internal

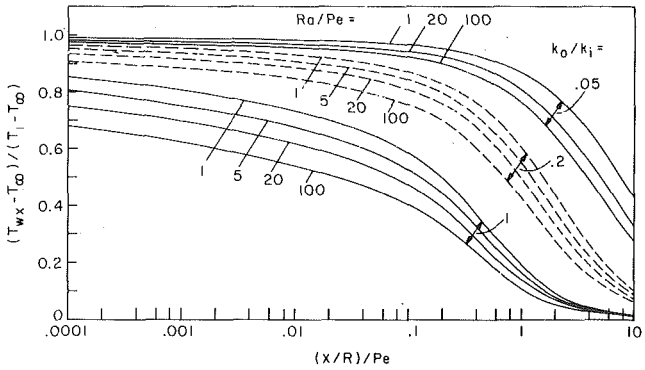

Fig. 5 Wall temperature distributions, $Pr_o = 0.7$

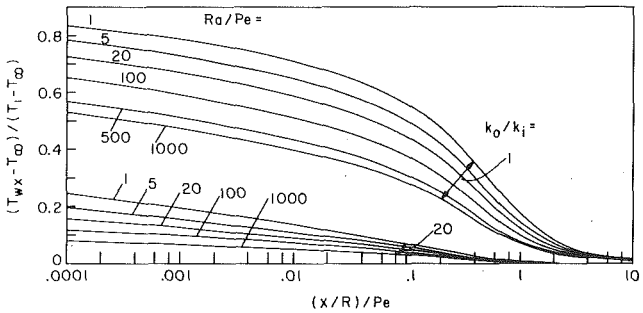

Fig. 6 Wall temperature distributions, $Pr_o = 5$

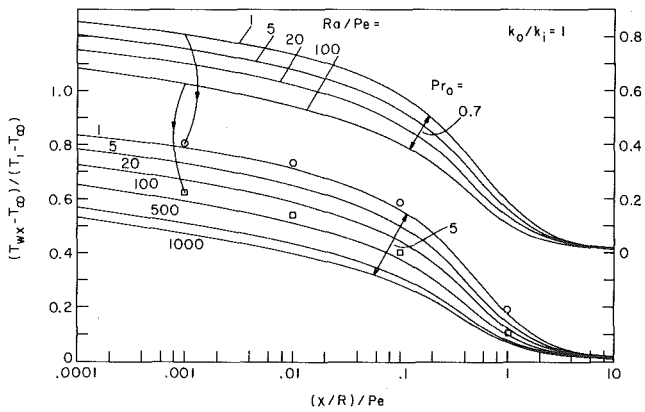

Fig. 7 Wall temperature distributions for $k_o/k_i = 1$, $Pr_o = 0.7$ and 5

[4] This assumes that $T_1 > T_\infty$.

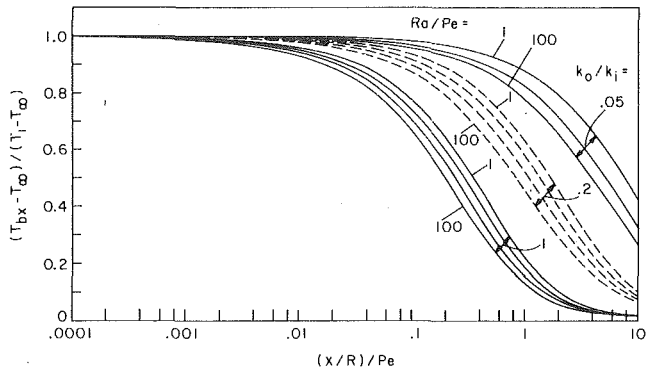

Fig. 8 Distributions of the pipe-flow bulk temperature, $Pr_o = 0.7$

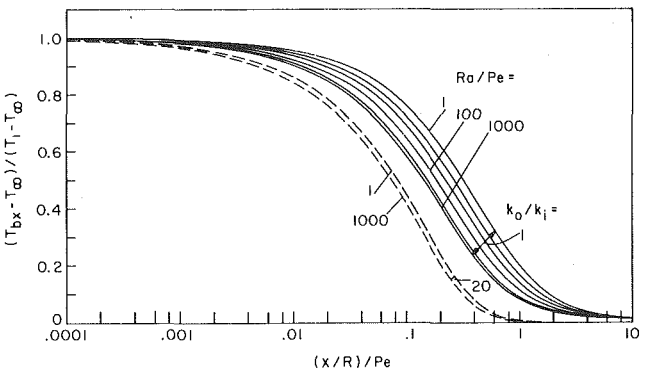

Fig. 9 Distributions of the pipe-flow bulk temperature, $Pr_o = 5$

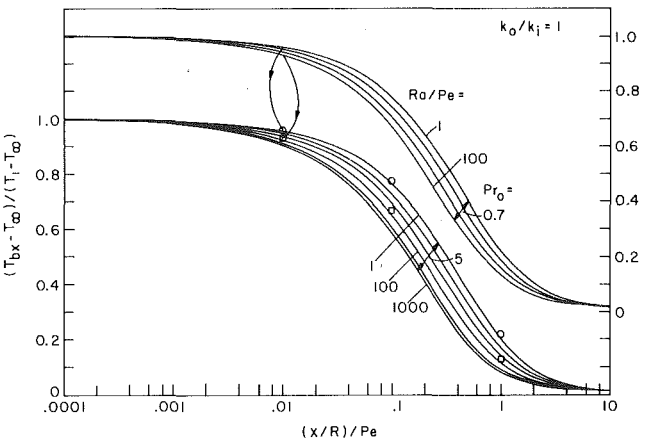

Fig. 10 Bulk temperature distributions for $k_o/k_i = 1$, $Pr_o = 0.7$ and 5

resistance (a truth verified by the results of Fig. 2) and then recognizing that increasing values of k_o/k_i and Ra/Pe cause a decrease in the external resistance. This results in a lower overall resistance and higher rates of heat transfer. The bulk temperature decreases in evidence in Fig. 9 are more rapid than those of Fig. 8 because the k_o/k_i values in the former are ≥ 1, while $k_o/k_i \leq 1$ for the latter.

A comparison of Figs. 8 and 9 with Figs. 5 and 6 shows that, as expected, $T_{wx} < T_{bx}$. It is also seen that the deviations between T_{wx} and T_{bx} at any axial station are more marked as k_o/k_i increases. This finding can be rationalized by noting that the difference between T_{wx} and T_{bx} depends on the ratio of the internal resistance to the overall resistance. As k_o/k_i increases, the internal resistance becomes a larger fraction of the overall resistance, thereby increasing $|T_{wx} - T_{bx}|$.

Figure 10 was prepared to examine the degree of sensitivity of the bulk temperature results to the Prandtl number Pr_o at a fixed k_o/k_i when Ra is used as a correlating parameter. The figure shows results for $Pr_o = 0.7$ and 5, both for $k_o/k_i = 1$. As in Fig. 7, the comparison of the results for the two Prandtl numbers is facilitated by the use of discrete data symbols for the replotting of selected $Pr_o = 0.7$ results for Ra/Pe = 1 and 100 among the results for $Pr_o = 5$.

Examination of the figure shows that the bulk temperature results for the two Prandtl numbers differ only slightly. Since the bulk temperature is a reflection of the streamwise-integrated heat transfer rate, it follows that at a fixed value of k_o/k_i, the latter is virtually independent of Pr_o in the range investigated, provided that Ra is used as the correlating parameter.

Concluding Remarks

The fluid-to-fluid conjugate convection problem considered here is believed to be the first combined duct flow—boundary layer problem to be solved from first principles; that is, without prior knowledge of the heat transfer coefficients for at least one of the flows. An iterative method was employed to deal with this complex physical situation, the special feature of which is that information transferred between the two flows is in the form of heat transfer coefficients rather than wall temperatures, heat fluxes, and bulk temperatures. The rapid convergence of the iteration scheme validates the utility of this approach.

From the solutions, it was found that at any dimensionless axial station $(x/R)/Pe$, the internal Nusselt number Nu_i is nearly independent of the specific values of the parameters. Nu_i is bounded between the values for uniform wall temperature and uniform heat flux. It was also observed that Nu_i for the conjugate problem does not attain an x-independent fully developed regime. Rather, at large downstream distances, the Nu_i curves attain a shallow minimum and then rise very gradually.

In contrast to the insensitivity of Nu_i to the parameters, the external (natural convection) Nusselt number Nu_o is highly sensitive. In general, Nu_o is smaller than the Nusselt number $(Nu_o)_{uwt}$ for natural convection on an isothermal vertical cylinder (with wall temperature = T_1). The deviations between Nu_o and $(Nu_o)_{uwt}$ become larger with increasing downstream distance and are accentuated at higher values of k_o/k_i and Ra/Pe.

Both the wall temperature and the pipe-flow bulk temperature decrease along the length of the tube, the decrease being more rapid at large k_o/k_i and Ra/Pe. The wall-to-bulk temperature difference is enlarged with increasing values of k_o/k_i. At a fixed value of Ra/Pe and for $k_o/k_i = 1$, both the wall and bulk temperature distributions are quite insensitive to the external Prandtl number Pr_o, with the bulk temperature being least sensitive. This finding indicates that the Rayleigh number is an effective correlating parameter in the Pr_o range investigated (0.7–5).

Acknowledgment

This research was performed, in part, under the auspices of the National Science Foundation (ENG-7518141 A01) and with support (to M. Faghri) from the Iranian Ministry of Education. The authors gratefully acknowledge the valuable suggestions of Professor S. V. Patankar.

References

1 Shah, R. K. and London, A. L., *Laminar Flow Forced Convection in Ducts*, Academic Press, New York, 1978.

2 Payvar, P., "Convective Heat Transfer to Laminar Flow over a Plate of Finite Thickness," *International Journal of Heat and Mass Transfer*, Vol. 20, 1977, pp. 431–433.

3 Luikov, A. V., "Conjugate Convective Heat Transfer Problems," *International Journal of Heat and Mass Transfer*, Vol. 17, 1974, pp. 257–265.

4 Patankar, S. V. and Spalding, D. B., *Heat and Mass Transfer in Boundary Layers*, Second ed., Intertext Books, London, 1970.

5 Sparrow, E. M. and Patankar, S. V., "Relationships Among Boundary Conditions and Nusselt Numbers for Thermally Developed Duct Flows," ASME JOURNAL OF HEAT TRANSFER, Vol. 99, 1978, pp. 483–485.

6 Minkowycz, W. J. and Sparrow, E. M., "Interaction Between Surface Mass Transfer and Transverse Curvature in Natural Convection Boundary Layers," *International Journal of Heat and Mass Transfer*, Vol. 22, 1979, pp. 1445–1454.

7 Hsu, C. J., "Exact Solution to Entry-Region Laminar Heat Transfer with Axial Conduction and the Boundary Condition of the Third Kind," *Chemical Engineering Science*, Vol. 23, 1968, pp. 457–468.

8 Minkowycz, W. J. and Sparrow, E. M., "Local Nonsimilar Solutions for Natural Convection on a Vertical Cylinder," ASME JOURNAL OF HEAT TRANSFER, Vol. 96, 1974, pp. 178–183.

9 Cebeci, T., "Laminar Free Convective Heat Transfer from the Outer Surface of a Vertical Slender Circular Cylinder," Paper NC1.4, *Proceedings, Fifth International Heat Transfer Conference*, Vol. III, 1974, pp. 15–19.

Heat Transfer Coefficients on the Downstream Face of an Abrupt Enlargement or Inlet Constriction in a Pipe

E. M. Sparrow
Fellow ASME

J. E. O'Brien

Department of Mechanical Engineering,
University of Minnesota,
Minneapolis, Minn. 55455

Measurements were made of the local and average heat transfer coefficients on the downstream face of an enlargement step in a pipe. Two flow configurations were investigated: (a) an abrupt enlargement from a smaller diameter pipe to a larger diameter pipe and (b) partial constriction of a pipe inlet by a large baffle plate. Air was the working fluid. The transfer coefficients were determined by means of the naphthalene sublimation technique; axial pressure distributions were also measured. The highest values of the local transfer coefficient were found to occur on the portion of the enlargement face adjacent to the aperture through which the flow enters the enlarged space. On the other hand, the lowest coefficients occur in the corner where the enlargement face meets the wall of the enlarged pipe. The radial distributions of the transfer coefficient on the enlargement face vary with the Reynolds number. With regard to average transfer coefficients, higher values (by at least 50 percent) are attained for the constricted inlet than for the abrupt enlargement. The average coefficients for the enlargement face are much higher (by a factor of two or three) than those on the wall of the enlarged pipe for fully developed flow conditions.

Introduction

Turbulent heat transfer in tubes and ducts has been a subject of intensive study for many years. Nevertheless, important problem areas exist for which basic data are either unavailable or incomplete. One such problem area is the heat transfer characteristics in a flow passage in which separation and reattachment occur. Flow separation and subsequent reattachment take place, for example, at an abrupt enlargement in the cross section of a tube or duct; such enlargements are frequently encountered in practice. These flow processes also occur when there is a partial constriction of the cross section due, for example, to the presence of a baffle or an orifice plate.

In recent years, some experimental work has been performed involving duct flows with either an abrupt enlargement [1, 2] or with a partially constricted cross section [3–6]. In the main, these studies were concerned with the effect of the separated region on the heat transfer coefficients along the duct walls downstream of the enlargement or constriction. In general, it was found that the heat transfer coefficients were substantially enhanced along the portion of the wall that is washed by the recirculating flow contained within the separation bubble, with the largest coefficients occurring at the reattachment of the flow to the wall.

The present research is concerned with a virtually unexplored problem involving separated duct flows, namely, the heat transfer on the downstream face of an abrupt enlargement or a constriction plate. Such surfaces are washed by the recirculating flow which occupies the separated region downstream of the respective change in cross section. For an abrupt enlargement in a circular tube, the downstream face of the step is washed by a flow which moves radially inward along the face. A similarly oriented flow washes the downstream face of an annular constriction plate situated in a tube. These flows are different from the predominantly axial flows which wash the tube walls.

The research encompasses two complementary sets of experiments. In the first set, a hydrodynamically developed turbulent pipe flow was passed through an abrupt enlargement, with the diameter of the downstream pipe being twice that of the upstream pipe. In the second set of experiments, flow was drawn into a pipe whose inlet cross section was partially constricted by a large circular baffle plate having a central aperture. The pipe diameter was twice that of the aperture, while the outer diameter of the baffle was ten times the aperture diameter.

The two investigated configurations give rise to markedly different flow fields at the inlet of the enlargement step. In the first case, the flow is axial, both in the turbulent core and in the boundary layer. On the other hand, in the second case, the entering flow carries both axial and radial momentum. The core flow enters more or less axially, but the inward-moving boundary layer which builds up on the baffle plate possesses a significant amount of radial momentum. The radial flow must turn as it passes into the aperture of the baffle plate.

The differences in the nature of the flow entering the enlargement step are expected to affect the heat transfer coefficients on the enlargement face. The inclusion of both configurations in the research enabled quantitative assessment of these effects.

A special feature of the research is the focus of the distribution of the local heat transfer coefficient on the enlargement face. Average transfer coefficients were determined by integration of the local data. To facilitate the acquisition of highly accurate and highly localized data, the experiments were performed with a mass transfer technique—naphthalene sublimation. The mass transfer coefficients determined from the experiments were transformed into heat transfer coefficients by applying the well-established analogy between the two transfer processes. Taking account of the boundary conditions for the mass transfer experiments, the analogous heat transfer results correspond to uniform wall temperature on the enlargement face.

For each of the two flow configurations investigated, a succession of experiments was performed in which the Reynolds number was varied parametrically. The Reynolds number used here to characterize the experiments is based on the flow cross section just upstream of the enlargement step; the value of the Reynolds number was varied from 5000 to 45,000.

Pressure distributions were measured in the first set of experiments in order to establish the existence of fully developed flow in the pipe upstream of the abrupt enlargement. Pressure measurements were also made in the pipe downstream of the enlargement to verify that there was sufficient length for reattachment and redevelopment to take place.

In the presentation of results, radial distributions of the local mass

Contributed by the Heat Transfer Division for publication in the JOURNAL OF HEAT TRANSFER. Manuscript received by the Heat Transfer Division January 17, 1980.

(heat) transfer coefficient on the enlargement face are plotted for both flow configurations with the Reynolds number as parameter. The average coefficients for the two configurations are also compared, and further comparisons are made with the coefficients for related turbulent pipe flows.

As a final comparison, the average transfer coefficients from the constricted-inlet experiments of the present study are brought together with those of [6]. In [6], experiments were performed to determine the average coefficients on the faces of a wall-attached transverse plate which partially blocks the cross section of a square duct. Although the flow configuration of [6] is markedly different from that of the present, the data are used for comparison because [6] is the only prior study of enlargement-face transfer coefficients known to the authors.

The Experiments

The two separation-inducing flow configurations to be investigated here are pictured schematically in Figs. 1 and 2. As seen in Fig. 1, a long hydrodynamic starting length delivers a fully developed turbulent pipe flow to a cross section where an abrupt enlargement takes place. In the second flow configuration, Fig. 2, the hydrodynamic development pipe is replaced by a thin, circular baffle plate having a central aperture. The diameter of the aperture is equal to that of the inside diameter of the replaced hydrodynamic development pipe, thereby constricting the inlet of the downstream pipe. Thus, the enlargement of the cross section downstream of the inlet constriction is identical to the pipe-to-pipe cross sectional enlargement of the first configuration.

Experimental Apparatus. The experimental apparatus will now be described more fully, with attention first focused on the configuration of Fig. 1 and then on the configuration of Fig. 2. For both cases, the experiments were performed in the suction mode. Air from the temperature-controlled laboratory room was drawn through the test section and then exited into a large plenum chamber. From the plenum, the air passed through a flow metering station (either of two calibrated rotameters, depending on the flow rate), a control valve, and a blower. The blower was situated outside the laboratory room, and its discharge was ducted to an exhaust at the roof of the building.

The use of the suction mode avoided preheating of the air by the blower, while the outside discharge enabled the laboratory to be maintained free of naphthalene vapor. These features contributed significantly to the accuracy of the data.

For the flow configuration of Fig. 1, both the hydrodynamic development pipe and the enlargement pipe were internally polished to a high degree of smoothness with a specially designed hone, and the polishing was repeated after the installation of the pressure taps. The respective finished inside diameters of the pipes were 5.08 and 10.16 cm, with corresponding lengths of 48 and 15 diameters. The two pipes were interconnected with the aid of flanges, as shown in Fig. 1. To avoid thermal distortions which might have resulted from welding, the flanges were affixed to the respective pipes with a high-strength epoxy. The flanges were sealed with O-rings and positively positioned by pins.

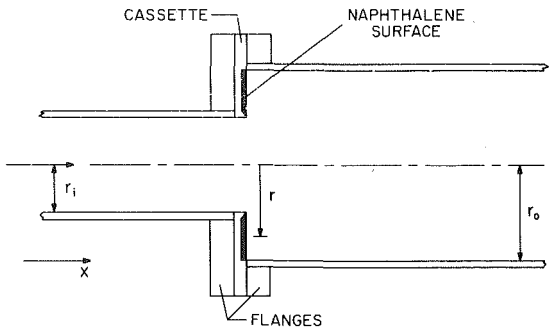

Fig. 1 Abrupt enlargement from a smaller pipe diameter to a larger pipe diameter

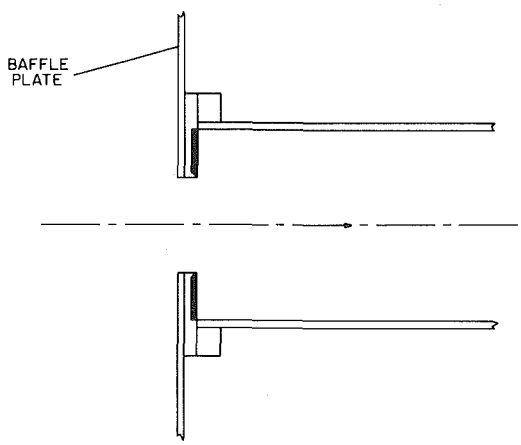

Fig. 2 Partial constriction of a pipe inlet by a large baffle plate

For the experiments, an aluminum disk was sandwiched between the flanges in the manner illustrated in Fig. 1. The aluminum disk was made from 0.635-cm thick tooling plate. A central aperture, 5.08-cm in diameter, was machined into the disk, with special care being taken to achieve a precise fit with the inside diameter of the hydrodynamic development tube. In addition, a 2.54-cm wide annular recess, 0.3175-cm deep, was cut into one face of the disk in order to accommodate the naphthalene test surface. The naphthalene was introduced into the recess by a casting process, to be described shortly, in which the aluminum disk was actually a part of the mold. Since it served as a housing for the naphthalene, the disk will hereafter be referred to as the cassette.

Pressure taps were positioned along the hydrodynamic development pipe and the enlargement pipe, with ten taps in the former and thirteen in the latter. The axial positions of the taps will be evident from pressure distribution data to be presented later. The pressure signals from the respective taps were conveyed via plastic tubing to a pressure selector switch, the output of which was sensed by a Baratron capacitance-type pressure meter with a smallest scale division of 10^{-4} mm Hg.

Nomenclature

A = surface area of enlargement face
D_i = inner diameter of enlargement step
D_o = outer diameter of enlargement step
$\mathcal{D}$ = naphthalene-air diffusion coefficient
h = local heat transfer coefficient
$\overline{h}$ = average heat transfer coefficient
K = local mass transfer coefficient, $\dot{m}/(\rho_{nw} - \rho_{nb})$
$\overline{K}$ = average mass transfer coefficient, $(\dot{M}/A)/(\rho_{nw} - \rho_{nb})$
k = thermal conductivity
$\dot{M}$ = rate of mass transfer on enlargement face
$\dot{m}$ = local mass transfer rate per unit area
$\overline{\mathrm{Nu}}$ = average Nusselt number, $\overline{h}(D_o - D_i)/k$
p = static pressure at x
p_{atm} = atmospheric pressure
r = radial position on enlargement face
r_i = inner radius of enlargement step
r_o = outer radius of enlargement step
Re = Reynolds number based on D_i, $4\dot{w}/\mu\pi D_i$
Re′ = Reynolds number based on D_o, $4\dot{w}/\mu\pi D_o$
$\overline{\mathrm{Sh}}$ = average Sherwood number, $\overline{K}(D_o - D_i)/\mathcal{D}$
Sc = Schmidt number
x = axial coordinate
$\dot{w}$ = mass flow rate of air
μ = viscosity
ν = kinematic viscosity
ρ_{nb} = density of naphthalene vapor in the bulk flow
ρ_{nw} = density of naphthalene vapor at the wall

Attention may now be turned to the flow configuration of Fig. 2. For these experiments, the 10.16-cm diameter pipe and the cassette were retained as before, but the hydrodynamic development pipe was replaced by a 0.3175-cm thick aluminum circular baffle with an outer diameter of 50.8 cm. A 5.08-cm dia aperture was machined into the center of the baffle so as to match with the aperture in the cassette. The ratio of ten in the diameters of the baffle and the aperture was selected so that the aperture would be small compared with the size of the baffle. Aside from the aforementioned changes, the flow circuit for the second configuration is the same as that for the first configuration.

Naphthalene Test Surface. The naphthalene test surfaces were made in a casting process involving a two-piece mold. One of the mold parts was the cassette that has already been discussed in connection with Figs. 1 and 2. The other part of the mold is a flat, highly polished stainless steel plate.

As a prelude to the casting process, the naphthalene occupying the cassette (from a prior data run) was removed by melting, leaving a vacant annular cavity. Then, the cassette was placed on the stainless steel plate with the cavity facing downward. Molten naphthalene was poured into the cavity through an opening in the back face of the cassette. Once the naphthalene had solidified, the mold parts were separated by a deft hammer blow, with the naphthalene remaining in the cassette. The exposed face of the naphthalene was an annulus, with inner and outer diameters equal to 5.08 and 10.16 cm, respectively. The naphthalene surface possessed a remarkable degree of smoothness, corresponding to the surface finish of the stainless steel plate.

When the casting process was completed, the access holes in the back face of the cassette were taped and the exposed surface of the naphthalene placed against a glass plate—both steps being taken to avoid extraneous sublimation. The cassette was then left overnight in the temperature-controlled laboratory in order to attain thermal equilibrium.

A new casting was made for each data run, using fresh (unused) reagent grade naphthalene (Eastman 168).

Mass Transfer Instrumentation. Measurements of the surface contour of the naphthalene face, made both before and after a data run, enabled the determination of local mass transfer rates and mass transfer coefficients. These contour measurements were performed with the cassette situated on a movable coordinate table which provided two directions of accurately controlled horizontal travel. The table was equipped with a guide and pins to facilitate horizontal positioning of the cassette. In addition, clamps affixed to the table were employed to provide a downward force on the cassette, thereby aiding in the attainment of a consistent vertical positioning of the naphthalene test surface.

The surface contours were measured with instrumentation which converts the movement of a sensor tip (similar to the tip of a dial gage) into an electrical signal that can be read and recorded by a digital voltmeter [8]. Taken together, the sensor and the voltmeter are able to resolve elevation differences as small as 7.6×10^{-5} cm.

For each data run, local elevation measurements were made at 100 points on the naphthalene test surface, both before and after the period of exposure to the air flow. The contours were measured at 25 stations along four radial lines displaced by 90 deg from each other.

Additional before and after elevation measurements were made at a number of reference points on the surface of the cassette adjacent to the naphthalene. The purpose of these measurements was to establish a means for correcting for slight imperfections of vertical positioning inherent in removing and subsequently replacing the test plate on the coordinate table. Since the cassette does not participate in the mass transfer process, any before/after changes in its elevation are due solely to vertical positioning imperfections. Typical repositioning corrections were 1.3×10^{-4} cm.

Besides the contour measurements which provide the local mass transfer results, the overall mass transfer was measured for each run by before and after weighings with a Mettler analytical balance having a smallest scale division of 0.1 mg. The total mass transfer for a typical data run was 200 mg.

Experimental Procedure. Various aspects of the experimental procedure have already been described in the preceding sections, and further information will now be conveyed.

For each data run, the first step was the preparation of the naphthalene casting on the day prior to the run. To prepare for the run itself, the blower was activated and allowed to operate until a steady state was attained with the control valve set at the desired flow rate. At the initiation of the surface contour measurements, the blower was turned off to insure quiescent conditions in the laboratory. During the contour measurements, which required about 25 min to complete, records of duration time and temperature were kept to facilitate corrections that will soon be described. Then, the cassette was installed in the apparatus, the installation being accomplished in about $2\frac{1}{2}$ min (time was of the essence to minimize extraneous losses).

The airflow was then initiated and maintained at a steady value for a period ranging from 2 to $4\frac{1}{2}$ hr, depending on the Reynolds number. The run times were chosen so that the mean change in the surface elevation was about 0.003 cm. During the run, records were kept of the air temperature, read with a precision-grade thermometer to 0.05°F. To terminate the run, the blower was shut off and the final contour measurements carried out.

Certain auxiliary experiments were also performed to determine corrections for extraneous losses. One of these experiments was concerned with extraneous sublimation which occurred when the cassette was positioned on the coordinate table. Surface contours were measured at a succession of times and a loss coefficient was devised which involved the duration of the contour measuring period and the temperature in the neighborhood of the coordinate table. In a second auxiliary experiment, the mass loss during the installation of the cassette in the apparatus and its subsequent removal was determined by direct weighing.

The pressure distribution measurements were performed in separate experiments that preceded the mass transfer studies.

Data Reduction. Local mass transfer coefficients were deduced by differencing the before and after contour measurements and applying three corrections which have already been mentioned in the paper. These corrections are:

(a) vertical positioning correction to account for elevation changes inherent in removal and subsequent replacement of the cassette on the coordinate table,

(b) correction for sublimation during the period when contour measurements were being made,

(c) correction for sublimation during installation and removal of the cassette from the experimental apparatus.

Typical correction values were 1.3×10^{-4}, 0.1×10^{-4}, and 0.5×10^{-4} cm, respectively, for a, b, and (c). As noted earlier, the average change in surface elevation during a data run was 2.5×10^{-3} cm.

If the change in local surface elevation at a radial station r, after correction, is denoted by $\Delta(r)$, then the local rate of mass transfer $\dot{m}(r)$ per unit area is given by

$$\dot{m}(r) = \rho_s \Delta(r)/\tau \tag{1}$$

in which ρ_s is the density of solid naphthalene ($\rho_s = 1.145$ g/cm^3) and τ is the duration of the data run. A local mass transfer coefficient K may then be evaluated from

$$K = \dot{m}/(\rho_{nw} - \rho_{nb}) \tag{2}$$

where ρ_{nw} and ρ_{nb}, respectively, denote the densities of the naphthalene vapor at the face of the enlargement step (i.e., adjacent to the surface of the solid naphthalene) and in the bulk flow. The former was evaluated from the Sogin vapor pressure–temperature relation [7] in conjunction with the perfect gas law, whereas the latter was zero in these experiments because the flow was drawn from a space which is free of naphthalene vapor.

An average mass transfer coefficient $\overline{K}$ was determined from its definition

$$\overline{K} = (\dot{M}/A)/(\rho_{nw} - \rho_{nb}) \tag{3}$$

in which $\dot{M}$ is the rate of mass transfer from the entire face of the enlargement step and A is the surface area of the face. The quantity $\dot{M}$ is found by a two-step procedure. First, at a given radial station r, the four local values of $\dot{m}(r)$ corresponding to the traverses along the four radial lines were averaged to give $\{\dot{m}(r)\}_{av}$. Then, with these

$$\dot{M}/A = \int_{r_i}^{r_o} \{\dot{m}(r)\}_{av} 2rdr/(r_o^2 - r_i^2) \tag{4}$$

where r_i and r_o denote the inner and outer radii of the enlargement step, respectively. The indicated integration was carried out using the trapezoidal rule.

The dimensionless counterpart of the average mass transfer coefficient is the average Sherwood number $\overline{\text{Sh}}$. For these experiments, $\overline{\text{Sh}}$ was defined as

$$\overline{\text{Sh}} = \overline{K}(D_o - D_i)/\mathcal{D} \tag{5}$$

with the diameter difference $(D_o - D_i)$ serving as the characteristic dimension. The quantity $\mathcal{D}$ is the naphthalene-air diffusion coefficient, the value of which was obtained from the Schmidt number Sc via the relation, $\mathcal{D} = \nu/\text{Sc}$, with ν denoting the kinematic viscosity of pure air and Sc = 2.5 [7].

The experiments were parameterized by the Reynolds number Re of the flow entering the enlargement step. If $\dot{w}$ denotes the mass rate of airflow, then

$$\text{Re} = 4\dot{w}/\mu\pi D_i \tag{6}$$

Results and Discussion

The presentation of results will first focus on the distributions of local transfer coefficients on the enlargement face, after which the average transfer coefficients will be presented. The axial pressure distributions will be illustrated in the final part of the Results section.

In view of the analogy between heat and mass transfer, the results to be presented here can be regarded as corresponding to heat transfer as well as to mass transfer. In recognition of this, the ordinates of the forthcoming figures will be labeled in terms of both the mass transfer coefficient K and the heat transfer coefficient h. Furthermore, in the discussion, the phrases heat transfer and mass transfer will be employed interchangeably.

Local Transfer Coefficients. For the case of the abrupt enlargement, data runs were made for Reynolds numbers of 5, 10, 15, 20, 25, 35, and 45 thousand. A selection of these will be used here in order to illustrate the key trends (data not reported here are available in [8]).

Radial distributions of the mass (heat) transfer coefficient along the enlargement face are presented in Figs. 3–6 for Reynolds numbers of 5, 10, 15, 25, and 45 thousand. In each figure, the local coefficient is plotted relative to the average coefficient for the Reynolds number in question, with an abscissa variable $(r - r_i)/(r_o - r_i)$ which runs from zero to one as the radial coordinate r runs from the inner radius r_i to the outer radius r_o. Thus, the data of Figs. 3–6 provide information about shapes of the distributions, but no inferences should be drawn about absolute magnitudes. Information about magnitudes will be made available shortly in terms of the (dimensionless) average transfer coefficients. Curves have been passed through the data points to provide continuity.

Examination of Figs. 3–6 shows that the distribution of the local coefficient is markedly affected by the Reynolds number. At the lowest Reynolds number investigated, Re = 5000 (Fig. 3), there is a very large variation of the transfer coefficient across the enlargement face, with $K/\overline{K}$ (or $h/\overline{h}$) decreasing from about 2.5 to 0.3. The highest coefficients occur on the portion of the enlargement face adjacent to the opening through which the flow enters the enlarged cross section; the lowest coefficients are in the corner where the enlargement face meets the wall of the enlarged pipe. The very high value attained by

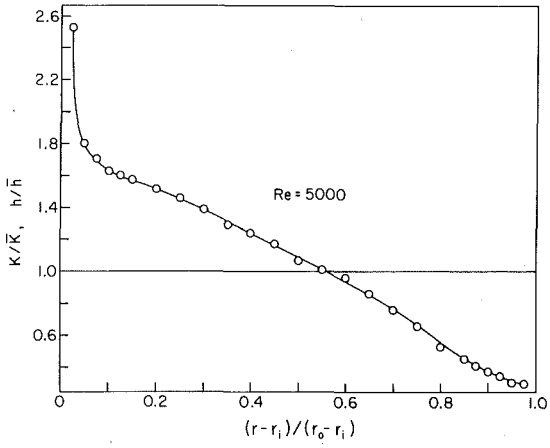

Fig. 3 Radial distribution of the mass (heat) transfer coefficient on the downstream face of an abrupt enlargement, Re = 5000

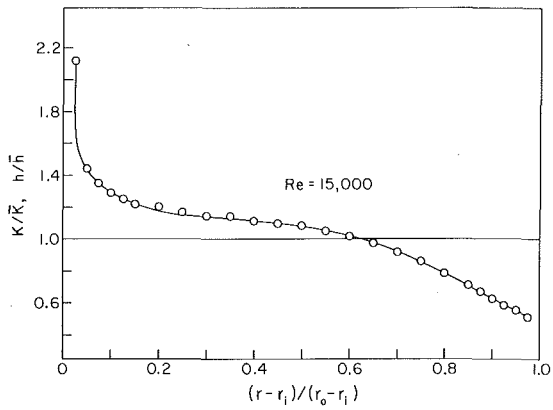

Fig. 5 Radial distribution of the mass (heat) transfer coefficient on the downstream face of an abrupt enlargement, Re = 15,000

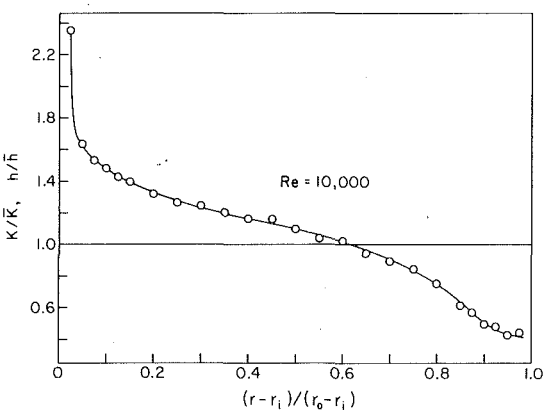

Fig. 4 Radial distribution of the mass (heat) transfer coefficient on the downstream face of an abrupt enlargement, Re = 10,000

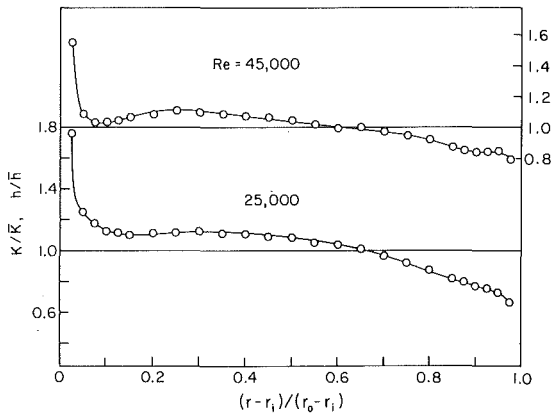

Fig. 6 Radial distributions of the mass (heat) transfer coefficient on the downstream face of an abrupt enlargement, Re = 25,000 and 45,000

the coefficient immediately adjacent to the opening is especially noteworthy. Aside from this point, the decrease of K (or h) with r is more or less linear at this Reynolds number.

The general character of the distribution shown in Fig. 3 is not unexpected. The jet-like flow which enters the enlarged cross section impresses a highly chaotic mixing region on the adjacent portion of the enlargement face, giving rise to relatively high transfer coefficients. On the other hand, the constraints imposed by the meeting of the enlargement face and the wall of the enlarged pipe dampens both the velocity and the turbulence, with resulting low values of the transfer coefficient. As the recirculating flow moves radially inward along the enlargement face, its velocity increases and the transfer coefficients increase correspondingly.

As the Reynolds number increases, an orderly progression of change occurs in the nature of the distribution curves. First of all, the overall extent of the variation across the face decreases markedly. Thus, for example, whereas $K/\overline{K}$ (or $h/\bar{h}$) ranged from 2.5 to 0.3 for Re = 5000, the range is 1.55 to 0.8 for Re = 45,000. Also, there is a tendency toward the attainment of uniformity in K (or h) over most of the face, with a shallow minimum and an adjacent shallow maximum developing on the inner half of the face. In particular, aside from the point immediately adjacent to the inlet aperture, K is constant to within ± 15 percent at the highest Reynolds number.

Another interesting characteristic, not evident from the figures included here, is the attainment, with increasing Reynolds number, of a distribution that is independent of the Reynolds number. A comparison of the distributions for Re = 35,000 and 45,000 (Figs. 4.5(f) and 4.5(g) of [8]) shows a high degree of similarity, with the major deviation being encountered at the point nearest the aperture, where the $K/\overline{K}$ values are 1.65 and 1.55.

The Reynolds-number-related changes described in the preceding paragraphs are indicative of a change in the structure of the recirculation zone. It would appear that with increasing Reynolds number, the entire enlargement face is washed by a more and more well-mixed flow which tends to wipe out significant radial variations of K. The sharp maximum at the innermost point remains, as it must because of the extreme mixing associated with the entry of the jet into the enlargement zone. There is also a tendency for the coefficients to fall off at radial stations near the corner, which is expected because of the constraints imposed by the meeting of the walls.

Attention is now turned to the local coefficients on the enlargement face downstream of a partially constricted inlet. Data runs were made for Reynolds numbers of 5, 10, 20 and 45 thousand. In general, departures from circumferential uniformity were found to be greater in this case than in the prior case where the enlargement step was fed by a long upstream hydrodynamic development section. This finding, while disconcerting, can be rationalized.

For the prior case, the presence of a long length of circular pipe upstream of the enlargement step tends to produce an axisymmetric flow at the inlet to the step. In the present case, where the inlet to the step is open to the laboratory room, the symmetry of the inlet flow is not as well controlled. For instance, air currents in a highly ventilated room might affect axi-symmetry, especially at the lower Reynolds numbers. Also, a slight misalignment of the large baffle plate situated at the inlet could also cause departures from symmetry, with a greater effect expected at low Reynolds numbers because of the thicker boundary layer buildup on the baffle plate.

The experimental data displayed satisfactory symmetry for the higher Reynolds numbers (20,000 and 45,000) but not for the lower Reynolds numbers (5000 and 10,000), and realignment of the baffle plate did not lead to the desired symmetries. In view of this, distribution curves will be presented here only for Re = 20,000 and 45,000, while the results for the other Reynolds numbers will be discussed qualitatively.

Local transfer coefficient distributions for Re = 20,000 and 45,000 are presented in Figs. 7 and 8. Each figure contains two sets of data. The black symbols denote the data for the partially constricted inlet while the open symbols are for the abrupt enlargement (i.e., the case discussed earlier in this section). The respective data sets are normalized by their own values of $\overline{K}$ (or $\bar{h}$). In general structure, Figs. 7 and 8 are similar to Figs. 3–6.

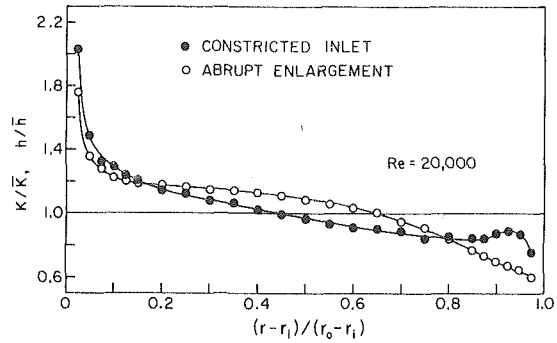

Fig. 7 Radial distributions of the mass (heat) transfer coefficient on the downstream face of a constricted inlet or an abrupt enlargement, Re = 20,000

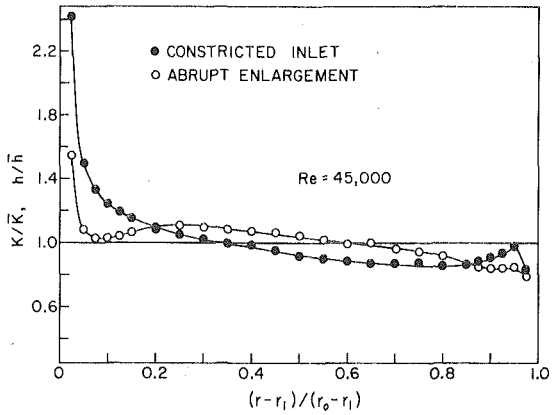

Fig. 8 Radial distributions of the mass (heat) transfer coefficient on the downstream face of a constricted inlet or an abrupt enlargement, Re = 45,000

Figures 7 and 8 enable comparisons to be made of the shapes of the distribution curves for the two types of inlet conditions (magnitude comparisons will be deferred until the $\overline{K}$ results are presented). Consider first the highest Reynolds number, Re = 45,000. Figure 8 shows that in the case of the constricted inlet, the transfer coefficient distribution is much more peaked toward the inner radius of the enlargement face than is that for the abrupt enlargement. However, as the Reynolds number decreases to 20,000 (Fig. 7), the sharp peaking of the constriction case diminishes, so that there is a lesser deviation between the distribution curves for the two cases at the smaller radii. In addition, the coefficients for the constricted inlet case do not drop off at larger $(r - r_i)/(r_o - r_i)$ as do those for the abrupt enlargement. At both Reynolds numbers for the constricted inlet, there is a local maximum near the outer radius of the enlargement face which suggests the presence of a secondary eddy.

As the Reynolds number decreases still further, the trends identified in the preceding paragraph are perpetuated. In this range, the $K/\overline{K}$ distribution curve for the constricted inlet is generally flatter than that for the abrupt enlargement, being less sharply peaked at smaller radii and tending to drop off less at larger radii.

The precise cause and effect relationships which give rise to the measured differences in the distribution curves for the two cases are difficult to identify with the information at hand. A number of contributing factors may, however, be pointed out. In the case of the abrupt enlargement, the flow which enters the enlargement step carries only axial momentum, both in the viscous layer and in the core. Upon entering the step, the flow becomes a jet which tends to spread radially outward to fill the enlarged space. The spreading of the jet and its interaction with the recirculation zone are materially affected by the thickness of the viscous layer of the entering flow, which depends on the Reynolds number.

In contrast, for the constricted inlet case, the entering flow carries both axial and radial momentum. The core flow enters more or less

axially, but the inward-moving boundary layer which builds up on the baffle plate carries a significant amount of radial momentum. Thus, the flow enters the enlargement step with a radially inward-directed velocity superposed on the main axial motion. Since the flow must ultimately attain an outward-directed velocity in order to fill the enlargement space, a significant turning must occur. This turning is expected to have a marked influence on the structure of the jet which enters the enlargement space. The extent of the turning depends on the radial momentum carried by the entering flow which, in turn, depends on the boundary layer buildup on the baffle plate—which is governed by the Reynolds number.

From the foregoing discussion, it is evident that whereas Reynolds number variations are expected to affect both of the flows under investigation, the nature of the effects may differ because of the different structures of the entering jets.

Average Transfer Coefficients. The average transfer coefficients for the enlargement face as a whole will be reported in dimensionless form in terms of the average Sherwood number $\overline{Sh}$ or its heat transfer counterpart $\overline{Nu}$ (note that $\overline{Sh} = \overline{Nu}$ when Sc = Pr). In both of these dimensionless groups, the diameter difference $(D_o - D_i)$ is used as the characteristic dimension.

Figure 9 shows the dependence of $\overline{Sh}$ (or $\overline{Nu}$) on the Reynolds number for both of the flow configurations investigated. As expected, the transfer coefficients increase with the Reynolds number. For each configuration, the increase appears to be well represented by a power law given by

$$\overline{Sh} = 0.145Re^{0.65}, \quad \overline{Sh} = 0.0475Re^{0.72} \tag{7}$$

respectively, for the constricted inlet and the abrupt enlargement. The Reynolds number exponents of equation (7) are quite close to the 2/3 power found by Sogin [10] for heat transfer from the rear face of a plate positioned in crossflow in a wind tunnel.

The fact that the Reynolds number dependences for the two cases are somewhat different is not surprising in view of the foregoing discussion. The higher coefficients for the constricted inlet are probably due to more vigorous mixing associated with the aforementioned turning of the flow.

It is relevant to provide perspectives about the magnitude of the average transfer coefficients and, for this purpose, comparisons may be made with results for a physical situation which has some relationship to that investigated here. The case chosen for comparison is that of fully developed heat (mass) transfer on the wall of the enlarged pipe. The fully developed values of K or h (denoted by K_{fd} and h_{fd}) were evaluated from the Petukov-Popov correlation ([9], pp. 351–352). With these, the ratio $\overline{K}/K_{fd}$ $(\overline{h}/h_{fd})$ was formed and the results listed in Table 1.

From the table, it is seen that the average transfer coefficient for the enlargement face is substantially larger than that for the related fully developed pipe flow. For the case of the constricted inlet, the $\overline{K}$ values exceed K_{fd} by at least a factor of three, while the $\overline{K}$ for the abrupt enlargement are about twice as large as K_{fd}. These results demonstrate that the region of recirculating flow is by no means a "dead water" region. One of the reasons for the primacy of $\overline{K}$ relative to K_{fd} is the fact that over most of the interface between the recirculation zone and the main flow, the mainflow velocities are higher than those in the fully developed region of the enlarged pipe.

As a final comparison, the average coefficients determined here will be brought together with those of [6]. The flow configuration of [6], illustrated schematically at the upper left of Fig. 10, is a square duct which is partially blocked by a wall-attached baffle plate. Average transfer coefficients on the upstream and downstream faces of the plate were determined by means of the naphthalene sublimation technique (only the downstream-face coefficients are of interest here). The flow configuration of [6] is quite different from that investigated here, so that there is no reason to expect very close agreement of the results. Notwithstanding this, it was deemed appropriate to make comparisons because the results of [6] are the only downstream-face coefficients available in the literature.

In Fig. 10, the average coefficients for the present constricted inlet case are compared with the downstream-face coefficients of [6]. On the ordinate, the coefficients are presented in dimensional form because it was not possible to identify a characteristic dimension suitable to both configurations which could be used in defining a Sherwood number. The results are plotted as a function of the Reynolds number Re′ which corresponds to conditions in the duct downstream of the enlargement. The data of [6] used in the comparison are for an area ratio (blocked area to total cross-sectional area) approximately equal to that of the present data.

The most striking feature of the comparison, as witnessed by the least-squares lines passed through the data, is the identical Reynolds number dependence of the two sets of results. The $\overline{K}$ results for the configuration of [6] are about 50 percent higher than those of the present case. This level of agreement is believed to be very good in view of the striking differences in the flow configurations.

Pressure Distributions. Measurements of the axial pressure distribution were made for the abrupt enlargement case to verify the existence of fully developed flow at the inlet to the enlargement step. The measurements were also intended to verify that there was ample length of pipe downstream of the enlargement for both flow reattachment and redevelopment to occur.

Figure 11 shows a representative axial pressure distribution which corresponds to Re = 25,000. The ordinate is the local pressure at an axial station x relative to the atmospheric pressure in the laboratory from which the air was drawn. The origin of the axial coordinate is a

Table 1 Comparison of enlargement face and fully developed transfer coefficients, $\overline{K}/K_{fd}$ or $\overline{h}/h_{fd}$

	Re × 10^{-3}						
	5	10	15	20	25	35	45
Enlargement	2.18	2.11	2.22	2.18	2.11	2.00	1.96
Constriction	3.72	3.39		3.16			2.93

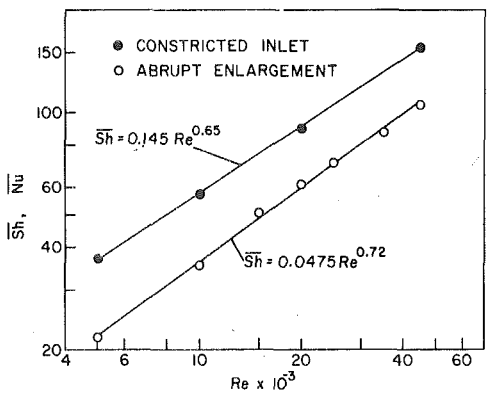

Fig. 9 Average Sherwood (Nusselt) numbers for the downstream face of an abrupt enlargement or a constricted inlet

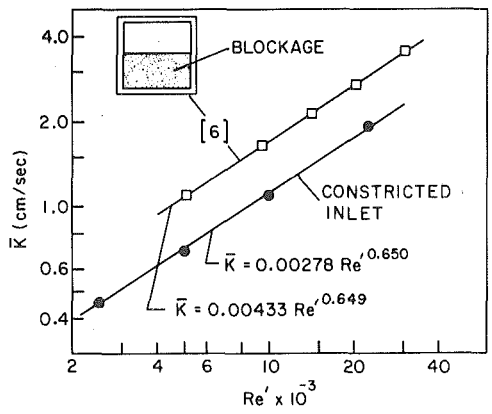

Fig. 10 Comparison of average coefficients for the constricted inlet with those for the downstream face of a plate which partially blocks a square duct

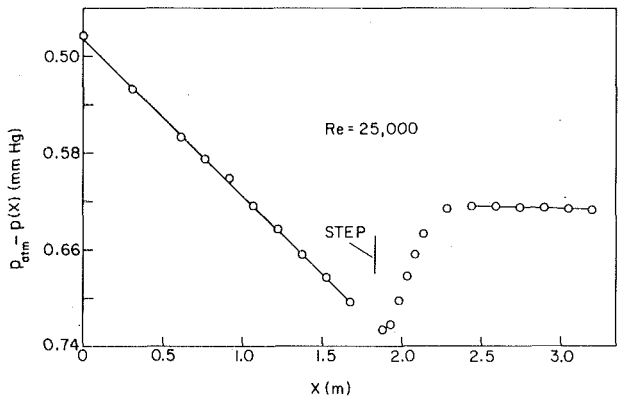

Fig. 11 Illustrative axial pressure distribution for an abrupt enlargement from a smaller diameter pipe to a larger diameter pipe

station situated 61 cm (2 ft) from the inlet of the hydrodynamic development section.

The figure indicates a linear pressure distribution at all measurement stations in the hydrodynamic development section, thereby signalling the attainment of a developed flow. Friction factors deduced from least-square fits of the pressure data agreed to within a few percent with those from the Prandtl-Karman correlation for all of the Reynolds numbers investigated. Downstream of the enlargement step, there is a pressure recovery followed by the re-establishment of a linear pressure distribution. The pressure gradient in the enlarged pipe is very small relative to that in the hydrodynamic development pipe owing to the relatively lower velocities that prevail.

The pressure distribution of Fig. 11 is typical of all the others that were measured [8].

Concluding Remarks

Measurements of the heat (mass) transfer coefficients on the face of an enlargement step in a circular pipe revealed the important roles of the Reynolds number and of the flow configuration. In general, the highest transfer coefficients occur adjacent to the opening through which the flow enters the enlarged cross section. The lowest coefficients are in the corner where the enlargement face meets the wall of the enlarged pipe.

For the case of an abrupt enlargement from a smaller pipe diameter to a larger pipe diameter, the variation of the heat transfer coefficient across the enlargement face decreases with the Reynolds number. Thus, while $h/\overline{h}$ varies from 2.5 to 0.3 for Re = 5000, the variation for Re = 45,000 is from 1.55 to 0.8. Furthermore, at the higher Reynolds numbers, $h/\overline{h}$ is very nearly constant across the enlargement face except very near the flow inlet aperture. At these Reynolds numbers, there is a tendency for the $h/\overline{h}$ distribution to become independent of the Reynolds number.

When the inlet to the enlargement step is partially blocked by a large baffle plate, axi-symmetry was not attained to the same degree as for the aforementioned abrupt enlargement configuration. At lower Reynolds numbers, the overall variation of $h/\overline{h}$ for the constricted inlet case is smaller than that for the abrupt enlargement case. For larger Reynolds numbers, the overall variations for the two cases become comparable, except that there is a higher peak adjacent to the inlet aperture for the constricted inlet case.

With regard to the average transfer coefficients, higher values (by at least fifty percent) are attained for the constricted inlet than for the abrupt enlargement. These coefficients are substantially greater (by a factor of two or three) than those for fully developed flow in the enlarged pipe. A comparison of the present results with average coefficients for the downstream face of a plate which partially blocks a square duct indicated an identical Reynolds number dependence.

Acknowledgment

This research was performed under the auspices of the National Science Foundation.

References

1 Filetti, E. G., and Kays, W. M., "Heat Transfer in Separated, Reattached, and Redevelopment Regions Behind a Double Step at Entrance to a Flat Duct," ASME JOURNAL OF HEAT TRANSFER, Vol. 89, 1967, pp. 163–168.

2 Zemanick, P. P., and Dougall, R. S., "Local Heat Transfer Downstream of an Abrupt Circular Channel Expansion," ASME JOURNAL OF HEAT TRANSFER, Vol. 92, 1970, pp. 43–60.

3. Krall, K. M., and Sparrow, E. M., "Turbulent Heat Transfer in the Separated, Reattached, and Redevelopment Regions of a Circular Tube," ASME JOURNAL OF HEAT TRANSFER, Vol. 88, 1966, pp. 131–136.

4 Seki, N., Fukusako, S., and Hirata, T., "Effect of Stall Length on Heat Transfer in Reattached Region Behind a Double Step at Entrance to an Enlarged Flat Duct," *International Journal of Heat and Mass Transfer,* Vol. 19, 1976, pp. 700–702.

5 Sparrow, E. M., and Kalejs, J. P., "Local Convective Transfer Coefficients in a Channel Downstream of a Partially Constricted Inlet," *International Journal of Heat and Mass Transfer,* Vol. 20, 1977, pp. 1241–1249.

6 Sparrow, E. M., and Wachtler, K P., "Transfer Coefficients on the Surfaces of a Transverse Plate Situated in a Duct Flow," *International Journal of Heat and Mass Transfer,* Vol. 21, 1978, pp. 761–767.

7 Sogin, H. H., "Sublimation from Disks to Air Streams Flowing Normal to their Surfaces," *Trans. ASME,* Vol. 80, 1958, pp. 61–71.

8 O'Brien, J. E., "Heat Transfer Coefficients on the Downstream Face of an Enlargement Step or an Inlet Constriction in a Tube," Thesis, Department of Mechanical Engineering, University of Minnesota, Minneapolis, Minn. 1979.

9 Karlekar, B. V., and Desmond, R. M., *Engineering Heat Transfer,* West Publishing, St. Paul, Minn. 1977.

10 Sogin, H. H., "A Summary of Experiments on Local Heat Transfer from the Rear of Bluff Obstacles to a Low Speed Airstream," ASME JOURNAL OF HEAT TRANSFER, Vol. 86, 1964, pp. 200–202.

New Parametrizations for Heat Transfer in Fins and Spines

A. D. Kraus
College of Engineering
Fellow ASME

A. D. Snider
College of Natural Sciences
University of South Florida,
Tampa, Fla 33620

A previous paper by the authors introduced a new set of parameters for describing the heat transfer properties of fins, namely, the thermal transmission matrices or ratios. They were devised to facilitate the analysis of a conglomerate of such fins in an array of extended surface. The present paper elaborates on the status and validity of the new parameters, discussing their superiority over the classic notion of fin efficiency with regard to adaptability and versatility. Tabulations of the new parameters for spines and radial fins are also included.

Introduction

The exact analysis of the heat transfer over an extended surface is a very complicated problem, involving such considerations as three-dimensional heat flow in the fins and the coolant, convection between the fins and coolant, boundary layer inhibition at the fin-coolant interface, and the flow pattern of the coolant. Thus, to compare the performance of any two proposed fin configurations in a realistic setting is an enormous, perhaps impossible, undertaking. The traditional approach of design engineers has been to invoke a set of idealizing assumptions usually attributed to Murray [1] and Gardner [2]. This simplification results in a model whose mathematical description is tractible (cf. [3–6] and the classic papers of Schmidt [7], Duffin [8], and Harper and Brown [9]). The model presumably approximates reality sufficiently well to justify design decisions; i.e., if one array performs twice as well as another under the idealized conditions, it will hopefully perform roughly twice as well in practice.

Probably the least realistic of these simplifying assumptions is the modeling of the coolant by a constant temperature bath and the concommitant hypothesizing that all of the complex physics of the heat transfer process can be expressed by Newton's law of cooling.

$$dq(x) = h(x)\theta(x)dS(x) \tag{1}$$

Here dq is the heat transferred (per unit time) from the fin to the coolant through a section of fin surface area dS; θ is the difference in temperature between the fin and the coolant (the temperature excess); and h is the heat transfer coefficient.

The authors described a new and efficient way of analyzing the idealized model ([10], hereinafter referred to as KSD). In fact, the model itself was improved slightly in that the assumptions were slightly weaker than those of Murray and Gardner. For example, KSD's general formalism took into account the slant profile contribution to dS and it allowed spatially varying thermal conductivities and heat transfer coefficients. (These effects have been studied in [11–14].) However, these features were minor; indeed none of the examples in KSD, nor here, exploit this added generality.

The essential contributions of KSD were (1) a new set of parameters for characterizing the thermal behavior of a single fin, and (2) an algorithm, based on these parameters, for treating combinations of fins. The algorithm has been generalized [15]. The present paper seeks to clarify the relationships of the new parameters with the classical fin efficiency, and to tabulate these parameters for spines and radial fins.

The New Parameters and the Fin Efficiency

Starting from the differential equation for idealized heat flow, KSD showed that the thermal transfer properties of any fin could be characterized in one of two ways. As before, let θ equal the temperature excess and let q equal the heat flow along the fin. The subscripts a and b indicate the fin tip and base, respectively. The heat flow *into* the base is denoted q_b and the heat flow *out of* the tip is denoted q_a.

Contributed by the Heat Transfer Division for publication in the JOURNAL OF HEAT TRANSFER. Manuscript received by the Heat Transfer Division May 29, 1979.

Then,

1 for a fin with finite (nonzero) tip thickness, i.e., a "regular" fin, there is a two by two *thermal transmission matrix*, Γ, which relates tip conditions to base conditions via the equation

$$\begin{bmatrix}\theta_a \\ q_a\end{bmatrix} = [\Gamma]\begin{bmatrix}\theta_b \\ q_b\end{bmatrix} \tag{2}$$

2 for a fin with zero tip thickness, i.e., a "singular" fin, there is a single *thermal transmission ratio*, μ, which governs the base conditions via the equation

$$q_b/\theta_b = \mu \tag{3}$$

It turns out that Γ always has a determinant equal to unity.

Denoting the elements of Γ by γ_{ij}, one can see from (2) that the $q{:}\theta$ ratios at the base and tip of a regular fin are related by a bilinear transformation

$$\frac{q_b}{\theta_b} = \frac{\gamma_{21} - \gamma_{11}(q_a/\theta_a)}{-\gamma_{22} + \gamma_{12}(q_a/\theta_a)} \tag{4}$$

Now, the efficiency η of a fin is defined as the dimensionless ratio Q_1/Q_0, where Q_1 is the heat actually dissipated by the fin, and Q_0 is the heat that the fin would dissipate if its temperature were uniformly equal to the base temperature $T(x) \equiv T_b$. Equivalently, Q_0 is the heat dissipated by a dimensionally identical fin with infinite thermal conductivity. Thus,

$$Q_0 = \theta_b \int h dS \tag{5}$$

integrated over the exposed surface of the fin. For a singular fin, $Q_1 = q_b$ and, thanks to (3), η and μ are related.

$$\eta = \mu / \int h dS \tag{6}$$

For a regular fin, things are not so simple. If the fin tip is adiabatic, $q_a = 0$ and $Q_1 = q_b$ so from (4) one deduces

$$\eta = \frac{-\gamma_{21}}{\gamma_{22}} \frac{1}{\int h dS} \tag{7}$$

If the tip is exposed to the coolant so that q_a is governed by a tip heat transfer coefficient h_a and tip area A, then $Q_1 = q_b$ (again) and

$$q_a = h_a A \theta_a \tag{8}$$

Combining (8) with (4) one derives

$$\eta = \frac{\gamma_{21} - \gamma_{11} h_a A}{-\gamma_{22} + \gamma_{12} h_a A} \frac{1}{\int h dS} \tag{9}$$

for the efficiency. This is somewhat academic because A is usually quite small and the value of h_a is often uncertain and seldom known. But, in principle, the efficiency for the fin with exposed tip is different from that for the fin with adiabatic tip.

Other values for the efficiency obtain if the fin is part of a network of extended surface with further fins attached to its tip. In such a case $Q_1 = q_b - q_a$ and (4) can be manipulated to produce

$$\eta = \frac{1}{\int hdS} \frac{\gamma_{21} + (1 - \gamma_{11})\,(q_a/\theta_a)}{-\gamma_{22} + \gamma_{12}\,(q_a/\theta_a)} \tag{10}$$

Thus the efficiency becomes a function of the overall array characteristics, through the ratio q_a/θ_a.

This is one of the inadequacies of the concept of fin efficiency. It cannot be computed for a regular fin a priori. Given the fin dimensions, thermal conductivity and the heat transfer coefficient, one *can* compute Γ; but η still depends on how the fin is mounted in the array. Most references that quote η do so for the conditions of (7).

An example will help to illustrate the differences between Γ, μ, and η. Consider the fin array shown in Fig. 1, where the base temperature excess is $\theta_b = 55.6°C$. Fins 1, 2, 4, and 5 are identical longitudinal fins of rectangular profile and fins 3 and 6 are identical triangular profile fins. The specifications, in the terminology of KSD, are as follows.

$$\text{Fins 1, 2, 4, 5; } \delta = 9.525 \times 10^{-3}\text{ m, } \sigma = 3.810 \times 10^{-2}\text{ m}$$

$$\text{Fins 3, 6; } \delta_b = 9.525 \times 10^{-3}\text{ m, } b = 3.810 \times 10^{-2}\text{ m}$$

For all fins, $L = 0.3048$ m, $k = 173.03$ W/m-°C and $h = 113.54$ W/m^2-°C. All of the temperature excesses and heat flows indicated were found by the technique in KSD.

Now one can tabulate the efficiencies (note that for fins 1, 2, 4, and 5, $hS = 2.637$ W/°C and for fins 3 and 6, $hS = 2.658$ W/°C.

$$\eta_1 = \frac{137.5}{2.637(55.6)} = 0.94$$

$$\eta_2 = \frac{232.1 - 104.2}{2.637(55.6)} = 0.87$$

$$\eta_3 = \frac{104.2}{2.658(43.1)} = 0.91 \tag{11}$$

$$\eta_4 = \frac{284.9 - 162.4}{2.637(55.6)} = 0.84$$

$$\eta_5 = \frac{162.4 - 73.0}{2.637(55.6)} = 0.87$$

$$\eta_6 = \frac{73.0}{2.658(30.1)} = 0.91$$

Thus the identical rectangular fins, operated in the same environment (h), do not all have the same efficiency. However, the thermal transmission matrix Γ, *is the same for all four.*

$$\Gamma = \begin{bmatrix} 1.1017 & -0.0784 \\ -2.7260 & 1.1017 \end{bmatrix} \tag{12a}$$

and for the singular triangular profile fins

$$\mu = 2.4213\text{ W/°C} \tag{12b}$$

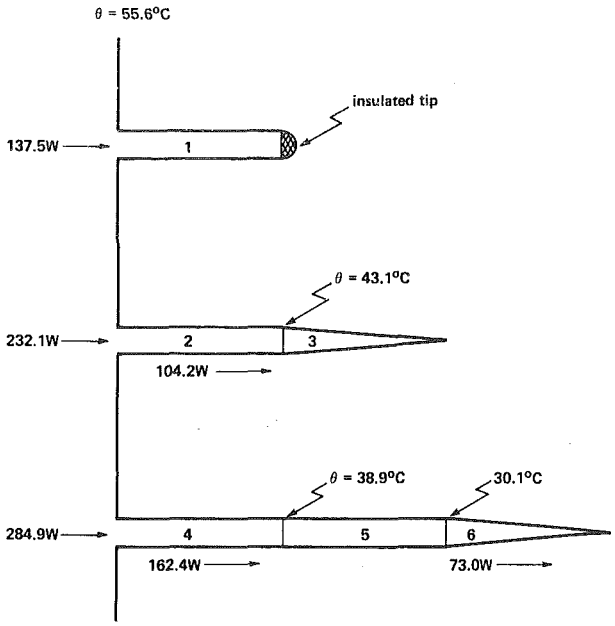

Fig. 1 An array of six fins with heat flows and temperature excesses indicated

For *singular fins* η and μ are related (6), but they still are not equivalent. Knowing only that the efficiency of fin 3 is 0.91, one knows that it dissipates 91 percent as much heat as an identical fin having infinite thermal conductivity. But how much heat does this "ideal" fin dissipate? For such a fin,

$$\frac{q_b}{\theta_b} = \eta \int hdS \tag{13}$$

So one must know $\int hdS$ in addition to η, in order to answer any questions about fin 3. But the single number μ is sufficient (as shown in KSD).

This illustrates the second inadequacy of the concept of fin efficiency. The general idea of an efficiency for a performance parameter is sound; it is a dimensionless ratio comparing the value of a parameter with a certain standard. However, the manner in which efficiency has been defined for fins compares every fin with a different standard; there are almost as many standards as there are fins. Two fins in the same environment having the same efficiency but different size and shape will dissipate different amounts of heat. *However, if they have the same μ, they will behave identically.*

The coup de grace for fin efficiency is administered as follows: Suppose a designer has somehow divined a priori all the efficiencies

Nomenclature

A = cross-sectional area, ft^2 (m^2)
$\mathcal{A}i$ = Airy function
a = location of fin tip, ft (m)
$\mathcal{B}i$ = Airy function
b = location of fin base, ft (m)
d = diameter of spine, ft (m)
f = a function
h = heat transfer coefficient, Btu/ft^2 – hr – °F (W/m^2 – °C)
I = modified Bessel function of first kind
K = modified Bessel function of second kind
k = thermal conductivity, Btu/ft – hr – °F (W/m – °C)
m = fin performance factor, ft^{-1} (m^{-1})
M = adjusted fin performance factor, ft^{-1} (m^{-1})
n = fin performance factor, ft^{-1} (m^{-1})
N = adjusted fin performance factor, ft^{-1} (m^{-1})
Q = actual and ideal fin heat dissipations (see equation (5)), Btu/hr (W)
q = heat flow, Btu/hr (W)
r = radial coordinate, ft (m)
S = surface, ft^2 (m^2)
u = transformed variable (see equation (27))
v = transformed variable (see equation (27))
x = rectangular coordinate, ft (m)
y = rectangular coordinate, ft (m)
z = rectangular coordinate, ft (m)
α = transformed variable (see equation (22))
β = transformed variable (see equation (22))
Γ = thermal transmission matrix
γ = element of thermal transmission matrix
δ = fin width, ft (m)
η = fin efficiency, dimensionless
θ = temperature excess, °F (°C)
μ = thermal transmission ratio, Btu/hr – °F (W/°C)
ρ = profile function for spine
σ = fin height, ft (m)
τ = ratio of tip to base locations, dimensionless (see equation (27))

Subscripts

a = fin tip
b = fin base
p = order of Bessel function
0 = ideal heat dissipation or base fin width
1 = actual heat dissipation

Superscripts

r = fin operated in reverse
-1 = matrix inverse
$'$ = derivative

for the array in Fig. 1 as given by (11), and he wishes to solve for the q's and θ's. From the earlier paragraph it is clear that he also needs all the quantities $\int h dS$. Working from the base of fin 2, where $\theta_b = 100°F$, (55.6°C) he computes $(q_b - q_a)$ from η_2. To try to get q_a, he now applies (6) to fin 3, whose *base* heat flow is this q_a and whose tip heat flow is zero. This gives q_a in terms of θ_b, the temperature excess at the interface of fins 2 and 3. But now all of the given information is exhausted and there is no way to find this θ_b.

The fact of the matter is that a regular fin simply cannot be characterized by a single parameter (η); it takes three parameters (four elements of Γ minus one determinant condition). And although a singular fin *can* be so characterized, η is not the best parameter to do it.

The conclusion is inescapable. The new thermal transmission parameters Γ and μ are more precise, versatile and useful for characterizing fins than the classical fin efficiency.

Formulas for the new parameters were given in KSD for regular longitudinal fins of rectangular, trapezoidal, and truncated concave parabolic profiles, and for singular longitudinal fins of triangular and concave parabolic profiles. The following sections extend this list to spines and radial fins. This rounds out the tabulations for the commonly used fin shapes.

Thermal Transmission Parameters for Spines

First consider the spines of circular cross section. Figure 2 illustrates the terminology. The analysis employs a cylindrical coordinate system with the x axis along the axis of symmetry, directed from tip ($x = a$) to base ($x = b$), and with ρ denoting distance from this axis. The x, rather than the customary z, axis is used in order to facilitate comparison with the longitudinal fins treated previously. Under the Murray-Gardner conditions, the flow will be axially symmetric, so the polar angle can be ignored.

The steady-state temperature excess, $\theta = T - T_s$, depends only on x; and the heat flow q, taken positive from base to tip, is given by

$$q(x) = k(x)A(x)\frac{d\theta(x)}{dx} = k(x)\pi[\rho(x)]^2\frac{d\theta}{dx} \tag{14}$$

Here $k(x)$ is the thermal conductivity, $A(x)$ is the cross section area, and $\rho = \rho(x)$ describes the profile of the spine. The heat dissipated through the surface is given, under the idealized conditions, by

$$dq(x) = \theta(x)h(x)dS(x) = \theta(x)h(x)2\pi\rho(x)\,[1 + \rho'(x)^2]^{1/2}dx \tag{15}$$

where $h(x)$ is the coefficient of heat transfer and $dS(x)$ is the element of surface area. Thus the equilibrium equation for $\theta = \theta(x)$ reads

$$\frac{d}{dx}\left[k(x)\rho(x)^2\frac{d\theta}{dx}\right] - 2h(x)\rho(x)\,[1 + \rho'(x)^2]^{1/2}\theta = 0 \tag{16}$$

In the case of spines with constant k and h this becomes

$$\rho(x)\frac{d^2\theta}{dx^2} + 2\frac{d\rho(x)}{dx}\frac{d\theta}{dx} - \frac{2h}{k}\,[1 + \rho'(x)^2]^{1/2}\theta = 0 \tag{17}$$

(This is at variance with [16, p. 114] because of misprints therein.)

For the *cylindrical spine of diameter d* (Fig. 3), $\rho(x) = d/2$ and proper interpretation of the theory developed in [16, p. 114] produces

$$\Gamma = \begin{bmatrix} \cosh m\sigma & -(2\sinh m\sigma)/\pi d(hkd)^{1/2} \\ -\pi d(hkd)^{1/2}(\sinh m\sigma)/2 & \cosh m\sigma \end{bmatrix} \tag{18}$$

where

$$m = 2(h/dk)^{1/2} \text{ and } \sigma = b - a \tag{19}$$

For the *truncated conical spine* (Fig. 4),

$$\rho(x) = xd/2b \tag{20}$$

where d is the diameter of the base. Then one finds the elements γ_{ij} of Γ given by

$$\begin{aligned} \gamma_{11} &= [K_2(\beta)I_1(\alpha) + I_2(\beta)K_1(\alpha)]2Mba^{-1/2} \\ \gamma_{12} &= [K_1(\beta)I_1(\alpha) - I_1(\beta)K_1(\alpha)]8b^{3/2}/k\pi d^2a^{1/2} \\ \gamma_{21} &= [K_2(\beta)I_2(\alpha) - I_2(\beta)K_2(\alpha)]\pi M^2kd^2a/2b \\ \gamma_{22} &= [K_1(\beta)\mathrm{I}_2(\alpha) + \mathrm{I}_1(\beta)K_2(\alpha)]2Ma/b^{1/2} \end{aligned} \tag{21}$$

where

$$\alpha = 2\mathrm{Ma}^{1/2}, \quad \beta = 2Mb^{1/2} \tag{22}$$

and

$$M = \left[\frac{4h^2(4b^2 + d^2)}{k^2d^2}\right]^{1/4} \tag{23}$$

and I_p, K_p are modified Bessel functions (cf. [16, p. 117] and [17, p. 355], but observe the corrected value for M).

For the *singular* ($a = 0$) *conical spine* the condition that θ_a remains finite as $a \to 0$ in (21) requires that the coefficient of $K_1(\alpha)$ equal zero in the expression for θ_a. Hence one finds the thermal transmission ratio equals

$$q_b/\theta_b = \mu = Mk\pi d^2\mathrm{I}_2(\beta)/4I_1(\beta)b^{1/2} \tag{24}$$

with β and M as in (22) and (23).

The *truncated spine of concave parabolic profile* (Fig. 5) has as its profile function

$$\rho(x) = x^2d/2b^2 \tag{25}$$

Inserted into (17), this yields a complicated differential equation unless one assumes the spine is long and thin, so that the ratio d/b can be neglected in comparison with unity. In that case the computations in [16, p. 119] can be modified to yield

$$\Gamma = (9 + 4M^2)^{-1/2}\begin{bmatrix} u\tau^v - v\tau^u & 4b(\tau^u - \tau^v)/k\pi d^2 \\ \pi dah(\tau^{u+2} - \tau^{v+2}) & u\tau^{u+3} - v\tau^{v+3} \end{bmatrix} \tag{26}$$

where

$$\begin{aligned} M &= (4b^2h/kd)^{1/2},\ u = -\frac{3}{2} + \frac{1}{2}(9 + 4M^2)^{1/2} \\ v &= -\frac{3}{2} - \frac{1}{2}(9 + 4M^2)^{1/2},\ \tau = a/b \end{aligned} \tag{27}$$

The *singular concave parabolic spine* is analyzed by letting $a \to$

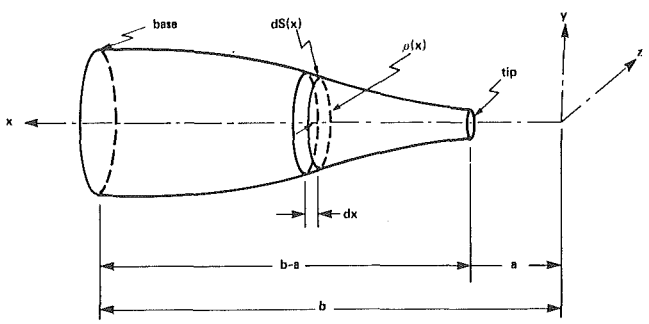

Fig. 2 Terminology and coordinate system for generalized spine

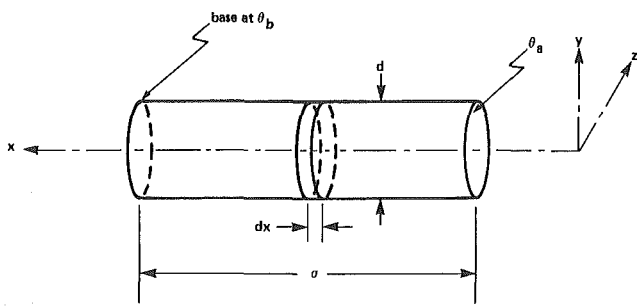

Fig. 3 Cylindrical spine

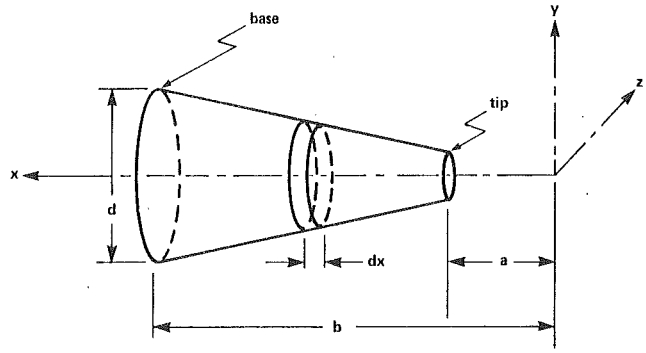

Fig. 4 Truncated conical spine

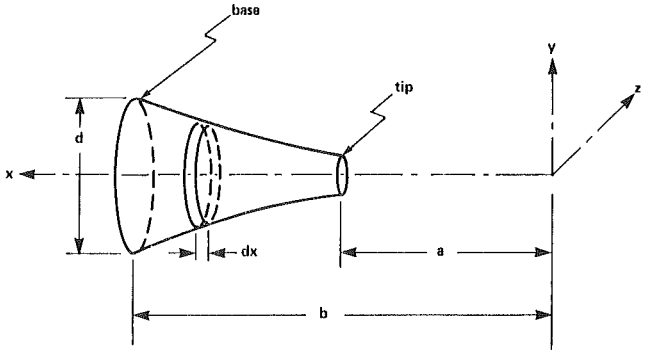

Fig. 5 Truncated concave parabolic spine

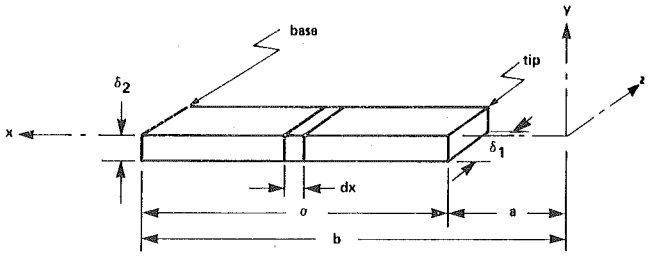

Fig. 6 Rectangular spine

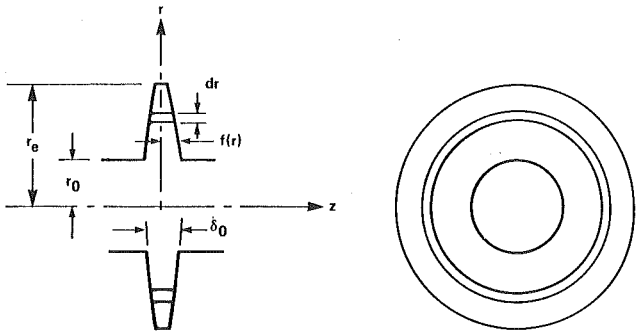

Fig. 7 Generalized radial fin

0 in (26). Since $v < 0 < u$, the finiteness condition yields the thermal transmission ratio

$$q_b/\theta_b = \mu = uk\pi d^2/4b \tag{28}$$

Specialists may note that the present paper, as well as KSD, has avoided discussion of fins of convex parabolic profile. The reason for this is that most previous treatments of this case drop the term $(\rho')^2$ in the element of surface area, equation (15); yet $\rho'(x)$ becomes infinite for such a profile! These fins will be reconsidered in a future paper.

Spines of constant rectangular cross section (Fig. 6), when operated under the Murray-Gardner conditions, are practically identical to longitudinal fins of rectangular profile. The only difference is that a spine transfers heat out of all four sides, while one usually treats the edges of a longitudinal fin as adiabatic [KSD], [16]. The thermal transmission matrix for the spine is readily obtained from the previous work by taking this effect, and the modified dimensions, into account. The result is

$$\Gamma = \begin{bmatrix} \cosh m\sigma & -(\sinh m\sigma)/k\delta_1\delta_2 m \\ -k\delta_1\delta_2 m \sinh m\sigma & \cosh m\sigma \end{bmatrix} \tag{29}$$

where

$$m = [2h(\delta_1 + \delta_2)/k\delta_1\delta_2]^{1/2};\ \sigma = b - a \tag{30}$$

(There is a typographical error in the 1, 2 entry of equation (17) of KSD, which becomes obvious when compared with equation (16) therein.) The square spine, of course, results if $\delta_1 = \delta_2$.

Thermal Transmission Parameters for Radial Fins

The general radial fin is depicted in Fig. 7. In the cylindrical coordinate system illustrated, the fin is described by the profile equation $z = f(r)$. Under the Murray-Gardner conditions heat flows in the radial direction only. The cross section area is $A(r) = (2\pi r)(2z)$ and the corresponding (two-sided) surface element for heat transfer is

$$dS = 2(2\pi r)\left[1 + \left(\frac{dz}{dr}\right)^2\right]^{1/2} dr \tag{31}$$

Thus the equilibrium heat flow equation, for constant k and h, becomes

$$\frac{d}{dr}\left[rf(r)\frac{d\theta}{dr}\right] - \frac{h}{k} r[1 + f'(r)^2]^{1/2}\theta = 0 \tag{32}$$

Notice, however, that because the radial coordinate now runs from base to tip, q and θ are related by

$$q(\mathrm{r}) = -k(r)A(r)\frac{d\theta}{dr} \tag{33}$$

(heat flow is still taken as positive from base to tip). This introduces slight changes in the formalism of KSD which will be incorporated without further comment in the following equations.

For the *radial fin of rectangular profile* (Fig. 8), $f(r) = \delta_0/2$ and one finds for the elements of Γ (cf., [16, p. 102] for a related computation).

$$\gamma_{11} = mr_0[K_1(mr_0)I_0(mr_e) + I_1(mr_0)K_0(mr_e)]$$

$$\gamma_{12} = -[K_0(mr_0)I_0(mr_e) - I_0(mr_0)K_0(mr_e)]/2\pi k\delta_0$$

$$\gamma_{21} = -2\pi k r_e r_0 \delta_0 m^2[K_1(mr_0)I_1(mr_e) - I_1(mr_0)K_1(mr_e)]$$

$$\gamma_{22} = mr_e[K_0(mr_0)I_1(mr_e) + I_0(mr_0)K_1(mr_e)] \tag{34}$$

where

$$m = (2h/k\delta_0)^{1/2} \tag{35}$$

For the *radial fin of hyperbolic profile* (Fig. 9) the profile equation is

$$z = f(r) = \delta_0 r_0/2r \tag{36}$$

Insertion of (36) into (32) leads to an intractible equation unless one can ignore f'^2 in comparison with unity; this requires $\delta_0/r_0 \ll 1$. In this case one arrives at

$$\gamma_{11} = \pi[\mathcal{B}i'(Nr_0)\mathcal{A}i(Nr_e) - \mathcal{A}i'(Nr_0)\mathcal{B}i(Nr_e)]$$

$$\gamma_{12} = -[\mathcal{A}i(Nr_0)\mathcal{B}i(Nr_e) - \mathcal{A}i(Nr_e)\mathcal{B}i(Nr_0)]/2kr_0\delta_0 N$$

$$\gamma_{21} = -2\pi^2 k r_0 \delta_0 N[\mathcal{B}i'(Nr_0)\mathcal{A}i'(Nr_e) - \mathcal{A}i'(Nr_0)\mathcal{B}i'(Nr_e)]$$

$$\gamma_{22} = \pi[\mathcal{A}i(Nr_0)\mathcal{B}i'(Nr_e) - \mathcal{B}i(Nr_0)\mathcal{A}i'(Nr_e)] \tag{37}$$

with

$$N = (2\mathrm{h}/r_0 k\delta_0)^{1/3} \tag{38}$$

and $\mathcal{A}i$, $\mathcal{B}i$ denoting Airy functions ([17, p. 446–447; compare 16, p. 106]).

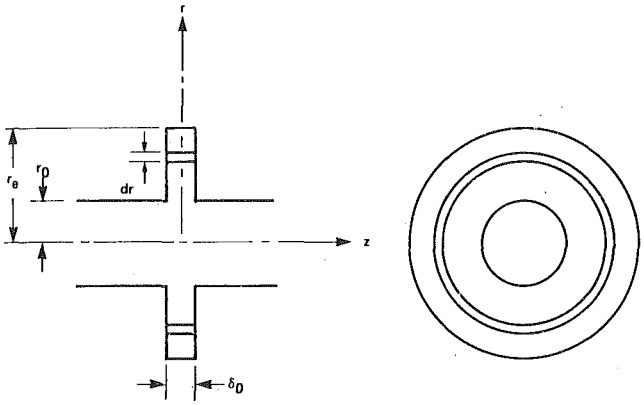

Fig. 8 Radial fin of rectangular profile

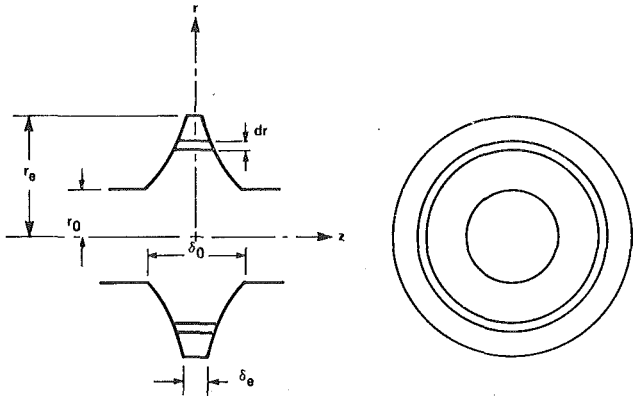

Fig. 9 Radial fin of hyperbolic profile

This completes the tabulation of the thermal transmission parameters for the commonly used fin shapes.

Fins Operated in Reverse

Circumstances may arise in which, after Γ is computed for a regular fin, one finds it convenient to reverse the base and tip designations of the fin. This involves more than a mere matrix inversion of Γ because the reference direction for q is also reversed. In fact, if the superscript r designates the reversed orientation, one identifies

$$\theta_a{}^{(r)} = \theta_b,\ \theta_b{}^{(r)} = \theta_a,\ q_a{}^{(r)} = -q_b,\ q_b{}^{(r)} = -q_a \tag{39}$$

Then it is not hard to see that the appropriate modification of (2) is

$$\begin{bmatrix} \theta_a{}^{(r)} \\ q_a{}^{(r)} \end{bmatrix} = \Gamma^{(r)} \begin{bmatrix} \theta_b{}^{(r)} \\ q_b{}^{(r)} \end{bmatrix} \tag{40}$$

where the reversed thermal transmission matrix $\Gamma^{(r)}$ is

$$\Gamma^{(r)} = \begin{bmatrix} 1 & 0 \\ 0 & -1 \end{bmatrix} \Gamma^{-1} \begin{bmatrix} 1 & 0 \\ 0 & -1 \end{bmatrix}$$

Thus $\Gamma^{(r)}$ differs from Γ^{-1} in the signs of the off-diagonal elements.

Conclusion and Summary

This paper complements [KSD] in that it rounds out the tabulation of the thermal transmission parameters introduced therein, for the commonly used fin shapes. Additionally, it presents alternative techniques for handling reversed fins. In the process, some clarifications and simplifications of previous analyses have been pointed out and incorporated.

In closing, one should remark that, although the exposition is directed to the problem of using extended surface for cooling, the results are, of course, equally valid for heating applications.

Acknowledgment

Some of the material contained in this paper was developed under National Science Foundation Grant ENG-7701297.

References

1 Murray, W. M., "Heat Dissipation through an Annular Disk or Fin of Uniform Thickness," *Journal of Applied Mechanics*, 5:A78 (1938).

2 Gardner, K. A., "Efficiency of Extended Surfaces," *Trans. ASME*, Vol. 67, 1945, p. 621.

3 Jakob, M.: *Heat Transfer*, Vols. I and II, assisted by S. P. Kezios, John Wiley & Sons, New York, 1949, 1957.

4 Kreith, F. *Principles of Heat Transfer*, 3rd ed., Intext Educational Publishers, New York, 1973.

5 Chapman, A. J., *Heat Transfer*, 3rd ed, Macmillan Publishing, New York, 1974.

6 Holman, J. P., *Heat Transfer*, 4th ed, McGraw-Hill, New York, 1976.

7 Schmidt, E., *Zeitschrift des Verins Deutscher Ingenieure*, Vol 70, 1926, pp. 885–889, 947–951.

8 Harper, D. R., and Brown, W. B., NACA Report 158, 1922.

9 Duffin, R. J., *Journal Math. Mech.*, 8(1), 1959, pp. 47–56.

10 Kraus, A. D., Snider, A. D., and L. F. Doty, "An Efficient Algorithm for Evaluating Arrays of Extended Surface," ASME JOURNAL OF HEAT TRANSFER, Vol. 100, May 1978, p. 288.

11 Maday, C. J., "The Minimum Weight One-Dimensional Straight Fin," ASME *Journal of Engineering for Industry*, Vol. 96. 1974, pp. 161–165.

12 Guneri, S., and Maday, C. J., "A Least Weight Circular Cooling Fin," ASME *Journal of Engineering for Industry*, Vol. 97, 1975, pp. 1190–1193.

13. Ghai, L. M., and Jacob, M., "Local Coefficients of Heat Transfer on Fins," ASME Paper No. 50, 1950.

14 Stachiewicz, W. J., "Effect of Variation of Local Film Coefficients of Pipe Performance," ASME JOURNAL OF HEAT TRANSFER, Vol. 91, No. 1, 1969, pp. 21–26.

15 Snider, A. D. and Kraus, A. D., "A General Extended Surface Analysis Method," submitted to JOURNAL OF HEAT TRANSFER, 1979.

16 Kern, D. Q., and Kraus, A. D., *Extended Surface Heat Transfer*, McGraw-Hill, New York, 1972.

17 Stegun, I. A., and Abramowitz, M., "Handbook of Mathematical Functions," Nat'l Bureau of Standards AMS 55, 1964.

The Optimum Dimensions of Circular Fins with Variable Thermal Parameters

P. Razelos
Department of Applied Sciences,
Mem. ASME

K. Imre
Department of Mathematics

College of Staten Island,
City University of New York,
Staten Island, NY 10301

Optimum dimensions of circular fins of trapezoidal profile with variable thermal conductivity and heat transfer coefficients are obtained. Linear variation of the thermal conductivity is considered of the form $k = k_0(1 + \epsilon T/T_0)$, and the heat transfer coefficient is assumed to vary according to a power law with distance from the bore, expressed as $h = K[(r - r_0)/(r_0 - r_e)]^m$. The results for $m = 0$, 0.8, 2.0, and $-0.4 \leq \epsilon \leq 0.4$, have been expressed by suitable nondimensional parameters which are presented graphically. It is shown that considering the thermal conductivity as constant, the optimum base thickness and volume of the fin are inversely proportional to the thermal conductivity of the material of the fin, while the optimum length and effectiveness are independent of the properties of the material used.

Introduction

Circular fins are used extensively in heat exchange devices to increase the heat transfer rate. The fin optimization problem, referred to in the literature as the optimum volume or the least material problem, is to find the shape of the fin which would minimize the fin volume for a given amount of heat dissipation, or, alternatively, to maximize the heat dissipation for a given volume. For purely conductive and convective fins the criterion for this optimum fin problem was first proposed intuitively by Schmidt [1], and later proved by Duffin [2]. Several investigators have obtained optimum fin profiles in which the effects of curvature, radiation, and variable thermal conductivity were also included [3–6]. The authors recently determined the optimum fin shapes [7] for longitudinal, circular, and spine fins, with variable heat transfer coefficient.

Unfortunately, problems of this type have the serious disadvantage that the resulting profiles are too complex to manufacture, and fragile at the sharp ends. However, the results are useful, serving as a measure of comparison for related optimization problems in which more practical fin profiles are utilized. One of the related problems is to select a suitable simple profile, and then determine the dimensions of the fin to yield maximum heat dissipation for a given fin volume. This type of optimization for convective longitudinal fins of several profiles, under the assumptions of one dimensional approximation, constant thermal parameters, and negligible effects of surface curvature and heat transfer from the tip, is treated in many texts [8–10], while constant thickness fin with variable thermal conductivity is considered in [11]. The optimum dimensions of the circular constant thickness fin are given in [12]. Several investigators have also considered the problem of optimizing a total array of fins [13–16].

The most severe restriction in all previous analytical work, is the assumption of a constant heat transfer coefficient, which is shown both theoretically and experimentally [17–25] to increase, in general and often radically, towards the fin tip.

In this paper, we consider the optimization of circular fins with a profile of constant slope, including the effect of the variable thermal conductivity (which depends on temperature linearly), as well as the effect of a variable heat transfer coefficient. We assume that the predominant modes of heat transfer are conduction and convection, and the effect of radiation is ignored. Unfortunately, the spatial dependence of the heat transfer coefficient cannot be fully specified without the knowledge of the coolant flow around the fin. In order to estimate its effect on the optimal fin dimensions (at least qualitatively) we have assumed a power law variation similar to those observed in longitudinal fins [17–18]. The experimental results for circular fins reported in [22], show a similar behavior of the heat transfer coefficient; but the variation is substantially different at different angles around the fin.

Although the results presented here are for a single circular fin, they undoubtedly are of valuable help in designing and analyzing total fin arrays. They also contain more information than those previously reported in literature with more restrictive assumptions, and some important conclusions are also valid with or without the presence of adjacent fins. The method presented here may also be helpful in the design of experiments for determining local heat transfer coefficients in fins.

Statement of the Problem

Consider a circular fin of uniform density, with a symmetric profile, attached to a cylindrical surface of radius r_0 with a temperature T_0 measured in excess to the ambient fluid (coolant) temperature. The profile of the fin is $y = y(r)$, with thermal conductivity $k(T)$, heat transfer coefficient $h(r)$, and both faces are exposed to an environment of temperature zero. The geometry of this arrangement is shown schematically in Fig. 1. Assuming one-dimensional conduction, the steady-state temperatures must satisfy the following problem.

$$d/dr[kry dT/dr] = h(r)rT(1 + y'^2)^{1/2} \tag{1}$$

$$T(r_0) = T_0 \tag{2}$$

$$[kdT/dr + h_e T]_{r_e} = 0, \quad \text{if } y(r_e) = w_e \neq 0 \tag{3a}$$

$$T(r_e), \text{ bounded} \quad \text{if } y(r_e) = 0 \tag{3b}$$

where $y' = dy/dr$

The temperature T_0 is considered constant but not necessarily known a priori.

Given the volume of the fin

$$V = 4\pi \int_{r_0}^{r_e} y(r) r dr \tag{4}$$

we seek the bore semi-thickness w and the length $L = r_e - r_0$ which will maximize the heat dissipated by the fin

$$q = -4\pi r_0 w k(T_0)(dT/dr)_{r=r_0} \tag{5}$$

under the condition that

$$q > q_b = 4\pi r_0 w h_b T_b \tag{6}$$

where q_b, h_b, T_b refer to the values of the corresponding quantities when no fin is present. We assume further that the thermal conductivity and the heat transfer coefficient are expressed by

$$k = k_0[1 + \epsilon(T/T_0)] = k_0[1 + \epsilon\theta] \tag{7}$$

$$h = h_a H(r/r_0), \tag{8}$$

Contributed by the Heat Transfer Division and presented at the ASME Winter Annual Meeting, December 2–7, New York, New York, 1979. Revised manuscript received at ASME Headquarters November 30, 1979. Paper No. 79-WA/HT-48.

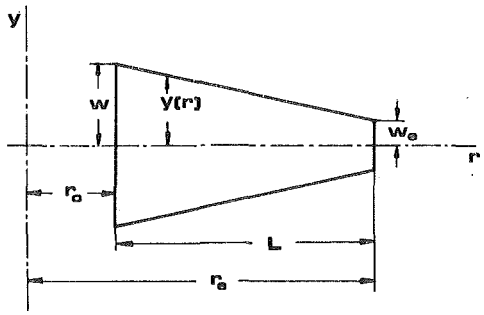

Fig. 1 Schematic cross-sectional view of circular fin

respectively, where h_a is the value of h averaged over the fin surface.

Introducing the dimensionless variables $\xi = r/r_0$, $\theta = T/T_0$, and $\eta = y/w$, into equations (1–3), we obtain

$$d/d\xi[(1 + \epsilon\theta)\eta\xi\, d\theta/d\xi] = \upsilon^2 H\, \xi\theta[1 + (B_r\eta'/\upsilon^2)^2]^{1/2} \quad (9)$$

$$\theta = 1, \quad \xi = 1 \quad (10)$$

$$d\theta/d\xi + (h_e/h_a)HB_r\theta = 0, \text{ at } \xi = \beta, \text{ if } \eta(\beta) \neq 0 \quad (11a)$$

$$\theta, \text{ bounded} \quad \text{at } \xi = \beta, \text{ if } \eta(\beta) = 0 \quad (11b)$$

where $\eta' = d\eta/d\xi$, $B_r = h_a r_0/k_0$ is a parameter specified by the problem, $\upsilon = r_0(h_a/k_0 w)^{1/2}$ and $\beta = r_e/r_0$ are the parameters to be determined during the optimization process. The dimensionless temperature θ, is obtained by solving the above problem as a function of ξ and the parameters β, υ, ϵ and B_r. The dimensionless volume U is defined as

$$U = k_0 V/4\pi r_0^4 h_a = \int_0^1 g(\beta)/\upsilon^2 \quad (12)$$

where

$$V = 4\pi r_0^2 w g(\beta) \quad (13a)$$

$$g(\beta) \equiv \int_0^1 \xi\eta d\xi \quad (13b)$$

The problem at hand is, in terms of the dimensionless parameters, for a given value of U to determine the values of υ and β which will maximize the dimensionless heat dissipation which is defined as

$$Q = q/(4\pi r_0^2 h_a T_0) = -(1 + \epsilon)\theta'(1)/\upsilon^2 \quad (14)$$

where $\theta' = d\theta/d\xi$

The optimum values of υ and β must be such that the condition (6) must be satisfied, i.e.,

$$N_r \equiv q/q_b = (h_a T_0/h_b T_b)\upsilon^2 Q/B_r > 1 \quad (15)$$

The above ratio N_r is usually referred in the literature as the removal number.

Solution

Regarding the parameters r_0, B_r, ϵ as given, one can obtain the solution of the boundary value problem (9–11) to calculate $\theta'(1)$, hence the heat dissipation at the fin bore, as a function of β and υ, which characterize the length and the bore semi-thickness of the fin, respectively. The volume U is also calculated in terms of these variables. Thus the stationary values of Q for a given U must satisfy the relation

$$(\partial Q/\partial\beta)(\partial U/\partial\upsilon) - (\partial Q/\partial\upsilon)(\partial U/\partial\beta) = 0 \quad (16)$$

Note that the problem of maximizing Q for a given U is equivalent to the problem of minimizing U for a given Q, since both problems are characterized by the root of equation (16), which can alternatively be written, using equation (12), as

$$2g\partial Q/\partial\beta + \upsilon(dg/d\beta)\partial Q/\partial\upsilon = 0 \quad (17)$$

If an analytic solution for the problem (9–11) was available (as is the case for a few simple profiles with constant h and k [26]), then the optimum values of β and υ (thus Q or U) could be determined using equation (17) together with that analytic solution. In the absence of such a solution one must resort to numerical methods in evaluating optimal values.

We also note that the dependence of the optimal values on the parameter B_r is rather weak, so that for almost all practical purposes it may be ignored. This is due to the fact that (1) the slope of the profile is much smaller in magnitude compared to one, and (2) the heat transfer from the fin tip is much smaller than the total convective heat dissipation. When these assumptions (the validity of which will be examined later) are adopted, the boundary value problem is reduced to

$$X_1' = X_2/[\eta\xi(1 + \epsilon X_1)] \quad (18a)$$

$$X_2' = \upsilon^2 H\xi X_1 \quad (18b)$$

$$X_1(1) = 1, X_2(\beta) = 0 \quad (19)$$

where we have set $X_1 \equiv \theta$, $X_2 \equiv (1 + \epsilon\theta)\eta\xi\theta'$. In the present work, we have chosen the trapezoidal profile

$$\eta = y/w = (1 - \lambda)(\beta - \xi)/(\beta - 1) + \lambda \quad (20)$$

where λ denotes the ratio of fin tip thickness to bore thickness, and the spatial variation of the heat transfer coefficient was assumed to be

$$H(\xi) = K(\beta,m)\,[(\xi - 1)/(\beta - 1)]^m \quad (21)$$

where

$$K(\beta,m) = (\beta + 1)(m + 1)(m + 2)/2[(m + 1)\beta + 1] \quad (22)$$

Corresponding to the profile (20)

Nomenclature

B = Biot number $h_a w/k_0$
B_r = parameter $h_a r_0/k_0$
E = fin's effectiveness
$g(\beta)$ = the ratio $V/4\pi r_0^2 w = \int_0^1 \xi\eta d\xi$
H = dimensionless heat transfer coefficient = h/h_a
h = heat transfer coefficient
h_a = average heat transfer coefficient
h_e = heat transfer coefficient at the tip of the fin
k = thermal conductivity
L = Length of the fin
m = parameter describing the variation h
N_r = removal number q/q_b
q = heat dissipated by the fin
q_b = heat dissipated by the bore surface in the absence of the fin
Q = dimensionless heat dissipation = $q/4\pi h_a r_0^2$
r = coordinate
r_e = tip radius
r_0 = bore radius
T = temperature in excess of the ambient fluid temperature
U = dimensionless volume = $k_0 V/4\pi r_0^4 h_a$
V = volume of the fin
$V(0)$ = volume of the fin when m or $\epsilon = 0$
V_c = volume of the constant thickness fin
υ = dimensionless parameter = $r_0(h_a/k_0 w)^{1/2}$
y = coordinate
w = fin's base semi-thickness
$w(0)$ = fin's base semi-thickness when m or $\epsilon = 0$
w_c = base semi-thickness of the constant thickness fin
w_e = tip semi-thickness
β = ratio of radii r_e/r_0
ϵ = parameter describing the variation of thermal conductivity
η = dimensionless coordinate y/w
λ = ratio of tip to base thickness = w/w_e
ξ = dimensionless coordinate = r/r_0

$$g(\beta) = (\beta - 1)[(1 - \lambda)(\beta + 2) + 3\lambda(\beta + 1)]/6 \quad (23)$$

The temperature dependence of the thermal conductivity was also chosen as given in equation (7).

The differential equation (18) is integrated backwards using a routine based on Verner's fifth and sixth order Runge-Kutta formulas. The terminal values $X_1(1)$ and $X_2(1)$ are then fed into another routine which utilizes a quasi-Newton algorithm, originally discussed by Fletcher [27] to find the minimum value of $X_2(1)/(X_1(1)v^2) = -Q$, as v^2 being evaluated from equation (12) for the specified value of U, by optimizing the parameter β. We also employed an additional root finding routine in which U is varied along the optimal trajectories until a given value of β (or a given value of Q) is obtained. The program also takes into account the effects of convective tip and the curvature of the profile, which can be suppressed or included.

Before proceeding to present the numerical results for some specific cases in the next section, let us examine the properties of the optimum solution for the case of constant thermal conductivity ($\epsilon = 0$), a condition often met in practice when there are moderate temperature excursions, such as in an air cooled process. In this case the optimum values of β and v will depend only on U, or only on Q, whenever U, or Q, is specified, respectively. If the values of β_{op} and v_{op} are determined for a given Q, which is independent of k, we can conclude that the length of the fin is independent of the properties of the material. The same is also true for the optimum effectiveness, E_{op}, which in this case is equal to $2Q/(\beta^2 - 1)$. Similarly, since v_{op} is independent of k, it follows from its definition that the base thickness, (and hence the volume of the fin), is inversely proportional to the thermal conductivity of the material of the fin. These properties also hold in the least material case [7].

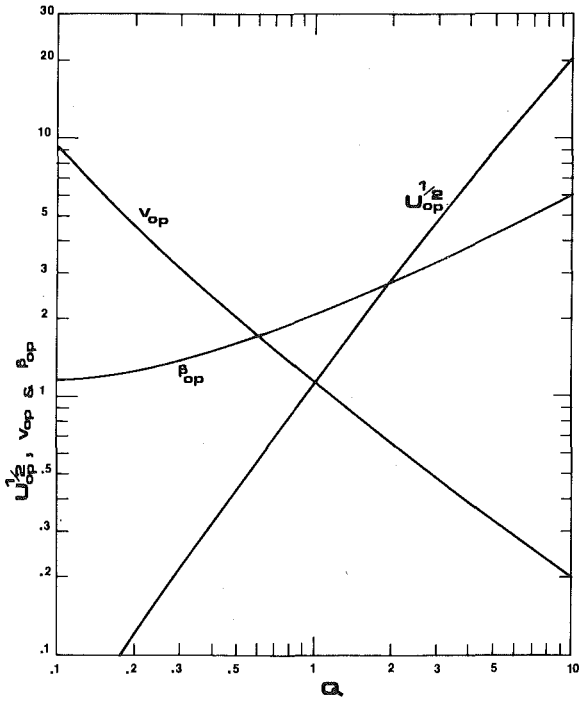

Fig. 2 Optimum dimensions of the constant thickness annular fin, with $\epsilon = m = 0$

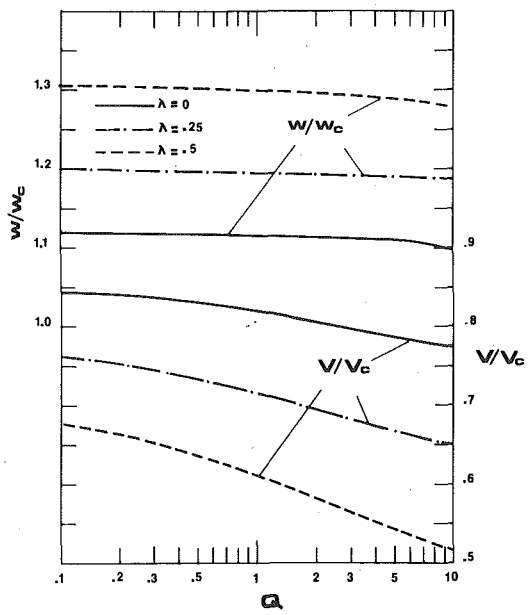

Fig. 3 Influence of the fin's profile, upon the optimum dimensions

Results and Discussion

In Fig. 2 the optimum values of v_{op} and U_{op} are plotted versus Q, for the constant thickness fin with $m = \epsilon = 0$. Note that these two curves correspond to the same problem treated in [12], where the solution was given in a para-metric form. Since in many practical problems the length of the fin is specified rather, than the heat dissipation or the volume, the variation of β_{op} with Q is also plotted in Fig. 2 which can be used to obtain directly the optimum fin dimensions in these cases.

The influence of the fin's profile upon the optimum dimensions, is shown in Fig. 3 where the ratios w/w_c and V/V_c are plotted versus Q, for the trapezoidal ($\lambda = 0.5$) and triangular profiles ($\lambda = 0$). This figure shows that as λ decreases the fin becomes thicker at the base, while the volume decreases. The calculated values of β_{op} show a corresponding increase of the optimum length, but this variation has a maximum of approximately 3 percent, even for the triangular fin.

In order to study the effect of the variable thermal conductivity, we have considered several values of the parameter ϵ between $\pm$ 0.4. The results indicate that for positive or negative ϵ the base thickness and volume decrease or increase respectively, while the variation of ϵ has no appreciable effect on the optimum length (β_{op}). It is also found that any variation of the base thickness and volume caused by any $\epsilon \neq 0$ is almost independent of the profile of the fin. The results are shown graphically in Fig. 4 where $w/w(0)$ and $V/V(0)$ are plotted versus ϵ.

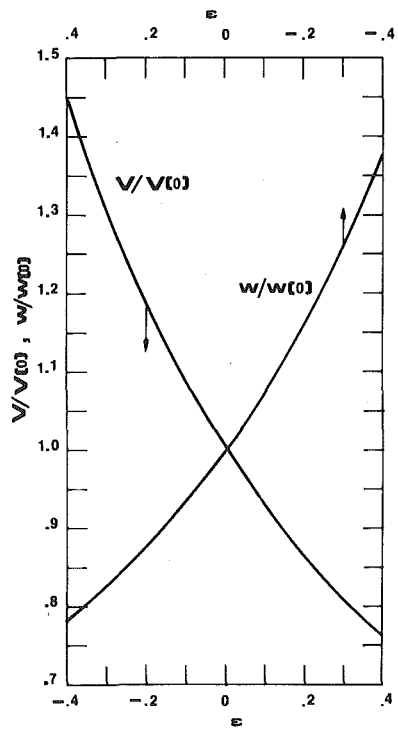

Fig. 4 The effect of variable thermal conductivity on the fin's optimum dimensions

The effect of the variable heat transfer coefficient is demonstrated in Fig. 5, where for the constant thickness and triangular profile fins, the ratios $w/w(0)$ and $V/V(0)$ are plotted versus Q, for two different values of the exponent $m = 0.8$ and 2. This figure shows that the dimensions of the fin increase appreciably with increasing m, while the calculated values of β_{op} were smaller, but no more than 3 percent. We should emphasize here that the above two values of m were selected only, for a qualitative examination of its influence upon the optimum dimensions, and the results should not be used for design purposes, before a complete knowledge of the variation of h is known.

In Fig. 5, for comparison, the ratios of the optimum volumes to the least material fin volume, are also known. It can be seen that the effect of variable h is more pronounced in the triangular fins, and generally decreases as Q increases. On the other hand, the departure of the results from those of the least material case, increases with increasing Q, and decreases drastically with increasing m. The results presented in Figs. 2–4 can be used in the entire range of practical applications for preliminary design purposes, since they cover the range of β_{op} from 1.25 to 6.0.

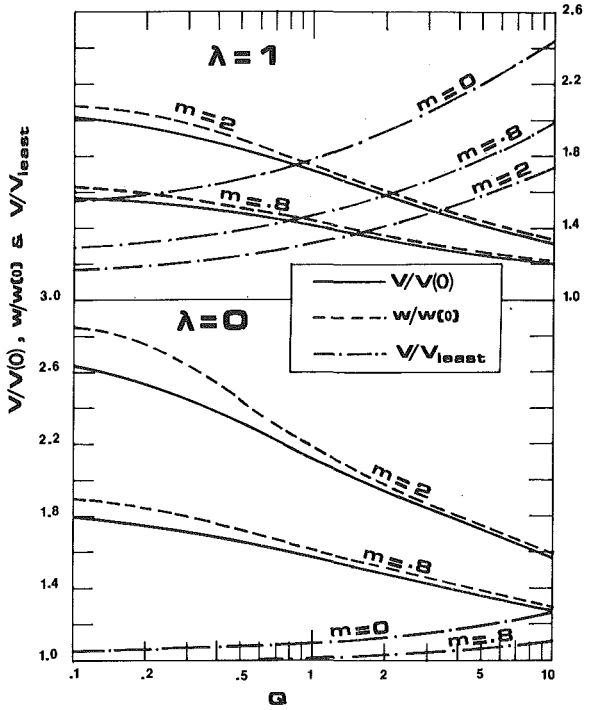

Fig. 5 The effect of the variable heat transfer coefficient on the optimum dimensions, and comparison with least material fin

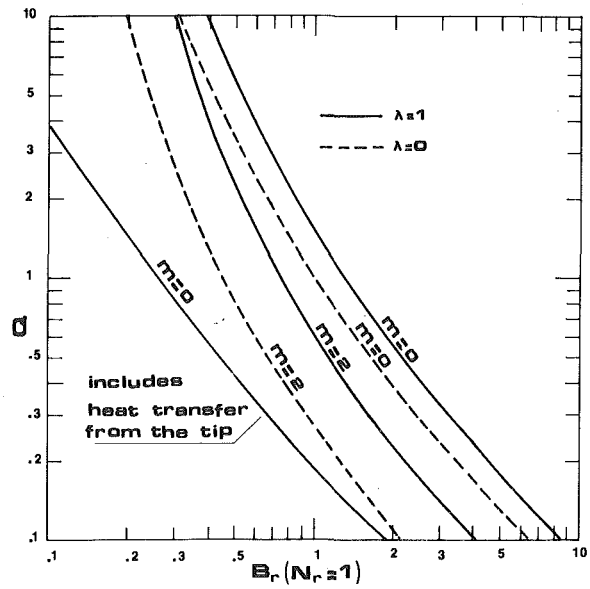

Fig. 6 Limiting values of the heat dissipation $Q(N_r = 1)$ in optimized constant thickness and triangular profile circular fins

The results presented in Fig. 2 show that as $Q \to 0$, $\beta \to 1$, and the circular fin becomes at the limit longitudinal. In this case as $Q \to 0$, $v \to \infty$ and $U \to 0$; however the product Qv and the ratio U/Q^3 approach definite limits, which for the constant thickness fin, are determined by extrapolation, and their values are 0.8895 and 2.0172, respectively. We now use the same formulation for the dimensionless semi-thickness w^* and V^*, as in the longitudinal fins [9, 28]

$$w^* = h_a k_0 w_{op}/(q_r/T_0)^2 \tag{24}$$

$$V^* = h_a{}^2 k_0 (V_r)_{op}/(q_r/T_0)^3 \tag{25}$$

where $q_r = q/2\pi r_0$ and $V_r = V/2\pi r_0$, the heat dissipation and volume per unit bore length. Inserting the expressions for U and Q from (12, 14), into the above relationships, we obtain

$$w^* = 0.25/(Qv)^2 = 0.3160 \tag{24a}$$

$$V^* = 0.25U/Q^3 = 0.5043 \tag{25a}$$

where the numerical answers are obtained, using the limiting values of Qv and U/Q^3 given above. These values of w^* and V^* are exactly those reported in [9, 28]. Note that equations (25, 25a) show that the optimum volume V_r is proportional to the third power of q_r, as in the longitudinal fins.

In order to evaluate the usefulness of the fin, one must estimate the ratio $h_a T_0/h_b T_b$ which occurs in the inequality (15), taking into account that T_0 is less than T_b due to the temperature depression [29, 30], and evaluating h_b as described in [9]. Since equation (15) is an inequality, the exact value of this ratio is not critical, and for the present purposes we take its value to be one. The product $N_r B_r$ is completely determined by Q under the simplifying assumptions stated earlier. Figure 6 displays the relationship between Q and B_r, with $N_r = 1$, for different cases under consideration. Since N_r must be greater than one, the usefulness region for the values of Q lies below the curves shown in Fig. 6. This figure shows qualitatively how the ability of the fin to dissipate heat is increased by using materials with higher k.

We conclude our discussion by examining briefly the validity of our assumptions. We have calculated several cases of triangular fins in which the surface effect is taken into account, and also several cases of constant thickness fins with convective tips. In general, the resulting optimum fins are shorter, thicker and with smaller volume. It was found that the curvature effect contributed to a maximum of 2.5 percent reduction of volume, and, therefore, can be neglected. The effect of the convective tips can reduce the volume as much as 16 percent, however, it can be neglected for all cases $Q \leq 1$, and $B_r \leq 0.1$. Finally, the one-dimension approximation overestimates the thermal performance of the fin as does the approximation of the constant h and the negligible curvature effect. It is shown in [31] that under these simplifications for any circular fin

$$N_r < Qv/B^{1/2} \tag{26}$$

where $B = h_a w/k$ is the Biot number. The product Qv is found to have a maximum value of 1.5 for constant thickness fins, and 1 for the triangular fins in the range of practical applications. If we assume that fins are economically justified when $N_r \geq 5$, then, according to equation (24), B must be less than 0.1. It was shown in [32] that for those Biot numbers the error in heat dissipation is less than 1 percent.

The following example serves as an illustration of the method presented here. Determine the optimum dimensions of a circular fin of bore radius 0.05m, which will dissipate 500 W when the heat transfer coefficient is 200 $W/m^2 - K$ and the temperature difference between the bore and the coolant is 100 K, for three different typical materials and fin profile uniform or triangular. The physical properties of the various materials and the optimum dimensions of the corresponding fins, as obtained from Figs. 5 and 6 are set forth in Tables 1 and 2, while in Table 3 the optimum dimensions of the least

Table 1 Optimum dimensions of constant thickness circular fins

q = 500 W, r_0 = 0.05m, h_a = 200 W/m^2 − K, T_0 = 100 K, Q = 0.7958

Material	k [W/m − K]	B_r	υ	$U^{1/2}$	r_0/r_e	$2w$ [cm]	V [cm^3]	E	B	N_r	V/V_{least}
CASE 1.1					Insulated tip, m = 0						
Copper	382	0.0262	1.374	0.838	1.911	0.139	28.91	0.6002	0.0004	57.4	1.76
Aluminum	228	0.0439	1.374	0.838	1.911	0.232	48.44	0.6002	0.0010	34.2	1.76
Cb. Steel	47	0.2128	1.374	0.838	1.911	1.127	234.79	0.6002	0.0240	7.1	1.76
CASE 1.2					Insulated tip, m = 0.8						
Copper	382	0.0262	1.140	1.001	1.898	0.202	41.21	0.6116	0.0005	39.5	1.44
Aluminum	228	0.0439	1.140	1.001	1.898	0.338	69.05	0.6116	0.0015	23.6	1.44
Cb. Steel	47	0.2128	1.140	1.001	1.898	1.637	334.73	0.6116	0.0348	4.9	1.44
CASE 1.3					Including heat transfer from the tip $h_e = h_a$, m = 0						
Copper	382	0.0262	1.368	0.830	1.891	0.140	28.32	0.6058	0.0004	56.8	1.72
Aluminum	228	0.0439	1.363	0.824	1.876	0.236	46.79	0.6099	0.0001	33.7	1.70
Cb. Steel	47	0.2128	1.291	0.767	1.720	1.277	196.41	0.6637	0.0272	6.2	1.47

Table 2 Optimum dimensions of triangular profile circular fins

q = 500W, r_0 = 0.05m, h_a = 200 W/m^2 − K, T_0 = 100K, Q = 0.7958

Material	k [W/m − K]	B_r	υ	$U^{1/2}$	r_0/r_e	$2w$ [cm]	V [cm^3]	E	B	N_r	V/V_{least}
CASE 2.1					m = 0 Negligible curvature effect						
Copper	382	0.0262	1.202	0.661	1.958	0.181	17.98	0.5617	0.0005	43.9	1.094
Aluminum	228	0.0439	1.202	0.662	1.958	0.304	30.13	0.5617	0.0013	26.2	1.094
Cb. Steel	47	0.2128	1.202	0.661	1.958	1.474	146.15	0.5617	0.0314	5.4	1.094
CASE 2.2					m = 0.8 Negligible curvature effect						
Copper	382	0.0262	0.937	0.836	1.935	0.298	28.75	0.5800	0.0008	26.7	1.004
Aluminum	228	0.0439	0.937	0.836	1.935	0.500	48.17	0.5800	0.0022	15.9	1.004
Cb. Steel	47	0.2128	0.937	0.836	1.935	2.426	233.65	0.5800	0.0516	3.3	1.004
CASE 2.3					m = 0 Including curvature effect						
Copper	382	0.0262	1.202	0.661	1.958	0.181	17.98	0.5619	0.0005	43.9	1.093
Aluminum	228	0.0439	1.201	0.661	1.957	0.304	30.12	0.5623	0.0011	26.2	1.093
Cb. Steel	47	0.2128	1.192	0.654	1.929	1.498	143.18	0.5775	0.0319	5.3	1.072

Table 3 Dimensions of least material fins [7]

q = 500W, r_0 = 0.05m, h_a = 200 W/m^2 − K, T_0 = 100 K, Q = 0.7958

Material	k [W/m − K]	B_r	υ	$U^{1/2}$	r_0/r_e	$2w$ [cm]	V [cm^3]	E	B	N_r
CASE 3.1					m = 0					
Copper	382	0.0262	0.950	0.632	2.1504	0.290	16.44	0.4391	0.0008	27.4
Aluminum	228	0.0439	0.950	0.632	2.1504	0.486	27.54	0.4391	0.0021	16.4
Cb. Steel	47	0.2128	0.950	0.632	2.1504	2.356	133.60	0.0501	0.0501	3.4
CASE 3.2					m = 0.8					
Copper	382	0.0262	0.838	0.834	1.943	0.373	28.63	0.5735	0.0010	21.4
Aluminum	228	0.0439	0.838	0.834	1.943	0.627	47.96	0.5735	0.0027	12.7
Cb. Steel	47	0.2128	0.838	0.834	1.943	3.033	232.66	0.5735	0.0645	2.6

material fins are listed. Comparing the results for cases 1.1 and 1.2 for the constant thickness fin shown in Table 1, it is seen that the fins with the variable heat transfer coefficient require 43 percent more volume, and are thicker at the base by 45 percent than those with constant h; the length remains almost unchanged. In case 1.1 the fins require 76 percent more volume than the least material fins. While in case 1.2, the increase is only 44 percent. A comparison of cases 1.2 and 1.3 reveals that if the heat transfer from the tip is taken into account, the fins are thicker and shorter with smaller volume; however, for all practical purposes, the 16 percent reduction is only appreciable for carbon steel. Note that in all cases the largest Biot number is 0.035, making the one-dimensional approximation justifiable. Comparing the results for cases 2.1 and 2.2 shown in Table 2 for the triangular profile fin, we can see that, for the variable heat transfer coefficient, the fins require 60 percent more volume and are thicker by 65 percent; once again, the length remains almost unchanged. Comparing for the least material, the fins in case 1.1 require 9 percent more volume, while in case 2.2 the required volume is increased by only 0.4 percent. We may note that in case 2.2 the use of carbon steel may not be economically justified. By examining cases 2.2 and 2.3, we can conclude that, for all practical purposes, the slope effect upon the optimum fin dimensions is negligible.

Concluding Remarks

In the present analysis, the optimum dimensions of circular fins with constant slope profile have been obtained assuming one di-

mensional approximation, neglecting the effect of curvature, and the heat transfer from the tip. The cases considered include (1) the constant heat transfer coefficient with thermal conductivity varying linearly with temperature, and (2) the constant thermal conductivity with heat transfer coefficient increasing with the distance from the bore according to a power law. The results are expressed in terms of suitable dimensionless parameters and for certain typical cases are presented graphically; they can be used for design purposes, within the specific variation of the thermal parameters considered, whenever the required heat removal, or the weight, or the length of the fin is specified. The numerical methods utilized, however, are not restricted to these specific forms, and can be used to handle more refined variations suitable for a given situation.

It is shown that in both cases (1) and (2) stated above, the optimal thickness of the fin base and the volume are mainly affected, while the length remains practically unchanged. It was also shown that, when k is constant and Q is given, (1) the base thickness and volume are inversely proportional to k, (2) the length and the effectiveness are independent of k. These results are also true for fins which are parts of an array, since the presence of the adjacent fins merely changes the heat transfer coefficient. The analysis presented here clearly shows that the effect of the variable heat transfer coefficient cannot be ignored.

Acknowledgments

The authors acknowledge the generous support of the City University Computer Center for providing its facilities to be used in numerical computations presented in this paper.

References

1 Schmidt, E., "Die Warmeubertragung durch Rippen, *"Zeitschrift des VDI,* Vol. 70, No. 26, p. 885, No. 28, p. 947, 1926.

2 Duffin, R. J., "A Variation Problem Related to Cooling Fins," *Journal of Mathematics and Mechanics,* Vol. 8, No. 1, 1959, pp. 47–56.

3 Maday, C. J., "The Minimum Weight One-Dimensional Straight Fin," ASME *Journal of Engineering for Industry,* Vol. 96, 1974, pp. 161–165.

4 Guneri, S., and Maday, C. J., "A Least Weight Circular Cooling Fin," ASME *Journal of Engineeri for Industry,* Vol. 97, 1975, pp. 1190–1193.

5 Wilkins, J. E., Jr., "Minimum-Mass Thin Fins Which Transfer Heat Only by Radiation to Surroundings at Absolute Zero," *Journal of Society Industrial Applied Mathematics,* Vol. 8, No. 4, 1960, pp. 630–639.

6 Cobble, M. H., "Optimum Fin Shape," *Journal of the Franklin Institute,* Vol. 291, No. 4, 1971, pp. 630–639.

7 Razelos, P., and Imre, K., "Application of Optimum Control Theory to Certain Heat Transfer Problems," to be presented at the Second International Conference on Information Sciences and Systems, University of Patras, Greece, July 9–13, 1979.

8 Schneider, P. J., *Conduction Heat Transfer,* Addison-Wesley, Reading, Mass., 1955.

9 Jacob, M., *Heat Transfer,* Vol. 1, fifth edition, John Wiley and Sons, New York, 1956.

10 Kern, Q. D. and Kraus, D. A., *Extended Surface Heat Transfer,* McGraw-Hill, New York, 1972.

11 Aziz, A., and Huq, S. M., "Perturbation Solution for Convective Fins with Variable Thermal Conductivity," ASME JOURNAL OF HEAT TRANSFER, Vol. 97, 1975, pp. 300–301.

12 Brown, A., "Optimum Dimensions of Uniform Annular Fins," *International Journal of Heat and Mass Transfer,* Vol. 8, 1965, pp. 665–662.

13 Appl, C. F., and Hung, M. H., "Finned Surfaces with Optimum Fins of Restricted Length," *Symposium on Air-Cooled Heat Exchangers,* ASME, New York, 1964, pp. 37–44.

14 Dhar, L. P., and Arora, P. C., "Optimum Design of Finned Surfaces," *Journal of Franklin Institute,* Vol. 301, No. 4, 1976, pp. 379–392.

15 Siegel, R. and Graham, W. R., "Effect of Fin Passage Length on Optimization of Cylinder Head Cooling Fins," *NASA Technical Paper* 1054, Lewis Research Center, Cleveland, Ohio, Sept. 1977.

16 Jones, D. C. and Smith, F. L., "Optimization Arrangement of Rectangular Fins of Horizontal Surfaces for Free-Convection Heat Transfer," ASME JOURNAL OF HEAT TRANSFER, Vol. 92, 1970, pp 6–10.

17 Ghai, L. M., and Jacob, M., "Local Coefficients of Heat Transfer on Fins," ASME Paper No. 50, 5-18-1950.

18 Stachiewicz, W. J., "Effect of Variation of Local Film Coefficients of Pipe Performance," ASME JOURNAL OF HEAT TRANSFER, Vol. 91, No. 1, 1969, pp. 21–26.

19 Yudin, F. V., and Tokhtarova, S. L., "Investigation of the Correction Factor for the Theoretical Effectiveness of a Round Fin," *Thermal Engineering,* Vol. 21, No. 8, 1974, pp. 58–62.

20 Kuznetsov, V. N., and Pshenisnov, F., "The Effect of Nonuniformity of the Heat Transfer over the Surface of Continuous Spiral and Wire Finning on the Finning Effectiveness," *Thermal Engineering,* Vol. 21, No. 6, 1974,

21 Kuznetsov, V. N. and Pshenisnov, F., "The Effect of Nonuniformity of the Heat Transfer Along the Surface of a Round Fin on its Effectiveness," *Thermal Engineering,* Vol. 21, No. 8, 1974, pp. 58–62.

22 Jones, V. T. and Russel, B. M. C., "Heat Transfer Distribution on Annular Fins," ASME Paper 78-HT-30, 1978.

23 Saboya, F. E. M., and Sparrow, E. M., "Local and Averaged Transfer Coefficients for One-row Plate Fin and Tube Heat Exchanger Configurations," ASME JOURNAL OF HEAT TRANSFER, Vol. 96, No. 3, 1974, pp. 265–272.

24 Masliyah, J. H. and Nandakumar, K. "Heat Transfer in Internally Finned Tubes," ASME JOURNAL OF HEAT TRANSFER, Vol. 98, No. 2, 1978, pp. 257–261.

25 Sparrow, E. M., Baliga, R. B., and Pantakar, V. S., "Forced Convection Heat Transfer from a Shrouded Fin Array with and without Tip Clearance," ASME JOURNAL OF HEAT TRANSFER, Vol. 100, No. 4, 1978, pp. 572–579.

26 Gardner, K. A., "Efficiency of Extended Surfaces," *Trans. ASME,* Vol. 67, No. 8, 1945, pp. 621–631.

27 Fletcher, R., "Fortran Subroutines for Minimization by Quasi-Newton Methods," Report R7125 AERE, Harwell, England.

28 Razelos, P., "The Optimization of Longitudinal Convective Fins with Internal Heat Generation" *Nuclear Engineering and Design,* Vol. 54, No. 2, 1979, pp. 289–299.

29 Sparrow, E. M., and Hennecke, K. D., "Temperature Depression at the Base of a Fin," ASME JOURNAL OF HEAT TRANSFER, Vol. 92, No. 1, 1970, pp. 204–206.

30 Sparrow, E. M., and Lee, L., "Effects of Fin Base-Temperature Depression in a Multifin Array," ASME JOURNAL OF HEAT TRANSFER, Vol. 97, No. 3, 1975, pp. 463–465.

31 Razelos, P., "A Note on the Heat Transfer in Convective Fins," *Warme-und Stoffubertragung,* Vol. 12, 1979, pp. 113–119.

32 Wan, L. and Tan, W. C., "Errors in One Dimensional Heat Transfer Analysis in Straight and Annular Fins," *Trans. ASME,* Vol. 95, No. 4, 1973, pp. 549–551.

E. M. Sparrow
Fellow ASME

A. Hajiloo
Department of Mechanical Engineering,
University of Minnesota,
Minneapolis, Minn. 55455

Measurements of Heat Transfer and Pressure Drop for an Array of Staggered Plates Aligned Parallel to an Air Flow

The heat transfer and pressure drop characteristics of an array of staggered plates, aligned parallel to the direction of a forced convection air flow, have been studied experimentally. During the course of the experiments, the plate thickness and Reynolds number were varied parametrically. Mass transfer measurements employing the naphthalene sublimation technique were made to obtain the heat transfer results via the heat-mass transfer analogy. For a given operating condition, the per-plate heat transfer coefficients were found to be the same for the second and all subsequent rows. The fully developed heat transfer coefficients increase with Reynolds number for all the plate thicknesses investigated, but in a different manner for the different thicknesses. In general, thicker plates give rise to higher heat transfer coefficients, especially at the larger Reynolds numbers. The measured friction factors also increase with plate thickness. For the thickest plates, the friction factor was found to be independent of the Reynolds number, signalling the dominance of inertial losses.

Introduction

The pioneering experiments of Norris and Spofford [1] first revealed the enhancement of heat transfer obtainable for fluid flow along a succession of discrete plate segments compared to that for flow along a continuous wall. These researchers and those that followed [2–6] dealt with actual or model heat exchangers consisting of an array of discrete plates aligned parallel to the airflow passing through the exchanger. The plates were arranged in parallel columns, with streamwise gaps between the plates in each column. In those applications, the plates were actually fins which bridged between the walls of the heat exchanger passages. Typically, condensing steam served as the other fluid in the heat exchanger.

In experiments involving such heat exchange devices, measurements typically include the air temperatures and pressures at inlet and exit, the air flowrate, the steam temperature and pressure and, perhaps, the condensate rate. Thus, only overall results are obtained. Furthermore, the determination of average air-side heat transfer coefficients involves numerous assumptions which, when seriously scrutinized, gives rise to a degree of uncertainty in the results.

It appears that there are no reported heat transfer or pressure drop measurements internal to a heat exchange device of the discrete-plate type, and with good reason, since such measurements are well-nigh impossible. More detailed measurements have been made for simpler discrete-plate systems, including two colinear plates [7–9] and eight colinear plates [10] aligned parallel to the flow. Thus, up to the present, the only cases for which detailed measurements have been made are limited to a single column of plates.

The present experiments were performed with a multicolumn array of discrete plates. In each column, ten plates were positioned colinearly, with the streamwise gap between successive plates being equal to the plate length. The plates in adjacent columns were arranged so that a plate in one column is abreast of a gap in the adjacent column. This arrangement may alternatively be characterized as offset or staggered.

Both heat transfer and pressure drop measurements were made. In lieu of direct heat transfer measurements, a mass transfer technique—naphthalene sublimation—was employed to good advantage both with respect to accuracy and attainment of standard boundary conditions. The mass transfer results were converted to heat transfer results via the well-established analogy between the two processes. Taking account of the boundary conditions for the mass transfer experiments, the analogous heat transfer results correspond to uniform wall temperature and to fins with an efficiency of unity. Per-plate heat transfer coefficients were determined both in the entrance region of the array and in the fully developed regime. The thermal development was found to be so rapid that the entrance region is of little practical relevance, so that the presentation of results is focused on the developed regime.

The pressure measurements included detailed axial distributions along the length of the discrete-plate array as well as in the upstream and downstream ductwork. These measurements enabled determination of a net loss coefficient for the array (reported on a per-row basis) and an apparent friction factor.

Two parameters were varied during the course of the investigation: the plate thickness and the Reynolds number. Plate thicknesses equal to 4, 8, and 12 percent of the plate length were employed. The ramifications of these thickness variations on other geometrical quantities (e.g., free flow area) will become evident when diagrams of the experimental set-up are presented. The Reynolds number, based on the Kays-London definition [3], ranged from about 1000 to 9000.

The Experiments

In the design of the experimental apparatus, special features were incorporated to facilitate the use of the naphthalene sublimation technique and to enable the thickness of the plates to be changed without a major rebuilding. With regard to the naphthalene technique, it involves the installation of coated test plates into the apparatus at the beginning of each data run and their removal at the end of the run. Furthermore, the installation and removal operations have to be performed in as short a time as possible in order to minimize extraneous sublimation. Thus, it is necessary that the test section include an access port that can be opened and closed rapidly, and the seating arrangement for the plates must provide positive positioning without adjustments. In addition, the seating and positioning arrangement must be capable of accommodating plates of different thickness with only simple modifications. The test section which was designed and fabricated to fulfill these objectives will now be described.

Test Section. The test section was housed in a 50.8 cm length of a flat rectangular duct whose overall length of 275 cm encompassed

Contributed by the Heat Transfer Division for publication in the JOURNAL OF HEAT TRANSFER. Manuscript received by the Heat Transfer Division December 31, 1979.

an upstream hydrodynamic development section and a downstream redevelopment section. A schematic side view of the test section showing the placement of the staggered plate array is presented in the upper diagram of Fig. 1. As can be seen in the diagram, there are five flow-aligned columns of plates. Three of the columns, those situated away from the top and bottom walls of the duct, contain plates of thickness t. To more closely approximate an infinitely high stack, the plates in the columns adjacent to the top and bottom walls are of thickness $t/2$. All columns contain ten plates. Whereas t was varied parametrically during the course of the experiments, the plate length L and the streamwise separation distance (also equal to L) were fixed at 2.54 cm. Also fixed was the transverse distance H between the centerlines of adjacent columns—$H = 0.667$ cm (note that the overall height of the host rectangular duct is $4 \times 0.667 = 2.668$ cm).

Two types of plates were employed in the experiments. For the mass transfer studies, the plates were composites consisting of a mild steel core sandwiched between thin layers (0.015 cm thick) of naphthalene. The plates which did not participate in the mass transfer process were of stainless steel. The overall thickness of the composite plates was made equal to that of the solid metal plates. Nominally, the plate thicknesses corresponded to t/L ratios of 0.04, 0.08, and 0.12. However, since metallic sheets are available only in discrete standard thicknesses, the actual t/L values for the experiments were 0.042, 0.078, and 0.123. For this same reason, the actual thickness/length ratios of the wall-adjacent plates were 0.025, 0.042, and 0.058. The leading and trailing edges of the plates were squared off to present a blunt face to the flow.

The spanwise distance (i.e., between the side walls) bridged by each plate was 13.34 cm. Thus, with a subchannel height dimension such as H or $(H - t)$, the subchannel aspect ratio (span/height) is at least 20. Such a large aspect ratio tends to minimize end (i.e., side wall) effects. This characteristic constitutes a major difference between the present laboratory-type experiments and the previous performance-oriented experiments,where aspect ratios were generally small and end effects correspondingly large.

The plates were supported and positioned by specially designed side walls. Each of the test section side walls consisted of a stack of four bars as shown in the lower diagram of Fig. 1. As seen in the diagram, two sets of periodic recesses were machined into the lowermost bar 1—row A along the lower surface of the bar and row B along the upper surface. Each of the other bars 2, 3, and 4 contained a single set of periodic recesses along their respective upper surfaces. These recesses housed extensions of the test plates to such close tolerances as to ensure precise positioning.

Recesses A and E, respectively adjacent to the top and bottom walls of the host duct, were initially machined to accommodate the thinnest of the half-thickness plates. These recesses were subsequently enlarged to accommodate the intermediate and the thickest of the half-thickness plates. With regard to recesses B, C, D, they were initially machined to mate with the thinnest of the plates, and no further modifications were made during the course of the experiments. For the accommodation of the thicker plates in these recesses, the extensions of the plates were machined symmetrically on their upper and lower surfaces so that the remaining thickness of the extensions

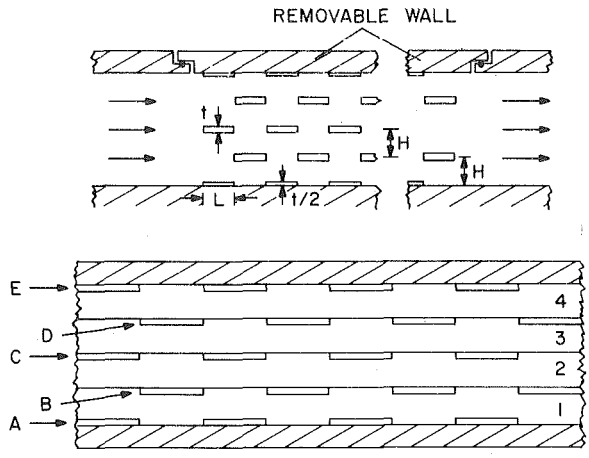

Fig. 1 Test section diagrams. Upper diagram: placement of the staggered plates; Lower diagram: built-up side wall showing recesses for positioning of plates

fitted precisely into the recesses.

This pattern of fabrication was devised so that the transverse center-to-center distance H (upper diagram of Fig. 1) was maintained the same regardless of the thickness of the test plates. To achieve this result, the appropriate heights of bars 1, 2, 3, and 4 are 0.720, 0.667, 0.667, and 0.614 cm.

Bars 1 and 2 were bolted together, and the unit was rigidly attached to the lower wall of the duct; bars 3 and 4 were similarly attached to the upper duct wall. The test-section side walls, as formed from the bars, mated smoothly with the conventional (i.e., one-piece) side walls of the (upstream) hydrodynamic development section and (downstream) flow redevelopment section. Both for alignment purposes and to prevent leaks, each of the test-section side walls was backed by a one-piece backing plate.

The upper wall of the test section was removable, with the act of removal being accomplished in a matter of seconds by releasing six quick-opening clamps. Since bars 3 and 4 were rigidly attached to the upper wall, the removal of the wall also removed the upper portions of the two side walls,thereby exposing the recesses C and the test plates situated in these recesses. Consequently, plates could be inserted into or removed from recesses C in a very short time. Thus, the entire sequence of operations encompassing the opening of the test section wall, the insertion (removal) of test plates in recesses C, and the closing of the wall could be accomplished within about a minute. Since recesses C lie along the central column of the test section, mass transfer measurements were confined to plates positioned in these recesses.

Experimental Apparatus. In the course of its flow, air was drawn from the temperature-controlled laboratory room through a hydrodynamic development section (37 hydraulic diameters in length), the test section, and a flow redevelopment section ($13\frac{1}{2}$ diameters long). All of these sections were parts of a flat rectangular duct, 13.34×2.668 cm in cross section and 275 cm long. From the duct exit, the air passed

Nomenclature

A = transfer area for naphthalene sublimation
A_{min} = minimum free flow area
D_h = hydraulic diameter (Kays-London)
$\mathcal{D}$ = mass diffusion coefficient
f = apparent friction factor, equation (6)
G = mass velocity, $\dot{m}/A_{min}$
H = transverse center-to-center distance, Fig. 1
h = per-plate heat transfer coefficient
K = per-plate mass transfer coefficient, equation (1)
K_p = per-row average pressure loss coefficient, equation (7)
k = thermal conductivity
L = plate length
ΔM = per-plate naphthalene mass transfer
$\dot{m}$ = air flow rate
Nu = per-plate Nusselt number, hD_h/k
N = number of rows
Pr = Prandtl number
ΔP = net of entrance and exit pressure losses
p = static pressure
Δp^* = net pressure drop due to array
Sc = Schmidt number
Sh = Sherwood number, $KD_h/\mathcal{D}$
St = Stanton number, Sh/ReSc or Nu/RePr
Re = Reynolds number, D_hG/μ
x = axial coordinate
t = plate thickness
V = mean velocity, G/ρ
μ = viscosity
ρ = air density
ρ_{nw} = naphthalene vapor density at plate surface
ρ_{nb} = bulk naphthalene vapor density
τ = duration of data run

via a rectangular-to-circular transition piece to a flow metering station (calibrated ASME-type orifice), through a control valve, and to a blower situated outside of the laboratory. The efflux from the blower was discharged to the outdoors, insuring that the air in the laboratory and at the duct inlet was free of naphthalene vapor.

The axial pressure distribution along the test section and the hydrodynamic development and redevelopment sections was measured with a Baratron capacitance-type pressure meter capable of being read to 10^{-4} mm Hg. The axial positions of the pressure taps will be evident from the pressure distributions that will be presented later.

The sublimation mass transfer from a naphthalene-coated plate was determined from weighings of the plate before and after a data run. The weighings were performed with a Mettler analytical balance with a capacity of 200 g and a smallest scale reading of 0.1 mg.

Naphthalene Test Plates. The naphthalene coatings for the test plates were applied by a combination casting-machining procedure. To ensure good adhesion of the coating, the surfaces of the plates were sand blasted and holes were drilled in the surface to enable the naphthalene to anchor itself.

The casting was performed in an open-topped mold, with the metal core of the test plate situated at the bottom of the mold cavity. Molten naphthalene was poured into the mold through the open top to a depth of about ¼ cm and, after solidification had taken place, the plate was turned over and a poured coating applied to the other surface. Then, the coated plate was detached from the other parts of the mold and subsequently positioned in a special vise clamped to the bed of a vertical milling machine. The naphthalene surfaces were then machined to the desired thickness of 0.015 cm by means of a fly cutter held in the chuck of the milling machine. The resulting surface finish, as sensed by touch, was similar to that of glass.

Subsequent to the machining, the plates were sandwiched between glass and an impermeable plastic was wrapped around the sandwich. The thus-wrapped plates were then placed in the laboratory room for at least twelve hours in order to attain thermal equilibrium with the surroundings.

Experimental Procedure. The data runs for the determination of fluid flow (i.e., pressure distribution) information were performed separately from the mass transfer data runs. For the fluid flow runs, only metal plates (i.e., not coated with naphthalene) were employed. Consequently, during a sequence of experiments for a given plate thickness and various Reynolds numbers, the plates were left in place and the test-section access capability was not employed. Once such a sequence was completed, all 50 plates of the array were removed and replaced by another set having a different thickness.

In each mass transfer data run, only one naphthalene-coated plate was employed, the others being stainless steel plates of thickness identical to that of the coated plate. For each plate thickness and for each preselected Reynolds number, a succession of data runs was performed in which the active plate was respectively placed in the first, second, third, etc. row. As noted earlier, the active plates were positioned in recesses C (lower diagram of Fig. 1), which house the center column of plates. This central placement was made with a view to minimizing the effects of the finite height of the stack of plates.

Immediately before the beginning of a data run, the mass of the test plate was determined by weighing with the analytical balance. Then, the plate was installed in a preselected row of the array and the airflow passed through the system for a period of time depending on the Reynolds number. Run times varied from 30 to 120 min, with longer times at lower Reynolds numbers. Upon termination of the run, the naphthalene coated plate was removed from the test section and its mass determined by weighing.

Then, an additional procedure was executed to find a correction for any extraneous mass transfer which might have occurred during the installation of the test plate in the apparatus and its subsequent removal. To this end, following the weighing of the test plate at the conclusion of the data run, the installation and removal procedures were repeated without the forced convection mass transfer period, after which the plate was weighed again. The difference between the final weighing and that just after the run was used as a correction for the extraneous sublimation.

The run times were adjusted so that the change in the thickness of the naphthalene coating during a data run was comfortably below 0.0025 cm, which corresponds to a change in mass of about 150 mg per plate. The corrections described in the prior paragraph were typically about 2 mg.

Data Reduction. The per-plate mass transfer coefficient K was evaluated from the corrected change in mass ΔM and the duration time τ of the data run by means of the defining equation

$$K = \Delta M/A\tau(\rho_{nw} - \rho_{nb}) \tag{1}$$

where A is the transfer area for naphthalene sublimation, and ρ_{nw} and ρ_{nb} are, respectively, the naphthalene densities at the plate surface and in the bulk flow. The quantity ρ_{nw} was evaluated from the Sogin vapor pressure—temperature relation [11] in conjunction with the perfect gas law; ρ_{nb} is zero in the present experiments because the entering air is free of naphthalene vapor and because there is no mass transfer upstream of the active test plate.

The per-plate Sherwood number Sh, the dimensionless form of K, was evaluated as

$$\mathrm{Sh} = KD_h/\mathcal{D} \tag{2}$$

in which D_h is the hydraulic diameter according to the Kays-London definition [3]. The values of D_h corresponding to the arrays with the thinnest, intermediate, and thickest plates are 2.35, 2.11, and 1.82 cm. The diffusion coefficient $\mathcal{D}$ was obtained via the Schmidt number Sc $= \nu/\mathcal{D}$, with Sc = 2.5 and ν evaluated as the kinematic viscosity of pure air.

The Reynolds number employed here is the standard one for heat exchangers [3], namely

$$\mathrm{Re} = D_hG/\mu, \quad G = \dot{m}/A_{\min} \tag{3}$$

with $A_{\min}$ denoting the minimum free flow area. With the use of the Reynolds number, a mass transfer Stanton number St may be introduced as

$$\mathrm{St} = \mathrm{Sh}/\mathrm{ReSc} \tag{4}$$

Furthermore, to generalize the results to other Sc (or Pr), a modified Colburn j-factor was employed. The conventional j-factor is based on the assumption that Sh $\sim$ Sc$^{1/3}$. The ⅓ power dependence may be valid at high Schmidt numbers, but a 0.4 power is believed to be a better representation at intermediate values of Schmidt number. Consequently, the results will be presented in the form

$$\mathrm{StSc}^{0.6} = \mathrm{Sh}/\mathrm{ReSc}^{0.4} \tag{5}$$

Furthermore, it will be assumed that StSc$^{0.6}$ for mass transfer equals StPr$^{0.6}$ for heat transfer.

Attention will now be turned to evaluation of dimensionless quantities which represent the pressure drop characteristics of the array. As will be illustrated later, in any given data run, the pressures at all test section taps (i.e., at all taps along the axial length of the array) fall along a straight line, enabling the gradient $-dp/dx$ to be evaluated. With this, an apparent friction factor f was evaluated from the defining equation

$$f = (-dp/dx)D_h/\tfrac{1}{2}\rho V^2 \tag{6}$$

where the quantity ρV^2 is related to the mass velocity G of equation (3) via $\rho V^2 = G^2/\rho$. The apparent friction factor was determined as a function of the Reynolds number in the range between 1000 and 9000 for each of the three plate thicknesses investigated.

The apparent friction factor, as defined in the foregoing, characterizes the pressure drop that is internal to the array. Aside from the internal pressure drop, the presence of the array gives rise to pressure effects adjacent to the inlet and exit cross sections. Flow acceleration and deceleration at the inlet and exit, respectively, are reflected as a pressure decrease and a recovery. Separation and eddy losses at these sections cause a pressure drop, as does the flow redevelopment downstream of the array. In addition, there may have been a short hydrodynamic development region in the initial portion of the array

which was not detected owing to the placement of the first pressure tap.

These considerations motivated the evaluation of an overall pressure drop $|\Delta p^*|$ which encompasses all pressure effects related to the presence of the array. This quantity was determined as follows: On a graph of p versus x, the pressure data in the hydrodynamic development section (upstream of the test section) fall on a straight line. Also, in the downstream redevelopment section, there is a region where p versus x is a straight line with a slope identical to that of the straight line in the hydrodynamic development section.

In the absence of the array, these straight lines would be colinear. However, with the array in place, the downstream segment is displaced vertically downward with respect to the upstream segment. The amount of the displacement is $|\Delta p^*|$.

A dimensionless form of the array pressure drop may be obtained in terms of a per-row pressure coefficient K_p defined as follows

$$K_p = |\Delta p^*| / \tfrac{1}{2}\rho V^2 N \tag{7}$$

where N is the number of rows in the array, equal to 20 in the present experiments. K_p was evaluated for all three plate thicknesses for the same Reynolds number range as was the friction factor f. The relationship between K_p and f will be discussed later.

Heat Transfer Coefficients

In view of the well-established relationship between the two processes, the dimensionless mass transfer results will be regarded as being equally applicable to corresponding heat transfer situations. Therefore, in what follows, the phrases heat transfer and mass transfer will be used interchangeably.

The per-plate heat (mass) transfer measurements for plates in consecutive rows enable assessment of the thermal and hydrodynamic development characteristics of the staggered array configuration. From an examination of these results (which are tabulated in [12]), it is readily seen that the development is remarkably rapid, such that for a given operating condition, the transfer coefficients are the same for the second and all subsequent rows.

The first-row heat transfer coefficients were lower than those for the downstream rows by about 25 percent, except for the thinnest plates at the lowest Reynolds numbers, where the deviations were hardly perceptible. The lower first-row coefficient values are attributable to the absence of mixing, due to vortex roll-up and/or turbulence, which augments the coefficients of downstream rows.

The attainment of a per-plate heat transfer coefficient that is constant from row to row signals the existence of the periodic fully developed regime. Such a regime, which was already identified analytically in [13], occurs in duct flows where either the cross sectional area or the velocity boundary conditions vary periodically in the streamwise direction. The periodic fully developed regime differs from the conventional fully developed regime in that the velocity distribution does not become independent of the streamwise coordinate. Rather, the velocity field varies in the streamwise direction, but the variation repeats itself in each geometrically periodic module. Depending on the thermal boundary conditions, the temperature field may also become periodically fully developed. In the present experiments, where heat (mass) transfer occurred in only one row of the array in any given data run, the attainment of the fully developed regime is reflective of the development of the velocity field.

Fully Developed Heat Transfer Coefficients. In view of their rapid attainment, the forthcoming discussion will be focused on the fully developed transfer coefficients. These results will be presented from two perspectives. The first exhibits the variation of the Sherwood (or Nusselt) number with the Reynolds number while the second shows the Reynolds number dependence of $StSc^{0.6}$ (or $StPr^{0.6}$). Graphs in which the experimental results are plotted in terms of these variables are respectively presented in Figs. 2 and 3, where curves have been faired through the data to provide continuity. The curves are parameterized by the plate thickness-length ratio t/L.

Inspection of Fig. 2 shows that, as expected, the Nusselt (Sherwood) number increases with the Reynolds number, but the detailed nature of the increase depends on the plate thickness. For the thinnest plates,

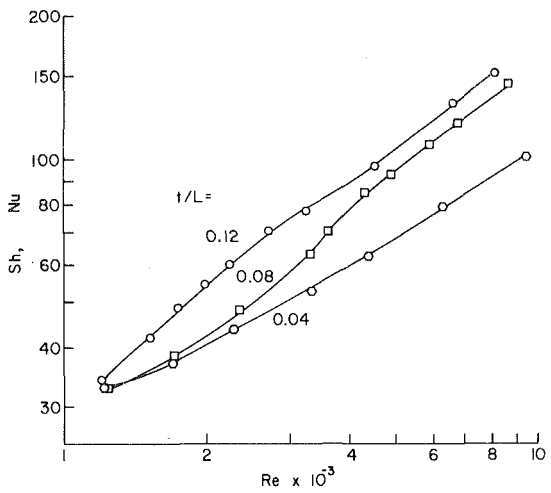

Fig. 2 Nusselt (Sherwood) number results

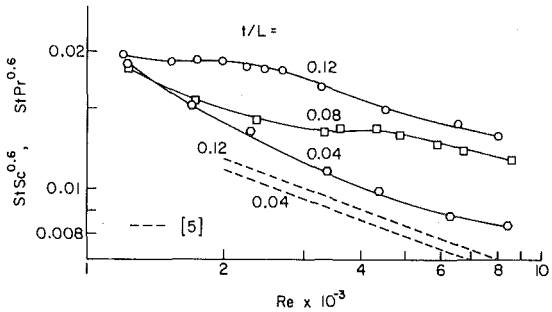

Fig. 3 Results for $StPr^{0.6}$ ($StSc^{0.6}$)

there is a smooth increase marked by a gradual steepening of slope. On the other hand, the Nusselt numbers for the intermediate plates show a relatively sharp rise in the Reynolds number range between 2000 to 5000, with more moderate rates of increase at lower and higher Reynolds numbers. The results for the thickest plates exhibit a distribution where there is a lesser slope in the range of Re between 3000 and 5000, flanked by regions of higher slope.

The aforementioned variations are reflective of the nature of the patterns of fluid flow. The flow field for the thinnest plates is expected to be the simplest of those encountered in these experiments (although it is far more complex than that of a conventional duct flow). For this case, an increase in Reynolds number activates wake-related augmentation and increased turbulence, but no sharp transitions. For thicker plates, a variety of transitions and resonances have been identified in simpler systems—a single plate or two colinear plates situated in an unbounded space [8, 14, 15]. Although the present configuration is much more complex than those of [8, 14, 15], their findings are suggestive of thickness-related flow phenomena which could be responsible for the observed irregularities in the Nu versus Re distribution of Fig. 2.

Further inspection of Fig. 2 shows that thickness has virtually no effect on the Nusselt number at the lowest of the Reynolds numbers investigated (~1200). As the Reynolds number increases, strong thickness-related augmentation is first felt by the thickest plates and then by the intermediate plates. At the larger Reynolds numbers, the Nusselt numbers for the thickest plates are 60 percent greater than those for the thinnest plates.

An alternate presentation of the present data is made in Fig. 3 in terms of $StSc^{0.6}$ (= $StPr^{0.6}$). As explained earlier, this parameter is a modified j-factor with $Sc^{0.6}$ being employed instead of $Sc^{2/3}$. Since the transformation of Sh to St involves division of the former by the Reynolds number, it is not surprising that the upsloping trend of Sh versus Re becomes a downsloping trend for $StSc^{0.6}$ versus Re.

For the thinnest plates, $StSc^{0.6}$ decreases smoothly with Re, with

a gradually decreasing slope. The shape of this curve may be regarded as conventional for plate-fin arrays [3]. The curves for the thicker plates reflect sharp transition and resonance phenomena, as discussed earlier in connection with Fig. 2. At the higher Reynolds numbers, the substantial augmentation associated with plate thickness is clearly in evidence.

Comparisons with the Literature. It is, of course, relevant to compare the present results with literature information. However, as noted in the Introduction, all of the prior work on multiplate arrays has involved full-scale or model two-fluid heat exchangers, with only overall measurements being made. Thus, there are differences in the geometrical and thermal configurations between the present experiments and those of the literature. In view of this, precise agreement between the results should not be expected.

From an examination of the literature, it was noted that on two separate occasions, first in 1950 and then in 1975, the available data for interrupted-plate heat exchangers were brought together and correlated, respectively in [2] and [5]. The data dealt with in [2] were primarily taken from limited circulation documents and since [2] does not describe the underlying experiments, there is no way to assess their merits. As assembled in [2], the j-factor results show considerable scatter. The present thin-plate heat transfer results fall within the scatter band (see Fig. 5.3 of [12]), while the high-Reynolds-number data for the intermediate plates fall high, as do the data for the thickest plates.

To assess this comparison, the parameter values of [2] were carefully examined. It was noted that for some of the data reported there, the stagger of plates was not symmetric. For the symmetric stagger data, the plates of [2] were generally longer, relative to the hydraulic diameter, than those of the present investigation. It is reasonable to expect that longer plates are less affected by enhancement due to wake turbulence and mixing than are shorter plates. This enhancement should be most effective for the thickest plates and at the higher Reynolds numbers for the intermediate plates.

A more interesting comparison can be made with the correlation of [5], which is based on more modern data than that of [2]. The data assembled in [5] show considerable scatter, and a power-law j versus Re relation was threaded through the data band. The data scatter about the correlating line is about ±15–20 percent. When the correlation equation of [5] is evaluated for the present parameters, the straight lines appearing in the lower portion of Fig. 3 result (the correlation does not apply below Re = 2000). Examination of Fig. 3 shows that for the thinnest plates, there is good trendwise agreement between the present data and the correlation of [5], with the correlation line lying about 20 percent below the data. For the other plates, the deviations are greater, both in trend and in magnitude. The outcome of these comparisons will now be rationalized.

One factor which affects the comparison is differences in geometry. In the present experiments, the sub-channel aspect ratio (span/height) is at least twenty. Among the 24 experiments reported in [5], only four had aspect ratios as large as 10–15, with the other aspect ratios being much smaller. Thus, the majority of the data reported in [5] were characterized by strong end effects, with an expected reduction in heat transfer coefficient.

Another issue worthy of mention is the fact that the data reported in [5] are averages over both the sidewalls and the fins of the participating heat exchangers. For hydrodynamic reasons, it is expected that the heat transfer coefficients for the former should be lower than those for the latter. Thus, the averaging produces coefficient values below those for the fin. In contrast, the results reported here are for the fins alone.

Still another factor of difference is the thermal boundary conditions. The data of [5] are for systems in which all surfaces are thermally active. On the other hand, in the present experiments, only a single plate participated in the heat transfer process. Multiple participating surfaces and a single participating surface yield identical heat transfer coefficients if there is a high degree of thermal mixing in the streamwise gaps between the plates. For less than perfect mixing, the single participating surface will yield higher coefficients.

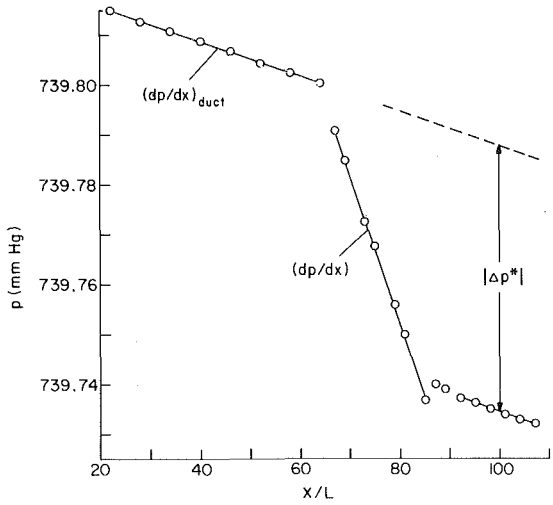

Fig. 4 Representative axial pressure distribution; Re ~ 3300, t/L = 0.04

The aforementioned factors are sufficient to explain the 20 percent deviation between the present thin-plate data and the correlation of [5]. For the thicker plates, the issue of flow blockage is relevant. From an examination of the parameters of the experiments, it was noted that both the intermediate and thickest plates of the present study gave rise to a substantially greater blockage of the sub-channel cross section than did the plates of [5]. This higher blockage is believed to be the key factor in the deviations in evidence in Fig. 3.

Pressure Drop Results

A typical graph of the axial pressure distribution along the length of the test apparatus is shown in Fig. 4 (the specific data are for Re ~ 3300 and t/L = 0.04). The ordinate shows the pressure as recorded during the experiments, whereas the abscissa is the dimensionless axial position, with x being measured from the inlet of the hydrodynamic development section and L, the plate length, serving as a reference dimension. The data shown in the figure encompass the hydrodynamic development length, the multiplate array (i.e., the test section), and the redevelopment length. As seen there, the overall pressure drop is only 0.08 mm Hg, thereby reinforcing the need for highly sensitive instrumentation.

The data for the successive sections of the apparatus lie on straight lines. The straight lines for the hydrodynamic development section and the downstream redevelopment section are parallel. Their vertical separation defines a quantity $|\Delta p^*|$ which encompasses all pressure effects caused by the presence of the array. As defined by equation (7), Δp^* forms the basis of the dimensionless per-row pressure coefficient K_p.

The pressure data for the test section also lie on a straight line. This line is steeper than the others, reflecting the higher pressure losses associated with the multi-plate array. The slope dp/dx of the line forms the basis of the apparent friction factor defined in equation (6). The rapid establishment of the linear p versus x relationship in the array is noteworthy.

The variations of f and K_p with Reynolds number are presented in Figs. 5 and 6, with t/L as the data parameter. Curves have been faired through the data to provide continuity.

From an examination of Fig. 5, it is seen that the apparent friction factor is markedly affected by the plate thickness, both with regard to magnitude and trend. In general, larger friction factors accompany the use of thicker plates. As t/L increases from 0.04 to 0.08, f increases by a factor of two at the higher Reynolds numbers, and a similar increase occurs as t/L increases from 0.08 to 0.12.

With regard to trend, f is seen to decrease gradually with Re for the thinnest plates, with a tendency to level off at the higher Reynolds numbers (i.e., for Re > 7000). The decrease is more rapid for the intermediate plates, and the leveling off is accomplished at Re = 2500.

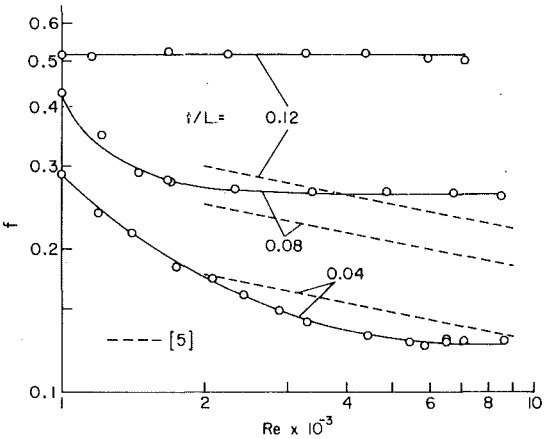

Fig. 5 Friction factor results

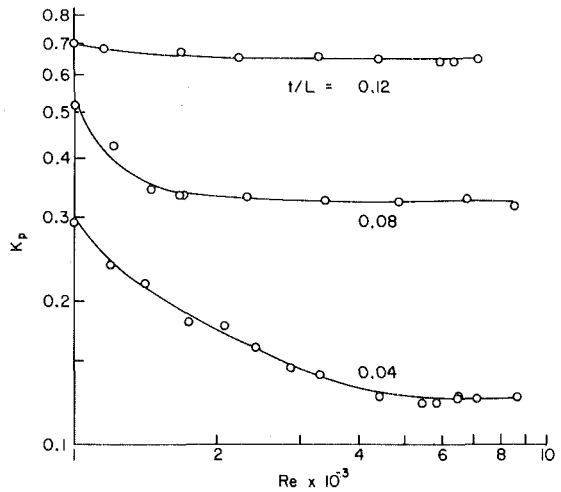

Fig. 6 Results for per-row pressure loss coefficient K_p

For the thickest plates, f is constant in the entire range investigated.

These trends are readily rationalized by noting that inertial losses (e.g., separation and recirculation) are proportional to V^2. Thus, f = constant is indicative of the dominance of inertial losses. For the thinnest plates, there is a significant contribution of wall friction at lower Reynolds numbers, while at higher Reynolds numbers the losses are due primarily to inertia. For the thickest plates, inertial losses dominate for the entire investigated range of Reynolds numbers.

The friction factor results of Fig. 5 are reminiscent of the well-known Moody diagram for turbulent pipe flows. There, the progressive evolution of the curves for pipes of different roughness is similar to the evolution of the present data with t/L.

The present friction factor results may be compared with the correlation of [5]. In [5], a power-law f versus Re relation was fitted through data which scatter by ± 50–60 percent about the correlating line in the Reynolds number range between 2000 and 9000. The use of such a power law tends to ignore the growing importance of inertial losses with increasing Reynolds number.

The correlation of [5], evaluated in terms of the parameters of the present experiments, is plotted in Fig. 5 (dashed lines). The agreement of the present thin-plate data with the correlation is remarkably good, especially when viewed with respect to the broad data band which formed the basis of the correlation. As t/L increases, the deviations grow larger, but the deviations for the intermediate plates are still within the scatter band of [5].

The fixed slopes of the correlation lines are not consonant with the leveling-off tendency of the present data. This disparity reflects, in part, the global nature of the correlation. Another factor in the disparity is the high degree of cross-sectional blockage imposed by the intermediate and thickest plates, giving rise to greater inertia-related losses than in any of the experiments brought together in [5].

The results for the dimensionless per-row pressure loss coefficient K_p are plotted in Fig. 6. This graph is remarkably similar in form to Fig. 5, and all of the trends identified for the former carry over to the latter. In this connection, it is interesting to show the relationship between the friction factor and K_p. From a careful accounting of all pressure drops and making use of Fig. 4, there follows

$$[(-dp/dx) - (-dp/dx)_{\text{duct}}]L_{\text{array}} = |\Delta p^*| + \Delta P \tag{8}$$

in which L_{array} is the streamwise length of the array, i.e.,

$$L_{\text{array}} = NL \tag{9}$$

and $N = 20$ in the present instance. The quantity ΔP is the net of the entrance losses and exit losses (or gains).

Equation (8) can be used to determine ΔP since all other quantities appearing in the equation were measured during the experiments. In general, it was found ΔP was too small to be determined with any degree of certainty so that, within the accuracy of the data, it may be deleted from equation (8). Then, upon introduction of dimensionless variables

$$f = (D_h/L)K_p + (D_h)(-dp/dx)_{\text{duct}}/\tfrac{1}{2}\rho V^2 \tag{10}$$

For the three plate thicknesses investigated, $(D_h/L) = 0.925, 0.830$, and 0.716 (thinnest to thickest). The second term on the right is positive but not very large, so that $f \simeq (1, 0.85, 0.75)K_p$ for $t/L = (0.04, 0.08, 0.12)$.

Concluding Remarks

The present per-plate heat (mass) transfer measurements in a staggered multiplate array have indicated the existence of a periodic fully developed regime whereby the per-plate Nusselt number is constant for the second and all subsequent rows. In view of this, attention was focused on the fully developed Nusselt (Sherwood) numbers.

It was found that the Nusselt number increases with the Reynolds number for all cases, but the detailed nature of the increase depends on the thickness of the plates. For the thinnest plates, there is a smooth increase marked by a gradual steepening of slope. On the other hand, for the thicker plates, the Nu vs. Re curves display segments of relatively rapid variation, indicating flow transition or resonance. In general, the Nusselt number increases with plate thickness, with greater effects in evidence at higher Reynolds numbers. These characteristics are also reflected in the distributions of $\text{StPr}^{0.6}$ versus Re.

The present heat transfer coefficients were found to lie higher than literature information based on overall heat transfer tests. The factors causing the deviations were identified.

The axial pressure distributions along the staggered-plate array are linear at all measurement points. The friction factors deduced from the data are markedly affected by plate thickness. For the thinnest plates, the f versus Re curve decreases gradually with Re and then levels off to a constant value. On the other hand, f is independent of Re for the thickest plates. The constancy of f with Re is indicative of the dominance of inertial losses associated with separation and mixing.

Acknowledgment

This research was performed under the auspices of the Power Program of the Office of Naval Research contract number N00014-76-C-0246.

References

1 Norris, R. H., and Spofford, W. A., "High Performance Fins for Heat Transfer," *Trans. ASME*, Vol. 64, 1942, pp. 489–496.

2 Manson, S. V., "Correlations of Heat Transfer Data and of Friction Data for Interrupted Plane Fins Staggered in Successive Rows," NACA TN 2237, 1950.

3 Kays, W. M., and London, A. L., *Compact Heat Exchangers*, 2nd ed., McGraw-Hill, New York, 1964.

4 Shah, R. K., and London, A. L., "Offset Rectangular Plate-Fin Surfaces—Heat Transfer and Flow Friction Characteristics," ASME *Journal of Engineering for Power*, Vol. 90, 1968, pp. 218–228.

5 Wieting, A. R., "Empirical Correlation for Heat Transfer and Flow Friction Characteristics of Offset-Fin Plate-Fin Heat Exchangers," ASME JOURNAL OF HEAT TRANSFER, Vol. 97, 1975, pp. 488–490.

6 Mochizuki, S., and Yoshinao, Y., "Heat Transfer and Friction Characteristics of Strip Fins," *Heat Transfer, Japanese Research,* Vol. 6, No. 3, 1977, pp. 36–59.

7 Adarkar, D. B. and Kays, W. M., "Heat Transfer in Wakes," Technical Report No. 55, Department of Mechanical Engineering, Stanford University, Stanford, Calif., 1963.

8 Loehrke, R. I., Roadman, R. E., and Reed, G. W., "Low Reynolds Number Flow in Plate Wakes," ASME Paper No. 76-WA/HT-30, 1976.

9 Cur, N., and Sparrow, E. M., "Experiments on Heat Transfer and Pressure Drop for a Pair of Colinear, Interrupted Plates Aligned with the Flow," *International Journal of Heat and Mass Transfer,* Vol. 21, 1978, pp. 1069–1080.

10 Cur, N., and Sparrow, E. M., "Measurements of Developing and Fully Developed Heat Transfer Coefficients along a Periodically Interrupted Surface," ASME JOURNAL OF HEAT TRANSFER, Vol. 101, 1979, pp. 211–216.

11 Sogin, H. H., "Sublimation from Disks to Air Streams Flowing Normal to Their Surfaces," *Trans. ASME,* Vol. 89, 1958, pp. 61–69.

12 Hajiloo, A., "Heat Transfer and Pressure Drop for an Array of Staggered Plates Aligned Parallel to an Air Flow," Thesis, Department of Mechanical Engineering, University of Minnesota, Minneapolis, Minn., 1979.

13 Patankar, S. V., Liu, C. H., and Sparrow, E. M., "Fully Developed Flow and Heat Transfer in Ducts Having Streamwise-Periodic Variations of Cross Sectional Area," ASME JOURNAL OF HEAT TRANSFER, Vol. 99, 1977, pp. 180–186.

14 Kottke, V., Blenke, H., and Schmidt, K. G., "The Influence of Nose Section and Turbulence Intensity on the Flow around Thick Plates in Parallel Flow," *Wärme- und Stoffübertragung,* Vol. 10, 1977, pp. 159–174.

15 Kottke, V., Blenke, H., and Schmidt, K. G., "Determination of Local and Average Mass Transfer on Thick Plates in Parallel Flow with Flow Separation and Reattachment," *Wärme- und Stoffübertragung,* Vol. 10, 1977, pp. 217–232.

Md. Alamgir[1]
Engineer,
General Electric Co.,
San Jose, Calif. 95125

C. Y. Kan[1]
Engineer,
Nutech,
San Jose, Calif. 95119
Assoc. Mem. ASME

J. H. Lienhard[1]
Professor,
Department of Mechanical Engineering,
University of Houston,
Houston, Tex 77004
Fellow ASME

An Experimental Study of the Rapid Depressurization of Hot Water[2]

New measurements of the pressure history in 5.08 and 1.27 cm i.d. tubes during extremely rapid depressurization from BWR and PWR conditions are presented. The pressure to which the present system (as well as the systems of other investigators) returns, is successfully correlated using a suggestion by Stuhmiller. New pressure undershoot data are given here, but they are rationalized elsewhere. The rate of opening, and the rarefaction wave speed, in the present system are also presented and correlated. The present study suggests that scaled replications of the early process of depressurization are reliable.

Introduction

The problem of insuring that the design of nuclear reactors is safe has led to the need for a variety of fundamental experiments. One such safety problem is that of knowing exactly what behavior would follow a guillotine break of a major BWR or PWR recirculation pipe, both from the standpoint of rate-of-loss of cooling water, and from the standpoint of the structural loads that it could impose. Data obtained in a fundamental experiment that reduces this kind of break to its most elementary form, namely the very sudden opening of a straight horizontal pipe containing hot water at BWR or PWR conditions, have helped us to understand how a system might react to such a break.

Experimental results of this kind have been obtained by Edwards and O'Brien [1], Bogartz, et al. [2–4], Rassokhin, et al. [5], Gallagher [6], Brockett, et al. [7], Allemann, et al. [8], Sozzi and Fedrick [9], and Lienhard, et al. [10]. The prediction of the behavior following such a break in a pipe is called the "Standard Problem 1."

All prior tests, except our own [10], used burst-diaphragm techniques that yielded rates of depressurization equal to or less than about 0.75 Matm/s. Our experiments involved the very rapid depressurization of water from pressures as high as 153 atm (2250 psia) and temperatures as high as 321°C, in a 1.27 cm i.d. tube. With the aid of a recently-patented opening device [11][3] we achieved depressurization rates as high as 1.8 Matm/s with correspondingly higher pressure undershoots than previous investigators reached.

Our objective in this paper is to present observations similar to those presented in [10], but to include data for a much larger tube than was used previously (5.08 cm i.d. or 16 times the cross-sectional area). With these data and those of previous investigators we shall:

- Develop a correlation of pressure undershoot which represents all previous and present data (This is done elsewhere in this journal [12].),
- Develop a general correlation of the quasi-static pressure to which the water first returns after pressure undershoot,
- Arrive at some general conclusions about the role of geometric scale and water purity upon the performance of such experiments or prototype behavior.

Experiment

Figure 1 is a schematic diagram of the 5.08 cm i.d. tube. It consists of an 11 m long stainless steel (ASTM A213) pipe connected to a 0.2 m stainless steel block, bored to match the pipe. The first 2.32 m of pipe behind the block is the heated test section; the rest of the pipe is simply present to delay the return of reflection of the rarefaction wave to the test section for about 13 ms after the pipe is opened.

The POP the QORC opening mechanism was incorporated into the front block as shown in Fig. 2. This is a fairly direct adaptation of the 1.27 cm dia pipe opening mechanism described more fully in [10, 11, 13, and 14]. But the structural design in this case had to be based on forces 16 times larger than in the previous design. It was arranged as follows.

The discharge end of the pipe was sealed with a disk-shaped plug and an O-ring. The plugs were made of mild steel or titanium. Silicon O-rings were used for temperatures up to 250°C. For higher temperature Kalrez O-rings were employed. Two titanium arms (see Fig. 2) secured the plug over the open end of the tube. A pair of L-shaped brackets were fastened to the front end on each side of the block. A common hinge pin passed through these two brackets and the arm. Each arm could be swung in and out of position about its hinge. This arrangement largely eliminated thermal-expansion-related binding between the contact surface of the plug and the arms. A weighted main cam guided on two vertical shafts was dropped from a height of 3.65 m, using a manual remote control. The falling main-cam engages a mating cam on each arm and drives them apart to release the edges of the plug. The plug is then forced out by the higher internal liquid pressure and depressurization ensues.

The test section was heated with semi-cylindrical strip heaters fitted on the outside of the pipe. To offset large vertical temperature differences resulting from natural convection only the bottom-half of the test section was heated. At a given location the water temperatures at the top, bottom and side of the pipe could generally be maintained within 5°C of each other.

Figure 3 shows the location of the pressure transducers (PT-) and the thermocouples (TC-) in the test section. In the present test, a Sundstrand 601B1 water-cooled quartz pressure transducer was mounted flush with the pipe i.d. at each of the locations PT-1 and PT-3. Transient pressure signals during depressurization, were transmitted to and stored on a pair of Tektronix 7613 storage oscilloscopes through a pair of dual mode charge amplifiers. The oscilloscopes were triggered by an external battery circuit about 3 to 5 ms prior to depressurization. A total of 11 grounded-junction sheathed chromel-alumel thermocouples were located at top, bottom, and sides of the pipe, and were connected to a common digital temperature readout device that could be read accurately within 0.6°C

The test preparation proceeded as follows: the discharge end of the pipe was sealed using the plug and the arm, and the falling weight was positioned at its upper level. The pipe was evacuated to a pressure of about 0.05 atm using the vacuum pump. The pipe was then filled with double distilled water that had been degassed by boiling for about an hour. All the valves were closed and the system was cold-tested at high pressure for possible leaks. Next the test section heaters were switched on. While the water was being heated the system pressure, read from a standard Bourdon gage (accuracy ± 2 psi), was maintained 20 to 30 atm above the saturation pressure at the current water temperature. For a typical hot water test the heating duration was about 3 to 5 hr. When the desired temperature and pressure were reached the heaters

---

[1] This work was done when the authors were with the Mechanical Engineering Department of the University of Kentucky, Lexington, KY.

[2] The present work was done under support of the Electric Power Research Institute (Contract No. RP-687-1) with B. Sehgal as Contract Manager.

[3] Called *POP the QORC* (Push Out the Plug in the Quick Opening Release Configuration)—the ultimate nuclear acronym.

Contributed by the Heat Transfer Division for publication in the JOURNAL OF HEAT TRANSFER. Manuscript received by the Heat Transfer Division October 29, 1979.

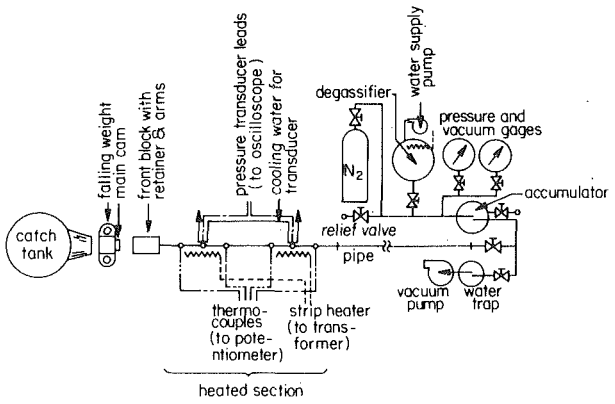

Fig. 1 Layout of apparatus for 5.08 cm i.d. pipe experiment

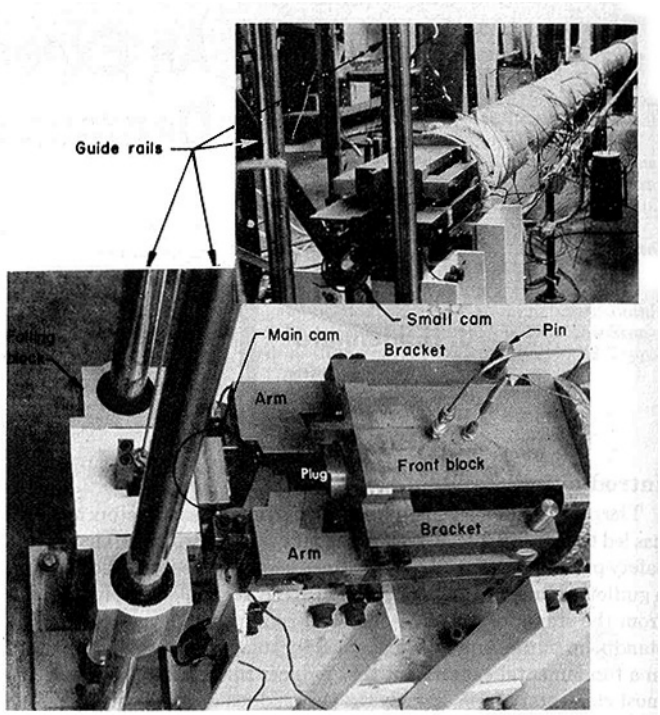

Fig. 2 Front block with plug release mechanism. Inset shows release configuration in relation to entire apparatus.

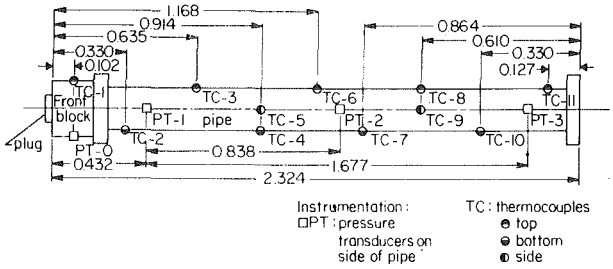

Fig. 3 Locations of thermocouples and pressure transducers in the heated section of the pipe (All dimensions are in meters.)

were switched off and some time (usually 30 s) was allowed for reversal of heat flow direction. Finally, the falling weight was released by remote control. The depressurization began as the plug was released and the transient pressure history at the PT locations was stored on the oscilloscope screen during the first 20 ms or so. These traces were subsequently photographed.

The data reported in this paper also include some new results obtained in the older 1.27 cm i.d. apparatus. Since these experiments and their accuracy are described in detail by Alamgir [14] and in references [10] and [13], we simply present the results here without further comment.

Results and Discussion

Results. The initiation of depressurization is accompanied with the generation of a rarefaction wave that propagates away from the pipe-break location into the high pressure liquid. At any axial location of the pipe, the pressure starts to change upon the arrival of this wave. Figure 4 is a representative selection of pressure-time histories in the 5.08 cm i.d. pipe for the two transducer locations PT-1 and PT-3. Included alongside the traces are the pressure and temperature of the water just prior to decompression. The latter temperature was linearly interpolated between the adjacent thermocouples.

The pressure transients show some characteristic features that have already been displayed in [10] and [13]: As the retainers move across the plug faces the pressure drops a little and rather slowly. Once the plug edges are cleared the pressure falls with great rapidity, almost linearly with time, to well below the saturation pressure. This rapid depressurization rate, designated as Σ matm/s, is either totally halted or else greatly attenuated as a result of bubble nucleation. The drop of pressure below p_{sat}, which we call the *pressure undershoot*, has been correlated [12] as a function of the initial water temperature and the depressurization rate in the superheated liquid, Σ'.

Following the pressure undershoot, bubble growth causes the pressure to recover, in most cases nearly exponentially with time, to a quasi-static level $p_{qs} < p_{sat}$. This happens within a few milliseconds of the undershoot and the level persists for 20 ms or longer. In the present 5.08 cm i.d. pipe experiments with hot water, the pressure traces do not show any sign of the return of the reflected rarefaction wave since we used a long pipe.

Table 1 lists the initial test conditions, the measured Σ and Σ', the measured nucleation or minimum pressure and the rarefaction speed for various runs.[3] The measured values of Σ and Σ' were fairly close to one another in the 5.08 cm i.d. pipe tests. Table 2 gives new test data[3] obtained in the 1.27 cm pipe.

The Rate of Depressurization, Σ. The rate of depressurization is a representation of how fast a break area is created or how quickly

[3] Estimated accuracies for the original and reduced data are, for Σ and Σ': ±15 percent, all pressures: ±2 percent of p_i, all temperatures: ±0.6°C.

Nomenclature

c = speed of sound in water
c_{pf} = specific heat of water
D = pipe or tube diameter
h_{fg} = latent heat of vaporization of water
Ja_{qs} = a Jakob number defined in equation (5)
m = mass of plug divided by cross-sectional area of pipe
p, p_i, p_n, p_{qs}, p_{sat} = pressure, initial system pressure prior to depressurization, local minimum pressure reached by system immediately following depressurization, quasi-static pressure to which system momentarily recovers following depressurization, saturation pressure at T_i.
R = radius of a bubble
T, T_i, T_{qs} = temperature, initial system temperature, temperature at p_{qs}
t = time
$V_{eff} = \kappa c p_i$
v = specific volume
$v_p = \kappa c(p_i - p)$
δ = effective thickness of cooled layer around a growing vapor bubble
κ = isothermal compressibility of water
ν = kinematic viscosity of water
ρ, ρ_f, ρ_g = density, density of liquid, density of vapor
Σ, Σ' = the approximately constant rate of depressurization from p_i to p_n, Σ evaluated between p_{sat} and p_n
$\tau = m\kappa c$

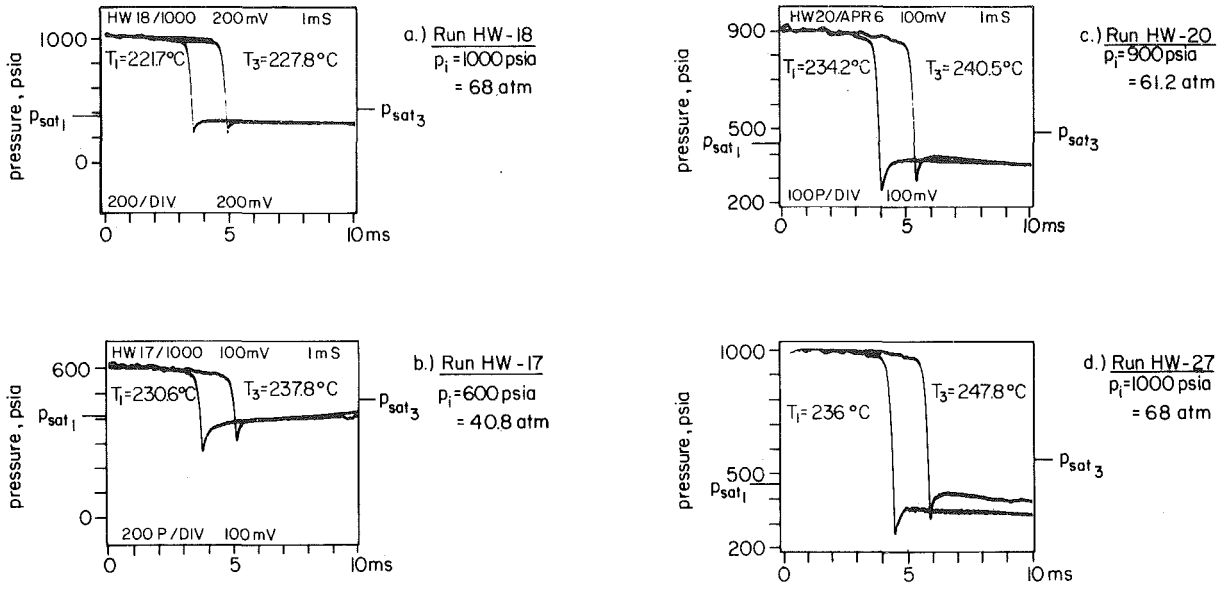

Fig. 4 Pressure-time histories at PT-1 (left trace) and PT-3 (right trace) locations in the 5.08 cm i.d. pipe

Table 1 Experimental results for the 5.08 cm i.d. pipe

Run No.	Pressure p_i (atm)	Interpolated Temperatures T_i PT-1 (°C)	PT-3 (°C)	Saturation Pressure Psat PT-1 (atm)	PT-3 (atm)	Minimum or Nucleation Pressure Pn PT-1 (atm)	PT-3 (atm)	Overall Depressurization Rate Σ PT-1 (Matm/sec)	PT-3 (Matm/sec)	Depressurization Rate in Superheated Water Σ' PT-1 (Matm/sec)	PT-3 (Matm/sec)	Measured Rarefaction Speed C (m/sec)	Plug Mass Per Unit Area m (gm/cm²)	Water Condition
CW-01	17	21	21	0.024	0.024	2.38	1	0.017	0.02	–	–	1448	12.38	Unboiled, distilled
CW-02	34	21	21	0.024	0.024	5.1	1	0.061	0.065	–	–	1505	12.38	Boiled, distilled
CW-04	6.8	22	22	0.027	0.027	1.63	2.31	0.0014	–	–	–	1450	13.57	Unboiled, distilled
HW-01	17	141	154	3.674	5.307	2.72	4.01	0.048	0.046	0.077	0.075	1500	12.38	Boiled tap water
HW-21	3.4	117.2	121.7	1.793	2.066	1.5	1.84	0.002	0.00028	0.002	0.00028	–	13.43	Boiled, distilled
HW-26	7.15	135	140.6	3.089	3.623	2.25	3	0.0067	0.0056	0.0067	0.0056	1449	13.43	"
HW-24	6.12	140.6	145.6	3.623	4.164	2.96	3.47	0.005	0.0058	0.01	0.0037	1480	13.57	"
HW-22	10.2	144.4	153.1	4.04	5.13	3.40	4.15	0.0136	0.0147	0.023	0.0147	1463	13.43	"
HW-23	10.9	148.6	157.8	4.55	5.76	3.54	4.63	0.0194	0.0167	0.0234	0.018	1429	13.43	"
HW-13	58	167.2	169.4	7.35	7.69	4.63	4.7	0.032	0.033	0.032	0.033	1430	13.57	"
HW-15	68	201.7	208.3	15.87	17.83	10.21	11.57	0.211	0.195	0.227	0.199	1327	13.57	"
HW-10	68	215.6	216.7	21.03	21.43	12.59	17.28	0.212	0.204	0.212	0.209	1256	12.38	Unboiled, distilled
HW-18	68	221.7	227.8	23.54	26.54	15.11	15.99	0.220	0.224	0.196	0.203	1255	13.43	"
HW-16	68	226.7	234.4	26	29.94	16.47	17.69	0.259	0.255	0.259	0.255	1245	13.57	"
HW-25	40.83	228.9	234.4	27.05	29.94	18.03	19.39	0.156	0.135	0.156	0.135	1188	13.43	Boiled, distilled
HW-17	40.83	230.6	237.8	27.76	31.78	19.05	22.11	0.099	0.098	0.099	0.098	1245	13.43	"
HW-20	61.24	234.2	240.6	29.76	33.34	17.69	20.41	0.170	0.176	0.170	0.176	1217	13.43	"
HW-27	68	236.1	247.8	30.84	37.80	18.17	22.6	0.189	0.182	0.189	0.182	1189	13.88	"
HW-14	68	251.7	257.2	40.35	44.23	27.22	30.62	0.186	0.18	0.199	0.193	1191	13.57	"
HW-12	68	253.3	257.2	41.51	44.23	–	31.30	–	0.133	–	0.133	–	12.38	"
HW-19	102	–	239.4	–	33.07	–	20.41	–	0.3	–	0.314	–	13.43	"
HW-07	57.15	211.1	221.1	19.19	23.34	12.25	15.31	0.245	0.251	0.245	0.251	1311	7.03	"
HW-30	63.96	251.9	258.9	41.51	45.50	28.78	30.62	0.136	0.143	0.136	0.156	1159	13.57	"

the high pressure liquid is allowed to expand. The magnitude of Σ thus depends on the extent of inertia associated with the break that the expanding liquid has to overcome. For our experiments, a dynamic force balance between the moving plug and rarefied liquid behind it yielded[4] (see [10])

$$\frac{dp}{dt} = -\frac{p}{\tau} \tag{1}$$

where the velocity of the expanding liquid (which also equals that of the plug) is $v_p = \kappa c(p_i - p)$ and $\tau \equiv m\kappa c$. A characteristic depressurization rate, $p_i/m\kappa c$, and an effective liquid velocity, $V_{\text{eff}} = \kappa c p_i$, can then be identified as parameters that govern Σ. In the preceding one-dimensional considerations we have ignored the liquid viscosity and the size of the system.

When these system variables are used, we may write the functional form for Σ as

[4] Certain undefined terms in this section are defined in the Nomenclature. In [10], equation (1) had an area-ratio factor that would arise if the liquid jet immediately expanded to the plug diameter. Recent photographic evidence suggests that this expansion does not occur.

Table 2 New data for the 1.27 cm i.d. Pipe

Run No.	Pressure Transducer Location	Pressure p_i (atm)	Temperature (°C)	Saturation Pressure p_{sat} (atm)	Minimum or Nucleation Pressure p_n (atm)	Overall Depressurization Rate Σ (Matm/sec)	Depressurization Rate in Superheated Water Σ' (Matm/sec)	Water Condition
AHW07	PT-1*	6.46	137.2	3.295	2.729	0.0075	0.0079	distilled and boiled
AHW06		7.14	129.4	2.622	2.177	0.0067	0.007	"
AHW08		49.3	223.9	24.65	11.57	0.331	0.348	"
AHW05		65.3	264.4	49.77	23.14	0.492	0.517	"
AHW04	PT-2	68	232.8	29.04	17.69	0.258	0.272	distilled but unboiled
AHW03	PT-2	68	260	46.33	29.26	0.363	0.375	"

$$\Sigma = fn\left[\frac{p_i}{m\kappa c}, V_{\text{eff}}, \nu, D\right] \tag{2}$$

where ν is the kinematic viscosity of water and D, the pipe i.d., is used as the characteristic size of the system. Dimensional analysis results in two dimensionless groups consistent with the Pi-Theorem.

$$\frac{\Sigma m\kappa c}{p_i} = fn\left(\frac{V_{\text{eff}}D}{\nu}\right) \tag{3}$$

where the group $\kappa c p_i D/\nu$ may be called a depressurization "Reynolds number". The isothermal compressibility of water $\kappa \equiv -(1/v)(\partial v/\partial p)_T$ has been calculated[5] from the equation of state for water given by the 1967 E.R.A. Steam Tables [15] and is presented in Fig. 5.

Figure 6 shows that the nondimensional depressurization rate, $\Sigma m\kappa c/p_i$, in all of our tests increases monotonically with $V_{\text{eff}}D/\nu$. The overall behavior of the data supports the validity of equation (3). The maximum value of the ordinate in the figure is given by equation (1) as unity. The (+) symbols are for certain 1.27 cm i.d. pipe tests with a slit or orifice constriction in the pipe. For these data the Reynolds number was based on either the orifice diameter (0.52 cm) or square-root of the slit area (0.45 cm). Ninety percent of all data lie within ±30 percent of the faired curve.

Speed of the Rarefaction Wave. In pipe decompression experiments the rarefaction speed can exceed the speed of sound in the liquid as the result of bonding between the liquid and the steel pipe wall. Evidence of this fact was provided by the measured rarefaction speed in our 1.27 cm i.d. pipe tests [10]. 5.08 cm pipe rarefaction speed data, shown in Fig. 7, also indicate a similar trend, but the speed augmentation is less because the ratio of the theoretical mean sound speeds for the two pipes (see equation (5) of [10]) is $\bar{c}_{5.08}/\bar{c}_{1.27} = 0.975$.

Quasi-Static Pressure Recovery Following the Pressure Undershoot. We have noted that the system pressure recovers to a quasi-static level, a few milliseconds after the plug is released. This pressure is less than p_{sat} at the initial water temperature. The time dependence of this recovery process appears to be related to bubble growth rate in the associated variable pressure field and to the gross liquid motion around the location of interest. However, for the purpose of predicting the recovery pressure level, p_{qs}, we use the following idealized model, developed by modifying a similar analysis by Stuhmiller [16].

Stuhmiller considered a growing vapor bubble of radius R with the vapor saturated at the current liquid pressure. The thermal energy required to grow this bubble is provided by cooling of a thin liquid layer around the interface. Instead of accepting Stuhmiller's suggestion that a lump-cooling of this layer takes place, we consider the existence of a time-dependent temperature profile in this developing thermal layer. We define $T_{qs} \equiv T_{sat}(p_{qs})$ and observe that the temperature increases asymptotically from this value to T_i with x, the radial distance from the bubble interface. Thus

[5] We are grateful to Amir Karimi for this calculation.

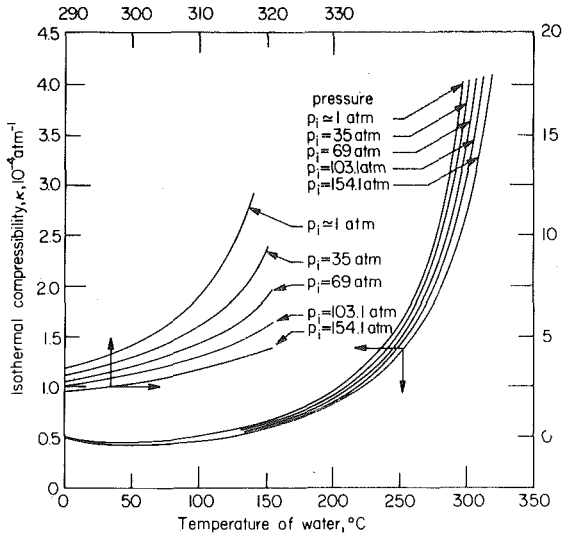

Fig. 5 The isothermal compressibility of subcooled and moderately superheated water

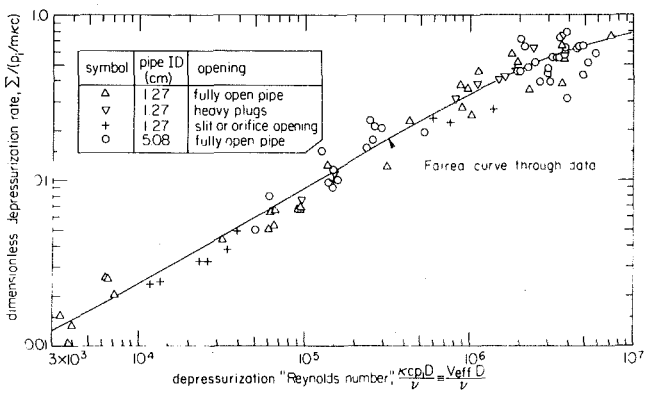

Fig. 6 Correlation of all opening-rate data for both pipes using the POP the QORC device

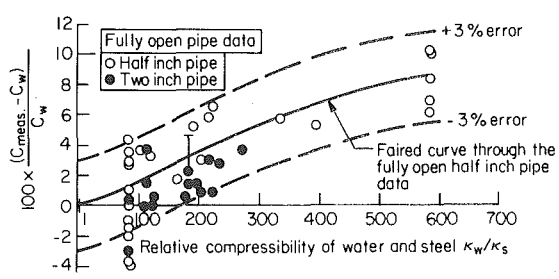

Fig. 7 Deviation of measured rarefaction speed from the calculated sound speed

$$\frac{4}{3}\pi R^3 \rho_g h_{fg} = 4\pi R^2 \rho_f c_{pf} \int_0^\infty (T_i - T)dx \tag{4}$$

where ρ_f, ρ_g, c_{pf} and h_{fg} are the saturated liquid and vapor densities, the liquid specific heat, and the latent heat of vaporization, all evaluated at T_i. Drawing an analogy with the displacement thickness in a hydrodynamic boundary layer, we introduce an energy thickness, δ, defined as

$$\delta(T_i - T_{qs}) = \int_0^\infty (T_i - T)dx \tag{5}$$

Combining equation (5) with equation (4), we get

$$\frac{4}{3}\pi R^3 \rho_g h_{fg} = 4\pi R^2 \rho_f c_{pf} \delta (T_i - T_{qs}) \tag{6}$$

Equation (6) can be rewritten to give a volumetric Jakob number

$$\mathrm{Ja}_{qs} \equiv \frac{\rho_f c_{pf}(T_i - T_{qs})}{\rho_g h_{fg}} = \frac{1}{3}\frac{R}{\delta} \tag{7}$$

The temperature T_{qs} can be calculated from equation (7) if we know the ratio of the bubble radius R to the equivalent thickness, δ, at p_{qs}.

The liquid around the growing bubble interface is not stationary, but agitated, as a result of instabilities that arise when a less dense vapor is accelerated into a dense liquid. Stuhmiller invoked a turbulent diffusivity argument and obtained $\delta/R \cong 0.265$. If we accept this value we get a constant value of Ja_{qs} from equation (7)

$$\mathrm{Ja}_{qs} = \frac{\rho_f c_{pf}(T_i - T_{qs})}{\rho_g h_{fg}} \simeq 1.26 \tag{8}$$

This result is based on several assumptions and should really only be viewed as a correlation in which 1.26 might be replaced with an adjustable constant. That this constant subsequently turns out to be exactly 1.26, is no doubt fortuitous.

Equation (8) immediately allows us to evaluate the recovery pressure level, p_{qs}, as p_{sat} at T_{qs}, once the initial water temperature T_i is known. Figure 8 shows the variation of the predicted p_{qs} with T_i for water as the solid curve, with ρ_f, c_{pf}, ρ_g and h_{fg} being evaluated as saturation properties at T_i. The saturation pressure, p_{sat} (T_i), is shown as the dashed curve. Figure 8 verifies an important claim, made previously by Brown [17], that $p_{qs} \neq f_n$ $(\Sigma', p_n$, or other opening-rate parameters.)

The difference, $p_{\mathrm{sat}}(T_i) - p_{qs}$, is a monotonically increasing function of the initial temperature T_i that dwindles to a negligible value only at very low temperatures. Experimental data for p_{qs} from the many available sources have been plotted on the same graph and they show very good agreement with the predicted curve. They match the prediction with an rms deviation of 4.27 percent and maximum deviation of 14 percent.

A point may be made about the data of Sozzi and Fedrick [9], shown by plus symbols. Their depressurization apparatus used a short pipe (3.25 m or 0.56 m) connected to a very large reservoir. In their experiments the pressure first recovered to a plateau below the saturation pressure and then was kicked up above the saturation pressure. We suspect the latter behavior to be the combined result of the presence of the reservoir and the reflected rarefaction wave interacting with the recovering pressure. When these effects are absent, the first pressure plateau, which we have chosen to plot, would represent the true recovery pressure.

Correction of previously Reported 1.27 cm Pipe PT-1 Temperatures. The high temperature blowdown tests with the half-inch pipe were carried out with a water cooled front section of the pipe [10]. This was necessary to avoid the thermal expansion binding between the plug and the retainers. The temperatures at the first transducer (PT-1) location were obtained by extrapolating the thermocouple readings without realizing how abruptly the water-cooling caused the temperature to change, near it. It now appears that the reported PT-1 temperatures were high.

The true local temperature, T_i, for these runs, can be estimated using the measured value of the quasi-static pressure p_{qs} (and hence

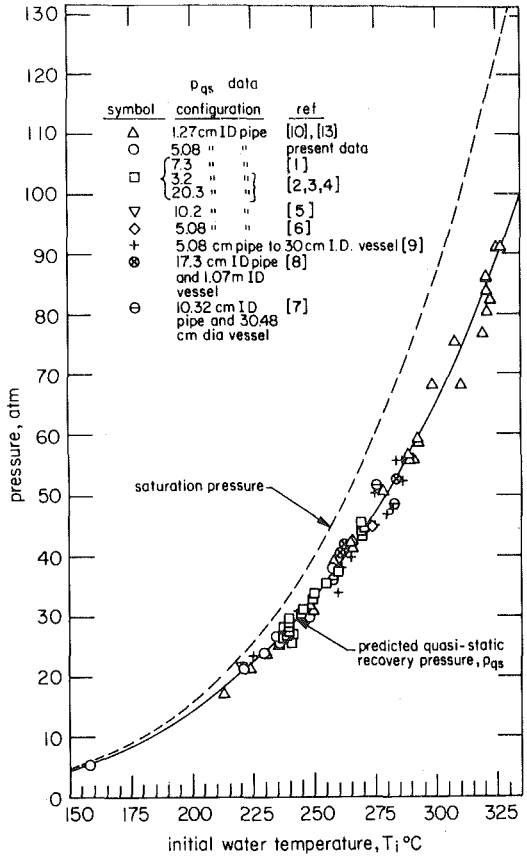

Fig. 8 Comparison of predicted quasi-static recovery pressure with experimental data

$T_{qs} = T_{\mathrm{sat}}(p_{qs})$) in equation (8). Table 3 shows the correct temperatures for the eleven tests in question and the magnitude of the errors in the originally measured temperature range from 8.3°C to 17.3°C. These data, of course do not appear in Fig. 8.

The Problem of Dimensional Scale and Water Purity in Reactor Blowdown Experiments. We present correlations of four different dependent variables here and in [12]. These are: (1) pressure undershoot, (2) quasistatic pressure recovery, (3) rarefaction wave speed, and (4) opening rate.

The first two parameters are the most important for the nuclear engineer who is interested in predicting the early blowdown behavior. Data for these parameters, measured over a *256-fold* variation of pipe area, have been correlated without showing any apparent influence of pipe size.

The rarefaction speed can be increased by a few percent of the speed of sound by pipe size, only if the pipe is quite small and thick-walled. The opening rate is a *dependent* variable in our scheme of experimentation, and dimensional scale must be included in its correlation. However, in most nuclear safety analyses it must be specified as an independent variable.

Thus, the present results suggest that reduced-scale modeling is entirely reliable, at least for specifying the primary features of the initial response of hot water to sudden depressurization.

Furthermore, the present experiments include 10 cases in which the water was either undistilled, or unboiled prior to pressurization, or both. These data correlate perfectly well with the other data, some of which reflect different preparation schemes from that which we normally used. Probably, the act of bringing water to BWR and PWR conditions constitutes a more significant preparation (in terms of, say, degassing) than anything that can be done at atmospheric pressure. Of course these remarks do not apply if a system is exposed[6] to large amounts of soluble noncondensible gases at p_i.

Table 3 Correction of 11 values of T_i at PT-1 previously reported in [10]

Run No.	Initial Pressure p_i (atm)	Temperature at PT-1 Location T_i Previously Reported in [10] (°C)	Temperature at PT-1 Location T_i Corrected Using Equation (6) (°C)	Measured Minimum or Nucleation Pressure p_n (atm)	Overall Rate of Depressurization Σ (Matm/sec)	Rate of Depressurization in Superheated Water Σ' (Matm/sec)
51	102	268	256.6	10.2	1.36	1.65
45	102	271	262.9	10.2	1.12	1.35
42	144.3	290.6	282.2	25.2	1.18	1.48
30	153.1	293.3	278.1	29.3	1.05	1.05
50	153.1	293.3	281.1	20.4	1.49	1.74
44	153.1	293.3	282.8	27.9	1.41	1.41
64	153.1	296	287.2	26.5	1.62	1.62
4-HV	68	231.1	215	12.9	0.15	0.12
2-H	102	262.8	246.1	23.1	0.19	0.21
5-HV	102	263.3	246.1	20.3	0.54	0.54
3-H	129.3	302.2	287	42.2	0.3	0.3

Conclusions and Summary

1 New data that bring the element of dimensional scale into the present experimental program are presented. They show the initial response of a pressurized hot water pipe to sudden depressurization.

2 These data include new pressure undershoot data that are correlated in a companion paper [12].

3 The data show that after pressure undershoot, the system pressure recovers to within about 4.2 percent of a sub-saturated value which corresponds to T_{qs} as correlated by equation (8).

4 The most important aspects of system response following sudden depressurization appear not to be influenced by dimensional scale, even when the pipe is as small as 1.27 cm i.d.

5 No perceptible influence of water preparation upon system response has been revealed by these tests.

6 The rarefaction wave speed is very slightly increased by the pipe walls. This increase is consistent with our discussion of such behavior in [10].

7 The opening rate in experiments such as these can be predicted within ±30 percent by the correlation in Fig. 6.

References

1 Edwards, A. R., and O'Brien, T. P., *Journal of the British Nuclear Energy Society*, Vol. 9, 1970, p. 125.

2 Borgartz, B. O., Goodman, R. M. E., O'Brien, T. P., Rawlingson, M., and Edwards, A. R., "Depressurization Studies, Phase 2: Results of Tests 115 and 130," UKAEA Report SRD-R-115, 1978.

3 Ibid, "Depressurization Studies, Phase 3: Results of Tests 144 and 145," UKAEA Report SRD-R-77, 1977.

4 Ibid, "Depressurization Studies, Phase 3: Results of Tests 142 and 143," UKAEA Report SRD-R-76, 1977.

5 Rassokhin, N. G., Kuzevanov, V. S., Tsiklauri, G. V., Marinchek, Z., and Sella, J., "Critical Conditions with Unsteady Outflow of a Two-Phase Medium with a Pipeline Break," *Teplofizika Vysokikh Temperatur*, Vol. 15, No. 3, 1977, p. 589.

6 Gallagher, E. V., "Water Decompression Analysis for Blowdown of Nuclear Reactors," IITRI-578, IIT Research Institute, Chicago, 1970.

7 Brockett, G. F., Curet, H. D., and Heiselmann, H. W., "Experimental Investigations of Reactor System Blowdown," IN-1348, Idaho Nuclear Corporation, 1970.

8 Allemann, R. T., McElfresh, A. J., Neuls, A. S., Townsend, W. C., Wilburn, N. P., and Witherspoon, M. E., 1971a USAEC Report BNWL-1463 and 1971b USAEC Report BNWL-1470.

9 Sozzi, G. L., and Fedrick, N. A., "Decompression Waves in a Pipe and Vessel Containing Subcooled Water at 1000 psi," NEDE-13333, General Electric Company, Mar. 1973.

10 Lienhard, J. H.; Alamgir, Md.; and Trela, M., "Early Response of Hot Water to Sudden Release from High Pressure," ASME JOURNAL OF HEAT TRANSFER, Vol. 100, 1978, pp. 473–479.

11 Lienhard, J. H., and Borkar, G. S., "Quick Opening Pressure Release Device and Method," U.S. Patent No. 4, 154, 361, May 15, 1979.

12 Alamgir, Md., and Lienhard, J. H., "Correlation of Pressure Undershoot During Hot-Water Depressurization," under review.

13 Borkar, G. S., Trela, M., and Lienhard, J. H., "A Rapid Hot-Water Depressurization Experiment," EPRI Report NP-527, Dec. 1977.

14 Alamgir, Md., "Initial Response of Pressurized Hot Water in A Suddenly Opened Pipe," Doctoral dissertation, Univ. of Kentucky, Mechanical Engineering Department, 1979.

15 Electric Research Association, *1967 Steam Tables*, St. Martin's Press, New York, 1967.

16 Stuhmiller, J. H., "The Physical Process in Pipe Blowdown," *Computational Techniques for Non-Equilibrium Two-Phase Phenomena*, (R. W. Lyczkowski and W. Mathers, eds.) National Heat Transfer Conference, Salt Lake City, Utah, 1977.

17 Brown, E. A., "Experiments on the Explosive Decompression of Water," Armour Research Foundation Report ARF 4132-9, Nov. 1959.

[6] While our system is pressurized by N_2 at the cold end of the pipe, the pressurizer is too far from the test section to influence it.

O. C. Jones, Jr.
Department of Nuclear Energy,
Brookhaven National Laboratory,
Upton, NY 11973
Mem. ASME

Flashing Inception in Flowing Liquids

The inception of net vaporization in flashing flows is examined. It is suggested that the flashing inception can be expressed as two additive effects. One is due to the static decompression which is a function of the initial temperature and also of the expansion rate. The other effect which is a function of Reynolds number and flashing index, is due to the turbulent fluctuations of the flowing liquid. It is shown that by taking a three standard deviation band on the turbulent velocity fluctuations, an adequate representation of the inverse mass flux effect on flashing inception for existing data is obtained. The turbulence effects are combined with the correlation of Alamgir and Lienhard to provide predictive methods recommended for the case where both static and convective decompression effects exist.

Introduction

In the event of a leak in a hot high pressure water system, the subcooled liquid will undergo decompression as it flows from the system to the surroundings. This may be a geometrically controlled decompression such as in the case of leakage through a relief valve subsystem. On the other hand, the decompression may be uncontrolled as in the case of a system rupture. In many cases, subcooled water flowing towards the leak experiences decompression to pressures below the saturation pressure and at some lower pressure begins to flash to vapor. Flashing may occur in regions of constant cross section such as in pipes, or in regions of varying geometry such as valves, fittings, or regions of a break in the piping system itself. In cases of concern from a safety standpoint, the resulting two-phase mixture will experience flow limitations due to choking. The actual discharge flow rate, which is especially sensitive to the vapor content, directly affects the system response. This is especially true in nuclear steam supply systems where the heat transfer characteristics of the fuel are quite sensitive to the system liquid inventory. At present there is no general model for the vapor generation rate under nonequilibrium conditions, or for any of the three major factors which affect the void development under such conditions: flashing inception point, interfacial area available for vaporization, and rate of mass exchange per unit interfacial area. It is the purpose of this paper to address the question of flashing inception as affected by velocity effects. It will be shown that a model based on turbulent fluctuation intensity does a reasonably acceptable job of accounting for these effects when applied to the few data available.

Background

It is well known that the mass flow rates in critical flow conditions are highly dependent on the vapor content of the flow. Saha [1] has reviewed and evaluated critical flow research concluding that currently accepted equilibrium models underpredict critical flows for "short" pipes especially for subcooled or nearly saturated sources. While thermal nonequilibrium must be taken into account for short pipes, it is not clear how the combination of length and diameter enters the picture. Wu, et al. [2] have shown that a model based on spherical bubble growth in fields of variable superheat adequately predicts the data of Reocreux [3] for void fractions less than 0.3. These predictions require accurate knowledge of both the voiding inception point and an initial nucleation density parameter. It is well known [4] that the initial degree of superheat markedly affects bubble growth in both constant and variable pressure fields. The degree of superheat has also been shown to play a strong role in void development in flashing critical flows [2]. Since the point at which flashing inception occurs directly affects the initial superheat, the flashing inception can also be expected to play a strong role in the critical mass flow rates under flashing conditions.

Little work has been accomplished examining the point of flashing inception. Seynhaeve, et al. [5] ran experiments with inlet temperatures between 111 and 167°C and at mass fluxes between 10 and 20 $Mg/m^2 \cdot s$. They determined the superheat at flashing inception to behave inversely with mass flux. Although their data were quite scattered, the superheat apparently decreased to almost zero at the higher mass fluxes, and even became negative in a few cases. In their evaluation of Reocreux's 1.74 bar data, Wu, et al. [2] obtained results similar to those shown in Fig. 1. In this figure, the superheat is expressed in terms of the overexpansion at the inception point denoted by Δp_{Fi}. (Note that throughout this paper the terms overexpansion and superheat are used interchangeably and are, of course, coupled along the saturation line.) Unfortunately, no other experiment appears to have been undertaken allowing suitable definition for determination of flashing inception superheats.

The boiling inception and onset of net vapor generation in flowing liquids has undergone much scrutiny in the case of heating, having been the subject of such well-known works as those of Hsu [6], and of Saha and Zuber [7], among others. Unfortunately, flashing inception does not appear to be characterized by models applicable to heated liquids where the superheat is generally confined to the wall

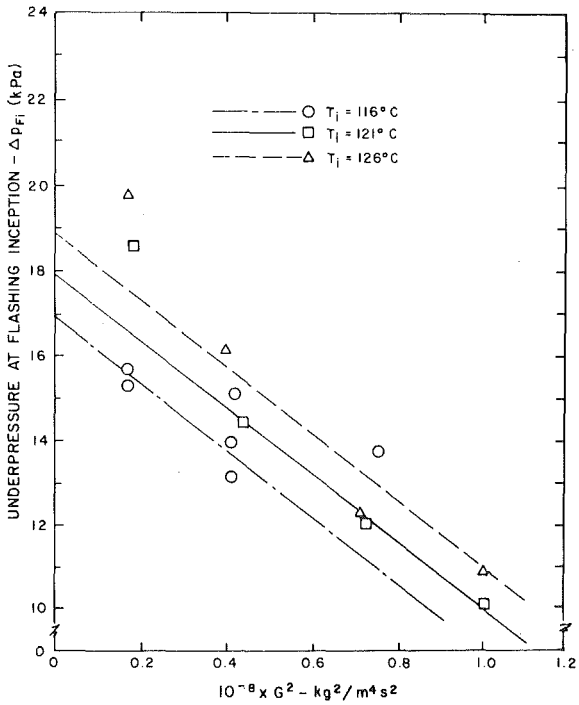

Fig. 1 Observed mass flux effect on overexpansion (underpressure) at flashing inception for the data of Reocreux [3]

Contributed by the Heat Transfer Division for publication in the JOURNAL OF HEAT TRANSFER. Manuscript received by the Heat Transfer Division April 18, 1980.

layer in bulk subcooled liquids. Instead, bulk superheating occurs prior to flashing inception while the initial voiding still seems generally relegated to the wall layer.

In the case of static liquids undergoing rapid decompression, the work of Lienhard, et al. [8], and Alamgir and Lienhard [9] are clearly applicable for predicting the flashing inception superheat in nonflowing systems. Reference [8] showed the limit of overexpansion to be dependent on the fluid expansion rate (rate of decompression) prior to nucleation up to a value of about 65 percent of the spinodal limit. This limit itself depends on the initial temperature. A correlation based on a wide range of data was proposed [9] for the underpressure in the form

$$\Delta p_{Fio} = \Delta p_{Fio}{}^{\circ} \sqrt{1 + 13.25\Sigma'^{0.8}} \tag{1}$$

where the expansion rate was given in units of Matm/s. The limiting value at vanishing decompression rates was given as a constant dependent on the initial temperature of the fluid only in the form

$$\Delta p_{Fio}{}^{\circ} = 0.258 \frac{\sigma^{3/2}}{\sqrt{kT_c}} \frac{T_r{}^{13.76}}{\left(1 - \frac{v_f}{v_g}\right)} \tag{2}$$

where σ is the surface tension, T_c the critical temperature, T_r the initial reduced temperature, v_f and v_g the saturation specific volumes of the liquid and vapor, respectively, at T_r, and k is Boltzman's constant. This correlation predicted the static undershoot to an rms accuracy of 10.6 percent in the ranges $0.515 < T_r < 0.935$ and $0.004 < \Sigma' < 1.803$ Matm/s. A suggestion was made that imperfections in cleaning and preparation of a given system as well as history of preparation may be important. However, this appears unlikely—at least within their data scatter—since several different systems were indeed correlated.

The superheats predicted by Alamgir and Lienhard [9] range up to 50°C or higher at the highest expansion rates and initial temperatures. Under such severe nonequilibrium conditions, the actual vapor content can be substantially reduced below equilibrium values and actual flow rates very much larger than those can be predicted on the basis of an equilibrium or near equilibrium critical flow model. Even at very low expansion rates, superheats of over 10°C are predicted and observed in fact. The existance of such superheats at flashing inception can be a major factor in inaccurate prediction of two-phase critical flow rates with subcooled initial (or inlet) conditions.

Another major factor identified in the correlation of reference [9] is the direct behavior of inception superheat predicted with increasing expansion rate. This trend, although in agreement with normally expected homogeneous nucleation behavior, is in direct opposition to the flowing data shown in Fig. 1, and the data of reference [5]. Unfortunately, however, the decompression rates in these latter experiments were approximately three orders of magnitude slower than those upon which the correlation of [9] is based.

Decompression times in the static systems data of references [8] and [9] are generally less than a millisecond. Decompression times in the flowing systems of [3] and [5] range up to several tens or hundreds of milliseconds. The only other differences between the static and dynamic flashing systems seem to be those of fluid motion. Of the factors influenced by these motions, the turbulent pressure fluctuations appear to be those most likely to have an effect.

It thus seems that decompressive flashing inception might be characterized by at least three considerations: initial temperature, decompression rate, and degree of liquid turbulence. Based on these considerations, the balance of this paper will be devoted to attempting to characterize flashing inception in flowing systems to the extent possible in view of the limited data available. Indeed, it will be shown that the inverse mass flux effects of both references [3] and [5] may be explained by effects of turbulent fluctuations.

Analysis

In view of the preceding remarks, it appears that the condition of the fluid at the onset of flashing, either static or flowing, might be characterized in terms of the turbulent pressure fluctuations. In the static systems of references [8] and [9], it is not likely that turbulence had time to develop. In the flowing systems of references [3] and [5], fully developed turbulence was most certainly present at the high Reynolds numbers encountered (order of 10^5). Thus, the following hypotheses seem reasonable.

1 Static flashing overexpansion is a function only of initial temperature and expansion rate, and represents the true inception potential according to equation (1).

2 Dynamic flashing overexpansion at inception is subject to the additive effects of turbulence giving an apparent alteration in the inception potential.

It is suggested that the overexpansion at flashing inception may be expressed as

$$\Delta p_{Fi} = f[\Delta p_{Fio}(T_i, \Sigma'), p'] \tag{3}$$

where $\Delta p_{Fio}(T_i, \Sigma')$ is the overexpansion under zero flow conditions as dependent on initial temperature, T_i, and expansion rate, Σ', and p' is the pressure fluctuation.

To see how the pressure fluctuations might enter into the picture, the fluctuation envelope may be envisioned as sketched in Fig. 2 depending on the mass flux. As the flux increases, so does the turbulence intensity. According to the hypotheses, the bottom of the envelope would represent the true *minimum* pressure at any mass flux. If this minimum pressure is taken as identical to the static value at inception represented by hypothesis (1), then the average pressure at the inception point would have to increase with increasing mass flux as shown in Fig. 3. Since the overexpansion at inception is the difference between the saturation pressure and the observed average pressure, this value, Δp_{Fi}, is seen to decrease in accordance with observation. If we define the apparent overexpansion at flashing inception as

$$\Delta p_{Fi} = p_s - \bar{p}_{Fi} \tag{4}$$

and the true value is taken to be identical with the static value as

$$\Delta p_{Fio} = p_s - p_{\min} \tag{5}$$

Nomenclature

A = duct cross section area
d = diameter
f = D'Arcy friction factor
F_i = flashing index, $G^2/2\rho_\ell \Delta p_{Fio}$
k = Boltzman's constant
G = mass flux
p = pressure
T = temperature
u', v', w' = velocity fluctuation components
U = local channel mass-averaged velocity at inception point
z = streamwise coordinate
Δ = difference
Φ = parameter defined by equation (12)
μ = viscosity
ρ = density
σ = surface tension
Σ' = rate of pressure decrease (expansion rate)
Σ_0' = static expansion rate, $\partial p/\partial t$
$\Delta\Sigma'$ = convective expansion rate, $v\partial p/\partial z$
ψ = parameter defined by equation (13)

Subscripts

c = critical
f = saturated liquid
Fi = flashing inception
Fio = flashing inception under static conditions
g = saturated vapor
i = initial
l = liquid
max = maximum
min = minimum
0 = static value without convective effects
r = reduced minimum
s = saturation value

Superscripts

+ = dimensionless based on Δp_{Fio}
′ = fluctuation
− = averaged
° = at vanishing expansion rates

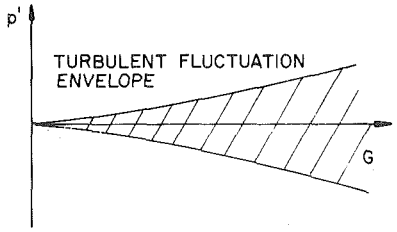

Fig. 2 Sketch of pressure fluctuation envelope with varying mass flux

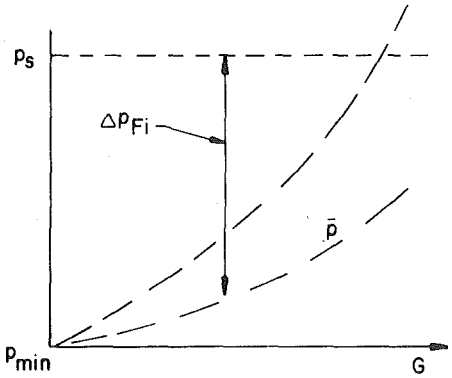

Fig. 3 Qualitative effects of pressure fluctuations on observed overexpansion at flashing inception

then the relationship between the two, in view of Figs. 2 and 3, is simply

$$\Delta p_{Fi} = \Delta p_{Fio} - \text{Max}|p'| \tag{6}$$

Note that the importance of turbulent pressure fluctuations in cavitation has been previously recognized by Daily and Johnson [10]. They, in fact, point out that the effects of dissolved gas or preexisting gas nuclei will be to reduce the cavitation or flashing inception superheat.

The maximum in the pressure fluctuation envelope is assumed to coincide with the maximum kinetic fluctuations so that

$$\text{Max}|p'| = \tfrac{1}{2}\rho_\ell[(u'_{\max}{}^2 + v'_{\max}{}^2 + w'_{\max}{}^2) \tag{7}$$

The nucleation density monotonically increases with increasing superheat while the probability density of the kinetic energy fluctuations first increases then decreases. The product of nucleation density and superheat probability density is expected to yield a maximum with increasing superheat. This maximum would probably represent the inception point and is expected to fall within the 99 percent probability band. If the maximum fluctuation in each velocity component is assumed to be represented by the three sigma value (three standard deviations), then

$$\text{Max}|p'| = \tfrac{1}{2}\rho_\ell[(3\sqrt{\overline{u'^2}})^2 + (3\sqrt{\overline{v'^2}})^2 + (3\sqrt{\overline{w'^2}})^2] \tag{8}$$

so that, for the case of isotropic turbulence (6) becomes

$$\Delta p_{Fi} = \Delta p_{Fio} - 27\left(\frac{\overline{u'^2}}{U^2}\right)\frac{G^2}{2\rho_\ell} \tag{9}$$

where U is the mean velocity of the flow at the inception location and $\overline{u'^2}/U^2$ is expected to be dependent to some extent on Reynolds number.

It is seen from equation (9) that the apparent flashing inception undershoot decreases from the static value as the mass flux increases. Without considering a possible limit on this decrease due to critical flow conditions, an expected limit is a decrease to vanishingly small superheat where the turbulence effects just balance the expansion rate effects at the given temperature. While there is nothing actually prohibiting the turbulent pressure fluctuations from exceeding the values required to overcome the zero-flow incipient superheat, bubbles thus generated would probably collapse almost immediately in the bulk subcooled liquid unless carried to lower pressure regions before this could happen. In dimensionless terms, then, equation (9) may thus be written considering the latter expectation as

$$\Delta p_{Fi}{}^* = \text{Max}\begin{cases}0\\ 1 - 27\left(\dfrac{\overline{u'^2}}{U^2}\right)F_i\end{cases} \tag{10}$$

where F_i is termed the flashing index and is the reciprocal of the well-known cavitation index. Note that the apparent flashing inception undershoot has been rendered dimensionless with respect to the static value, which may be predicted by equation (1).

Results and Discussion

Equation (9) shows that the apparent overexpansion at flashing inception should be linear in the square of the mass flux with an intercept of the static inception value, Δp_{Fio}. If the ideas previously expressed are at all valid, using extrapolated values of Δp_{Fio}, turbulent fluctuation intensities obtained at known inception points should match those found, for instance by Laufer [11], of 0.07–0.08.

Figure 1 shows the data of Reocreux [3] which appear to be the only data available where inception points are given or can be determined. It should be noticed that 1°C represents approximately 6.5 kPa at these temperatures for water. Stated another way, 1 kPa represents ~0.15°C. It is virtually impossible to determine significant trends within the scatter of the data. For this reason, straight lines were utilized to attempt to extrapolate the three sets of data in Fig. 1 to a small mass flux consistent with vanishing turbulence, taken to be zero flow herein. The values of Δp_{Fio} thus obtained were 17, 18, and 19 kPa, respectively. These represent actual superheats of approximately 3.5°C. The Alamgir and Lienhard correlation was not used for this purpose since it was not recommended for decompression rates below 4000 bar/s and the maximum values encountered in reference [3] were approximately 5 bar/s. (It may be noted that if the correlation is used for these conditions, predictions of approximately 40 kPa, or twice those observed, are obtained.)

Using the values of Δp_{Fio} obtained from Fig. 1, the mean fluctuation intensities may be computed from the data. These are shown in Fig. 4, (solid symbols). The average of the velocity fluctuation intensities obtained is 0.072 in good agreement with the measurements of Daily and Johnson [10] based on their measurements of bubble motion and also of Laufer [11]. No observable trend with mass flux is noticed. Also, there is surprisingly little scatter in the results so obtained.

Reocreux's data are replotted in Fig. 5 on dimensionless coordinates suggested by equation (10). Unfortunately, there are no data with reasonably good values of Δp_{Fio} available at higher flashing indices so the equilibrium limit can not be tested.

On the other hand, the data of Seynhaeve, et al. [5] do consist of higher flashing indices but do not give sufficient information to determine the static inception undershoots. However, these data have expansion rates where negligible change from the limiting value Δp_{Fio} would be expected. Thus, it might be expected that the data of reference [5] which lies in the same temperature range as the Reocreux data may exhibit the same behavior. Both sets of data are plotted in Fig. 6. Also shown in this figure is the prediction based on a static inception underpressure of 18 kPa. The trends observed appear to support the conclusions previously stated. Note that the lower limit of zero superheat also appears reasonable and tentatively supported by the relatively meager amount of data available.

To provide the reader with some physical insight into the actual behavior of the combined static decompression and flowing effects, the two correlations, that of reference [9] and that developed herein, may be combined. To demonstrate the effects adequately and simply requires some unfolding of the parameters included in the correlation. A very descriptive and yet simple combination results when the flashing index is written in terms of the expansion rate yielding

$$\Delta p_{Fi}{}^+ = \sqrt{1 + 13.25\,(\Sigma_0' + \Delta\Sigma')^{0.8}} - \frac{27}{2}\left(\frac{\overline{u'^2}}{U^2}\right)\Phi(\Delta\Sigma')^{2/3} \tag{11}$$

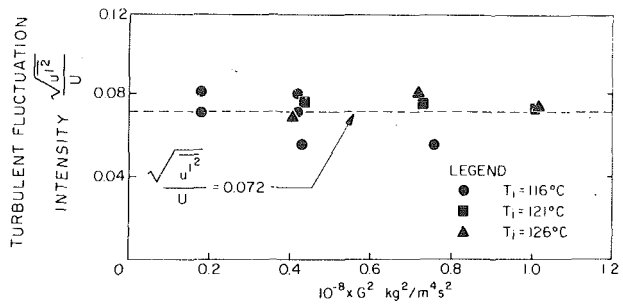

Fig. 4 Velocity fluctuation intensities calculated from the overexpansion data of Reocreux [3] at flashing inception

Note that the total expansion rate, Σ', has been broken into its static and convective components, Σ_0' and $\Delta\Sigma'$, given in the normal Lagrangian manner for a fluid element while the flashing inception undershoot has been rendered dimensionless through $\Delta p_{Fio}{}^\circ$ given by equation (2). Parameters in equation (11) are seen to be the static and flowing expansion rates and a parameter Φ given by

$$\Phi = \frac{\psi}{\Delta p_{Fio}{}^\circ} \tag{12}$$

For purposes of this discussion, the turbulence intensity is considered fixed at a value of 0.072. Indeed, variations from this value as normally found in variable hydrodynamic situations are not expected to be important in view of the stated accuracy of equation (1).

The parameter ψ is given differently depending on the factor causing the flowing expansion.

Friction $$\psi = [2d\sqrt{\rho_\ell}/f]^{2/3} \tag{13a}$$

Acceleration $$\psi = [A\sqrt{\rho_\ell}/(dA/dz)]^{2/3} \tag{13b}$$

It should be noted that the streamwise area contraction denoted by dA/dz is also expected to have a significant effect on the local turbulence intensity. This will be discussed in a following paper on nozzle flows.

In a physical plane of Δp_{fi} versus Σ', the static flashing inception ($\Delta\Sigma' = 0$) would appear as a family of curves beginning at constant values, $\Delta p_{Fio}{}^\circ$, with vanishingly small expansion rates. Then, Δp_{Fi} increases slowly assymptotic to $\Sigma_0{}'^{0.4}$ at high expansion rates. These are shown as the lighter lines at fixed temperature in Fig. 7.[1] For practical purposes, $\Delta p_{Fio}{}^\circ$ is limited between ~0.2 bar at 100°C and ~9.5 bar at ~300°C after which it decreases again to zero due to vanishing surface tension as the critical point is approached. Less than 15 percent increase in inception undershoot is noticed for expansion rates less than 10 kbar/s while almost a tenfold increase is predicted at 10 Mbar/s expansion rates (beyond the correlation range).

When the convective expansion rate effects are taken into account, four parameters must be considered: $\Delta p_{Fio}{}^\circ$, Σ_0', ψ, and, $\Delta\Sigma'$. In this case a curve starting at the static coordinate values of (Δp_{Fio}, Σ_0') departs by increasingly larger amounts from the static curve for increasing *total* expansion rates depending on the parameter ψ. These are the two typical families of lines shown as the dark curves in Fig. 7 departing the 175°C static decompression curve at values of 0.001 and 0.1 Mbar/s for Σ_0'. Whether this curve first increases, or decreases monotonically, with increasing Σ' depends on the initial slope at the departure point. If two given rates of static decompression are sufficiently small and dominated by large values of convective expansion rates such that a given total value of Σ' is large with respect to the two static values, curves of the same value of ψ will tend to coalesce. This is seen for the two curves in Fig. 7 where $\psi = 10^{-4}$ (Mbar-s^2)$^{1/3}$. Indeed, for Σ' greater than approximately 0.1, the two different curves for $\psi = 5 \times 10^{-5}$ are virtually indistinguishable.

The dimensionless plane suggested by equation (11) reduces the complexity by one dimension while still keeping the general pictorial

[1] In evaluating equation (2), surface tension values from the equation given by Schmidt in *Properties of Water and Steam in SI-Units* (Springer-Verlag, New York, 1969) were used. These values differ from those in the 1979 edition but appear to be more accurate.

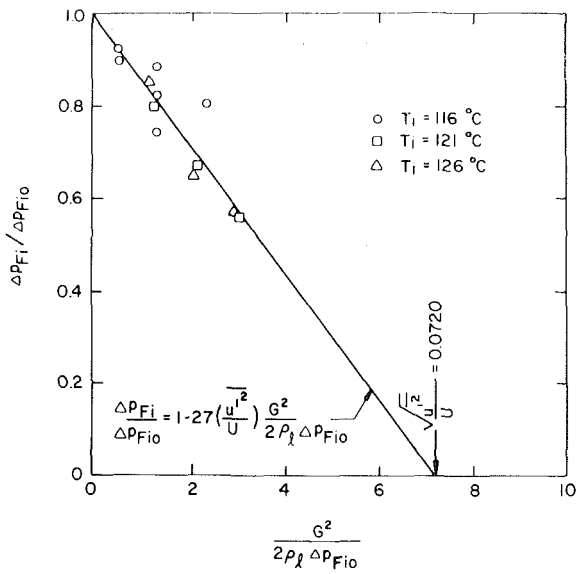

Fig. 5 Dimensionless correlation of Reocreux's [3] overexpansion data at flashing inception

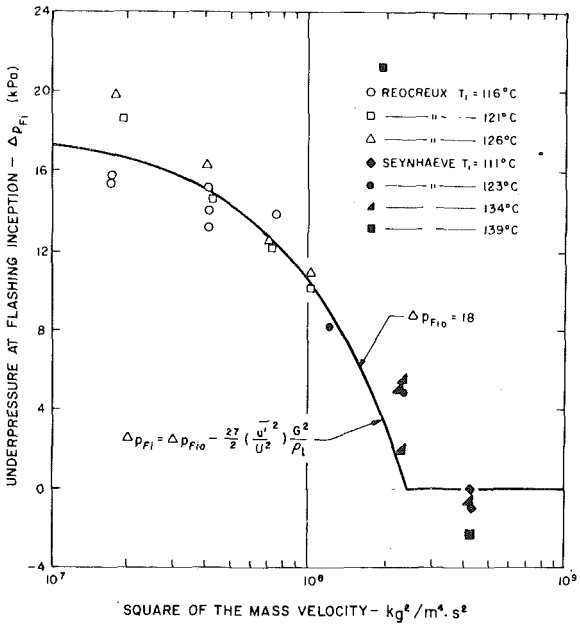

Fig. 6 Comparison of the flashing inception data of Reocreux [3] and of Seynhaeve, et al. [5] with the theory developed herein using the approximate static flashing overexpansion value of 18 kPa for the computation

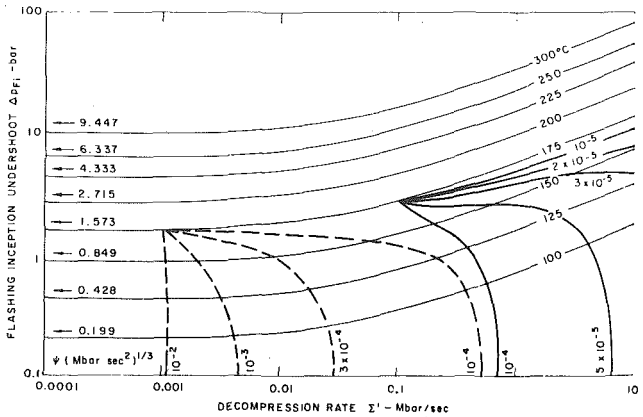

Fig. 7 Physical combination of the static flashing inception correlation of Alamgir and Lienhard [9] with the flowing turbulence effects described herein. Light lines: static decompression effects only. Dark lines: turbulence effects included

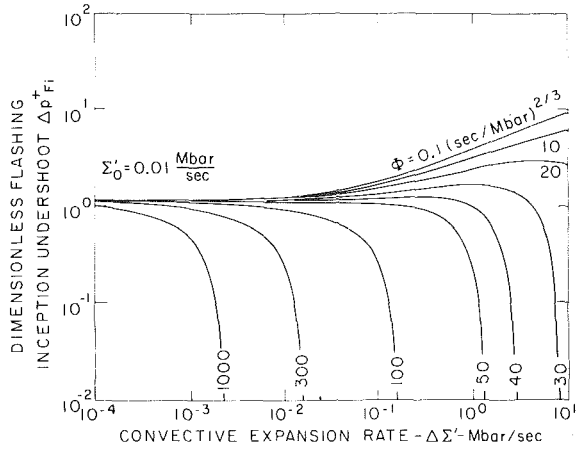

Fig. 8(*a*) 0.01 Mbar/s

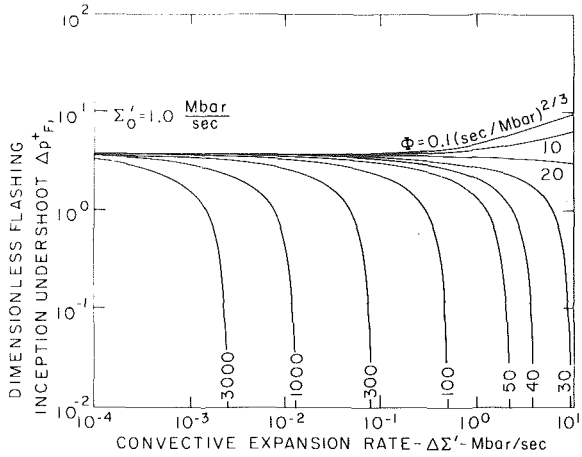

Fig. 8(*c*) 1.0 Mbar/s

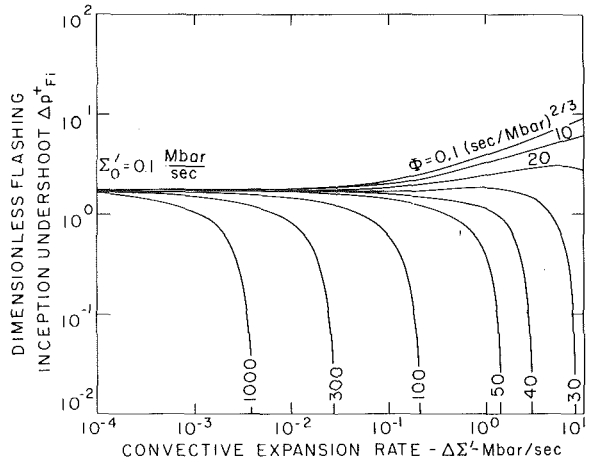

Fig. 8(*b*) 0.1 Mbar/s

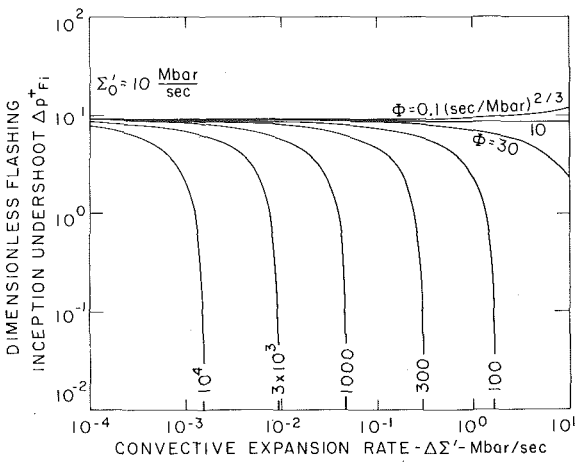

Fig. 8(*d*) 10 Mbar/s

Fig. 8 Dimensionless flashing inception correlation combining Alamgir and Lienhard [9] with the turbulence effects developed herein

behavior of the phenomenon unchanged. By plotting the dimensionless undershoot, $\Delta p_{Fi}{}^+$, as a function of the *convective expansion* rate, $\Delta\Sigma'$, (Fig. 8), the essence of the physical behavior is maintained while providing a much simplified picture. It is noted that the expected range of ψ for friction-caused expansions is 10^{-4} to 10^{-2} (Mbar $s^2)^{1/3}$ while those for accelerated cases is one to two orders of magnitude smaller for the various nozzles encountered in the critical flow literature. The normal range for Φ is then seen to be a six-order range between 0.1 and 10^5 (s/Mbar)$^{2/3}$. In the case of the reference [3] experiments, ψ is near 0.004 (Mbar $s^2)^{1/3}$ while, based on the extrapolated values of Δp_{Fio}, Φ is near 20,000 (s/Mbar)$^{2/3}$.

As seen in Fig. 8, at a given value of Σ_0' the curves become asymptotic at small Σ' to the ratio of the static value of undershoot to that for vanishing expansion rates at a given temperature. For increasing convective expansions, the undershoot may or may not first increase, depending on Σ_0' and Φ, but then decreases rapidly to zero, indicating the disappearance of any significant amounts of nonequilibrium.

In estimating the degree of nonequilibrium superheat to be expected at the onset of flashing in constant area ducts (a following paper will describe application to variable area geometries), it seems easiest to utilize equations (1, 2), and (10) with the turbulence intensity taken as 0.072 (unless a clear and substantially different value is known a priori for a particular geometry). In practice, the light lines in Fig. 7 can probably be used to estimate Δp_{Fio} with sufficient accuracy in many cases so that equations (1) and (2) need not be used. On the other hand, conditions near atmospheric pressure similar to those of references (3) and (5) where expansions on the order of 20 × 10^{-6} Mbar/s (20 bar/s) and less were encountered, it appears that the static inception criteria (reference [9]) may be considerably in error if extrapolated below its range of applicability. In such cases, independent means of developing static inception estimates do not exist and alternate methods are required.

Conclusions and Recommendations

1 Flashing inception superheat in flowing systems appears to be described by the effects of turbulent fluctuations (equation (10)). This suggests that the flowing and static superheats at inception are identical once turbulent fluctuations are taken into account.

2 Under flowing conditions where flashing occurs under the combined effects of system decompression and convective decompression caused by friction and/or acceleration, the flashing inception superheat may be either very large (50°C or more) or may instead be negligible. The actual superheat depends on the relative balance between apparent expansion rate and turbulence effects. Since the degree of nonequilibrium depends heavily on the initial superheat at flashing inception, the resultant void development is expected to be strongly affected.

3 It is suggested that since critical flow rates of two-phase mixtures are very dependent on the actual vapor content of the flowing mixture and hence on the void development, that the variations in flashing inception superheat may be of overriding importance in such flows and, in fact, may be the prime cause of much of the apparent scatter in the existing data.

4 It is suggested that the limit of flashing inception with vanishing

mass flux in flowing systems coincides with that value that would be obtained by static decompression at the same expansion rates.

5 Methods of accurately extending the static flashing inception superheat correlation of Alamgir and Lienhard [9] to lower values of expansion rate are required.

6 Additional data are needed for flashing inception in flowing systems at higher pressures. Sufficient details are required to accurately determine the inception point due to the sensitivity of void development to small changes in superheat at inception. Sufficient range in mass flux is required to allow extrapolative determination of the case of vanishing turbulence.

Acknowledgments

The author is grateful for numerous enlightening discussions with Prof. J. H. Lienhard, and Drs. N. Abuaf and B. J. C. Wu. This work was performed under the auspices of the U.S. Nuclear Regulatory Commission.

References

1 Saha, P., "A Review of Two-Phase Steam-Water Critical Flow Models with Emphasis on Thermal Nonequilibrium," BNL-NUREG-50907, Sept. 1978.

2 Wu, B. J. C., Saha, P., Abuaf, N., and Jones, Jr., O. C., "A One-Dimensional Model of Vapor Generation in Steady Flashing Flow: Interim Milestone Report," BNL-NUREG-25709, Oct., 1978.

3 Reocreux, M., "Contribution a l'Etude des Debits Critiques en Ecoulement Diphasique Eau-Vapeur," PhD Thesis, Universite Scientifique et Medicale de Grenoble, France, 1974.

4 Jones, Jr., O. C., and Zuber, N., "Bubble Growth in Variable Pressure Fields," ASME JOURNAL OF HEAT TRANSFER, Vol. 100, 1978, pp. 453–459.

5 Seynhaeve, J. M., Giot, M. M., and Fritte, A. A., "Non-Equilibrium Effects on Critical Flow Rates at Low Qualities," presented at the Specialists Meeting on Transient Two-Phase Flow-Toronto, Canada, Aug. 3–4, 1976.

6 Hsu, Y. Y., "On the Size Range of Active Nucleation Cavities on a Heating Surface," ASME JOURNAL OF HEAT TRANSFER, Vol. 84, 1962, pp. 207–216.

7 Saha, P., and Zuber, N., "Point of Net Vapor Generation and Vapor Void Fraction in Subcooled Boiling," *Heat Transfer 1974, Proceedings of the 5th International Heat Transfer Conference,* Vol. IV, 1974, pp. 175–179.

8 Lienhard, J. H., Alamgir, Md., and Trela, M., "Early Response of Hot Water to Sudden Release from High Pressure," ASME JOURNAL OF HEAT TRANSFER, Vol. 100, 1978, pp. 473–479.

9 Alamgir, Md., and Lienhard, J. H., "Correlation of Pressure Undershoot During Hot-Water Depressurization," ASME JOURNAL OF HEAT TRANSFER in press.

10 Daily, J. W., and Johnson, Jr., V. E., "Turbulence and Boundary Layer Effects on Cavitation Inception from Gas Nuclei," *Trans. ASME,* Vol. 78 1956, pp. 1695–1706.

11 Laufer, J., "Investigation of Turbulent Flow in a Two-Dimensional Channel," NACA TN 2123, July, 1950.

W. Nakayama
Chief Researcher, Mem. ASME

T. Daikoku
Researcher.

H. Kuwahara
Researcher.

T. Nakajima
Researcher.

Mechanical Engineering Research Laboratory, Hitachi, Ltd., 502 Kandatsu, Tsuchiura, Ibaraki, Japan

Dynamic Model of Enhanced Boiling Heat Transfer on Porous Surfaces

Part I: Experimental Investigation

Enhancement of nucleate boiling heat transfer has been studied with the structured surfaces composed of interconnected internal cavities in the form of tunnels and small pores connecting the pool liquid and the tunnels. The boiling curves of R-11, water and nitrogen show 80 to 90 percent reduction of wall superheat required to transfer the same heat flux as that on plain surfaces, when the pore diameter is set around 0.1 mm. The experimental data on bubble formation showed a significant contribution of latent heat transport to the enhancement. A visualization study made with a transparent structured model suggested that the liquid suction into the tunnel is triggered by the bubble growth at active pores and subsequent evaporation inside the tunnel plays a vital role in driving the bubble formation cycle. This observation led to a conception of the dynamic model expounded in Part II.

Introduction

On porous surfaces, wall superheat of a very small degree can start nucleate boiling, thereby raising the heat transfer coefficient order of magnitudes higher than that of convective heat transfer. High heat transfer coefficients with such small temperature differences make the porous surface structure very attractive to high-efficiency heat exchangers which are earnestly needed in the new energy source developments.

Surveying previously filed patents, one can find many ideas on how to utilize this enhancement. They differ mainly in the method of providing porous structures on surfaces: sintering the layer of metal particles, for example [1, 2], machining with a cutter and a press [3–6], etc. Although there are a large variety of ideas, only a few have been put to actual use in industrial heat exchangers [7, 8].

In anticipation of wide commercial use in a forthcoming energy shortage era, the greatest requirement for further advances in this enhancing technique is to understand the mechanism of enhancement. Setting up an analytical model and proving it by a specifically designed experiment is the only way to obtain more efficient and more economically enhanced surfaces. O'Neil, et al [7] assumed a static bubble within the porous media and determined the minimum superheat required for the growth of a bubble in a sintered metal layer of a given porosity. Czikk and O'Neil [9] extended the theory of [7] by relating the heat transfer performance to the distribution of pore sizes. However, the observations made by the present authors and other authors [11–13] indicate that the phenomena are highly dynamic. Macbeth [10] attempted to explain high heat transfer rates of boiling from porous scales on boiler tubes. Although his analysis considers the resistance to liquid flow, the dynamic nature is not fully taken into account and, moreover, it is not applicable to the surfaces of homogeneous porosity. Farrell and Alleavitch [11], based on their observation of beds of monel beads, showed the condition of vapor ejection through the bed by computing the pressure drop of vapor flow which was generated close to the heated base surface. The model in their experiment had a relatively large bed thickness. Hence, it is not certain that the dynamics of fluid motion satisfies a similarity to the phenomena in much thinner and finer porous layers. In addition to the aforementioned references, some of the patent literature [1–6] also discussed the enhancement mechanism in rather qualitative ways. Analytical works other than those cited above dealt with the case of porous layers exposed to the vapor, a common situation in the heat pipes, which is beyond the scope of the present paper.

Observations of phenomena within the porous layers have been attempted by several authors [11–13]. The existence of the vapor blanket regions in the layer, in some cases migrating is commonly observed. Also noteworthy is the lack of nucleation within the layer; that is, bubbles much smaller than the pore sizes were not observed. These observations suggest the need for the development of an analytical model. However, they must be viewed with some caution in regard to the inadequate dynamic similarity inherent in the enlarged model layers.

In the present report and its companion paper [20], the authors attempt to shed some more light on the mechanism of nucleate boiling on porous surfaces. In order to avoid as much complexity as possible, the surface studied here has geometrical simplicity and regularity, as described in the next chapter. Analytical approach is made with a model taking into account dynamic aspects which have not been fully considered in the previous literature.

Heat Transfer Performance

The essential feature of porous surface structure is represented by small interconnected cavities and openings through which the cavities communicate to the exterior liquid. Figure 1 shows the geometry of the present surface. The internal cavity is a row of tunnels which run under the lid with pitch λ_t. The tunnels' cross section is nearly rectangular and measures $H_t \times W_t$. The openings are here called pores; they are triangular in shape and provided along the tunnel with pitch

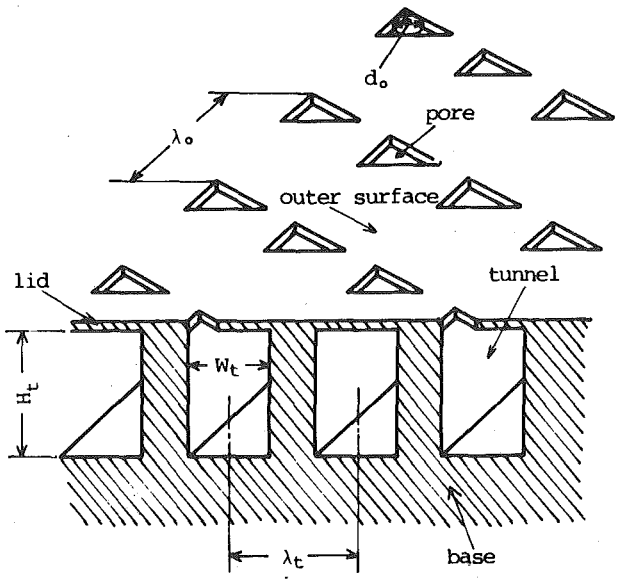

Fig. 1 Geometry of the surface structure

Contributed by The Heat Transfer Division for publication in the JOURNAL OF HEAT TRANSFER. Manuscript received by the Heat Transfer Division November 9, 1979.

λ_0. The pore size is represented by the diameter of a circle inscribed in a triangle. In case this structure is on the surface of a circular tube, the tunnels run in a closely spaced spiral. On a flat surface they run parallel to each other. Figure 2 consists of photographs of the surface structure provided on a copper plate by machining.

Table 1 gives the dimensions of the surface structures, and the boiling curves obtained with these surfaces are shown in Figs. 3(*a–c*). The surface material is oxygen-free copper. The microscopic ruggedness of their cross-sectional contours is similar to the one seen in Fig. 2. The real surface area (A_r) was estimated from the cross-sectional photographs. On the far right hand column of Table 1, the ratio of A_r to the projected base area (A) is shown. The most widely varied among the geometrical dimensions was the pore diameter d_0 which was considered crucial for the ejection of vapor bubbles from the tunnel. The other dimensions were not changed in a systematic way partly due to the constraint arising from the manufacturing technique itself.

The boiling curves of water, R-11, and nitrogen are reported here, the latter two as representatives of fluorocarbon refrigerants and cryogenic fluids, respectively. The test pieces were placed in a pool of liquids, with their heat transfer surfaces facing upward. System pressure was set at an atmospheric in all experiments. The liquids were held at saturation temperatures except for the case of water where a little subcooling (~2 K) was inevitable.

In presenting the boiling curves, heat flux (q) is defined on the base area (A). Wall superheat (ΔT) is the difference between the wall temperature at the bottom of the tunnels and the saturation temperature of the fluid. The experimental apparatus, the method of measurement, and the estimated accuracy of experiment are described in the Appendix. The data in Figs. 3(*a–c*) were all taken with decreasing heat flux, although hysteresis behavior on these surfaces was found to be a less pronounced one than that observed on plain surfaces. The symbols X are the data for the plain surfaces made of the same oxygen-free copper and lapped by the grains #1000 (grain diameter 16μ). They are found to agree with the existing formulas [14, 15].

From Figs. 3(*a–c*) one can make the following summary.

1 The present surface is highly efficient in promoting boiling heat transfer especially in the range of small wall superheats. Superheats required to transfer a given heat flux are reduced to nearly one tenth, at best, of those on the plain surfaces.

2 Some curves for different d_0 are seen to intersect at some ΔT. In those cases, a surface with larger d_0 is superior in a range of large ΔT, while at smaller ΔT a great deal of enhancement is achieved by a surface with smaller d_0.

The surface No. R(11)-1 was manufactured with special care so that the surface was relatively free from structural deformation compared to other surfaces. (The pore diameter scatters around the mean value especially when it is small, for example ±50 percent when d_0 = 0.04 mm). This surface provides the basic data for later analytical development.

Preliminary Examination of Enhancement Mechanism

It is apparent by quantitative comparison as well as by consideration on the involved physics that the increase in actual heat transfer area is not a major contributor to the attained enhancement.

Three routes exist for heat transfer from the surface to the ambient liquid: (1) convective heat transfer from the outer surface enhanced by agitating force of bubble formation, (2) vaporization of liquid near the outer surface into growing bubbles and (3) vaporization of liquid in the tunnels. The first two correspond to the conventional mechanism working on plain surfaces. In order to see the relative importance of (1) and (2), measurements were made of the number of bubble formation sites N_A, the formation frequency f_b, and the diameter of departing bubbles d_b by boiling R-11 on the structured surfaces (R(11)-1,-3) and the plain surface. The latent heat flux q_L was computed from

Table 1 Structural dimension of the tested surfaces

fluid	Surface No.	d_o	λ_o	λ_t	H_t	W_t	A_r/A
water	W-1	0.20	0.60	0.60	0.62	0.25	2.93
	W-2	0.14	0.72	0.50	0.50	0.20	3.40
	W-3	0.08	0.72	0.50	0.60	0.15	3.70
R-11	R(11)-1	0.10	0.70	0.55	0.40	0.25	3.36
	R(11)-2	0.06	0.70	0.55	0.40	0.25	3.36
	R(11)-3	0.04	0.70	0.55	0.40	0.25	3.36
liquid nitrogen (LN)	LN-1	0.20	0.72	0.40	0.40	0.18	3.33
	LN-2	0.12	0.72	0.40	0.50	0.14	3.71
	LN-3	0.09	0.72	0.40	0.56	0.16	4.05
	LN-4	0.06	0.72	0.40	0.52	0.18	4.05
	LN-5	0.03	0.72	0.40	0.56	0.18	4.09

(mm)

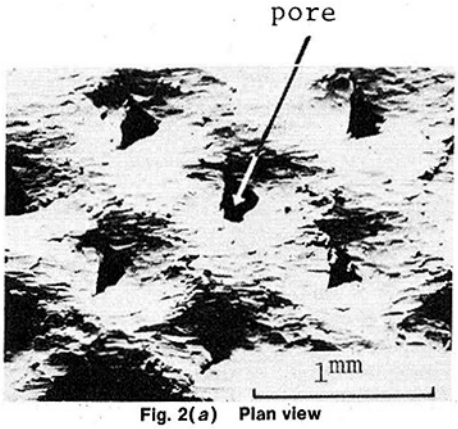

Fig. 2(*a*) Plan view

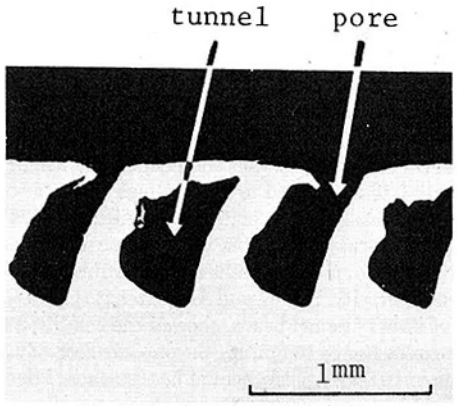

Fig. 2(*b*) Cross-sectional view

Fig. 2 Magnified view of the surface

Nomenclature

A = base heat transfer area (cm^2)
A_r = real surface area of structured surface (cm^2)
A_t = surface area of tunnel wall (cm^2)
C_q = empirical coefficient for equation (2) [K(cm^2/W)$^{3/5}$(1/cm^2)$^{1/5}$]
d_b = bubble departure diameter (cm)
d_0 = diameter of pore (cm or mm)
f_b = bubble formation frequency (Hz)
H_t = tunnel height (cm or mm)
h_{fg} = latent heat of vaporization (J/g)
h_{max} = roughness height (mm)
N_A = number of active pores
q = heat flux (W/cm^2)
q_{ex} = heat flux on the outer surface (W/cm^2)
q_L = latent heat flux (W/cm^2)
r_0 = pore radius (cm)
T_w = temperature of wall (K)
ΔT = wall superheat (K)
W_t = tunnel width (cm or mm)
x = empirical constant for equation (2)
y = empirical constant for equation (2)
λ_0 = pore pitch (cm or mm)
λ_t = tunnel pitch (cm or mm)
ρ_v = vapor density (g/cm^3)

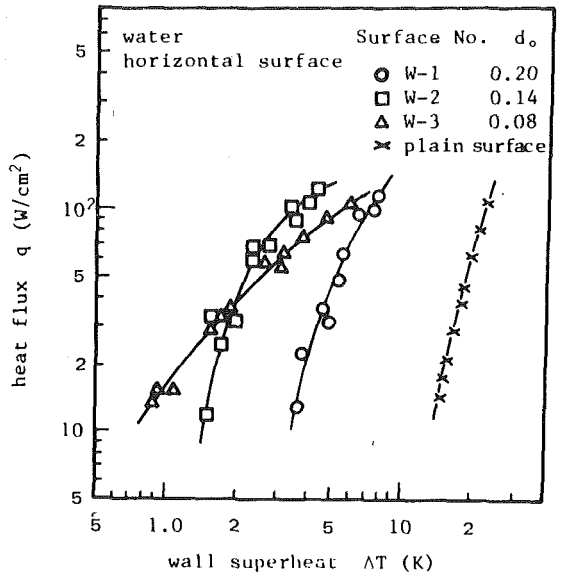

Fig. 3(*a*) Boiling curves of water

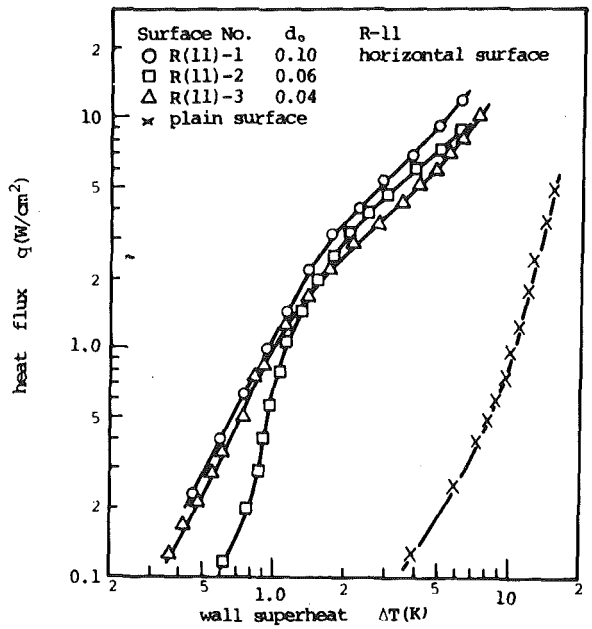

Fig. 3(*b*) Boiling curves of R-11

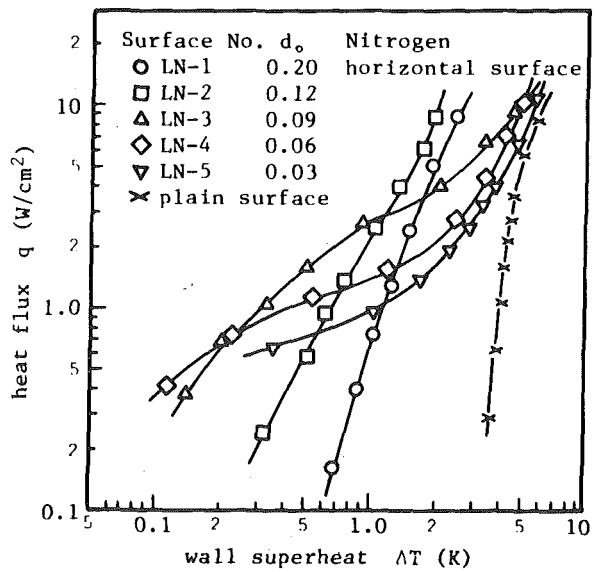

Fig. 3(*c*) Boiling curves of liquid nitrogen

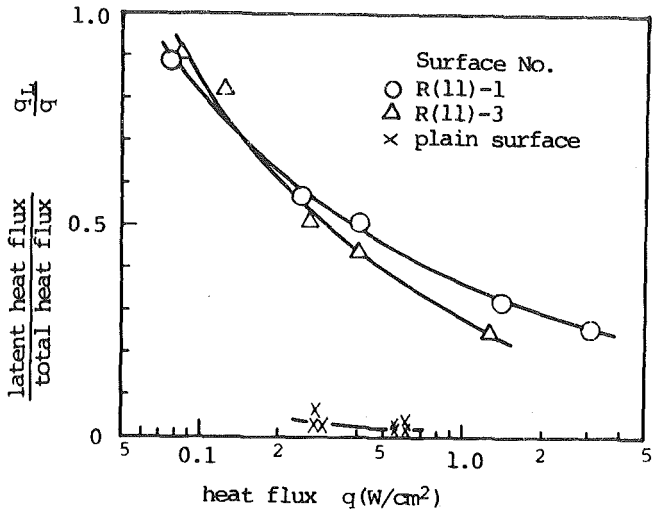

Fig. 4 Contribution of latent heat transport to total heat flux

$$q_L = (N_A/A) f_b h_{fg} \rho_v (\pi d_b^3/6), \quad (1)$$

where ρ_v is vapor density, h_{fg} latent heat of vaporization, and N_A/A bubble population density.

The ratio of q_L to the total heat flux q is shown against q in Fig. 4. The data on the plain surface confirmed the well-established finding by many investigators of insignificant contribution of latent heat. However, the latent heat transport has a large percentage for the structured surfaces and shows a marked dependence on q. This is thought to imply that a significant role is played by the vaporization process in the tunnels (3).

Assuming that the heat flux from the outer surface of the structured surface q_{ex} is controlled by the same mechanism working on plain surfaces, one attempts to find, for later use, a formula correlating q_{ex} with the bubble population density as follows. According to the literature [16–18], the heat flux on a plain surface is proportional to the $\frac{1}{4}$ to $\frac{1}{3}$ power of bubble population density. The coefficient of proportionality is known to differ for different fluids. In order to find the relationship between q, ΔT and N_A/A for R-11, measurements were made with the plain copper surfaces having different roughness heights. The results are plotted in Fig. 5 together with the data for the structured surfaces. The numbers attached to the groups of data symbols give the values of q_{ex} which were computed by subtracting q_L of equation (1) from q. The structured surface data are not large in number to allow drawing of constant heat flux lines. This is due to the difficulty in preparing the surfaces to permit their heat transfer performance to vary systematically in a wide range.

The solid curves in Fig. 5 are represented by the following formula

$$q_{ex} = (\Delta T/C_q)^{1/y} (N_A/A)^{-x/y}, \quad (2)$$

where $x = -1/6$, $y = 2/3$ and $C_q = 18.0$ [K(cm²/W)$^{2/3}$(1/cm²)$^{1/6}$]. The values of x and y coincide with those reported by Nishikawa and Fujita [17] who have summarized the previous investigations including [16] and [18]. According to [17], the above values of x and y are valid in the laminar flow regime, which lies to the left of a broken line in Fig. 5. For the turbulent flow regime, which is to the right of a demarcation line, Nishikawa and Fujita [17] quoted from Zuber [18]: $x = -1/5$ and $y = 3/5$. The demarcation between laminar and turbulent regimes is defined by a point on the boiling curve where its relatively moderate slope in a small ΔT range changes to a steep slope in a large ΔT range. The line in Fig. 5 was drawn from the present data of R-11; however, it should be noted that the transition points were rather arbitrarily located in a certain range of ΔT (or q) where the change of slope is gradual, as exemplified by the curve in Fig. 3(*b*).

On the premise that those values of x and y are valid for q_{ex} on the structured surfaces, one finds the values of C_q by data fitting from Fig. 5. All data except for the lowest ($q_{ex} = 0.008$ W/cm²) are corre-

lated by equation (2) with

$$x = -1/5, y = 3/5,$$

$$C_q = 1.95[\mathrm{K(cm^2/W)^{3/5}(1/cm^2)^{1/5}}] \quad (3)$$

within the range $-20 \sim +30$ percent; whereas the data for $q_{ex} = 0.008$ W/cm^2 coincide within 51 percent with the laminar regime correlation for the plain surface. The order of magnitude of C_q in equation (3) agrees with the value given by Zuber [18] (C_q = 3.93). This result implies that a demarcation line for the structured surfaces could be far left, in Fig. 5, of the demarcation line for the plain surfaces. The convective flow on the outer surface is assumed to be turbulent, so that the values given in equation (3) will be used in the analysis of Part II [20].

In the foregoing argument to determine q_{ex}, the temperature drop between the tunnel bottom and the outer surface is not considered. It is estimated to be very small; in water, for example, it amounts to only 0.13K at q = 50 W/cm^2.

Observation of Phenomena in the Tunnels

The implication given by the foregoing study that vaporization in the tunnels plays an important role has prompted the visualization experiment described in this section.

The apparatus (Fig. 6) consists of a base block, two glass plates (30 mm × 30 mm, 1 mm thick) forming a pool space above the base block, and a thin metal lid having a row of through holes (pores). A tunnel space is formed between the lid and the base. Those components were pasted together carefully with adhesives, so that no microscopic paths for the fluid exist between the tunnel and the pool other than the holes in the lid. The pool was filled with R-11; its top was open to the atmosphere. Liquid R-11 was continuously replenished through a needle connected to an outside reservoir.

In one experiment, heat was added from the copper base block by means of cartridge heaters inserted in the block. The lid was made of the same copper and had a thickness of 0.4 mm. The tunnel height was varied between 0.5 to 1.0 mm and the hole diameter between 0.05 to 0.5 mm in several steps. In this setup, the lid was heated indirectly by thermal conduction from the base through the glass plates.

In another experiment, the lid was made of a stainless steel strip of 0.05 mm thick, and heated directly by passing d-c current through it. This experiment was made to measure the lid temperature from the change of electrical resistance in the strip. Correspondence of the thermal condition between this model and the surfaces used in the boiling experiment was partly checked by this measurement. Although a complete correspondence was impossible for this type of visualization experiment, it was considered that essential features of the phenomena could be reproduced in the model. The power input in either method was given in small increasing or decreasing steps with a sufficiently long interval for the observed events to get stabilized.

A sequence of events was recorded by a high speed movie camera or a still camera. Illumination was provided by passing light behind the glasses at short intervals so that radiant heat did not alter the physical process.

The events summarized below were commonly observed in both the aforementioned experiments. No essential difference was caused in the physical process by different methods of heating. The photographs reproduced in Fig. 7 were chosen from a group of similar photographs for their qualities for reproduction.

1 In an unheated state, a vapor region exists in the tunnel. Its volume depends on the temperature of the room. When the temperature is low enough, it is reduced to a bubble smaller than the tunnel size. The rest of the tunnel space is filled by the liquid.

2 As heat is added by turning on the heater or passing current to the lid, the vapor region expands driving the liquid out of the tunnel through the holes (Fig. 7(a)). The advancing liquid-vapor interface leaves meniscuses in the upper corners formed by the glass plates and the lid and in the lower corners formed by the glass and the base. These remaining liquids are seen to evaporate rapidly; however, small meniscuses remain in the corners.

3 Until the wall superheat (defined here by the difference between

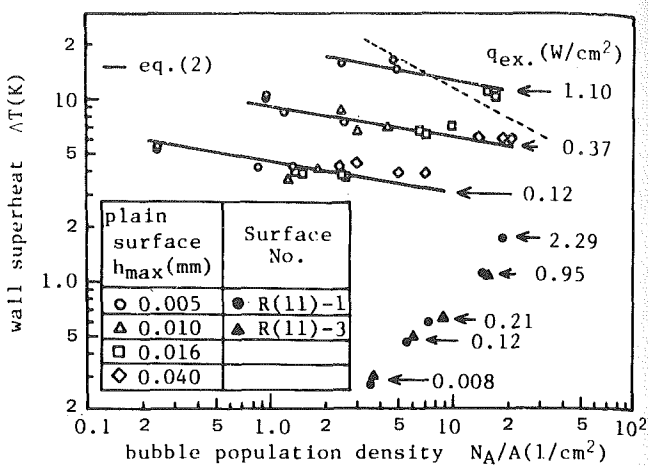

Fig. 5 Correlation of wall superheat, heat flux and bubble population density on the roughened plain surfaces (h_{max} = roughness height) and the structured surfaces

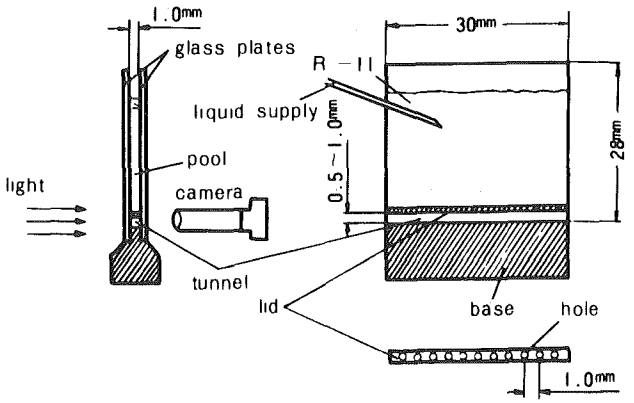

Fig. 6 Apparatus for observation experiment

the lid temperature and the liquid temperature) reaches around 0.6 K, there are no appreciable changes in the state in the tunnel. The surface of the base is seen to be wet, and thin liquid hold-up persists in the corners; it is particularly conspicuous in the upper corners.

4 When the superheat exceeds about 0.6 K, bubbles start to emerge from one or two of the holes. The interval of their emergence in this initial phase is around 8 s. In phase with the bubble ejection, the meniscuses in the upper corners are seen to pulsate. The pulsation occurs in a relatively wide span, extending over remote locations from the active holes (Fig. 7(b)). This seems to indicate that intake of the liquid from the exterior pool occurs and spreads in the axial direction over the corners. Whether and how the liquid intake is made through the inactive holes was not clearly recorded. However, in some experiments with imperfect joints between the glass plates and the lid, liquid was seen to be sucked in the tunnel through crevices on the joining face.

5 Increasing the superheat does not change the essential character of the above process; it merely increases the frequency and the number of active holes. Identifying the pulsating meniscuses becomes increasingly difficult due to diminishing liquid hold-up and increased frequency.

6 The process was commonly observed in all the tunnel heights investigated. It was also common to all the hole diameters except for the largest one (0.5 mm). In the last case, expulsion of the liquid from the tunnel was never completed. Liquid was seen to be sloshing in the tunnel, its volume occupying 10–50 percent of the entire volume, depending on the superheat.

From these observations, one may conjecture a machinery of bubble formation sustained by the pumping action of departing bubbles

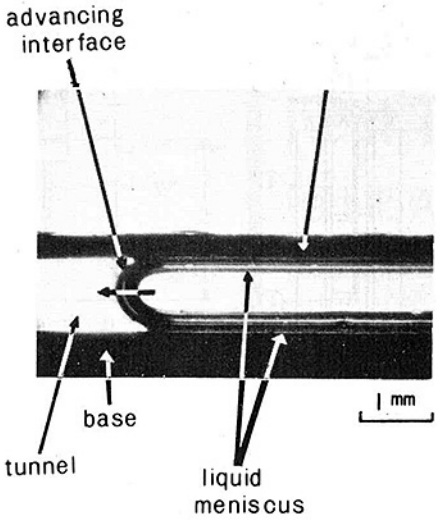

Fig. 7(*a*) Expanding vapor region in the initial phase of heating

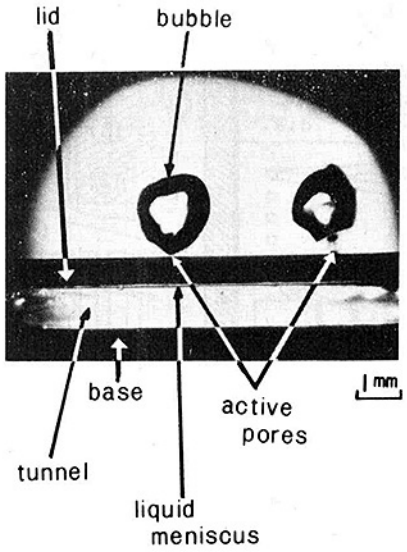

Fig. 7(*b*) Bubble formation and liquid meniscus held in the tunnel

sucking liquid into the tunnel, spreading of the introduced liquid in angled corners by capillary forces, and subsequent evaporation of the liquid to form another generation of bubbles. The base surface seemed never to be dried even when the base block was directly heated. The explanation for this may be found in the existence of an equilibrium layer [19]; but this could not be confirmed.

Concluding Remarks

Experimental investigation of pool boiling heat transfer on the horizontal structured surfaces has led to the following conclusions.

1 The surface structure having a pore diameter of around 0.1 mm is highly efficient in enhancing heat transfer. The boiling curves of R-11, water and nitrogen show a 80 to 90 percent reduction of wall superheat required to transfer the same heat flux as that on plain surfaces.

2 Detailed measurement of bubble formation in R-11 indicated a significant contribution of latent heat flux to the total heat flux.

3 A visualization study made with the transparent model suggested the important role played by vaporization inside the tunnel in enhancing heat transfer.

4 Heat flux on the outer surface, resulting from convection caused by bubble formation, is related to the population density of active pores and the wall superheat by the empirical equation (2) with the constants $x = -1/5$, $y = 3/5$, $C_q = 1.95[\mathrm{K(cm^2/W)^{3/5}(1/cm^2)^{1/5}}]$ for R-11.

Acknowledgment

The authors wish to thank Mr. H. Yoshida, Senior Researcher, Hitachi Cable Ltd., for his cooperation in preparation of the test surfaces.

References

1 Milton, R. M., "Heat Exchanger System," U.S. Patent 3,384,154, May, 1968.

2 Dahl, M. M., and Erb, L. D., "Liquid Heat Exchanger Interface and Method," U.S. Patent 3,990,862, Nov., 1976.

3 Kun, L. C., and Czikk, A. M., "Surface for Boiling Liquids," U.S. Patent 3,454,081, July, 1969.

4 Webb, R. L., "Heat Transfer Surface Having a High Boiling Heat Transfer Coefficient," U.S. Patent 3,696,861, Oct., 1972.

5 Zatell, V. A., "Method of Modifying a Finned Tube for Boiling Enhancement," U.S. Patent 3,768,290, Oct., 1973.

6 Fujie, K., Nakayama, W., Kuwahara, H., and Kakizaki, K., "Heat Transfer Wall for Boiling Liquids," U.S. Patent 4,060,125, Nov., 1977.

7 O'Neill, P. S., Gottzmann, C. F., and Terbot, J. W., "Novel Heat Exchanger Increases Cascade Cycle Efficiency for Natural Gas Liquefaction," *Advances in Cryogenic Engineering,* Vol. 17, 1972, pp. 420–437.

8 Arai, N., Fukushima, T., Arai, A., Nakajima, T., Fujie, K., and Nakayama, Y., "Heat Transfer Tubes Enhancing Boiling and Condensation in Heat Exchangers of a Refrigerating Machine," *ASHRAE Trans.* Vol. 83, Pt 2, 1977, pp. 58–69.

9 Czikk, A. M., and O'Neill, P. S., "Correlation of Nucleate Boiling from Porous Metal Films," *Advances in Enhanced Heat Transfer,* ASME, New York, 1979, pp. 53–59.

10 Macbeth, R. V., "Boiling on Surfaces Overlayed with a Porous Deposit: Heat Transfer Rates Obtainable by Capillary Action," AEEW-R. 711, U.K.A.E.A., 1971.

11 Ferrell, J. K, and Alleavitch, J., "Vaporization Heat Transfer in Capillary Wick Structures," *Chemical Engineering Symposium Series,* Vol. 2, No. 66, 1970, pp. 82–91.

12 Gregory, F. C., "An Investigation of Nucleate Boiling from Mesh Covered Surfaces," Thesis, U.S. Naval Postgraduate School, June, 1970.

13 Cornwell, K., Nair, B. G., and Patten, T. D., "Observation of Boiling in Porous Media," *International Journal of Heat and Mass Transfer,* Vol. 19, 1976, pp. 236–238.

14 Nishikawa, K., and Yamagata, K., "On the Correlation of Nucleate Boiling Heat Transfer," *International Journal of Heat and Mass Transfer,* Vol. 1, 1960, pp. 219–235.

15 Brentari, E. G., and Smith, R. V., "Nucleate and Film Pool Boiling Design Correlations for O_2, N_2, H_2 and H_e," *Advances in Cryogenic Engineering,* Vol. 10, 1965, pp. 325–341.

16 Kurihara, H. M., and Myers, J. E., "The Effects of Superheat and Surface Roughness on Boiling Coefficients," *AIChE Journal,* Vol. 6, No. 1, 1960, pp. 83–91.

17 Nishikawa, K., and Fujita, Y., "Correlation of Nucleate Boiling Heat Transfer Based on Bubble Population Density," *International Journal of Heat and Mass Transfer,* Vol. 20, 1977, pp. 233–245.

18 Zuber, N., "Nucleate Boiling, The Region of Isolated Bubbles and the Similarity with Natural Convection," *International Journal of Heat and Mass Transfer,* Vol. 6, 1963, pp. 53–78.

19 Potash, Jr. M., and Wayner, Jr. P. C., "Evaporation From a Two-Dimensional Extended Meniscus," *International Journal of Heat and Mass Transfer,* Vol. 15, 1972, pp. 1851–1863.

20 Nakayama, W., Daikoku, T., Kuwahara, H., and Nakajima, T., "Dynamic Model of Enhanced Boiling Heat Transfer on Porous Surfaces—Part II. Analytical Modeling," ASME JOURNAL OF HEAT TRANSFER, Vol. 102, No. 3, 1980, pp. 451–456.

Appendix

Figure A-1 shows the apparatus used for the experiment of water. The main parts are: a stainless steel vessel ①, an auxiliary heater ③, a copper block ⑤ with a test surface ⑥ and thermal insulation ⑧⑨⑩. The vessel is open to the air through a vent ④. The block ⑥ was heated by the resistance heaters inserted from the bottom ⑦. The heat flow rate was determined from the temperature gradient in the copper block; four copper-constantan thermocouples (0.2 mm dia) imbedded at a 5 mm spacing gave the temperature gradient.

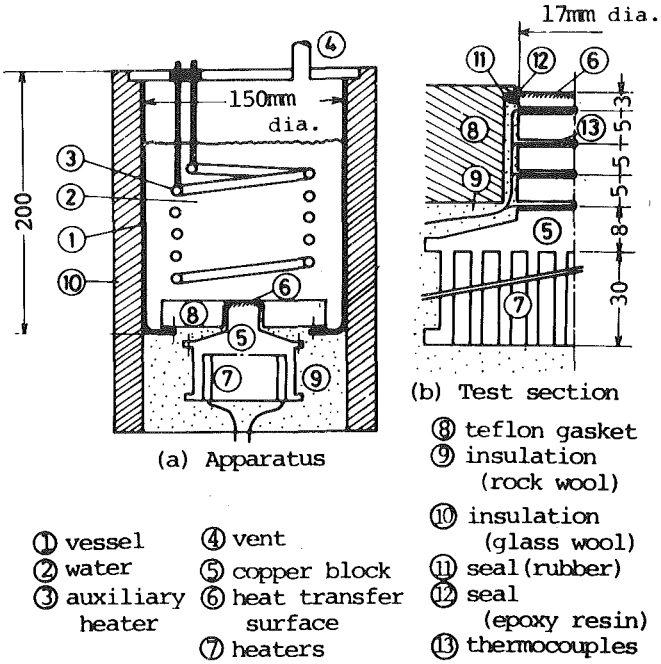

Fig. A-1 Apparatus for boiling water

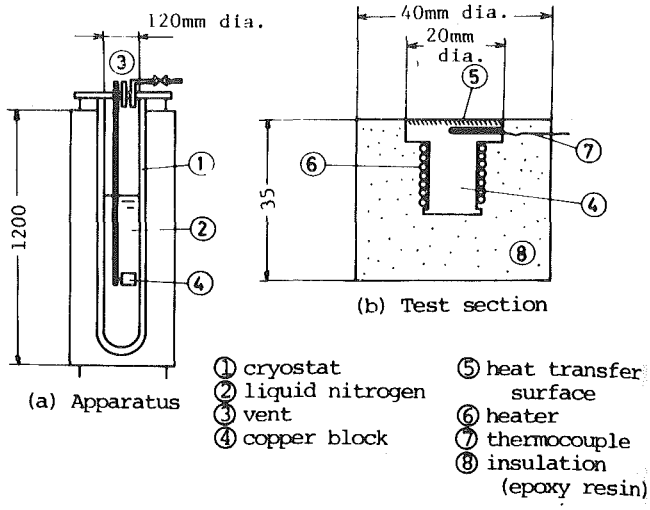

Fig. A-2 Apparatus for boiling liquid nitrogen

The apparatuses for R-11 and nitrogen are similar. Figure A-2 shows the apparatus used for the experiment of nitrogen.

In the cases of water and R-11, the temperature at the bottom of the tunnel was determined by extrapolating the thermocouple readings at four locations in the block, and this was defined as the surface temperature. For nitrogen, the temperature at 2.5 mm below the heat transfer surface was measured by a copper-constantan (0.2 mm dia) thermocouple. The surface temperature was defined as the temperature at the bottom of the tunnel, which was determined by computation of heat conduction from the thermocouple to the tunnel bottom.

The causes of inaccuracy in surface temperature and heat flux measurements come from the instruments, the sensors, the nonlinearity of temperature distribution in the blocks, and the uncertainty in thermal conductivities and the heat leak estimations. The estimated accuracies are summarized as follows

R-11 and water

ΔT, $\pm(0.10 - 0.34)$K; q, max. 9 percent

Nitrogen

if the heat flux is assumed to be accurate, ΔT is uncertain in the ranges, ±2.3 percent at ΔT = 5 K, ±33.3 percent at ΔT = 0.2 K.

The measurements of the departure diameter and departure frequency were made by either photographic recording or an optical method utilizing laser light. In the latter case, the departing bubble was stilled by synchronization of light pulse and its diameter was measured through a microscope. The frequency was measured by amplifying light signal dispersed by the bubble and processing it in an autocorrelation functioner to find the mean value. The population density was measured by counting the number of active sites on many photographs.

W. Nakayama
Chief Researcher,
Mem. ASME

T. Daikoku
Researcher.

H. Kuwahara
Researcher.

T. Nakajima
Researcher.

Mechanical Engineering Research Laboratory,
Hitachi, Ltd.,
502 Kandatsu, Tsuchiura,
Ibaraki, Japan

Dynamic Model of Enhanced Boiling Heat Transfer on Porous Surfaces

Part II: Analytical Modeling

Based on the experimental results reported in Part I, an analytical model of the dynamic cycle of bubble formation is proposed. The cycle consists of a waiting period and a bubble growth period; in the former the pressure in the tunnel is increased due to evaporation from internally held meniscuses and in the latter a certain amount of pool liquid is sucked in the tunnel to be subsequently evaporated. The equations are formulated with the adoption of a moderate number of empirical constants. Their solutions give the predictions of latent heat flux due to internal evaporation, population density of active sites, and frequency of bubble formation. The population density is then used to estimate convective heat flux on the outer surface from the empirical correlation established in Part I. The analytical predictions are compared with the experimental data of Part I. The results are encouraging and indicate the course of future study to implement the model.

Introduction

It has been known that on porous surfaces nucleation begins with the imposition of a much lower degree of wall superheat than is usually observed on plain surfaces. Bubble generation raises the heat flux to a higher order of magnitude in a range of small wall superheats where natural convection is normally the sole mode of heat transfer.

The structure of the porous surface is characterized by continuous internal cavities and a number of pores on the outer surface. One might conjecture that the porous surface structure functions as a cluster of isolated re-entrant type cavities, ignoring the continuity of internal cavities. From this viewpoint, the enhanced heat transfer is explained by the intensification of convection on the outer surface brought by the increased population density of bubbles. However, the experimental data on bubble formation, reported in the companion paper Part I [1], showed that this is not the case. When the wall superheat is moderate, bubbles are formed at a relatively small number of pores and the majority of pores remain inactive; enhancement is largely brought about by the latent heat transport, not the convective component. It is therefore essential for the understanding of porous surface boiling to consider internal cavities, inactive, and active pores as integrated parts of the surface structure, all having important functions to drive the dynamic cycle of bubble generation. That the latent heat transport is a large contributer to the enhancement suggests the importance of evaporation in the continuous internal cavity (called the tunnel in the present report).

In this part of the report, a mathematical model is set up to simulate the dynamic cycle driven by internal evaporation. The ultimate goal is the establishment of a method of performance prediction which facilitates the determination of optimum structural size for a given heat load condition. The base of the analytical model was provided by the experimental investigation in Part I. To the authors' knowledge, there has never been any published work that takes into account the dynamic process considered in this report.

Dynamic Model of Bubble Formation

The surface structure under consideration has a number of tunnels and pores, located with the spacings of λ_t and λ_0, respectively (Fig. 1). However, the analytical model developed here is intended not only for the present surface but for a class of porous layers that have a relatively large volume of interconnected cavities and narrow openings on the exterior surface.

Throughout the analysis, the following assumptions were made.

1 The pool liquid is at saturation temperature (T_s) corresponding to system pressure (P_s).

2 The temperature of the tunnel wall (T_w) is uniform.

3 The vapor in the tunnels and bubbles is in saturated state.

4 The case of large pores and, hence, the situation where the tunnel is flooded by a large volume of liquid, is not considered. The tunnels are filled with vapor except in the neighborhood of angled corners where liquid is held.

Other assumptions will be stated wherever appropriate.

The sequence of events is divided into the following phases (see Fig. 2).

I Pressure Build-Up Phase. Pressure is built up in the tunnel by evaporation of liquid held in the corners. This phase continues until the meniscus at the pores reaches a hemispherical shape of radius $r_0(=d_0/2)$. At the end of this phase, the pressure in the tunnel is at its maximum.

II Pressure Reduction Phase. At some pores, the meniscuses begin growing into bubbles faster than those at other pores due to naturally existing perturbation. The pressure built up in Phase I is reduced as the vapor flows into the growing bubbles. The meniscuses at inactive pores are unable to grow due to the reduction of pressure of the vapor. In the initial period of bubble growth, the bubble expands under high internal pressure. Later the growth is governed by the inertia of receding liquid around the bubble.

III Liquid Intake Phase. In this phase, the inertia of the liquid forces expansion of the bubble to a point where the pressure in the

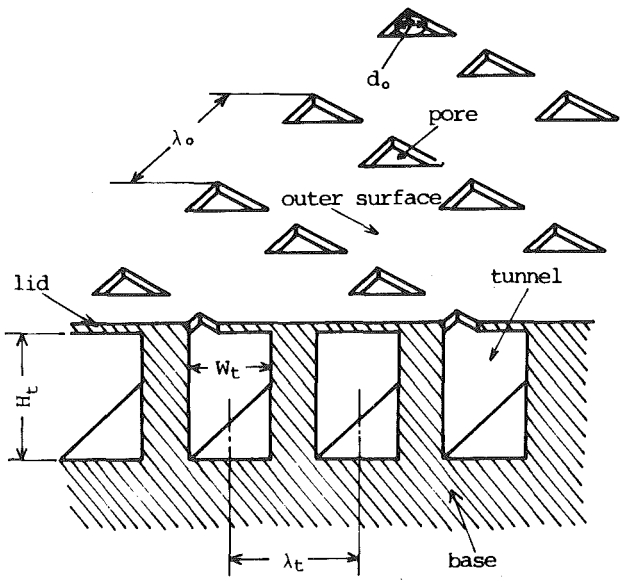

Fig. 1 Geometry of the surface structure

Contributed by the Heat Transfer Division for publication in the JOURNAL OF HEAT TRANSFER. Manuscript received by The Heat Transfer Division November 9, 1979.

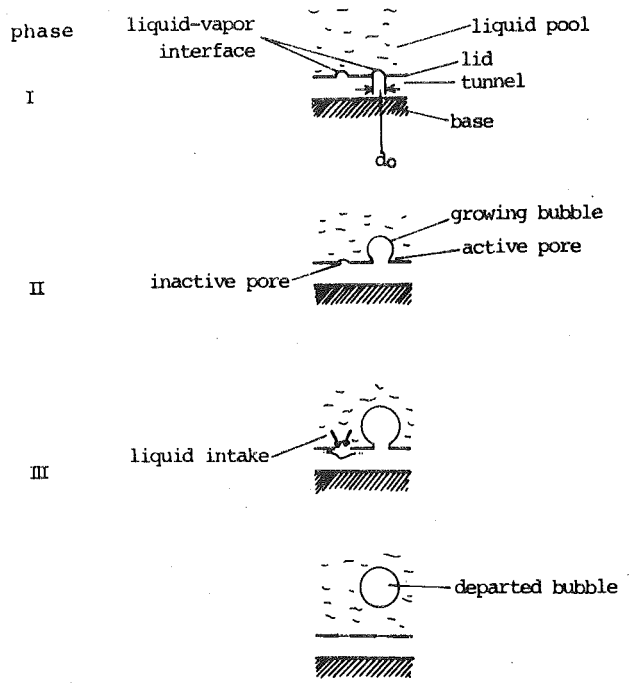

Fig. 2 Physical model for the analysis

bubble and, consequently, the pressure in the tunnel is lowered below the pool pressure. During this short interval of pressure depression, liquid flows into the tunnel through the inactive pores. At the end of this phase, the bubble departs and all pores are closed by the meniscuses. The introduced liquid spreads along the angled corners by capillary forces. The cycle starts again from Phase I.

The mathematical formulation follows.

Phase I. At the initiation of this phase (time $t = 0$), the pressure, density and temperature of the vapor in the tunnel are P_{v0}, ρ_{v0} and T_{v0}, respectively. Clapeyron-Clausius relation,

$$dT_v/dp_v = g_c T_{v0}/\rho_{v0} h_{fg}, \tag{1}$$

and the equation of state

$$p_v = g_c^{-1} \rho_v R T_v \tag{2}$$

are combined to give the temperature and density of the vapor at the end of the phase ($t = \theta_1$), where

$$P_v = P_{v1} \equiv 2\sigma/r_0, \tag{3}$$

$$T_{v1} = T_{v0} + g_c(2\sigma/r_0) T_{v0}/(\rho_{v0} h_{fg}), \tag{4}$$

$$\rho_{v1} = \rho_{v0} + g_c(2\sigma/r_0)(1 - RT_{v0}/h_{fg})/RT_{v0} \tag{5}$$

In the above equations, R is gas constant, and σ is surface tension.

Denoting heat transfer coefficient and heat transfer area in the tunnel by h_t and A_t, respectively, one writes the heat balance equation,

$$h_t A_t (T_w - T_v) = h_{fg} dm_v/dt, \tag{6}$$

where dm_v/dt is the rate of increase of vapor mass and given by the sum

$$dm_v/dt = V_v d\rho_v/dt + \rho_{vm1} dV_v/dt. \tag{7}$$

V_v is the volume of vapor and $\rho_{vm1} = (\rho_{v0} + \rho_{v1})/2$.

For the heat transfer process on the tunnel walls, the following assumptions were made. (1) The mass of introduced liquid is so small that its heat capacity is negligible. (2) Evaporation takes place from the liquid held in the angled corners. Its rate is proportional to $k_\ell(T_w - T_v)/\delta_\ell$, where k_ℓ is liquid thermal conductivity and δ_ℓ represents the thickness of the held-up liquid, decreasing with time. (3) Actual heat transfer area A_{ta} is distributed in the neighborhood of the corners and much smaller than the tunnel wall area. A_{ta} decreases in proportion to δ_ℓ due to evaporation of the liquid.

The first assumption could be examined aposteriori. Based on assumptions (2) and (3), one sets

$$h_t A_t = k_\ell C_{t1}, \tag{8}$$

where C_{t1} is a constant independent of time. For justification of (2) and (3), and determination of C_{t1}, one has to await further detailed investigations on vaporizing process of meniscuses in each specific type of angled corners. Presently, C_{t1} is set as empirical constant.

Nomenclature

A = base heat transfer area (cm^2)
A_c = cross-sectional area of tunnel (cm^2)
A_t = surface area of tunnel wall (cm^2)
A_{ta} = actual heat transfer area of tunnel wall (cm^2)
C_b = empirical coefficient of departure diameter
C_q = empirical coefficient for equation (34) [K(cm^2/W)$^{3/5}$(1/cm^2)$^{1/5}$]
C_t = empirical coefficient for internal heat transfer (cm)
C_0 = coefficient, equation (27)
C_3 = empirical coefficient for meniscus recession
d_b = bubble departure diameter (cm)
d_0 = diameter of pore (cm or mm)
f_b = bubble formation frequency (Hz)
g = gravity acceleration (cm/s^2)
g_c = conversion factor 10^{-7} (J/dyne-cm)
H_t = tunnel height (cm or mm)
h_{fg} = latent heat of vaporization (J/g)
h_t = internal heat transfer coefficient (W/cm^{2}K)
k_ℓ = liquid thermal conductivity (W/cm K)
$\dot{m}$ = mass flow rate at the pore (g/s)
m_ℓ = liquid mass (g)
m_v = vapor mass (g)
N = number of pores
N_A = number of active pores
P = pressure ($P_a \times 0.1$)
P_0 = initial pressure ($P_a \times 0.1$)
P_v = pressure of the vapor ($P_a \times 0.1$)
$P^* = P/(\sigma/r_0)$
q = heat flux (W/cm^2)
q_{ex} = heat flux on the outer surface (W/cm^2)
q_L = latent heat flux (W/cm^2)
R = gas constant (J/gK)
r_0 = pore radius (cm)
T = temperature (K)
T_v = temperature of vapor (K)
T_w = temperature of wall (K)
ΔT = wall superheat (K)
ΔT_t = temperature difference between the wall and the internal vapor (K)
t = time (s)
V_t = tunnel volume (cm^3)
V_v = vapor volume (cm^3)
W_t = tunnel width (cm or mm)
$X = \sqrt{2/3} \cdot \eta^{3/2}$
Z = nondimensional mass flux at the active pore
Z_i = nondimensional mass flux at the inactive pore
$\beta = N_A/N$
δ_ℓ = representative liquid thickness in the tunnel (cm)
$\eta = \eta'/r_0$
η_d = value of η at the time of bubble departure
η' = distance between the bubble top and the outer surface at the active pore (cm)
λ_0 = pore pitch (cm or mm)
λ_t = tunnel pitch (cm or mm)
ξ = non-dimensional distance between the bubble top and the outer surface at the inactive pore
ξ_3 = ξ in phase III
ρ_v = vapor density (g/cm^3)
ρ_ℓ = liquid density (g/cm^3)
σ = surface tension (dyne/cm)
$\tau = t/\sqrt{\rho_\ell r_0^3/\sigma}$
Φ^* = equation (17)
0 = initial value
1 = phase I
2 = phase II
$m1$ = mean value in phase I
$m2$ = mean value in phase II
S = saturated state
vb = vapor in the bubble
* = nondimensional
Z_{max} = maximum mass flow

Substituting equations (7) and (8) into equation (6), making use of equations (1, 2), and adopting some linearizing manipulations, one determines the period of Phase I as

$$\theta_1 = \frac{V_{vm}h_{fg}}{k_\ell C_{t1}}\left\{\frac{\rho_{vm1}(h_{fg} - RT_{v0})}{RT_{v0}^2}\ln\left(\frac{T_v - T_{v0}}{T_w - T_{v1}}\right) + \frac{\rho_{vm1}}{\Delta T_{t1}}\ln\left(\frac{V_{v1}}{V_t}\right)\right\}. \tag{9}$$

In equation (9), V_t is the volume of the tunnel. When the total number and pitch of the pores are N and λ_0, respectively, and the tunnel cross-sectional area is A_c, $V_t = N\lambda_0 A_c$. Another assumption is made here that, at $t = 0$, the meniscuses at the pores are flush with the lid. Hence, at $t = 0$, $V_v = V_t$, and at $t = \theta_1$, $V_v = V_{v1} \equiv V_t + N(\pi d_0^3/12)$. Other notations in equation (9), $V_{vm} = (V_t + V_{v1})/2$, $\Delta T_{t1} = T_w - (T_{v0} + T_{v1})/2$. The mass of liquid evaporated during θ_1 is

$$m_{\ell 1} = V_{vm}(\rho_{v1} - \rho_{v0}) + N(\pi d_0^3/12)\rho_{vm1}. \tag{10}$$

Phases II and III. The basic assumption here is that, at the active pore, viscous forces and evaporation from the bubble boundary make a negligible contribution to the dynamics of bubble growth. Predominance of inertia forces over viscous forces in bubble growth has been reported by Cooper and Lloyd [2] and L'Ecuyer and Murtby [3]; the latter made a numerical analysis of the growth of bubbles driven by a gas flow from the submerged orifice.

Nondimensional variables are introduced for the purpose of conciseness. The conservation equations of mass and momentum are written in terms of the meniscus height at the pore, i.e., the distance between the top of the meniscus and the lid surface. These equations are derived by referring to [3]; the derivation is given in the Appendix. The meniscus height at the active pore is denoted by η', in nondimensional form $\eta \equiv \eta'/r_0$, and the nondimensional height at the inactive pore by ξ. Nondimensional time $\tau(\equiv t/\sqrt{\rho_\ell r_0^3/\sigma})$ is zero at the initiation of Phase II and θ_2^* at the end of Phase III.

Assuming the density change is negligible compared to the volume change in these phases, mass conservation equations at an individual active pore and an inactive pore are written as

$$\frac{d}{d\tau}\{\eta(\eta^2 + 3)\} = Z, \tag{11}$$

$$\frac{d}{d\tau}\{\xi(\xi^2 + 3)\} = Z_i, \tag{12}$$

respectively, where $Z(Z_i)$ is defined by

$$Z \equiv \frac{6}{\rho_{vm2}\sqrt{\sigma/r_0\rho_\ell}}\cdot\frac{\dot{m}}{\pi r_0^2} \tag{13}$$

and $\dot{m}$ is the rate of mass flow at the pore. The average density during the phase, ρ_{vm2}, is

$$\begin{aligned}\rho_{vm2} &= (\rho_{v1} + \rho_{v2})/2\\ \rho_{v2} &= \rho_{v0} + g_c(4\sigma/d_b)(1 - RT_{v0}/h_{fg})/RT_{v0}\end{aligned} \tag{14}$$

where d_b is the departure diameter. The departure diameter is given here by a conventional formula with an empirical constant C_b,

$$d_b = C_b\sqrt{2\sigma/g(\rho_\ell - \rho_{vm2})}. \tag{15}$$

Adopting the same assumption made for Phase I about the heat transfer coefficient in the tunnel, heat transfer rate on the tunnel wall is given by $k_\ell C_{t2}\Delta T_{t2}$, where C_{t2} is an empirical constant, and $\Delta T_{t2} \equiv T_w - (T_{v1} + T_{v2})/2$,

$$T_{v2} \equiv T_{v0} + g_c(4\sigma/d_b)T_{v0}/(\rho_{vm2}h_{fg}) \tag{16}$$

Then, vapor generation rate divided by the total number of pores is represented by a nondimensional parameter,

$$\Phi^* \equiv \frac{6k_\ell C_{t2}\Delta T_{t2}}{\rho_{vm2}h_{fg}\sqrt{\sigma/r_0\rho_\ell}N\pi r_0^2}. \tag{17}$$

This is treated as time-independent in the following analysis.

Denoting the ratio of the number of active pores to the total number of pores by $\beta(\equiv N_A/N)$, and assuming $\beta \ll 1$ as observed in the experiment [1], one writes the equation of instantaneous mass conservation for the whole set of active and inactive pores as

$$\beta Z + Z_i = \Phi^*. \tag{18}$$

Substitution of equations (11) and (12) into equation (18) and integration with τ from $\tau = 0$ to $\tau = \theta_2^*$ yield

$$\beta = \frac{\Phi^*\theta^*_2 - \xi_3(\xi_3^2 + 3) + 4}{\eta_d(\eta_d^2 + 3) - 4}, \tag{19}$$

where η_d is related to the departure diameter by

$$\eta_d = \frac{d_b}{2r_0}\{1 + \sqrt{1 - (2r_0/d_b)^2}\}, \tag{20}$$

and ξ_3 is the recession distance of the meniscus at the inactive pore at the end of Phase III. Note that $\eta = \xi = 1$ at $\tau = 0$ for integration of equations (11) and (12). The recession ξ_3 is assumed to be proportional to the cube root of the volume of liquid introduced during the cycle. With an empirical constant C_3, one writes

$$\xi_3 = -C_3\{(m_{\ell 1} + m_{\ell 2})/\rho_\ell N\pi r_0^3\}^{1/3}, \tag{21}$$

where $m_{\ell 2}$ is the mass of evaporated liquid during Phases II and III.

Equation of momentum for the growing bubble at the active pore is written in non-dimensional form

$$P_{vb}^* - P_s^* = \frac{4\eta}{\eta^2 + 1} + \frac{5\eta^4 - 3\eta^2 + 6}{16\eta^4}\left(\frac{d\eta}{d\tau}\right)^2 + \frac{(\eta^2 + 1)(2\eta^2 - 1)}{8\eta^3}\frac{d^2\eta}{d\tau^2}, \tag{22}$$

where P_{vb}^* is the averaged pressure in the bubble made dimensionless by (σ/r_0) and P_s^* ambient pressure. Rigorous integration of equation (22), if not impossible, would not yield results in a manageable form. Therefore, approximate treatment is done by adopting an intuitive argument that the momentum balance at the time of maximum mass flow rate into the growing bubble is crucial to determine the duration of Phases II and III combined. Assuming $\eta \gg 1$, and setting $X \equiv \sqrt{2/3}\,\eta^{3/2}$, one rewrites equation (11) as

$$Z = 3XdX/d\tau. \tag{23}$$

The following quadratic equation is written to approximate the relationship between X and τ,

$$X = \sqrt{2/3} + 2(X_d - \sqrt{2/3})(\tau/\theta_2^*) - (X_d - \sqrt{2/3})(\tau/\theta_2^*)^2 \tag{24}$$

which satisfies $X = \sqrt{2/3}$ at $\tau = 0$ and $X = X_d(\equiv\sqrt{2/3}\eta_d^{3/2})$, $dX/d\tau = 0$ at $\tau = \theta_2^*$. Substituting equation (24) into equation (23) one obtains the maximum values of X and Z,

$$X = (2/3)X_d,\ Z = 2.309X_d^2/\theta_2^* \equiv Z_{\max},$$

when

$$\tau = 0.423\theta_2^* \equiv \tau_{Z_{\max}}. \tag{25}$$

Conversion of X to η and substitution of equations (25) yield the values of η, $d\eta/d\tau$ and $d^2\eta/d\tau^2$ corresponding to $Z_{\max}$. Equation (22) then becomes

$$P_{vb}^* - P_s^* = \frac{5.242}{\eta_d} - 0.1457\frac{\eta_d^2}{\theta_2^{*2}}. \tag{26}$$

The average pressure in the bubble P_{vb}^* is lower than the pressure in the tunnel P_v^* due to pressure drop caused by the vapor flow through the pore. With an empirical coefficient C_0, P_{vb}^* is related to P_v^* by

$$P_v^* - P_{vb}^* = \frac{C_0}{72}\left(\frac{\rho_{vm2}}{\rho_\ell}\right)Z^2 = 0.0329\,C_0\left(\frac{\rho_{vm2}}{\rho_\ell}\right)\frac{\eta_d^6}{\theta_2^{*2}}. \tag{27}$$

It should be noted that this term becomes crucial in the case of small pore diameters as it determines the possibility of liquid intake necessary to maintain the cycle.

In the last step of the analysis, the relationship between P_v^* and P_s^* is sought from the force balance equation at the inactive pore,

$$P_v^* - P_s^* = 4\xi, \tag{28}$$

where $\xi \ll 1$ is assumed. Integration of equation (12) from $\tau = 0$ to $\tau_{Z_{max}}$ and use of equation (18) yield

$$\xi = \frac{1}{3}\left\{-\beta \int_0^{\tau_{Z_{max}}} Z d\tau + \Phi^* \tau_{Z_{max}} + 3\right\}. \quad (29)$$

Substituting equations (23) and (24) into equation (29) and setting $\beta \approx \Phi^* \theta_2^* / \eta_d^{*3}$, one obtains

$$\xi_{Z_{max}} = 1 - 0.007\, \Phi^* \theta_2^*. \quad (30)$$

From preliminary computations, it turned out that $\xi_{Z_{max}} \approx 0$, hence, by setting $P_v^* = P_s^*$ in equations (26) and (27) and adding both equations, one obtains

$$\theta_2^* = \sqrt{\frac{\eta_d 3}{5.242}\left\{0.1457 - 0.0329 C_0 \left(\frac{\rho_{vm2}}{\rho_\ell}\right) \eta_d{}^4\right\}}. \quad (31)$$

Determination of Constants

The empirical constants introduced in the above analysis were determined by referring to the experimental data on bubble formation reported in Part I [1]. Refer to Table 1 of Part I for a specific list of the test surfaces designated by, for example, R(11)-1 and W-2. For the initial state of Phase I, one has no concrete information to specify it, hence, has to adopt an approximation that $P_{v0} = P_s$, $T_{v0} = T_s$ and $\rho_{v0} = P_s/RT_s$.

For R-11, the surface R(11)-1 provides the most detailed and reliable data to determine other empirical constants. The reference state was arbitrarily chosen at $\Delta T = 1$K, where $q = 1.12$ W/cm^2, $f_b = 130$ Hz, $d_b = 0.7$ mm and $N_A/A = 13.5$ cm^{-2}. Based on these values, it is estimated that $q_L = 0.34$ W/cm^2. The total number of pores is $N = 2050$, hence, $\beta = 0.053$. Using physical properties of R-11, $\sigma = 18$ dyne/cm, $h_{fg} = 179.8$ J/g and $R = 0.0563$ J/g K, and setting $C_0 = 0$ as described later, the empirical constants were determined as

$$C_b = 0.442, \qquad C_3 = 3.172,$$
$$C_{t1} = 3.13 \times 10^2 \text{ (cm)}, \qquad C_{t2} = 2.77 \times 10^4 \text{ (cm)}.$$

From these values of C_{t1} and C_{t2}, the equivalent heat transfer coefficients (W/cm^{2}K) based on the tunnel wall area A_t are computed as $h_{t1} = 0.016$ and $h_{t2} = 1.46$. These coefficients should be viewed as the average values during each phase; h_{t2} is greater than h_{t1}. Although nothing definite can be said about the reason for this before more detailed investigation is carried out, it does not contradict one's supposition that an extremely high heat transfer coefficient is attained during the dynamic period.

As for the value of C_0, one could infer that on a surface having too small pore diameters, the inertial force of bubble growth to suck liquid into the tunnel is annulled by the flow resistance at the pore mouth; hence, no supply of liquid is vaporized in the tunnel. The critical pore diameter for which the present mechanism fails to work would provide the ground to determine C_0. Until now, there has been no reliable data on the critical diameter. Instead of relying on uncertain data, survey computations have been conducted to see the effect of variation of C_0. It is found that C_0 is much smaller than unity and the variation of C_0 has had little effect on the predicted values of q, β and f_b unless the right hand side of equation (31) becomes nearly zero. On the basis of this computational experience, and for the simplicity of the formula, one tentatively sets $C_0 = 0$.

Some data on the density and frequency of bubble formation were also obtained with the surface R(11)-3. Based on these data, C_3, C_{t1} and C_{t2} were determined as $C_3 = 5.675$, $C_{t1} = 3.32 \times 10^2$ cm ($h_{t1} = 0.022$ W/cm^{2}K), $C_{t2} = 3.20 \times 10^4$ cm ($h_{t2} = 2.11$ W/cm^{2}K).

The other constants are set equal to the values for R(11)-1. It should be noted here that on this surface a small fraction of the pores have an oblate form, the minor axis extending 0.4 (±0.2) mm, the major axis about 1 mm, and some others (37 percent of the total number) are found to be entirely closed. The effective total number of pores is estimated at $N = 1300$.

For water, the constant C_b is chosen among many previously reported data as $C_b = 0.22$. There are no basic data to determine C_0, C_3, C_{t1} and C_{t2}, hence, the values of C_0 and C_3 obtained for R-11 are adopted, and a multiplier is introduced for C_{t1} and C_{t2} to fit the analytical heat flux to the experimental data at a certain ΔT.

For nitrogen, any detailed measurements could not be made. Therefore, the values for R-11 are employed for C_0 and C_3, and C_{t1} and C_{t2} are multiplied by an adjustable factor. The value for C_b is determined from the reported data on departure diameter of nitrogen on plain surfaces [4] as $C_b = 1.67$.

Procedure of Predictive Computation

In the authors' view, more thorough comparison of the analytical results with more experimental data are required before writing a summarized correlation of $q - \Delta T$ in a concise form. Instead, the procedure of computation is described below. It is understood that the specifications of the surface structure geometry, physical properties of the fluid, the system pressure and the wall temperature are given.

1 Compute θ_1 and $m_{\ell 1}$ from equations (9) and (10), respectively.

2 Find θ_2^* from equation (31) and convert it to

$$\theta_2 \equiv \theta_2^* \sqrt{\rho_\ell r_0^3/\sigma}\,.$$

3 Compute $m_{\ell 2}$ from $m_{\ell 2} = \theta_2 (k_\ell C_{t2})\, \Delta T_{t2}/h_{fg}$. (32)

4 ξ_3 from equation (21).

5 β from equation (19).

6 q_L from $q_L = (m_{\ell 1} + m_{\ell 2}) h_{fg}/(\theta_1 + \theta_2) A$. (33)

7 Using β, one finds $N_A = \beta N$, then q_{ex} is computed from

$$q_{ex} = (\Delta T/C_q)^{5/3}\, (N_A/A)^{1/3}, \quad (34)$$

where $C_q = 1.95$ [K(cm^2/W)$^{3/5}$(1/cm^2)$^{1/5}$] for R-11 [1],
$C_q = 3.93$ [K(cm^2/W)$^{3/5}$(1/cm^2)$^{1/5}$] for water [5], and
$\Delta T \equiv T_w - T_s$.

8 $q = q_L + q_{ex}$. (35)

Results and Discussion

The predicted heat flux for R-11 is compared to the measured heat flux in Fig. 3. Within the range $0.2 < q < 4$ W/cm^2, the prediction agrees fairly well with the experimental data. The slope of the boiling curves is reproduced well by the analysis. In Fig. 3 (b) of Part I [1] the empirical boiling curves are seen to moderate their slope in a high heat flux range. It remains open to future investigation to explain this transition.

In Fig. 4, the experimental data of bubble departure frequency (Fig. 4 (a)) and population density of bubble formation sites (Fig. 4 (b)) taken with the surface R(11)-1 are compared with the predictions. They are in good agreement. The experimental surface actually has

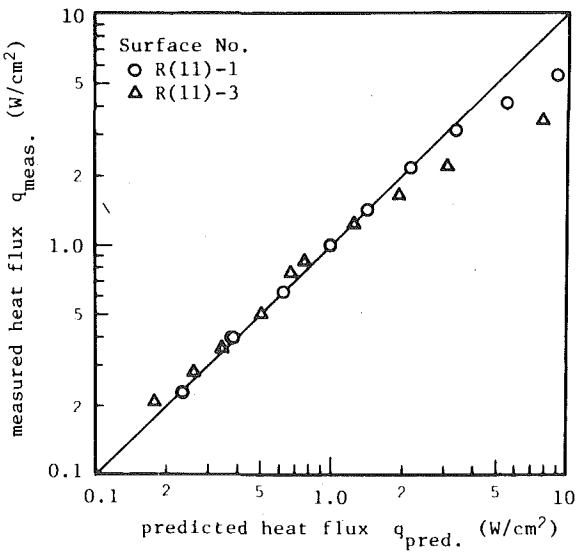

Fig. 3 Comparison between the measured heat flux and predicted heat flux for R-11

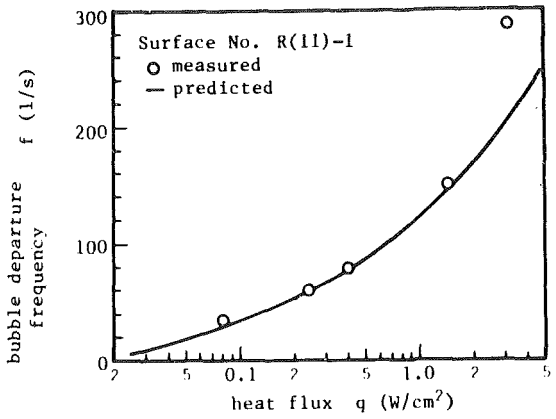

Fig. 4(*a*) Bubble departure frequency

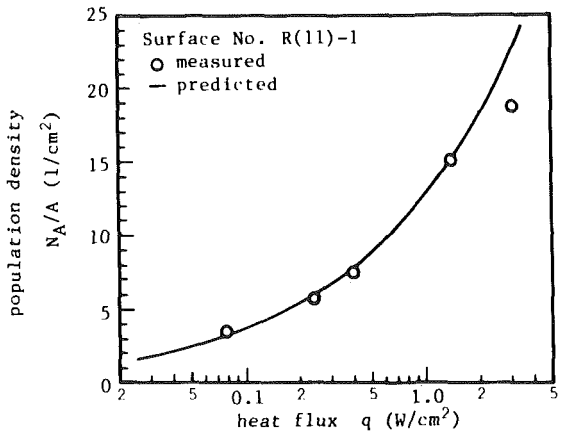

Fig. 4(*b*) Population density

Fig. 4 Comparison between the measured and predicted bubble formation characteristics

a row of 72 independent parallel tunnels, each having a length of 2 cm and 28 to 29 pores, whereas, in the analysis, this set of individual tunnels are treated as one single space. Similar comparisons were attempted for the surface R(11)-3. However, for small pore diameters, computed results are particularly sensitive to the change of geometrical dimensions. The uniformity of the structural geometry must be established before making a meaningful comparison. Another source of uncertainty exists in the assumption of departure diameter independent of the heat flux. The diameter actually varies ±20 percent within the heat flux range studied; the higher the heat flux, the smaller the departure diameter. This variation tends to make dependence of the departure frequency upon the heat flux less pronounced than the present prediction does in the case of small pore diameters. Introduction of another empirical coefficient to account for the variation of d_b was avoided because it requires a further complication in the analysis to model the physical process of departure.

The number of active sites was determined in the present analysis without resorting to any stochastic model which has been employed to interpret the data on plain surfaces [6]. This could be done on the premise that the active and inactive pores are interconnected by the internal tunnels.

For water and nitrogen, heat fluxes are compared in Fig. 5. The multipliers for $C_{t1}(h_{t1})$ and $C_{t2}(h_{t2})$ had to be determined for each boiling curve at a certain ΔT in about the middle of the range of superheats. This was inevitable due to lack of sufficient information needed to determine other empirical coefficients. Figure 5 should be viewed as offering a comparison between the predicted and measured slopes of the boiling curves. Computational experience showed that the internal heat transfer coefficient is one to two orders of magnitude higher in water than in R-11, and the same order of magnitude in nitrogen. It was also found that the latent heat transport is especially

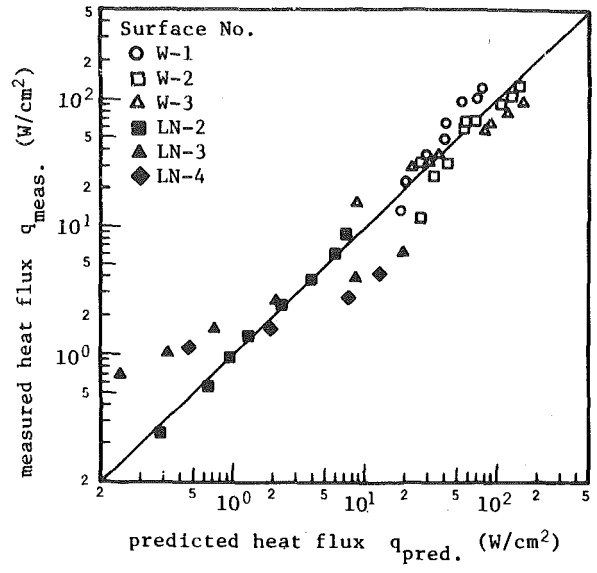

Fig. 5 Comparison between the measured heat flux and the predicted heat flux for water and nitrogen

larger in case of water (almost 95 percent). Deviation of some data from the predicted values amounts to as much as 300 percent as seen in Fig. 5. However, the analytical model yields generally satisfactory predictions for the surfaces W-2 and LN-2. Further experiment is needed before a general statement about the accuracy of the present analysis when applied to various fluids could be made.

Finally, the analytical model is used to predict the optimum pore diameter for a given heat flux. An example for water is shown in Fig. 6. The computation was performed by setting $h_{t1} = 0.29$, $h_{t2} = 25.4$ (W/cm²K) (the values for W-2) and the other constants as determined previously. The minimum superheat is produced by the interplay of lengthening waiting period of Phase I with decreasing the pore diameter and reduction of population density with increasing the pore diameter. Further increase of d_0 tends to reduce ΔT again, however, the analysis may not be applicable to the case of too large pore diameters because of the possibility of liquid flooding. The curve should be useful as a guide to optimization, however, as one can observe from the actual boiling curves of Fig. 3 (*a*) of Part I [1], the optimization analysis of real use has to await more data providing the firm bases for the empirical coefficients, refinement of the analytical model itself, and more rigorously controlled geometry of the surface structure.

The relationships between ΔT versus d_0 for R-11 and nitrogen have been sought, and the examples are shown in Fig. 6. The empirical constants are those of R(11)-1 for R-11, and $h_{t1} = 0.02$, $h_{t2} = 1.37$ (W/cm²K) for nitrogen. For those low surface tension fluids, the minimums of superheat are not as clearly defined as that for water. Near the left ends of the computed curves, there exist minimum values of d_0 for which the pressure build-up during Phase I becomes so high that the internal vapor temperature reaches the wall temperature before the initiation of Phase II. Hence, no vapor release occurs unless the bubble grows by the ordinary mechanism absorbing heat from the exterior boundary layer. In view of the flatness of the $\Delta T - d_0$ curves, the optimum pore diameters in practical terms are considered to exist in a range bounded to the lower end just discussed and to the higher end determined by liquid flooding. Decreasing heat transfer performance of the surfaces having large pore diameters in the low superheat range, as exemplified in Figs. 3 of Part I [1]. is thought to imply the ill effect of liquid flooding. The analysis has not yet been developed to predict the point of flooding.

Concluding Remarks

The following remarks are made to indicate the direction of future study.

1 Justification of the present analytical model by other type of porous layers could not be made, because the reported data with

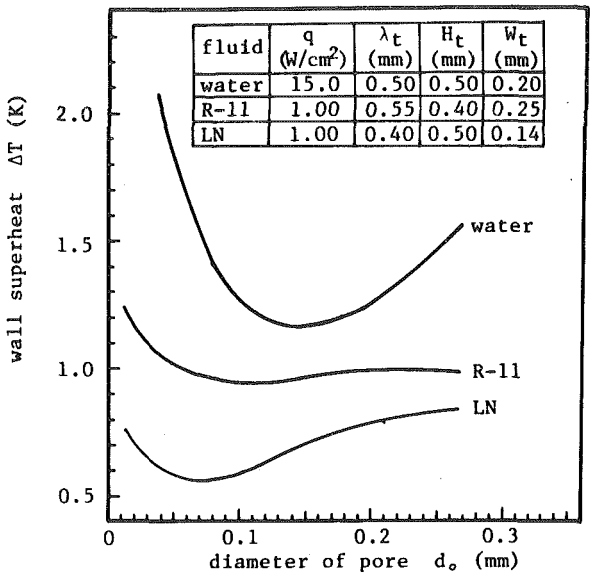

Fig. 6 Analytical prediction of optimum pore diameter

geometrical specifications are scarce. More experiments with geometrically uniform surface structures are needed.

2 The study on evaporation process in the internal cavities is important to produce more efficient surface structures. Refinement of analysis should be made by incorporating the analysis of this process.

3 The present study provides a guide to optimization of the surface structure. As manufacturing techniques are advanced to produce more uniform surface structures, the optimization analysis should become an increasingly useful tool to best utilize the enhancement mechanism discussed here.

References

1 Nakayama, W., Daikoku, T., Kuwahara, H., and Nakajima, T., "Dynamic Model of Enhanced Boiling Heat Transfer on Porous Surfaces—Part I. Experimental Investigation," ASME JOURNAL OF HEAT TRANSFER, Vol. 102, No. 3, 1980, pp. 445–450.

2 Cooper, M. G., and Lloyd, A. J. P., "The Microlayer in Nucleate Pool Boiling," *International Journal of Heat and Mass Transfer*, Vol. 12, 1969, pp. 895–913.

3 L'Ecuyer, M. R. L., and Murtby, S. N. B., "Energy Transfer From a Liquid to Gas Bubbles Forming at a Submerged Orifice," NASA TN D-2547, 1965.

4 Bewilogua, L., Knoener, R. and Wolf, G., "Heat Transfer in Boiling Hydrogen, Neon, Nitrogen and Argon," *Cryogenics*, Vol. 2, 1962, pp. 36–39.

5 Zuber, N., "Nucleate Boiling, The Region of Isolated Bubbles and the Similarity with Natural Convection," *International Journal of Heat and Mass Transfer*, Vol. 6, 1963, pp. 53–78.

6 Sultan, M., and Judd, R. L., "Spatial Distribution of Active Sites and Bubble Flux Density," ASME JOURNAL OF HEAT TRANSFER Vol. 100, 1978, pp. 56–62.

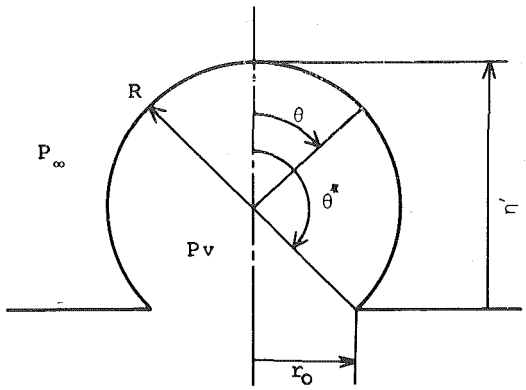

Fig. A-1 Growing bubble from the pore

Appendix

Using the coordinate system (R, θ) shown in Fig. A-1, L'Ecuyer and Murtby [3] derived the equation of momentum for a spherical bubble,

$$\frac{1}{\rho_\ell}\left(P_v - P_\infty - \frac{2\sigma}{R}\right) = R\frac{d^2R}{dt^2} + \frac{3}{2}\left(\frac{dR}{dt}\right)^2 + \frac{3}{2}V_y\cos\theta\frac{dR}{dt} + \frac{1}{2}R\cos\theta\frac{dV_y}{dt} + V_y{}^2\left(\frac{1}{2}\cos^2\theta - \frac{5}{8}\sin^2\theta\right), \quad \text{(A-1)}$$

where

$$V_y = -\frac{1}{\cos\theta^*}\frac{dR}{dt}, \quad \text{(A-2)}$$

and the viscous terms are neglected.

In terms of the distance between the bubble top and the outer surface (η'),

$$R = (\eta'^2 + r_0^2)/2\eta',\ V_y = \{(\eta'^2 + r_0^2)/2\eta'^2\}(d\eta'/dt).$$

Equation (A-1) is written by the new variable as

$$\frac{1}{\rho_\ell}\left(P_v - P_s - \frac{4\sigma\eta'}{\eta'^2 + r_0^2}\right) = \frac{1}{8\eta'^4}\left\{3\eta'^4 - 2r_0^2\eta'^2 + 7r_0^4 + (3\eta'^2 - 5r_0^2)(\eta'^2 + r_0^2)\cos\theta + (\eta'^2 + r_0^2)^2\left(\cos^2\theta - \frac{5}{4}\sin^2\theta\right)\right\}\left(\frac{d\eta'}{dt}\right)^2 + \frac{1}{8\eta'^3}\{2(\eta'^2 - r_0^2) + (\eta'^2 + r_0^2)\cos\theta\}(\eta'^2 + r_0^2)\frac{d^2\eta'}{dt^2} \quad \text{(A-3)}$$

Multiplying $2\pi(R/r_0)^2 \sin\theta d\theta = \{\pi(\eta'^2 + r_0^2)/2\eta' r_0\}^2 \sin\theta d\theta$ on equation (A-3) and integrating with respect to θ from $\theta = 0$ to θ^* ($\cos\theta^* = -(\eta'^2 - r_0^2)/(\eta'^2 + r_0^2)$) one obtains the area-integrated equation. This is further divided by the instantaneous surface area of the bubble $\pi(\eta'^2 + r_0^2)$. Assuming the pressure is uniform in the bubble and using the nondimensional variables, one obtains equation (22).

J. H. Lienhard
Mechanical Engineering Department,
University of Houston,
Houston, Tex 77004,
Fellow ASME

V. K. Dhir
School of Engineering and Applied Science,
University of California,
Los Angeles, Calif. 90024
Mem. ASME

On the Prediction of the Minimum Pool Boiling Heat Flux

A criterion is offered for the collapse of film boiling in a saturated liquid at the minimum heat flux. The criterion says the vapor film collapse occurs when insufficient vapor is generated to sustain the growing wave after it reaches a constant rate of increase of amplitude. This criterion yields an accurate prediction for horizontal flat plates and cylinders. The prediction requires the use of empirical generalizations about the configuration of film boiling, which are also developed here.

Objective

The literature on the prediction of $q_{\min}$, the minimum saturated pool boiling heat flux, includes several basic papers, each of which was written before certain relevant information became available. We wish to refine the theory on the basis of more recent information. First let us review what has been done.

History

Chang [1] appears to be the first investigator who recognized that, to understand film boiling behavior, one had to understand the Taylor unstable wave action in the liquid-vapor interface above the heater. Zuber and Tribus (see, e.g., [2]) showed how $q_{\min}$ could be predicted on the basis of this action. Their development was restricted to the infinite horizontal flat heater. It can be paraphrased in the following way. They began by noting that

$$\frac{q_{\min}}{\rho_g h_{fg}} = u_g = \left(\frac{\text{volume of bubbles}}{\text{heater area-cycle}}\right)\left(f\,\frac{\text{cycle}}{\text{s}}\right) \tag{1}$$

Here we designate volume of vapor created per unit area of heater as the velocity, u_g, and the lowest frequency at which bubbles can leave each node, as f. Figure 1 is a typical photograph of film boiling from a horizontal wire. It illustrates the collapsing Taylor wave motion. (It is much harder to photograph film boiling on a large flat plate, although Dhir, Castle, and Catton [3] have photographed analogical behavior during the sublimation of a slab of dry ice under warm water.) Above a horizontal plate, the Taylor wave action is as shown in Fig. 2.

Zuber completed his derivation subject to several assumptions. They are

1 The bubble radius is $\lambda_{d_1}/4$ where λ_{d_1} is the length of a one-dimensional wave given by [4]

$$\lambda_{d_1} = \frac{2\pi\sqrt{3}}{\sqrt{\dfrac{g(\rho_f - \rho_g)}{\sigma}}} \tag{2}$$

2 The minimum frequency was taken as the inverse of the time needed for a wave to grow to an amplitude of λ_{d_1}, based on its amplitude-averaged growth rate up to an amplitude of $0.4\lambda_{d_1}$ (assuming that during this period, the growth can be predicted by the simple linear theory.)

3 Two bubbles are released per cycle per area equal to $\lambda_{d_1}^2$

The first assumption has stood up to several people's subsequent measurements (see, e.g., [5]). Berenson [6] noted in 1961 that Zuber's amplitude average should have been a time average and that nonlinear growth, beyond an amplitude of $0.4\lambda_d$, could not be obtained by an extrapolation in any event. His $q_{\min}$ formula therefore took the form

$$u_g = A\sqrt[4]{\frac{\sigma g(\rho_f - \rho_g)}{(\rho_f + \rho_g)^2}} \tag{3}$$

where A was set at 0.09, based on two carefully measured data points.

[1] This work was done when the author was with the Department of Mechanical Engineering, University of Kentucky, Lexington, KY.

Contributed by the Heat Transfer Division for publication in the JOURNAL OF HEAT TRANSFER. Manuscript received by the Heat Transfer Division January 11, 1980.

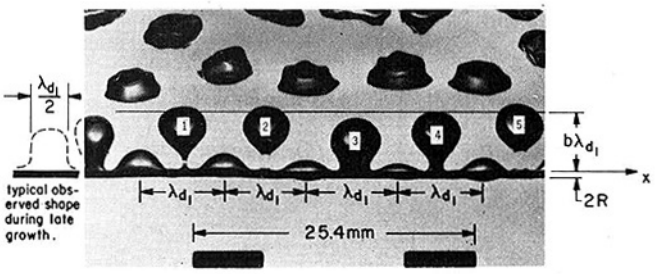

Fig. 1 Typical bubble departure pattern during film boiling (Radius of wire, R = 0.323mm, q = 1.3 × 10^5 W/m^2, fluid is acetone at 1 atm, R' = 0.0203, b_4 = 0.65)

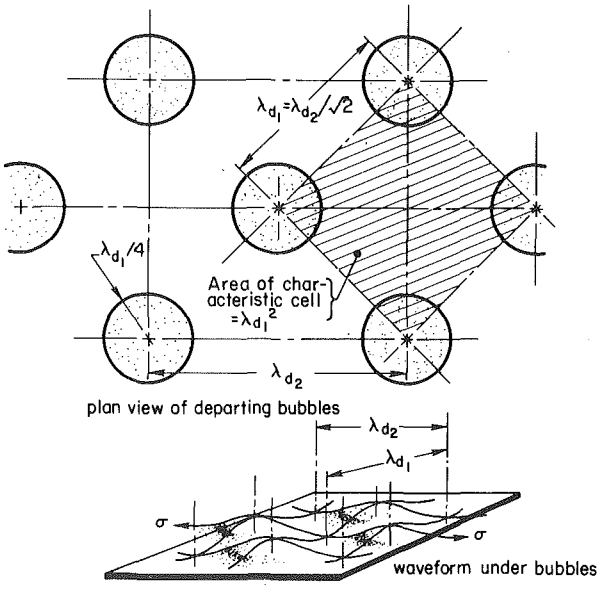

Fig. 2 The array of vapor jets as seen on an infinite horizontal heater surface

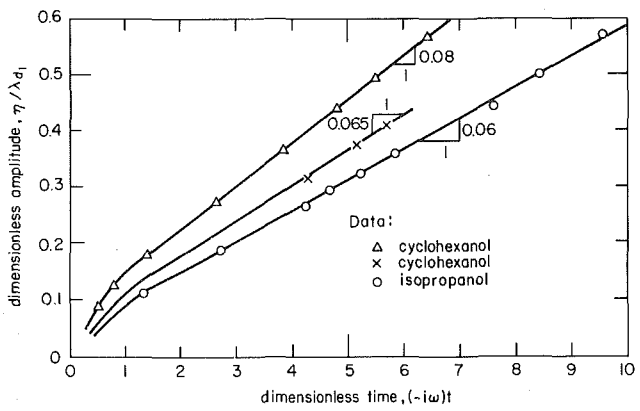

Fig. 3 Typical observations of late bubble growth during film boiling

Zuber's prediction gave $A = 0.177$.

In 1969, Sernas [7] showed that the wavelength in a horizontal plane interface—what we shall call the two-dimensional wavelength, λ_{d_2},—is

$$\lambda_{d_2} = \sqrt{2}\lambda_{d_1} \tag{4}$$

(see Fig. 2). He attempted to correct Zuber's formula but he assumed that the bubble diameter was still $\lambda_{d_1}/2$ instead of $\lambda_{d_2}/2$, and following Zuber he counted two bubbles in each area of $\lambda_{d_2}^2$, instead of the correct number, four. (See Fig. 2. He corrected the latter point in 1973 [8].) He also retained Zuber's estimate of f.

Meanwhile Lienhard and Wong [5] had redone Zuber's flat plate analysis for a horizontal cylinder, after they had first derived λ_{d_1} for such a configuration:

$$(\lambda_{d_1})_{cyl.} = \frac{2\pi\sqrt{3}}{\sqrt{\dfrac{g(\rho_f - \rho_g)}{\sigma} + \dfrac{1}{2R^2}}} \tag{5}$$

The resulting $q_{\min}$ prediction can be written as

$$u_g = B\sqrt[4]{\frac{g\sigma(\rho_f - \rho_g)}{(\rho_f - \rho_g)^2}} \Big/ [R'^2(2R'^2 + 1)]^{1/4}, \tag{6}$$

where

$$R' \equiv R\sqrt{\frac{g(\rho_f - \rho_g)}{\sigma}} \tag{7}$$

The Criterion for the Collapse of Film Boiling

The prediction of $q_{\min}$ using equation (1) only requires knowledge of the average velocity of vapor needed to maintain the cyclic growth and collapse of the interface. To understand the physical circumstances that specify the minimum vapor volume flow that can be sustained, we first consider the observed vapor removal configuration on a flat plate and above a horizontal cylinder (see Figs. 1 and 2).

The horizontal cylinder and horizontal flat plate generate vapor at a nearly constant rate and deliver it to an escapement process in the collapsing Taylor wave above the heater. Thus, $q_{\min}$ will occur when, as q is reduced, there is one point in the cycle where the constant rate of vapor production becomes insufficient to supply the instantaneous natural rate of wave motion. Then the wave can no longer stay off the heater, and film boiling must collapse. This criterion differs from that used by Zuber [2] in obtaining u_g in equation (1). As we have noted, Zuber attempted to determine the slowest overall natural frequency of oscillation that the wave can sustain.

To make use of the criterion we have to know the instantaneous rate of change of volume of a bubble during its growth period, and to find this we must set down some experimental observations of bubble growth during film boiling near $q_{\min}$.

Observed Bubble Action During Film Boiling

Consider the numbered bubbles in Fig. 1. Bubbles No. 2 and 5 have severed from the vapor film removing themselves as an avenue of vapor escape. Bubble No. 1 has just barely broken away and bubble No. 3 has a little way to go. Bubble No. 4 is just ceasing to provide means for vapor to escape, and its top has reached a height which is a fraction, $b = 0.65$, of the wavelength. We also observe that, although bubble height at departure is about $0.65\lambda_{d_1}$, the bubble radius of curvature is never less than $\lambda_{d_1}/4$ (see Fig. 1)

In the early stages, the growth process is exponential with an amplitude, η_m, given by

$$\eta_m = \eta_{m0}e^{-i\omega t}\cos\frac{2\pi x}{\lambda_{d_1}} \tag{8}$$

where x is an axial coordinate (see Fig. 1), η_m, evaluated at time, $t = 0$; and $(-i\omega)$ is the wave growth rate—a positive real number. Several observations of wave amplitude, η_m, as a function of time in isopropanol [9, 10] and cyclohexanol [10], show that exponential growth blends into a linear growth after the amplitude reaches a value of $0.12 \le \eta_m/\lambda_{d_1} \le 0.25$. A sampling of these data is shown in Fig. 3. It is also very clear from the data plotted in Fig. 3 that a linear growth rate is maintained until the bubble detaches from the interface. The growth rate in the linear region can be written as

$$\frac{d\eta}{dt} = c\lambda_{d_1}(-i\omega) \tag{9}$$

The value of the constant c is listed in Table 1 along with the values of b, the bubble height at detachment divided by λ_{d_1}.

Model for Instantaneous Bubble Volume Growth Rate

Figure 4(*a*) shows a geometrical model for bubble shape in the exponential and early linear growth period. If the growing interface is a part of a sphere, the bubble volume at any instant is

$$V = \pi R\eta^2\left(1 - \frac{\eta}{3R}\right) \tag{10}$$

The base radius, r, of the bubble is generally less than or equal to its curvature. To distinguish between r and R we observe that

$$r^2 = R^2 - (R - \eta)^2$$

The instantaneous rate of change of bubble volume is obtained by differentiating equation (10).

$$\frac{dV}{dt} = \pi(R\eta - \eta^2)\frac{d\eta}{dt} + \pi\eta^2\frac{dR}{dt} \tag{12}$$

However, we noted earlier that the radius of curvature of the bubble stays constant after the bubble becomes hemispherical and its height reaches $\lambda_{d_1}/4$. Thus for bubble heights equal to or slightly greater than $\lambda_{d_1}/4$, equation (12) reduces to

$$\frac{dV}{dt} = \pi(2R\eta - \eta^2)\frac{d\eta}{dt} \tag{13}$$

In all cases we have observed, the bubble reaches a linear growth

Table 1 Observed values of c and b during film boiling in organic liquids [5,9,10], for various wire sizes and (in some cases) at elevated gravity

$\bar{c}$	Standard Deviation of c	$\bar{b} \equiv \overline{\dfrac{\text{height}}{\lambda_{d_1}}}$	Standard Deviation of b
0.069	0.011	0.645	0.097

Nomenclature

A,B = constants defined in equations (3) and (6), and evaluated in equations (19) and (23)

b = (height of top of a detaching bubble) ÷ (appropriate λ_d)

c = constant of proportionality as used in equation (9)

f = frequency of bubble departures from a node

g = acceleration of gravity or other body force

h_{fg} = latent heat of vaporization

$-i\omega$ = growth rate of a wave (a real number)

q, q_{min} = heat flux; minimum pool boiling heat flux

u_g = velocity of vapor leaving a surface at $q_{\min}$, equal to $q_{\min}/\rho_g h_{fg}$

r, R, R' = radius of bubble at base, radius of top of bubble, $R\sqrt{\sigma/g(\rho_f - \rho_g)}$

t = time

V = volume of growing bubble

x,y = coordinates parallel with, and normal to, liquid-vapor interface

η_m, η_{m0} = amplitude of wave; amplitude at time $t = 0$

$\lambda_{d_1}, \lambda_{d_2}$ = the most susceptible wavelength in a one-dimensional interface, in a two-dimensional interface

ρ_f, ρ_g = saturated liquid and vapor densities

σ = surface tension

τ = period of bubble cycle, equal to $1/f$

ω = circular frequency of a traveling wave (a pure imaginary number)

rate by the time the bubble is a hemisphere. Therefore we can substitute $d\eta/dt$ from equation (9) in equation (13) and get

$$\frac{dV}{dt} = \pi c(-i\omega)\lambda_{d_1}(2R\eta - R^2) \tag{14}$$

We are interested in a maximum of dV/dt during a growth cycle. According to equation (14), dV/dt will be maximum when the interface height, η, equals the radius of curvature, R. This is true when the bubble is hemispherical and $\eta = R = \lambda_{d_1}/4$. Thus the equation for the maximum value of dV/dt is

$$\frac{dV}{dt} = \frac{\pi c}{16}(-i\omega)\lambda_{d_1}^3 \tag{15}$$

Following the criterion developed earlier, film boiling will collapse when the vapor generation rate at the heater falls below the value given by equation (15).

The Minimum Heat Flux on Flat Plates

Figure 2 shows that, on the average, one bubble at a time is supported in a heater area, $\lambda_{d_1}^2$. Thus we obtain the minimum vapor velocity, u_g, from equation (15), as

$$u_g = \frac{dV}{dt}\frac{1}{\lambda_{d_1}^2} = \frac{\pi c}{16}(-i\omega)\lambda_{d_1} \tag{16}$$

But the growth rate is given [4] as

$$(-i\omega) = \sqrt{\frac{\pi}{\lambda_{d_1}}\left[\frac{g(\rho_f - \rho_g)}{\rho_f + \rho_g} - \frac{\pi^2\sigma}{\lambda_{d_1}^2(\rho_f + \rho_g)}\right]} \tag{17}$$

Substituting $(-i\omega)$ from equation (17), and λ_{d_1} from equation (2), into equation (16) we get

$$u_g = 1.32c\sqrt[4]{\frac{g\sigma(\rho_f - \rho_g)}{(\rho_f + \rho_g)^2}} \tag{18}$$

Finally, making use of the value of c from Table 1, we obtain minimum heat flux on a flat plate as

$$(q_{\min})_{\text{flat plate}} = \underbrace{0.091^{0.078}_{0.104}}_{A}\rho_g h_{fg}\sqrt[4]{\frac{g\sigma(\rho_f - \rho_g)}{(\rho_f + \rho_g)^2}} \tag{19}$$

where the range of A corresponds with the standard deviation of c.

Berenson's measurements indicated that the best experimental values for n-pentance and CCl_4, respectively, gave the lead constant in equation (19) equal to 0.089 and 0.091. Berenson chose a mean value of 0.09 for the constant. The constant obtained using the present criterion is nearly the same as Berenson's. (Other flat heater data can be found, but all are inadequate for one or more of three reasons: They lack vertical sidewalls to eliminate induced flows, they are not enough larger than λ_{d_2} in size, or they have not been obtained with Berenson's attention to cleanliness.)

A few minimum heat flux data obtained during the sublimination of a horizontal slab of dry ice placed beneath a pool of water or benzene have been reported in reference [3]. During sublimation, the gas-liquid interface was found to grow, collapse and regrow at the same location rather than to alternate between nodes and antinodes as observed in film boiling on cylinders (Fig. 1) and as proposed in Fig. 2 for film boiling on flat plates. This peculiar behavior during "pseudo film boiling" is caused by uneven sublimation of the surface underneath the gas releasing nodes and under the gas film. The antinodes of the wave that coincided with the valleys on the surface remained inactive because of the concave nature of the valley. Visual observations showed that, on the average, the bubble release nodes fall on a square grid with a spacing of λ_{d_1} (See Fig. 2). For the cyclic bubble release process to continue on dry ice with a nearly uniform gas evolution rate, the neighboring bubbles must have a staggered growth pattern. This suggests that pseudo film boiling on dry ice will be sustained as long as the gas volume flux can support a maximum volume growth rate between one-half and one bubble in an area of $\lambda_{d_1}^2$.

This means that during pseudo film boiling the lead constant in equation (19) should be cut in half. The minimum heat flux data reported in [3] for water over dry ice are indeed correlated to within 3 percent with equation (19), when the numerical constant is reduced from 0.091 to 0.0455. Likewise, pseudo film boiling data for benzene are within 5 percent when the numerical constant in equation (19) is reduced by 75 percent. This is because the shift from one bubble to one half bubble is incomplete in the case of benzene.

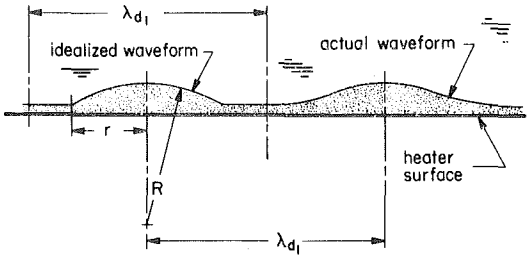

Fig. 4(*a*) Idealization of waveform during early growth for a flat heater

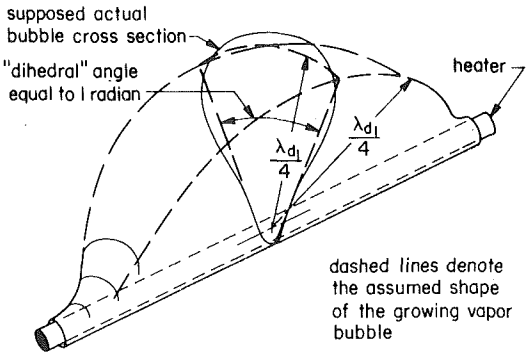

Fig. 4(*b*) Idealization of bubble growing on a horizontal wire

Fig. 4 Bubble shapes during film boiling

The Minimum Heat Flux on a Horizontal Cylinder

An average of one bubble is supported on a surface area, $2\pi R\lambda_{d_1}$, of a cylindrical heater. However, because the diameter of the cylinder is much smaller than the width of the bubble at the top, the bubble will be a spherical wedge, as shown in Fig. 4(*b*), rather than a hemisphere during its early period of growth. The top of the bubble is taken to be a spherical surface with both radius of curvature and arc length equal to $\lambda_{d_1}/4$. The contribution of the volume of the heater to the volume of the spherical wedge is ignored. After correcting equation (15) to give the volume of a spherical wedge whose diahedral angle is unity instead of π, we get the following expression for the vapor volume flux.

$$u_g = \frac{\frac{\pi c}{16\pi}(-i\omega)\lambda_{d_1}^3}{2\pi R\lambda_{d_1}} = \frac{c}{32\pi}(-i\omega)\frac{\lambda_{d_1}^3}{R} \tag{20}$$

The growth rate for waves above a cylinder has been given in [5] as

$$(-i\omega) = \sqrt{\frac{2\pi}{\lambda_{d_1}}\left[\frac{g(\rho_f - \rho_g)}{\rho_f + \rho_g} - \frac{4\pi^2\sigma}{\lambda_{d_1}^2(\rho_f + \rho_g)} + \frac{\sigma}{2(\rho_f + \rho_g)(R + \delta)^2}\right]}^{1/2} \tag{21}$$

Substituting the wavelength from equation (7), and this growth rate, into equation (20), we get

$$u_g = 0.866c\sqrt[4]{\frac{g\sigma(\rho_f - \rho_g)}{(\rho_f + \rho_g)^2}}[R'^2(2R'^2 + 1)]^{-1/4} \tag{22}$$

where $R' \equiv R\sqrt{\sigma/g(\rho_f - \rho_g)}$. Using a mean value of c from Table 1,

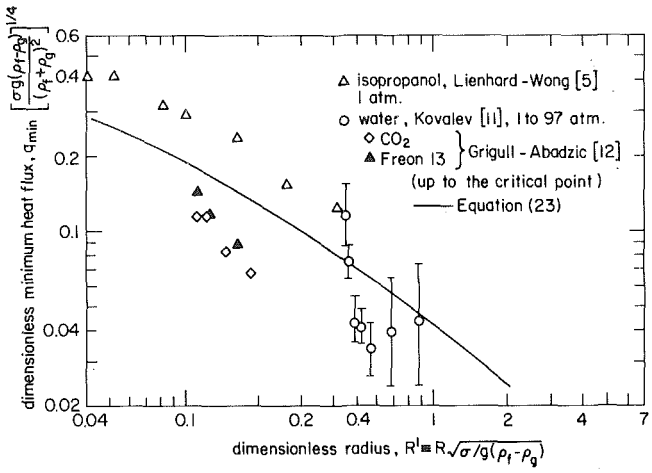

Fig. 5 Comparison of the q_{min} prediction with the rather scattered available data

we obtain for the minimum heat flux on a cylindrical heater

$$q_{min} = \underbrace{0.06^{0.051}_{0.068}}_{B} \rho_g h_{fg} \sqrt[4]{\frac{g\sigma(\rho_f-\rho_g)}{(\rho_f+\rho_g)^2}} [R'^2(2R'^2+1)]^{-1/4} \quad (23)$$

Very few of the available q_{min} data for cylinders can be used to test the validity of equation (23). All but the data of Kovalev [11] involve end mounting effects[1] that have the effect of raising q_{min} above its true value. The data in [5] probably suffer from end effects although precautions were taken to minimize them. The data of Grigull and Abadzic [12] were obtained with submerged ends in CO_2 near the critical point. Their wires doubtless had thick vapor blankets around them. This would have the influence of making q_{min} lower than it is when the blanket is thin, in conformity with the theory.

Consequently, the data exhibit about ±50 percent scatter on appropriately nondimensionlized coordinates in Fig. 5. But the important fact is that equation (23) falls in the middle of these data as the discussion above would lead us to expect. It is also interesting to note that the present equation falls within 3 percent of the expression established experimentally by Lienhard and Sun [9].

[1] Kovalev bent the ends of his heater wire upward, in a U-shape, so they exited from the liquid without ending in it.

Conclusions

A criterion for minimum pool boiling heat flux on horizontal flat plates and cylindrical heaters has been proposed. According to this criterion, the minimum heat flux occurs when the vapor volume flux is just sufficient to maintain the maximum volume growth rate of a bubble in a given cycle. This maximum volume flux occurs when interface grows linearly with time, the radius of curvature of the bubble is $\lambda_{d_1}/4$ and the bubble is either a hemisphere (for a flat plate) or a spherical wedge (for a cylindrical heater). The numerical constants obtained in this work are nearly the same as those obtained experimentally, and previously reported in the literature.

References

1 Chang, Y. P., "A Theoretical Analysis of Heat Transfer in Natural Convection and in Boiling," *Trans. ASME*, Vol. 79, 1957, p. 1501.

2 Zuber, N., "Hydrodynamic Aspects of Boiling Heat Transfer," AEC Rept. No. AECU-4439, *Physics and Mathematics*, June 1959.

3 Dhir, V. K., Castle J. N., and Catton, I., "Role of Taylor Instability on Sublimmation of a Horizontal Slab of Dry Ice," ASME *Journal of Heat Transfer*, Vol. 99, No. 3, 1977, pp. 411–418.

4 Bellman R., and Pennington, R. H., "Effects of Surface Tension and Viscosity on Taylor Instability," *Quarterly Journal of Applied Mathematics*, Vol. 12, 1974, p. 151.

5 Lienhard J. H., and Wong, P. T. Y., "The Dominant Unstable Wavelength and Minimum Heat Flux during Film Boiling on a Horizontal Cylinder," ASME *Journal of Heat Transfer*, Vol. 86, No. 2, 1964, pp. 220–226.

6 Berenson, P. J., "Transition Boiling Heat Transfer from a Horizontal Surface," M.I.T. Heat Transfer Lab. Rept. #17, 1960.

7 Sernas, V., "Minimum Heat Flux in Film Boiling—A Three-Dimensional Model," *Proc. Second Canadian Cong. of Applied Mechanics*, University of Waterloo, Canada, May 1969, p. 425–426.

8 Sernas, V., Lienhard J. H., and Dhir, V. K., "The Taylor Wave Configuration during Boiling from a Flat Plate," *Internal Journal of Heat and Mass Transfer*, Vol. 16, 1973, pp. 1820–1821.

9 Lienhard J. H., and Sun, K. H., "Effects of Gravity and Size upon Film Boiling from Horizontal Cylinders," ASME *Journal of Heat Transfer*, Vol. 92, No. 2, 1970, pp. 292–298.

10 Dhir, V. K., "Viscous Hydrodynamic Instability Theory of the Peak and Minimum Pool Boiling Heat Fluxes," University of Kentucky, College of Engineering Report, UKY BU100, Lexington, Ky, Nov. 1972.

11 Kovalev, S. A., "An Investigation of Minimum Heat Fluxes in Pool Boiling of Water," *International Journal of Heat and Mass Transfer*, Vol. 9, 1966, pp. 1219–1226.

12 Grigull U., and Abadzic, E., "Heat Transfer from a Wire in the Critical Region," *Proceedings Institution of Mechanical Engineers*, Vol. 182, pt. 31, 1967–1968, pp. 52–57.

The Nature of Nucleation Site Interaction

R. L. Judd
Professor,
Mem. ASME

C. H. Lavdas
Student Assistant,
Student Mem. ASME

McMaster University,
Hamilton, Ontario,
Canada

Bubble emission at a nucleation site is capable of either initiating or terminating bubble emission at an adjacent nucleation site. The former ensues from the creation of a nucleus by a bubble which covers a potentially active nucleation site with its dry spot whereas the latter ensues from interference between a bubble and the nucleus standing at an active nucleation site. Photographic evidence of both these occurrences is presented. Site interaction is at least partly responsible for overlapping of areas of influence surrounding the nucleation sites; the extent of the influence exerted by the emission of bubbles at an active nucleation site is presented herein.

Introduction

Although the phenomena relating to nucleation and growth of boiling bubbles are reasonably well understood, more specific knowledge of the mechanisms of heat transfer in the vicinity of the nucleation sites is required before the rate of heat transfer can be predicted reliably. It is particularly important to know how the emission of bubbles at a nucleation site promotes the transfer of heat from the boiling surface within the area influenced by the emission process. For those boiling conditions in which the nucleation site density is so great that overlapping of influence areas occurs, the consequence of such overlapping upon the overall rate of heat transfer will have to be known. It is this topic which the present paper addresses.

Site Interaction

It is commonly recognized that nucleation and bubble emission occurs continuously at some nucleation sites and intermittently at others. Kirby and Westwater [1] alluded to this when they discussed the effect of varying the time period during which photographic data were obtained in order to obtain a count of the number of active sites within the field of view of their camera. Cole [2] touched on this aspect of nucleation and bubble formation in his discussion of the stability of nucleation cavities in which the articles he reviewed postulated that sites remained active only so long as the flow of liquid penetrating the cavity after bubble departure was reversed before it reached the bottom. Eddington and Kenning [3] observed instances in which boiling sites were seen to have been active when, according to their gas nucleation experiments, they should not have been and, conversely, instances in which apparently stable nucleation sites according to their gas nucleation experiments did not nucleate at all in boiling. These observations are evidence of nucleation site instability which manifests itself by intermittent bubble emission in contrast to continuous bubble emission from the more stable sites.

The explanation for intermittent bubble emission lies in the interaction of the processes occurring at adjacent nucleation sites according to our research. Four thousand frame/s motion picture films from Judd and Hwang's [4] study of dichloromethane boiling on a glass surface using laser interferometry and high speed photography for nine different combinations of heat flux and subcooling were examined to determine the nature of the interactions occurring during bubble emission. Tables 1 and 2 depict the history of bubble formation for the experiments conducted at 5.3°C subcooling and 60 kW/m^2 and 41 kW/m^2 heat flux, respectively, at the 18 active nucleation sites lying within the field of view of the high speed camera. The numbers entered under each of the column headings representing the active nucleation sites correspond to the frame on the motion picture film at which bubbles were nucleated. It can be seen that at the higher heat flux, sites 7, 9 and 15 were continuously active during the time interval spanned by the film whereas at the lower heat flux, only site 4 appears to be continuously active. Site 15 has apparently been deactivated during the step decrease in heat flux; sites 7 and 9 show evidence of intermittent bubble emission as discussed above.

Closer examination of the motion picture films revealed the reasons for intermittent activation and deactivation of nucleation sites. As depicted in Fig. 1, a bubble nucleated by site 4 at frame 1786 is just about to depart from the surface at frame 1800. Subsequently, a bubble nucleated by site 6 at frame 1807 begins to grow until, at frame 1830, the periphery of the bubble reaches site 4 but does not encompass it. This bubble departs from the surface shortly after frame 1870, but site 4 does not nucleate any further bubbles for the duration of the film. Presumably, the nucleus existing at site 4 was displaced by the advancing bubble periphery or absorbed by the bubble itself. This sequence of events represents site deactivation and is consistent with

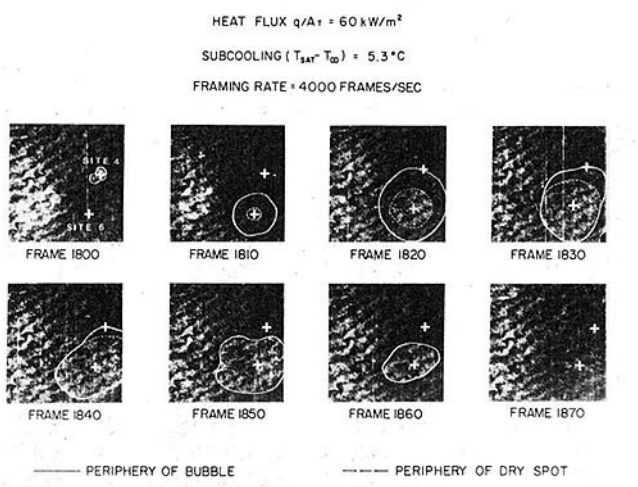

Fig. 1 Nucleation site deactivation

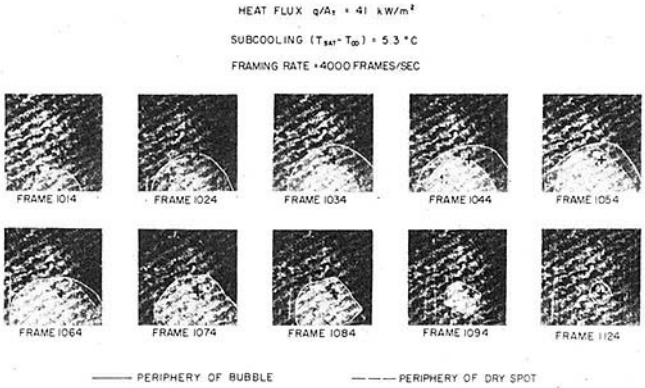

Fig. 2 Nucleation site activation

Contributed by the Heat Transfer Division for publication in the JOURNAL OF HEAT TRANSFER. Manuscript received by the Heat Transfer Division September 27, 1979.

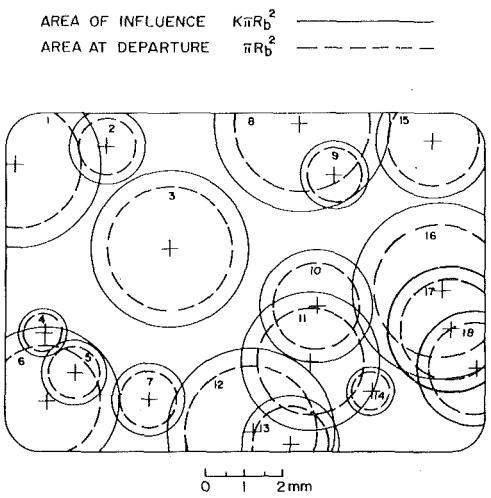

Fig. 3 Typical site plan within camera field of view

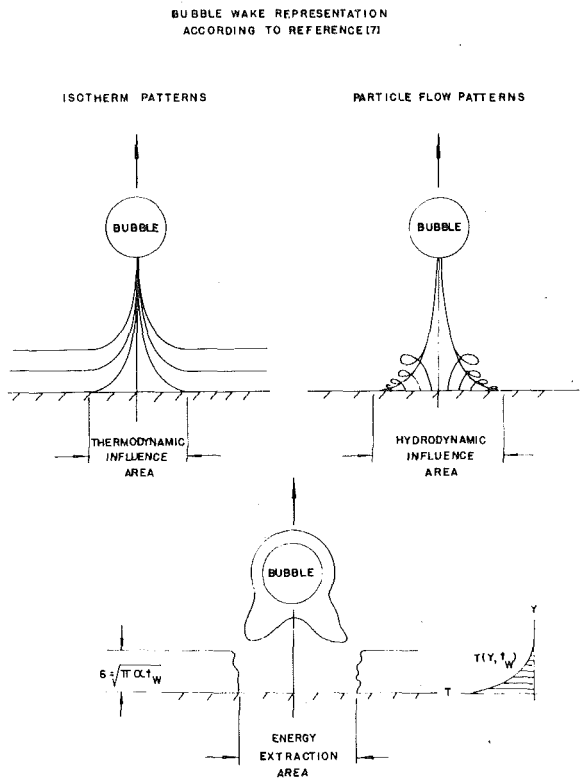

Fig. 4 Illustration of various influence areas

the phenomenon of "thermal interference" postulated by Eddington and Kenning.

As depicted in Fig. 2, site 7 was activated by an exceedingly large bubble nucleated by a site outside of the field of view of the high speed camera whose dry spot covered it from frame 1054 to frame 1094. After the bubble had departed from the surface, bubble formation was observed to occur at site 7 from frame 1124 onward to the end of the film. Presumably, a nucleus was formed at the site when the dry spot receded. This observation is consistent with Eddington and Kenning's description of "site seeding."

Area of Influence

The interdependency of events occurring at adjacent nucleation sites is important to the prediction of heat transfer from a boiling surface since neglect of this factor will inevitably lead to error. Wherever the sites are close enough to interact, the areas of influence of the bubbles forming at these sites will almost assuredly overlap. Therefore, while it might be reasonable to consider the area of influence of a bubble to be a circle centered at the nucleation site with a radius equal to the departure diameter in accordance with Han and Griffith [5] and Hsu and Graham [6], among others, it does not necessarily follow that the areas of influence will not be overlapping.

Sites which exist outside of the areas of influence of bubbles forming at surrounding sites, such as sites 3 and 7 in Fig. 3, contribute directly to the boiling heat transfer rate in proportion to the surface area under their influence. Other sites which are interdependent, such as sites 10–14 in Fig. 3, may be considered similarly, provided that sufficient time elapses after the departure of each bubble for the conditions necessary for the formation of the subsequent bubbles to reestablish themselves. The essential difference then, in considering influence areas to be interdependent versus independent, concerns the evaluation of the surface area outside the influence of the nucleation sites in which natural convection occurs.

Using the results of the aforementioned photographic investigation, Judd and Hwang devised a predictive equation incorporating the contributions of microlayer evaporation, nucleate boiling (enthalpy transport), and natural convection. It was assumed that there was no overlapping of areas of influence around the nucleation sites and average values were used to describe the frequency of bubble emission, bubble departure radius, and volume of microlayer evaporated for the boiling conditions investigated. Boiling heat flux was satisfactorily predicted by

$$q_P/A_T = \rho_\ell h_{fg}(N/A_T)\overline{fV}_{ME} + 2\sqrt{\pi}\sqrt{\rho_\ell C_\ell k_\ell}\,K\overline{R}_b{}^2\sqrt{\overline{f}}(N/A_T)(T_w - T_\infty) + 0.18k_\ell[(g\beta/\nu_\ell{}^2)(\mu_\ell C_\ell/k_\ell)]^{1/3}(T_w - T_\infty)^{4/3}[1 - K\pi\overline{R}_b{}^2(N/A_T)]$$

in which K is a parameter greater than or equal to unity relating the projected bubble area at departure to the area around a nucleation site from which a departing bubble extracts energy by displacement of the thermal boundary layer as depicted schematically in Fig. 4. The various components of the predictive model are represented in Fig. 5 where the areas devoted to microlayer evaporation, nucleate boiling, and natural convection can be identified.

Stephan [7] has shown how the wake of a rising bubble can displace the liquid in the vicinity of the boiling surface and distort the temperature distribution; but, in as much as there is as yet no theoretical solution to predict the quantity of energy transported into the bulk liquid, such analytical approaches are not capable of yielding quantitative results so far as the formulation of a predictive model is concerned. Accordingly, Judd and Hwang introduced the influence of a

Nomenclature

A_T = heater surface area
A_{NC}/A_T = area fraction devoted to natural convection
A_{NB}/A_T = area fraction devoted to nucleate boiling
C_ℓ = liquid specific heat
f = frequency of bubble emission
g = gravitational constant
h_{fg} = latent heat
k_ℓ = liquid thermal conductivity
K = influence area factor
N = number of active nucleation sites
N/A_T = active site density
q_{NB}/A_T = nucleate boiling component of predicted heat flux
q_{NC}/A_T = natural convection component of predicted heat flux
q_{ME}/A_T = microlayer evaporation component of predicted heat flux
q_P/A_T = predicted heat flux
t_w = waiting period
$(T_w - T_\infty)$ = temperature difference
V_{ME} = volume of microlayer evaporated
y = distance from boiling surface
α = thermal diffusivity
β = volumetric coefficient of expansion
δ = thermal layer thickness
μ_ℓ = liquid dynamic viscosity
ν_ℓ = liquid kinematic viscosity
ρ_ℓ = liquid density

Table 1 Nucleation history at 60 KW/m² heat flux and 5.3°C subcooling

SITE NUMBER																	
1	2	3	4	5	6	7	8	9	10	11	12	13	14	15	16	17	18
-	-	-	-	-	-	-	-	-	-	-	-	-	-	-	-	72	-
-	-	-	-	-	-	-	-	-	-	-	-	-	-	109	-	-	-
-	-	120	-	-	-	-	-	-	-	-	-	-	-	-	-	-	-
-	-	-	124	-	-	-	-	-	-	-	-	-	-	-	-	-	-
-	-	-	137	-	-	-	-	-	-	-	-	-	-	-	-	-	-
-	-	-	157	-	-	-	-	-	-	-	-	-	-	-	-	-	-
-	-	-	168	-	-	-	-	-	-	-	-	-	-	-	-	-	-
-	-	-	-	-	-	-	-	169	-	-	-	-	-	-	-	-	-
-	-	-	198	-	-	-	-	-	-	-	-	-	-	-	-	-	-
-	-	-	-	-	-	-	-	-	-	-	-	-	-	237	-	-	-
-	-	-	-	-	-	-	237	-	-	-	-	-	-	-	-	-	-
-	-	-	303	-	-	-	-	-	-	-	-	-	-	-	-	-	-
-	-	-	-	-	-	-	-	339	-	-	-	-	-	-	-	-	-
-	-	-	344	-	-	-	-	-	-	-	-	-	-	-	-	-	-
-	-	-	-	-	-	348	-	-	-	-	-	-	-	-	-	-	-
-	-	-	-	-	358	-	-	-	-	-	-	-	-	-	-	-	-
-	-	-	-	-	-	-	-	-	-	-	-	-	-	366	-	-	-
-	-	-	-	-	-	-	-	387	-	-	-	-	-	-	-	-	-
-	-	-	-	-	-	400	-	-	-	-	-	-	-	-	-	-	-
-	-	-	-	422	-	-	-	-	-	-	-	-	-	-	-	-	-
-	-	-	-	-	-	446	-	-	-	-	-	-	-	-	-	-	-
-	-	-	-	-	-	-	451	-	-	-	-	-	-	-	-	-	-
-	-	-	461	-	-	-	-	-	-	-	-	-	-	-	-	-	-
-	-	-	-	-	-	-	-	484	-	-	-	-	-	-	-	-	-
-	-	-	-	-	-	530	-	-	-	-	-	-	-	-	-	-	-
-	-	-	-	-	-	-	-	-	563	-	-	-	-	-	-	-	-
-	-	-	564	-	-	-	-	-	-	-	-	-	-	-	-	-	-
-	-	-	-	572	-	-	-	-	-	-	-	-	-	-	-	-	-
573	-	-	-	-	-	-	-	-	-	-	-	-	-	-	-	-	-
-	-	-	-	-	-	-	-	574	-	-	-	-	-	-	-	-	-
-	-	-	618	-	-	-	-	-	-	-	-	-	-	-	-	-	-
-	-	-	-	-	-	628	-	-	-	-	-	-	-	-	-	-	-
-	-	-	664	-	-	-	-	-	-	-	-	-	-	-	-	-	-
-	-	-	-	-	-	-	-	670	-	-	-	-	-	-	-	-	-
-	-	-	-	-	-	707	-	-	-	-	-	-	-	-	-	-	-
-	-	-	-	-	-	-	-	-	-	-	-	-	-	721	-	-	-
-	-	-	-	-	-	-	-	728	-	-	-	-	-	-	-	-	-
-	-	-	732	-	-	-	-	-	-	-	-	-	-	-	-	-	-
-	-	-	-	-	-	-	-	-	753	-	-	-	-	-	-	-	-
-	-	759	-	-	-	-	-	-	-	-	-	-	-	-	-	-	-
-	-	-	773	-	-	-	-	-	-	-	-	-	-	-	-	-	-
-	-	-	-	-	-	-	775	-	-	-	-	-	-	-	-	-	-
-	-	-	-	-	-	-	-	790	-	-	-	-	-	-	-	-	-
-	-	-	-	-	-	-	-	-	-	-	-	-	-	-	-	-	792
-	-	-	-	-	-	-	-	-	-	-	-	-	-	835	-	-	-
-	-	-	837	-	-	-	-	-	-	-	-	-	-	-	-	-	-
-	-	-	-	-	-	839	-	-	-	-	-	-	-	-	-	-	-
-	-	-	-	-	-	-	-	849	-	-	-	-	-	-	-	-	-
-	-	-	878	-	-	-	-	-	-	-	-	-	-	-	-	-	-
-	-	-	-	-	-	-	-	-	-	-	-	-	-	-	-	-	880
-	-	-	-	-	-	-	-	-	-	-	-	-	-	886	-	-	-
-	-	-	919	-	-	-	-	-	-	-	-	-	-	-	-	-	-
-	-	-	-	-	-	928	-	-	-	-	-	-	-	-	-	-	-
-	-	-	-	-	-	-	-	929	-	-	-	-	-	-	-	-	-
-	-	-	-	-	-	-	-	-	-	-	-	-	-	957	-	-	-
-	-	-	968	-	-	-	-	-	-	-	-	-	-	-	-	-	-
-	-	-	-	-	-	-	-	-	-	-	-	-	-	-	-	-	970
-	-	-	-	-	-	-	-	996	-	-	-	-	-	-	-	-	-
-	-	-	1009	-	-	-	-	-	-	-	-	-	-	-	-	-	-
1014	-	-	-	-	-	-	-	-	-	-	-	-	-	-	-	-	-
-	-	-	-	-	-	1031	-	-	-	-	-	-	-	-	-	-	-
-	-	-	1043	-	-	-	-	-	-	-	-	-	-	-	-	-	-
-	-	-	-	-	-	-	-	1088	-	-	-	-	-	-	-	-	-
-	-	-	-	-	-	1094	-	-	-	-	-	-	-	-	-	-	-
-	-	-	-	-	-	-	-	-	1096	-	-	-	-	-	-	-	-
-	-	-	-	-	-	-	-	-	-	-	-	-	-	-	-	-	1133
-	-	-	1140	-	-	-	-	-	-	-	-	-	-	-	-	-	-
-	-	1160	-	-	-	-	-	-	-	-	-	-	-	-	-	-	-
-	-	-	-	-	-	1170	-	-	-	-	-	-	-	-	-	-	-
-	-	-	-	-	-	-	-	1171	-	-	-	-	-	-	-	-	-
-	-	-	1187	-	-	-	-	-	-	-	-	-	-	-	-	-	-
-	-	-	-	-	-	-	-	-	-	-	-	-	-	1196	-	-	-
-	-	-	-	-	-	-	-	1219	-	-	-	-	-	-	-	-	-
-	-	-	1230	-	-	-	-	-	-	-	-	-	-	-	-	-	-
-	-	-	-	-	-	1265	-	-	-	-	-	-	-	-	-	-	-
-	-	-	1279	-	-	-	-	-	-	-	-	-	-	-	-	-	-
-	-	-	-	-	-	-	-	-	-	-	-	-	-	-	-	-	1288
-	-	-	-	-	-	-	-	1311	-	-	-	-	-	-	-	-	-
-	-	-	-	-	-	-	1315	-	-	-	-	-	-	-	-	-	-
-	-	-	1329	-	-	-	-	-	-	-	-	-	-	-	-	-	-
-	-	-	-	-	-	1342	-	-	-	-	-	-	-	-	-	-	-
-	-	-	1360	-	-	-	-	-	-	-	-	-	-	-	-	-	-
-	-	1383	-	-	-	-	-	-	-	-	-	-	-	-	-	-	-
-	-	-	1400	-	-	-	-	-	-	-	-	-	-	-	-	-	-
-	-	-	1405	-	-	-	-	-	-	-	-	-	-	-	-	-	-
-	-	-	-	-	-	1431	-	-	-	-	-	-	-	-	-	-	-
-	-	-	-	-	-	-	1433	-	-	-	-	-	-	-	-	-	-
-	-	-	-	-	-	-	-	1435	-	-	-	-	-	-	-	-	-
-	-	-	1452	-	-	-	-	-	-	-	-	-	-	-	-	-	-
-	-	-	-	-	-	-	-	-	-	-	-	-	-	-	-	-	1462
-	-	-	-	-	-	1484	-	-	-	-	-	-	-	-	-	-	-
-	-	-	1494	-	-	-	-	-	-	-	-	-	-	-	-	-	-
-	-	-	-	-	-	-	-	-	1528	-	-	-	-	-	-	-	-
-	-	-	-	-	-	-	1537	-	-	-	-	-	-	-	-	-	-
-	-	-	1552	-	-	-	-	-	-	-	-	-	-	-	-	-	-
-	-	-	-	-	-	-	-	-	-	-	-	-	-	1576	-	-	-
-	-	-	1590	-	-	-	-	-	-	-	-	-	-	-	-	-	-
-	-	-	-	-	-	-	1604	-	-	-	-	-	-	-	-	-	-
-	-	-	-	-	-	-	-	-	-	-	-	-	-	-	1622	-	-
-	-	-	-	-	-	-	-	1628	-	-	-	-	-	-	-	-	-
-	-	-	1655	-	-	-	-	-	-	-	-	-	-	-	-	-	-
-	-	-	-	-	-	1669	-	-	-	-	-	-	-	-	-	-	-
-	-	-	1717	-	-	-	-	-	-	-	-	-	-	-	-	-	-
-	-	-	-	-	-	-	-	-	-	-	-	-	-	-	-	-	1726
-	-	-	-	-	-	1766	-	-	-	-	-	-	-	-	-	-	-
-	-	-	1786	-	-	-	-	-	-	-	-	-	-	-	-	-	-
-	-	-	-	-	-	-	-	-	1798	-	-	-	-	-	-	-	-
-	-	-	-	-	1807	-	-	-	-	-	-	-	-	-	-	-	-
-	-	-	-	-	-	-	1818	-	-	-	-	-	-	-	-	-	-
-	-	-	-	-	-	-	-	-	-	-	-	-	-	-	-	-	1861
-	-	-	-	-	-	1877	-	-	-	-	-	-	-	-	-	-	-
-	-	-	-	-	-	-	1891	-	-	-	-	-	-	-	-	-	-
-	-	-	-	-	-	-	-	-	1919	-	-	-	-	-	-	-	-
-	-	-	-	-	-	-	1976	-	-	-	-	-	-	-	-	-	-
1976	-	-	-	-	-	-	-	-	-	-	-	-	-	1987	-	-	-
-	-	-	-	-	-	-	-	-	-	2042	-	-	-	-	-	-	-
-	-	-	-	-	-	2061	-	-	-	-	-	-	-	-	-	-	-
2065	-	-	-	-	-	-	-	-	-	-	-	-	-	-	-	-	-
-	-	-	-	-	-	-	-	-	-	-	-	-	-	-	-	-	2065
-	-	-	-	-	-	-	2082	-	-	-	-	-	-	-	-	-	-
-	-	-	-	-	-	-	-	2097	-	-	-	-	-	-	-	-	-
-	-	-	-	-	-	-	-	-	-	-	2136	-	-	-	-	-	-
-	-	-	-	-	-	2145	-	-	-	-	-	-	-	-	-	-	-
-	-	-	-	-	-	-	-	2154	-	-	-	-	-	-	-	-	-
-	-	-	-	-	-	-	-	-	-	-	-	-	-	2216	-	-	-
-	-	-	-	-	-	-	2223	-	-	-	-	-	-	-	-	-	-
-	-	-	-	-	-	-	-	-	-	2235	-	-	-	-	-	-	-
2250	-	-	-	-	-	-	-	-	-	-	-	-	-	-	-	-	-
-	-	-	-	-	-	2270	-	-	-	-	-	-	-	-	-	-	-
-	-	-	-	-	-	-	-	-	-	-	-	-	-	2287	-	-	-

Table 2 Nucleation history at 41 KW/m² heat flux and 5.3°C subcooling

SITE NUMBER																	
1	2	3	4	5	6	7	8	9	10	11	12	13	14	15	16	17	18
-	-	-	74	-	-	-	-	-	-	-	-	-	-	-	-	-	-
-	-	112	-	-	-	-	-	-	-	-	-	-	-	-	-	-	-
-	-	-	-	-	-	-	128	-	-	-	-	-	-	-	-	-	-
-	-	-	-	-	-	-	-	171	-	-	-	-	-	-	-	-	-
-	-	-	-	-	-	-	186	-	-	-	-	-	-	-	-	-	-
-	-	-	-	-	-	-	244	-	-	-	-	-	-	-	-	-	-
-	-	-	275	-	-	-	-	-	-	-	-	-	-	-	-	-	-
-	343	-	-	-	-	-	-	-	-	-	-	-	-	-	-	-	-
-	-	-	357	-	-	-	-	-	-	-	-	-	-	-	-	-	-
-	-	-	-	-	-	-	-	-	-	-	-	-	-	-	375	-	-
-	-	-	-	-	-	-	399	-	-	-	-	-	-	-	-	-	-
-	-	-	471	-	-	-	-	-	-	-	-	-	-	-	-	-	-
-	-	-	540	-	-	-	-	-	-	-	-	-	-	-	-	-	-
-	-	-	-	-	-	-	588	-	-	-	-	-	-	-	-	-	-
-	-	-	-	-	-	-	-	-	-	-	-	-	-	-	-	-	618
-	-	-	626	-	-	-	-	-	-	-	-	-	-	-	-	-	-
-	-	-	-	-	-	-	-	-	674	-	-	-	-	-	-	-	-
-	-	-	-	-	-	-	681	-	-	-	-	-	-	-	-	-	-
-	-	-	704	-	-	-	-	-	-	-	-	-	-	-	-	-	-
-	-	-	780	-	-	-	-	-	-	-	-	-	-	-	-	-	-
-	-	-	-	-	-	-	820	-	-	-	-	-	-	-	-	-	-
-	-	-	859	-	-	-	-	-	-	-	-	-	-	-	-	-	-
-	-	-	-	-	-	-	-	-	-	-	-	-	-	-	-	-	870
-	-	-	-	-	-	900	-	-	-	-	-	-	-	-	-	-	-
-	-	-	920	-	-	-	-	-	-	-	-	-	-	-	-	-	-
-	-	-	984	-	-	-	-	-	-	-	-	-	-	-	-	-	-
-	-	-1120	-	-	-	-	-	-	-	-	-	-	-	-	-	-	-
-	-	-	-	-	-1124	-	-	-	-	-	-	-	-	-	-	-	-
-	-	-	-	-	-	-1140	-	-	-	-	-	-	-	-	-	-	-
-	-	-1149	-	-	-	-	-	-	-	-	-	-	-	-	-	-	-
-	-	-	-	-	-1159	-	-	-	-	-	-	-	-	-	-	-	-
-1170	-	-	-	-	-	-	-	-	-	-	-	-	-	-	-	-	-
-	-	-	-	-	-1215	-	-	-	-	-	-	-	-	-	-	-	-
-	-	-	-	-	-	-	-1238	-	-	-	-	-	-	-	-	-	-
-	-1243	-	-	-	-	-	-	-	-	-	-	-	-	-	-	-	-
-	-	-1253	-	-	-	-	-	-	-	-	-	-	-	-	-	-	-
-	-	-	-	-	-1270	-	-	-	-	-	-	-	-	-	-	-	-
-	-	-1337	-	-	-	-	-	-	-	-	-	-	-	-	-	-	-
-	-	-	-	-	-	-	-	-	-	-	-	-	-	-	-	-	-1340
-	-	-1400	-	-	-	-	-	-	-	-	-	-	-	-	-	-	-
-	-	-	-	-	-1422	-	-	-	-	-	-	-	-	-	-	-	-
-	-	-1470	-	-	-	-	-	-	-	-	-	-	-	-	-	-	-
-	-	-1493	-	-	-	-	-	-	-	-	-	-	-	-	-	-	-
-	-	-	-	-	-	-	-1536	-	-	-	-	-	-	-	-	-	-
-	-	-	-	-	-1575	-	-	-	-	-	-	-	-	-	-	-	-

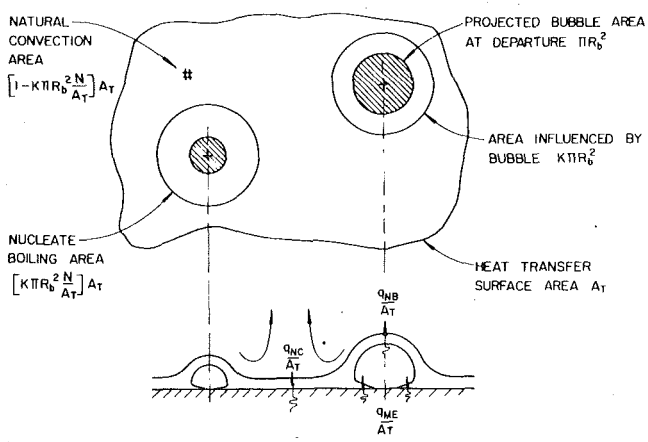

Fig. 5 Schematic representation of boiling heat transfer model

departing bubble into their predictive model by defining an "energy extraction area" such that the energy accumulated within this area during the formation of the superheated thermal layer $\delta = \sqrt{\pi \alpha t_w}$ was transported into the bulk liquid each time that a bubble was formed. By matching the predicted heat flux with the impressed heat flux, a single value of K defined according to

K = energy extraction area/projected bubble area at departure

was obtained for each combination of boiling conditions. The model used by Judd and Hwang in the development of their predictive equation is not unlike that adopted by Graham and Hendricks [8], except that Graham and Hendricks assumed that all of the energy transferred during the waiting period to the liquid which replaced the bubble within the "hydrodynamic influence area", taken to be four times the bubble area at departure, was transported into the bulk liquid by the next departing bubble.

A value of $K = 1.8$ gave the best overall agreement between theory and experiment for the nine different combinations of heat flux and subcooling investigated, individual differences ranging from −21.1 to +9.7 percent. This finding has been reexamined in light of the

aforementioned site interdependency since it is now apparent that considerable overlapping of influence areas occurred. It was assumed that the conditions required for successive bubble emissions in overlapping areas of influence were continually satisfied and that a single different value of K existed for each of the nine different boiling conditions. The latter assumption is partly justified by arguing that the boiling condition establishes the level of activity in the vicinity of the surface which would determine the extent to which the disturbance created by the formation of a bubble at an active nucleation site would propagate.

The predictive equation was reformulated on an individual site basis according to

$$q_P/A_T = \sum_{i=1}^{N} \{\rho_\ell h_{fg} f_i V_{ME_i}/A_T + 2\sqrt{\pi}\sqrt{\rho_\ell C_\ell k_\ell}\, K R_{bi}^2 \sqrt{f_i}\,(T_w - T_\infty)/A_T\} + 0.18 k_\ell [(g\beta/\nu_\ell^2)(\mu_\ell C_\ell/k_\ell)]^{1/3}(T_w - T_\infty)^{4/3} A_{NC}/A_T$$

where $A_{NC}/A_T = 1 - A_{NB}/A_T$ is obtained from the determination of the area unaffected by nucleate boiling in diagrams such as Fig. 3. In general, A_{NB} will be less than

$$\sum_{i=1}^{N} K\pi R_{bi}^2$$

because of overlapping of areas of influence and will only equal

$$\sum_{i=1}^{N} K\pi R_{bi}^2$$

when the areas of influence are not overlapping.

Determining $A_{NC}/A_T = 1 - A_{NB}/A_T$ by graphical integration of plots, such as Fig. 3, and equating the predicted heat flux to the measured heat flux, numerical values of influence area factor K were obtained for each of the nine different boiling conditions which ranged from 1 to 8. The highest value is somewhat suspect because there were so few active nucleation sites within the field of view of the high speed camera for the boiling condition concerned that the measured values might not be representative. Figure 6 shows that all of the values of influence area factor K tend to form a single curve when plotted as a function boiling area fraction A_{NB}/A_T. This contrasts with Han and Griffith's value $K = 4.0$ and Judd and Hwang's value $K = 1.8$.

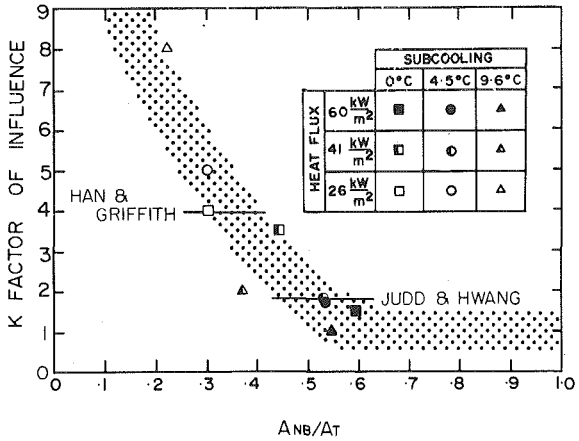

Fig. 6 Influence area factor

Implications for Heat Transfer

Given that nucleate boiling heat transfer can be adequately expressed by the combination of the contributions of microlayer evaporation, nucleate boiling and natural convection suggested above, then the results of Hwang and Judd's experiments reinterpreted to account for overlapping of the areas of influence, demonstrate that the influence area factor K decreases as the boiling area fraction A_{NB}/A_T increases. When A_{NB}/A_T exceeds 50 percent, the influence area factor K approaches unity which means that the disturbance induced by bubble formation extends no further than the bubble departure radius. In as much as the boiling conditions for which this occurs are associated with increasing heat flux, the implication is that bubble coalescence in the vicinity of the surface accompanying increasing values of active site density has diminished the ability of each active site to promote the transfer of heat.

It was evident throughout the study that bubble formation at widely separated nucleation sites was far more effective at promoting heat transfer than bubble formation at closely spaced nucleation sites. This was especially true for boiling at low heat flux and high subcooling where the sites were effectively isolated from one another. One explanation is that relatively large spacings permit the development of intense upward directed flow patterns around the nucleation sites which could account for the more effective heat transfer. However, this hypothesis is unsupported by the data and requires further investigation.

All of this is not unknown. Nucleate boiling heat transfer characteristics are governed by the hydrodynamic processes taking place in the local regions surrounding the active sites, and Zuber [9] has explained how, when the active site density is small, the sites are isolated so far as their hydrodynamic regions of influence are concerned; whereas when the active site density is large, congestion occurs in the vicinity of the sites which then begin to compete for a supply of the liquid from the superheated thermal layer. What the present paper accomplished was to identify the mechanisms by which nucleation site interactions occur and to quantify the variation of influence area.

The ultimate goal of this type of research is to be able to predict boiling heat transfer relationships given surface material, fluid and a limited amount of additional information to represent the nucleation site characteristics of the surface. However, this will only be possible if bubble interactions can be properly represented, including the interdependency of closely spaced nucleation sites which this paper addresses. It is hoped that the information reported will be useful in the development of such boiling heat transfer models in the future.

References

1 Kirby, D. W., and Westwater, J. W., "Bubble and Vapour Behaviour on a Horizontal Plate during Pool Boiling near Burnout," *Chemical Engineering Progress Symposium Series,* Vol. 61, No. 57, 1965.

2 Cole, R., "Boiling Nucleation," *Advances in Heat Transfer,* Academic Press, New York, Vol. 10, 1974.

3 Eddington, R. I., and Kenning, D. B. R., "The Prediction of Flow Boiling Bubble Populations from Gas Bubble Nucleation Experiments," *Proceedings of the Sixth International Heat Transfer Conference,* Toronto, Canada, Aug. 7–11, 1978.

4 Judd, R. L., and Hwang, K. S., "A Comprehensive Model for Nucleate Pool Boiling Heat Transfer Including Microlayer Evaporation," ASME JOURNAL OF HEAT TRANSFER, Vol. 98, No. 4, Nov. 1976.

5 Han, C-Y., and Griffith, P., "The Mechanism of Heat Transfer in Nucleate Pool Boiling: Part I. Bubble Initiation, Growth and Departure: Part II. The Heat Flux—Temperature Difference Relation," *International Journal of Heat and Mass Transfer,* Vol. 8, 1965.

6 Hsu, Y. Y., and Graham, R. W., "An Analytical and Experimental Study of Thermal Boundary Layer and Ebullition Cycle in Nucleate Boiling," NASA Technical Note D-594, May 1961.

7 Stephen, K., "Bubble Formation and Heat Transfer in Natural Convection Boiling," *Heat Transfer in Boiling,* Chapter 1, Hemisphere Publishing, 1977.

8 Graham, R. W., and Hendricks, R. C., "Assessment of Convection, Conduction and Evaporation in Nucleate Boiling," NASA TND-3943, 1967.

9 Zuber, N., "Hydrodynamic Aspects of Boiling Heat Transfer," Ph.D. Thesis, University of California, Los Angeles, 1959.

S. Nijhawan
Research Assistant.

J. C. Chen
Professor,
Mem. ASME

R. K. Sundaram
Asst. Professor.

E. J. London
Research Engineer.

Institute of Thermo-Fluid Engineering and Science,
Lehigh University,
Bethlehem, Pa. 18015

Measurement of Vapor Superheat in Post-Critical-Heat-Flux Boiling

A differentially-aspirated superheat probe was developed to measure vapor temperatures in post-critical-heat-flux, dispersed-flow boiling. Measurements obtained for water, at low-to-moderate pressures and mass flow rates in a tube, indicated very significant non-equilibrium, with vapor superheats of several hundred degrees (°C). Predictions of published correlations showed unsatisfactory agreement with the experimental results.

Introduction

Boiling two-phase flow, subsequent to exceeding critical heat flux (post-CHF), can occur with two different flow patterns. When critical heat flux is reached at low or subcooled qualities, the post-CHF flow occurs with an inverse annular flow pattern where a liquid core is surrounded by an annular vapor film. When the critical heat flux occurs at moderate to high qualities (dryout), the post-CHF flow exists in a dispersed flow pattern where liquid droplets are entrained in a continuous vapor phase. This investigation is concerned with the latter class of post-CHF, dispersed flow boiling.

Heat transfer in the post-dryout flow regime has often been modeled with the assumption of thermodynamic equilibrium between liquid and vapor phases. In such equilibrium models, the heat transferred from hot wall is assumed to be totally absorbed by the evaporation of the liquid phase. The vapor temperature would thus be equal to the local saturation temperature, so long as the equilibrium quality of the two-phase mixture does not exceed unity. Other more phenomenological models have attempted to consider the possible existence of thermodynamic nonequilibrium, where superheated vapor would coexist with entrained liquid droplets.

Thermodynamic nonequilibrium in dispersed two-phase flow was first suggested by Parker and Grosh [1]. In their experiments, liquid droplets were seen to exist even at equilibrium mixture qualities exceeding unity. Laverty and Rohsenow [2] published an early attempt to analyze nonequilibrium dispersed flow boiling. That work was continued by Forslund and Rohsenow [3], and by Hynek, et al. [4]. More recently, several semi-empirical correlations incorporating nonequilibrium concepts have been proposed by Plummer, et al. [5], Saha, et al. [6], and Jones and Zuber [7]. All these correlations and models are history-dependent in the sense that knowledge of the location and conditions of the fluid at the dryout (critical heat flux) point is required. A second group of nonequilibrium correlations for dispersed flow boiling attempts to use only local parameters to predict wall heat transfer. Within this class of models are those of Tong and Young [8], Groeneveld and Delorme [9], and Chen, et al. [10].

All the analytical models and correlations, whether of the history-dependent or local parameter class, have emphasized the need for determining the nonequilibrium vapor temperature as a first step in calculating post-dryout heat transfer. In this flow regime, liquid-wall contact is minimal and the major mechanism for heat transfer from the wall is by turbulent convection to the vapor phase. All analyses utilize convective heat transfer models for this vapor heat flux, of the functional form

$$Q_{vc} = h_{vc} \cdot (T_w - T_v) \tag{1}$$

$$h_{vc} = f(G, X_a, D, \text{vapor properties})$$

If thermodynamic equilibrium is not assumed, then the vapor temperature T_v and actual vapor quality X_a are normally unknown. One relationship between these two unknowns is found from heat balance

$$\frac{X_a}{X_e} = \frac{H_{fg}}{H_v(P,T_v) - H_L(P,T_s)} \tag{2}$$

To permit predictions of the vapor heat flux (Q_{vc}), a second independent relationship between X_a and T_v is necessary. The various analytical models and correlations differ primarily in the formulation proposed for this necessary second relationship.

Attempts to verify or improve the correlational models have been greatly hampered by a lack of experimental data on the existence and magnitude of thermodynamic nonequilibrium. Post-CHF experiments provide measurements of wall heat flux, wall temperature, system pressure, and equilibrium quality (X_e). Corresponding measurements for the nonequilibrium vapor quality (X_a) and for the superheated vapor temperature (T_v) are generally not available. Thus, in comparing correlational models with experiment, the uncertainties involved in prediction of h_{vc}, X_a, and T_v are lumped together and it has not been possible to isolate possible sources of error in the proposed phenomenological models.

The objective of this investigation was to develop an experiment in which measurements of wall heat flux, system pressure, fluid flow rate, equilibrium vapor quality, and nonequilibrium quality (X_a) or superheated vapor temperature (T_v), were all obtained simultaneously. Data from such experiments would then permit independent assessments of the phenomenological model for prediction of nonequilibrium conditions (X_a, T_v) and for prediction of the post-CHF heat transfer (Q_{vc}, T_w).

Measurement Method

The key to this experimental investigation is the measurement of the nonequilibrium state. It was desired to directly measure either the actual vapor flow quality (X_a) or the average superheated vapor temperature (T_v). Knowing one, the other parameter can be calculated by equation (2). The work described below was based on measurements of the superheated vapor temperature.

Measurement of the vapor temperature in dispersed, post-dryout flow is an extremely difficult task. The entrained liquid droplets, which are at essentially the saturation temperature, tend to quench any temperature sensor and prevent detection of superheated vapor temperature. In addition, the presence of high temperature walls in the test section is a second complication since radiation heat transfer to the sensor could cause measurement errors. It is due to these difficulties that there have been only two recorded attempts to measure vapor superheats in post-CHF flow. Mueller [11] utilized a thermocouple probe inserted through the side wall of the flow channel. The two-phase fluid was drawn into the thermocouple probe through the

Contributed by the Heat Transfer Division for publication in the JOURNAL OF HEAT TRANSFER. Manuscript received by the Heat Transfer Division October 1, 1979.

open end of the probe tubes. The probe was limited in use to flows at fairly high qualities (minimal entrained liquid droplets) in order to avoid quenching the thermocouple junction. This probe design was used by Polomik [12] to obtain a limited number of measurements in steam/water tests for post-CHF flows at 1000 psia pressure. More recently, vapor superheat measurements were obtained for post-CHF tests in rod bundles [13]. A shielded thermocouple was placed in one tube of the rod bundle and fluid was drawn past the thermocouple through a hole in the tube wall. Significant vapor superheats were observed for tests at high vapor qualities. It was reported that this measurement method was again hampered at low or moderate vapor qualities by liquid quenching of the thermocouple junction.

The first phase of the present investigation was the development of a reliable method for measurement of the superheated vapor temperature. Primary concerns included (*a*) preventing sensor quench by entrained droplets, (*b*) reducing radiation heat transfer from nearby hot walls, (*c*) minimizing temperature equilization between liquid and vapor phases during the measurement process, and (*d*) extending operable range to moderate or low vapor qualities (to X_e of 40 percent or less).

Following feasibility evaluations, a microthermocouple probe using differential aspiration was selected for detailed development. The concept utilized (a) inertial separation of liquid droplets from the sampled vapor, (*b*) differential aspiration of the separated phases to minimize probe quench by liquid, and (*c*) multiple radiation shielding of the thermocouple junction to minimize radiation heat transfer from the neighboring hot walls. A great number of different probe designs were built and tested in flows of hot air and superheated steam with entrained cold water sprays. These included probes of (*a*) bare thermocouple, (*b*) bare thermocouple in single aspirated tube, (*c*) shielded thermocouple in aspirated tube (shield placed in front of thermocouple to deflect liquid droplets, five different designs tested), and (*d*) thermocouple in concentric tubes with aspiration. This development work resulted in the final "vapor probe" shown in Fig. 1. A microthermocouple with 0.07 mm dia wires and an exposed hot junction was placed within the inner of two concentric capillary tubes. The ends of both capillary tubes were insulated and welded closed. Access holes to the outer and inner tubes were drilled at 90 deg displacement as indicated in Fig. 1. The probe assembly was then inserted into the two-phase flow in such a manner that the sampled fluid had to traverse through a 180 deg and a second 90 deg change of direction before passing over the thermocouple junction. These directional changes provided the inertial shielding for separation of liquid drops from the vapor. Due to the small linear dimensions involved, residence time of the sample fluid within the probe is minimal, thus preventing any significant equilibration between the phase temperatures. It was found that the small fraction of liquid drops which are aspirated into the probe would collect in the outer annulus, to be drawn off by aspiration through the annular space. Essentially liquid-free vapor would then be aspirated through the inner tube past the sensing thermocouple junction. Judicious control of the differential aspiration between the inner tube and outer annulus permitted adjustment of the liquid quenching frequency. The double annular shield arrangement also provided radiation shielding. For this design, the error caused by radiation from hot walls at operating conditions was calculated to be less than 2°C.

Figure 2 shows a sketch of the bench test apparatus used to characterize the vapor probe and indicates a typical probe signal trace. In this test apparatus, superheated steam with cold water spray was flowed past the vapor probe in vertical down-flow or up-flow. Dif-

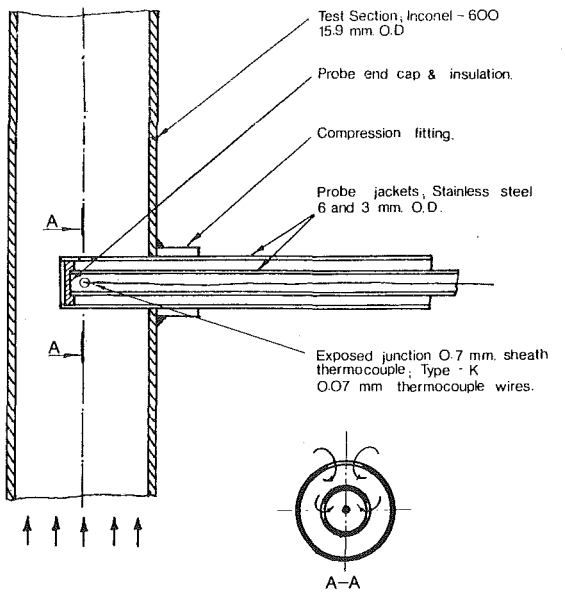

Fig. 1 The vapor probe

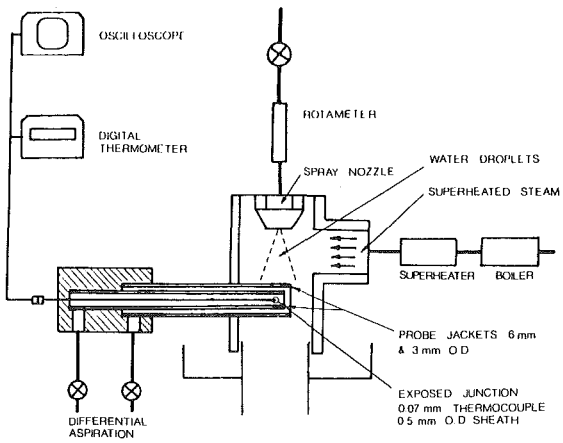

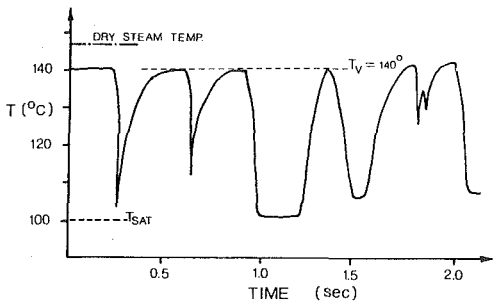

Fig. 2 Test facility for vapor probe and sample probe signal

Nomenclature

D = tube diameter
G = flow rate
H = enthalpy
h = heat transfer coefficient
H_{fg} = latent heat of vaporization
P = pressure
Q = heat flux
t = time
T = temperature
X = quality
Z = distance from the test section inlet

Subscripts

a = actual
e = equilibrium
L = liquid
s = saturation
v = vapor
vc = convective to vapor
w = wall

ferential aspiration on the probe was then adjusted to obtain an output signal of the type shown in Fig. 2. The objective was to provide sufficient time between liquid quenches for the thermocouple to recover to the vapor temperature. As seen from the probe signal shown in Fig. 2, this objective was successfully obtained in that the measured temperature approached a maximum asymptotic reading. For conditions of this run, the asymptotic temperature was only a few degrees lower than the known inlet (dry) steam temperature. This maximum temperature was taken to be the mean vapor superheated temperature (approximately 140°C in the case shown). It is also seen that at moment of liquid quenches, the measured temperature approached saturated liquid temperature of 100°C. In using this superheat probe in actual post-CHF experiments, differential aspiration was always adjusted to obtain this same type of characteristic probe response.

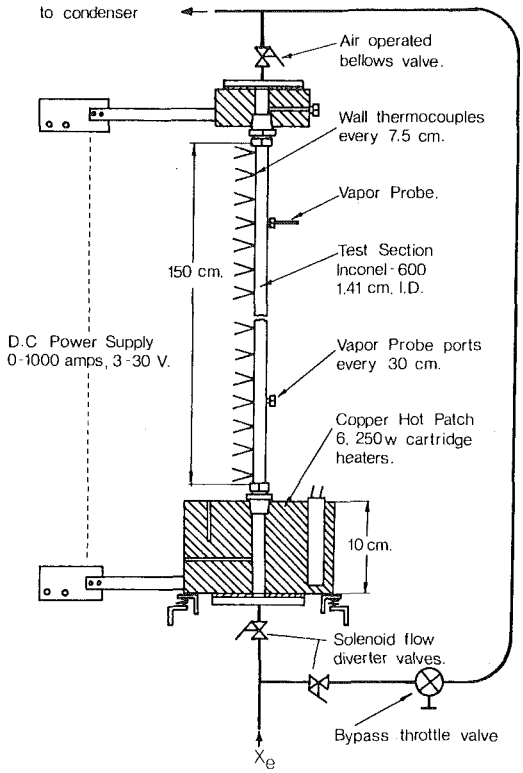

Fig. 3 Post-CHF test section

The data taken with the probe in post-CHF tests involved operation in two-phase flow with much higher vapor superheats (of the order of 300°C) and much lower liquid volume fraction. This resulted in longer periods between droplet quenches (see Fig. 4) so that a less stringent transient response was required of the probe. It is felt that this qualification of the probe in the bench-test was much more stringent than required for the actual experiment.

Post-CHF Experiment

The post-critical-heat-flux experiments were performed in a forced convection boiling two phase loop. The basic process loop supplied a steady flow of saturated steam and water to the inlet of the post-CHF test section. Details of the test section are shown in Fig. 3. At the inlet, the two-phase fluid flowed first through a 1.41 cm dia channel in a heavy copper hot patch. The hot patch was heated by cartridge heaters inserted close to its outside perimeter. From the hot patch, the two-phase flow then proceeded vertically upward through a thin-wall tube of 1.41 cm i.d. and 150 cm length. Joule heating of this tube by direct current passage through the wall was obtained using a variable d-c power supply of 30 kW. Stations for insertion of the vapor probe were located at 30 cm intervals. During the first experiments reported here, only the top probe station (30 cm below the exit of the tube) was used for the vapor superheated measurements. External thermocouples were fixed to the o.d. of the test section tube at 7.5 cm intervals to provide measurement of the wall temperatures. All runs were carried out with vertical upflow through the test section. A bypass line with flow-diverting valves was provided around the hot patch and test section tube, as indicated in Fig. 3. It should be noted that this type of post-CHF test section was first used by Groeneveld, et al. [14] in their post-CHF experiments.

To establish post-CHF conditions during the experiment, the two-phase flow was first directed through the bypass, with the hot patch and test section isolated from the loop. Under inert gas cover, the hot patch and test section were preheated to temperatures well above Liendenfrost wetting temperature (to approximately 450°C). The two-phase flow was then switched from the bypass line to the hot patch and test section. The thermal inertia of the massive hot patch delays its quenching by the two-phase flow. With sufficient time lag, the operator was able to adjust power input to the hot patch and to the test section, maintaining both in the post-CHF condition. Normally, the quench front would remain anchored within the 10 cm length of the hot patch. In most runs, this procedure was used to obtain steady state, post-CHF conditions throughout the length of the test-section tube. In a few runs, the test section power was reduced to permit a gradual progression of the quench front up the test section.

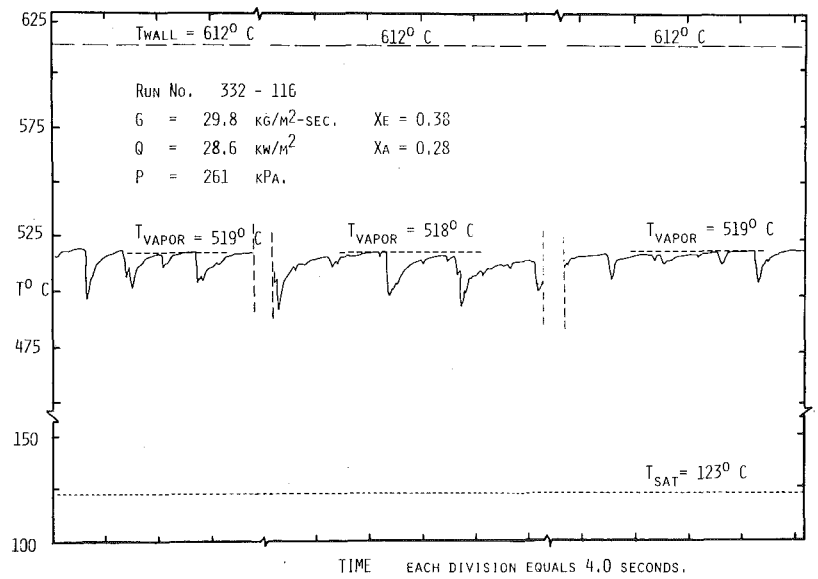

Fig. 4 Example of vapor-probe signal in post-CHF test

With judicious setting on the input power, relatively slow quench front progression could be obtained, thus providing pseudo-steady state measurements under low-flow "reflood" conditions.

For each run, the total mass flow rate and mixture equilibrium-quality at the inlet to the hot patch were determined from measurements made in the process loop. At the test section, continuous records were obtained for the inlet and outlet pressures, power inputs to the hot patch and to the test section tube, wall temperatures along the length of the test section, and vapor superheat temperatures at the last probe station (30 cm below the exit of the test section). These measurements, along with previously obtained heat loss calibration, provided the desired data on local fluid conditions (mass flux G, equilibrium quality X_e, saturation temperature T_s) and on the local heat transfer behavior (heat flux Q, wall temperature T_w, and the nonequilibrium vapor temperature T_v).

Results and Discussion

Twelve experimental runs in the post-CHF regime were completed and the results are reported here. The ranges of parameters in these twelve runs are shown in Table 1. Groeneveld [15] had pointed out that published data for post-CHF heat transfer are particularly lacking at low pressures, low flow rates, and low equilibrium qualities. It is hoped that these present results will help to fill this information void, as well as addressing the primary question of vapor superheating.

In all twelve experimental cases, significant nonequilibrium vapor superheating was detected by the vapor probe. A typical signal trace from the vapor probe for one of the runs is indicated in Fig. 4. Three different segments of the probe signal are shown, representing three different probe aspiration rates at approximately constant system conditions. It is seen that reasonably complete recovery to an asymptotic vapor temperature was obtained between quenches. The best indication that correct vapor temperatures were in fact measured comes from the observation that the "asymptotic" vapor temperatures were approximately the same for different aspiration rates and different droplet quench frequencies (as shown in Fig. 4). For conditions of this run, the vapor temperature was measured to be 519°C. The corresponding local wall temperature was 612°C and fluid saturation temperature was 123°C, at the axial position of the probe station. Thus, for this post-CHF case, the vapor was determined to be at nonequilibrium thermodynamic state of 396°C superheat. It is noteworthy that such substantial superheating was found even for this two-phase flow of relatively moderate vapor equilibrium quality ($X_e = 0.38$).

Typical axial variation of local wall temperature, saturation temperature, and equilibrium vapor quality, are shown in Fig. 5. The wall temperatures indicated by open circles in the figure were obtained from thermocouple measurements on the o.d. of the tubular test section, with a minor correction calculated for the temperature drop through the tube wall. The dashed line indicates a very slight variation in local saturation temperature, as interpolated from measured inlet and outlet pressures. The equilibrium quality, X_e, was calculated by heat balance. The axial coordinate (Z) is given in meters measured from the junction of the hot patch with the post-CHF tubular test-section. Heat flux was essentially constant over the length of the test section. For conditions of this run, the difference between wall temperature and saturation temperature increased along the direction of flow from approximately 200°C to approximately 370°C, indicating a decrease in the effective heat transfer coefficient along the direction of flow. The vapor temperature at the probe station is shown as the square point on Fig. 5. The vapor superheat for this run was greater than 57 percent of the local wall superheat. From the measured vapor temperature, the local actual quality (X_a) was calculated by equation (2) and is plotted as the dark square symbol on Fig. 5. It is seen that this actual quality, though greater than the inlet equilibrium quality, was noticeably less than the local equilibrium quality. Thus, the two phase flow in the post-CHF regime behaved neither as an equilibrium mixture (i.e., $X_a = X_e$ at all Z) nor as a frozen mixture (i.e., X_a = inlet X_e). Obviously the dynamic balance between heat transfer from the wall to the vapor and the heat transfer from the superheated vapor

Table 1

Pressure (P)	up to 3 bars
Mass Flux (G)	18 to 80 kg/m²-s
Heat Flux (Q)	1.1×10^4 to 4.2×10^4 W/m²
Wall Temperature (T_w)	up to 550°C
Equil. Quality (X_e)	0.08 to 0.36 at T.S. Inlet 0.17 to 0.49 at Probe Station

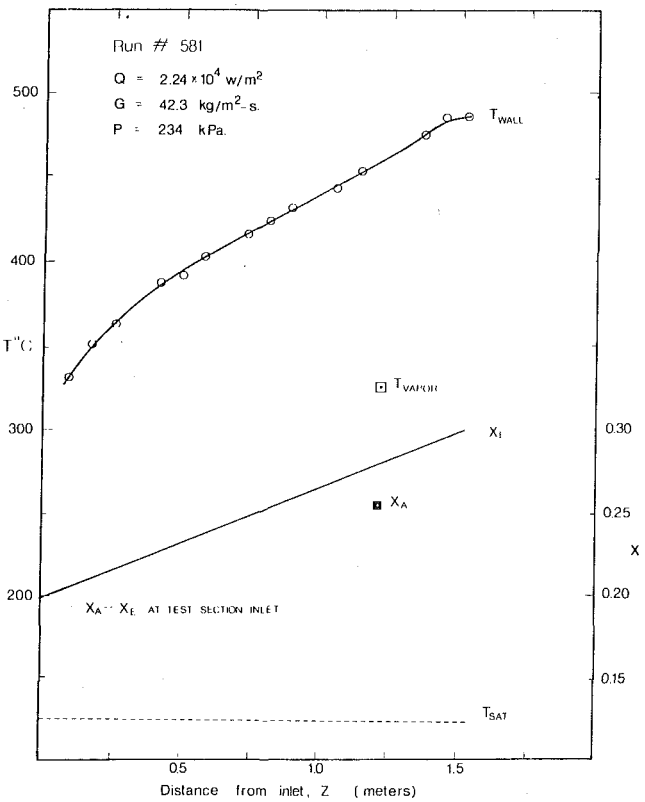

Fig. 5 Conditions along test sections in post-CHF experiment

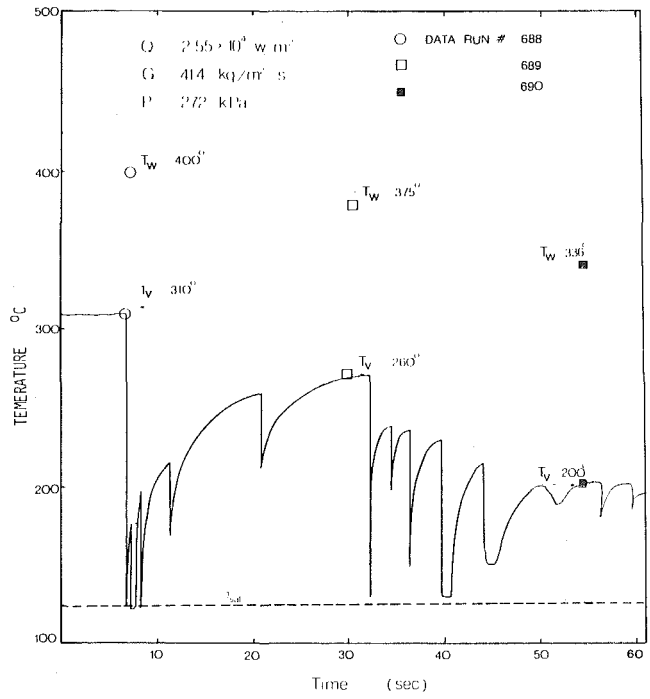

Fig. 6 Variation of vapor and wall superheats during slow reflood

to entrained droplets resulted in an intermediate rate of evaporation for the liquid in the two phase mixture.

Figure 6 shows conditions at the probe station during a slow reflood, wherein the quench front moved slowly upward along the test section. Under such conditions, as the quench front approached closer to the probe station, the measured vapor temperatures decreased with time. For the case shown, vapor temperatures of approximately 325, 260 and 200°C were measured at times corresponding to 8 s, 32 s, and 55 s, respectively. During this time span, the local wall temperatures also decreased slightly as indicated on Fig. 6, while the saturation temperature remained essentially constant.

The axial conditions for these three sample times are indicated in Fig. 7. Local wall temperatures along the test section are indicated by the three curves with individual temperature symbols. The top curve, corresponding to the 8 s time sample, indicated a quench front outside of the test section length. The latter two curves show the progression of the quench front as it moved upward into the test section length. The corresponding vapor temperatures are also shown in this figure. For this case, the saturation temperature remained at 125°C so that the measured vapor temperatures corresponded to superheats of 185, 135, and 75°C, respectively, for the three sample times. The three values of the local actual quality (X_a) calculated by equation (2) are also plotted on Fig. 7. As would be expected, these actual qualities increased with time and approached closer to the local equilibrium quality as the quench front moved up the test section toward the probe location.

An attempt was made to compare these superheat data with predictions calculated by two of the more recent nonequilibrium correlations. Figure 8 shows a plot (dark points) of the measured vapor superheat ($T_v - T_s$) versus local wall superheat ($T_w - T_s$) for the twelve experimental runs. For each run, using the known heat flux and wall temperatures, the correlations of Groeneveld and Delorme [9] and of Chen, et al. [16] were used to predict the corresponding vapor superheats. These predicted values are indicated by the open symbols on Fig. 8 for comparison with the experimental data. It is seen that both correlations indicated the correct trend but are significantly in error on the magnitude of the vapor superheat. Groeneveld and Delorme's model consistently overpredicted vapor superheats while the Chen, et al. correlation consistently underpredicted the vapor superheat, with deviations of up to 100 percent for both correlations.

The same two correlations were also compared with the experimental heat transfer data obtained in these tests. For each run, using the known local wall temperature and equilibrium quality, a prediction of the total heat flux was calculated by each of the two correlations. Figure 9 shows a plot of the predicted versus the measured heat fluxes. It is seen that the correlation of Groeneveld and Delorme underpredicted the heat flux for all twelve experimental cases. Deviation

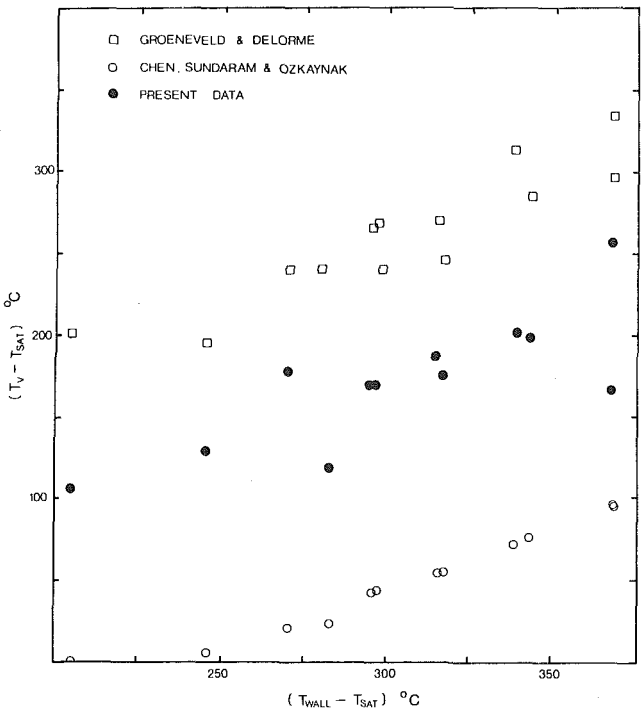

Fig. 8 Comparison of measured vapor superheats with predictions from nonequilibrium correlations

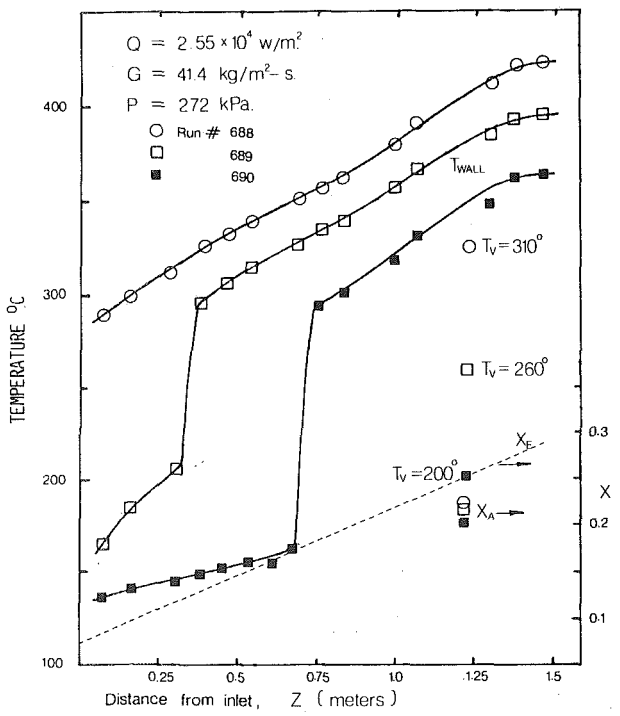

Fig. 7 Time-varying conditions in post-CHF test section during slow reflood

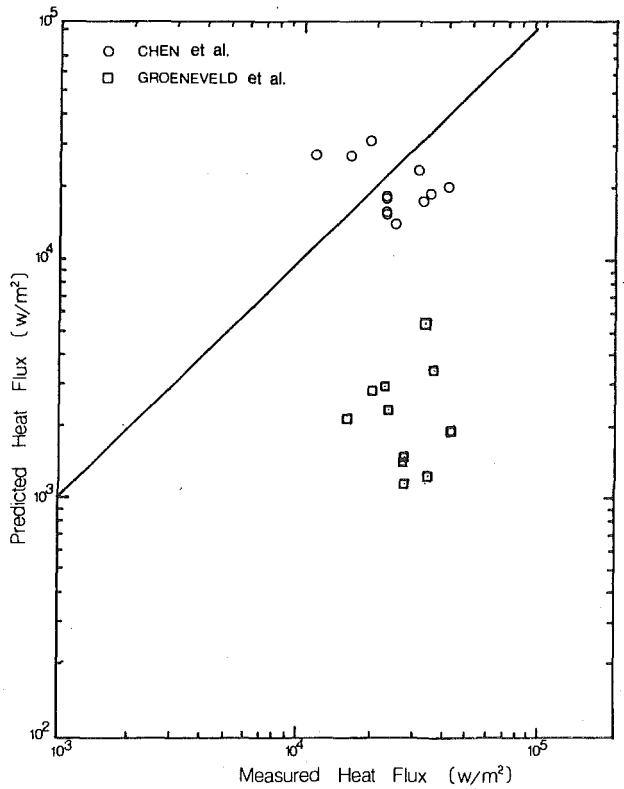

Fig. 9 Comparison of measured heat fluxes with predictions

between calculated and measured heat fluxes were approximately of one order of magnitude. Some underprediction is expected because this correlation does not account for direct wall-liquid contact. However, at the relatively high void fractions of the test conditions, the contribution to total heat transfer due to this mechanism is expected to be far less than the magnitude of underprediction indicated by the correlation. The correlation of Chen, et al. did predict the correct order of magnitude, though noticeable scatter is evident. The average deviation between predicted and measured heat fluxes for this second correlation was approximately 30 to 40 percent.

From the above comparisons, it appears that even the most recent nonequilibrium correlations are not able to predict nonequilibrium superheats for vapor in post-CHF boiling. This is not surprising since there has been an almost complete lack of experimental superheat data for development of such models and correlations. In terms of correlating post-CHF heat fluxes, a large data base does exist, although the great bulk of the data are limited to high-pressure and high-quality conditions. When compared against the present low-pressure data, the correlation of Groeneveld and Delorme was not successful. The correlation of Chen, et al. did surprisingly well for these low-pressure data, especially since the vapor superheats were not well predicted. It would appear that the model, with its empirical constants, made compensating adjustments for uncertainties in the prediction of the vapor superheat in order to still predict approximately correct heat fluxes.

Summary

This experimental program developed a vapor probe that was demonstrated to be useful in the difficult measurement of vapor temperatures in dispersed two-phase flow. Using this probe, post-CHF experiments were carried out in water/steam two-phase flows. Very significant amounts of superheat were indeed measured, even at fairly low equilibrium qualities (i.e., approximately 30 percent).

Measurements of heat transfer in the post-CHF regime were also obtained. These data, obtained at low pressures and low-equilibrium qualities, are in a parametric range where published results have been lacking to date.

In comparing experimental measurements with predictions by two of the more recent nonequilibrium models, it was found that the degree of vapor superheat was not satisfactorily predicted by either models, while one model did predict the right order of magnitude for the heat fluxes. It is clear that much more experimental measurements of this nature must be obtained to aid the improvement of phenomenological models for nonequilibrium, post-CHF heat transfer.

Acknowledgments

The authors wish to express their appreciation to Dr. Philip Kosky of General Electric Company and Dr. Y. Y. Hsu of the Nuclear Regulatory Commission for their invaluable support and advice given during various stages of this investigation. This research was funded by the United States Nuclear Regulatory Commission.

References

1 Parker, J. D., and Grosh, R. J., "Heat Transfer to a Mist Flow," ANL-6291, 1962.

2 Laverty, W. F., and Rohsenow, W. M., "Film Boiling of Saturated Nitrogen Flowing in a Vertical Tube," ASME JOURNAL OF HEAT TRANSFER, Vol. 80, 1967, pp. 90–98.

3 Forslund, R. P., and Rohsenow, W. M., "Dispersed Flow Film Boiling," ASME Paper 68-HT-44, ASME JOURNAL OF HEAT TRANSFER, Nov. 1968.

4 Hynek, S. J., Rohsenow, W. M., and Bergles, A. E., "Forced Convection Dispersed Flow Film Boiling," MIT Heat Transfer Lab, Report DSR 70586-63, 1969.

5 Plummer, D. N., Griffith, P., and Rohsenow, W. M., "Post-critical Heat Transfer to Flowing Liquid in a Vertical Tube," Paper No. 76-CSME/CS ChE-13, *16th National Heat Transfer Conference*, St. Louis, 1976.

6 Saha, P., Shiralkar, B. S., and Dix, G. E., "A Post-dryout Heat Transfer Model Based on Actual Vapor Generating Rate in Dispersed Droplet Regime," ASME Paper 77-HT-80, 1977.

7 Jones, O. C., and Zuber, N, "Post CHF Heat Transfer: A Nonequilibrium, Relaxation Model," presented at the 17th National Heat Transfer Conference, Salt Lake City, 1977.

8 Tong, L. S., and Young, J. D., "A Phenomenological Transition and Film Boiling Correlation," *Proceedings of the 5th International Heat Transfer Conference*, Vol. IV, B3.9, Tokyo, 1974.

9 Groeneveld, D. C., and Delorme, G. G. J., "Prediction of Thermal Nonequilibrium in the Post-dryout Regime," *Nuclear Engineering and Design*, Vol. 36, 1976, pp. 17–26.

10 Chen, J. C., Ozkaynak, F. T., and Sundaram, R. K., "Vapor Heat Transfer in Post-CHF Region Including the Effect of Thermodynamic Nonequilibrium," *Nuclear Engineering and Design*, Vol. 51, 1979, pp. 143–155.

11 Mueller, R. E., "Film Boiling Heat Transfer Measurements in a Tubular Test Section," EURAEC-1871/GEAP-5423, 1967.

12 Polomik, E. E., "Transition Boiling Heat Transfer Program—Final Summary Report for Feb. 1973–Oct. 1967," GEAP-5563, October 1967.

13 Hochreiter, L. E., "NRC/Westinghouse/EPRI FLECHT Low Flooding Rate Skew Axial Profile Results," Presented at the 5th Water Reactor Safety Information Meeting, sponsored by USNRC, Washington, D.C., 1977.

14 Groeneveld, D. C., and Gardiner, S. R. M., "A Method of Obtaining Flow Film Boiling Data for Subcooled Water," *International Journal of Heat and Mass Transfer*, Vol. 21, 1978, pp. 664–665.

15 Groeneveld, D. C., and Gardiner, S. R. M., "Post-CHF Heat Transfer under Forced Convective Conditions," Invited paper, Nuclear Reactor Safety Symposium, ASME Winter Annual Meeting, Atlanta, 1977.

16 Chen, J. C., Sundaram, R. K., and Ozkaynak, F. T., "A Phenomenological Correlation for Post-CHF Heat Transfer," USNRC Report NUREG-0237, June 1977.

Prediction of Horizontal Tubeside Condensation of Pure Components Using Flow Regime Criteria

G. Breber
J. W. Palen
J. Taborek

Heat Transfer Research, Inc.,
1000 South Fremont Avenue,
Alhambra, Calif. 91802

In order to select the appropriate correlations for prediction of horizontal tubeside condensation heat transfer coefficients, it is necessary to estimate what types of flow patterns exist at various points along the tube. The main criteria required are shown to be the ratio of shear to gravity forces on the condensate film and the ratio of vapor volume to liquid volume. A recently proposed prediction method by Taitel and Dukler is compared with observed flow regimes for condensation in horizontal tubes. The theoretically obtained parameters are shown to characterize the flow regimes well. Based on these parameters, a simplified procedure for prediction of local heat transfer coefficients for pure component condensation in horizontal tubes is proposed.

Introduction

Condensation in horizontal tubes is important in the power and chemical process industries. Because of the increasing industrial requirements for more efficiency and less overdesign, it was necessary to take a closer look at methods for predicting the condensation heat transfer coefficients for this configuration. In this presentation only condensation of pure components is considered.

An initial review in 1970 by Bell, et al. [1] clearly showed that not only did available methods in the literature give drastically different answers, but that even the trends with flow rate were not consistent. This variation was not because of poor correlations, since all the methods predicted the data upon which they were based very well. As Bell et al. correctly analyzed, different types of correlations are necessary for prediction in different condensation flow regimes, and the failure to select the proper type can result in severe errors. This leads to the conclusion that determination of the flow regime is one of the most important steps in proper prediction of horizontal tubeside condensing heat-transfer coefficients.

Flow regime prediction is especially important and especially difficult in phase change processes because the vapor fraction changes along the tube so that several different local flow patterns may occur between inlet and outlet of the tube. A logical question is whether flow regime maps developed from adiabatic two-phase systems such as air and water mixtures will hold for phase change processes, such as condensation of hydrocarbons and refrigerants.

In this paper a relatively new method of flow regime prediction by Taitel and Dukler [2] is compared for the first time with over 700 flow regime observations for condensation in horizontal tubes. It was mentioned in an earlier paper [3] that this new method apparently was based on the proper parameters for prediction of condensation flow regimes but had not at that time been tested against condensation data. In this paper it is shown that the parameters recommended by Taitel and Dukler are indeed significant for condensation. The original theoretical boundaries can be somewhat simplified for the purpose of condensation mechanism selection based on the general approach described in the following section.

General Characteristics of Condensation Flow Regime Transitions

Flow regimes change as condensation takes place because of two conditions caused by the decreasing vapor fraction.

1 The ratio of shear forces to gravity forces on the condensate film decreases.

2 The ratio of liquid volume to vapor volume increases.

A schematic diagram of the kinds of flow regimes which are observed as a function of these two ratios is shown in Fig. 1.

The major flow regimes in horizontal tubeside condensation may be thought of as four quadrants on a two-dimensional map relating the ratio of forces and the liquid volume fraction. Taitel and Dukler used an adaptation of the Kelvin-Helmholtz theory for wave instability to obtain dimensionless parameters for their model. An admittedly much cruder but still logical approach can be used to obtain the parameters for a map such as Fig. 1.

Liquid Volume Fraction. The true liquid volume fraction is not known because the amount of slip cannot be theoretically determined for all regimes. However, it is well known that the liquid volume fraction can be correlated as a function of the Martinelli parameter, X. Therefore, X will replace liquid volume fraction for the abscissa of the map, where

$$X = \sqrt{\Delta P_\ell / \Delta P_v} \cong \left(\frac{1-y}{y}\right)^{0.9} \left(\frac{\rho_v}{\rho_\ell}\right)^{0.5} \left(\frac{\mu_\ell}{\mu_v}\right)^{0.1} \tag{1}$$

if both phases are turbulent.

Force Ratio. As discussed in reference [3], it is very important in condensation to determine whether flow is *shear-controlled* or *gravity-controlled*. Let us write simple equations for pressure gradients for the two limiting cases.

1 Vapor Shear Axial Gradient, $$F_a = \frac{dP_s}{dL} = \frac{4f_v}{D_i}\frac{G_v^2}{2\rho_v} \tag{2}$$

2 Gravity Radial Gradient, $$F_r = \frac{dP_g}{dD_i} = g(\rho_\ell - \rho_v) \tag{3}$$

Taking a ratio of F_a to F_r, $$\frac{F_a}{F_r} = \frac{2f_v G_v^2}{D_i g \rho_v (\rho_\ell - \rho_v)} \tag{4}$$

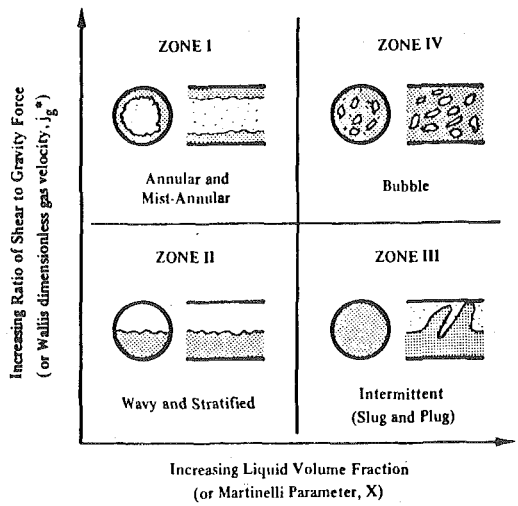

Fig. 1 Conceptual diagram of flow regimes in a horizontal tube

Contributed by the Heat Transfer Division for publication in the JOURNAL OF HEAT TRANSFER. Manuscript received by the Heat Transfer Division October 30, 1979.

It is interesting that F_a/F_r is related to the "dimensionless gas velocity," j_g*, defined by Wallis [4].

$$j_g^* = \frac{G_t y}{\sqrt{D_i g \rho_v (\rho_\ell - \rho_v)}} = \left[\left(\frac{F_a}{F_r}\right)\left(\frac{1}{2f_v}\right)\right]^{0.5} \quad (5)$$

The vapor-phase friction factor at the two-phase interface, f_v, can be considered almost a constant, especially for a rough wavy interface. Therefore, the Wallis j_g* factor is directly related to the ratio of the forces involved and can be used in place of F_a/F_r for the ordinate of Fig. 1.

As will be shown in the next section, j_g and X are identical to the parameters derived by Taitel and Dukler using a unique theoretical approach.

Description of Taitel-Dukler Flow Regime Map

The model by Taitel and Dukler was originally developed for transition between adjacent flow patterns for the case of steady adiabatic flow without phase change in horizontal or inclined tubes. We will consider only the horizontal case for simplicity.

Transition between Wavy and Annular or Intermittent Patterns is given as a function of F and X where $F = j_g$* (equation (5)). The graphical illustration of the numerical determination of this boundary is the curve A in Fig. 2.

The transition takes place either to the intermittent or annular pattern. (The intermittent pattern has been previously referred to in the literature as slug or plug flow.)

Transition between Intermittent and Annular Patterns is done by a single value of X as illustrated by boundary B in Fig. 2.

Transition between Intermittent and Dispersed Bubble Patterns is a function of X and T, where

$$T = \frac{\left(\frac{dP}{dL}\right)_\ell}{(\rho_\ell - \rho_v)g} \quad (6)$$

The numerical solution appears as curve D in Fig. 2.

Transition between Stratified-Smooth and Stratified-Wavy Patterns is a function of X and K, where

$$K = (F)(\mathrm{Re}_\ell)^{1/2} \quad (7)$$

The term Re_ℓ is a superficial Reynolds number of the liquid. The numerical solution resulted in curve C in Fig. 2.

A comparison of the above approaches with visual data for condensation will now be described.

Description of the Data

Data sources used for this investigation are listed in Table 1. This includes all known condensation data from open literature for which flow patterns were systematically studied and reported, as well as some selected unpublished HTRI data. These data had been subjected to consistency tests and other culling procedures. Although all fluids were either refrigerants, steam, or n-pentane, a wide range of physical properties and flow parameters were covered, as is shown in Table 2.

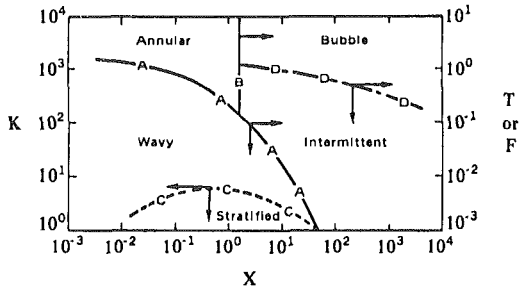

Fig. 2 Original Taitel-Dukler flow regime map for horizontal tubes (ref (2))

Table 1 Condensation flow pattern data sources

Reference	Fluid	Tube Inside Diameter, mm	Test Section Length, m	Number of Data Points	Symbol on Figs. 3-7
6	R-12	8.0	4.42	83	⊖
7	R-12	12.7	0.61	91	●
8	R-12	4.8	0.61	66	○
		15.9	0.61	123	○
	R-113	4.8	0.61	74	◇
		12.7	0.61	70	◇
		15.9	0.61	86	◇
9	R-12	12.7	0.61	25	▼
10	R-12	12.7	0.61	9	■
11	steam (no condensation)	25.4	1.27	4	□
		50.8	1.27	4	□
12	steam	22.0	6.70	14	▲
12	n-Pentane	22.0	6.70	74	▲
13	R-113	14.5	0.72	17	▽
17	R-11	16.0	4.40	13	△

Nomenclature

D_i = inside tube diameter, m
F = modified Froude number defined in reference [2]
F_a = vapor shear axial gradient, equation (2), kPa/m
F_g = correction to Nusselt relation for stratified layer inside horizontal tube
F_r = gravity radial gradient, equation (3), kPa/m
f_v = friction factor for vapor
g = acceleration of gravity, m/s^2
G_t = total mass velocity, kg/m^{2}s
G_v = vapor mass velocity, kg/m^{2}s
h_{cg} = local condensation heat transfer coefficient in gravity-controlled flow or natural convection, W/m^{2}K
h_{cs} = local condensation heat transfer coefficient in shear-controlled flow or forced convection, W/m^{2}K
h_ℓ = convective heat transfer coefficient for liquid flowing alone, W/m^{2}K
h_N = Nusselt model heat transfer coefficient for a draining film, W/m^{2}K
j_g* = Wallis dimensionless gas velocity, equation (5)
K = wavy flow, dimensionless parameter, equation (7)
k_ℓ = liquid thermal conductivity, W/mK
K_p = constant, equation (9)
L = tube length, m
m = exponent relating two-phase pressure drop correction to two-phase heat transfer correction
P = operating pressure, kPa
P_g = gravity force, kPa
P_s = shear force, kPa
Re_ℓ = Reynolds number for liquid flowing alone
T = dispersed bubble flow dimensionless parameter, equation (6)
X = Martinelli parameter, equation (1)
y = local weight fraction vapor
ΔL = distance from tube entrance to point of local evaluation of h_ℓ, m
ΔP_ℓ = pressure drop for liquid flowing alone in the tube, kPa
ΔP_{tp} = pressure drop for two-phase mixture, kPa
ΔP_v = pressure drop for vapor flowing alone in the tube, kPa
ΔT_c = difference between bulk temperature of condensing fluid and wall, K
λ = heat of vaporization, J/kg
μ_ℓ = liquid bulk viscosity, N s/m^2
μ_v = vapor bulk viscosity, N s/m^2
μ_w = liquid viscosity at the tube wall temperature, N s/m^2
ρ_ℓ = liquid density, kg/m^3
ρ_v = vapor density, kg/m^3
σ = surface tension, N/m
ϕ_ℓ^2 = Martinelli ratio of two-phase pressure drop to pressure drop for liquid flowing alone

Table 2 Range of parameter values for data used in this study

Inside pipe diameter	(D_i)	4.8 – 22.0 (50.8) mm
Liquid density	(ρ_ℓ)	560.6 – 1 505.7 kg/m^3
Vapor density	(ρ_v)	4.8 – 70.5 kg/m^3
Liquid viscosity	(μ_ℓ)	150 (140) – 500 N s/m^2
Vapor viscosity	(μ_v)	7.6 – 13.5 (16.1) N s/m^2
Surface tension	(σ)	0.0058 – 0.0573 N/m
Operating pressure	(P)	108.2 – 1 248.6 (2 489) kPa
Total mass velocity	(G_t)	17.63 – 990.0 (1 600.3) kg/m^{2}s

Calder (11) hot water flash data parameter values are shown in parentheses for cases where they exceeded parameter ranges for condensation data.

Traviss and Rohsenow data [6] consisted of 83 points for refrigerant R12. A glass observation section was located 15 tube diameters downstream from the end of the test section and allowed a description of one flow pattern per run. The runs were all at high mass velocities, so the wavy and stratified patterns were not observed.

Soliman and Azer [7] described 41 runs with refrigerant R12, which provided 91 data points. The test section consisted of three separate counterflow condensers, with lengths of 0.51, 0.61, and 0.61 m respectively. The condensers were joined together by three transparent sections with a visual length of about 0.13 m. The authors identified a very broad spectrum of flow patterns from mist through wavy to slug flow.

Soliman [8] presented 201 runs with 419 data points. Condensation of two refrigerants was tested, R-12 and R-113. Soliman visually identified nine different flow patterns, including all major patterns except dispersed bubble flow and stratified flow. He also described several transitional flow patterns, which he termed semiannular, semiannular-wavy, and annular-wavy. The differences between these patterns are very hard to identify, and "subjective factors" must be considered. For the purpose of this study, all mentioned transition flows were included in the category of the annular-wavy flow transition.

Brauser [9] reported 25 runs and Chen [10] 9 runs with refrigerant R-12. The flow pattern entering and leaving the test section was observed through sight glasses. Brauser and Chen mostly provided data in the shear-controlled region at high velocities and high vapor weight fractions.

Calder [11] data, measured at Lawrence Livermore Laboratory, consisted of 8 runs with steam. The glass sections, intended for observation of flow patterns, were sandwiched between stainless-steel pipes of the same corresponding diameters. The experimental facility was constructed for investigation of two-phase geothermal flows. Basically, it was a hot-water generator from which the pressurized water was flashed to desired low pressure conditions for test purposes. The test section pressure ranged from 750 to 2500 kPa, and total mass velocity reached 1630 kg/m^{2}s. These interesting data were added to this study for a comparison with the typical condensation data described above because of lack of water condensation data runs at described conditions. This source provided mist, annular, wavy, and slug patterns which were seen to be in very good agreement with the condensation data at the same values of the generalized flow regime parameters.

HTRI data observations were made along a 6.7 m glass tube in which the entire condensation process could be observed and location of regime transitions accurately determined. High speed still and motion picture studies documented the flow patterns along the length of the test section [12]. The HTRI data include all main flow patterns with an exception of dispersed bubbles which require system pressure above the limitation of a glass tube. For many runs, condensate was injected at the entrance to the test section at saturation temperature. This allowed observations of slug and plug patterns over a wide range

Chato [13]. The test section was a finned copper tube. Observation windows were located at both ends of the tube allowing observation in axial directions. Only smooth and wavy stratified flows were observed.

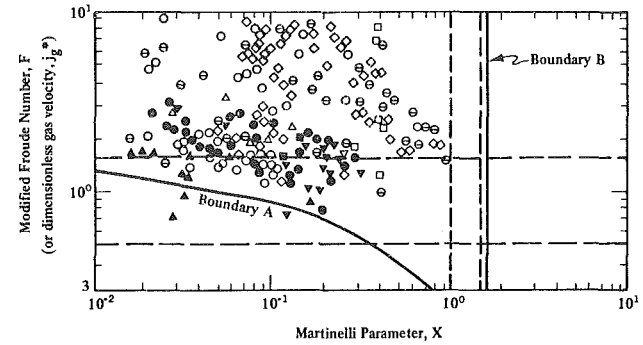

Fig. 3 Comparison of Taitel-Dukler flow map with annular flow condensation data

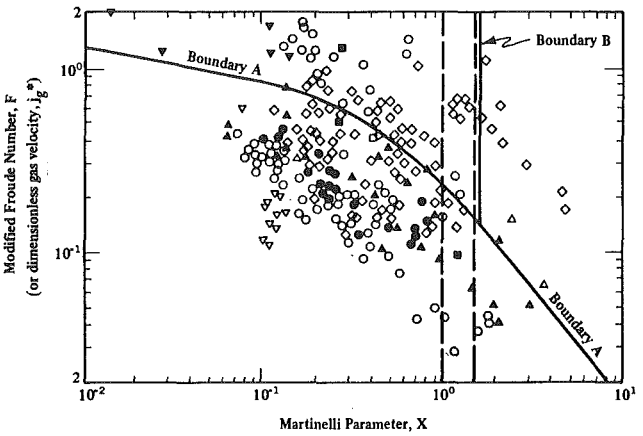

Fig. 4 Comparison of Taitel-Dukler flow map with wavy flow condensation data

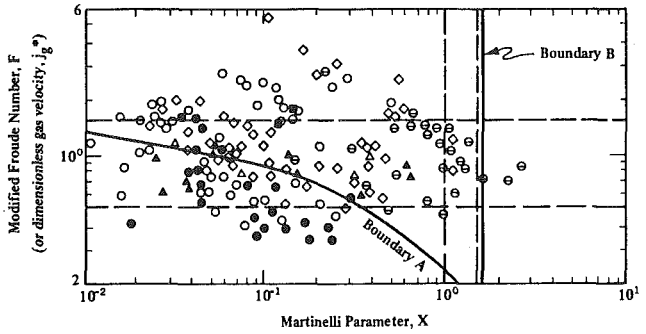

Fig. 5 Comparison of Taitel-Dukler flow map with annular-wavy transition flow condensation data

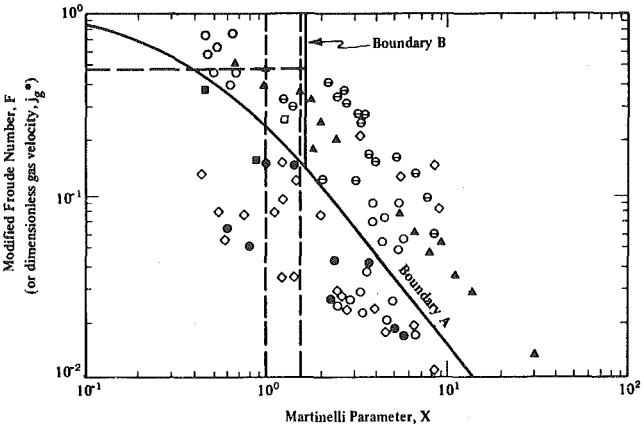

Fig. 6 Comparison of Taitel-Dukler flow map with intermittent (slug-plug) condensation data

Fujii [17]. The flow patterns were observed at five locations along the test section through 75mm long tube segments with the same diameter as the metalic tube.

Comparison of the Taitel-Dukler Map with Condensation Data

In Figs. 3–7 observed flow patterns are compared with their calculated positions on the Taitel-Dukler map. Different symbols are used for each data source and correspond to the designations given in Table 1. Relatively good agreement was found for tube diameters ranging from 8.0 to 22.0 mm. For Soliman's data with a very small tube diameter (4.8 mm), agreement was not good. Wavy and slug flows were predicted as annular. The reason for this deviation is not presently understood and may be due to surface tension effects which are not accounted for. However, much of the discrepancy may just be due to the fact that it is extremely difficult to tell the difference between wavy and semiannular flow for such a small tube. In any case, tubes of such small diameter are rarely used, at least in the process industries, so the anomaly is not serious with regard to practical condenser design.

Excellent agreement was found for annular data as can be seen from Fig. 3. Essentially all of the points observed to be in the annular or mist annular regimes were located above Boundary A and left of Boundary B as required. This is a remarkably good confirmation of the theoretical Boundary A as the lower limit of annular flow in condensation. Relatively good agreement between visually observed and predicted patterns was found for stratified-wavy data, where (neglecting the 4.8 mm tube data) 80 percent of the data points were located in the proper region, as shown in Fig. 4. Some of the points observed as wavy fall above the Boundary A which points out the fact that transition between annular and wavy is not abrupt and that a transition region rather than a single line is necessary to separate these two regimes. This was, in fact, mentioned by Taitel and Dukler. Figure 5 shows those points which were defined as annular-wavy or semiannular by the investigators. As can be seen, a rather broad transition region is required to encompass these data. However, they are approximately evenly distributed on either side of Boundary A (at least at low values of parameter X), further confirming the basic validity of this boundary.

The largest discrepancies were for data reported to be in the intermittent or slug flow area, as shown in Fig. 6. At high total mass velocities, some points observed to be in slug flow were indicated in the annular-dispersed liquid region on the Taitel-Dukler map. For some points with low total mass velocity, on the other hand, observed slug flow points were plotted in the stratified wavy region of the Taitel-Dukler map. Figure 6 shows that the observed slug and plug data points are divided by Boundaries A and B of the map.

Nevertheless, it should be noted that none of the slug flow points is found in the region to the left of $X = 0.4$ or above $F = 1.0$. Therefore, it is evident that these parameters do locate the slug region even though it is probable that the Boundary A should be shifted at least for high X values.

The Taitel-Dukler Boundaries A and B were of greatest interest for this work because in the selection of condensation mechanisms it is most important to distinguish the annular, wave, and slug regimes. However some of Chato's and HTRI data were available for condensation in stratified flow with a smooth interface. Figure 7 shows that the Taitel-Dukler K parameter does an excellent job of defining these points.

Condensation Path Prediction

In spite of the very logical basis for the flow parameters, the condensation path in the Taitel-Dukler map is a rather complicated curve.

An analytical expression of the condensation path in the Taitel-Dukler map can be deduced from the definition of the Wallis dimensionless gas velocity, (equation (5)). For the most common case, when vapor and condensate flow turbulently, the Martinelli parameter is given by equation (1). Substituting equation (1) into equation (5) results in

$$j_g^* = \frac{G_t}{\sqrt{\rho_v(\rho_\ell - \rho_v)D_i g}}\left(\frac{K_p}{X^{1.111} + K_p}\right) \tag{8}$$

K_p is a constant depending only on physical properties of fluid.

$$K_p = \left(\frac{\rho_v}{\rho_\ell}\right)^{0.555}\left(\frac{\mu_\ell}{\mu_v}\right)^{0.111} \tag{9}$$

Figure 8 illustrates the condensation path for two cases with condensing n-pentane at 138 kPa, one at high total mass velocity, G_t, and one at low. For the high velocity case, the transition is from the annular to the slug flow regime, while for the low velocity case the path passes from the annular into the wave regime. One difficulty in using this map for condensation is seen. The condensation path can be almost parallel to the Boundary A. Therefore, considering the actual broad transition region, illustrated in Fig. 5, it is very difficult to tell at what point in the condensation path to begin switching condensation correlations from the shear-controlled type to the gravity-controlled type. More specific recommendations are given in a later section.

Simplified Criteria for Condensation Heat Transfer Prediction

As was discussed in reference [3], there are two basic types of condensation heat transfer formulations for horizontal tubes. These also hold for other geometries.

Nusselt Type. This is based on modifications of the Nusselt equations for heat transfer to a draining film and applies to the gravity-controlled wavy or stratified regimes.

$$h_{cg} = h_N F_g \tag{10}$$

The factor h_N is the heat transfer coefficient for a draining liquid film as derived by Nusselt. For a horizontal tube the following expression is often used.

$$h_N = \left[\frac{k_\ell^3 \rho_\ell(\rho_\ell - \rho_v)g\lambda}{4\mu_\ell \Delta T_c D_i}\right]^{1/4} \tag{11}$$

The factor F_g can be shown to be a function of the true liquid volume fraction and the vapor Reynolds number. However, as a first

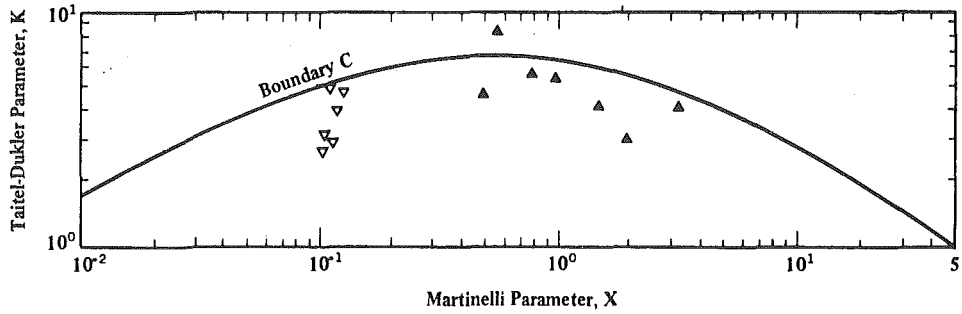

Fig. 7 Comparison of Taitel-Dukler flow map with smooth stratified condensation data

approximation a constant value of $F_g = 0.79$ is suggested in reference [3]. This also agrees with the data of Chato [13] and of Kroeger [14]. This value will become conservative as the annular flow boundary is approached. A slight downward slope of the tube can increase significantly the heat transfer.

Convective Type. A very good approximation for the annular flow regime, which can be used as a first estimate for the intermittent and bubble regimes is obtained by the following analogy relationship (also see reference [3]).

$$h_{cs} = h_\ell(\phi_\ell{}^2)^m \tag{12}$$

where

$$\phi_\ell{}^2 = \frac{\Delta P_{tp}}{\Delta P_\ell} \tag{13}$$

The factor $\phi_\ell{}^2$ can be obtained from the appropriate two-phase pressure drop correlation. The Lockhart-Martinelli correlations may be used as a good approximation. The simplified curve fit form by Chisholm as referenced by Collier [15] is recommended. The exponent m may be derived theoretically to range between 0.4 and 0.5, depending on assumptions. In reference [3] a value of 0.5 is suggested for intube correlation. However, for design estimations a conservative value of 0.45 is recommended.

The convective heat transfer coefficient for the liquid phase, h_ℓ, may be determined from boundary layer theory as was done by Traviss, et al. [16]. However, reasonably good results can be obtained using familiar empirical correlations for liquid-forced convection in a tube.

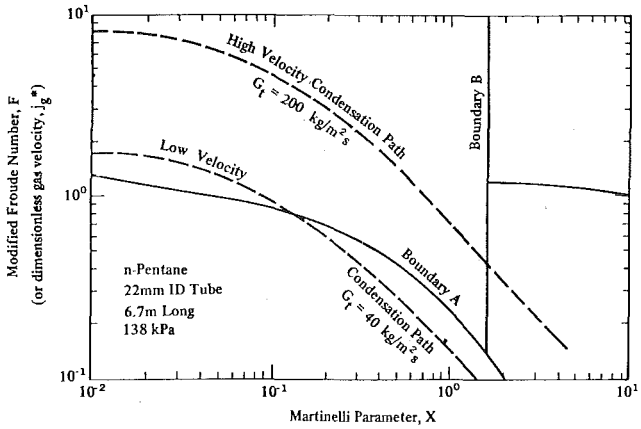

Fig. 8 Example condensation paths on Taitel-Dukler flow map

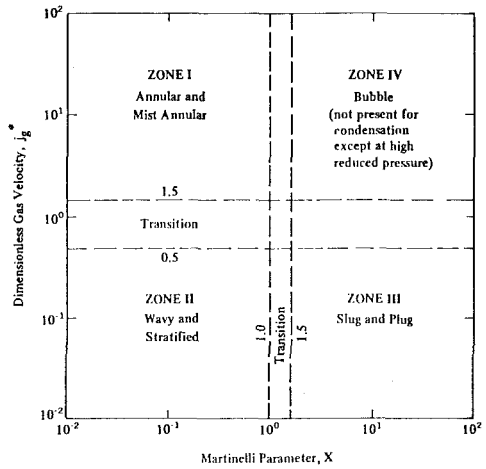

Fig. 9 Simplified criteria for horizontal tubeside condensation flow regimes, based on available data

As was seen in the above comparison, the original Taitel-Dukler boundaries should be broadened somewhat between the annular and wave regions to include a transition zone and shifted somewhat between the wave and slug regions to agree with available condensation data. The following simplified criteria are proposed for the purpose of condensation correlation selection.

Zone I $\quad j_g^* > 1.5, X < 1.0$

Assume annular flow and use equation (12)

Zone II $\quad j_g^* < 0.5, X < 1.0$

Assume wavy or stratified flow and use equation (10)

Zone III $\quad j_g^* < 1.5, X > 1.5$

Assume slug (intermittent flow).

For this regime few condensation heat transfer data are known to exist in the open literature, and recommendations must be tentative. Actually, both the convective mechanism and the draining film Nusselt mechanism may be involved alternately on a frequency corresponding to the frequency of the slugs. However, for an approximate method this model is too complicated, and there are too many unknowns. Therefore, it is tentatively recommended that equation (12) be used for this regime on the basis that the convective mechanism appears to be controlling and because this equation approaches the proper limit as the vapor fraction approaches 0 (as $y \rightarrow 0$, $F_{tp} \rightarrow 1.0$, and $h_{cs} \rightarrow h_\ell$).

Zone IV $\quad j_g^* > 1.5, X > 1.5$

Assume bubble flow and use equation (12).

Notice that more advanced correlations for ΔP_{tp} may give different relationships for ϕ_ℓ for different zones.

Transition between Zones I and II. Linearly prorate between h_{cg} and h_{cs} with respect to j_g^*.

Transition between Zones II and III. Linearly prorate between h_{cg} and h_{cs} with respect to X.

These simple recommendations actually give relatively good definitions of the observed condensation flow regimes as shown in the next section.

Comparison of Simplified Recommendations with Observed Condensation Flow Regimes

The boundaries given in the previous section are shown as dashed lines in Figs. 3–6. It is evident that these do a good job of separating the four main types of flow patterns as referred to in Fig. 1. A summary of the simplified criteria is shown in Fig. 9. Of course, no flow regime boundaries are exact, and the only realistic way of defining the flow regimes on a given map is to state what is the probability of finding a certain flow regime at a certain coordinate system location on the map.

In Table 3, the percentage of points for each flow pattern falling in a certain zone defined by the boundaries of Fig. 9 is illustrated. For example, for Zone I with $j_g^* > 1.5$ and $X < 1.0$, 84 percent of the enclosed points were observed to be annular or mist, 15 percent annular-wavy transition, and one percert wavy. The agreement for all zones is evidently quite good, considering the simple criteria.

As would be expected, the transition regions contain a broader distribution of points, including a significant number of points from the bordering zones. Therefore, proration of the heat transfer coefficient models of the bordering zones makes sense and is presently the only practical way seen to handle these complex regions.

Conclusions

It may be concluded from this study that dimensionless flow regime parameters used for adiabatic two-phase flow may also be applied for determination of local condensation flow regimes. The theoretically derived flow regime parameters by Taitel and Dukler were confirmed to be significant for condensation, both by an alternative derivation and by comparison with experimental data. The original theoretical Taitel-Dukler boundaries between annular and wave regimes agreed

Table 3 Distribution of observed flow patterns

Flow Pattern Zones Fig. 9	Percentage of Points of Each Type Observed in Each Zone			
	Annular and Mist I	Annular-Wavy Transition	Wavy and Stratified II	Slug and Plug III
Zone I Annular Mist and Annular	84	15	1	0
Zone II Wavy and Stratified	0	9	85	6
Zone III Slug and Plug	0	6	12	82
Transition Between Zones I and II	24	55	20	1
Transition Between Zones II and III	0	6	44	50

excellently with the observed data at low liquid loadings.

Excellent agreement was also seen for the wavy-stratified boundary. At high liquid loadings, corresponding to Martinelli parameter values greater than about 0.5, the agreement between slug flow data and the theoretical wavy-slug boundary was less good. However, an empirical shift of this boundary produced good results.

A set of simplified criteria in terms of flow regime parameters is proposed to select the appropriate correlation model (Nusselt or convective) for more accurate prediction of horizontal tubeside condensation heat transfer for pure components. Use of these criteria also gives somewhat better prediction of observed condensation flow patterns than the original theoretical boundaries for the data presently on hand.

Acknowledgment

The authors are grateful to the management and Technical Advisory Committee of HTRI for permission to publish this information. It should be noted that the above does not necessarily represent HTRI recommendations for design but is intended to provide a helpful interpretation of published literature in the light of HTRI experiences in the same area.

References

1 Bell, K. J., Taborek, J., and Fenoglio, F., "Interpretation of Horizontal Intube Condensation Heat Transfer Correlation with a Two-Phase Flow Map," *CEP Symposium Series,* Vol. 66, No. 102, 1970, pp. 150–163.

2 Taitel, Y., and Dukler, A. E., "A Model for Predicting Flow Regime Transitions in Horizontal and Near Horizontal Gas-Liquid Flow," *AIChE Journal,* Vol. 22, No. 1, 1976, pp. 47–55.

3 Palen, J. W., Breber, G., and Taborek, J., "Prediction of Flow Regimes in Horizontal Tubeside Condensation," AIChE Paper No. 5, presented at the 17th National Heat Transfer Conference, Sale Lake City, 1977.

4 Wallis, G. B., "Flooding Velocities for Air and Water in Vertical Tubes," UKAEA Report AEEW-R-123, 1962, and *One-Dimensional Two-Phase Flow,* McGraw-Hill, New York, 1969.

5 Dukler, A. E., "Modeling Two-Phase and Heat Transfer," Keynote Paper KS-11, presented at the Sixth International Heat Transfer Conf., Toronto, 1978.

6 Traviss, D. P. and Rohsenow, W. M., "Flow Regimes in Horizontal Two-Phase Flow with Condensation," *ASHRAE Transactions,* No. 2279, RP-63, 1973.

7 Soliman, H. M. and Azer, U. L., "Flow Patterns During Condensation Inside a Horizontal Tube," ASHRAE Transactions, Vol. 77, Part 1, 1971, p. 211.

8 Soliman, H. M., "Analytical and Experimental Studies of Flow Patterns During Condensation Inside Horizontal Tubes," PhD Thesis, Kansas State University, 1974.

9 Brauser, S. O., "Turbulent Condensation in a Horizontal Tube," PhD Thesis, Kansas State University, 1966.

10 Chen, J., "Condensing Heat Transfer in a Horizontal Tube," Masters Report, Kansas State University, 1962.

11 Calder, C. A., "Flow Regime Characterization for Horizontal Two-Phase Steam Flow," Microfiche No. UCRL-52186, October 1976, Lawrence Livermore Laboratory, University of California.

12 Movie Session, Sixth International Heat Transfer Conf., Toronto, 1978, HTRI Movie, "Flow Regimes in Tubeside Condensers."

13 Chato, J. C., "Laminar Condensation Inside Horizontal and Inclined Tubes," *ASHRAE Journal,* Vol. 4, No. 252, 1962.

14 Kroeger, D. G., "Laminar Condensation Heat Transfer Inside Inclined Tubes," paper presented at the 16th Natl. Heat Transfer Conf., St. Louis, 1978.

15 Collier, J. G., *Convective Boiling and Condensation,* McGraw-Hill, New York, 1972.

16 Traviss, D. P., Baron, A. B., Rohsenow, W. M., "Forced-Convection Condensation Inside Tubes," ASHRAE Contract RP63, MIT Report No. DSR 7291-74, July 1, 1971, Cambridge, Mass.

17 Fujii, T., Honda, H., Nagata, T., Fujii, F., and Nozu, S., "Condensation of R-11 Inside of Horizontal Tube," Report No. 1: Flow Regime Mapping and Pressure Drop, *Transactions of Japanese Society of Mechanical Engineers,* Vol. 42, No. 363, November 1976, pp. 3541–3550.

S. A. Stylianou
J. W. Rose

Department of Mechanical Engineering,
Queen Mary College,
University of London,
Mile End Road,
London E1 4NS,
England

Dropwise Condensation on Surfaces Having Different Thermal Conductivities

Heat flux and vapor-to-surface temperature difference measurements have been made for dropwise condensation of steam on copper, bronze, copper-plated bronze, and ptfe-coated copper surfaces. Except in the case of the ptfe surface the promoter used was dioctadecyl disulphide. Tests were carried out at various pressures ranging from atmospheric down to about 12 kPa. *Care was taken to insure that the apparatus was leak-tight and a local venting technique was used to obviate the effects of traces of non-condensing gases. The heat flux and surface temperature were obtained from temperatures indicated by fine-wire thermocouples accurately located at different distances from the condensing surface. In order to randomize the error in the extrapolated surface temperature for the bronze plate, the thermocouples were repeatedly removed and re-installed. Tests were carried out using a total of six different thermocouple installations. The results for the copper and bronze surfaces were in close agreement with each other and with earlier results for dioctadecyl disulphide-promoted copper surfaces. For the ptfe-coated copper surface, when the ptfe layer resistance was accounted for on the basis of simple one-dimensional steady conduction, the residual vapor-to-(ptfe) surface temperature differences were found to be very close to those obtained for the dioctadecyl disulphide-promoted copper surface.*

Introduction

In recent years many of the uncertainties relating to dropwise condensation heat transfer have been resolved. Notably, there is now broad agreement concerning the heat flux-temperature difference-pressure relationship for condensation of steam on copper surfaces. Even for the case of steam, however, it appears that one point, at least, needs to be settled: namely, the importance or otherwise of the thermal properties of the material of the condensing surface. Various experimental investigations to date have led to opposite conclusions. Roughly speaking, half have indicated that there is a significant systematic dependence of the heat-transfer coefficient on the surface thermal conductivity, while in the remaining half no evidence of such dependence was found.

The main factors which have hindered the settlement of this issue are:

1 Promoter effectiveness is different for different surface materials. This leads to differences in observed heat-transfer coefficients which obscure those which might be due to the thermal properties of the material.
2 The accuracy with which the temperature of the condensing surface (as found by the technique of extrapolation from temperatures observed at different distances from the surface) can be measured, decreases with decreasing thermal conductivity of the condenser material. The (systematic) error in the extrapolated surface temperature arises from the fact that the thermocouples do not record the temperatures precisely at the centre lines of the thermocouple holes. Moreover, once the thermocouples are installed, the positional bias of the system is fixed, so that the error in the extrapolated temperature always has the same sign.
3 When using low conductivity test plates the heat fluxes, and hence the vapor-to-surface temperature differences, are small. Under these circumstances quite small errors in the surface temperature lead to large errors in the vapor-side heat-transfer coefficient.

The fact that a significant portion of the condensing surface is essentially adiabatic should lead to an additional effective thermal resistance. A model for estimating this "constriction resistance" has been given by Hannemann and Mikic [1]. The present authors accept, in principle, the existence of a constriction resistance. However, for reasons discussed below, they consider the experimental evidence (with the possible exception of results recently reported by Hannemann and Mikic [2]) for a significant systematic dependence of heat-transfer coefficient on the thermal conductivity of the surface material to be unconvincing.

Discussion of Previous Experimental Investigations

In earlier investigations, vapor-side heat-transfer data have been

(a) inferred (for various metal surfaces with monolayer promoters) from overall vapor-to-coolant measurements [3, 4],
(b) inferred (for ptfe surfaces) from measurements of the combined temperature difference due to the condensate and the relatively thick promoter layer [5, 6],
(c) determined (for various metal surfaces with monolayer promoters) using surface temperatures obtained by extrapolation from temperatures observed at different distances from the condensing surface [7–9], and
(d) determined (for stainless steel [2] and glass [10] with monolayer promoters) using surface temperatures obtained from thin-film surface thermometers.

(a) Overall Measurements. In view of the high vapor-side heat-transfer coefficients for dropwise condensation, vapor-side coefficients inferred from overall measurements (a procedure which involves the subtraction of quantities of similar magnitude) are susceptible to relatively large errors.

Wilkins and Bromley [3] condensed steam at atmospheric pressure on long vertical tubes of copper, gold, Admiralty, Cu-Ni 90-10 and Monel, using various promoters. The estimated vapor-side coefficients were found to decrease with decreasing tube conductivity. With the exception of Monel, the differences are of similar magnitude to the probable uncertainty in the values.

To test the hypothesis that the results of Wilkins and Bromley were, at least in part, due to differences in promoter effectiveness on the different surfaces, Rose [4] made overall measurements for condensation of steam on horizontal tubes of copper, brass, aluminium and stainless steel using dioctadecyl disulphide as promoter. The inferred vapor-side coefficients for aluminum and stainless steel were mark-

Contributed by the Heat Transfer Division for publication in the JOURNAL OF HEAT TRANSFER. Manuscript received by The Heat Transfer Division November 19, 1979.

edly lower (by a factor of around 20) than those found for copper and brass. When the aluminum and stainless steel tubes were given a thin (~9 μm) copper coating prior to promoting, to insure promoter effectiveness, dramatic increases in overall coefficients were obtained and the calculated vapor-side coefficients found to be essentially the same as those for the copper and brass tubes.

The clear implication of the above investigations is that, surface chemistry differences can lead to significant differences in vapour-side heat-transfer coefficient but, for identical surface chemistries, differences in vapor-side coefficient which might be attributable to differences in thermal conductivity of the bulk condenser material are certainly smaller than can be reliably determined by this type of measurement.

(b) ptfe Layers. In two investigations [5, 6] steam was condensed on teflon surfaces. The thermal conductivity of this material is around 1/1500 that of copper. Graham [5] and Wilmshurst and Rose [6] used teflon layer thicknesses of 1.5 μm and 10 μm, respectively, on copper plates. In both cases, thermocouples located in the copper plates served to measure the heat flux and, by extrapolation, the temperature at the copper-teflon interface. When the teflon layer resistance was accounted for on the basis of simple one-dimensional steady conduction, the heat-transfer coefficient (teflon surface-to-vapor) was, in both cases, found to be very close to that obtained with dioctadecyl disulphide-promoted copper surfaces.

(c) Surface Temperature Obtained by Extrapolation. In two of the three experimental investigations of this type, evidence of significant dependence of the vapor-side coefficient on the material of the condensing surface was reported.

Tanner, et al. [7] obtained results which indicate steam-side coefficients, for stainless steel promoted with montanic acid, lower than those for copper by factors generally varying between 3 and 5. The authors suggested that the low coefficients might be attributable to surface chemistry effects. Moreover, in this work, the maximum observed vapor-to-surface temperature difference for the stainless steel condenser was about 0.7 K. An estimate of the possible systematic error (calculated as indicated by Wilcox and Rohsenow [11]) in the surface temperature obtained by extrapolation gives about 0.5 K. On this basis, the vapor-side heat-transfer coefficients could have been about 3.5 times larger than those reported.

Griffith and Lee [8] used horizontal downward-facing condensing surfaces of copper, zinc, and stainless steel. All three surfaces were gold plated so as to obtain identical surface chemistries as well as readily promotable surfaces. The promoter used was oleic acid. In the case of the zinc and stainless steel surfaces, thin disks of these materials were respectively soft-soldered and silver-soldered to thicker copper disks in which the temperature distributions were measured. These authors reported heat-transfer coefficients in the approximate ratios 5 : 2.2 : 1 for copper, zinc and stainless steel respectively. Estimates of the Wilcox-Rohsenow [11] extrapolation errors indicate that the reported coefficients might have been incorrect by about 8, 10 and 30 percent for the copper, zinc, and stainless steel, respectively. The observed differences in heat-transfer coefficients for the different metals cannot therefore be explained on this basis. It is possible however that the thermal resistances of the soldered interfaces (not accounted for in [8]) were significant. If the resistance of the silver-soldered copper-steel joint exceeded that of the soft-soldered zinc-copper joint, this would have led to apparent steam-side heat-transfer coefficients decreasing in the order copper, zinc, stainless steel. It is also to be noted that the reported coefficient for copper is much lower than has been found in more recent investigations.

Aksan and Rose [9] condensed steam on copper and copper-plated (12 μm) steel promoted with dioctadecyl disulphide. The coefficients for copper were in good agreement with established values while those for steel were *higher* on average by about 10 percent. However, the surface temperature extrapolation could have led to an error of around 20 percent. The fact that the observed coefficient for steel was higher than for copper is therefore probably not significant. It is however evident that, unless other errors were present in this work, the coefficient for steel does not differ greatly from that for copper.

Table 1

Mean heat flux	Range of ΔT/K	
kW/m^2	stainless steel [2]	copper [7, 9, 12, 13]
70	0.8–1.1	0.4–0.8
140	1.8–3.2	0.6–1.3

(d) Surface Thermometry. Hannemann and Mikic [2] have recently obtained results using two stainless steel condensing plates. The surface temperature was measured in each case by a titanium thin-film resistance thermometer, sandwiched between layers of silicon nitride. The surfaces were finally gold plated and promotion achieved by adding dioctadecyl disulphide to the water in the boiler.

The results reported lie in two quite narrow heat flux bands and are compared in Table 1 with earlier data for dioctadecyl disulphied-promoted copper surfaces. It may be seen that, for the lower heat flux, the stainless steel results of [2] just overlap the copper data, while at the higher heat flux the ΔT-values for steel are on average around 1.5 K higher. The fact that the scatter of the steel data, particularly at the higher heat flux, is greater than the discrepancies between the results of the different investigations using copper surfaces, may be due in part to the method of promoting used in [2].

Tanasawa and Shibata [10] condensed steam on a glass plate of thickness 0.5 mm on which a thin-film constantan-copper thermocouple had been deposited. The promoter used was oleic acid. The glass plate was attached with silicone resin to one end of a heat-flux meter, in the form of a copper rod containing fine-wire thermocouples, the rear surface of which was cooled. The primary objective of this work was to study the heat-transfer behaviour at very low vapor-to-surface temperature differences where lower heat-transfer coefficients might be expected to result from a paucity of active nucleation sites.

Evidence for a decrease in coefficient with decreasing ΔT was found for ΔT < about 1.0 K. For ΔT > 0.5 K, however, the mean value of the vapor-to-surface heat-transfer coefficient was about 80 kW/m^2 K. This is somewhat lower than an average value for copper surfaces over the same range of heat flux (up to about 0.1 MW/m^2). It may be noted nowever that, notwithstanding the fact that the conductivity of the glass was around 30 times smaller than that of the steel used in [2], the above coefficient is larger than that reported for steel.

The Present Work

In the light of the foregoing discussion it seems clear that the results of the various investigations, taken together and examined in the light of surface chemistry considerations and possible experimental errors, do not provide a convincing case for a systematic dependence of vapor-to-surface heat-transfer coefficient on the conductivity of the surface material. Doubts raised by the Hannemann and Mikic results [2] prompted the present investigation.

In the present work, measurements were made for dropwise condensation of steam at various pressures ranging from atmospheric down to about 12 kPa using copper, bronze, copper-coated bronze and ptfe-coated[1] copper surfaces. The surface temperature was determined, in all cases, by extrapolation from temperatures indicated by fine-wire thermocouples accurately located at different distances from the surface. The hole size and spacing were such as to render small the extrapolation error [11]. In the case of the bronze plate the ther-

[1] ptfe layer thickness 13.7 μm ± 0.4 μm by eddy current determination.

Nomenclature

k = thermal conductivity of ptfe
q = heat flux
T_v = vapor temperature
t = thickness of ptfe layer
ΔT = vapor-to-surface temperature difference

mocouples were repeatedly removed from the test plate and reinstalled so as to randomize this error. To obtain reasonably high values of ΔT for the low-conductivity plate the rear side of this (and of the copper plate) was finned and provision made for high coolant flow rates. Bronze was chosen since good long-lived dropwise condensation can readily and reliably be obtained with this surface. The results obtained leave no doubt in the minds of the present authors that, if a thermal conductivity effect is present, it is certainly much weaker than has been suggested by some earlier reports.

Apparatus

Referring to Fig. 1, steam was generated from distilled water in a glass boiler (7) by two 3-kW immersion heaters (8). One of the heaters was connected via a variable transformer so that the heater power could be varied continuously from 0 to 6 kW.

The vapor passed from the boiler into a cruciform glass steam chamber (6). One of the horizontal limbs of the steam chamber was closed by an electrically-heated double-glazed observation window (5) and the other by the test plate and cooling box assembly (4). The test plate (condensing area 50 mm high × 30 mm wide) was cooled by mains water. The condensate was returned by gravity to the boiler.

A stainless steel vent tube (9) was sited close to the condensing surface. During operation, the vented vapour was passed through a well-insulated stainless steel tube and into a stainless-steel auxiliary condenser (12), from which the condensate returned by gravity to the boiler. A spherical glass receiving vessel (14), located between the auxiliary condenser outlet and the boiler, was connected via two ice traps (15) to a vacuum pump (17) for removal of noncondensing gas. The venting rate could be varied by means of a valve (11) in the vapor line between the boiler and auxiliary condenser, and observed by means of a graduated glass cylinder (19) located between the receiving vessel and the boiler return line. To measure the venting rate the boiler return valve (20) was closed and condensate from the auxiliary condenser collected over a measured time interval.

Strenuous efforts were made to ensure a good leak-tight apparatus. All joints were either welded or were flanged couplings with viton gaskets. The assembled apparatus could be pumped down to a pressure of about 0.1 Torr in 15 min and the pressure rise over a 12-hr interval, when isolated, was about 1 Torr.

Two test plates of identical dimensions were used (see Fig. 2), one of high-conductivity copper and the other of phosphor bronze. In order to achieve sufficiently high heat fluxes in the case of the bronze plate, the cooling side was finned and provision for high coolant flow rates made by using a 7.5 kW pump (1) (see Fig. 1).

Five thermocouple holes, 0.4 mm dia were drilled horizontally at the mid-height of each test plate and their positions precisely determined by travelling microscope. The nominal distances from the condensing surface were 2 mm, 3.4 mm, 4.8 mm, 6.2 mm and 7.6 mm. Insulated butt-welded nichrome-constantan thermocouples (wire diameter 0.15 mm) were inserted in the holes so that the junctions were in the central vertical plane of the plate and the leads ran to either side along isotherms.

The vapor temperature was measured by two thermocouples in stainless-steel tubes. One junction was located above the surface of the water in the boiler and the other near to the condensing surface. The difference between the temperatures indicated by the two thermocouples was highest at the highest vapor temperature but was generally less than 0.1 K and never exceeded 0.15 K. Thermocouple tubes were also located in the coolant inlet and outlet pipes. The coolant could be heated by externally wound heating tape (3) and its flow rate measured by flowmeters (2) (see Fig. 1).

The leads from the plate, steam and coolant thermocouples were taken via reference junction tubes to a precision copper thermocouple selector switch and thence to a digital voltmeter reading to 1 μV. The reference junctions were placed in closely-fitting thin-walled glass tubes (one for each thermocouple), which were immersed to a depth of about 250 mm in finely-ground closely-packed melting ice contained in a large vacuum-walled vessel. Care was taken to avoid bunching of the cold-junction tubes. All thermocouples used were from the same reels.

Two thermocouples were calibrated against a standard thermocouple calibrated by the National Physical Laboratory (U.K.) One of the thermocouples was made from the beginning of the reels and the second after removing sufficient wire to provide the thermocouples required for the investigation. The three junctions were bound tightly together with copper wire and placed in a copper tube immersed in an oil bath. The bath was fitted with a stirrer and an immersion heater supplied by a variable transformer. Calibration points were obtained at 5 K intervals in the working temperature range. The indications of the two thermocouples under calibration differed by amounts corresponding to temperature differences less than 0.02 K at the lower temperatures and less than 0.04 K at the higher temperatures. A polynomial was fitted to the combined data (r.m.s. deviation less than 0.03 K) and used for all thermocouples. The aforementioned cali-

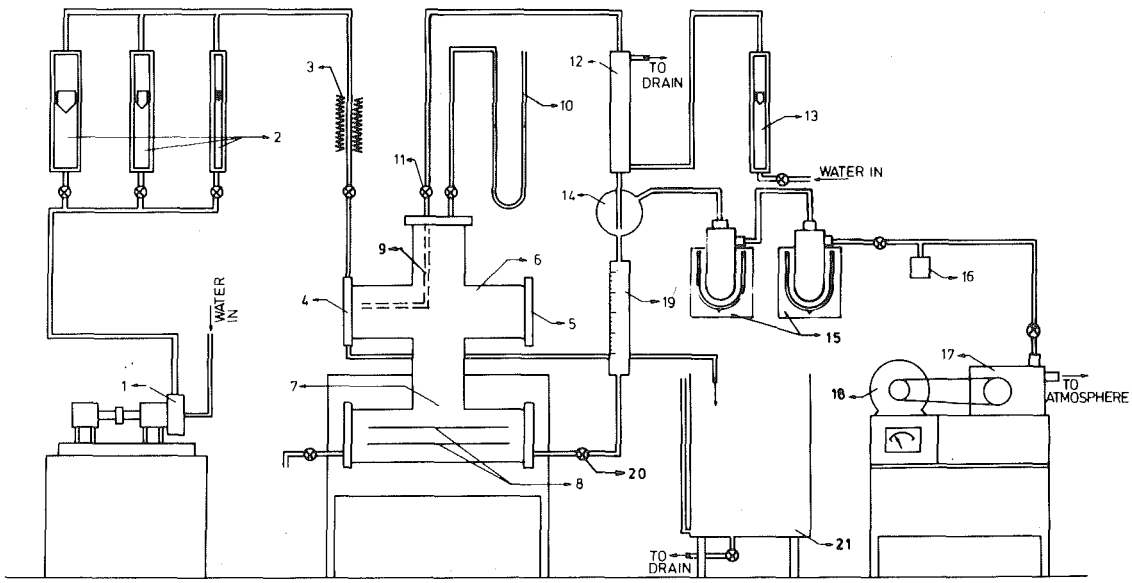

Fig. 1 Apparatus: (1) pump, (2) flowmeters, (3) heater, (4) test plate and cooling box, (5) electrically heated window, (6) steam chamber, (7) boiler, (8) immersion heaters, (9) vent tube, (10) manometer, (11) vent control valve, (12) auxiliary condenser, (13) flowmeter, (14) noncondensing gas receiver, (15) cold traps, (16) pressure gauge, (17) vacuum pump, (18) motor, (19) collecting cylinder, (20) condensate return valve, (21) coolant collecting tank

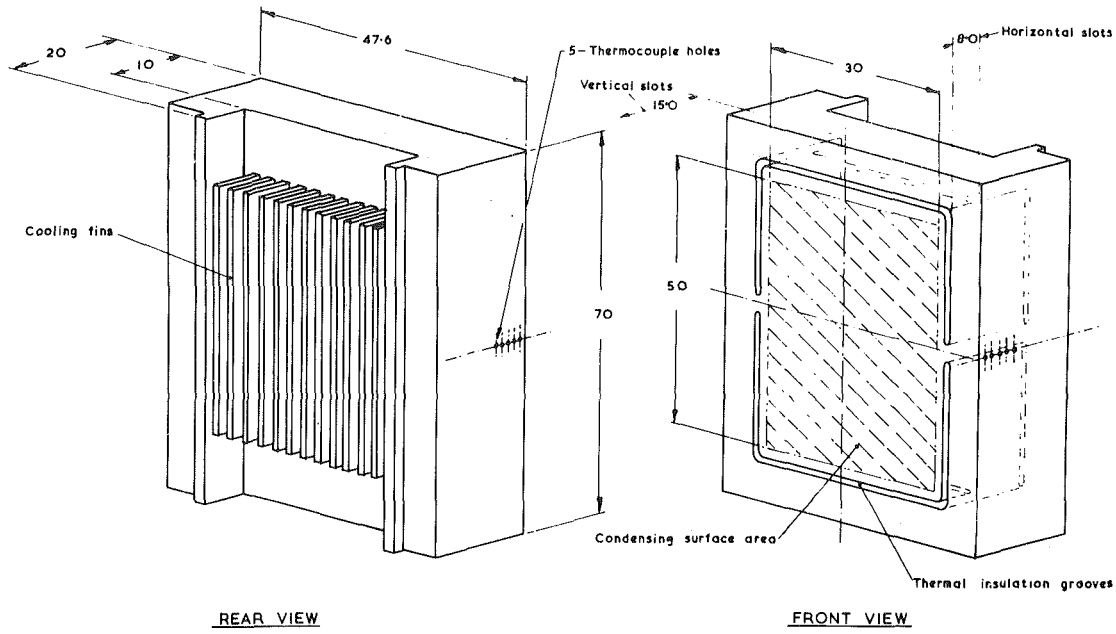

Fig. 2 Test Plate

bration procedure was checked by comparing the standard with a thermocouple calibrated against a platinum resistance thermometer in a high-precision constant temperature bath.[2] The two standards were found to agree within around 0.05 K. Prior to use, all thermocouples were annealed at a temperature of 230 °C for 2 hr.

Procedures and Observations

Except in the case of the ptfe surface, the following procedure was carried out prior to each test run. The surface was first given a mirror finish using metal polish. It was then thoroughly cleaned with an acetone-soaked cloth before being immersed in carbon tetrachloride for about 20 minutes. The surface was then immersed in promoter solution (1 percent dioctadecyl disulphide in carbon tetrachloride) for about 30 min. The plate was then quickly assembled with the steam chamber and the coolant turned on and set to a flow rate intermediate between the extreme values to be used. The assembling procedure took about 7 min. When using the ptfe-coated copper plate, the surface was initially cleaned with carbon tetrachloride and all tests were carried out without removing the test plate from the vapor chamber.

Before turning on the power supply to the boiler heaters, the apparatus was evacuated for about 30 min. The valve in the vacuum line was then closed, the power supply was turned on and the apparatus brought to the required operating temperature. During the time taken to achieve a steady state at the required vapor temperature, the valve in the vacuum line was frequently opened for a short time. (This was always done prior to taking observations). In the case of the copper and copper-coated bronze surfaces it was found that an interval of around 3 to 4 hr was needed to establish steady conditions. During this time the vapor-to-surface temperature difference fell by between 0.2 K and 0.5 K. The final steady values were achieved more quickly at high condensation rates suggesting that excess promoter was removed during the preliminary interval. It is of interest to note however that, in the case of the bronze surface, once a steady vapor temperature has been established (this generally took around 30–45 min from the onset of boiling) no further time-dependence of the surface temperature was observed.

Following the earlier studies relating to close venting during dropwise condensation [12] the following procedure was carried out for each test plate in turn and for each vapor temperature. With the coolant flow rate set to an intermediate value (that which gave approximately the mean heat flux), the venting rate was slowly increased by opening the vent control valve (11) (see Fig. 1) until it was observed that the falling drops were slightly disturbed. The venting rate was then measured and a set of observations made for a range of coolant flow rates. For each coolant flow rate the boiler heater power was adjusted so as to maintain a constant vapor temperature. Further sets of observations were then made at higher and lower venting rates. Figure 3 shows typical results. No significant differences were found for the venting rates used. In all subsequent measurements, venting rates within the ranges established by the above procedure were used.

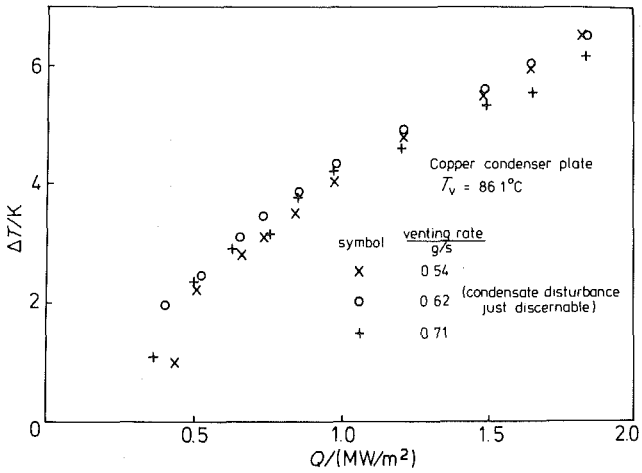

Fig. 3 Tests with different venting rates

The heat flux and condensing surface temperature were determined from the observed plate temperatures by a least squares procedure which incorporated the temperature dependence of the thermal conductivity of the plates. For the case of the bronze plate this led to significantly lower surface temperatures than obtained using a constant value for the thermal conductivity. For the bronze plate the thermal conductivity was determined from the electrical resistivity[3] [14] using a specimen machined from the same block as the test plate so as to give the resistivity, and hence thermal conductivity, in the

[2] The authors are grateful to Dr. M. R. Nightingale, Department of Mechanical Engineering, Queen Mary College, for providing this second standard.

[3] For resistivity measurements the authors are grateful to Mr. J. Morris, Dept. of Electrical and Electronic Engineering, Queen Mary College (University of London).

same direction as the heat flux in the plate. The copper-to-bronze thermal conductivity ratio was 7.00 at 100 °C and 8.20 at 30 °C. Except at the high coolant flow rates, where the temperature rise of the coolant was very small (~0.1 K), the heat flux determined from the coolant measurements agreed with that found as indicated above to within 5 percent (no special precautions had been taken to obtain high accuracy coolant measurements).

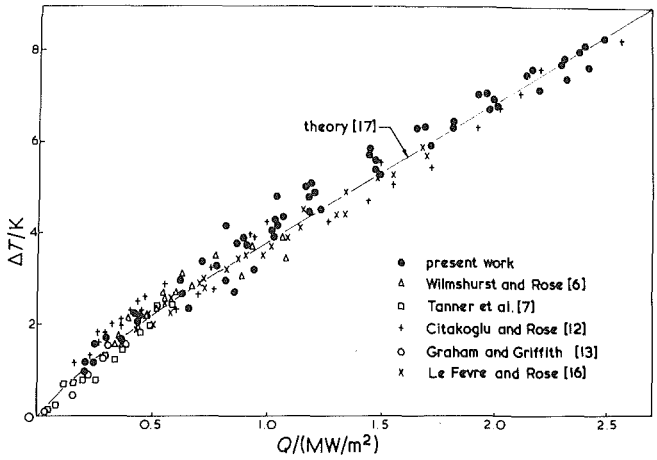

Fig. 4 Comparison of present results with earlier data (dioctadecyl disulphide promoted copper surfaces, vapor pressure ≈ 1 atm)

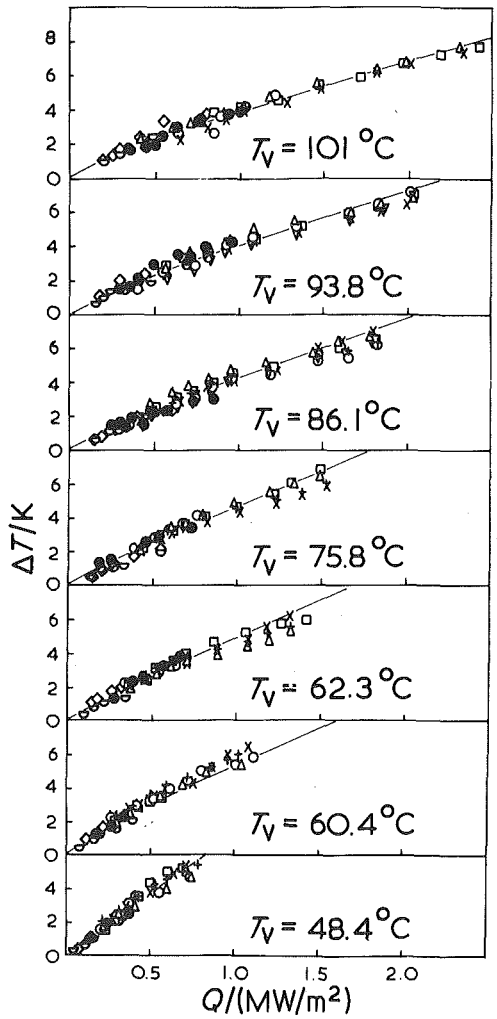

Fig. 5 Comparison of present results with earlier data (dioctadecyl disulphide promoted copper surfaces at various vapor pressures). ● denotes data of Wilmshurst and Rose [6]. Other symbols denote runs on (eight) different days. The lines are given by theory [17].

In the case of the bronze plate, when measurements had been completed at all vapor temperatures, the thermocouples were removed from the plate and re-installed and a fresh set of measurements taken. This was repeated twice more so that, in all, four different thermocouple installations were used. Following these tests the bronze surface was copper-plated to a thickness of 25 μm and further measurements, involving two different thermocouple installations were carried out.

Results

It may be seen from Figs. 4 and 5 that, for the whole range of heat flux and vapor pressure, the present results for the copper plate are in very close agreement with those of previous workers using the same

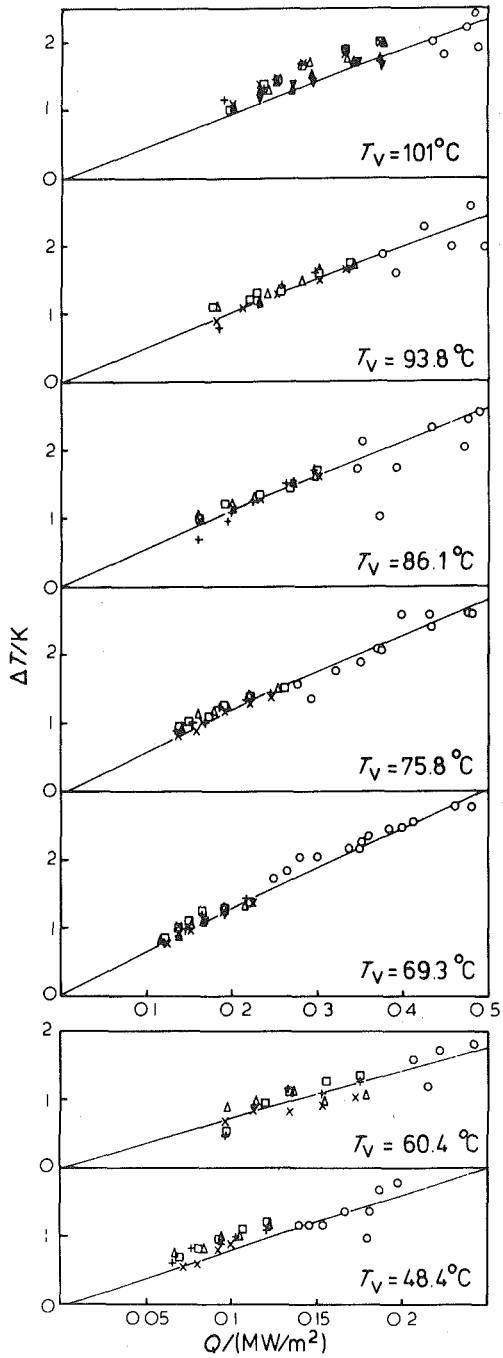

Fig. 6 Comparison of results for bronze and ptfe surfaces with data for copper. ○ denotes ptfe data; △ × □ + denote bronze data, the different symbols indicate different thermocouple installations; ▲ ▼ denote data for copper-plated bronze. The lines are those given by theory [17] and represent data for copper surfaces as may be seen from Fig. 5.

promoter and surface. Tanner, et al. [15] and Graham and Griffith [13] have obtained results for lower vapour temperatures. These give slightly higher values of ΔT consistent with the trend indicated by the results given in Fig. 5. All of these data are in good agreement with theory [17].

Figure 6 shows the bronze data. The different symbols denote different thermocouple installations. Also shown are the results for the ptfe surface, where the values of ΔT plotted are the observed temperature differences between the vapor and the copper-ptfe interface minus the temperature drop across the ptfe layer estimated on the basis of simple one-dimensional conduction, i.e. Qt/k, ($k = 0.251$ W/m K). The lines shown on Fig. 6 are those given by theory [17] which, as may be seen from Fig. 5, conveniently represents the copper results. It is evident that the results for copper, bronze and ptfe surfaces do not differ significantly.

For the bronze plate, the results for the four different thermocouple installations (six for $T_v = 101$ °C) are in close agreement with each other. The differences are, in general, somewhat less than the scatter of the copper results and are also less than might have been expected on the basis of the Wilcox-Rohsenow error analysis [11]. For the size and spacing of the thermocouple holes in the bronze plate the estimated possible error in the extrapolated surface temperature is about 0.9 K at a heat flux of 0.3 MW/m^2 and about 0.3 K at 0.1 MW/m^2.

Conclusions

For the present ranges of heat flux and vapor pressure, the $Q - \Delta T$ relationships for bronze and for ptfe do not differ significantly from that for copper. The results for the bronze plate suggest that the analysis of Wilcox and Rohsenow [11] might overestimate the surface temperature error. It could be that the use of an effective hole radius, twice that of the actual hole radius, as suggested in [11] to account for "distortion of isotherms around a hole," may be overly conservative.

References

1 Hannemann, R. J., and Mikic, B. B., "An Analysis of the Effect of Surface Thermal Conductivity on the Rate of Heat-Transfer in Dropwise Condensation," *International Journal of Heat Mass Transfer,* Vol. 19, 1976, pp. 1299–1307.

2 Hannemann, R. J., and Mikic, B. B., "An Experimental Investigation into the Effect of Surface Thermal Conductivity on the Rate of Heat Transfer in Dropwise Condensation," *International Journal of Heat Mass Transfer,* Vol. 19, 1976, pp. 1309–1317.

3 Wilkins, D., and Bromley, L., "Dropwise Condensation Phenomena," *AIChE Journal,* Vol. 19, 1973, pp. 839–845.

4 Rose, J. W., "Effect of Condenser Tube Material on Heat Transfer During Dropwise Condensation of Steam," *International Journal of Heat Mass Transfer,* Vol. 21 1978, pp. 835–840.

5 Graham, C., "The Limiting Heat Transfer Mechanisms of Dropwise Condensation," Ph.D Thesis, Massachusetts Institute of Technology, 1969.

6 Wilmshurst, R., and Rose, J. W., "Dropwise Condensation—Further Heat-Transfer Measurements," *Proceedings of the Fourth International Heat Transfer Conference,* Vol. 6, paper Cs 1.4, 1970.

7 Tanner, D. W., Pope, D., Potter, C. J., and West, D., "Heat Transfer in Dropwise Condensation—Part II," *International Journal of Heat Mass Transfer,* Vol. 8 1965, pp. 427–436.

8 Griffith, P., and Lee, M. S., "The Effect of Surface Thermal Properties and Finish on Dropwise Condensation," *International Journal of Heat Mass Transfer,* Vol. 10, 1967, pp. 697–707.

9 Aksan, S. N., and Rose, J. W., "Dropwise Condensation—the Effect of Thermal Properties of the Condenser Material," *International Journal of Heat Mass Transfer,* Vol. 16, 1973, pp. 461–467.

10 Tanasawa, I., and Shibata, Y., "Dropwise Condensation at Low Heat Flux and Small Surface Sub-Cooling," *Condensation Heat Transfer, Proceedings of the 18th National Heat Transfer Conference*, San Diego, Aug. 6–8, 1979, ASME, pp. 79–84.

11 Wilcox S., and Rohsenow, W., "Film Condensation of Potassium Using Copper Condensing Block for Precise Wall Temperature Measurements," ASME JOURNAL OF HEAT TRANSFER, Vol. 92, 1970, pp. 359–371.

12 Citakoğlu, E., and Rose, J. W., "Dropwise Condensation—some Factors Influencing the Validity of Heat-Transfer Measurements," *International Journal of Heat Mass Transfer,* Vol. 11, 1968, pp. 523–537.

13 Graham, C., and Griffith, P., "Drop Size Distributions and Heat Transfer in Dropwise Condensation," *International Journal of Heat Mass Transfer,* Vol. 16, 1973, pp. 337–346.

14 Powell, R. W., "Correlation of Metallic Thermal and Electrical Conductivities for Both Solid and Liquid Phases," *International Journal of Heat Mass Transfer,* Vol. 8, 1965, pp. 1033–1045.

15. Tanner, D. W., Pope, D., Potter C. J., and West, D., "Heat Transfer in Dropwise Condensation at Low Steam Pressures in the Absence and Presence of Noncondensable Gas," *International Journal of Heat Mass Transfer,* Vol. 11, 1968, pp. 181–190.

16 Le Fevre, E. J., and Rose, J. W., "An Experimental Study of Heat Transfer by Dropwise Condensation, "*International Journal of Heat Mass Transfer,* Vol. 8, 1965, pp. 1117–1133.

17. Le Fevre, E. J., and Rose, J. W., "A Theory of Heat Transfer by Dropwise Condensation," *Proceedings of the Third International Heat Transfer Conference,* Vol. 2, 1966, pp. 362–375.

M. Ünsal
Middle East Technical University,
Gaziantep Campus,
Gaziantep, Turkey

W. C. Thomas
Virginia Polytechnic Institute and
State University,
Blacksburg, VA 24061

Nonlinear Stability of Film Condensation

Perturbation methods are used to investigate the nonlinear stability of a vertical condensate film adjacent to quiescent saturated vapor. The analysis presented leads to closed-form expressions for the wave amplification rate and the wave velocity. Application of the results to steam condensation show that supercritically unstable infinitesimal disturbances reach finite equilibrium amplitudes while subcritically stable finite-amplitude wave motion is not possible. The nondimensional parameters which affect the supercritically-stable finite-amplitude wave motion are identified and the effects on the stability of the condensate film are discussed.

Introduction

A closed-form approximate solution of the linearized stability problem of film condensation was previously reported [1]. The linearized theory, while valid for infinitesimal disturbances on the film, does not apply for predicting film stability characteristics when an initially-unstable infinitesimal disturbance grows to a finite amplitude or for initially finite amplitude disturbances. Since any wave observed experimentally will have finite amplitude, the stability characteristics of finite-amplitude waves on condensate films, which is subject of the present theoretical investigation, is important.

The solution methodology used in this paper is different from the previous linearized stability analysis of laminar film condensation. The previous analysis leads to the classical Orr-Sommerfeld equation and appropriate boundary conditions. In the present study, the nondimensional stream function and temperature are expanded in an asymptotic series with respect to the wavenumber. These expansions are determined to first order as a function of the unsteady condensate film thickness. The expansions are substituted into the interfacial energy condition yielding a nonlinear equation for the film thickness. The film thickness is then separated into time-averaged and disturbance components. This solution method gives an equation for the average film thickness and another nonlinear equation for the disturbance film thickness. The latter equation is solved to second order with respect to the disturbance film amplitude by the method of multiple scales [2] for the case of an initially-sinusoidal disturbance. Closed-form equations are obtained for the nonlinear wave amplification rates and the wave velocities.

Governing Equations

The equations governing the motion in a two-dimensional vertical condensate film are the $\tilde{x}$ and $\tilde{y}$ components of the constant-property Navier-Stokes equation. These equations are used to determine the stream function and liquid pressure distribution. The two-dimensional constant-property energy equation governs the temperature distribution in the liquid film. The boundary conditions at the wall-liquid interface are the vanishing of the $\tilde{x}$ and $\tilde{y}$ components of the liquid velocity and a constant wall temperature. The boundary conditions at the liquid-vapor interface are the equality of normal and tangential stresses, the interface energy balance reported previously [1, equations (9–11)], and equality of liquid and vapor temperature. The three partial differential equations and associated boundary conditions are nondimensionalized by the following transformations.

$$(\tilde{p} - \tilde{p}_g)/\rho U_0^2 \rightarrow p$$

$$\tilde{\psi}/U_0\tilde{\eta}_0 \rightarrow \psi$$

$$\tilde{\eta}/\tilde{\eta}_0 \rightarrow \eta$$

$$(\tilde{T} - \tilde{T}_w)/(\tilde{T}_s - \tilde{T}_w) \rightarrow \theta$$

$$\alpha\tilde{x}/\tilde{\eta}_0,\ \tilde{y}/\tilde{\eta}_0,\ \alpha\tilde{t}U_0/\tilde{\eta}_0 \rightarrow x, y, t \tag{1}$$

where the nondimensional wavenumber is given by

$$\alpha = 2\pi\tilde{\eta}_0/\lambda \tag{2}$$

and the hydrostatic pressure distribution in the vapor by

$$\tilde{p}_g = \rho_g g\tilde{x} \tag{3}$$

In dimensionless notation, the problem formulation, is

$$\psi_{yyy} = -2 + \alpha\mathrm{Re}(p_x + \psi_{yt} + \psi_y\psi_{xy} - \psi_x\psi_{yy}) - \alpha^2\psi_{xxy} \tag{4}$$

$$p_y = -\alpha\mathrm{Re}^{-1}\psi_{xyy} + \alpha^2(\psi_y\psi_{xx} - \psi_x\psi_{xy} + \psi_{xt}) - \alpha^3\mathrm{Re}^{-1}\psi_{xxx} \tag{5}$$

$$\theta_{yy} = \alpha\mathrm{Pe}(\psi_y\theta_x - \psi_x\theta_y + \theta_t) - \alpha^2\theta_{xx} \tag{6}$$

$$\psi = \psi_x = \psi_y = 0 \text{ at } y = 0 \tag{7}$$

$$\psi_{yy} = \alpha^2\psi_{xx} + \alpha^24\psi_{xy}\eta_x(1 - \alpha^2\eta_x{}^2)^{-1} \text{ at } y = \eta \tag{8}$$

$$p + \alpha 2\mathrm{Re}^{-1}\psi_{xy}(1 + \alpha^2\eta_x{}^2)(1 - \alpha^2\eta_x{}^2)^{-1} + \alpha^2N_\xi\mathrm{Re}^{-5/3}\eta_{xx}(1 + \alpha^2\eta_x{}^2)^{-3/2} + (\gamma - 1)Nd\mathrm{Re}^{-2}(\theta_y - \alpha^2\eta_x\theta_x)^2(1 + \alpha^2\eta_x{}^2)^{-1} = 0 \text{ at } y = \eta \tag{9}$$

$$\theta = 0 \text{ at } y = 0 \tag{10}$$

$$\theta = 1 \text{ at } y = \eta \tag{11}$$

$$\zeta(\theta_y - \alpha^2\eta_x\theta_x) - \alpha\mathrm{Pe}(\psi_x + \psi_y\eta_x + \eta_t) = 0 \text{ at } y = \eta \tag{12}$$

Derivation of the Wave Equation. The mathematical formulation given by equations (4–12) are analyzed to yield a nonlinear wave equation for the disturbance film thickness. The following expansions are assumed to obtain an asymptotic solution, valid for small wavenumbers, of the problem posed by equations (4–11).

$$\psi = \psi_0 + \alpha\psi_1 + 0(\alpha^2)$$

$$p = p_0 + \alpha p_1 + 0(\alpha^2)$$

$$\theta = \theta_0 + \alpha\theta_1 + 0(\alpha^2) \tag{13}$$

These expansions are substituted into (4–11) and a sequence of problems are obtained for ψ_i, p_i, and θ_i. Noting that N_ξ is large in practical applications, α^2N_ξ is taken to be of order one. Also, since the effect of Nd has been found to be negligible on stability [1], Nd/Re^2 is taken to be of order α^2. The solutions of the zeroth-order and the first-order problems are as follows.

$$\psi_0 = \eta y^2 - y^3/3$$

$$p_0 = -\alpha^2N_\xi\mathrm{Re}^{-5/3}\eta_{xx}$$

$$\theta_0 = y/\eta \tag{14}$$

Contributed by the Heat Transfer Division for publication in The JOURNAL OF HEAT TRANSFER. Manuscript received by The Heat Transfer Division December 13, 1979.

$$\psi_1 = \alpha^2 N_\xi \mathrm{Re}^{-2/3}\eta_{xxx}(\eta y^2/2 - y^3/6) + \mathrm{Re}(y^4/12 - \eta^2 y^2/2)\eta_t + \mathrm{Re}(y^5/30 - \eta^3 y^2/3)\eta\eta_x$$

$$p_1 = -2\mathrm{Re}^{-1}(y + \eta)\eta_x$$

$$\theta_1 = \mathrm{Pe}(\eta^{-2}\eta_x y^5/20 - \eta^{-1}\eta_x y^4/4 - \eta^{-2}\eta_t y^3/6 + \eta^2\eta_x y/5 + \eta_t y/6) \quad (15)$$

The dimensionless stream function, pressure, and temperature as given by equations (13–15) depend on the normal coordinate y as well as on x and t. The x and t dependence comes through the film thickness η.

The equation governing film thickness is obtained by substituting (13–15) into the interfacial energy balance (12) which gives

$$k_0\eta^{-1} - k_1\eta^2\eta_x - k_2\eta_t - k_3(\eta^2\eta_x\eta_{xxx} + \eta^3\eta_{xxxx}/3) + k_4(5\eta^4\eta_{xt}/24 + 5\eta^3\eta_x\eta_t/6 + 9\eta^5\eta_x{}^2/10 + 3\eta^6\eta_{xx}/20) + 0(\alpha^3) = 0 \quad (16)$$

where

$$k_0 = \zeta/2\mathrm{Pe},\ k_1 = (1 + 11\zeta/40)\alpha,\ k_2 = (1 + \zeta/3)\alpha/2,\ k_3 = N_\xi \mathrm{Re}^{-2/3}\alpha^4/2,\ k_4 = \mathrm{Re}\alpha^2$$

It is convenient to separate the time-average and the disturbance (unsteady) components of the film thickness to investigate the stability characteristics of the condensate film. Accordingly, η is decomposed by

$$\eta \to \bar{\eta}(x) + \epsilon\eta(x, t) \quad (17)$$

where $\bar{\eta}$ is the time-averaged part of the film thickness and $\epsilon\eta$ is the unsteady part of the film thickness. The parameter ϵ is introduced as a measure of the disturbance amplitude. From this point on, η represents the disturbance component of the film thickness.

Substituting equation (17) into (16) and separating time-averaged and unsteady parts, two equations are obtained. The problem is further simplified by neglecting the x-derivatives of the average film thickness in the unsteady equation and by letting $\bar{\eta} = 1$ in the unsteady equation. The former simplification is the parallel-flow approximation while the latter simplification implies that the simplified unsteady equation is only locally valid. The resulting equations are given below.

The equation for the average film thickness

$$k_0/\bar{\eta} - k_1\bar{\eta}^2\bar{\eta}_x - k_3(\bar{\eta}^2\bar{\eta}_x\bar{\eta}_{xxx} + \bar{\eta}^3\bar{\eta}_{xxxx}/3) + k_4(9\bar{\eta}^5\bar{\eta}_x{}^2/10 + 3\bar{\eta}^6\bar{\eta}_{xx}/20) + \epsilon^2 S = 0 \quad (18)$$

The (unsteady) wave equation

$$k_0\eta + k_1\eta_x + k_2\eta_t + k_3\eta_{xxxx}/3 - k_4(5\eta_{xt}/24 + 3\eta_{xx}/20) = \epsilon[k_0\eta^2 - 2k_1\eta\eta_x - k_3(\eta_x\eta_{xxx} + \eta\eta_{xxxx}) + k_4(5\eta\eta_{xt}/6 + 5\eta_x\eta_t/6 + 9\eta_x{}^2/10 + 9\eta\eta_{xx}/10 - S] + \epsilon^2[-k_0\eta^3 - k_1\eta^2\eta_x - k_3(2\eta\eta_x\eta_{xxx} + \eta^2\eta_{xxxx}) + k_4(5\eta^2\eta_{xt}/4 + 5\eta\eta_x\eta_t/2 + 9\eta\eta_x{}^2/2 + 9\eta^2\eta_{xx}/4)] + 0(\epsilon^3) \quad (19)$$

A new parameter, S, has been introduced into equations (18) and (19) in order to separate equation (16) into average and disturbance parts. The nonlinearity in the unsteady equation introduces terms which must appear in the time-averaged equation. The parameter S eliminates these terms in the unsteady equation. By this means, the time-averaged terms in the unsteady equation (19) are carried over to equation (18). The solution of equation (18) gives the average film thickness in the condensate film. If one takes $\zeta = 0$, the first two terms of equation (18), when equated to zero, give the film thickness corresponding to the Nusselt solution. When ζ is finite, the parameter k_1 takes into account the heat convection effects while the parameter k_4 takes into account the acceleration effects in the condensate film. The parameter k_3 takes into account the effects of surface tension on the steady film thickness. The last term in equation (18) accounts for the effect of the finite-amplitude wave motion on the average film thickness. Since the purpose of the present study is to investigate the stability of the condensate film, equation (18) is not discussed in detail.

An Asymptotic Solution for the Wave Equation. Equation (19) governs the behavior of finite-amplitude disturbances on the condensate film. In this section, this equation is used to predict the timewise behavior of an initially-sinusoidal disturbance on the condensate film. The linear part of (19) admits travelling wave solutions of the form

$$\eta = \exp(i(x - ct)) + CC \quad (20)$$

Here, $c = c_{r1} + ic_{i1}$ is the complex wave celerity corresponding to the linear stability problem and CC stands for complex conjugate. The wave-speed and the wave amplification rate obtained by letting (20) satisfy the linear part of (19) are given below by equations (38) and (34). These equations are exactly the same as equations (24) and (25) of reference [1] with Nd set equal to zero. This result is expected since the effect of the parameter Nd has been neglected in the present investigation. The neutral stability curve obtained by letting $c_{i1} = 0$ in equation (34) is depicted in Fig. 1 for saturated steam at atmospheric

Nomenclature

a = amplitude function defined in equation (31)
A = amplitude function defined in equation (25)
b = defined following equation (29)
B = defined in equation (29)
c_p = liquid specific heat
$c = c_{r1} + ic_{i1}$ = complex wave celerity
C_1 = defined in equation (21)
c_{i1} = amplification rate of infinitesimal disturbances
c_{i3} = second Landau coefficient, equation (35)
c_{r1} = wave speed of infinitesimal disturbances
c_{r3} = nonlinear component of wave speed
g = gravitational acceleration
h_{fg} = latent heat
k = liquid thermal conductivity
k_0, k_1, k_2, k_3, k_4 = parameters defined following equation (16)
$Nd = \zeta^2/\gamma\mathrm{Pr}^2$
$N_\xi = 2^{1/3}\sigma\rho^{-1}\nu^{-4/3}g^{-1/3}(1 - \gamma)^{-1/3}$
$\tilde{p}$ = liquid pressure
$\tilde{p}_g$ = vapor pressure
p = dimensionless pressure
Pe = PrRe, local Peclet number
$\mathrm{Pr} = \rho c_p\nu/k$, Prandtl number
$\mathrm{Re} = U_0\tilde{\eta}_0/\nu$, local Reynolds number
S = parameter defined following equation (19)
$\tilde{t}$ = time
t = dimensionless time
$\tilde{T}$ = liquid temperature
$\tilde{T}_s$ = vapor saturation temperature
$\tilde{T}_w$ = wall temperature
T_0, T_1, T_2 = dimensionless time scales
$U_0 = g(1 - \gamma)\tilde{\eta}_0{}^2/2\nu$, reference velocity
$\tilde{x}$ = parallel coordinate
x = dimensionless parallel coordinate
$\tilde{y}$ = normal coordinate
y = dimensionless normal coordinate
α = dimensionless wave number
α_n = upper neutrally-stable wave number
β = phase function defined in equation (31)
$\gamma = \rho_g/\rho$
Γ = defined in equation (21)
ϵ = disturbance amplitude
$\zeta = c_p(\tilde{T}_s - \tilde{T}_w)/h_{fg}$, heat capacity parameter
$\tilde{\eta}_0$ = local time-average component of the film thickness
$\bar{\eta}$ = dimensionless average film thickness
η = dimensionless film thickness, dimensionless disturbance film thickness
θ = dimensionless temperature
λ = disturbance wavelength
ν = kinematic viscosity
ρ_g = vapor density
ρ = liquid density
σ = surface tension
ϕ = phase function defined in equation (25)
$\tilde{\psi}$ = liquid stream function
ψ = dimensionless stream function

Subscripts

x, y, t, T_0, T_1, T_2 = partial differentiation with respect to the subscript

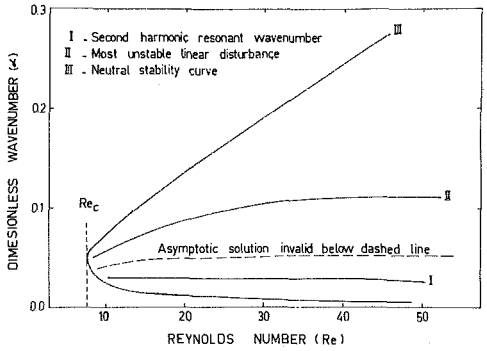

Fig. 1 Neutral stability curve for saturated steam, T_s = 373 K, ΔT = 47 K

pressure and $\Delta T = 47K$. Those α-Re pairs lying to the right (left) of the neutral stability curve correspond to unstable (stable) linear disturbances. Equation (38) shows that waves of different wavenumber travel at different speeds. Equation (34) shows that the infinitesimal disturbances are damped or amplified with time except for those α and Re combinations corresponding to the neutral stability curve. It is clear, therefore, that equation (19) is typical of a dispersive and dissipative wave equation. Analysis of equations (38) and (34) shows that for any Reynolds number larger than the critical Reynolds number, the wavespeed is equal to k_1/k_2 (approximately 2) at the two neutrally-stable wavenumbers. The wavespeed is smaller than k_1/k_2 for wavenumbers in the unstable region bounded by the two neutrally-stable wavenumbers. In order to determine an asymptotic solution of equation (19) for waves traveling at speeds differing from k_1/k_2, let

$$k_1 = k_2 C_1 + \epsilon\Gamma \tag{21}$$

where C_1 is a first approximation to the wavespeed of the disturbances and $\epsilon\Gamma$ is a parameter giving the magnitude of the deviation of the wavespeed from k_1/k_2. The method of multiple scales [2] is used to find a temporal uniformly-valid asymptotic solution of equation (19). Multiple time scales are introduced according to

$$T_0 = t,\ T_1 = \epsilon t,\ T_2 = \epsilon^2 t \tag{22}$$

The partial time derivative is transformed according to

$$\frac{\partial}{\partial t} \rightarrow \frac{\partial}{\partial T_0} + \epsilon\frac{\partial}{\partial T_1} + \epsilon^2\frac{\partial}{\partial T_2} \tag{23}$$

and the disturbance film thickness is expanded as follows

$$\eta = \eta_0 + \epsilon\eta_1 + \epsilon^2\eta_2 + 0(\epsilon^3) \tag{24}$$

When the parameter k_1 is eliminated from the left side of equation (19) by the equality in (21) and the expansions (23) and (24) are substituted into (19), three problems are obtained for the determination of η_0, η_1, and η_2. (The details are omitted in the present paper.)

The zeroth-order problem for η_0 admits travelling wave solutions of the form

$$\eta_0 = A\exp(i\phi) + \overline{A}\exp(-i\phi) \tag{25}$$

Where $\overline{A}$ stands for the complex conjugate of A and

$$A = A(T_1, T_2),\ \phi = x - C_1 T_0$$

$$C_1 = 24(k_0 + k_3/3 + 3k_4/20)/5k_4 \tag{26}$$

In the present study, the solution of the zeroth-order problem is taken as given by equation (25). Hence, the stability of an initially-sinusoidal disturbance on the condensate film is investigated.

When (25) is substituted into the first-order problem, the time-averaged part is eliminated by choosing

$$S = 2k_0 A\overline{A} \tag{27}$$

The first-order problem contains secular terms proportional to $e^{i\phi}$. To obtain a timewise uniformly-valid solution, the coefficient of $e^{i\phi}$ is set to zero giving

$$(-k_2 + i5k_4/24)\frac{\partial A}{\partial T_1} - i\Gamma A = 0 \tag{28}$$

The solution for the first-order problem then becomes

$$\eta_1 = B\exp(i2\phi) + \overline{B}\exp(-i2\phi) \tag{29}$$

where

$$B = bA^2$$

$$b = (9k_0 + 2k_3/3 - 3k_4/5 - i2k_1)/(4k_3 - 3k_0)$$

When equations (25) and (29) are substituted into the second-order problem, secular terms proportional to $e^{i\phi}$ appear. The coefficient of $e^{i\phi}$ must vanish in order that the expansion is uniformly valid to second order in ϵ. This condition gives

$$(-k_2 + i5k_4/24)\frac{\partial A}{\partial T_2} + [k_0(2b - 3) - ik_1(2b + 1) - k_3(7b + 1) + k_4(5C_1 b/6 - 9b/10 + 5C_1/4 - 9/4)]A^2\overline{A} = 0 \tag{30}$$

The wave amplification rate and the wave velocity are obtained by letting

$$A = \frac{1}{2}ae^{i\beta} \tag{31}$$

where a and β are real functions. Substituting equation (21) into (28) and (30), separating real and imaginary parts, and noting that the wave amplification rate is given by

$$\alpha = \frac{d(\epsilon a)}{dt} = \alpha\left[\epsilon\frac{\partial(\epsilon a)}{\partial T_1} + \epsilon^2\frac{\partial(\epsilon a)}{\partial T_2}\right] \tag{32}$$

one obtains

$$\alpha\frac{d(\epsilon a)}{dt} = \alpha[c_{i1} + c_{i3}(\epsilon a)^2]\epsilon a \tag{33}$$

where

$$c_{i1} = (5k_1k_4/24 - k_0k_2 - k_2k_3/3 - 3k_2k_4/20)/(k_2^2 + 25k_4^2/576) \tag{34}$$

$$c_{i3} = (45k_0^2k_2 + 2k_2k_3^2/9 + 9k_2k_4^2/50 + 45k_0k_1k_4/8 - 38k_0k_2k_3 - 113k_0k_2k_4/60 - 4k_1^2k_2 - 53k_2k_3k_4/5 - 5k_1k_3k_4/4 - 3k_1k_4^2/8)/[(4k_3 - 3k_0)(4k_2^2 + 25k_4^2/144)] \tag{35}$$

Noting that the wavespeed, c_r, is given by

$$c_r = C_1 - \frac{d\beta}{dt} = C_1 - \left(\epsilon\frac{\partial\beta}{\partial T_1} + \epsilon^2\frac{\partial\beta}{\partial T_2}\right) \tag{36}$$

one obtains

$$c_r = c_{r1} + c_{r3}(\epsilon a)^2 \tag{37}$$

where

$$c_{r1} = (k_1k_2 + 5k_3k_4/72 + k_4^2/32)/(k_2^2 + 25k_4^2/576) \tag{38}$$

$$c_{r3} = (27k_0k_1k_2 + 95k_0k_3k_4/12 + 113k_0k_4^2/288 + 5k_1^2k_4/6 + 53k_3k_4^2/24 - 6k_1k_2k_3 - 9k_1k_2k_4/5 - 75k_0^2k_4/8 - 5k_3^2k_4/108 - 3k_4^3/80)/[(4k_3 - 3k_0)(4k_2^2 + 25k_4^2/144)] \tag{39}$$

The expression for c_{i1} in equation (34) gives the amplification of infinitesimal disturbances on the condensate film. The parameter c_{i3} in equation (35) gives the nonlinear amplification rate. This parameter is sometimes called the second Landau coefficient [3]. Equations (38) and (39) give the linear and the nonlinear components of the wavespeed.

Limitations on the Results

One of the limitations on the results obtained is that the solution

obtained to the problem posed by equations (4–11) is only a first-order solution with respect to the wavenumber. The previous linearized stability results [1] indicate that the first-order solution gives accurate results provided the Reynolds number is not large compared to 50. A similar situation is expected in the nonlinear stability analysis and accuracy considerations limit the applicability of the results to Re < 50.

The validity of the asymptotic expansion for the disturbance film thickness, equation (24), must also be considered. The present expansion for the disturbance film thickness breaks down when $\epsilon\eta_1$ is of the same order of η_0. The parameter b in equation (29) shows that η_1 would be infinite when $4k_3 - 3k_0 = 0$. Substituting the expressions for k_3 and k_0, this situation corresponds to

$$\alpha^4 = 3\zeta \mathrm{Re}^{2/3}/(4\mathrm{Pe}N_\xi) \tag{40}$$

The wavenumber given by equation (40) is the second harmonic resonant wavenumber. The first and the second harmonics in a disturbance travel at the same speed when the wavenumber is given by (40). The amplitudes of the two harmonics are both finite at this wavenumber, and the second harmonic cannot be a small correction to the first harmonic as was assumed in the present study. Consequently, the present stability results are invalid when α is close to the resonant wavenumber. The second harmonic resonant wavenumber given by equation (40) is depicted in Fig. 1. Also shown on this figure is the most unstable linear disturbance wavenumber corresponding to the maximum of αc_{i1}. It is noted that the locus of the most unstable linear disturbance lies well above the locus for the second harmonic resonant wavenumber. This result implies that the practically-observed wavenumbers are likely to fall in the region of validity of the present theory. A quantitative measure on the region of validity of the present results is obtained by requiring $\epsilon\eta_1$ to be smaller than a 50 percent correction to η_0. The condition determining the validity region is then

$$|b|\ \epsilon a \leq 1 \tag{41}$$

It is noted without proof that an infinite number of higher-order resonant wavenumbers exist which are smaller than the second harmonic resonant wavenumber. This fact renders the present results invalid for very small wavenumbers. The inadequacy of the present solution at small wavenumbers lies in the fact that a single harmonic (cf. equation (25)) alone cannot describe the shape of long waves. An experimentally-observed long wave takes the form of a smooth hump which cannot be represented by a single harmonic [4, p. 428]. A proper representation for the profile of long waves may be obtained by taking more than a single harmonic in the solution of the zeroth-order problem [5, p. 324]. The analysis, however, is beyond the scope of the present study.

In the following sections, the graphical results are presented only for those regions where equation (41) is satisfied and where the wavenumber is larger than the second harmonic resonant wavenumber.

Stability Characteristics of Finite Amplitude Disturbances

It is noted that the linear component of the wave amplification rate, αc_{i1}, and the linear component of the wavespeed, c_{r1}, obtained in this paper are identical with equations (24) and (25) of reference [1] when Nd is set equal to zero. Hence, the solution in [1] and the present solution, although obtained by different procedures, yields the same result for the stability characteristics of infinitesimal disturbances.

When c_{i1} is set equal to zero, equation (34) yields the neutral stability curve for infinitesimal disturbances. The neutral stability curve separates the α – Re plane into two regions: one region where small disturbances decay with time (the stable region) and another region where small disturbances grow with time (the unstable region). The present nonlinear stability analysis is used to study the behavior of a finite disturbance in the stable region (subcritical stability) as well as the study of the subsequent nonlinear development of a linearly-unstable disturbance in the unstable region (supercritical stability). Subcritical and supercritical stability of a condensate film is discussed here by means of an example.

Consider the film condensation of saturated steam at 373 K on a cooled vertical surface with $\tilde{T}_s - \tilde{T}_w = 47$ K. Evaluating surface tension and latent heat at 373 K and the other physical properties at the reference temperature $\tilde{T}_w + [\tilde{T}_s - \tilde{T}_w]/3$, one finds $N_\xi = 12347$, $\zeta = 0.0872$, and Pr = 2.62. The critical Reynolds number for this example is calculated as 7.9 by equation (29) of reference [1]. The linear wave amplification rate, αc_{i1}, and the nonlinear wave amplification rate, αc_{i3}, are presented for Reynolds numbers of 5, 20, and 50 in Figs. 2, 3, and 4, respectively. The parameter α_n is the upper neutrally-stable wavenumber and has been arbitrarily taken equal to 0.1 in Fig. 2 because a neutrally-stable wavenumber does not exist when Re = 5. For Figs. 3 and 4, α_n is calculated from equation (34) by letting $c_{i1} = 0$. The dashed curves in Figs. 2 and 3 correspond to an isothermal liquid film flowing at the same Reynolds number and are calculated

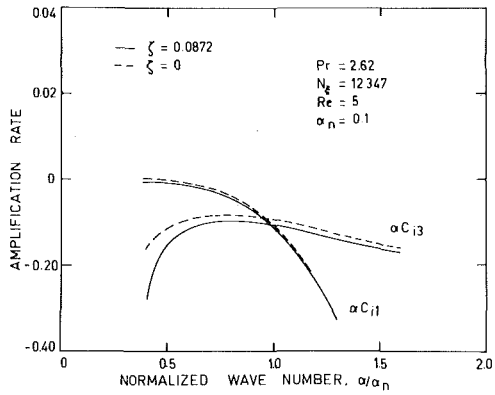

Fig. 2 Linear and nonlinear amplification rates when Re = 5

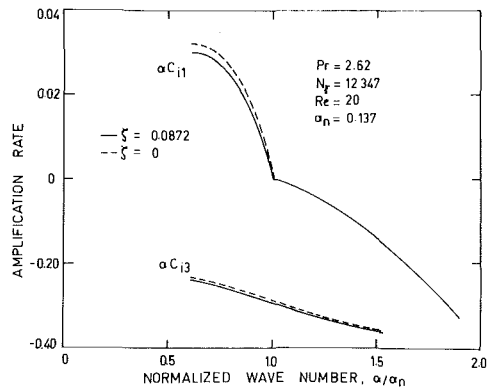

Fig. 3 Linear and nonlinear amplification rates when Re = 20

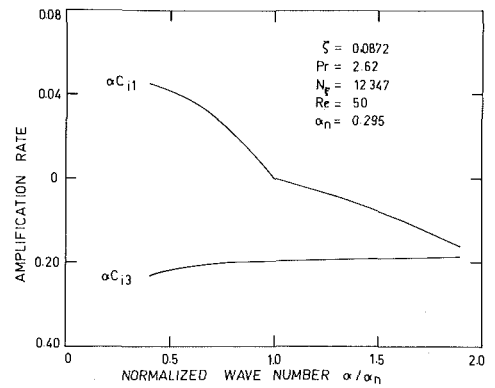

Fig. 4 Linear and nonlinear amplification rates when Re = 50

from equation (34) by setting the heat capacity parameter to zero in equations (34) and (35). There is no observable difference between the amplification rates of an isothermal liquid film and a condensing liquid film in Fig. 4 where Re = 50. Figure 2 shows that the condensation mass transfer increases the wave decay rate over the value corresponding to an isothermal liquid film. Figure 3 shows that the condensation mass transfer decreases the wave amplification rate below the value corresponding to an isothermal liquid film. Consequently, condensation mass transfer has a stabilizing effect on both linear and nonlinear disturbances. This stabilizing effect becomes negligible as the Reynolds number increases as observed in Figs. 2, 3, and 4.

In Figs. 2–4, the nonlinear wave amplification rate, αc_{i3}, is always negative. This result implies that a finite-amplitude disturbance decays in the stable region or that subcritically-stable wave motion is not possible. In the unstable region, the linear amplification rate is positive while the nonlinear amplification rate is negative. Therefore, the linearly-unstable infinitesimal disturbances in the unstable region do not grow indefinitely but, rather, reach equilibrium amplitudes. Hence, supercritically-stable finite-amplitude wave motion exists on the condensate film. The equilibrium amplitude of the supercritically-stable wave motion is obtained by equating the wave amplification rate in equation (33) to zero which gives

$$(\epsilon a)^2 = -c_{i1}/c_{i3} \tag{42}$$

The equilibrium amplitudes of supercritically-stable waves as predicted by equation (42) are plotted in Fig. 5 for the values of the parameters corresponding to Figs. 2–4. The solid curves in Fig. 5 correspond to a condensate film while the dashed curves correspond to an isothermal film. When Re = 5, the condensate film equilibrium amplitude is zero. An isothermal film at this Reynolds number will admit supercritically-stable waves with amplitudes shown by the dashed curve. When the Reynolds number is larger than the critical Reynolds number, the condensate film will have supercritically-stable waves. The amplitudes of such waves are smaller than the equilibrium amplitudes of waves on an isothermal film at the same Reynolds number. The difference between the amplitudes on the condensate film and the isothermal film decreases as the Reynolds number increases and becomes negligible when Re $\gg$ 20 for the example considered. Figure 5 also shows that the equilibrium amplitude increases as the Reynolds number increases.

Inspection of equations (34) and (35) shows that the condensate film stability is determined by the four parameters ζ, Pr, N_ξ, and Re. The discussion of the example considered above showed that increasing ζ decreases the equilibrium amplitude while increasing Re increases the equilibrium amplitude. Figures 6 and 7 are plotted by using equation (42) in order to display the effects of N_ξ and Pr. Figure 6 shows that increasing the surface tension parameter, N_ξ, decreases the equilibrium amplitude and, hence, has a stabilizing effect. Figure 7 shows that increasing the Prandtl number increases the wave amplitude and has a destabilizing effect.

Prediction of Wavespeeds

The wavespeed of infinitesimal disturbances is given by equation (38). The wavespeed of supercritically-stable finite-amplitude waves is given by equation (37) where the wave amplitude, ϵa, is evaluated from equation (42). The wavespeed of infinitesimal disturbances, c_{r1}, and the wavespeed of supercritically-stable finite-amplitude disturbances, c_r, are plotted in Fig. 8 for the example considered in the previous section. The wavespeed presented in Fig. 8 correspond to Reynolds numbers of 20 and 50. The predicted wavespeed of infinitesimal disturbances, c_{r1}, is shown by the dashed curves. The wavespeeds of supercritically-stable finite-amplitude waves given by the solid curves in Fig. 8 are larger than the wavespeed of infinitesimal disturbances. In this respect, the supercritically-stable finite-amplitude waves given by the solid curves in Fig. 8 are larger than the wavespeed of infinitesimal disturbances. In this respect, the supercritically-stable waves on the condensate film have the characteristics of gravity waves. This observation is in agreement with the results

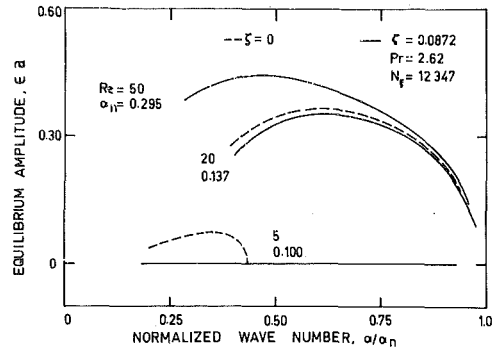

Fig. 5 Equilibrium amplitude of supercritically-stable wave motion at different Reynolds numbers

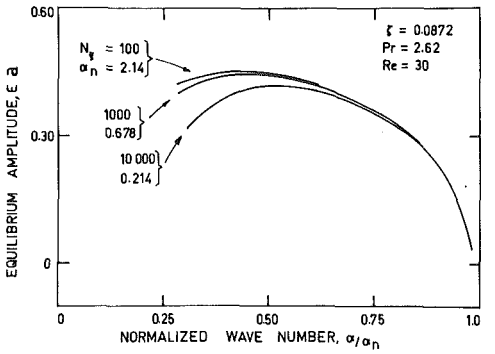

Fig. 6 Equilibrium amplitude of supercritically-stable wave motion at different values of N_ξ

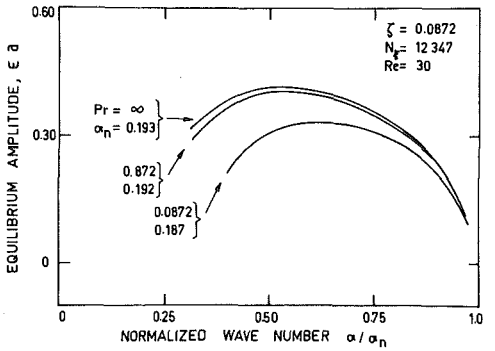

Fig. 7 Equilibrium amplitude of supercritically-stable wave motion at different Prandtl numbers

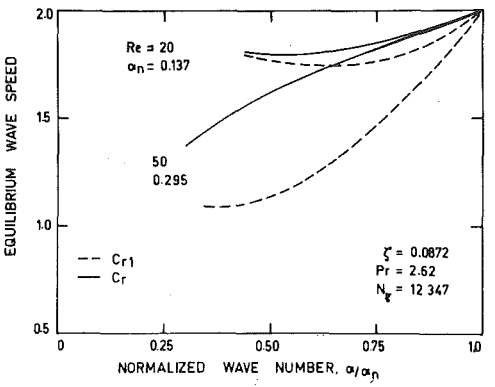

Fig. 8 Comparison of the wavespeed of infinitesimal disturbances, c_{r1}, with the wavespeed of supercritically-stable finite-amplitude waves, c_r

obtained for the supercritically-stable wave motion on an isothermal liquid film [6].

Applications to Isothermal Liquid Films

Equations (4–12) reduce to the equations governing the motion in an isothermal liquid film falling down a vertical surface when the heat capacity parameter, ζ, is set equal to zero. In this sense, the nonlinear stability analysis of laminar film condensation is a generalization to the nonlinear stability analysis of an isothermal liquid film. Letting $\zeta = 0$ in equations (42) and (37), gives, after simplification,

$$(\epsilon a)^2 = (8/15 - N_\xi\alpha^2/3\mathrm{Re}^{5/3})N_\xi\mathrm{Re}^{1/3}\alpha^4/(1 + 131N_\xi\mathrm{Re}^{1/3}\alpha^4/80 + 57\mathrm{Re}^2\alpha^2/400 - N_\xi^2\alpha^6/72\mathrm{Re}^{4/3}) \quad (43)$$

$$c_r = (2 + 5N_\xi\mathrm{Re}^{1/3}\alpha^4/36 + \mathrm{Re}^2\alpha^2/8)/(1 + 25\alpha^2\mathrm{Re}^2/144) + (\epsilon a)^2(53\alpha^2\mathrm{Re}^2/96 - 3/4 - \mathrm{Re}^{5/3}/30N_\xi\alpha^2 - 5N_\xi\mathrm{Re}^{1/3}\alpha^4/864 - 3\mathrm{Re}^{11/3}/160N_\xi)/(1 + 25\alpha^2\mathrm{Re}^2/144) \quad (44)$$

The equilibrium amplitude and wavespeed predictions from equations (43) and (44) are compared with the predictions from the previous nonlinear stability studies [3, 4, 7].

Consider the waves on an alcohol film at 288 K which was studied experimentally by Kapitza [8]. From page 704 of [8], $\alpha = 0.143$, $\sigma/\rho = 29$ cm^3/s^2, $\nu = 0.0202$ cm^2/s, and Re = 5.025 (which is 3/2 the Reynolds number in [3, 7]). Substituting $N_\xi = 668.4$, Re, and α into equation (43) gives an equilibrium wave amplitude $\epsilon a = 0.241$. The corresponding predictions in [3] and [7] are 0.217 and 0.253, respectively. With $\epsilon a = 0.241$, equation (44) gives $c_r = 1.93$. The corresponding predictions in [3, 4], and [7] are 2.05, 1.80, and 1.73, respectively. Note that in the present paper ϵa corresponds to $4A/3$ and c_r corresponds to $2c/3$ in [3–7].

Considering the waves on a water film at 288 K, Kapitza's data [8] gives $\alpha = 0.092$, $\sigma/\rho = 74$ cm^3/s^2, $\nu = 0.0114$ cm^2/s, and Re = 8.06. With $N_\xi = 3657$, equation (43) gives $\epsilon a = 0.240$. The corresponding predictions in [3] and [7] are 0.208 and 0.253, respectively. Equation (44) gives $c_r = 1.93$ and the corresponding predictions in [3, 4], and [7] are 2.02, 1.81, and 1.78, respectively.

The present predictions are between those of reference [3] and reference [7]. Since the results in [7] are improvements over the previous results in [3], it is concluded that the present theory gives reasonable predictions for the wave amplitudes and fair predictions for the wavespeed. It should be noted, however, that the present closed-form expressions (43) and (44) are much simpler than the lengthy expressions in [3, 4]. The effect of various parameters on the wave amplitude and the wavespeed is more readily identified.

Conclusions

The long-wave asymptotic solution of the equations governing the motion and temperature in a two dimensional laminar condensate film results in a nonlinear dispersive-dissipative wave equation for the disturbance film thickness. The analysis of the wave equation by the method of multiple scales yields simple closed-form expressions for the wave amplification rates and the wavespeeds of finite-amplitude disturbances on the condensate film.

The long-wave approximation limits the applicability of the results to small Reynolds numbers while harmonic resonance renders the results invalid for wavenumbers near zero.

When the wall-to-vapor temperature difference is 47 K and the vapor temperature is 373 K during the condensation of saturated steam, the film will possess supercritically-stable finite-amplitude waves. Such a condensate film will not admit subcritically-stable wave motion.

Increasing the heat capacity parameter ζ or the surface tension parameter N_ξ decreases the equilibrium amplitude of supercritically-stable waves on the condensate film. Increasing the Reynolds number or the Prandtl number increases the equilibrium amplitude. The condensation mass transfer has a stabilizing effect on both small and finite-amplitude disturbances.

Finite amplitude waves on a condensate vertical water film travel at larger wavespeeds than infinitesimal disturbances.

Simple closed-form expressions for the nonlinear stability of an isothermal liquid film is recovered from the present results in the limit as the heat capacity parameter approaches zero.

The effect of the condensation mass transfer on the nonlinear stability of a condensate film becomes negligible at large Reynolds numbers. The stability characteristics of condensate films are identical to those of an isothermal film at the same Reynolds number when the condensate film Reynolds number is large compared with the critical Reynolds number from the linearized stability theory.

References

1 Ünsal, M., and Thomas, W. C., "Linearized Stability Analysis of Film Condensation," ASME JOURNAL OF HEAT TRANSFER, Vol. 100, 1978, pp. 629–634.

2 Nayfeh, A. H., *Perturbation Methods,* Wiley-Interscience, New York, 1973, Ch. 6.

3 Lin, S. P., "Finite-Amplitude Stability of a Parallel Flow with a Free Surface," *Journal of Fluid Mechanics,* Vol. 36, Part 1, 1969, pp. 113–126.

4 Lin, S. P., "Finite-Amplitude Side-band Stability of a Viscous Film," *Journal of Fluid Mechanics,* Vol. 63, Part 3, 1974, pp. 417–429.

5 Nayfeh, A. H., and Saric, W. S., "Nonlinear Waves in a Kelvin-Hemholtz Flow," *Journal of Fluid Mechanics,* Vol. 55, Part 2, 1972, pp. 311–327.

6 Lin, S. P., "Roles of Surface Tension and Reynolds Stresses on the Finite Amplitude Stability of a Parallel Flow with a Free Surface," *Journal of Fluid Mechanics,* Vol. 40, Part 2, 1970, pp. 307–314.

7 Lin, S. P., "Profile and Speed of Finite Amplitude Waves in a Falling Liquid Layer," *The Physics of Fluids,* Vol. 14, No. 2, 1971, pp. 263–268.

8 ter Haar, D. (Editor), *Collected Papers of P. L. Kapitza,* Vol. 2, Pergamon Press, Oxford, 1965, pp. 662–709.

Experiments on Transient Condensing Flow through a Porous Medium[2]

R. H. Nilson
P. C. Montoya

Heat Transfer and Fluid Mechanics Department,
Sandia Laboratories,[1]
Albuquerque, NM

A cold, initially-dry column of sand receives a sudden inflow of dry saturated Freon vapor (CCl_3F) from a high-pressure high-temperature reservoir. Condensation occurs as the hot vapor penetrates into the cold sand, resulting in a co-current liquid/vapor flow. The axial distribution of condensate is wave-like with a (Buckley/Leverett-type) saturation-jump on the leading edge. Temperature and pressure profiles are in good agreement with a simple integral analysis which includes the essential features of the process: vapor-phase mass transfer, fluid/solid energy transfer by condensation, and liquid-phase flooding of the pore volume. The reported ensemble of experiments confirms the theoretical model over a broad range of saturation (from nearly dry to liquid-full) and over a broad range of Reynolds number (from Darcy flow to inertia-dominated flow). The considered problem is exemplary of the phase-change flows which occur in a number of geologic applications: containment of underground nuclear tests, steam stimulation of oil fields, geothermal energy, and in situ combustion processes.

1 Introduction

Multiphase flow through porous media is of importance in a wide variety of current applications: unsaturated groundwater flow [1], oil and gas production [2], drying processes [3], steam stimulation of oil fields [4], geothermal energy [5], transpiration cooling, nuclear reactor safety, containment of underground nuclear tests [6], and in situ combustion processes such as coal gasification and oil-shale retorting. Energy transfer is often an important consideration, particularly since phase-change and latent-heat effects are paramount in all but the first two of the noted applications.

Multiphase mass-transfer in porous media occurs as a consequence of pressure forces, buoyancy forces, and capillarity. (Occasionally, the gradients in chemical species and in temperature are also important.) In opposition to these driving forces, there are viscous stresses which are usually accounted for by Darcy's law which postulates a simple proportionality between the viscous stresses and the nominal fluid velocity. In its original form, Darcy's law is restricted to single-phase flow at low Reynolds number. The extension to high Reynolds number is addressed by the empirical model of Forchheimer [2] which includes the inertial component of the flow resistance as well as Darcy's viscous component. The extension to multiphase flow is accomplished by the introduction of relative permeability functions [1, 2] which empirically describe the macroscopic effects of the microscopic phase-interactions.

Energy transfer occurs by conduction and convection. In the aforementioned applications, it is generally true that the flowing fluid is in local thermal equilibrium with the solid matrix, as occurs whenever the intraparticle thermal resistance and the convective surface resistance are both small. The rate of energy transfer is then controlled only by the bulk macroscopic transport mechanisms of advection and interparticle conduction.

Experimental work has not been extensive, considering the great diversity of the operative transport phenomena. At the one extreme, there are some fundamental experiments which address specific phenomena such as Darcy-flow, in the absence of other effects. At the opposite extreme, there have been laboratory simulations and field tests which involve a host of interactive transport mechanisms, as exemplified by reservoir engineering studies. Lying between these extremes, there is an intermediate realm which includes those problems which, although strongly coupled, are still amenable to elementary analysis and simple interpretation. Exemplary of this intermediate category are the studies of conduction-drying of porous media [3], as well as the geothermal blow-down experiment of Arihara [7], in which a rarefaction disturbance produced an evaporation wave. Here we address the complementary problem of a compression-induced condensation wave.

The present experimental/analytical study concerns transient condensing flow of a pure substance (Freon 11) in a column of porous sand. The initially dry medium is subjected to a step-increase in temperature and pressure at the boundary. Condensation occurs as the hot high-pressure vapor penetrates into the cold porous matrix. The fluid velocities are sufficiently large that capillarity, buoyancy, and heat conduction are all negligible. Attention is focused on the early semi-infinite time period, so that far-boundary effects need not be considered. This problem is more fundamental than previous studies concerning steam driven displacement of oil [4, 8], and a very rudimentary analysis is sufficient to capture the essential features. The results provide strong confirmation of the theory over a broad range of the parameters, as explained in the summary at the end of the paper.

2 Theoretical Model

Conservation of mass and energy are respectively stated as follows for a transient, one-dimensional, two-phase flow of a pure substance in a porous medium [3, 5].

$$\frac{\partial}{\partial t}\{\epsilon s\rho_\ell + \epsilon(1-s)\rho_v\} + \frac{\partial}{\partial x}\{\rho_\ell u_\ell + \rho_v u_v\} = 0$$

$$\frac{\partial}{\partial t}\{\epsilon s\rho_\ell h_\ell + \epsilon(1-s)\rho_v h_v + (1-\epsilon)\rho_m h_m\} + \frac{\partial}{\partial x}\{\rho_\ell h_\ell u_\ell + \rho_v h_v u_v\} - \frac{\partial}{\partial x}\left\{k\frac{\partial T}{\partial x}\right\} - \frac{DP}{Dt} = 0. \quad (1)$$

The subscripts ℓ, v, and m, respectively, refer to the liquid, the vapor, and the solid matrix; s is the local volume fraction of the pore space which is occupied by the liquid, ϵ is porosity, k is bulk thermal conductivity of the fluid-saturated medium, and the other symbols have their usual meaning. The apparent or superficial velocities, u_ℓ and u_v, represent average volumetric flow rates per unit sectional area of the medium. In phase-change applications, it is usually reasonable to make the following simplifications: Assume fluid and solid in local thermal equilibrium; neglect conduction energy transfer (high Peclet number); neglect compression work (DP/Dt) [5]; neglect local density change due to vapor compression ($\partial\rho_v/\partial t \ll \rho_{\ell v}\partial s/\partial t$).

Contributed by the Heat Transfer Division for publication in the JOURNAL OF HEAT TRANSFER. Manuscript received by the Heat Transfer Division November 16, 1979.

[1] A U. S. Department of Energy Facility.

[2] This work was supported by U. S. Department of Energy under Contract AT(29-1)-789.

Conservation of momentum is customarily expressed by the Forchheimer equation [2]

$$-\frac{\kappa}{\mu}\frac{\partial P}{\partial x} = u + \lambda\frac{\rho}{\mu}u^2 \tag{2}$$

which, like the Colebrook equation of pipe flow, relates the frictional pressure loss to the velocity.

1 When the Reynolds number ($\mathrm{Re} = \rho u d/\mu$) is small, the pressure gradient is proportional to velocity in accordance with Darcy's law. The proportionality constant contains the permeability, κ, which depends on the porosity, ϵ, and on the characteristic pore dimension, d, roughly in the manner described by the Kozeny equation [2], $\kappa \simeq 0.006\, d^2\epsilon^3/(1-\epsilon)^2$.

2 When the Reynolds number is large, the pressure gradient is proportional to the square of the velocity. The flow resistance of the matrix is then characterized by the proportionality constant, λ, which is related to the other structural properties (ϵ, κ, d) roughly in the manner suggested by Ergun or by Ward [2] alternatively, $\lambda \simeq 0.012\, d/(1-\epsilon)$ or $\lambda \simeq 0.55\sqrt{\kappa}$.

Since $\lambda \sim \sqrt{\kappa} \sim d$, the right hand side of the Forchheimer equation (2) can be rewritten in the form, $u(1 + \mathrm{Re}/C)$, which emphasizes the effect of the local Reynolds number (here, C is a constant which depends on the porosity; $C \simeq 40$–55 for $\epsilon \simeq .35$).

In multiphase flow through porous media it is customary, for low Reynolds number at least, to generalize the constitutive relationship by the introduction of relative-permeability functions [1, 2] which account for the fact that each phase occupies only a certain fraction of the local pore volume. For a nonwetting phase (here, vapor) at low Re, it is usually true that the relative permeability, κ_v, is nearly linear (i.e., $\kappa_v = 1 - s$) [2], so that the corrected superficial velocity, $\hat{u}_v = \kappa_v u_v$, is simply proportional to the available pore volume (i.e., $\hat{u}_v = u(1-s)$). This behavior suggests that the nonwetting phase simply "see" a reduction in flow area due to wetting of the matrix. It is, therefore, reasonable to expect that the same linear approximation has validity at high Reynolds number, even though the distribution of phases may become island-like [1] rather than the pendular and funicular distributions which occur at low Reynolds number. Fortunately, there is no need to estimate the relative-permeability of the wetting liquid-phase, because the chosen integral method of analysis depends only on the incoming mass flow which consists of vapor alone.

3 Integral Analysis

The integral form of the transport equations requires only that the conservation principles be satisfied in a global sense

$$\frac{d}{dt}\int_0^\infty \epsilon s \rho_{\ell v} dx = (\rho_v \hat{u}_v)_0 \tag{3}$$

$$\frac{d}{dt}\int_0^\infty \{\epsilon s \rho_\ell h_\ell + \epsilon(1-s)\rho_v h_v + (1-\epsilon)\rho_m h_m\} dx = (\rho_v \hat{u}_v h_v)_0 \tag{4}$$

which insures that the internal rate of accumulation of mass and energy within the medium is accounted for by the inflow of mass and energy. In the present case, this inflow consists of dry saturated-vapor alone; no liquid enters.

The axial profiles of temperature, pressure, and saturation are presumed to be explicit functions of the normalized boundary-layer coordinate $\eta = x/\delta$, in which $\delta(t)$ is the penetration depth of the disturbance. The following choice of these profiles is motivated by simplicity and is guided both by prior knowledge of the forthcoming experimental results and by knowledge gained in previous analytical/numerical studies [9] of the condensing flow problem.

$$T^* = 1 - \eta,\ P^* = 1 - \eta,\ s = \langle s\rangle;\ 0 \le \eta \le 1 \tag{5}$$

$$T^* = 0,\ P^* = 0,\ s = 0;\ 1 \le \eta \le \infty \tag{6}$$

in which $T^* = (T - T_\infty)/\Delta T$ and $P^* = (P - P_\infty)/\Delta P$. The presumed linearity of T^* and P^* is a fairly realistic approximation to the actual profiles which are erfc-shaped for small ΔT but become nearly linear at large ΔT. In contrast, the presumed uniformity of the s-profile is a very crude approximation to the actual s-profile which is believed to be rather complex and to vary in structure, depending upon ΔT (i.e., depending upon the nominal amount of condensate and the mobility of that condensate) [9]: (1) For small ΔT, the s-profile rises abruptly to a maximum, but small, value just inside the boundary, then jumps down slightly, and then falls smoothly like $\mathrm{erfc}(\eta)$ in the far field. (2) For moderate ΔT, the forward-facing saturation-jump moves forward into the flow and becomes more pronounced. (3) For large ΔT, the single s-jump broadens into an imbedded slug of liquid which is punctuated by s-jumps on both sides. It is permissible to suppress the structure of the s-profile because, in the integral analysis at least, it is only necessary to establish (through the energy-integral equation) an approximate relationship between the overall temperature change ΔT and the bulk amount of condensate $\langle s\rangle$. The detailed spatial distribution of the condensate is important only in so far as it influences the spatial variations in: relative permeability of vapor, bulk specific heat, convective transport associated with liquid motion. Here we chose to ignore the fine structure of the flow in order to provide the simplest possible explanation of the gross features which are observed in the experiments. Indeed, the algebraic and interpretive advantage of the integral approach is greatest when the profile assumptions are simplest and, as known from previous applications to heat conduction and viscous boundary layers, low-order approximations give reasonable results in spite of slope-discontinuities and other such profile inconsistencies which lie imbedded within the interval of integration.

Substitution of the presumed profiles into the integral equations and subsequent rearrangement results in a differential equation for δ and an algebraic expression for the nominal amount of saturation $\langle s\rangle$.

$$\frac{d\delta}{dt} = 2\frac{h_{\ell v}}{\langle \rho c\rangle \Delta T}(\rho_v \hat{u}_v)_0, \quad \langle s\rangle = \frac{1}{2}\frac{\langle \rho c\rangle \Delta T}{\epsilon \rho_\ell h_{\ell v}} \tag{7, 8}$$

in which $\langle \rho c\rangle = \epsilon\langle s\rangle \rho_\ell c_\ell + \epsilon(1 - \langle s\rangle)\rho_v c_v + (1-\epsilon)\rho_m c_m$. Furthermore, under the presumed linear pressure distribution, $\partial P/\partial x \sim \Delta P/\delta$ and the Forchheimer equation (2) constrains the relationship between the inlet vapor velocity, u_0, and the boundary layer thickness δ. Applying the quadratic formula to (2),

$$u_0 = (u_v)_0 = \frac{1}{2}\left\{-\frac{\mu_0}{\rho_0\lambda} + \left[\left(\frac{\mu_0}{\rho_0\lambda}\right)^2 + 4\frac{\kappa}{\rho_0\lambda}\frac{\Delta P}{\delta}\right]^{1/2}\right\} \tag{9}$$

Nomenclature

ϵ, κ, d, λ = matrix properties (porosity, permeability, characteristic length, Forchheimer constant)

ρ, μ, h, c = fluid properties (density, viscosity, enthalpy, specific heat)

$\rho_{\ell v}$, $h_{\ell v}$ = phase-change quantities: $\rho_{\ell v} = \rho_\ell - \rho_v > 0$, $h_{\ell v} = h_v - h_\ell > 0$

ℓ, v, m = material subscripts (liquid, vapor, matrix)

0, ∞ = position subscripts ($x = 0$, $x \to \infty$)

x, η = position variable, $\eta = x/\delta(t)$

t, τ = time variable, $\tau = t(3(1 - \langle s\rangle)\mu_0{}^3)/(16\langle s\rangle \epsilon \rho_\ell \rho_0 \lambda^2 \kappa \Delta P)$

θ, $\hat{\theta}$ = similarity variables $\hat{\theta} = x/(\langle \rho c\rangle \Delta T/3h_{\ell v} t \rho_0 (1 - \langle s\rangle))^{2/3}(\lambda\rho_0/\kappa\Delta P)^{1/3}$, $\theta = x/(\langle \rho c\rangle \Delta T \mu_0/4h_{\ell v} t \rho_0 (1 - \langle s\rangle)\kappa\Delta P)^{1/2}$

δ, δ^* = penetration depth (i.e., boundary-layer thickness), $\delta^* = \delta(\langle \rho c\rangle \Delta T/3h_{\ell v} t \rho_0 (1 - \langle s\rangle))^{2/3}(\lambda\rho_0/\kappa\Delta P)^{1/3}$

P, P^* = pressure, $P^* = (P - P_\infty)/\Delta P$, $\Delta P = P_0 - P_\infty$

T, T^* = temperature, $T^* = (T - T_\infty)/\Delta T$, $\Delta T = T_0 - T_\infty$

s = liquid saturation (volume fraction of the pore volume)

$\langle s\rangle$, $\langle \rho c\rangle$ = average values of saturation and heat capacity as defined in and below equation (8)

u, $\hat{u}$ = velocity, $\hat{u}_v = \kappa_v u_v$ (κ_v = relative permeability of vapor)

Re = Reynolds number: $\mathrm{Re} = \rho u d/\mu$

Here and hereafter, there is no ambiguity in using the subscript 0 to designate the properties of the incoming vapor, since the inflow consists of vapor alone.

The boundary-layer growth $\delta(t)$ is predicted by solving the ordinary differential equation (7), $\delta' = f(u_0)$, accompanied by the Forchheimer equation (9), $u_0 = g(\delta)$, subject to the initial condition $\delta(0) = 0$.

1 At early times, the Reynolds number is high (since $u_0 \to \infty$ as $\delta \to 0$) so the solution starts out like

$$\delta = \left\{3 \frac{h_{\ell v} \rho_0 (1 - \langle s \rangle)}{\langle \rho c \rangle \Delta T} \sqrt{\frac{\kappa \Delta P}{\lambda \rho_0}}\right\}^{2/3} t^{2/3} \tag{10}$$

as obtained by substitution of the $\delta \to 0$ limit of (9) into (7), followed by analytical integration of the resulting ordinary differential equation.

2 At late times, the Reynolds number is low (since $u_0 \to 0$ as $\delta \to \infty$) so the solution eventually passes onto the asymptote

$$\delta = \left\{4 \frac{h_{\ell v} \rho_0 (1 - \langle s \rangle)}{\langle \rho c \rangle \Delta T} \frac{\kappa \Delta P}{\mu_0}\right\}^{1/2} t^{1/2} \tag{11}$$

as obtained by taking the $\delta \to \infty$ expansion of the square root in (9), substituting into (7), and integrating.

The transition between the early and late asymptotics can be expressed as a universal relationship between the dimensionless variables δ^* and τ which are defined in the Nomenclature (δ^* is simply δ, scaled by the early-time high-Re solution (10)). With this change of variables, the problem statement (7,9) can be rewritten as

$$\frac{3}{2} \tau \sqrt{\delta^*} \frac{d\delta^*}{d\tau} = \sqrt{1 + \delta^* \tau^{2/3}} - \sqrt{\delta^* \tau^{2/3}} - \delta^{*3/2} \tag{12}$$

subject to the initial condition $\delta^*(0) = 1$. The integration of (12) is done numerically with a standard Runge-Kutta routine, starting off from $\tau = 0$ with the singular expansion $\delta^* = 1 - \frac{1}{2} \sqrt[3]{\tau} + \cdots$. As seen in Fig. 1, the solution gradually departs from the early asymptote, $\delta^* = 1$, and then passes smoothly onto the late asymptote, $\delta^* = \sqrt{2/3}\, \tau^{-1/6}$.

Although the integral analysis is very rough, it has the advantage of simplicity and it provides reasonable estimates of the engineering information such as $\delta(t)$, inlet mass flow rate, and gross amount of condensation (although it reveals nothing about the flow structure, or where within the boundary-layer the condensation actually takes place). Indeed, an examination of the partial differential equations (1,2) will show that the formal solution possesses two self-similar asymptotics [6, 9, 10, 11].

1 an early high-Re domain in which the similarity variable is $\hat{\theta} \sim x/t^{2/3}$ (defined in the Nomenclature),

2 a late low-Re domain in which the similarity variable is $\theta \sim x/\sqrt{t}$ (defined in the Nomenclature).

So, within these asymptotic domains the integral analysis (which tacitly assumes self-similarity) predicts the engineering information in a form which is functionally correct, within unity-order constants which depend on the profile assumptions.

4 Experimental Apparatus and Procedure

A porous sample of white silica sand is contained within a vertically-standing plexiglass tube which measures 88.9 mm in diameter and 1.04 m in length. The sample is axially constrained between perforated plexiglass plates which are covered with a cloth mesh in order to prevent passage of sand while not obstructing the vapor flow. The ends of the tube are sealed by removable plates, leaving cylindrical enclosures at the ends which serve as inlet and outlet plenums.

The axial temperature profile is monitored by seven thermocouples with junctions equally spaced along the axis of the tube. The pressure profile is monitored by four (Statham) transducers which are mounted in the side walls of the tube on uniform axial intervals. The driver unit for the condensing flows is a two-phase reservoir containing saturated-vapor and saturated-liquid of Freon 11. During an experiment, saturated-vapor flows out of the reservoir and is continually replenished by the evaporation of saturated-liquid. In spite of this evaporative cooling effect within the reservoir, the internal temperature and pressure hold nearly steady, because of the large volume and large thermal mass of the reservoir.

Before the condensing flows were run, a number of preliminary experiments were performed in order to characterize the porous sample. The porosity of the sample ($\epsilon \simeq 0.32$) was determined by measurement of the pressure change during isothermal gas-flooding from an auxilliary reservoir, and this was checked by comparing the bulk density of the sample with the density of SiO_2. The permeability of the sample ($\kappa \simeq 20 \times 10^{-8}$ cm^2 (20 Darcy)) was determined by measurement of pressure drop and flow rate during steady gas flow within a Reynolds number range $0.3 < \mathrm{Re} < 2.0$. Photomicrographs showed relatively uniform sand grains with a mean diameter of order $d \simeq 100$ μm, as compared with the estimate $d \simeq 220$ μm calculated from the Kozeny equation using measured values of ϵ and κ. The departure from Darcy's law at high Reynolds number was investigated by measurement of pressure drop and flow rate during steady isothermal gas-flow and was found to agree with the predictions of the Forchheimer/Ergun model to within 10 percent throughout the Reynolds number range $0.5 < \mathrm{Re} < 300$ (i.e., $2.6 < u < 500$ cm/s). Finally, transient compressible flow of air through the porous sample was found to be in good agreement with the numerical solutions by Morrison [10], providing an independent confirmation of the κ/ϵ ratio which controls the time scale of the transient. This series of experiments provided redundant and supportive estimates of the macroscopic flow parameters (ϵ, κ, λ, d), thereby eliminating any adjustable parameters in the two-phase flow model. Confidence was gained in the Forchheimer/Ergun relationship and in the experimental procedure for transient flow through porous media.

Transient condensing flow of Freon 11 in porous sand was investigated using the following experimental procedure. (1) Loading and mild compaction of the sand is achieved by shaking the tube with its axis held vertically. (2) Cooling of the sand-filled test section to 283 K is accomplished by immersion in a temperature-controlled bath for 3 hr. (3) Purging and charging of the test section requires a series of evacuation/recharge cycles. (4) Initiation occurs when the Freon valve is thrown open allowing the saturated-vapor to abruptly pressurize the inlet plenum and to flow forward into the sample. (5) After the transient has run its course, the sample is vacuum-pumped until dry and the porosity and the permeability are rechecked. No appreciable changes were observed.

Verification runs afforded the opportunity to correct experimental difficulties and to make checks on consistency and reproducibility. Cross-checking of temperature and pressure records indicated good agreement with the vapor pressure curve of Freon 11. Gravitational forces were proved negligible by comparing the results for three different orientations: horizontal, vertical upflow, and vertical downflow. Heat conduction effects, both axial and radial, are clearly negligible since hours are required for bath-cooling, whereas only seconds are required to complete the condensation transient. Plenum pressure was measured during the transients to check rise-time and subsequent flatness. Reproducibility was checked by making a pair of duplicate runs with the same initial and boundary conditions. In all such checks of consistency, sensitivity, and reproducibility, the deviations and scatter did not exceed 5 to 10 percent of the overall change in measured quantities.

5 Results

The ensemble of experiments consists of six condensing flows, all with the same sample and all with the same initial condition of dry saturated-vapor at 283 K. The varied parameter is the temperature/pressure of the driving saturated-vapor state. As indicated in Table 1, increases in the temperature difference and in the pressure difference, respectively, cause increases in the nominal amount of condensate $\langle s \rangle$ and in the nominal vapor velocity (and, hence, in the nominal Reynolds number Re_L which is defined in Table 1).

The temperature profiles of Figs. 2 and 4 are illustrative of the system response for the extremes of small ΔT and of large ΔT, respectively. Pressure profiles are redundant because $P = P(T)$ in an equilibrium two-phase flow, as verified in the test runs. Saturation profiles were not measured, primarily because of the associated ex-

Table 1 Parameter values for ensemble of experiments

Run	ΔT(K)	$\langle s \rangle^\dagger$	P_0/P_∞	$\mathrm{Re}_L{}^\dagger$
1	8.	.05	1.4	5.
2	20.	.13	2.0	17.
3	31.	.21	2.8	36.
4	43.	.30	3.9	72.
5	48.	.35	4.5	92.
6	54.	.40	5.2	120.

† The nominal saturation $\langle s \rangle$ is calculated from (8). The nominal Reynolds number $\mathrm{Re}_L = u_L d\rho_0/\mu_0$ is based on the inlet vapor velocity $u_L \sim \Delta P/L$, as calculated from (9) using the length of the tube L as the penetration depth δ.

perimental difficulties, but also because the motion of the condensate has only a secondary impact on the energy transfer.

The penetration depth of the flow is fairly well predicted by the theoretical model, as seen in the comparison of Fig. 1. For any particular flow there are several data points, each corresponding to a measurement of the entire temperature profile. The penetration depth, δ, is calculated from the temperature data using the following integral measure

$$\delta = \frac{2}{\Delta T} \int_0^\infty (T - T_\infty) dx \tag{13}$$

which, although somewhat arbitrary, has computational advantages over the alternative leading-edge definition and results in essentially the same outcome.

The transition region between high and low Reynolds number is nearly covered by the measured data which spans four time-decades in Fig. 1. In the first experiment of the ensemble ($\Delta T = 8$ K), the flow velocity is slow enough that low-Re conditions prevail throughout the experiment. In the last experiment ($\Delta T = 54$ K), the flow velocity is high enough that high-Re conditions prevail. All of the data lie along the theoretical curve, although somewhat on the low side of expectations, perhaps because of the factors which were suppressed in the integral analysis; i.e., distribution of condensate within the flow field, lack of self-similarity in the transition regime, or rough approximation of the presumed profiles.

The self-similarity of a low Reynolds number flow is demonstrated in Fig. 3 which presents the exact same data as Fig. 2, except that the abcissa is now $\theta \sim x/\sqrt{t}$. The integral method gives a good prediction of the temperature profile, as indicated by the dashed line in Fig. 3. The exponential tail of the experimental profile is characteristic of a linear diffusion process. In fact, it can be shown [9] that the formal solution to (1, 2) approaches $T^* = \mathrm{erfc}\,(\theta)$ in the limit as $\Delta T \to 0$ (In that limit it also happens that $s \to 2\langle s \rangle \mathrm{erfc}(\theta)$, for all but very small θ.)

The self-similarity of a high Reynolds number flow is demonstrated in Fig. 5 which presents identically the same data as Fig. 4, except that the abcissa is now $\hat{\theta} \sim x/t^{2/3}$. The integral method gives an acceptable prediction of the temperature profile, as indicated by the dashed line in Fig. 5. The analysis overpredicts the penetration depth, partly because the Reynolds number range of the experiment is not quite asymptotically high, as apparent in checking the τ-range in Fig. 1. The shape of the experimental temperature profile is characteristic of a nonlinear diffusive process (i.e., $P_t + (\psi(P)P_x)_x = 0$) in which the diffusivity function ψ(P) becomes vanishingly small at the leading edge of the disturbance [10, 12] (here, because ρ_v and κ_v are both small at the leading edge).

The progress of the condensation front is visually observable and is recorded in motion pictures and in microdensitometer scans of selected frames therefrom. When the amount of condensation is relatively small (e.g., $\langle s \rangle = 0.05, 0.13$), the wetting of the medium is hardly discernible; but with increasing $\langle s \rangle$ a distinctive condensation front, or saturation jump, becomes clearly apparent at the leading edge of the flow (see Fig. 6). Cross-checking with the thermocouple data reveals that the saturation front is nearly coincident with the leading edge of the temperature profile.

As the condensation wave traverses the tube, the structure of the saturation profile appears to remain essentially the same, except for

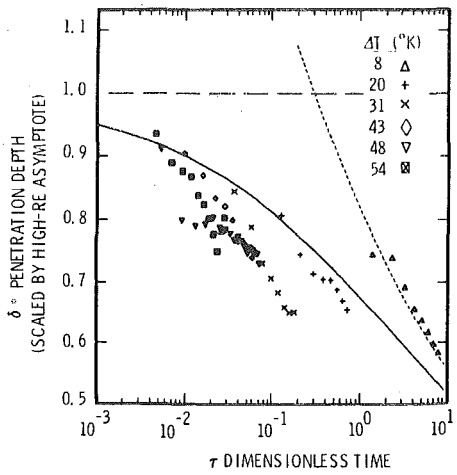

Fig. 1 Composite of boundary-layer growth. Comparison of all experimental data with high-Re asymptote (- - - -, equation (10)), low-Re asymptote (····, equation (11)), and transition analysis (—, equation (12))

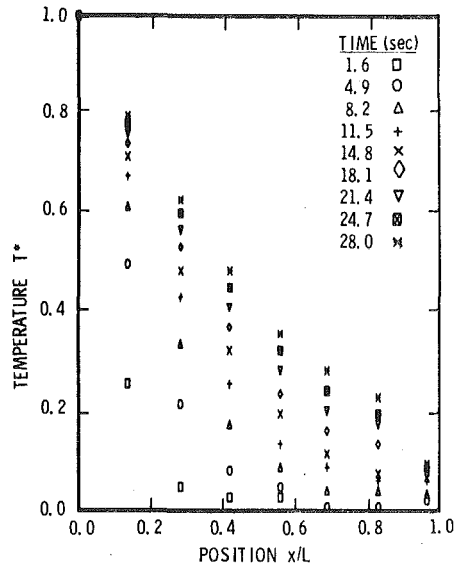

Fig. 2 Transient temperature profiles for $\Delta T = 8$ K

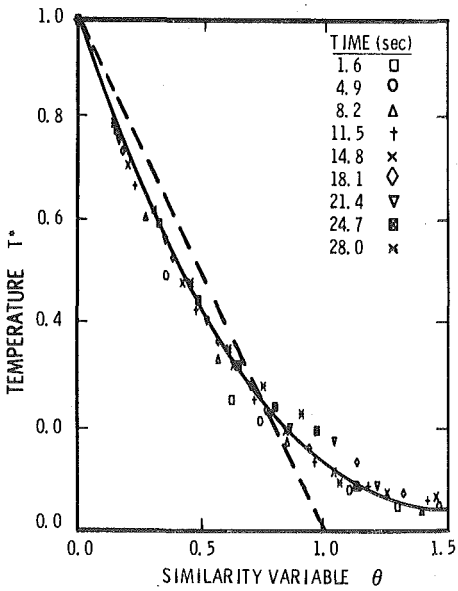

Fig. 3 Self similarity at low Reynolds number. Comparison of experimental data with integral estimate (- - - -, equation (11)) and with the complementary error function (—, formal solution [9] as $\Delta T \to 0$).

an overall self-similar stretching of the length scale. At the inflow surface the sand is relatively dry, since the early condensate has been swept out by incoming vapor, leaving behind only the so-called irreducible or residual saturation. In the central two-phase zone the wetness increases somewhat, but is relatively uniform. In the frontal fully-wet zone the saturation is again nearly uniform, but here the pore-volume appears to be liquid-full. Ahead of the fully-wet zone the sand is completely dry. These observations are consistent with predicted saturation profiles [6, 9] and with stability analysis [13] based on Darcy modeling. It is, moreover, noteworthy that the experimental results are indicative of a stable and orderly two-phase flow, even at high Reynolds number.

6 Summary

A comparison of experiment and theory demonstrates the following features of transient condensing flow in porous media.

1 Mass transfer in the vapor phase controls the rate of the process, since it is the condensation of the vapor which is the dominant mechanism of energy transfer between the fluid and the porous matrix.

2 Low Reynolds number flows are self-similar, as predicted by the generalized Darcy model (Fig. 3).

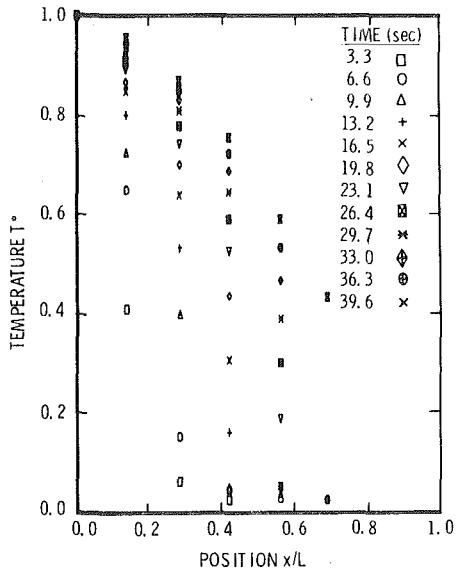

Fig. 4 Transient temperature profiles for $\Delta T = 54$ K

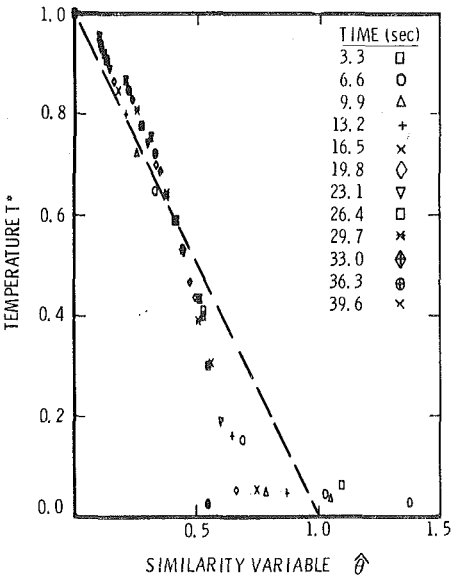

Fig. 5 Self similarity at high Reynolds number. Comparison of experimental data with integral estimate (- - -, equation (10)).

3 High Reynolds number flows are self-similar as predicted by the two-phase generalization of Ergun's model (Fig. 5).

4 The smooth transition between high and low Reynolds numbers is fairly well described by a universal function, $\delta^*(\tau)$, which derives from the Forchheimer model (Fig. 1).

5 The distribution of condensate is wave-like in character with a shock-like saturation jump at the leading edge (Fig. 6), as predicted by a formal analysis [9] based on the generalized Darcy model. Although the low-mobility liquid at the leading edge is driven by the incoming high-mobility vapor, the shock front appears to be stable, even at high Reynolds number.

Good theoretical/experimental agreement at this elementary level is encouraging, particularly since the required characterization of the medium is simple (only ϵ and κ) which is advantageous in the geologic applications where little information is available.

References

1 Wooding R. A., and Morel-Seytoux, H. J., "Multiphase Fluid Flow Through Porous Media," *Annual Review of Fluid Mechanics,* Vol. 8, 1976, pp. 233–274.

2 Scheidegger, A. H., *The Physics of Flow Through Porous Media* University of Toronto Press, 1974.

3 Whitaker, S., "Simultaneous Heat Mass and Momentum Transfer in Porous Media: A Theory of Drying," *Advances in Heat Transfer,* Vol. 13, 1977, pp. 119–203.

4 Weinstein, H. G., Wheeler, J. A., and Woods, E. G., "Numerical Model for Thermal Processes," *Society of Petroleum Engineers Journal,* Feb. 1977, pp. 65–77.

5 Cheng, P., "Heat Transfer in Geothermal Systems," *Advances in Heat Transfer,* Vol. 14, 1978, pp. 1–106.

6 Morrison, F. A., Jr., "Transient Multiphase Multicomponent Flow in Porous Media," *International Journal of Heat and Mass Transfer,* Vol. *16,* 1973, pp. 2331–2342.

7 Huyakorn, P. S., Pinder, G. F., Faust, C. R., and Mercer, J. W., "Finite Element Simulation of Two-Phase Flows in Porous Media," *Computational*

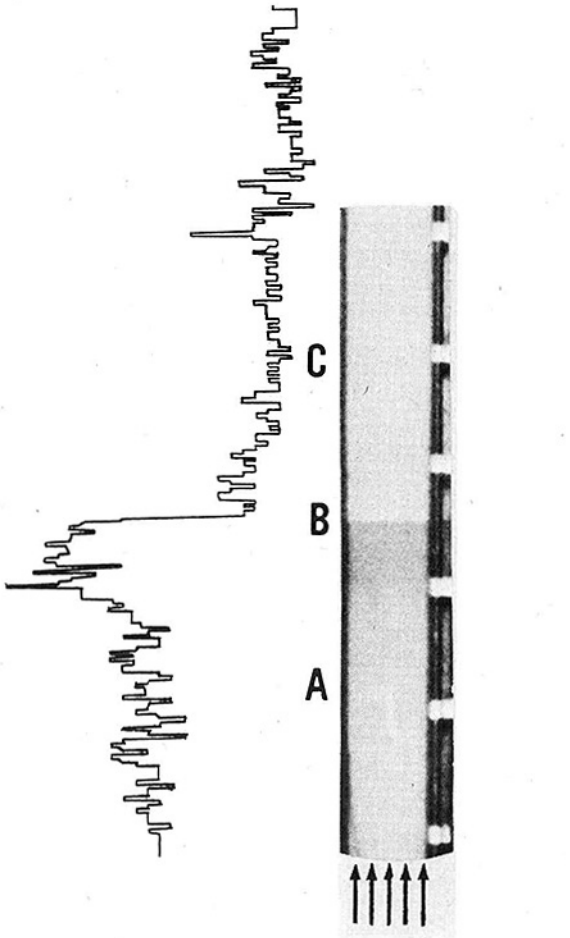

Fig. 6 Axial distribution of condensate as seen in photograph and in microdensitometer scan: (*A*) partially-wet two-phase zone, (*B*) condensation front with saturation jump, (*C*) undisturbed dry region

Techniques for Interface Problems, AMD—Vol. 30, ed. K. C. Park and D. K. Gartling, Special Symposium at 1978 Winter Annual Meeting of ASME, 1978, pp. 19–43.

8 Baker, P. E., "Effect of Pressure and Rate on Steam Zone Development in Steamflooding," *Society of Petroleum Engineers Journal,* Vol. 13, Oct. 1973, pp. 274–284.

9 Nilson, R. H., and Romero, L. A., "Self-Similar Condensing in Porous Media," *International Journal of Heat Mass Transfer,* in press.

10 Morrison, Jr., F. A., "Transient Gas Flow in a Porous Column," *I/EC Fundamentals,* Vol. *11,* 1972, pp. 191–197.

11 Morrison, Jr., F. A., "Similarity in Transient High Speed Gas Flow Through Porous Media," ASME *Journal of Fluids Engineering,* Vol. *98,* 1976, pp. 567–568.

12 Pimbley, Jr., G. H., "Wave Solutions Traveling Along Quadratic Paths for the Equation $u_t - (R(u)u_x)_x = 0$" *Quarterly of Applied Mathematics,* Vol. XXXV, Apr 1977, pp. 129–138.

13 Miller, C. A., "Stability of Moving Surfaces in Fluid Systems With Heat and Mass Transfer, III Stability of Displacement Fronts in Porous Media," *AIChE Journal* Vol. 21, No. 3, May 1975, pp. 474–479.

ERRATUM

Erratum: N. Shamsunder and E. M. Sparrow "Effect of Density Change on Multidimensional Heat Conduction Phase Change," published in the November 1976 issue of the JOURNAL OF HEAT TRANSFER, pp. 550–557.

In Fig. 8, the labels "vertical face" and "horizonal face" should be interchanged.

Transient and Frequency Response Characteristics of Two-Phase Condensing Flows: with and without Compressibility

B. L. Bhatt
Assistant Professor.

G. L. Wedekind
Professor,
Mem. ASME

Oakland University
Rochester, Mich.

In a tube-type condenser, involving complete condensation, small changes in the inlet vapor flowrate momentarily cause very large transient surges in the outlet liquid flowrate. Experimental data are presented which indicate that compressibility effects tend to attenuate the amplitude of these flow surges. The system mean void fraction model was extended to include compressibility effects and its predictions are shown to agree well with experimental data. The model is further extended to predict the response characteristics to an oscillatory inlet flowrate and compared with predictions based upon the drift-flux model.

Introduction

Two-phase condensing flow phenomena occur in a variety of industrial applications including reheat and reboiler systems associated with nuclear or conventional power plants, ocean thermal energy conversion, space power generation, solar energy conversion, vapor compression refrigeration, and chemical processing.

A survey of the literature indicates that the transient and frequency response characteristics of two-phase condensing flows have received very little attention compared to their evaporating flow counterparts. Apparently, the only published research papers are those of Schoenberg [1] and McMorran and Moeck [2]. The former is a study of the frequency response characteristics of inlet pressure and the condensation boundary of a gas cooled mercury condenser for a space power application. In this work, conservation equations for the vapor and liquid regions, together with the heat transfer dynamics of the tube-wall were first linearized for small perturbations and then Laplace transformed to derive the associated transfer functions. These were found to be sensitive to process heat transfer coefficients, vapor, and liquid pressure drop functions and tube-wall capacitance. The behavior of the transfer functions was experimentally verified. However, from this work, it is not apparent to what extent each of the various mechanisms considered contribute to the specific behavior of the transfer functions. On the other hand, McMorran and Moeck [2] theoretically analyzed the frequency response of the condensing side of a reboiler associated with a nuclear power system. Their analysis is based on the drift-flux model, considering only the simplest case of incompressible flow in an effort to obtain insight into the fundamental dynamics of the process. Further details about their work will be discussed later when some of their results will be compared with some of the findings of this present study. A few other investigations related to tube-type condenser dynamics are those associated with pressure [3] and flow [4] fluctuations, and the effects of liquid film instabilities [3, 5, 6] while operating in one and zero gravity environments. However, these studies do not have direct relevance to the present paper.

In a study by the present authors [7] of tube-type condensers involving complete condensation, small changes in the inlet vapor flowrate were shown to momentarily cause very large transient surges in the outlet liquid flowrate. Under certain circumstances, these flow surges have been observed to result in momentary flow reversals. The successful prediction of these transient flow surges was achieved using a system mean void fraction model [7, 8]. Experimental data were also presented which indicate that an effective means of attenuating the amplitude of the flow surges is to introduce viscous throttling at the condenser outlet. This has the effect of making the compressibility of the vapor an important mechanism in the attenuation process.

The primary purpose of this paper is to extend the system mean void fraction model to include these compressibility effects, and to compare its transient attenuation predictions with experimental data. The model will also be extended to predict the response characteristics to an oscillatory inlet flowrate, both with and without the effects of compressibility. Some supporting experimental frequency response data will also be presented. Finally, for the conditions of negligible compressibility, the frequency response predictions based on the system mean void fraction model will be compared with predictions based on the drift-flux model [2].

System Mean Void Fraction Model: with Compressibility

A schematic of a condensing flow system undergoing complete condensation is shown in Fig. 1. The system includes an upstream vapor volume and viscous throttling in the downstream subcooled liquid region at the condenser outlet. The symbol $\bar{\eta}(t)$ in this figure is used to represent the axial position of the non-fluctuating [7] effective point of complete condensation, and thus the effective length of the two-phase region.

In the formulation of the two-phase flow model that incorporates the compressibility effects, the concept of a system mean void fraction [7, 8] will be utilized. Therefore, the nonfluctuating system mean void fraction, $\bar{\alpha}_s$, will be defined as

$$\bar{\alpha}_s(t) \equiv \frac{1}{\bar{\eta}(t)} \int_{z=0}^{\bar{\eta}(t)} \bar{\alpha}_a(z,t)\, dz \tag{1}$$

Together with the concept of a system mean void fraction, the model is formulated around an application of both the conservation of mass and energy principles to the two-phase region, and the conservation of mass to both the upstream vapor region and the downstream subcooled liquid region. The governing equations for each region will be considered in order.

Two-Phase Region. The condensing flow system model for this region is based on the following assumptions.

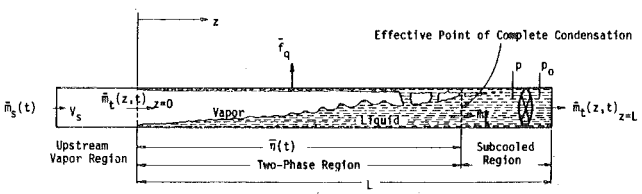

Fig. 1 Schematic of horizontal condensing flow system with upstream vapor region and downstream throttling

Contributed by the Heat Transfer Division for publication in the JOURNAL OF HEAT TRANSFER. Manuscript received by the Heat Transfer Division October 1, 1979.

The first four assumptions are the same as assumptions (1–3) and (5) of reference [7]. In addition, thermodynamic equilibrium in the two-phase region is assumed to exist at any instant of time. Consequently all thermodynamic properties are assumed to be saturated properties, independent of axial position, and evaluated at the mean system pressure which is, however, allowed to *vary with time*.

Conservation of Mass and Energy. The conservation of mass principle, simultaneously applied to the liquid and vapor in the two-phase region, can be expressed as

$$\frac{d}{dt}\int_{z=0}^{\bar{\eta}(t)} [\rho(1-\bar{\alpha}_a) + \rho'\bar{\alpha}_a]A_t dz = \bar{m}_t(z,t)_{z=0} - \bar{m}_t^* \tag{2}$$

The conservation of energy principle simultaneously applied to the liquid and vapor in the two-phase region can be expressed as

$$\frac{d}{dt}\int_{z=0}^{\bar{\eta}(t)} [\rho h(1-\bar{\alpha}_a) + \rho' h'\bar{\alpha}_a]A_t dz$$

$$= -\int_{z=0}^{\bar{\eta}(t)} f_q P\, dz + \{[h(1-\bar{x}) + h'\bar{x}]m_t(z,t)\}_{z=0} - h\bar{m}_t^* \tag{3}$$

The enthalpy rather than the internal energy is involved as a consequence of the flow work at the inlet and outlet, and, as a consequence of the boundary work which exists because the system boundary is moving with time. It is also assumed that slight changes in the system energy, due to changes in the system pressure, are small in comparison to each one of the individual terms on the right-hand side of the above equation. An order of magnitude check was carried out to confirm the validity of this assumption.

Upstream Vapor Region. The vapor in this region (see Fig. 1) is assumed to be saturated and at the mean condenser pressure, p. Also it is assumed to occupy a constant volume V_s, throughout which the vapor density, ρ', is uniform but time varying.

Conservation of Mass. The conservation of mass principle when applied to the upstream vapor region yields

$$V_s\frac{d\rho'}{dt} = \bar{m}_s(t) - \bar{m}_t(z,t)_{z=0} \tag{4}$$

Subcooled Liquid Region. Referring again to Fig. 1, the subcooled liquid region is represented by $\bar{\eta}(t) < z \leq L$. For simplicity, it is assumed that the density of liquid in the subcooled region is the same as that of the saturated liquid, ρ

Conservation of Mass. Since the liquid density is assumed constant, the conservation of mass for this region reduces to

$$-\rho A_t\frac{d\bar{\eta}(t)}{dt} = \bar{m}_t^* - \bar{m}_L(t) \tag{5}$$

where to simplify the notation, $\bar{m}_t(z,t)_{z=L}$ has been replaced by $\bar{m}_L(t)$.

Viscous Effects. The effects of downstream throttling at the condenser outlet can be taken into account by assuming that the subcooled liquid stream flows through a valve that has a lumped resistance equal to the resistance of the entire flow passage at the outlet of the condenser. The orifice coefficient of the valve will be designated by the symbol k_0. Also, it is assumed that the inertia effects are negligible. Therefore, the pressure drop between the mean condenser pressure, $p(t)$, and the pressure at the downstream side of the valve, p_0, which is assumed to be constant, can be expressed as

$$p(t) - p_0 = \frac{k_0}{\rho {A_t}^2}\bar{m}_L{}^2(t) \tag{6}$$

The above equation yields the following expression for the time rate of change of the saturated vapor density, ρ'.

$$\frac{d\rho'}{dt} = \frac{2\gamma k_0}{\rho {A_t}^2}\bar{m}_L(t)\frac{d\bar{m}_L(t)}{dt} \tag{7}$$

It can be seen that equation (7) makes it possible to couple the outlet flow resistance to the compressibility of the vapor within the condensing flow system.

Combined Condenser Flow System Equations. The governing differential equations for each one of the regions in the condenser can now be combined in a suitable way. In order to simplify the above system of equations, the time dependent coefficients were represented by their mean values and the nonlinear outlet resistance was linearized. Furthermore, in arriving at equation (12) below, the additional rate of condensation due to changes in the vapor density were found to be small in comparison to the rate of condensation due to the heat flux. For an alternate viewpoint, see references [10, 11]. The linearized system of differential equations can be expressed as follows:

$$\tau_f\frac{d\bar{m}_L(t)}{dt} + \bar{m}_L(t) = (\rho/\rho')\bar{m}_s(t) - [(\rho/\rho') - 1]\frac{\bar{f}_q P\bar{\eta}(t)}{(h'-h)} \tag{8}$$

where a compressible flow system time constant, τ_f, is given by

$$\tau_f = (\rho/\rho')[V_s + A_t\bar{\eta}_m(\bar{\alpha}_s + \beta_0)]\gamma\, k_0^* \tag{9}$$

$$\beta_0 = [\rho'\bar{\alpha}_s(\epsilon/\gamma) + \rho(1-\bar{\alpha}_s)(\beta/\gamma)]/(h'-h) \tag{10}$$

Nomenclature[a,b]

A = coefficient in equation (20), s^2
A_t = total cross-sectional area of tube, m^2
B = coefficient in equation (20), s
d = inside diameter of tube, m
f_q = local heat flux, W/m^2
$\bar{f}_q$ = spatially averaged heat flux, W/m^2
G_m = transfer function for outlet liquid flowrate
h = enthalpy of saturated liquid, J/Kg
h' = enthalpy of saturated vapor, J/Kg
k_0 = exit orifice coefficient, $\Delta p/\rho v^2$
k_0^* = linearized valve resistances at outlet, $2(k_0/\rho A_t^2)\bar{m}$, $KN{\cdot}s/m^2{\cdot}g$
$\bar{m}_L^*$ = outlet liquid flowrate in absence of compressibility, g/s
$\bar{m}_L = \bar{m}_t(z,t)_{z=L}$, g/s
$\bar{m}_s(t)$ = total mass flowrate at inlet of upstream compressible volume, g/s
$\bar{m}_t^*$ = instantaneous nonfluctuating total mass flowrate of fluid leaving two-phase region relative to moving boundary of the two-phase region, g/s
$\bar{m}_{t,i}$ = initial total mass flowrate at system inlet, g/s
$\bar{m}_{t,f}$ = final total mass flowrate at system inlet, g/s
P = inside perimeter of tube, m
p = spatial mean system pressure, KN/m^2
p_0 = pressure downstream of outlet throttling valve, KN/m^2
t = time, s
v = velocity, m/s
V_s = volume of vapor upstream of two-phase region, m^3
$\bar{x}$ = nonfluctuating local flow quality
$\bar{x}_0$ = nonfluctuating flow quality at condenser inlet, $z = 0$
z = spatial co-ordinate in the axial direction, m
$\bar{\alpha}_a$ = area mean void fraction (nonfluctuating)
$\bar{\alpha}_s$ = system mean void fraction (nonfluctuating)
$\beta = dh/dp$, $J{\cdot}m^2/Kg{\cdot}KN$
β_0 = dimensionless thermodynamic property, equation (10)
$\gamma = d\rho'/dp$, $g/m{\cdot}KN$, equation (7)
$\epsilon = dh'/dp$, $J{\cdot}m^2/Kg{\cdot}KN$, equation (10)
$\bar{\eta}(t)$ = nonfluctuating effective point of complete condensation, m
$\bar{\eta}_m$ = arithmetic mean of initial and final $\bar{\eta}$, $(\bar{\eta}_i + \bar{\eta})/2)$
ρ = density of saturated liquid, Kg/m^3 $(\bar{\eta}_i + \bar{\eta}_f/2)$
ρ = density of saturated liquid, Kg/m^3
ρ' = density of saturated vapor, Kg/m^3
τ_c = time constant of condensing flow system, s
τ_m = time constant of inlet mass flowrate variation, s
τ_f = compressible flow system time constant, s
ϕ_m = phase angle for flowrate, deg
ω = angular frequency, radians/s

[a] Unless otherwise indicated, barred (—) symbol of quantities generally refer to nonfluctuating quantities in reference to random fluctuations.

[b] All thermodynamic properties are assumed to be nonfluctuating. However, in order to simplify the notation, no bar (—) has been indicated on these quantities.

and the spatially averaged heat flux, $\bar{f}_q$, is defined as

$$\bar{f}_q \equiv \frac{1}{\bar{\eta}(t)} \int_{z=0}^{\bar{\eta}(t)} f_q \, dz \tag{11}$$

The differential equation governing the motion of the effective point of complete condensation is

$$\frac{d\bar{\eta}(t)}{dt} + \frac{1}{\tau_c}\bar{\eta}(t) = \left[\overline{m}_s(t) - V_s \frac{d\rho'}{dt}\right]\left(\frac{1}{\rho'\overline{\alpha}_s A_t}\right) \tag{12}$$

where

$$\tau_c = \frac{\rho'\overline{\alpha}_s(h' - h)A_t}{\bar{f}_q P} \tag{13}$$

represents the condensing system time constant, which is the same as the one given by equation (9) of reference [7]. The specific values for the system mean void fraction, $\overline{\alpha}_s$, for various flow situations are obtained from steady state void fraction-flow quality relationships, such as those given in the Appendix of reference [7]. After linearization equation (7) becomes

$$\frac{d\rho'}{dt} = \gamma \, k_0{}^* \frac{d\overline{m}_L(t)}{dt} \tag{14}$$

In their present form, equations (8, 12) and (14) are a complete set and must be solved simultaneously for the response of the outlet liquid flowrate to any arbitrary time varying inlet flowrate. However, it can be seen from equation (12) that if the mass storage in the upstream vapor volume, V_s, is small, then $V_s \, d\rho'/dt \ll \overline{m}_s(t)$, and can be neglected; otherwise, it should be retained.

Response to Exponential Inlet Flowrate Change. The response to an exponential inlet flowrate will be investigated for the condition[1] where $V_s \, d\rho'/dt \ll \overline{m}_s(t)$. Therefore, the motion of the effective point of complete condensation, $\bar{\eta}(t)$, as given by equation (12), becomes uncoupled from the other equations, and can be solved independently. For an exponentially varying inlet flowrate, represented by the expression

$$\overline{m}_s(t) = \overline{m}_{t,f} + (\overline{m}_{t,i} - \overline{m}_{t,f}) \, e^{-t/\tau_m} \tag{15}$$

solving equation (12), consistent with the condition that $\bar{\eta}(t)_{t=0} = \bar{\eta}_i$, and substituting the results into equation (8), the differential equation governing the outlet flowrate of subcooled liquid, $\overline{m}_L(t)$, becomes

$$\tau_f \frac{d\overline{m}_L(t)}{dt} + \overline{m}_L(t) = \overline{m}_L{}^*(t) \tag{16}$$

with the initial condition

$$\overline{m}_L(t)_{t=0} = \overline{m}_{t,i} \tag{17}$$

where

$$\overline{m}_L{}^*(t) = \overline{m}_{t,f} + (\overline{m}_{t,i} - \overline{m}_{t,f}) \left\{ e^{-(\tau_c/\tau_m)t/\tau_c} + \frac{\left(\frac{\tau_c}{\tau_m}\right)\left[\left(\frac{\rho}{\rho'}\right) - 1\right]}{\left[\left(\frac{\tau_c}{\tau_m}\right) - 1\right]} \times \left[e^{-(\tau_c/\tau_m)t/\tau_c} - e^{-t/\tau_c}\right] \right\} \tag{18}$$

It is interesting to note that the forcing function of equation (16), $\overline{m}_L{}^*(t)$, as given by equation (18), is the same as given by equation (13) of reference [7], which represents the outlet flowrate response in the absence of compressibility effects. The solution to differential equation (16) can be expressed as follows.

$$\frac{\overline{m}_L(t) - \overline{m}_{t,i}}{\overline{m}_{t,f} - \overline{m}_{t,i}} = [1 - e^{-t/\tau_f}] + \frac{\left[\left(\frac{\rho}{\rho'}\right) - 1\right]\left(\frac{\tau_c}{\tau_m}\right)}{\left[\left(\frac{\tau_c}{\tau_m}\right) - 1\right]} \{e^{-t/\tau_c} - e^{-t/\tau_f}\}$$

$$+ \frac{\left[\left(\frac{\rho}{\rho'}\right)\left(\frac{\tau_c}{\tau_m}\right) - 1\right]\left(\frac{\tau_m}{\tau_f}\right)}{\left[\left(\frac{\tau_c}{\tau_m}\right) - 1\right]\left[1 - \left(\frac{\tau_m}{\tau_f}\right)\right]} \{e^{-t/\tau_m} - e^{-t/\tau_f}\} \tag{19}$$

The characteristics of the above solution are displayed in Fig. 2, with the compressible flow system time constant, τ_f, as a parameter. The condensing flow system time constant, τ_c, and the inlet flowrate time constant, τ_m, are held constant. The graph clearly shows the effect of the compressible flow system time constant, τ_f, on the overshoot characteristics. It indicates that for a small upstream vapor volume, an increase in the outlet flow resistance has an appreciable influence in attenuating the amplitude of the outlet flowrate overshoot. However, it also indicates that substantial attenuation is obtainable only with large values of the compressible flow system time constant, τ_f.

Responses to Oscillatory Inlet Flowrate. As is customary for the study of frequency response of linear systems, Laplace transforms will be used in obtaining the desired transfer functions. This approach, however, will require some rearrangement of the governing differential equations.

With Effects of Compressibility. The analysis of the frequency response of a condensing flow system with compressibility will include the effects of an upstream vapor volume on the motion of the effective position of complete condensation, as given by equation (12). Therefore, equations (8, 12) and (14) are combined in such a way that $\bar{\eta}(t)$ and $(d\rho'/dt)$ are eliminated. The result, after considerable rearrangement, becomes a second order differential equation governing the outlet liquid flowrate, $\overline{m}_L(t)$; thus

$$A \frac{d^2\overline{m}_L(t)}{dt^2} + B \frac{d\overline{m}_L(t)}{dt} + \overline{m}_L(t) = \overline{m}_s(t) + \left(\frac{\rho}{\rho'}\right) \tau_c \frac{d\overline{m}_s(t)}{dt^s} \tag{20}$$

where

$$A = \tau_c \tau_f \tag{21}$$

and

$$B = \tau_c + \tau_f - [(\rho/\rho') - 1] \, V_s \gamma k_0{}^* \tag{22}$$

with the initial conditions

$$\overline{m}_L(t)_{t=0} = \overline{m}_{t,i}; \qquad \left.\frac{d\overline{m}_L(t)}{dt}\right|_{t=0} = 0 \tag{23}$$

Utilizing Laplace transforms, equation (20) yields the following gain and phase relationships.

$$G_m = \frac{\overline{m}_L(t) - \overline{m}}{\overline{m}_s(t) - \overline{m}} = \left\{\frac{1 + [(\rho/\rho')\tau_c\omega]^2}{(1 - A\omega^2)^2 + (B\omega)^2}\right\}^{1/2} \tag{24}$$

and

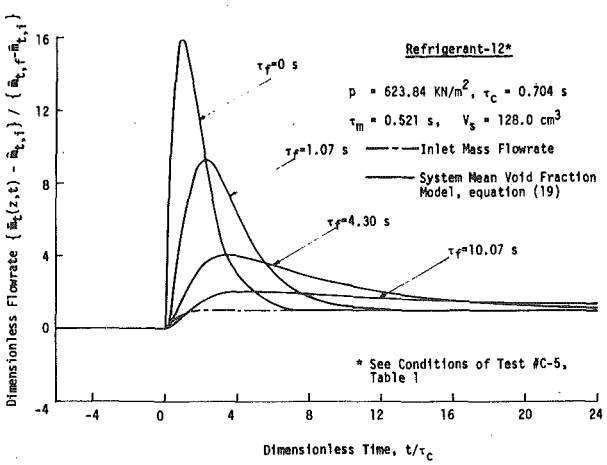

Fig. 2 Predicted effect of the compressible flow system time constant on outlet flowrate response

[1] This simplification is not necessary for a closed form solution. Without it, however, the resulting differential equation would be of second order.

$$\phi_m = \tan^{-1}\{(\rho/\rho')\tau_c\omega\} - \tan^{-1}\{B\omega/(1 - A\omega^2)\} \quad (25)$$

where $\overline{m}$ represents the nonoscillating mean or steady-state flowrate and ω is the angular frequency of the inlet flowrate oscillations.

Without Effects of Compressibility. Incompressibility can be expressed by

$$\frac{d\rho'}{dp} \equiv \gamma = 0 \quad (26)$$

Therefore, this flow situation can be considered to be a special case of the foregoing model. If $\gamma = 0$, then from equations (9, 21) and (22)

$$\tau_f = A = 0 \quad (27)$$

and

$$B = \tau_c \quad (28)$$

When these conditions are introduced into equations (24) and (25), the resulting gain and phase relationships are given by

$$G_m = \frac{\overline{m}_L(t) - \overline{m}}{\overline{m}_s(t) - \overline{m}} = \left\{\frac{1 + [(\rho/\rho')\tau_c\omega]^2}{1 + (\tau_c\omega)^2}\right\}^{1/2} \quad (29)$$

and

$$\phi_m = \tan^{-1}\{(\rho/\rho')\tau_c\omega\} - \tan^{-1}\{\tau_c\omega\} \quad (30)$$

Therefore the frequency response characteristic for an incompressible two-phase condensing flow system is seen to be a special case of the more general compressible flow model. A comparison of the predictive capabilities of the model with both experimental and other theoretical data is presented in the next section.

Experimental Apparatus

The experimental apparatus involved in the present study is the same as reported in an earlier paper [7]. The basic elements of this experimental apparatus are a high pressure reservoir, a tube in tube type horizontal condenser, and a low pressure reservoir. Vapor is generated in the high pressure reservoir. A regulating valve located at the outlet of this reservoir controls the flowrate of vapor that is supplied to the tube side of the condenser. The subcooled liquid at the outlet of the condenser is then collected and stored in the low pressure reservoir. A throttling valve was located between the outlet of the condenser and the inlet to the low pressure reservoir.

The objectives of the overall experimental program also include a visual observation of the two-phase condensing flow phenomena. Therefore in addition to the copper test section, an all glass test section was also used. The response of the outlet liquid flowrate to an oscillatory inlet vapor flowrate was studied on this test section. The sinusoidal oscillations in the inlet vapor flowrate were produced by operating the regulating valve, located at the outlet of the high pressure reservoir, with a crank mechanism which was driven through a variable speed gear box by an electrical motor.

In two-phase condensing flow, in fact in two-phase flows in general, even for what is conventionally accepted as steady-state conditions, there are random fluctuations in the outlet flowrate, as well as in other system parameters such as pressure and temperature. These fluctuations in two-phase condensing flows as also observed by Soliman and Berenson [3], have been attributed to local liquid film instabilities in the early stages of the condensation process. These instabilities or waves within the liquid film at the liquid vapor interface were seen to be initiated by higher velocity vapor, flowing within the annular flow regime, at the inlet of the condenser. Waves growing in amplitude on the thickening film of liquid were observed to propagate downstream into the semiannular/stratified flow regime. Smaller waves appeared to be overtaken by the larger waves, until the amplitude of these waves grew enough to hit the top inner surface of the tube. This initiated the beginning of the slug flow regime, followed by bubble entrapment and their subsequent collapse within the matrix of subcooled liquid. All of these local fluctuations and the transition to slug flow appear to be the major contributors to the observed stochastic fluctuations in the outlet liquid flowrate and other system parameters.

When sinusoidal oscillations are introduced in the inlet vapor flowrate, they seem to interact with the inherent fluctuations, resulting in the outlet flowrate response being partly random and partly sinusoidal. The degree of interaction seems to be large when the range of frequencies of the random fluctuations are near the frequencies of the inlet flowrate oscillations. Under these circumstances it is much more difficult to extract the information about the gain and phase relationships. However, at very low frequencies it was easier to discern between the random fluctuations and the sinusoidal oscillations. Therefore, they were assumed to be statistically independent of each other. Under this condition, the gain in the amplitude of the outlet flowrate was obtained for a few such low frequency tests. For more details see references [10, 11].

Comparison of Model with Experimental and Other Theoretical Observations

Transient Response Characteristics. The response of the outlet liquid flowrate, when the inlet vapor flowrate was increased by about 12 percent, is shown in Fig. 3. The three sets of data represent the transients for three different values of the downstream throttling; each giving rise to a different level of compressibility. During each of these tests, the upstream vapor volume was quite small, being that inherent in the piping between the vapor turbine and the inlet of the condenser test section. This upstream vapor volume is of about the same order of magnitude as the volume of the vapor in the two-phase region. The theoretical model predictions for the conditions of a small upstream vapor volume, equation (19), have been superimposed on the experimental data and are shown by the solid curves. The accuracy of the model in accounting for the attenuation of the transient flow surges as a result of an increase in the downstream throttling is reasonably good, especially when consideration is given to the complexity of the physical mechanisms involved, and the relative simplicity of theoretical model. It should be noted, however, that neither inertia effects nor the possible existence of a time dependent or nonuniform heat flux have been considered.

An examination of the above results indicate that downstream throttling, resulting in vapor compressibility, is a mechanism for attenuating the transient flow surges which have been observed in the outlet liquid flowrate [7]. The results also indicate, however, that the attenuation is obtainable at the cost of a substantial pressure loss at the condenser outlet. This can be verified from the fact that the response with heavy throttling as compared to the response with low throttling, both depicted in Fig. 3, requires about a fifty-fold increase in the outlet flow resistance.

Frequency Response Characteristics: General. The gain and phase characteristics of the outlet liquid flowrate response to sinusoidal oscillations in the inlet vapor flowrate, as predicted by the sys-

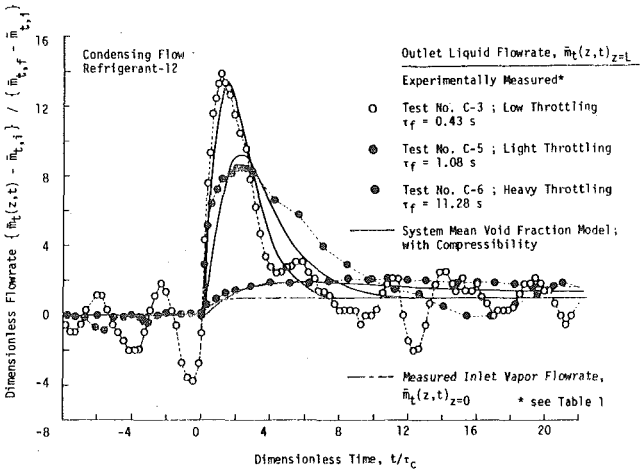

Fig. 3 Response of outlet liquid flowrate with downstream throttling

tem mean void fraction model are shown in Fig. 4. The model predictions which include the effects of compressibility indicate that as the frequency increases, the gain increases until a certain critical frequency. Thereafter, a further increase in frequency causes the compressibility of the vapor to absorb the oscillations, thereby reducing the gain. Also plotted in the same figure are the model predictions which exclude the effects of compressibility. These predictions indicate that the gain increases monotonically and then levels off to a constant value—a marked departure from the predictions of the model which include the effects of the compressibility.

Also plotted in Fig. 4 are a few experimental data points associated with the gain, obtained at low frequencies. In the narrow domain of frequencies where the experimental data were obtained, the effects of compressibility appear to be negligible and the models seem to be predicting the gain reasonably well. The validity of the models at higher frequencies, however, remains unverified because of the experimental difficulties indicated in the previous section.

Comparison with Predictions Based upon the Drift-Flux Model. As indicated earlier, one of the objectives of this paper was to compare the theoretical predictions based on the system mean void fraction model to other available theoretical results. It appears that the only other available results relevant to this particular section are those from the theoretical work of McMorran and Moeck [2]. Their analysis is based upon the drift-flux Model. They obtained transfer functions for the effective point of complete condensation and the outlet liquid flowrate as a result of perturbations in the inlet flowrate and in the time dependent component of the heat flux.

In order to compare the predictions of the system mean void fraction model, which were based on a time invariant average heat flux, the transfer functions developed by McMorran and Moeck [2] were evaluated for the condition when the time dependent component of the heat flux is zero. The resulting frequency response predictions of gain and phase for the response of the outlet flowrate of subcooled liquid, $\overline{m}_L(t)$, are given in Fig. 5. These predictions are for the condensation of steam at a pressure of 4964.0KN/m^2 in a Gentilly-1 nuclear reboiler [2].

Superimposed on the above graphs are the frequency response predictions for the same condensing flow conditions, but based on the system mean void fraction model without the effects of compressibility. Specifically, the predictions are those obtained from equations (29) and (30). An examination of Fig. 5 reveals that the frequency response predictions based upon the system mean void fraction model are very close to those predicted by the drift-flux model.[2] It should be pointed out that the predictions using the drift-flux model include the propagation delay which is embodied in the formulation of void propagation equation. However, as indicated by McMorran and Moeck [2], the delay effects are apparently negligible for the condensing flow system under consideration. The system mean void fraction model, on the other hand, does not account for the propagation delay. Taking into consideration the simplicity of the system mean void fraction model, including the capability of accounting for the compressibility effects, its inability to account for the delay effects does not appear to be a deficiency of major concern, at least for the present application.

It should be pointed out that McMorran and Moeck's model [2], which is based upon the drift-flux model, does not provide for reverse flows. Also, it would appear that the incorporation of the effects of compressibility in the drift-flux formulation would lead to substantial complexities, in part because the formulation involves partial differential equations. On the other hand, the capability of the system mean void fraction model to predict the reverse flows [7] and to account for compressibility effects for the present condensing flow situation is clearly demonstrated.

[2] Even when the time dependent component of heat flux in reference [2] is not set to zero, the predictions of system mean void fraction model with time invariant heat flux are still close to the predictions of [2]. This indicates that small perturbations in heat flux have very little influence on the overall dynamic response characteristics, as noted by McMorran and Moeck [2] as well.

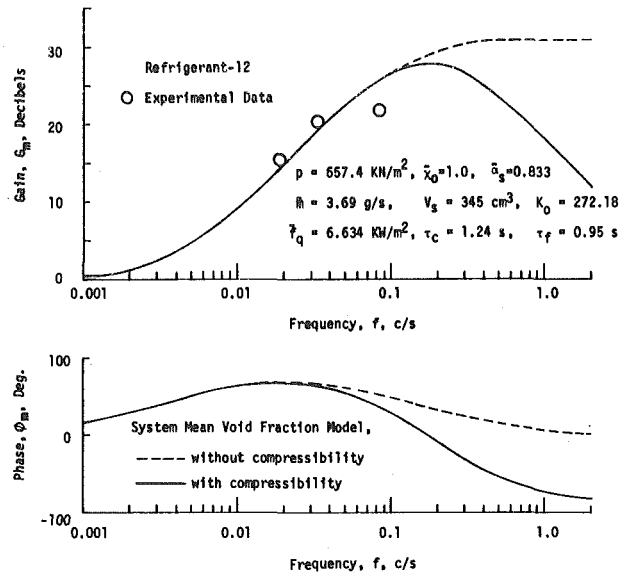

Fig. 4 Response of outlet liquid flowrate, comparison of system mean void fraction model, with and without compressibility

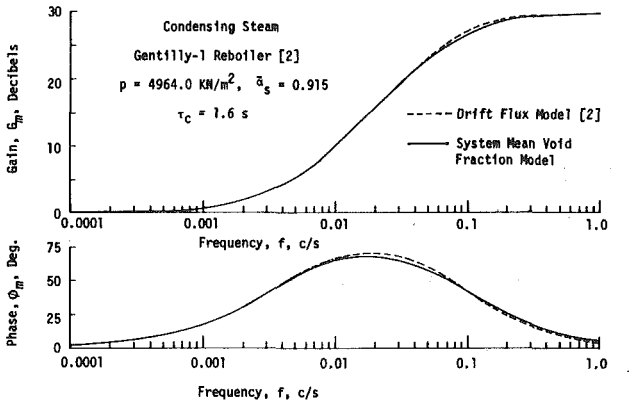

Fig. 5 Gain and phase relationships for the outlet liquid flowrate relative to the inlet vapor flowrate

Summary and Conclusions

In a study of tube-type condensers involving complete condensation, small changes in the inlet vapor flowrate have been shown to momentarily cause very large transient surges in the outlet liquid flowrate [7]. Under certain circumstances, these flow surges have been observed to result in momentary flow reversals. A system mean void fraction model has successfully predicted these transient flow surges [7]. Experimental data are presented in this paper which indicate that an effective means of attenuating the amplitude of these transient flow surges is to introduce throttling at the condenser outlet. This has the effect of making the compressibility of the vapor an important mechanism in the transient flow process.

The primary purpose of this paper has been to extend the system mean void fraction model to include these compressibility effects. Its attentuation predictions have been shown to agree well with experimental data. This model was further extended to predict the frequency response characteristics to an oscillatory inlet vapor flowrate, both with and without the effects of compressibility. A set of supporting experimental data at low frequencies was also presented.

Without compressibility, the system mean void fraction model was shown to predict an increase in the amplitude of the outlet liquid flowrate up to a certain critical frequency. Thereafter, an increase in frequency causes the compressibility of the vapor to absorb the oscillations, consequently reducing the gain in the amplitude of the outlet flowrate.

Without compressibility, the system mean void fraction model

Table 1 Physical properties and parameters for transients with compressibility

Test Number	p kN/m^2	$\bar{x}_o$	$\bar{m}_{t,i}$ g/s	$\bar{m}_{t,f}$ g/s	τ_m s	$\bar{f}_q$ kW/m^2	d cm	τ_c s	$\bar{\alpha}_s$	V_s cm^3	τ_f s	k_o^* $\frac{kN.s}{m^2 g}$	T_o ^oC	Test Section
C-3	620.0	1.0	4.690	5.22	0.44	13.0	0.800	0.65	0.840	128	0.425	0.5466	11.7	Copper
C-5	623.84	1.0	4.310	4.852	0.521	11.84	0.800	0.704	0.837	128	1.075	1.396	11.8	"
C-6	638.75	1.0	4.415	4.899	0.521	12.27	0.800	0.69	0.835	128	11.28	15.03	11.7	"

predicts a monotonic increase in the amplitude of outlet flowrate oscillations up to a certain frequency before it levels off to a constant value. These incompressible predictions were then compared with the predictions of McMorran and Moeck [2]. The predictions of the system mean void fraction model were shown to agree very well with their predictions, which are based upon the drift-flux model.

This comparable ability to predict the frequency response characteristics would appear to be an important and affirming observation, especially in view of the inherent simplicity of the system mean void fraction model, and its proven ability to predict reverse flows and the effects of vapor compressibility.

Acknowledgments

The authors would like to acknowledge the National Science Foundation Engineering Division, Mechanical Sciences and Engineering Section, Heat Transfer Program for its part of the support of this research under Grants GK-35884 and ENG-7823982. The Oakland University, Research Committee is also acknowledged for its equipment support during the experimental phase of this research.

References

1 Schoenberg, A. A., "Mathematical Model with Experimental Verification for the Dynamic Behavior of a Single-Tube Condenser," NASA TN D-3453, 1966.

2 McMorran, P. D., and Moeck, E. O., "Dynamic Model of Condensation in a Tube," AECL-5603, Chalk River Nuclear Laboratories,Chalk River, Ontario Aug. 1976.

3 Soliman, M., and Berenson, P. J., "Flow Stability and Gravitational Effect in Condenser Tubes," *Proceedings of the Fourth International Heat Transfer Conference,* Paris, Vol. VI, 1970, Paper No. Cs 1.8.

4 Doroshchuk, V. Y., and Frid, F. P., "The Critical Heat Flux for Water Flowing Through Round Tubes," *Problems of Heat Transfer and Hydraulics of Two-Phase Media,* S. S. Kutateladze, Editor, Pergamon Press, New York, 1969, Chapter 2, p. 38.

5 Vild, T. J., Schubert, F. H., and Snoke, D. R., "A System to Demonstrate the Zero Gravity Performance of an Organic Rankine Cycle," Inter-society Energy Conversion Engineering Conference, Boulder, Colo., 1968.

6 Williams, J. L., Keshock, E. G. and Wiggins, C. L., "Development of a Direct Condensing Radiator for Use in a Spacecraft Vapor Compression Refrigeration System," ASME *Journal of Engineering for Industry,* Nov. 1973, p. 1053.

7 Wedekind, G. L., and Bhatt, B. L., "An Experimental and Theoretical Investigation into Thermally Governed Transient Flow Surges in Two-Phase Condensing Flow," *Preceedings of the Two-Phase Flow and Heat Transfer Symposium-Workshop,* Ft. Lauderdale, Fla., Vol. 11, October 1976, pp. 691–711. Also, ASME JOURNAL OF HEAT TRANSFER, Vol. 99, No. 4, Nov. 1977. pp. 561–567.

8 Wedekind, G. L., Bhatt, B. L. and Beck, B. T., "A System Mean Void Fraction Model for Predicting Various Transient Phenomena Associated with Two-Phase Evaporating and Condensing Flows," *Proceedings of the NATO Advanced Study Institute on Two-Phase Flows and Heat Transfer,* Istanbul, Aug. 1976. Also, *International Journal of Multiphase Flow,* Vol. 4, 1978, pp. 97–114.

9 Collier, J. G., *Convective Boiling and Condensation,* McGraw-Hill, London, 1972.

10 Bhatt, B. L., "An Experimental and Theoretical Study of Various Transient and Oscillatory Flow Phenomena in Two-Phase Condensing Flow Systems," Ph.D. Thesis, School of Engineering, Oakland University, Rochester, Mich. 1978.

11 Bhatt, B. L., and Wedekind, G. L., "Transient and Frequency Response Characteristics of Two-Phase Condensing Flow; With and Without Compressibility," Paper presented at the Second Multi-Phase Flow and Heat Transfer Symposium Workshop, Miami Beach, Fla., Apr. 16–18, 1979.

C. F. Delale[1]
Lehigh University,
Bethlehem, PA 18015

Lower Bound Estimate for Droplet Size in Two-Phase Dispersed Flow

A theoretical post-dryout heat transfer model is developed based on one-dimensional two-phase dispersed flow and is applied to calculate the wall temperatures in the post-CHF regime. The model is also applied to reason the existence of a lower bound for average droplet diameter in two-phase dispersed flow. Results obtained using data by Bennett, et al. show lower droplet sizes than the experimentally measured values.

1 Introduction

In forced convection saturated boiling, the maximum heat flux, called the critical heat flux (CHF), will occur when the liquid phase can no longer maintain continuous contact with the heated surface. When this happens, depending on the quality, two possible flow patterns may occur (Figs. 1 (*a*) and (*b*)). At low qualities, the heated surface faces a vapor film after losing contact with the liquid phase. At sufficiently high qualities, the liquid film at the heated surface disappears because of surface evaporation and droplet entrainment. In both cases, the flow eventually develops into dispersed droplet regime. Normally, high heat flux boiling systems operate in nucleate boiling regime. However, post-CHF regimes have gained importance in recent years as a result of technological developments in cryogenics and rocketry. The post-CHF regime may also occur in some accident situations, primarily the loss-of-coolant accident (LOCA) in water-cooled nuclear reactors. In this case, the design of a safe nuclear reactor together with cooling emergency systems requires information on the heat removal from the nuclear reactor.

A number of studies in this regime, mostly experimental, has been made in recent years [1–4]. A convincing theoretical model that takes into account the spatial and transient behavior of the flow is still far from being developed. The spatial dependence is usually taken into account considering various relaxation models [3, 4], but one still has to depend mostly on experimental data.

In the present study, a new method of prediction is presented. Given the pressure P, the mass flux G, the wall temperature T_w, the wall heat flux q_w, the tube diameter D and the equilibrium quality x_e versus axial coordinate, a theoretical one-dimensional post-dryout model is developed and applied to obtain the lower bound estimate for average droplet size in the post-CHF regime.

2 Theoretical Model and Analysis

The model to be presented in this section is developed for a one-dimensional two-phase dispersed flow in a vertical tube of diameter D. In the case of one-dimensional dispersed flow in noncircular ducts, one has to consider the hydraulic diameter D_H instead. The flow is steady-state and the origin 0 of the axial coordinate z is arbitrarily set in the post-CHF regime. The droplets entrained in the flow are assumed to be spherical. The axial pressure gradient is assumed to be negligible though one can account for it by considering $P = P(z)$. The wall heat flux is axisymmetric, and the liquid droplets are taken to be at saturation temperature. The variations in kinetic and potential energy are neglected. Figure 2 indicates the physical model and coordinate system.

Equations Governing the Flow. The conservation of mass and energy together with energy and mass balance between phases for the infinitesimal control volume shown in Fig. 2 yields

$$\frac{d\dot{m}_\ell}{dz} + \frac{d\dot{m}_v}{dz} = 0 \tag{2.1}$$

$$\frac{d(\dot{m}_\ell h_\ell)}{dz} + \frac{d(\dot{m}_v h_v)}{dz} = q_w(z) \cdot \zeta \tag{2.2}$$

$$(\dot{m} dx_a)\{h_v - h_\ell\} = dQ_d(z) + \{q_\ell(z) + q_r(z)\} dA_w \tag{2.3}$$

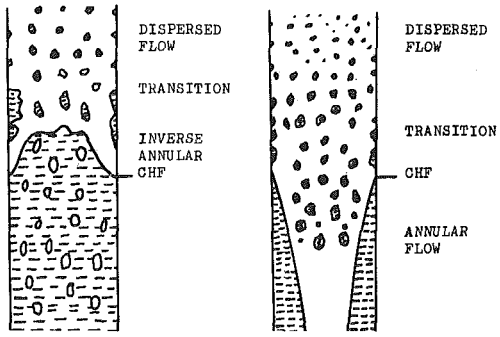

Fig. 1(*a*) At low quality Fig. 1(*b*) At high quality

Fig. 1 Post-CHF flow patterns

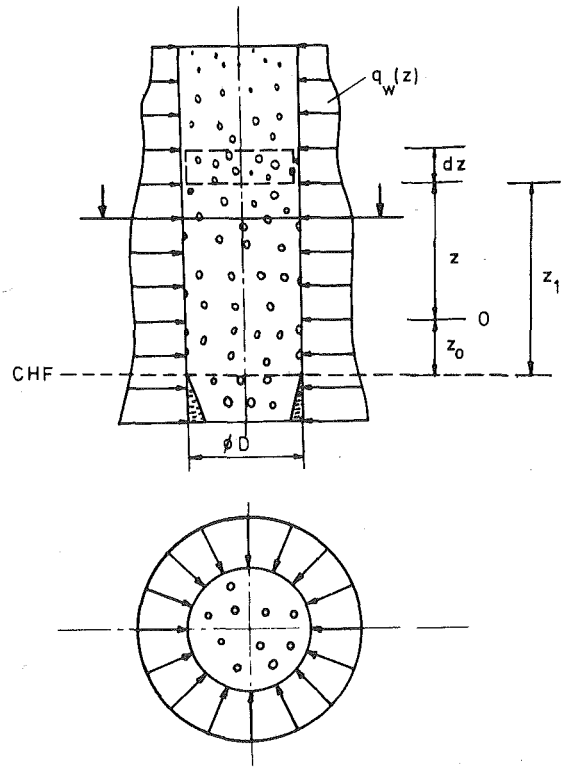

Fig. 2 The physical model and coordinate system

[1] Present Address: Division of Engineering, Brown University, Providence, RI 02912.

Contributed by the Heat Transfer Division for publication in the JOURNAL OF HEAT TRANSFER. Manuscript received by the Heat Transfer Division July 5, 1979.

dQ_d is the total heat transfer from the vapor to the droplets entrained in the flow between z and $z + dz$ and is given by

$$dQ_d(z) = h_d(T_v - T_{SAT})\pi d^2 dN \tag{2.4}$$

The number of droplets dN present between z and $z + dz$ can be calculated from

$$dN = \frac{6(1 - x_a)\dot{m}dz}{\pi \rho_\ell d^3 U_\ell} \tag{2.5}$$

By introducing the actual quality $x_a(z)$, equation (2.1) is automatically satisifed. If one considers a tube of circular cross section ($\zeta = \pi D$) keeping the pressure P constant and setting $T_\ell = T_{SAT}$ and introduces

$$\eta = \frac{z}{100D} = \frac{z_1 - z_0}{100D}, \tag{2.6}$$

equations (2.2) and (2.3) become

$$\{h_v(P, T_v) - h_\ell(P, T_{SAT})\}\frac{dx_a}{d\eta} + x_a c_{pv}(P, T_v)\frac{dT_v}{d\eta} = \frac{400 q_w(\eta)}{G} \tag{2.7}$$

$$\{h_v(P, T_v) - h_\ell(P, T_{SAT})\}\frac{dx_a}{d\eta} = \frac{600 D h_d(T_v - T_{SAT})(1 - x_a)}{\rho_\ell \cdot d \cdot U_\ell} + \frac{100 D(q_\ell + q_r)\zeta}{\dot{m}} \tag{2.8}$$

On the other hand, the actual quality x_a and the equilibrium quality x_e are related by heat balance

$$\frac{x_a}{x_e} = \frac{h_{fg}(P, T_{SAT})}{h_v(P, T_v) - h_\ell(P, T_{SAT})} \tag{2.9}$$

The three equations (2.7, 2.8) and (2.9) constitute the basic equations of the proposed model.

Evaluation of the Actual Quality x_a as a Functional of the Axial Coordinate. By combining (2.8) and (2.9) and integrating between limits $\eta = 0$ and $\eta = \eta$, one obtains

$$x_a(\eta) = \frac{x_0}{(1 - x_0)e^{-K(\eta)} + x_0} \tag{2.10}$$

where K(η) is a function of the axial coordinate defined by

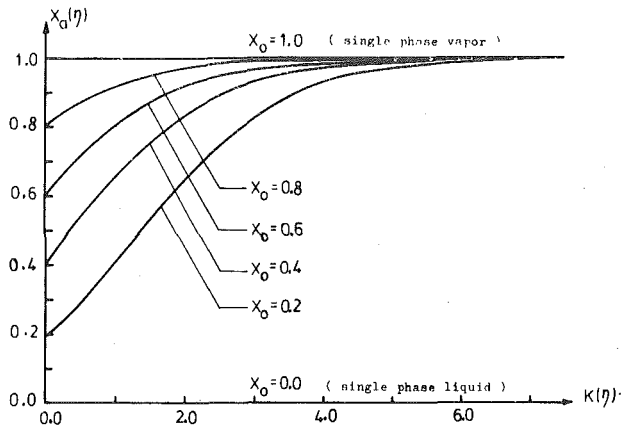

Fig. 3 Actual quality versus $K(\eta)$

$$K(\eta) = \int_0^\eta \left\{\frac{600 D h_d(T_v - T_{SAT})}{x_e(\eta) h_{fg} \rho_\ell \cdot d \cdot U_\ell} + \frac{100(q_\ell + q_r)\zeta D}{\dot{m}_\ell x_e(\eta) h_{fg}}\right\} d\eta \tag{2.11}$$

and x_0 is the actual quality at $\eta = 0$, assumed to be known. Typical behavior of $x_a(\eta)$ versus $K(\eta)$ is shown in Fig. 3 for different values of x_0. It is clearly seen that for $x_0 \geq 0.2$, $K(\eta)$ is practically between 0 and 6 for every $\eta \geq 0$ ($0 \leq K(\eta) \leq 6$). This shows that an upper bound for $K(\eta)$ is practically possible even though theoretically $K(\eta)$ can be infinite.

Method of Solution. The complete solution of the problem depends on the evaluation of $K(\eta)$. In the liquid-deficient region, for most cases, q_ℓ is negligible. In cases where thermal radiation effects can also be neglected, the second term of the integrand in equation (2.11) drops out. In such a situation,

$$K(\eta)\Big|_{\substack{q_\ell = 0 \\ q_r = 0}} = \int_0^\eta \frac{600 h_d(T_v - T_{SAT})D}{x_e(\eta) h_{fg} \rho_\ell U_\ell d}\Bigg|_{\substack{q_\ell = 0 \\ q_r = 0}} d\eta \tag{2.12}$$

Even in this case, one still needs to know h_d, d and U_ℓ to determine $K(\eta)$. When these quantities are determined, equations (2.7, 2.10) and (2.12) can be combined to solve for $T_v(\eta)$, $x_a(\eta)$ and $K(\eta)$. One then assumes a reasonable correlation for the heat transfer coefficient from the wall to the vapor and obtains $T_w(\eta)$ by

$$T_w(\eta) = T_v(\eta) + \frac{q_w(\eta)}{h_{w-v}} \tag{2.13}$$

The accuracy of the model can be tested by comparing this value of

Nomenclature

A_t = total cross-sectional area of the tube
A_w = total area of the wall
c_{pv} = specific heat of the vapor at constant pressure
D = tube diameter
D_H = hydraulic diameter
d = average droplet diameter
d_{min} = minimum average droplet diameter
G = mass velocity (flux)
h_d = heat transfer coefficient from the vapor to the droplets
h_{fg} = latent heat of evaporation
h_ℓ = specific enthalpy of the liquid
h_v = specific enthalpy of the vapor
h_{w-v} = heat transfer coefficient from the wall to the vapor
k_v = thermal conductivity of the vapor
L = total evaporation length measured from the CHF-point
$\dot{m}$ = total mass flow rate
$\dot{m}_\ell$ = mass flow rate of the liquid
$\dot{m}_v$ = mass flow rate of the vapor
Nu = Nusselt number
dN = number of droplets between z and $z + dz$
P = pressure
Pr = Prandtl number
Q_d = total heat transfer from the vapor to the droplets
q_ℓ = heat flux from the wall to the droplets based on unit area of the wall
q_r = heat flux from the wall to the droplets by radiation based on unit area of the wall
q_v = heat flux from the wall to the vapor based on unit area of the wall
q_w = total wall heat flux based on unit area of the wall
Re = Reynolds number
S = slip ratio
T_ℓ = liquid temperature
T_f = film temperature
T_{SAT} = saturation temperature
T_v = superheated vapor temperature
T_w = wall temperature
U_ℓ = actual velocity of the liquid
$U_{\ell 0}$ = terminal velocity in drift-flux model
U_m = mean velocity in the homogeneous flow model
U_v = actual velocity of the vapor
We = Weber number
x_a = actual quality
x_e = equilibrium quality
x_0 = actual initial quality
z = axial coordinate in the post-CHF regime
z_0 = distance between the origin 0 and the CHF-point
z_1 = axial coordinate measured from the CHF-point
α = void fraction
η = dimensionless axial coordinate
μ_v = dynamic viscosity of the vapor
ρ_ℓ = density of the liquid
ρ_m = mean density in homogeneous flow model
ρ_v = density of the vapor
σ = surface tension coefficient
ζ = perimeter of the tube

$T_w(\eta)$ with the experimentally measured value.

The most widely used correlation for the evaporation of droplets is Frössling formula [8]:

$$\mathrm{Nu}_d = \frac{h_d \cdot d}{k_v} = 2\left\{1 + 0.276\left(\frac{\rho_v d V_{\text{relative}}}{\mu_v}\right)^{1/2} \mathrm{Pr}_v^{1/3}\right\} \quad (2.14)$$

As can be clearly seen, one still requires information on d, U_ℓ, and V_{relative}. To calculate U_ℓ and V_{relative}, one has to know the void fraction $\alpha(\eta)$. Consequently, one has to consider correlations for d and α. Various correlations can be employed for d and α. It is here suggested that one use the lower bound estimate for d as calculated in Section 3. An alternative method of solution exists. When sufficient experimental data becomes available, one can correlate $K(\eta)$. It follows from equation (2.10) that $K(\eta)$ is a monotonically increasing function of η. The general form recommended here for $K(\eta)$ is

$$K(\eta) = A\eta^m + B\eta \quad (2.15)$$

where A, B and m are dimensionless constants to be obtained in terms of flow parameters. Constitutive equation (2.15) can be more simplified by assuming a linear relation ($A = 0$) for $K(\eta)$.

$$K(\eta) = \left(6.9 - Ln\frac{x_0}{1 - x_0}\right)\frac{\eta}{\eta_0} \quad (2.16)$$

η_0 is the value of the axial coordinate at which transition to single phase vapor occurs ($x_a = 0.999$). Setting $z_0 = 0$ ($z = z_1$) in Fig. 2 and assuming $(x_a)_{\text{CHF}} = (x_e)_{\text{CHF}}$, equations (2.16) and (2.10) yield

$$x_a(z_1) = \frac{(x_e)_{\text{CHF}}}{(1 - (x_e)_{\text{CHF}})\exp\left\{-\left(6.9 - Ln\frac{(x_e)_{\text{CHF}}}{1 - (x_e)_{\text{CHF}}}\right)\frac{z_1}{L}\right\} + (x_e)_{\text{CHF}}} \quad (2.17)$$

Here z_1 is the axial coordinate measured from the CHF-point, and L is the distance for total evaporation from the CHF-point. L is related to the flow parameters by

$$\int_0^L q_w(z_1)dz_1 = \frac{GD}{4}\{x_e(z_1 = L) - (x_e)_{\text{CHF}}\}h_{fg}(P, T_{\text{SAT}}) \quad (2.18)$$

For the case of constant wall heat flux, equation (2.18) for L reduces to

$$L = \frac{GD}{4q_w}\{x_e(z_1 = L) - (x_e)_{\text{CHF}}\}h_{fg}(P, T_{\text{SAT}}) \quad (2.19)$$

equations (2.9, 2.17) and (2.18) determine $x_a(z_1)$ and $T_v(z_1)$ provided that $x_e(z_1 = L)$ be known. Once $x_a(z_1)$ and $T_v(z_1)$ are determined, one can solve for the wall temperature $T_w(z_1)$ from

$$T_w(z_1) = T_v(z_1) + \frac{q_w(z_1)}{h_{w-v}} \quad (2.20)$$

The above model is tested against film boiling data of nitrogen by Forslund and Rohsenow [1]. In these data, the equilibrium quality at which transition to single-phase vapor occurs is reported to be of the order of magnitude of 3.0. For h_{w-v} in equation (2.20), an improved Dittus-Boelter type correlation is used,

$$h_{w-v} = 0.0135\left(\frac{k_{v,f}}{D}\right)\left\{\frac{GD}{\mu_{v,f}}\left[x_a + \frac{\rho_{v,f}}{\rho_\ell}(1 - x_a)\right]\right\}^{0.8}\mathrm{Pr}_{v,f}^{0.4}, \quad (2.21)$$

where the constant 0.0135 is fitted so that h_{w-v} matches its single-phase value asymptotically. The property values for the vapor are calculated at the film temperature

$$T_f = \frac{T_w + T_v}{2} \quad (2.22)$$

Results of $x_a(z_1)$, $T_v(z_1)$ and $T_w(z_1)$ predicted by the present model for a typical run are shown in Fig. 4. The comparison of wall temperatures for this run with the experimentally measured values shows a maximum error of 12 percent and a mean error of less than 7 percent in the dispersed flow film boiling regime. The error can be interpreted to be due to the deviation from the linear assumption for $K(\eta)$ (equation (2.16)) and due to the accuracy of equation (2.21) for h_{w-v}.

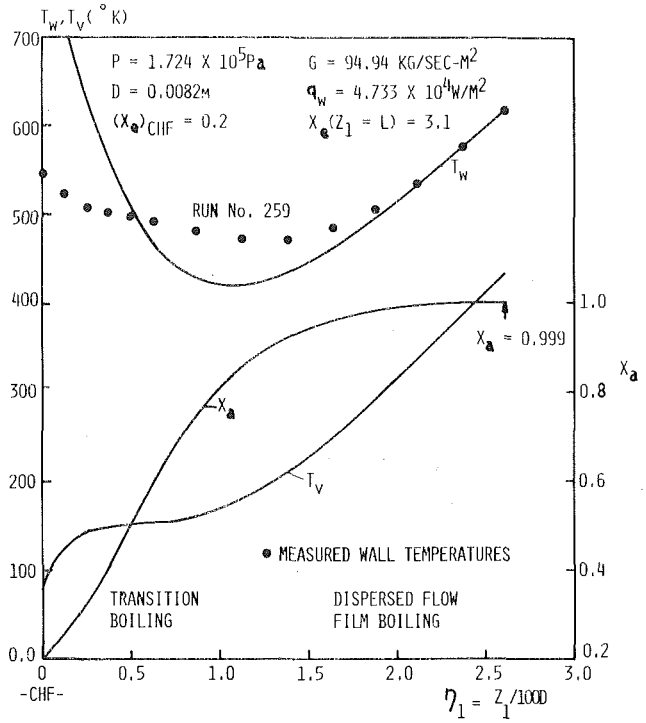

Fig. 4 Calculated values of X_a, T_v and T_w by the present model for film boiling of nitrogen and comparison with data by Forslund and Rohsenow [1]

Improvement on these assumptions is beyond the scope of the present work and will be considered in future studies. As expected, the model fails to predict the approximate wall temperatures in the transition boiling regime, i.e. very close to the CHF-point. This is because equation (2.20), used to calculate the wall temperatures, is no longer valid and has to be improved to account for the additional amount of heat transferred from the wall to a layer of droplets next to the surface of the tube (Leidenfrost effect).

3 Application of the Model to Estimate the Lower Bound for Droplet Size in Two-Phase Dispersed Flow

Given the pressure P, the mass flux G, the wall temperature $T_w(\eta)$, the wall heat flux $q_w(\eta)$, the equilibrium quality $x_e(\eta)$ and the tube diameter D, the lower bound for average droplet diameter is predicted using the post-dryout model developed above. Such a calculation is necessary for the estimate of the actual mean droplet diameter. The general proof for the existence of the lower bound for average droplet diameter is given in the appendix. It is shown that such a lower bound is obtained when $q_\ell = 0$, $q_r = 0$ and $S = 1$.

Evaluation of the Vapor Temperature T_v and Actual Quality x_a. Neglecting q_ℓ and q_r, one has

$$T_v(\eta) = T_w(\eta) - \frac{q_w(\eta)}{h_{w-v}} \quad (3.1)$$

In order to calculate T_v for given $T_w(\eta)$ and $q_w(\eta)$, only information on h_{w-v} is required. In this work, two correlations are used for h_{w-v}.

1 Heineman correlation [6] as employed by Saha-Shiralkar-Dix [3]

$$h_{w-v} = 0.0157\frac{k_{v,f}}{D}\mathrm{Re}_{v,f}^{0.84}\mathrm{Pr}_{v,f}^{0.33}\left(\frac{z_1}{D}\right)^{-0.04} \quad (3.2a)$$

for $6 < z_1/D < 60$

$$h_{w-v} = 0.0133\frac{k_{v,f}}{D}\mathrm{Re}_{v,f}^{0.84}\mathrm{Pr}_{v,f}^{0.33} \quad (3.2b)$$

for $z_1/D > 60$.

z_1 is the distance measured from the CHF-point, and

$$\mathrm{Re}_{v,f} = \frac{\rho_v U_v D}{\mu_{v,f}} = \frac{G x_a D}{\alpha \mu_{v,f}} \tag{3.3}$$

The void fraction α is calculated using the drift-flux model.

$$x_a = \frac{1 - (1-\alpha)\left(\dfrac{U_{\ell 0}\rho_\ell}{G}\alpha^2 + 1\right)}{1 - (1-\alpha)(1 - \rho_\ell/\rho_v)} \tag{3.4}$$

where $U_{\ell 0}$ is the terminal velocity given by

$$U_{\ell 0} = -1.4\left[\frac{\sigma g(\rho_\ell - \rho_v)}{{\rho_v}^2}\right]^{1/4} \tag{3.5}$$

Combining equations (2.9, 3.1, 3.2.*a*, *b*, 3.3) and (3.4), one can iteratively solve for x_a and T_v at any η.

2 Hadaller's correlation [5] as recommended by Groeneveld and Delorme [2]

In Hadaller's correlation, h_{w-v} is given by

$$h_{w-v} = 0.008348\frac{k_{v,f}}{D}\left[\frac{GD}{\mu_{v,f}}\left\{x_a + \frac{\rho_v}{\rho_\ell}(1-x_a)\right\}\right]^{0.8774}\mathrm{Pr}_{v,f}^{0.6112} \tag{3.6}$$

In a similar manner, one iteratively solves for x_a and T_v combining equations (2.9), (3.1) and (3.6).

Evaluation of $K(\eta)$ and Check for $x_a(\eta)$. By differentiating equation (2.10) with respect to η once and substituting in equation (2.7) for $x_a(\eta)$ and $dx_a/d\eta$, it follows that

$$\frac{dK}{d\eta} = \left\{\frac{400q_w(\eta)}{G} - \frac{x_0 c_{pv}\dfrac{dT_v}{d\eta}}{(1-x_0)e^{-K(\eta)} + x_0}\right\} \cdot \frac{\{x_0 + (1-x_0)e^{-K(\eta)}\}^2}{(h_v - h_\ell)x_0(1-x_0)e^{-K(\eta)}} \tag{3.7}$$

In equation (3.7) x_0, $q_w(\eta)$ and G are given. On the other hand, $T_v(\eta)$ is calculated in the previous section. Since one needs $dT_v/d\eta$, he has to consider a continuous curve for $T_v(\eta)$. A general curve fit expression is recommended here in the form

$$T_v(\eta) = \sum_{k=0}^{n} a_k \eta^k \tag{3.8}$$

where a_k's are the parameters to be fitted by the method of least squares. Integration of equation (3.7) with the initial condition $K(0) = 0$ yields

$$K(\eta) = \int_0^\eta \left\{\frac{400q_w(\eta)}{G} - \frac{x_0 c_{pv}\dfrac{dT_v}{d\eta}}{(1-x_0)e^{-K(\eta)} + x_0}\right\} \frac{\{x_0 + (1-x_0)e^{-K(\eta)}\}^2}{(h_v - h_\ell)x_0(1-x_0)e^{-K(\eta)}} d\eta \tag{3.9}$$

Equation (3.9) is a nonlinear Volterra integral equation and can be solved by means of successive approximations. Now that $K(\eta)$ can be solved, one can calculate $x_a(\eta)$ by equation (2.10) and compare it to the previously calculated value. Thus, one can check the accuracy in curve fit for T_v and in approximate calculation of $K(\eta)$. Invertedly, one can calculate $K(\eta)$ from equation (2.10) and find a curve fit expression for it; however, the procedure given above proves to be more convenient for the present calculations.

Evaluation of the minimum average droplet diameter. Neglecting q_ℓ and q_r, one has by equation (2.12)

$$\frac{dK}{d\eta} = \frac{600Dh_d(T_v - T_{\mathrm{SAT}})}{x_e(\eta)h_{fg}\rho_\ell U_\ell d} \tag{3.10}$$

For the minimum average droplet size, one also has to consider $S = 1$. This suggests

$$h_d = \frac{2k_v}{d_{\min}} \tag{3.11}$$

and

$$U_\ell = U_v = \frac{\dot{m}}{\rho_m A_t} = \frac{G}{\rho_m} \tag{3.12}$$

where

$$\rho_m = \frac{1}{\dfrac{x_a}{\rho_v} + \dfrac{1-x_a}{\rho_\ell}} \tag{3.13}$$

Substituting in equation (3.10) and solving for $d_{\min}$, it follows that

$$d_{\min}(\eta) = \sqrt{\frac{1200Dk_v\rho_m(T_v - T_{\mathrm{SAT}})}{x_e(\eta)h_{fg}\rho_\ell G\left(\dfrac{dK}{d\eta}\right)}} \tag{3.14}$$

In equation (3.14), T_v and x_a are to be calculated using one of the correlations for h_{w-v} suggested previously. $dK/d\eta$ is to be solved from equations (3.7) and (3.9), and ρ_m is to be calculated by equation (3.13). The rest of the quantities appearing in equation (3.14) are either given or they can be related to the given quantities.

Two Extreme Limits for the Lower Bound of Average Droplet Size. (1) The case of single-phase vapor flow ($x_a \to 1$): From equations (2.10) and (3.7), it follows that when $x_a \to 1$; $K \to \infty$ and $dK/d\eta \to \infty$. Therefore, equation (3.14) yields

$$\lim_{x_a \to 1} d_{\min}(\eta) \to 0 \tag{3.15}$$

(2) Estimate of lower bound for average initial droplet size ($x_a \to x_0$): When $x_a \to x_0$, by definition $K = 0$. Thus, combining equations

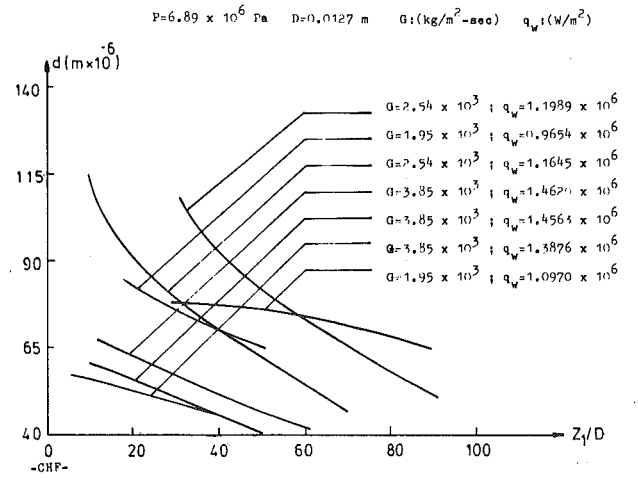

Fig. 5 Minimum average droplet diameter versus axial coordinate using Heineman correlation for h_{w-v}. Data source: Bennett, et al.

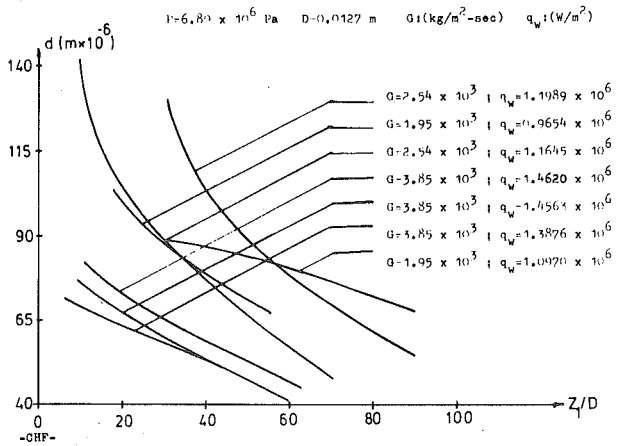

Fig. 6 Minimum average droplet diameter versus axial coordinate using Hadaller's correlation for h_{w-v}. Data source: Bennett, et al.

(3.7) and (3.14) one obtains

$$d_{\min}(0) = \sqrt{\frac{1200Dk_v\rho_m(T_v(0) - T_{SAT})(1 - x_0)}{\rho_\ell \left\{400q_w(0) - x_0Gc_{pv}\dfrac{dT_v(0)}{d\eta}\right\}}} \tag{3.16}$$

Results Obtained Using Data of Bennett, et al. [7]. The lower bound for average droplet size is calculated using data by Bennett, et al. for water-steam system. For these data, a parabolic vapor temperature distribution is assumed; therefore, equation (3.8) reduces to

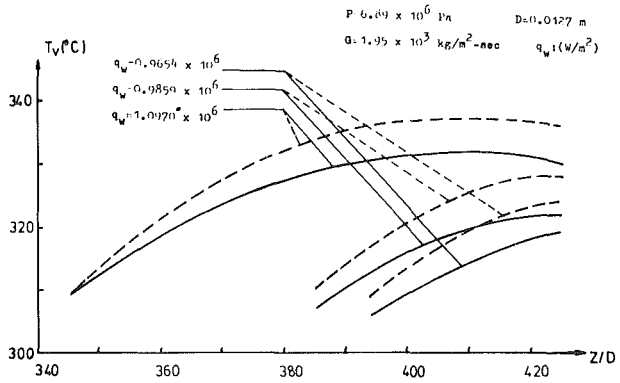

Fig. 7 Superheated vapor temperature versus axial coordinate. Data source: Bennett, et al.
—— Heineman correlation for h_{w-v}.
- - - Hadaller's correlation for h_{w-v}.

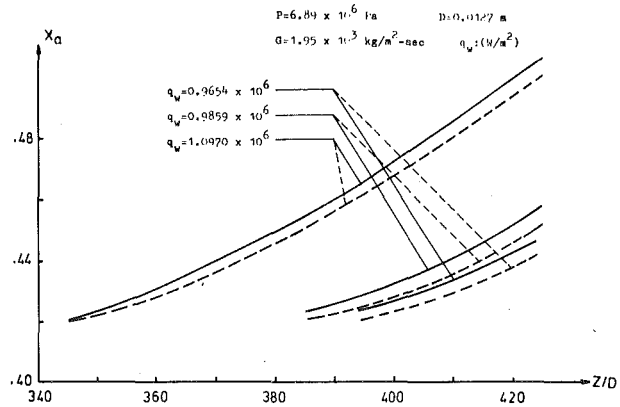

Fig. 8 Actual quality versus axial coordinate. Data source: Bennett, et al.
—— Heineman correlation for h_{w-v}.
- - - Hadaller's correlation for h_{w-v}.

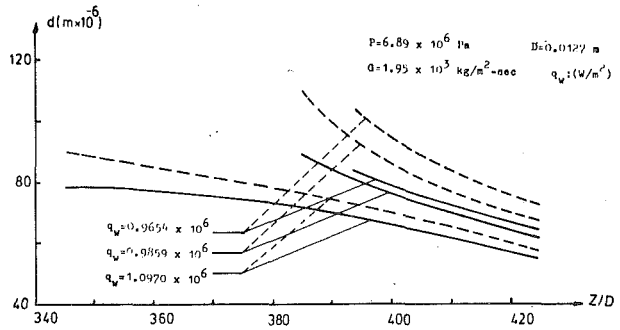

Fig. 9 Minimum average droplet diameter versus axial coordinate. Data source: Bennett, et al.
—— Heineman correlation for h_{w-v}.
- - - Hadaller's correlation for h_{w-v}.

$$T_v(\eta) = T_v(0) + a_1\eta + a_2\eta^2 \tag{3.17}$$

where a_1 and a_2 are fitted by the method of least squares.

Figures 7–9 show typical post-dryout characteristics of T_v, x_a and $d_{\min}$ as a function of the axial coordinate for water-steam data by Bennett, et al. The effect of q_w keeping D, G and P constant is shown on the plots. As is clearly seen, $d_{\min}$ decreases with increasing q_w. $d_{\min}$ is also plotted versus z_1/D (Figs. 5 and 6), z_1 being the distance measured from the CHF-point. The results obtained by the present lower bound calculation for average droplet diameter fall below the experimentally measured values of the mean droplet diameter in two-phase dispersed flow. Table 1 shows the experimentally measured values of the mean droplet diameter in two-phase dispersed flow.

Comparison with the Droplet Breakup Criteria. Prior to the present work, the mean droplet diameter in two-phase systems has been calculated using a critical Weber number at which the droplets are assumed to break up.

$$\mathrm{We}_{\text{critical}} = \frac{\rho_v(U_v - U_\ell)^2 d}{\sigma} \tag{3.18}$$

The critical Weber number based on the lower bound estimate of average droplet diameter by the present model is seen to vary significantly with the axial coordinate. Figure 10 shows that the critical Weber number based on the lower bound calculation varies continuously between the limits 0.045 and 0.025 for a particular run from Bennett's data; therefore, even for a particular flow regime the difficulty with which critical Weber number to pick remains a serious problem of the criteria. With the present lower bound calculation for average droplet diameter, such a difficulty is avoided.

4 Summary and Conclusions

A theoretical post-dryout heat transfer model is developed based on one-dimensional two-phase dispersed flow. The actual quality x_a is related to the axial coordinate η by the functional relation (2.10) introducing the function $K(\eta)$ from equation (2.11). The usual procedure of calculating $K(\eta)$ requires correlations for h_d, d and α. It is recommended that one use equation (2.14) for h_d, the minimum average droplet diameter—as calculated in the present paper–for d and the drift-flux model for α in order to calculate $K(\eta)$.

In an alternative method, a linear constitutive equation (equation (2.16)) is suggested for $K(\eta)$. This assumption may be arrived at

Table 1 Experimental data for mean droplet diameter [9]

Description of study	Flow conditions	Droplet Data	Remarks
Investigator -date system Fluid	Flow cross section Quality (x_a or x_e) Gas velocity (U_v)	Range	Measurement method Application Reference
Forslund and Rohsenow (1968) Vertical tube Upward flow Nitrogen	D = 0.0058 m D = 0.0082 m D = 0.0120 m x_a = 0.3 - 0.8 U_v = 15 - 45 m/sec	100 - 1000 (m x 10^{-6})	Photography Boiling burnout study 11
Cumo et.al. (1974) Vertical Rectangular Upward flow Freon	0.003 m x 0.005 m x_e = 0.91 - 1.46	24 - 52 (m x 10^{-6})	Photography Basic study 10
Pagson, Roberts and Waibler (1979) Vertical tube Upward flow Steam-water	x_a = 0.5 - 0.8	41 (m x 10^{-6})	Photography Basic study Heat Transfer 13
Mayinger and Langner (1976) Vertical tube Upward flow R-12		20 - 850 (m x 10^{-6})	Photography In tube boiling 12

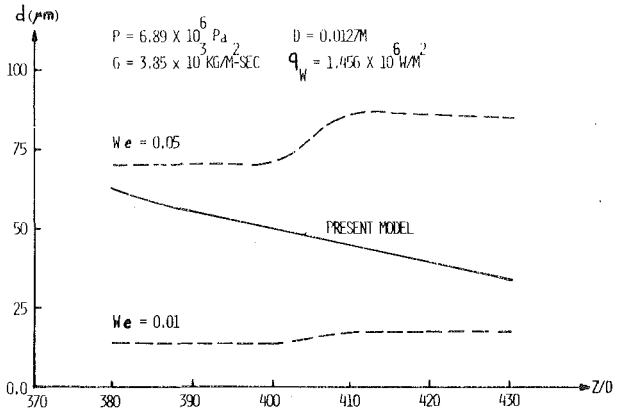

Fig. 10 Comparison of the present model with the droplet breakup criteria. (Heineman correlation is used for h_{w-v}). Data source: Bennett, et al.

through physical arguments; away from high thermal radiative fluxes, the integrand in equation (2.11) is nearly constant at least in the effective range of $K(\eta)$. Thus, x_a and T_v can be explicitly predicted by equations (2.9, 2.17) and (2.18) provided that the equilibrium quality at which transition to single phase vapor flow occurs be known. The above model is tested against film boiling data of nitrogen by Forslund and Rohsenow [1], and the results are shown in Fig. 4. The mean error in calculating the wall temperatures by the method described proves to be less than 7 percent in the film boiling regime of nitrogen for the particular run presented. Improvement on the model is a subject for future studies.

The post-dryout model is also applied to reason the existence of a lower bound for average droplet size in two-phase dispersed flow. The proof for the existence of such a bound is included in the Appendix. The lower bound for droplet diameter is explicitly given by equation (3.14). Moreover, it is obvious that when one uses the minimum possible h_{w-v} to calculate $d_{\min}$ by the present model, one obtains the minimum possible average droplet diameter.

Results obtained using data by Bennett, et al. show that the difficulty encountered in choosing the correct critical Weber number for a particular flow regime by the droplet breakup criteria can be avoided using the lower bound estimate for average droplet diameter predicted by the present model. One may also conclude that the average droplet diameter depends primarily on the wall heat flux and axial coordinate; it decreases with increasing wall heat flux and axial coordinate.

References

1 Forslund, R. P., and Rohsenow, W. M., "Dispersed Flow Film Boiling," ASME JOURNAL OF HEAT TRANSFER, Nov. 1968, pp. 399–407.

2 Groeneveld, D.C., and Delorme, G. G. J., "Prediction of Thermal Non-equilibrium in the Post-Dryout Regime," *Nuclear Engineering and Design*, Vol. 36, 1976, pp. 17–26.

3 Saha, P., Shiralkar, B. S., and Dix, G. E., "A Post-Dryout Heat Transfer Model Based on Actual Vapor Generation Rate in Dispersed Droplet Regime," ASME Paper No. 77-HT-80, 1977.

4 Jones, O. C., and Zuber, N., "Post-CHF Heat Transfer: A Nonequilibrium Relaxation Model," 76 NHTC at Salt Lake City, Utah.

5 Hadaller, G., and Banerjee, S., "Heat Transfer to Superheated Steam in Round Tubes," AECL unpublished report, 1969 (see reference [2]).

6 Heineman, J. B., "An Experimental Investigation of Heat Transfer to Superheated Steam in Round and Rectangular Tubes," ANL-6213, 1960.

7 Bennett, A. W., Hewitt, G. F., Kearsey, H. A., Keeys, R. K. F., "Heat Transfer to Steam Water Mixtures Flowing in Uniformly Heated Tubes in which the Critical Heat Flux Has been Exceeded," UKAEA Research Group Report AERE-R5373, 1967.

8 Spalding, D. B. *Convective Mass Transfer*, McGraw-Hill, London, 1963, pp. 48–49.

9 Smith, R. V., and Azzopardi, B. J., "Summary of Reported Droplet Size Distribution Data in Dispersed Two-Phase Flow" NUREG-CR-0476, 1978.

10 Cumo, M., Farello, G. E., Ferrari, G., and Palazzi, G., "On Two-Phase Highly Dispersed Flows," ASME JOURNAL OF HEAT TRANSFER, Vol. 96, Series C. No. 4, 1974.

11 Forslund, R. P., and Rohsenow, W. M., "Thermal Nonequilibrium in Dispersed Flow Film Boiling in a Vertical Tube," MIT Report No. 75312-44, 1966.

12 Mayinger, F., and Langner, H., "Steady State and Transient Entrainment Behavior in Upward Co-current Flow," NATO Advanced Study Institute in Two-Phase Flow, Istanbul, Turkey.

13 Pagson, J. T., Roberts, J. H., and Waibler, P. J., "An Investigation of the Liquid Distribution in Annular-Mist Flow," ASME JOURNAL OF HEAT TRANSFER, Vol. 92, 1970, pp. 651.

APPENDIX

General Proof of the Existence of the Lower Bound for Average Droplet Size in Two-Phase Dispersed Flow

For the total wall heat flux, one can write

$$q_w(\eta) = q_v(\eta) + q_\ell(\eta) + q_r(\eta) \tag{A1}$$

When q_ℓ and q_r are neglected as done in most cases in the liquid-deficient region, one predicts $q_v(\eta)$ maximum. From

$$q_v(\eta) = h_{w-v}(T_w - T_v) \tag{A2}$$

it follows that the prediction for $h_{w-v}(T_w - T_v)$ is also maximum. Thus, either h_{w-v} or $T_w - T_v$ or both are overpredicted. However, h_{w-v} is a single phase heat transfer coefficient and depends on T_v through property values of the vapor. Therefore, the dominant part in heat transfer from the wall to the vapor is the driving force $T_w - T_v$. $q_v(\eta)$ being predicted maximum, $T_w - T_v$ is also predicted maximum when q_ℓ and q_r are neglected. In this case, since T_w is fixed at a particular location, the prediction for T_v is minimum. From equation (2.9), it follows that x_a is predicted maximum. Therefore, one concludes that neglecting q_ℓ and q_r makes the prediction for T_v minimum and that for x_a maximum. Since x_a is predicted maximum, it follows from equation (2.10) that $K(\eta)$ is greater in the case when q_ℓ and q_r are neglected. Therefore,

$$\int_0^\eta \frac{600Dh_d(T_v - T_{SAT})}{x_e(\eta)h_{fg}\rho_\ell U_\ell d}\,d\eta\bigg|_{\substack{q_\ell=0\\q_r=0}} > \int_0^\eta \frac{600Dh_d(T_v - T_{SAT})}{x_e(\eta)h_{fg}\rho_\ell U_\ell d}\,d\eta\bigg|_{\substack{q_\ell\neq 0\\q_r\neq 0}} + \int_0^\eta \frac{100(q_\ell + q_r)\xi D}{\dot{m}_\ell x_e(\eta)h_{fg}}\,d\eta \tag{A3}$$

In equation (A3), the second term appearing on the right is always positive. Therefore, one can write

$$\int_0^\eta \left\{\frac{600Dh_d(T_v - T_{SAT})}{x_e(\eta)h_{fg}\rho_\ell U_\ell d}\bigg|_{\substack{q_\ell=0\\q_r=0}} - \frac{600Dh_d(T_v - T_{SAT})}{x_e(\eta)h_{fg}\rho_\ell U_\ell d}\bigg|_{\substack{q_\ell\neq 0\\q_r\neq 0}}\right\} d\eta > 0 \tag{A4}$$

Since for every η, the inequality is satisfied, i.e., the above integral is positive for every η, it follows that the integrand must also be positive. Noting that $x_e(\eta)$, h_{fg} and D are the same at a particular η whether or not q_ℓ and q_r are neglected, one obtains

$$\frac{h_d(T_v - T_{SAT})}{U_\ell d}\bigg|_{\substack{q_\ell=0\\q_r=0}} > \frac{h_d(T_v - T_{SAT})}{U_\ell d}\bigg|_{\substack{q_\ell\neq 0\\q_r\neq 0}} \tag{A5}$$

The above inequality holds regardless of the flow model to be used. It has already been shown that $T_v - T_{SAT}$ is minimum for a particular correlation of h_{w-v} in all flow models when q_ℓ and q_r are neglected.

Considering:

$$\frac{h_d(T_v - T_{SAT})}{U_\ell d}\bigg|_{\substack{q_\ell\neq 0\\q_r\neq 0}} \tag{A6}$$

a lower bound for d exists if one can choose a minimum h_d and a maximum U_ℓ simultaneously. On the other hand, the slip S is defined by

$$S = \frac{U_v}{U_\ell} \geq 1 \tag{A7}$$

Therefore, the maximum U_ℓ occurs when $S = 1$. h_d is minimum when the heat transfer from the vapor to the droplets is only by conduction

($S = 1$). Therefore, one obtains the lower bound for average droplet diameter when

$$q_\ell = 0,\ q_r = 0 \text{ and } S = 1 \tag{A8}$$

Fortunately, the homogeneous flow model gives $S = 1$. Therefore, the use of the homogeneous flow model for h_d and U_ℓ when q_ℓ and q_r are neglected will give the lower bound estimate for average droplet diameter in two-phase dispersed flow.

An Analysis of Heat Transfer to Axial Dispersed Flow between Rod Bundles under Reactor Emergency Cooling Conditions

S. Wong
L. E. Hochreiter

Nuclear Technology Division,
Westinghouse Electric Corporation,
Pittsburgh, Pa. 15230

Analysis is carried out for dispersed flow heat transfer under reactor emergency cooling conditions. The present formulation explicitly reveals an extra dependence of the heat transfer coefficient and Nusselt number on the mean vapor temperature for droplet dispersed flow which is not found in single phase flow heat transfer. The heat transfer results obtained from three different geometries—an infinite square array of cylindrical rods, an annulus and a circular pipe—are compared; all have the same hydraulic diameter. It is found that, within the framework of the present analysis, results for the annulus and the rod bundles agree well when the pitch-to-diameter ratio is 1.5 or greater. The circular pipe is in general a poor approximation for rod bundle geometries except at a pitch-to-diameter ratio of about 1.3 which is typical of present day light water reactor fuel assemblies.

1 Introduction

A model has been proposed by Sun, et al. [1] to calculate the combined convection and radiation heat transfer from the fuel rods to the steam-droplet mixture (dispersed flow) under reactor Emergency Core Cooling Systems (ECCS) operation conditions during a postulated loss-of-coolant accident. The rod bundles were treated as a system of parallel identical subchannels, with each subchannel defined as the open space among four adjacent rods (see Fig. 1). The subchannel was then characterized by a circular tube with the same hydraulic diameter, D_h.

The equivalent hydraulic diameter concept, however, is not always a good approximation to noncircular tube geometry. In this paper, the heat transfer characteristics of the steam-droplet flow (dispersed flow) will be analyzed for cylindrical rods arranged in an infinite square array (called square rod bundles hereafter) with uniform circumferential rod wall temperatures. The goal of the analysis is to check the use of the hydraulic diameter concept as an approximation to square rod bundles for dispersed two-phase flow heat transfer. The exact results obtained from the square rod bundles will also be compared with that obtained by using the equivalent annulus concept (i.e., the subchannel of the rod bundle is being replaced by an annulus such that the flow area between the annulus is identical to that in actual configuration).

2 Physical Model

Apart from geometry and the inclusion of circumferential dependence of wall heat flux and vapor temperature, the same physical model as that proposed by Sun, et al. is being considered; the reader is referred to reference [1] for details. Very briefly, the model considers the combined effects of convection and radiation heat transfer to quasi-steady laminar dispersed droplet flow under reactor ECC operation conditions. Neglecting the axial variation of vapor temperature, the vapor temperature field for the geometric configuration shown in Fig. 1 satisfies the following equation.

$$(1/r)\partial(r\partial\Omega/\partial r)/\partial r + (1/r^2)\,\partial^2\Omega/\partial\theta^2 = \xi^2\Omega \tag{1}$$

where

$$\Omega(r,\theta) = (T_v(r,\theta) - T_{\text{sat}}) + \psi/\xi^2 \tag{2}$$

$$\xi^2 = \beta\,[1 + C_p\,(T_m - T_{\text{sat}})/h_{fg}]/k \tag{3}$$

$$\psi = [C_p(T_m - T_{\text{sat}})\,(\phi_{w1} + \phi_{v1})/h_{fg} + \phi_{v1} - \phi_{wv}]/k \tag{4}$$

Calculations of the volumetric radiation heat flux, ϕ, is given in [1]. The droplet-vapor heat transfer factor, β, is defined as

$$\beta = \pi\, ndk\mathrm{Nu}_d \tag{5}$$

In this paper, the droplet Nusselt number, Nu_d, for the heat transfer between an evaporating droplet and the surrounding superheated steam will be computed by the Lee and Ryley [2] correlation.

$$\mathrm{Nu}_d = 2 + 0.74\,\mathrm{Re}_d^{0.5}\,\mathrm{Pr}^{0.33} \tag{6}$$

The boundary conditions that must be satisfied by the temperature field Ω are

$$\Omega = \Omega_w \qquad \text{at } r = r_w \tag{7}$$

$$\partial\Omega/\partial\theta = 0 \qquad \text{at } \theta = 0,\ \pi/4 \tag{8}$$

$$\partial\Omega/\partial N = 0 \qquad \text{at } r = s/\cos\theta,\ 0 \le \theta \le \pi/4 \tag{9}$$

where

$$\partial/\partial N = \cos\theta\ \partial/\partial r - (\sin\theta/r)\ \partial/\partial\theta \tag{10}$$

The conventional definition of the bulk mean temperature requires a knowledge of the vapor velocity distribution. An analytical expression for the velocity distribution in dispersed flow between rod bundles is not available in the open literature. It is beyond the scope of the present work to investigate the detailed hydrodynamic of dispersed flow. Hence, following reference [1], the mean vapor temperature is defined by assuming a uniform vapor velocity profile

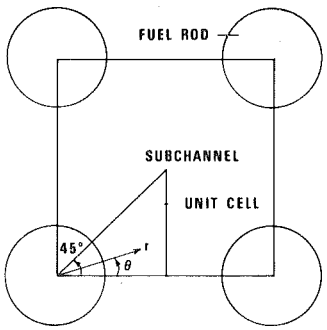

Fig. 1. Subchannel and unit cell in square rod bundles

Contributed by the Heat Transfer Division for publication in the JOURNAL OF HEAT TRANSFER. Manuscript received by The Heat Transfer Division October 25, 1979.

$$\Omega_m = (1/A) \int_0^{\pi/4} \int_{r_w}^{s/\cos\theta} \Omega(r, \theta)\, r dr d\theta \tag{11}$$

where

$$A = \int_0^{\pi/4} \int_{r_w}^{s/\cos\theta} r dr d\theta \tag{12}$$

is the flow area of the unit cell being considered.

3 Analysis

The solution to equation (1) can readily be obtained by the method of separation of variables. Remembering $\Omega(r, \theta)$ must satisfy

$$\Omega(r, \theta) = \Omega(r, \theta + 2\pi) \tag{13}$$

and the boundary condition as given by equation (8), the solution for $\Omega(r, \theta)$ must read

$$\Omega(r, \theta) = C_0 I_0(\xi r) + D_0 K_0(\xi r) + \sum_{k=1}^{\infty} (C_k I_{4k}(\xi r) + D_k K_{4k}(\xi r)) \cos 4k\theta \tag{14}$$

where

C_k; D_k = integration constants, $k = 0, 1, 2, \ldots$.

$(I_k(x); K_k(x))$ = modified Bessel's function of (1^{st}; 2^{nd}) kind and kth order.

The integration constants are to be determined by the appropriate boundary conditions. Applying equation (7) to equation (14), it is found that

$$\Omega_w = C_0 I_0(\xi r_w) + D_0 K_0(\xi r_w) \tag{15}$$

$$D_k = -C_k I_{4k}(\xi r_w)/K_{4k}(\xi r_w);\ k = 1, 2, \ldots. \tag{16}$$

The convective heat flux at the wall is given by

$$q''_{cv} = -k(\partial\Omega/\partial r)_{\text{wall}} \tag{17}$$

Substituting equation (14) into equation (17), and integrating along the wall circumference within the unit cell, one obtains

$$\int_0^{\pi/4} (\partial\Omega/\partial r)_{\text{wall}}\, r_w d\theta = \pi \xi r_w [C_0 I_1(\xi r_w) - D_0 K_1(\xi r_w)]/4 \tag{18}$$

In view of equations (8) and (9), the left hand side of equation (18) can be written as

$$\int_0^{\pi/4} (\partial\Omega/\partial r)_{\text{wall}}\, r_w d\theta = \oint \nabla_n \Omega\, dl \tag{19}$$

where dl is the differential displacement on the boundry of the unit cell; $\nabla_n \Omega$ is the normal gradient of $\Omega(r, \theta)$ along the boundary, and the integration $\oint$ is extended along the entire boundary of the unit cell in the clockwise direction. Utilizing Green's theorem and equation (1), equation (19) becomes

$$-\int_0^{\pi/4} (\partial\Omega/\partial r)_{\text{wall}}\, r_w\, d\theta = \int_0^{\pi/4} \int_{r_w}^{s/\cos\theta} (\xi^2 \Omega) r dr d\theta \tag{20}$$

Combining equations (18) and (20), and remembering equation (11) and the definition of hydraulic diameter, one easily obtains

$$\Omega_m \xi D_h/4 = -C_0 I_1(\xi r_w) + D_0 K_1(\xi r_w) \tag{21}$$

Equations (15) and (21) can readily be solved to obtain C_0 and D_0.

$$C_0 = \frac{\Omega_w K_1(\xi r_w) - \xi D_h \Omega_m K_0(\xi r_w)/4}{K_1(\xi r_w) I_0(\xi r_w) + K_0(\xi r_w) I_1(\xi r_w)} \tag{22}$$

$$D_0 = \frac{\Omega_w I_1(\xi r_w) + \xi D_h \Omega_m I_0(\xi r_w)/4}{K_1(\xi r_w) I_0(\xi r_w) + K_0(\xi r_w) I_1(\xi r_w)} \tag{23}$$

Summarizing the results obtained so far, the temperature field now reads

$$\Omega(r, \theta) = \frac{\Omega_w K_1(\xi r_w) - \xi D_h \Omega_m(\xi r_w)/4}{K_1(\xi r_w) I_0(\xi r_w) + K_0(\xi r_w) I_1(\xi r_w)} I_0(\xi r) + \frac{\Omega_w I_1(\xi r_w) + \xi D_h \Omega_m I_0(\xi r_w)/4}{K_1(\xi r_w) I_0(\xi r_w) + K_0(\xi r_w) I_1(\xi r_w)} K_0(\xi r) + \sum_{k=1}^{\infty} [I_{4k}(\xi r) - I_{4k}(\xi r_w) K_{4k}(\xi r)/K_{4k}(\xi r_w)] C_k \cos 4k\theta \tag{24}$$

The constants C_k are, of course, to be determined by the final boundary condition, equation (9). Direct differentiation of equation (24) gives, after some rearrangement, the following relations for C_k.

$$\sum_{k=1}^{\infty} C_k \{\xi [(I_{4k-1}(\xi r) - 4k I_{4k}(\xi r)/\xi r) + (I_{4k}(\xi r_w)/K_{4k}(\xi r_w)) \times (K_{4k-1}(\xi r) + 4k K_{4k}(\xi r)/\xi r)] \cos 4k\theta \cos\theta + 4k [I_{4k}(\xi r) - I_{4k}(\xi r_w) K_{4k}(\xi r)/K_{4k}(\xi r_w)] \times \sin 4k\theta \sin\theta/r\} = -C_0 \xi I_1(\xi r) \cos\theta + D_0 \xi K_1(\xi r) \cos\theta \tag{25}$$

where

$$r = s/\cos\theta$$

$$0 \le \theta \le \pi/4$$

and C_0 and D_0 are as defined in equations (22) and (23), respectively.

At this point, an approximate solution must be sought. The summation over the C_k terms is truncated after N_0 terms. Equation (25) is then applied successively at N_0 values of θ in the range $0 \le \theta \le \pi/4$. This yields N_0 linear equations from which the constants C_k ($k = 1, 2, \ldots. N_0$) can be solved. This method of collocation has been used successfully by Sparrow, et al. [3] to determine single phase laminar heat transfer coefficient in rod bundles. It will be seen later that only the first few C_k's are important and hence the method is justified.

Once the constant coefficients are completely determined, the mean vapor temperature can be obtained by direct integration of equation (24). The constant coefficients, however, are themselves functions of Ω_m (or the mean vapor temperature) as can be seen readily from equations (22, 23) and (25) (note also that ξ is a function of the mean vapor temperature). Hence, an iterative procedure must be employed; an initial guess of the mean vapor temperature is first made, and the constant coefficients are then computed by equations (22, 23) and (25). A new mean vapor temperature can then be obtained from equation (11) by direct integration and is compared with the initially assumed value. A better estimate of the mean vapor temperature can then be made and the procedure continues until convergence is achieved.

Nomenclature

A = flow area
C_p = specific heat of vapor at constant pressure
d = droplet diameter
D_h = hydraulic diameter
h = heat transfer coefficient
h_{fg} = latent heat of vaporization
k = thermal conductivity of vapor
n = droplet number density
Nu = Nusselt number
Pr = Prandtl number
q''_{cv} = convective heat flux
r = radial distance from center of fuel rod
s = pitch/2
Re_d = droplet Reynolds number
T = temperature
ϕ = volumetric radiation heat flux
θ = azimuth angular dependence

Subscripts

g, v = gas or vapor
d, l = droplet or liquid
w = wall
sat = saturation
m = mean
wl = from wall to liquid
wv = from wall to vapor
vl = from vapor to liquid

4 Heat Transfer Coefficient and Nusselt Number

The average convective heat transfer coefficient, using the mean vapor temperature as the reference temperature, can be defined as

$$h_m = (4/\pi) \int_0^{\pi/4} d\theta q''_{cv}/(\Omega_w - \Omega_m) \quad (26)$$

From equations (11, 17) and (20), h_m can readily be written as

$$h_m = k\xi^2 D_h \Omega_m / 4(\Omega_w - \Omega_m) \quad (27)$$

Or using the saturation liquid temperature as the reference temperature, one has

$$h_{sat} = k\xi^2 D_h \Omega_m / 4(\Omega_w - \Omega_{sat}) \quad (28)$$

Using the hydraulic diameter as the characteristic dimension, the corresponding Nusselt Numbers are

$$Nu_m = (\xi D_h)^2 \Omega_m / 4(\Omega_w - \Omega_m) \quad (29)$$

$$Nu_{sat} = (\xi D_h)^2 \Omega_m / 4(\Omega_w - \Omega_{sat}) \quad (30)$$

It is worthwhile to note that the dependence of the heat transfer coefficients and Nusselt numbers on the mean vapor temperature that appears explicitly in the numerators of equations (27–30) is a result of the convective heat exchange between the super-heated vapor and water droplets, and is not found in single phase flow heat transfer. The droplets serving as an additional heat sink in dispersed flow has already been discussed by previous authors (e.g., reference [1]).

5 Equivalent Hydraulic Diameter Formulation

The angular dependence, θ, in equation (1) has been neglected by Sun, et al. [1], and the resulting equation was solved for pipe flow with the same hydraulic diameter.

$$(1/r)d(rd\Omega/dr)/dr = \xi^2 \Omega \quad (31)$$

The boundary conditions are

$$\Omega = \Omega_w \quad \text{at} \quad r = D_h/2 \quad (32)$$

$$d\Omega/dr = 0 \quad \text{at} \quad r = 0 \quad (33)$$

The solution for (31) satisfying (32) and (33) is simply

$$\Omega = \Omega_w I_0(\xi r)/I_0(\xi D_h/2) \quad (34)$$

The mean vapor temperature can be obtained by direct integration

$$\Omega_m = 4\Omega_m I_1(\xi D_h/2)/\xi D_h I_0(\xi D_h/2) \quad (35)$$

The expressions for the heat transfer coefficients and Nusselt numbers are the same as equations (27–30).

6 Equivalent Annulus Formulation

Another approximation for the rod bundle geometry is the equivalent annulus concept. The inner radius of the annulus is simply the fuel rod radius, r_w. The outer radius, r^*, is such that the flow area between the annulus is identical to that in the actual configuration.

$$\pi(r^{*2} - r_w{}^2) = 8A \quad (36)$$

where A is as defined in equation (12).

Again the angular dependence of the temperature field is suppressed, and Ω obeys the same equation as for pipe flow (equation (31)). The boundary conditions are

$$\Omega = \Omega_w \quad \text{at} \quad r = r_w \quad (37)$$

$$d\Omega/dr = 0 \quad \text{at} \quad r = r^* \quad (38)$$

The solution for $\Omega(r)$ satisfying the above boundary conditions is

$$\frac{\Omega(r)}{\Omega_w} = \frac{I_0(\xi r)}{[I_0(\xi r_w) + I_1(\xi r^*)K_0(\xi r_w)/K_1(\xi r^*)]} + \frac{K_0(\xi r)}{[I_0(\xi r_w)K_1(\xi r^*)/I_1(\xi r^*) + K_0(\xi r_w)]} \quad (39)$$

The mean temperature is again obtained by direct integration:

$$\Omega_m = \frac{\Omega_w}{\pi\xi(r^{*2} - r_w{}^2)} \left\{ \frac{r^* I_1(\xi r^*) - r_w I_1(\xi r_w)}{[I_0(\xi r_w) + I_1(\xi r^*)K_0(\xi r_w)/K_1(\xi r^*)]} - \frac{r^* K_1(\xi r^*) - r_w K_1(\xi r_w)}{[I_0(\xi r_w)K_1(\xi r^*)/I_1(\xi r^*) + K_0(\xi r_w)]} \right\} \quad (40)$$

The expressions for the heat transfer coefficients and Nusselt numbers are the same as in equations (27–30). Also, because of the close resemblance in geometric configurations and boundary conditions, one expects that the equivalent annulus formulation is a good approximation for rod bundles when the variation of heat flux around the rod periphery can be neglected.

7 Input Data for Calculations

Typical PWR (pressurized water reactor) reflood data obtained from the Full-Length-Emergency-Cooling-Heat-Transfer (FLECHT) program is used for the present analysis. A complete set of data which is required for the calculations is

Fuel rod diameter	= 0.035 ft (0.01067 m)
Pitch-to-diameter ratio	= 1.3
System pressure	= 40 psia (2.8×10^5 Pa)
Wall temperature	= 1500°F (815.6°C)
Droplet mass flux	= 2 lbm/s-ft^2 (9.8 Kg/m^2-s)
Droplet diameter	= 0.002 ft (0.6 mm)
Droplet velocity	= 30 ft/s (9.1 m/s)
Vapor velocity	= 45 ft/s (13.7 m/s)

The numerical values cited above are typical of PWR reflood [4], and will be used throughout the present analysis. When studying the effect of geometry on heat transfer, the pitch to diameter ratio is varied from 1.01 to 2.0 while keeping all other parameters constant.

8 Results and Discussions

1 Errors due to Truncation of the Series Solution. Table 1 shows the results of truncating the series solution (equation (14)) after 2, 4, 6 and 8 terms, respectively. The series solution converges very rapidly, and satisfactory overall heat transfer results are obtained even only the first two terms (i.e., $N_0 = 2$) of the series are retained. In the remainder of this section, all results are presented with N_0 equal to 6.

2 Peripheral Variation of Wall Heat Flux. The peripheral variation of wall heat flux for different pitch-to-diameter ratios (PDR) is shown in Fig. 2. The location of minimum heat flux occurs at θ = 0 deg; hence, if the wall heat flux were prescribed to be constant while allowing the wall temperature to vary, the hot spot would occur at θ = 0 deg. Also, note that the peripheral variation of wall heat flux diminishes very rapidly as the PDR increases, and can practically be ignored for a PDR of 1.5 or greater. Hence, at high PDR (1.5 or greater), one expects that constant wall temperature and heat flux are simultaneously achieved and the equivalent annulus formulation is a good approximation for square rod bundles.

Table 1 Errors due to truncation of series solution

	No 2	No 4	No 6	No 8
T_m (°C)	619.8	620.1	620.1	620.1
h_m (watt/m^2-°C)	96.77	97.08	97.09	97.09
Nu_m	14.26	14.30	14.30	14.30
h_{sat} (watt/m^2-°C)	27.66	27.71	27.71	27.71
Nu_{sat}	4.075	4.081	4.081	4.081
C_0	27.56	27.49	27.49	27.49
$D_0 \times 10^{-6}$	2.203	2.205	2.205	2.205
$C_1 \times 10^{-2}$	1.549	1.530	1.530	1.530
$C_2 \times 10^{-3}$	3.127	3.569	3.593	3.593
$C_3 \times 10^{-5}$	0	1.952	1.958	1.953
$C_4 \times 10^{-7}$	0	−4.744	−17.47	−16.83
$C_5 \times 10^{-13}$	0	0	−8.280	−8.330
$C_6 \times 10^{-15}$	0	0	−3.344	−5.186
$C_7 \times 10^{-21}$	0	0	0	−5.620
$C_8 \times 10^{-24}$	0	0	0	−1.097

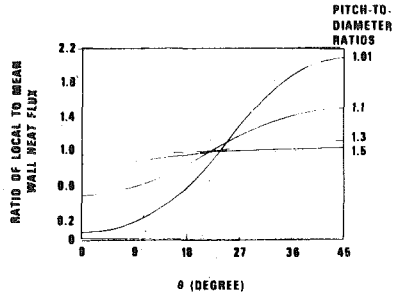

Fig. 2 Peripheral variation of heat flux for different pitch-to-diameter ratios

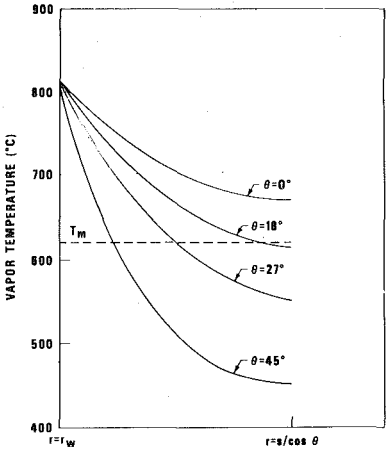

Fig. 3 Radial vapor temperature distributions for different values of θ

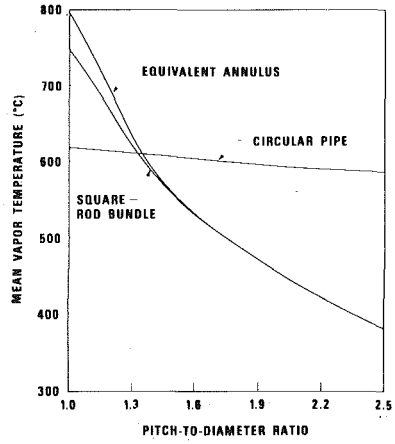

Fig. 4 Variation of mean vapor temperature with pitch-to-diameter ratio for various geometries

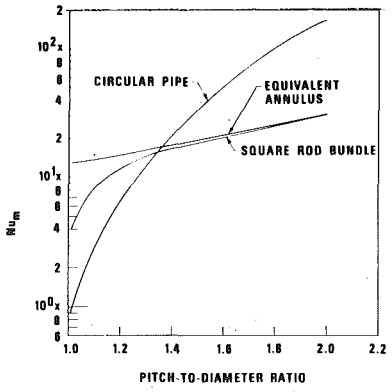

Fig. 5 Variation of Nu_m with pitch-to-diameter ratio for various geometries

3 **Radial Vapor Temperature Distribution.** The radial vapor temperature distributions for different values of θ are shown in Fig. 3. Comparing Fig. 2 with Fig. 3, one sees that a higher (lower) local heat flux corresponds to a lower (higher) local vapor temperature. This is in accord with intuition as a lower local vapor temperature implies a higher driving force ($T_w - T_v$) for convection between the wall and vapor, and hence, a better local heat transfer.

4 **Variation of Mean Vapor Temperature with Geometry.** Figure 4 shows the variations of the mean vapor temperature with PDR (or equivalently, the hydraulic diameter) for all three geometries being studied (square rod bundles, annulus and circular tube). The mean vapor temperature decreases as the PDR increases, and the mean vapor temperature for square rod bundles and annulus become practically identical when the PDR is 1.5 or greater. The variation of mean vapor temperature with PDR for pipe flow is relatively insensitive when compared to the other two geometries. Since the overall heat transfer is a function of the mean vapor temperature (see equations (27–30)), the heat transfer characteristics for dispersed flow in pipes behave differently from square rod bundles or annulus. It also suggests that the use of the hydraulic diameter concept as an approximation to rod bundle geometry is only valid for a small range of PDR (around 1.3).

5 **Variation of Nusselt Number with Geometry.** The Nusselt numbers (Nu_m and Nu_{sat}) increase monotonically with increasing PDR for all three geometries as shown in Figs. 5 and 6. Because of the different variations of the mean vapor temperature for these geometries (Fig. 4), the Nusselt number for pipe flow, depending on the PDR, can be quite different from the other two geometries.

Extensive experiments had been conducted with circular tubes in order to obtain the dispersed flow heat transfer coefficients (or Nusselt number). The results of the present analysis show that the hydraulic diameter concept is not necessarily a good approximation to rod bundle geometries over a wide range of PDR. One should not, therefore, apply results obtained from circular pipes to rod bundles unless the PDR is about 1.3. Fortunately, the pitch-to-diameter ratio of present day light water reactor fuel assemblies is about 1.3; Figs. 4–6 seem to indicate that the results of all three geometries converge at this pitch-to-diameter ratio. The present results also suggest that an annulus is a much better approximation to rod bundles than circular pipes.

9 Conclusions

1 The heat transfer coefficient for dispersed flow has an explicit dependence on the mean vapor temperature which is not present in single-phase flow heat transfer.

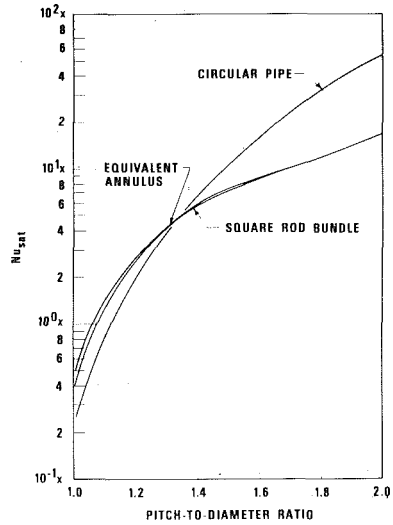

Fig. 6 Variation of Nu_{sat} with pitch-to-diameter ratio for various geometries

2 The variation of mean vapor temperature with hydraulic diameter can be different for pipe and rod bundle geometry. Within the framework of the present analysis, the equivalent hydraulic diameter concept is an unsatisfactory approximation for rod bundle geometries except for a PDR of about 1.3.

3 The equivalent annulus concept, on the other hand, is a good approximation to square rod bundle geometry when the pitch-to-diameter ratio is large (1.5 or greater under the conditions studied in the present analysis).

References

1 Sun, K. H., Gonzalez-Santalo, J. M., Tien, C. L., "Calculations of Combined Radiation and Convection Heat Transfer in Rod Bundles Under Emergency Cooling Conditions," ASME JOURNAL OF HEAT TRANSFER, Vol. 98, 1976, pp. 414–420.

2 Lee, K., Ryley, D. J., "The Evaporation of Water Droplets in Superheated Steam," ASME JOURNAL OF HEAT TRANSFER, Vol. 90, 1968, pp. 445–451.

3 Sparrow, E. M., Loeffler, Jr., A. L., Hubbard, H. A., "Heat Transfer to Longitudinal Laminar Flow Between Cylinders," ASME JOURNAL OF HEAT TRANSFER, 1961, pp. 415–422.

4 Lilly, G. P., Yeh, H. C., Dodge, C. E., Wong, S., "PWR FLECHT Skewed Profile Low Flooding Rate Test Series Evaluation Report," WCAP-9183, Nov. 1977.

K. Hishida
Graduate Student.

M. Maeda
Associate Professor.

S. Ikai
Professor.

Department of Mechanical Engineering,
Keio University,
3-14-1 Hiyoshi,
Kohoku-ku Yokohama 223, Japan

Heat Transfer from a Flat Plate in Two-Component Mist Flow

An experimental study concerning the characteristics of heat transfer from a dry isothermal flat plate in two-component (water-air) mist flow has been performed for lower water-air mass flow ratios up to 2.3 percent. Heat transfer coefficients in mist flow increase several times corresponding to single phase coefficients with increasing mass flow ratio and free stream velocity, and with decreasing wall temperature. The measurements of droplet velocity employing laser Doppler anemometry indicate the similarity of velocity distributions in boundary layer of mist flow, which approximately fit the laminar single phase one. It is confirmed that an augmentation of heat transfer is attributable to a latent heat due to evaporation of water droplets within the boundary layer, and that, at a constant Reynolds number and wall temperature, the enhanced rates of heat transfer coefficients are linearly correlated to water mass flow rates for unit cross-sectional area.

Introduction

Recently, numerous techniques of augmenting heat transfer have been developed in designing a compact heat exchanger for effective utilization of thermal energy. Suspending small amounts of liquid droplets in cooling gas medium has been considered as one of these techniques that can realize a remarkable enhancement of heat transfer rates from a hot solid surface by utilizing a latent heat due to evaporation of liquid phase. A knowledge of heat transfer characteristics in two-phase flow is demanded in a number of industrial applications such as steam evaporators, spray coolers, and atomization and combustion devices of liquid fuel.

A heat transfer in mist flow involving fine liquid particles can fit one of two cases, depending on the presence or absence of a liquid film on the heating surface. In the first case, realized at a lower wall temperature and in flow fields over bluff body, the boundary layer is composed of two regions, i.e., an inner liquid layer on the solid surface and an outer two-phase layer. Several investigations [1–8] have been performed experimentally and analytically on heat transfer of circular cylinder submerged in a mist flow, confirming a high potential for increasing heat transfer. Thomas and Sunderland [9], and Aihara et al. [10] studied the heat transfer from a wedge-shaped body exposed to a binary mist flow. Their reports have indicated an enhancement of heat transfer as high as 10–30 times compared with single phase flow. The second case, where the liquid film is not formed on the heating surface, is realized under the condition that liquid droplets evaporate before reaching the surface at higher temperature and/or instantaneously upon deposition on the hot surface. Heyt and Larsen [11] studied a forced convective binary mist flow over a dry isothermal heated surface, and discussed analytically the effect of particle presence and evaporation on boundary layer structure for the case of dilute concentration of fine particles less than 3 μm dia. Bhatti and Savery [12] reported on a theory developed for the restricted regime of a two-phase flow wherein droplets suspended in gas stream penetrate the boundary layer and vaporized without deposition. A similar mechanism in two-phase flow has been studied in the determination of dryout or burnout condition of heat transfer in the presence of dry wall for various internal flow regions [13, 14].

In spite of a number of published papers on experimental and theoretical studies of heat transfer concerned with circular or wedge-shaped bodies and a flat plate, the mechanism of heat transfer within two-phase boundary layer has remained unexplored, since the dispersed phase locally exchanges momentum, energy and mass with the continuous phase. Therefore, the present investigation makes an experimental study on heat transfer from an isothermal flat plate without liquid film on the heating surface in a two-component (water-air) mist flow, in order to find out basic correlations among various factors such as water-air mass flow ratio, heating wall temperature, and free stream velocity, with a view to helping the understanding of heat transfer characteristics in mist flow.

Experimental Apparatus and Procedure

Flow System. The experimental flow system consists of an air-suction type wind tunnel for minimizing a free stream turbulence, as is shown schematically in Fig. 1. The duct flow through the test section was set in the gravitational direction in order to prevent the accumulation of liquid droplets and the discordance between gas stream and droplet trajectory due to the effect of gravity on droplets. Air was sucked out of the room and mixed with liquid droplets in the settling duct ③. Pure water obtained from the ion-exchanger was atomized by four atomizing nozzles (DELAVAN, Type W 0.65 GPH) located within the settling duct, and then the contraction nozzle ④ made uniform the velocity distribution of water-air mist flow into the test section ⑦ which had a cross section of 150 mm × 100 mm and a length of 300 mm. The wall of the test section was made of a transparent acrylic plastic. The loading of water droplets was controlled by adjusting the distance from atomizing nozzles to the water mass flow controller ② which consisted of four cone-shaped collecting cups

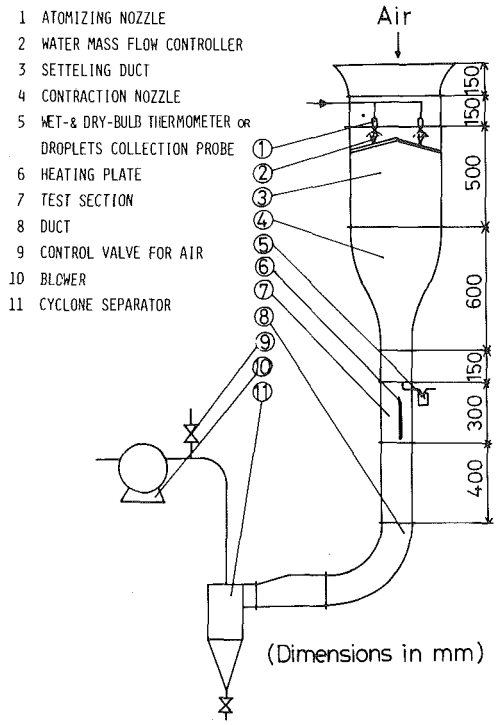

Fig. 1 Experimental flow system

Contributed by the Heat Transfer Division for publication in the JOURNAL OF HEAT TRANSFER. Manuscript received by the Heat Transfer Division February 6, 1980.

placed just below each atomizing nozzle. This method provided a constant distribution of droplet sizes independent of water-air mass flow ratio. The most difficult experimental problem was encountered in production of a water-air mist flow with uniform concentration over the cross section. In the present study, experiments were carried out under the condition that the maximum variation of the horizontal distribution over the heating plate was less than ±10 percent based on the overall average value.

Heating Plate. Figure 2 shows the construction of the heating plate. The leading edge ⑧ was made of a porous metal and connected to the top of the heating plate, in order to eliminate the accumulated liquid droplets which disturbed the flow field of the edge tip. The main heater ⑪, which had the bakelite surface plated with nickel for electrical heating, was divided into 14 sections, each connected to copper terminals. The nickel plated auxiliary heater ⑥, divided into four sections, was insulated just below each copper plate ③ of 0.5 mm thickness which provided a uniform temperature in the heating plate to reduce the backward heat loss from the main heater. Temperatures of main and auxiliary heaters were measured by copper/constantan thermocouples of 80 μm in diameter ⑩ whose coupling points were buried about 0.1 mm under the main heater surface and on the copper plate, respectively. Two thermocouples were set at both sides 2 mm apart from the edge of each heating surface to measure the sideward heat loss. Electric power supply to these sections was so controlled as to make an isothermal surface. Plate temperatures were set at from 50 to 80°C which maintained the accuracy, avoiding influence of natural convection and radiation. The variation of temperatures between main and auxiliary heaters was set at less than ±0.1°C. The output from any thermocouple could be read by a digital volt meter to the order of 1 μV. The heater power was obtained by the supplied voltage and amperage to each section. Heat transfer coefficients were evaluated from the local heat flux and the temperature difference between the heater and the free stream. The resultant accuracy of heat transfer coefficients was likely to be within 5 percent, taking into account the uncertainty in measurements of the heater and free stream temperatures and other factors.

Measurements of Wet and Dry-Bulb Temperatures and Droplet Mass Flow Rate. The gas phase temperature of water-air mist flow was measured by a wet- and dry-bulb thermometer which was located just over the leading edge of heating plate at position ⑤ in Fig. 1. After separating droplets from water-air mixture by a compact cyclone, the dry-bulb temperature of air was measured by a copper/constantan thermocouple of 80 μm in diameter and the wet-bulb temperature was measured by a thermocouple which was imbedded in a copper sphere (2 mm in diameter) covered with a saturated wick.

The droplet mass flow rate was measured by isokinetic sampling, and a collecting probe was set in place of the wet- and dry-bulb thermometer. The collected water was weighed by a chemical balance to the order of 1 mg.

Droplet Size and Velocity Measurement. The droplet size was measured by the immersion sampling technique in which water droplets were collected in a solvent medium of silicon, photographed at high magnification, and then counted and classified from the pictures. Examples of droplet size distribution, sampled just over the heating plate, are shown in Fig. 3. Δn is the number of droplets counted by a step of 5 μm in diameter. The total number counted, n, is over 700. Throughout the experiments, the droplet size distributions were constant, and droplets were from 34 to 38 μm in arithmetic mean diameter and from 52 to 60 μm in volume-surface mean diameter.

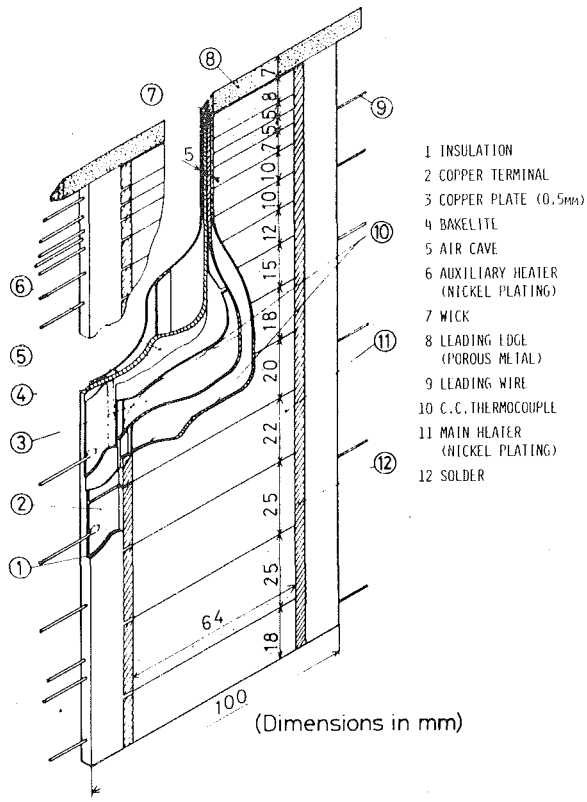

Fig. 2 Heating plate

A laser Doppler anemometer, operated in the forward scattering fringe mode, was employed for the measurement of droplet velocity, whose signal processing was modified for measuring the velocity of a larger particle. The mean relative velocity between air and droplets was evaluated by subtracting the gas phase velocity measured by a pitot tube in the absence of water droplets from the mean droplet velocity.

Results and Discussions

Heat Transfer to Single Phase Flow. In the present flow system, the turbulence intensity in the free stream measured by hot wire anemometry was less than 1.0 percent in the range of air velocities from 5.4 m/s to 9.8 m/s. Typical distributions of air velocities over the heating plate for single phase flow measured by hot wire anemometry are shown in Fig. 4, and compared with Blasius' solution for incompressible laminar boundary layer. The results almost agree with Blasius' solution.

The measured heat transfer coefficients to single phase flow are

Nomenclature

C_w = specific heat of water, KJ/kg K
d = droplet diameter, μm
$\overline{d}$ = arithmetic mean diameter of droplets, μm
h_m = heat transfer coefficient to mist flow, W/m^2 K
h_0 = heat transfer coefficient to single phase flow, W/m^2 K
M = water-air mass flow ratio, $= \dot{m}/\dot{m}_a$
$\dot{m}$ = water mass flow rate for unit cross-sectional area, kg/m^2 s
$\dot{m}_a$ = air mass flow rate for unit cross-sectional area, kg/m^2 s
Nu_x = Nusselt number, $= h_0 x/\lambda$
q_x = local heat flux, W/m^2
Re_x = Reynolds number, $= \overline{U}_{g\infty} x/\nu$
r_w = latent heat due to evaporation of water, KJ/kg
$t_{gd\infty}$, $t_{gw\infty}$ = dry- and wet-bulb temperatures of gas phase of mist in free stream, °C
t_v = temperature of vaporizing droplets, °C
t_w = wall temperature of heating plate, °C
$\overline{U}_d$ = droplet velocity in boundary layer, m/s
$\overline{U}_g$, $\overline{U}_{g\infty}$ = gas velocities in boundary layer and in free stream, m/s
x = axial coordinate along the plate, m
x_0 = unheated length from leading edge, m
y = transverse length normal to the plate, m
$\Delta t = t_w - t_{gd\infty}$, K
$\eta = y\sqrt{\overline{U}_{g\infty}/x\nu}$
λ = thermal conductivity of air, W/mK
ν = kinematic viscosity of air, m^2/s

plotted in Fig. 5 in terms of local Nusselt number Nu_x to Reynolds number Re_x, as a parameter of free stream velocity and wall temperature. The properties of the fluid are evaluated at the reference temperature defined by the arithmetic mean value of wall and free stream temperatures. The theoretical solution of heat transfer along a flat plate at zero incidence with unheated section of x_0 from the leading edge is expressed as

$$Nu_x = 0.332\,Pr^{1/3}\,Re_x^{1/2}(1-(x_0/x)^{3/4})^{-1/3} \quad (1)$$

The experimental results to single phase flow are in good accordance with the theoretical solution, independent of wall temperature. The error due to radiation and natural convection caused by a temperature difference can be neglected for forced convective heat transfer, the maximum estimated error relative to heat flux q_x being about 2.5 percent.

Heat Transfer to Two-Component Mist Flow. The heat transfer to a two-component mist flow was examined in the range of free stream velocities from 5.4 m/s to 9.8 m/s, water-air mass flow ratios from 0 to 2.3 percent, the wall temperatures of the isothermal heating plate from 50 to 80°C, the dry and wet-bulb temperatures in free stream from 18 to 24°C and from 15 to 20°C, respectively, and the relative humidities of air phase in mist flow from 75 to 88 percent.

The mean relative velocity between air and droplets in free stream was from 0.03 to 0.07 m/s. The terminal velocities of droplets with 34–38 μm in arithmetic mean diameter are calculated to range from 0.032 to 0.038 m/s by Stokes drag law. It is, therefore, considered that droplets in free stream have ceased to accelerate. Distributions of the droplet velocities over the plate, evaluated from more than 500 samples of droplet velocity, are shown in Fig. 6, and compared with the solution of Blasius for laminar single phase flow. As the air velocity near the wall is smaller, the droplet velocity becomes correspondingly smaller. The droplet velocity profiles near the wall in boundary layer are a little higher than the Blasius' profile. This phenomenon is considered to be caused by the inertia of droplets carried from free stream into the boundary layer. The distribution of droplet velocities approximately fits with Blasius' solution, unaffected by variations of wall temperature, water-air mass flow ratio and free stream velocity. This result indicates the similarity of velocity distributions in a boundary layer of a two-component mist flow involving fine droplets from 34 to 38 μm in arithmetic mean diameter, and confirms that the presence of water droplets in dilute concentration hardly induces a turbulence in boundary layer, as pointed out by Maeda, et al. [15] who reported that the addition of glass particles of 55 μm to a low turbulence boundary layer over a flat plate increased the turbulence intensity with mass flow ratio, increasing about three times at mass flow ratio $M = 1.0$ but was hardly influenced up to $M = 0.2$. Thus, the influence of turbulence in the presence of liquid droplets hardly enhances heat transfer, since the mass flow ratio is less than 2.3 percent (= 0.023) in this experiment.

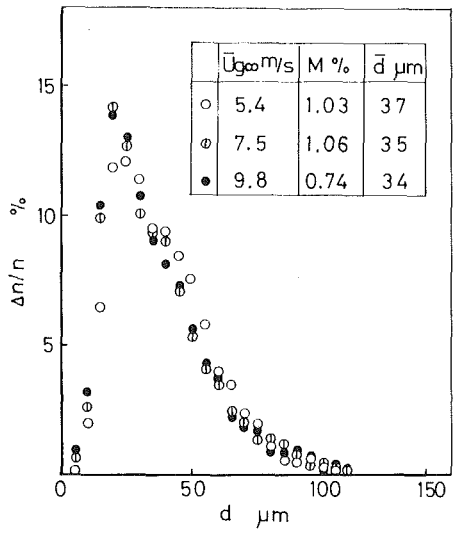

Fig. 3 Droplet size distribution

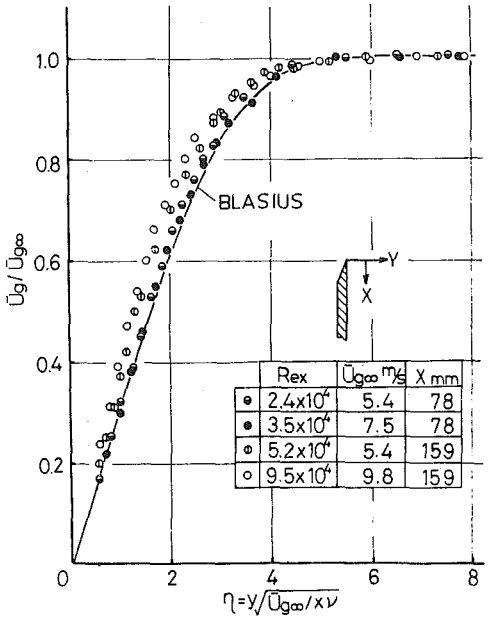

Fig. 4 Distribution of air velocities over a plate

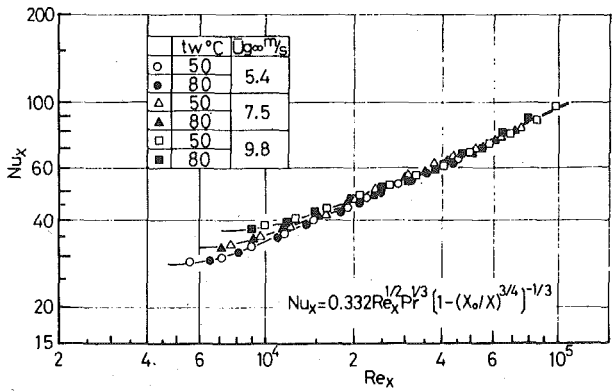

Fig. 5 Local heat transfer in single phase flow

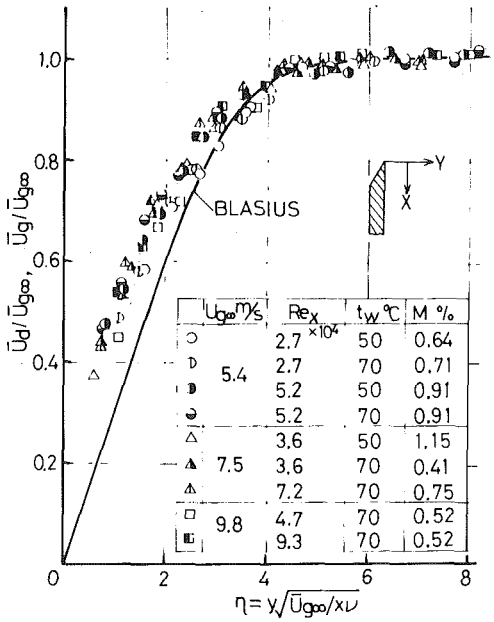

Fig. 6 Distribution of droplet velocities over a plate

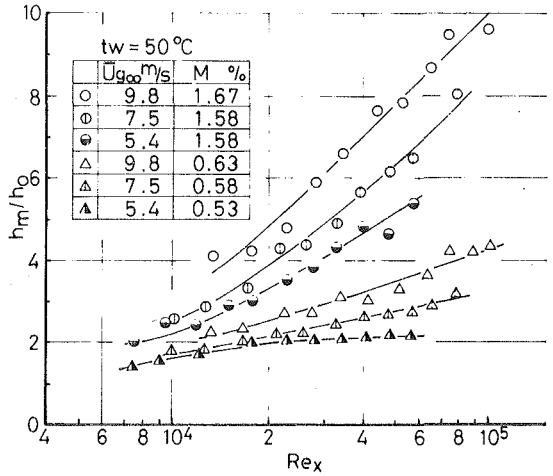

Fig. 7(*a*) Local heat transfer ratio in mist flow at t_w = 50°C

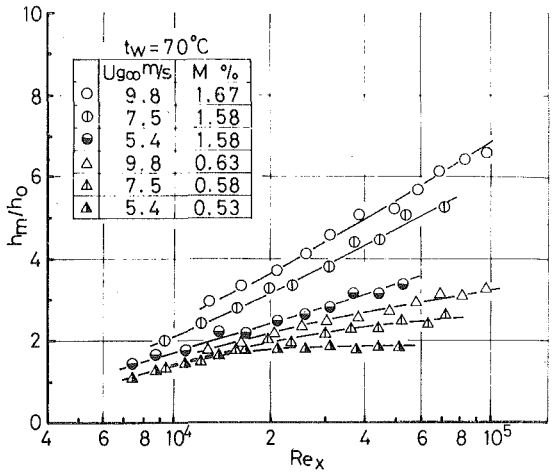

Fig. 7(*b*) Local heat transfer ratio in mist flow at t_w = 70°C

The local heat transfer coefficient h_m in two-component mist flow is defined as

$$h_m = q_x/(t_w - t_{gd\infty}) \tag{2}$$

where $t_{gd\infty}$ is a dry-bulb temperature of mist flow in free stream and q_x is a local heat flux. Typical local heat transfer data for ratio h_m/h_0 are given for Reynolds number Re_x in Figs. 7 (*a*) and (*b*). It is shown, as a general tendency, that the local heat transfer ratio increases with an increase in water-air mass flow ratio M, free stream velocity and/or Reynolds number, and with a decrease in wall temperature. The profile of local heat transfer ratio along the plate is affected by wall temperature even for a constant water-air mass flow ratio and a constant free stream velocity, as shown in Fig. 8. The local heat transfer ratio h_m/h_0 increases linearly with log Reynolds numbers Re_x at a lower wall temperature such as t_w = 50°C, and approaches a constant value with an increasing wall temperature such as t_w = 70, 80°C at higher Reynolds numbers, i.e., at the trailing parts of the plate for a constant free stream velocity. The tendency of the slope settling to a constant value of local heat transfer ratio at each velocity appears at low mass flow ratios and high wall temperatures. At a low mass flow ratio, as indicated by symbol ▲ in Fig. 7 (*a*) and symbols ▲ and ▲ in Fig. 7 (*b*), the tendency of the slope approaching a constant value of heat transfer ratio is recognized at a higher wall temperature for the condition of a higher free stream velocity. At a higher mass flow ratio, the rate of increase in heat transfer ratio with Reynolds number becomes larger at higher free stream velocity and lower wall temperature. These results indicate that an effective augmentation of heat transfer by adding small amounts of water droplets occurs at the trailing part of the plate, and the wall temperature becomes a very significant factor in heat transfer process of the system.

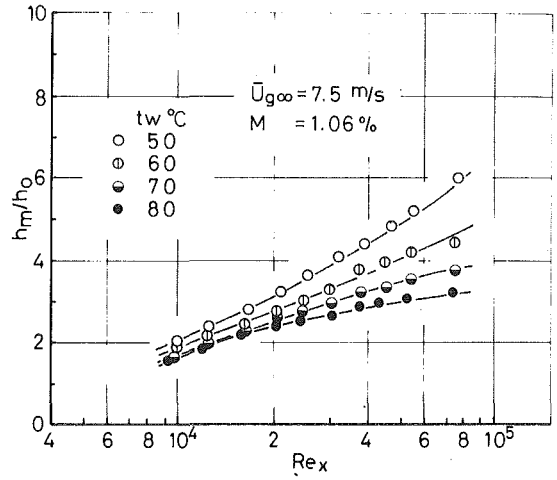

Fig. 8 Local heat transfer ratio in mist flow, $\bar{U}_{g\infty}$ = 7.5 m/s, M = 1.06 percent

Figure 9 shows the relation between heat transfer ratio and water-air mass flow ratio with Reynolds number set constant at $Re_x = 4.0 \times 10^4$, based on the similarity of velocity distributions for each phase in boundary layer of mist flow. However, the rate of enhancement in heat transfer ratio with mass flow ratio is positively affected by free stream velocity, and increases at higher free stream velocity and lower wall temperature.

In the range of mass flow ratios examined in this experiment, heat transfer coefficients are linearly enhanced with water-air mass flow ratio, as indicated in Fig. 9. Thus, evaporation of water droplets contributes at a certain rate to the quantity of droplets which penetrate the thermal boundary layer, and the augmentation of heat transfer is attributed to a latent heat due to evaporation of droplets which penetrate the boundary layer and/or deposit on the heating surface. The value of latent heat is determined by the total quantity of evaporating water droplets near and on the heating surface. An increase in the number of droplets in free stream has a high potential of enhancing heat transfer from a hot wall as a result of increasing water droplets which penetrate the boundary layer and deposit on the surface. The quantity of water droplets, which do not cease to

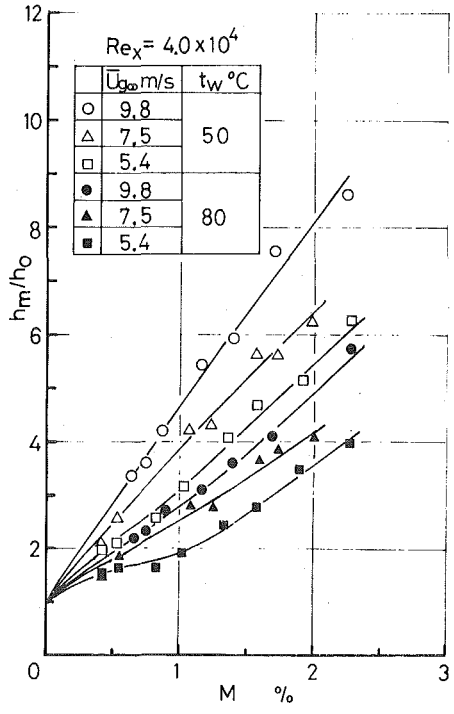

Fig. 9 Heat transfer ratio versus water-air mass flow ratio

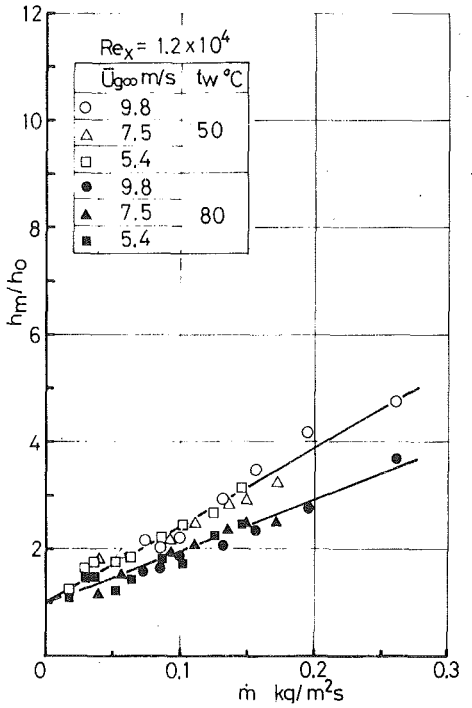

Fig. 10(*a*) Heat transfer ratio versus water mass flow rate at $Re_x = 1.2 \times 10^4$

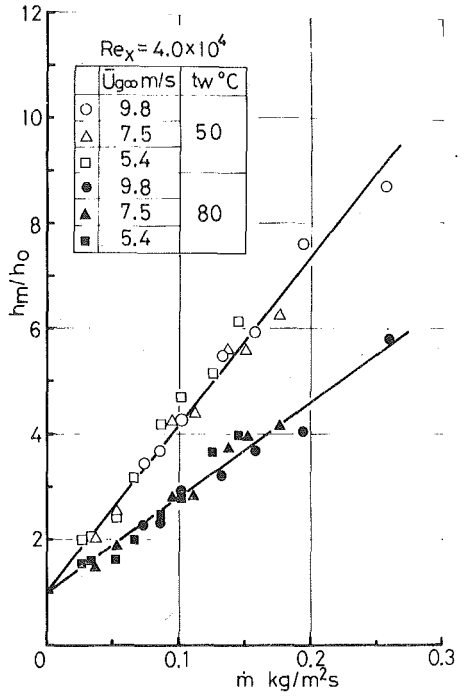

Fig. 10(*b*) Heat transfer ratio versus water mass flow rate at $Re_x = 4.0 \times 10^4$

evaporate and flow downstream, is considered to increase at low wall temperature and high free stream velocity, compared with that at high wall temperature and low free stream velocity. Consequently, the rate of enhancement in heat transfer ratio in mist flow increases in the trailing part of plate at lower wall temperature and higher free stream velocity.

Number densities of suspended droplets are identical for a constant mass flow ratio, but total number of droplets passing unit cross sectional area per unit time changes at different flow velocities. It is considered that the enhanced rate of heat transfer coefficient due to latent heat is determined by the total quantity of evaporating droplets, which depend on the quantity of droplets flowing per unit time in the boundary layer. Therefore, heat transfer ratio is correlated with water mass flow rate $\dot{m}$ instead of mass flow ratio, as indicated in Fig. 10. Linear correlation holds between h_m/h_0 and $\dot{m}$ for a constant Reynolds number and a constant wall temperature. The rate of enhancement in heat transfer ratio to water mass flow rate increases with a lowering wall temperature and with an increasing Reynolds number. Thus, the rate of evaporating water droplets in boundary layer which contributes to the enhanced rate of heat transfer is proportional to water mass flow rate.

Liquid film on the heating surface was not observed in this experimental condition. The following simple superposition model may be considered to simulate the heat transfer process in mist flow under the condition that liquid droplets evaporate before reaching the heating surface and/or vaporize instantaneously upon deposition; local heat flux to mist flow q_m could be evaluated by summing up local convective heat flux to air phase q_a, sensible heat of liquid q_s, and latent heat due to evaporation of liquid q_ℓ, and expressed as

$$q_m = q_a + q_s + q_\ell$$

$$q_a = h_0(t_w - t_{gd\infty}) = h_0\Delta t, \quad q_s \simeq \dot{m}_{ev}C_w(t_v - t_{gw\infty}), \qquad (3)$$

$$q_\ell = \dot{m}_{ev}r_w$$

where $\dot{m}_{ev}$ is an evaporating rate of liquid within boundary layer; q_a is evaluated from heat transfer coefficients to single phase flow h_0, since an enhancement of heat transfer due to turbulence induced by presence of particles is neglected at lower mass flow ratio; and t_v is taken as t_w so that wall temperature is lower than boiling point of water. Equation (3) is then reduced to

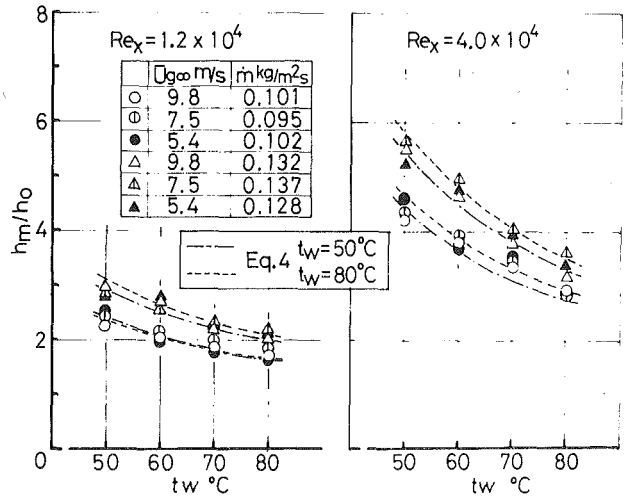

Fig. 11 Heat transfer ratio versus wall temperature

$$\frac{h_m}{h_0} = 1 + \frac{\dot{m}_{ev}}{h_0\Delta t}(r_w + C_w\Delta t') \qquad (4)$$

where $\Delta t' = t_w - t_{gw\infty}$. It has been very difficult to evaluate $\dot{m}_{ev}$ for lack of any previous detailed analysis of droplets behavior in boundary layer of mist flow. In order to compare the tendency of heat transfer estimated by equation (4) with experimental data, equation (4) is evaluated from $\dot{m}_{ev}$ calculated using mean values of experimental data at $t_w = 50$ and 80°C, respectively; i.e., heat transfer ratio h_m/h_0 to wall temperatures is predicted, based on experimental data at a certain wall temperature. Comparison of prediction with experimental data is made in Fig. 11 where heat transfer ratio is plotted against wall temperature for a constant water mass flow rate. A decrease in the heat transfer ratio with an increase in wall temperature becomes remarkable for larger Reynolds numbers. This tendency is explained by equation (4), but equation (4) calculated from the data at high wall temperature gives a little higher value than experimental data at low wall temperature, because $\dot{m}_{ev}$ is slightly changed by a variation in wall temperature. It is confirmed from the result that the enhanced

heat transfer in a two-component mist flow with dilute concentration contributes to a latent heat due to an evaporation of liquid droplets within boundary layer.

Concluding Remarks

An experimental study has been carried out concerning the heat transfer from a vertical isothermal flat plate to a two-component (water-air) mist flow containing water droplets of 34–38 μm in arithmetic mean diameter, for water-air mass flow ratios up to 2.3 percent, in the range of free stream velocities from 5.4 to 9.8 m/s and wall temperature of heating plate from 50 to 80°C. Conclusions reached from the study are as follows.

Heat transfer coefficients in mist flow increase to several times the corresponding single phase coefficients with an increase in mass flow ratio and/or in free stream velocity, and with a decrease in wall temperature. The profiles of local heat transfer ratio along the plate are affected by wall temperature and the rate of enhancement in heat transfer with Reynolds number becomes larger at lower wall temperature.

The measurements of droplet velocity employing laser Doppler anemometry indicate the similarity of velocity distributions in boundary layer of mist flow, unaffected by wall temperature, water-air mass flow ratio and free stream velocity. The velocity distribution of mist flow approximately fits Blasius' solution for laminar single phase flow.

At a fixed Reynolds number and wall temperature, the enhanced rates of heat transfer are linearly correlated to water mass flow rate passing per unit cross-sectional area. It is confirmed that an augmentation of heat transfer in mist flow is attributed to latent heat due to an evaporation of water droplets within the boundary layer, and that the rate of evaporating water droplets which contributes to the enhanced rate of heat transfer is proportional to water mass flow rate. Heat transfer characteristics such as a decrease of heat transfer coefficient with an increasing wall temperature are explained by a simple superposition model of convective heat transfer to gas phase, sensible heating of liquid and latent heating due to an evaporation of liquid.

Acknowledgment

The authors would like to acknowledge Messrs S. Hirose, H. Terada, T. Ohkoshi, and S. Gotoh for their assistance in performing the experiment.

References

1 Acrivos, A., Ahern, J. E. and Nagy, A. R., "Research Investigation of Two-Component Heat Transfer," The Marquart Corporation, ARL 64-1161, Wright-Patterson AFB 1964.

2 Tifford, A. N., "Exploratory Investigation of Laminar Boundary Layer Heat Transfer Characteristics of Gas Liquid-Spray Systems," ARL 64-136 1964.

3 Smith, J. E., "Heat Transfer Studies of Water-Spray Flows," ARL 66-0091, 1966.

4 Goldstein, M. E., Yang, W. J., and Clark, J. A., "Momentum and Heat Transfer in Laminar Flow of Gas with Liquid Droplet Suspension over a Circular Cylinder," ASME JOURNAL OF HEAT TRANSFER, Vol. 89, No. 2, 1967, pp. 185–194.

5 Hodgson, J. W., Saterbak, R. T., and Sunderland, J. E., "An Experimental Investigation of Heat Transfer from a Spray Cooled Isothermal Cylinder," ASME JOURNAL OF HEAT TRANFER, Vol. 90, No. 3, 1968, pp. 457–463.

6 Mednik, R. L., and Colver, C. P., "Heat Transfer from a Cylinder in an Air-Water Spray Flow Stream," *AIChE Journal*, Vol. 15, No. 3, 1969, pp. 357–362.

7 Kosky, P. G., "Heat Transfer to Saturated Mist Flowing Normally to a Heated Cylinder," *International Journal of Heat and Mass Transfer*, Vol. 19, No. 5, 1976, pp. 539–543.

8 Wilson, S. D., and Jones, A. F., "Heat Transfer from a Spray-Cooled Cylinder," *Industrial Engineering and Chemical Fundamentals*, Vol. 17, No. 3, 1978, pp. 183–189.

9 Thomas, W. C., and Sunderland, J. E., "Heat Transfer between a Plane Surface and Air Containing Suspended Water Droplets," *Industrial Engineering and Chemical Fundamentals*, Vol. 9, No. 3, 1970, pp. 368–374.

10 Aihara, T., Taga, M., and Haraguchi, T., "Heat Transfer from a Uniform Heat Flux Wedge in Air-Water Mist Flows," *International Journal of Heat and Mass Transfer*, Vol. 22, No. 1, 1979, pp. 51–60.

11 Heyt, J. W., and Larsen, P. S., "Heat Transfer to Binary Mist Flow," *International Journal of Heat and Mass Transfer*, Vol. 14, No. 9, 1971, pp. 1395–1405.

12 Bhatti, M. S., and Savery, C. W., "Augmentation of Heat Transfer in a Laminar External Gas Boundary Layer by the Vaporization of Suspended Droplets," ASME JOURNAL OF HEAT TRANSFER, Vol. 97, No. 3, 1975, pp. 179–184.

13 Takagi, T., and Ogasawara, M., "Some Characteristics of Heat and Mass Transfer in Binary Mist Flow," *Proceedings of the 5th International Heat Transfer Conference*, Tokyo, 1974, B7.10, pp. 350–354.

14 Ganić, E. N. and Rohsenow, W. M., "Dispersed Flow Heat Transfer," *International Journal of Heat and Mass Transfer*, Vol. 20, No. 8, 1977, pp. 855–865.

15 Maeda, M., Saigusa, T., and Ikai, S., "Study on Heat Transfer to Gas-Solids Suspension, Part I, Influence of Free Stream Turbulence on Heat Transfer," *Bulletin of the JSME*, Vol. 19, No. 137, 1976, pp. 1317–1325.

Heat Transfer to Curved Surfaces from Heat Generating Pools

J. D. Gabor
L. Baker, Jr.
J. C. Cassulo
D. J. Erskine
J. G. Warner

Reactor Analysis and Safety Division,
Argonne National Laboratory,
9700 S. Cass Avenue,
Argonne, Ill. 60439

Experiments were conducted on heat transfer from internally heated $ZnSO_4$-H_2O pools to curved surfaces. These experiments extended existing data for nonboiling pools to higher Rayleigh numbers. The data for convective downward heat transfer from nonboiling pools to a curved surface were reasonably close to the Mayinger correlation extrapolated to higher Rayleigh numbers and lower ratios of pool depth to radius of curvature. Sideward heat transfer to a surface could be described by $Nu = 0.7\ Ra^{0.2}$. Insulating the upper pool surface from the atmosphere had no effect on either sideward or downward heat transfer. An investigation was also made on effects of curvature on heat transfer from boiling pools. Nusselt numbers for sideward heat transfer were proportional to a boiling Reynolds number based on superficial vapor velocity to the 0.275 power and quite close to the correlation for a pool with flat vertical walls. Downward boiling heat transfer to a curved surface was proportional to the Reynolds number to the 0.1 power.

Introduction

This investigation on heat transfer to curved surfaces from an internally heated pool has particular application to nuclear reactor safety analysis. Knowledge of the possible magnitudes of the heat fluxes at the boundaries of a fuel pool is necessary to bound the extent of melting attack on containment structures and the rate at which heat must be removed to prevent melt-through and to stabilize the pool. This work also has application to chemical engineering and absorption of solar radiation in liquid pools.

Experiments were conducted in which heat transfer to curved surfaces was measured for both boiling and nonboiling liquid pools. These experiments extend the data for nonboiling pools to higher Rayleigh numbers and provide information on effects of curvature for boiling pools.

A variety of geometries have been studied for nonboiling pools generating heat internally at lower Rayleigh numbers. Kulacki and Goldstein [1] and Kulacki and Emara [2] correlated upward and downward heat transfer for rectangular geometries. Jahn and Reineke [3] theoretically and experimentally investigated free convection in rectangular and semicircular cavities. Mayinger, et al. [4] reported results for a semicircular geometry and a right circular cylinder. Watson [5] and Martin [6] analyzed free convection in a vertical cylinder. Min and Kulacki [7] measured thermal convection in a fluid layer bounded from below by a segment of a sphere.

Initial work on internally heated boiling liquids was reported by Stein, et al. [8]. Suo-Anttila, et al. [9] developed a model for downward heat transfer from an internally heated boiling pool of infinite width based on bubble induced fluid circulation. Gabor et al. [10] measured and correlated sideward and downward heat transfer for rectangular pools with various aspect ratios. Gustavson et al. [11] examined local values and correlated the results in terms of combined free and forced convection contributions. Greene, et al. [12] reexamined the data of Gustavson et al. in order to simplify the correlation of local heat transfer.

The results of this investigation will be discussed as follows:

1 Experimental Description
2 Experiments with Round-Bottom Apparatus
  A Nonboiling Pools
    i Total Downward Heat Transfer
    ii Local Downward Heat Transfer
  B Boiling Pool
3 Experiments with Curved-Electrode Apparatus
  A Nonboiling Pool
  B Boiling Pool
4 Conclusions

Contributed by the Heat Transfer Division for publication in the JOURNAL OF HEAT TRANSFER. Manuscript received by the Heat Transfer Division October 9, 1979.

1 Experimental Description

Two types of apparatus were used to measure heat transfer to curved surfaces in the downward and sideward directions. The apparatus for measuring downward heat transfer to a curved surface had a base consisting of 6 curved copper sections 0.376 m long by 0.113 m wide (see Fig. 1). Each curved section was water cooled and was electrically insulated with 0.076-mm thick teflon film. The base of the apparatus was an arc with a radius of 0.45 m and a subtended angle of 90 deg. For a pool of depth such that four of the six heat-transfer sections were covered, the subtended angle was 60 deg. The electrodes were two copper plates attached to opposite ends of the base cooling sections. The electrodes were also water-cooled to prevent nucleation on their surface during experiments with boiling pools. The pool depths were 55 mm where four sections were covered and 113 mm when six sections were covered.

The apparatus for measuring sideward heat transfer to a curved surface is shown in Fig. 2. In this pool container each electrode was concavely curved to form a semi-circle with a radius of curvature of 76 mm. The flat base plate (381 mm by 152 mm) of the apparatus was electrically insulated with 0.076-mm-thick Teflon film. The electrodes

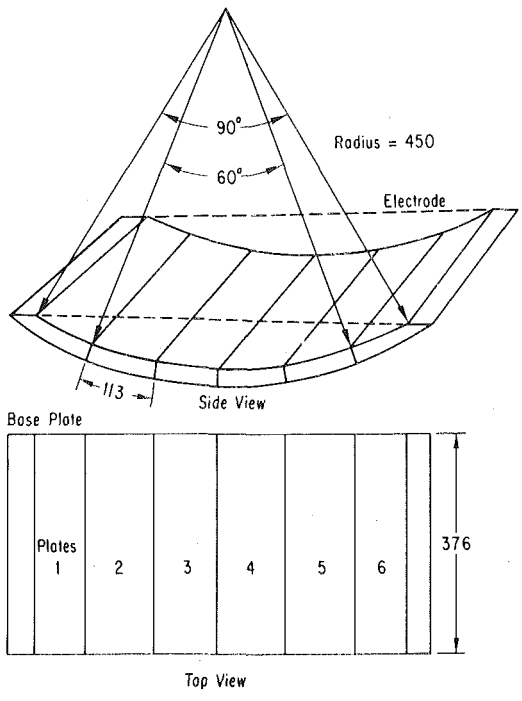

Fig. 1 Apparatus for downward heat flux experiments

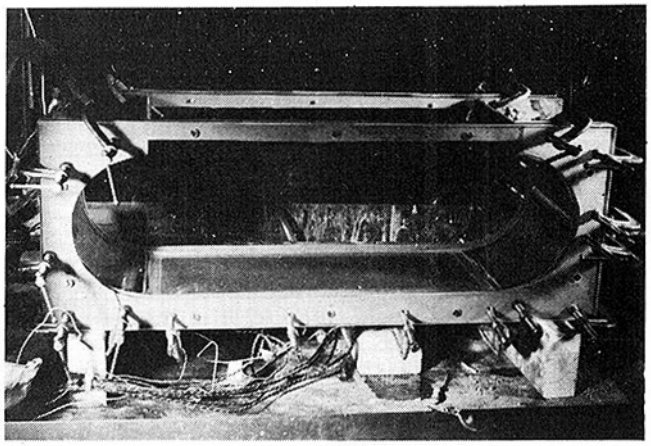

Fig. 2 Apparatus for measuring sideward heat transfer from an internally heated pool to curved surfaces

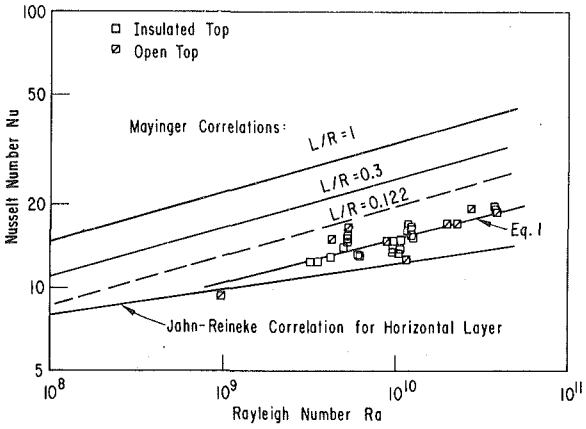

Fig. 3 Experimental results for total downward heat transfer to a curved surface having an included angle of 60 deg under nonboiling conditions

were curved copper plates attached to opposite ends at the base plate. The right electrode as shown in Fig. 2 was split into two sections in order to determine relative rates of heat transfer to the section near the top of the pool and to the section near the bottom of the pool. The front and back sides were each constructed from two 12.7-mm thick Lucite plates to minimize heat losses.

The temperatures of the base cooling plates, electrodes, and cooling water inlets and outlets were measured by Chromel-Alumel thermocouples. The thermocouples were mounted in holes drilled halfway into each heat-transfer plate. Seven thermocouples were mounted in each heat-transfer plate (plate thickness of 6.35 mm) of the round-bottomed apparatus. Six thermocouples were mounted in the right electrode (plate thickness of 4.76 mm) and six in the base plate of the apparatus with the curved electrodes. Three thermocouples were mounted in the upper half and three in the lower half of the split electrode. The temperatures from the round-bottom apparatus were recorded by a Doric Scientific Digitrend 210 data logger with 100 channels and 0.25°C precision. The temperatures of the curved-electrode apparatus were read from a Doric Trendicator type 400A with 0.1°C precision. Flow rates of cooling water were measured with either a stopwatch and graduate for low flow rates or a Brooks rotameter, Type 1307-08F1B1E, for higher flow rates (0.76 to 7.57 l/m). Heat fluxes to the surfaces were determined from the changes in cooling water temperature. In these experiments, the inlet temperatures and flow rates of the cooling water were adjusted so that the base plates all had the same surface temperature (within a range of 1°C). In the nonboiling experiments, pool temperatures were measured by a movable thermocouple within the pool. This thermocouple was not used in the boiling experiments because it was a nucleation site. The maximum temperature was in the center of the pool at the upper surface for both pool geometries. There was no temperature variation in the lateral direction (toward the electrodes of the round-bottom pool or toward the insulated side walls of the pool with curved electrodes).

The liquid level was controlled with a copper wire probe. When the liquid level receded, contact with the probe was broken and a solenoid valve was actuated releasing makeup water into the pool. The rate of vaporization was determined from the rate of makeup water addition.

Pools of $ZnSO_4$-H_2O electrolyte were Joule heated in these experiments. Experiments under nonboiling conditions were performed with (1) the top of the pool open to the atmosphere and (2) the top of the pool insulated with a floating layer of foam rubber.

Experimental error consisted of errors in measurement and uncertainties in thermophysical values. Errors in measurement of temperature, power input, water flow rates, and pool depth were estimated at 1 to 3 percent, 2 to 4 percent, 1 to 4 percent, and 0.5 to 1 percent. Uncertainties in the thermophysical values are estimated to be 0.5 to 1 percent for the Nusselt numbers and 4 percent for the Rayleigh number. The total uncertainty in the Nusselt numbers is then 5 to 13 percent and 8 to 16 percent in the Rayleigh numbers.

In these experiments, variations in electrical conductivity resulting from the changing temperature profile in the pool as well as the curvature of electrodes for the apparatus shown in Fig. 2 affected the uniformity of heat generation. The temperature variation was more significant in the nonboiling pools since the agitation by the vapor bubbles in the boiling pools produced a pool core with a uniform temperature. Peckover [13] addressed this problem for heat transfer to flat surfaces and determined that correction can be neglected for high Rayleigh numbers and lateral current flow which is the case for these experiments. However, previous analytical modelling efforts [3–6] on convective heat transfer were based on uniform heat generation which is not representative of practical experimentation (electric resistance heating) as well as the many applications for which the internal heat generation is nonuniform. Additional analytical work is needed to take into account nonuniform heat generation caused by temperature and geometry variations.

2 Experiments with Round-Bottom Apparatus

A Nonboiling Pools. *i Total Downward Heat Transfer.* The Nusselt numbers for total downward heat transfer to four sections under nonboiling conditions are plotted in Fig. 3. For each experiment, pool properties were calculated for an average temperature between the pool and the plate temperatures.

The experimental Nusselt numbers were largely independent of whether the top of pool was insulated or open. The experimental points were fitted by the method of least squares and the following correlation was obtained.

Nomenclature

C_p = specific heat
g = gravitational constant
k = thermal conductivity
L = pool depth
Nu = Nusselt number, $QL/k(T_p - T_s)$
Nu′ = modified Nusselt number, $Q/[kq(T_p - T_s)]^{1/2}$
q = volumetric heat generation rate
Q = heat flux
R = radius of curvature
Ra = Rayleigh number, $g\beta qL^5/\alpha\nu k$
Re = boiling Reynolds number, LV_0/ν
T = temperature
V_0 = superficial vapor velocity
α = thermal diffusivity, $k/\rho C_p$
β = volumetric expansion coefficient
ν = kinematic viscosity
ρ = density

Subscripts

1,2,3,4,5,6 = identification of section in round-bottom apparatus
B = boiling
c = conduction
D = downward
p = pool center
s = surface
S = sideward

$$\text{Nu} = 0.38\ \text{Ra}^{0.16} \pm 7.5 \text{ percent}$$

$$\text{for} \quad 1 \times 10^9 < \text{Ra} < 4 \times 10^{10} \tag{1}$$

The experimental results in Fig. 3 are compared with the correlation of Mayinger, et al. [4] for circular segments and with the Jahn-Reineke [3] correlation for horizontal layers. The Mayinger correlation is

$$\text{Nu} = 0.54\ \text{Ra}^{0.18}\ (L/R)^{0.26}$$

$$\text{for} \quad 0.3 < (L/R) < 1.0 \quad \text{and} \quad 10^7 < \text{Ra} < 5 \times 10^{10}. \tag{2}$$

where R = the radius of curvature of the segment. The Rayleigh number range of the Mayinger correlation includes that of the present study; however, the ratio of pool depth to radius of curvature in the four-section experiments ($L/R = 0.122$) is well below the lower limit of the correlation. The Mayinger correlation for $L/R = 0.122$ is shown as a dashed line in Fig. 3. The experimental data are found to fall below the extrapolated Mayinger correlation but above the well-established Jahn-Reineke correlation for downward heat transfer in a horizontal layer.

$$\text{Nu} = 1.389\ \text{Ra}^{0.095}$$

$$\text{for} \quad 4 \times 10^4 < \text{Ra} < 5 \times 10^{10}. \tag{3}$$

It is concluded that the downward heat transfer is increased relative to that for a horizontal surface but that the increase is much less than that for a full semicircle represented by the Mayinger correlation, equation (2), with $L/R = 1$.

The nonboiling experiments which used all six of the curved sections are plotted in Fig. 4. Again, the experimental Nusselt numbers did not depend significantly upon whether the top of the pool was insulated or open. The experimental points were reasonably close to the extrapolated Mayinger correlation for the appropriate ratio of $L/R = 0.25$. The following correlation was obtained with a least squares fit.

$$\text{Nu} = 5.34\ \text{Ra}^{0.068} \pm 16 \text{ percent}$$

$$\text{for} \quad 2 \times 10^{10} < \text{Ra} < 4 \times 10^{11}. \tag{4}$$

Equation (4) yields Nusselt numbers about 18 percent lower than that of equation (2) with $L/R = 0.25$.

ii Local Downward Heat Transfer. To evaluate the localized heat transfer, the ratios of the heat fluxes to each section to the total heat flux were calculated for each experiment. The values were averaged and the standard error of the estimate calculated. For the nonboiling data with four sections, the central sections (3–4) and the outer sections (2–5) gave the following averages:

$$\frac{Q_{3\text{-}4}}{Q_{\text{TOTAL}}} = 0.48 \pm 19 \text{ percent},$$

and

$$\frac{Q_{2\text{-}5}}{Q_{\text{TOTAL}}} = 1.52 \pm 6 \text{ percent}. \tag{5}$$

For the nonboiling data with all six sections covered, the average ratios were calculated as follows.

$$\frac{Q_{3\text{-}4}}{Q_{\text{TOTAL}}} = 0.51 \pm 35 \text{ percent},$$

$$\frac{Q_{2\text{-}5}}{Q_{\text{TOTAL}}} = 1.14 \pm 12 \text{ percent},$$

$$\frac{Q_{1\text{-}6}}{Q_{\text{TOTAL}}} = 1.51 \pm 15 \text{ percent}. \tag{6}$$

These ratios are plotted in Fig. 5 as a function of the average angle from the horizontal of the center of each heat transfer section. For comparison the results for a full semicircle (included angle = 180 deg) reported by Jahn and Reineke are also shown in Fig. 5. Curves are sketched in Fig. 5 following those of Jahn and Reineke. Although the curves sketched in Fig. 5 for the four and six section results are somewhat uncertain, it does appear likely that the maximum local

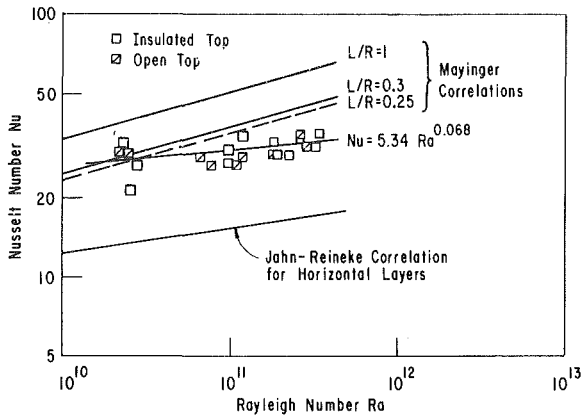

Fig. 4 Experimental results for total downward heat transfer to a curved surface having an included angle of 90 deg under nonboiling conditions

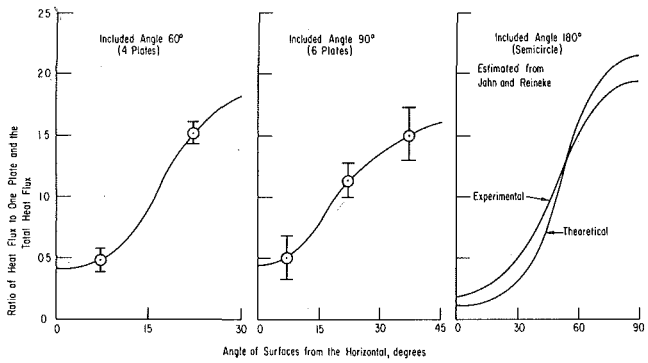

Fig. 5 Local values of downward heat flux to curved surfaces under nonboiling conditions

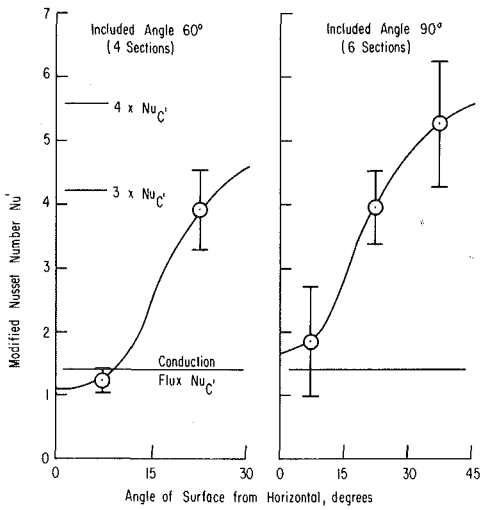

Fig. 6 Modified Nusselt numbers for downward heat transfer to curved surfaces under nonboiling conditions

to average ratio of the heat flux is less than two at the extreme edges of the pool. This conclusion is supported by the Jahn and Reineke results which indicate that the maximum value of heat flux at the upper corners of a full semicircle are only about twice the average value.

The local heat fluxes can also be considered in terms of the "conduction heat flux." In Fig. 6, the average values of the modified Nusselt numbers, Nu′, are plotted as a function of the angle from the horizontal. The results indicate that the local downward heat fluxes at the center of the pools are approximately equal to the conduction value of Nu′ = 1.414. At the extreme edges of the pool, the local values of heat flux are three to four times the conduction value.

B Boiling Pool. The boiling experiments used four sections and are listed in Table 1. The table presents the total pool power, the heat

Table 1 Experimental heat transfer data from an internally-heated water pool to a curved lower surface: boiling with four sections

Power kW	Heat Flux, kW/m² Q_{2-5}	Q_{3-4}	Q_{TOTAL}	Q_{VAP}	Surface Temperature °C	Heat Balance Error, Percent	Nu_{TOTAL}	$Re \times 10^4$
6.46	10.019	7.234	8.626	25.858	74.1	4.8	27.8	0.361
6.47	10.836	7.755	9.295	25.858	73.9	1.9	29.7	0.361
6.58	10.038	6.193	8.116	26.611	75.4	−1.6	27.5	0.374
6.60	10.858	7.169	9.014	26.611	77.0	−3.8	32.6	0.377
6.70	10.150	6.685	8.418	26.611	76.5	−0.8	29.8	0.376
6.63	10.254	7.543	8.899	25.858	75.1	3.8	29.8	0.363
7.33	12.837	8.711	10.774	31.632	76.7	−8.7	38.5	0.448
7.49	10.888	7.487	9.187	31.632	73.6	−2.4	29.0	0.440
7.55	11.555	8.269	9.912	31.632	75.6	−3.7	33.9	0.445
7.88	11.376	8.765	10.071	26.611	76.2	11.6	35.3	0.376
7.88	11.469	8.351	9.910	26.611	76.1	10.6	34.5	0.376
7.88	11.623	8.050	9.837	26.611	75.3	10.8	33.1	0.374
10.38	11.824	9.129	10.477	47.700	76.9	−2.1	37.7	0.676
10.38	12.234	8.764	10.499	47.700	75.9	−2.9	36.3	0.672
10.38	12.453	9.104	10.779	47.700	76.2	−3.5	37.7	0.673
12.02	12.705	8.983	10.844	55.231	77.7	0.1	40.5	0.786
12.02	12.528	8.461	10.494	55.231	77.2	0.8	38.3	0.784
12.02	12.678	8.730	10.704	55.231	77.3	0.1	39.2	0.785
13.53	11.790	8.946	10.368	65.273	75.8	−1.1	35.7	0.919
13.53	11.302	9.149	10.225	65.273	74.3	−0.8	33.1	0.912
13.73	11.908	8.854	10.381	65.273	76.3	0.1	36.5	0.922
14.70	12.362	9.101	10.732	75.315	76.8	−5.9	38.6	1.07
14.90	11.973	9.061	10.517	75.315	76.9	−4.1	37.8	1.07
15.66	13.030	8.841	10.936	80.838	78.0	−5.2	41.3	1.15
15.66	12.835	8.844	10.840	80.838	77.8	−5.2	40.5	1.15
17.25	12.759	9.024	10.892	90.378	75.6	−3.5	37.2	1.27
19.20	12.248	9.072	10.660	90.378	76.4	5.8	37.6	1.28
20.16	12.322	9.707	11.014	90.378	76.2	10.1	38.6	1.28
21.42	12.314	8.183	10.249	110.462	76.7	−0.5	36.7	1.56
21.42	12.508	9.269	10.888	110.462	77.0	−0.9	39.5	1.57
21.92	12.854	8.983	10.919	124.772	76.6	−9.6	38.8	1.77
21.92	12.650	8.659	10.654	124.772	76.3	−9.0	37.5	1.76
21.92	12.849	6.017	9.433	124.772	73.8	−8.3	30.0	1.74

fluxes to the individual sections, the average total heat flux, the upward or vaporization heat flux, the surface and pool temperatures and the heat balance error (difference between power input and heat transferred to cooling surfaces plus heat of vaporization).

The data for the total downward heat transfer under boiling conditions which were obtained with the four section configuration are plotted in Fig. 7. These data are plotted in terms of the Nusselt number versus the boiling Reynolds number. The Reynolds number is based on the superficial velocity of the vapor (volumetric vapor rate/cross-sectional area of surface) on the assumption that the agitation caused by the rising vapor bubbles predominates over natural convection caused by liquid density differences. The bubbles nucleate within the interior of an internally heated pool and not on a wall which is the usual case in boiling heat transfer. Therefore, the correlation must be made in terms of the mechanisms involved in boiling in internally heated pools [10]. The Nusselt numbers were a weak function of the Reynolds number as indicated by the least squares fit of the data.

$$Nu = 14.6\ Re^{0.1} \tag{7}$$

The data for boiling pools indicate that the variation of local heat flux with angle is very much less than that for nonboiling pools. This probably results from a destruction of the convection patterns within the pool by bubble agitation.

3 Experiments with Curved-Electrode Apparatus

A Nonboiling Pool. Experiments were conducted with pool temperatures at and below the boiling point. The surfaces of both electrodes and the base plate were maintained at the same temperature. The first set of runs (37 runs) was carried out with the upper pool surface open to the atmosphere. In the next series of runs (29 runs) the upper pool surface was covered with insulating foam rubber. In the experiments with the insulated top, the upward heat flux because of surface evaporation was eliminated.

The data were correlated in terms of Nusselt number versus Rayleigh number (see Fig. 8). The data for the "open-top" and the "in-

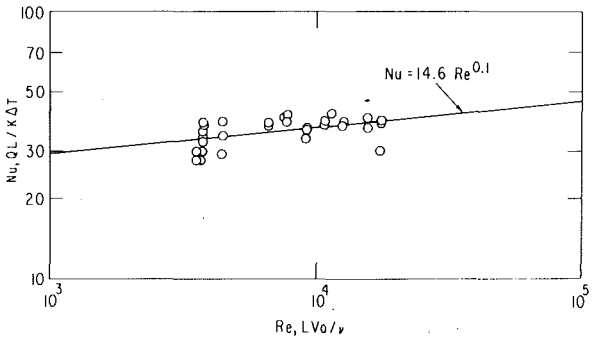

Fig. 7 Average downward heat transfer to a curved surface having an included angle of 60 deg under boiling conditions

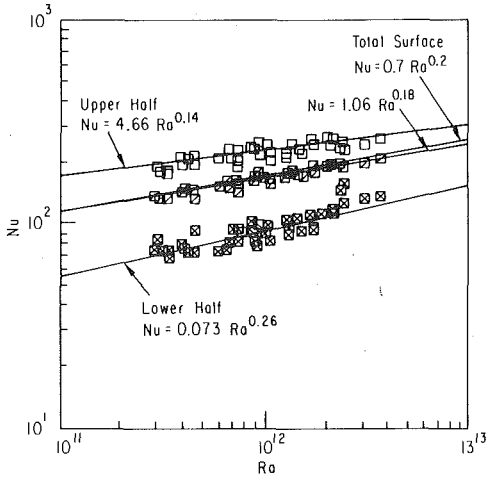

Fig. 8 Heat transfer to a semi-circular curved surface from an internally heated pool

Table 2 Experimental heat transfer data from an internally-heated $ZnSO_4$-H_2O pool to curved side electrodes (right electrode split into two equal sections)

Power kW	Heat Flux, kW/m² Q_{VAP}	$Q_{LOWER\ RIGHT}$	$Q_{UPPER\ RIGHT}$	Q_{LEFT}	Q_{DOWN}	Wall Temperature, °C	Heat Balance Error, Percent	Nu_{TOTAL}*	$Re \times 10^4$
6.14	22.68	44.64	82.75	68.19	4.15	40.1	3	276	0.560
6.24	24.07	44.25	84.39	70.36	4.89	39.7	5	280	0.593
10.13	63.33	51.19	104.35	81.25	14.52	43.8	2	353	1.60
10.17	63.61	50.71	106.49	80.70	13.93	43.1	2	350	1.60
13.97	109.59	53.69	105.96	86.81	29.76	49.2	3	408	2.88
13.97	108.41	52.95	108.88	85.33	30.01	49.9	2	412	2.86
15.39	131.30	59.42	112.40	90.82	33.93	51.7	2	453	3.50
15.90	136.16	57.42	114.85	86.87	31.96	50.1	3	430	3.60
19.31	171.12	59.66	113.36	93.99	39.56	56.2	0	508	4.70
19.04	172.71	59.06	114.55	95.13	38.73	55.7	2	507	4.73

* Total refers to total electrode surface.

sulated-top" experiments were in close agreement. Within the range of experimental error, there did not appear to be any effect of covering the top surface on the heat transfer to the electrodes. Therefore, the data from both sets of experiments are plotted on Fig. 8 and were combined for a least squares analysis.

The heat flux to the upper half of the curved split electrode was correlated by

$$Nu = 4.66\ Ra^{0.14}. \tag{8}$$

The heat flux to the lower half of the split electrode was less than to the upper half and was correlated by

$$Nu = 0.073\ Ra^{0.26}. \tag{9}$$

The average of the heat flux to the continuous left electrode and the total heat flux to both sections of the right electrode was correlated by

$$Nu = 1.06\ Ra^{0.18}. \tag{10}$$

Also shown on Fig. 8 is the curve

$$Nu = 0.7\ Ra^{0.2}. \tag{11}$$

This curve appears to correlate the data for heat transfer over the entire electrode surface quite well within the range of the data with little difference from the correlation obtained by least squares analysis. The correlation has the advantage that it is independent of pool depth since the pool depth term, L, appears to the first power on both sides of the equation.

The heat flux downward to the flat base plate was less than that predicted by conduction using the difference in temperature between the center of the pool and the surface of the base plate even though convective liquid flow was visually evident. The cooled liquid flowing down from the electrode surfaces and then across the base plate effectively reduced the temperature driving force at the base plate surface resulting in a lowered downward heat flux.

B Boiling Pool. The data for these boiling experiments are listed in Table 2. The data for sidewards heat transfer are plotted on Fig. 9 in terms of Nusselt number versus Reynolds number based on the superficial vapor velocity, V_0. The data of Gabor, et al. for vertical flat walls in a rectangular geometry with various aspect ratios were correlated in these terms by

$$Nu = 3.096\ Re^{1/2}. \tag{12}$$

Equation (14) is plotted on Fig. 9 and is not out of line with the data for the average of the total heat transfer to the curved electrodes. The Nusselt numbers for heat transfer to the upper and lower sections of the split electrodes are also given on Fig. 9. The heat flux to the upper section was about twice that to the lower section.

A least squares fit of the data gives the following correlations:

For heat transfer to the entire electrode surface,

$$Nu = 25.29\ Re^{0.275}. \tag{13}$$

For heat transfer to the upper half of the split right electrode,

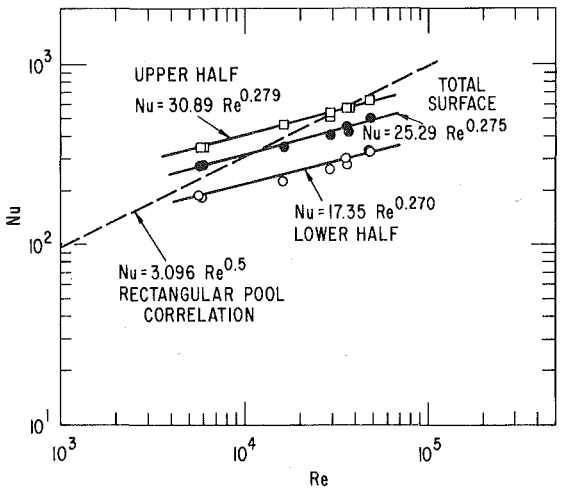

Fig. 9 Sideward heat transfer to a curved surface from an internally heated boiling pool

$$Nu = 30.89^{0.279}. \tag{14}$$

For heat transfer to the lower half of the split right electrode,

$$Nu = 17.35\ Re^{0.270}. \tag{15}$$

The pattern of liquid flow along the base of the pool is not a simple one-directional flow as along the electrode wall. Along the electrode wall, the liquid flows in a downward direction. The liquid cooled at the electrodes flows down onto both ends of the base plate. At low rates of boiling, a wave of cold liquid can be seen washing back and forth across the base. At higher boiling rates, with a thicker bubbly layer, turbulence from the bubbly layer destroys this wave motion.

This effect of change in flow pattern at the base of the pool is shown in Fig. 10 in which the ratio of horizontal to downward heat flux, Q_S/Q_D, is plotted against the boiling flux, Q_B. The parameters for this plot follow that used for pools of rectangular geometry and flat vertical walls [10]. This correlation applied for pool depth-to-length ratios varying from 0.17 to 1.2 for pool lengths of 191 and 381 mm. The current data are for only one aspect ratio and therefore Fig. 10 should be regarded primarily from the point of view of illustrating the heat transfer mechanism. At the lower boiling rates, the Q_S/Q_D ratio declines rapidly from about 16 to 3 as Q_B increases. As Q_B increases above 100 kW/m², the ratio declines less rapidly from about 2.8 to 2.3. This same behavior occurred with a pool of rectangular geometry and flat vertical walls [10]. However, at the higher boiling rates with the rectangular pool Q_S/Q_D leveled out fairly consistently at 3.8. This high Q_S/Q_D ratio for the rectangular pool compared to the pool with curved electrodes indicates higher downward heat transfer for the curved electrode pool. This is obviously a geometry effect in that the cooled downward liquid along the curved electrode flowed more smoothly onto the surface at the base. With the straight vertical electrodes, the

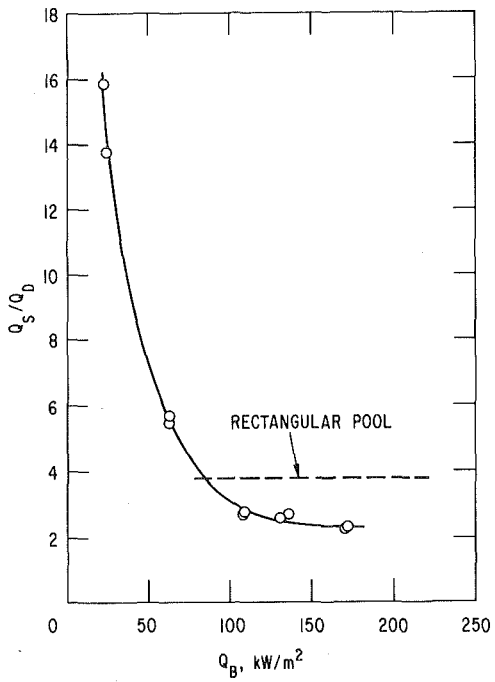

Fig. 10 Ratio of sideward to downward heat fluxes for boiling pool with curved electrodes

cooled liquid flowed directly normal to the base and after reaching the base of the electrode would flow into the lower liquid level at approximately a 45 deg angle from the bottom corner of the pool. Evidently the flow coming off the curved electrode was at a higher velocity as it moved into the liquid level near the base.

Conclusions

The experimental data for convective downward heat transfer to a curved surface were reasonably close to the Mayinger correlation when extrapolated to higher Rayleigh numbers and lower L/R ratios. Sideward heat transfer from a nonboiling pool can be described by

$$\mathrm{Nu} = 0.7\ \mathrm{Ra}^{0.2}. \tag{11}$$

Within the range of experimental error, there did not appear to be any effect of insulating the top surface on either sideward or downward heat transfer.

The Nusselt number for downward heat transfer to a curved surface for a boiling pool is proportional to $\mathrm{Re}^{0.1}$ and for sideward heat transfer to a curved surface is proportional to $\mathrm{Re}^{0.275}$.

References

1 Kulacki, F. A., and Goldstein, R. J., "Thermal Convection in a Horizontal Fluid Layer with Uniform Volumetric Energy Sources," *Journal of Fluid Mechanics*, Vol. 55, Part 2, 1972, pp. 271–287.

2 Kulacki, F. A., and Emara, A. A., "High Rayleigh Number Convection in Enclosed Fluid Layers with Internal Heat Sources," NUREG-75/06, July 1975, The Ohio State University, Columbus, Ohio.

3 Jahn, M., and Reineke, H. H., "Free Convection Heat Transfer with Internal Heat Sources, Calculations and Measurements," *Proceedings of the Fifth Int. Heat Transfer Conference*, Tokyo, Sept. 1974, Paper NC2.8.

4 Mayinger, F., Jahn, M., Reineke, H. H., and Steinbrenner, U., "Examination of Thermohydraulic Processes and Heat Transfer in a Core Melt," BMFT R8 48/1, 1976, Institute fur Verfahrenstechnik der T.U. Hannover.

5 Watson, A., "Natural Convection of a Heat Generating Fluid in a Closed Vertical Cylinder: An Examination of Theoretical Predictions," *Journal of Mechanical Engineering Science*, Vol. 13, No. 3, 1971, pp. 151–156.

6 Martin, B. W., "Free Convection in a Vertical Cylinder with Internal Heat Generation," *Proceedings of Royal Society A.*, Vol. 301, 1967, pp. 327–341.

7. Min, J. H. and Kulacki, F. A., "An Experimental Study of Thermal Convection with Volumetric Energy Sources in a Fluid Layer Bounded from Below by a Segment of a Sphere," *Sixth International Heat Transfer Conference*, Toronto, Canada, Aug. 7–11, 1978, paper NR-27.

8 Stein, R. P., *et al.*, "Studies of Heat Removal from Heat Generating Boiling Pools," CONF-740401-P2, *Proceedings of the Fast Reactor Safety Conference*, Beverly Hills, Calif., 1974, pp. 865–880.

9 Suo-Anttila, A. J., *et al.*, "Boiling Heat Transfer from Molten Fuel Layers," CONF-740401-P2, *Proceedings of the Fast Reactor Safety Conference*, Beverly Hills, Calif., 1974, pp. 845–864.

10 Gabor, J. D., Baker, L., Cassulo, J. C., and Mansoori, G. A., "Heat Transfer from Heat Generating Boiling Pools," *AIChE Symposium Series*, No. 164, Vol. 73, 1977, pp. 78–85.

11 Gustavson, W. R., Chen, J. C., and Kazimi, M. S., "Heat Transfer and Fluid Dynamic Characteristics of Internally Heated Boiling Pools," BNL-NUREG-21856, Sept. 1976, Brookhaven National Laboratory, Upton, New York.

12 Greene, G. A., Jones, O. C., and Schwarz, C. E., "Thermo-fluid Mechanics of Volume-heated Boiling Pools," BNL-NUREG-50759, Dec. 1977, Brookhaven National Laboratory, Upton, New York.

13 Peckover, R. S., "Directional Dependence and Non-Uniformity of Joule Heating in Natural Convection Experiments," *ASME/AIChE 18th National Heat Transfer Conference*, San Diego, Aug. 6–8, 1979, paper 79-HT-96.

J. L. Gillette
R. M. Singer
Mem. ASME

J. V. Tokar[1]
J. E. Sullivan

Argonne National Laboratory
Argonne, Ill. 60439

Experimental Study of the Transition from Forced to Natural Circulation in EBR-II at Low Power and Flow[2]

A series of tests was conducted in EBR-II which examined the dynamics of the transition from forced to natural circulation flow in a liquid-metal-cooled fast breeder reactor. Each test was initiated by abruptly tripping an electromagnetic pump which supplies 5–6 percent of the normal full operational primary flow rate. The ensuing flow coastdown reached a minimum value after which the flow increased as natural circulation was established. The effects of secondary system flow through the intermediate heat exchanger and reactor decay power level on the minimum in-core flow rates and maximum in-core temperatures were examined.

Introduction

During the normal operation of a liquid-metal-cooled fast breeder reactor (LMFBR), fuel temperatures are controlled by the forced circulation of liquid sodium. However, during certain events postulated to occur during the life-time of a reactor, power to the primary pumps (which maintain the forced flow) can be lost. As the forced flow starts to decrease, the plant protective system will, with extremely high reliability, shut down the plant. However, due to the generation of radioactive material within the fuel and structural components of the reactor during power operation, residual decay heat will be released even though the primary fission reactions have ceased. Therefore, there must be some continued circulation of coolant, albeit at a much reduced rate, following this event to prevent overheating of the reactor.

Although the design of LMFBR systems will include backup pumping systems such as redundant electrical power supplies, the ultimate "fall-back" heat transport mechanism is natural circulation cooling. To demonstrate that natural circulation is indeed a reliable fall-back mechanism, experimental data must be obtained which directly show the capability of this heat transfer mode in maintaining temperatures below prescribed limits and which can be used as bench-mark points in the development of analytical models describing this phenomenon.

One such test [1] was conducted in the Experimental Breeder Reactor No. II (EBR-II) and involved a sudden transition from operation at an initial steady-state of 5.3 percent of full flow (auxiliary primary pump on) and 1.6 percent of full power to a final purely natural convective state at 1.7 percent of full flow. A significant undershoot in flow rate and corresponding overshoot in temperature occurred when the pump was abruptly de-energized. During the transient, the total reactor coolant flow rate dropped to 1.1 percent, while that in an instrumented fueled subassembly (XX07) dropped to 0.7 percent of their full values. The delay in the establishment of natural convective flow was attributed to the slow development of the hot leg (upper reactor internals and/or outlet piping) temperatures corresponding to the final steady natural convective conditions.

Natural circulation experiments have also been conducted in other sodium-cooled reactors, e.g., SEFOR [2], HALLAM [3], Rapsodie [4], Phenix [5], and PFR [6]. However, because of a lack of in-core instrumentation and a lack of documentation of sufficient detail of the specific test results, these experiments are of limited value to the general technical community. This paper presents the results of an extensive series of transient natural circulation tests conducted in EBR-II which greatly extend the data presented in [1]. This series of tests, all of which were conducted at low power and flow conditions, investigated the effects of decay power level, initial temperature (or buoyancy) distribution in the primary heat transport circuit, secondary heat transport system dynamics, and intersubassembly phenomena upon the transition from forced to natural convective flow.

Description of Experiments

Reactor and Instrumentation Description. The EBR-II is a sodium-cooled fast breeder reactor with a complete steam-electric system. The reactor consists of 16 rows of subassemblies, the inner seven rows constituting the fueled core and the outer nine containing reflector and blanket subassemblies. The active fuel length in the core is 0.343 m. The driver fuel elements are 4.42 mm in diameter and are contained within a hexagonal can which has a flat-to-flat dimension of 56.1 mm. The normal operating power of the reactor is 60.0 MWt at a total coolant flow rate of 0.516 m^3/s. Additional descriptive information on EBR-II is available in [7] and a sketch of the primary heat transport circuit is shown in Fig. 1.

The instrumentation utilized in these tests includes both the normal plant sensors and special in-core sensors. The in-core instrumentation was located in a modified driver subassembly placed in a

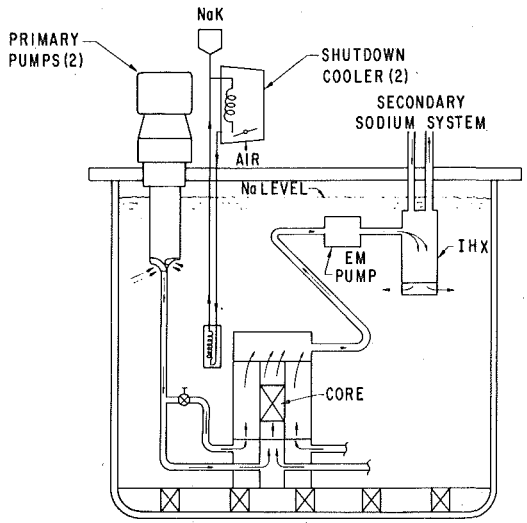

Fig. 1 Schematic diagram of the primary heat transport circuit of EBR-II

[1] Current address is Bell Laboratories, Naperville, Ill.

[2] Work supported by the U.S. Department of Energy.

Contributed by the Heat Transfer Division and presented at the 18th AIChE/ASME National Heat Transfer Conference, San Diego, Calif., Aug. 6–8, 1979. Revised manuscript received by the Heat Transfer Division October 17, 1979. Paper No. 79-HT-10.

converted control-rod position in the fifth row of the core. This subassembly, designated XX08, consisted of 61 elements, 58 of which were fueled. Within this subassembly, there were two inlet, permanent magnet flowmeters, six fuel centerline thermocouples, and 16 coolant thermocouples mounted as wire wrap spacers. Two of these coolant thermocouples, called BTCs, were located at the core bottom, two, called 4TCs, were at 0.4 of the core height, two, called 7TCs, were at 0.7 of the core height, nine, called TTCs, were near the core top (same height as the fuel thermocouples), and one, called 15C, was at 1.5 of the core height. In addition, two coolant thermocouples, called OTCs, were located above a flow mixer near the subassembly exit, but within the hex can at 0.933 m above core bottom, and measured the mixed-mean coolant outlet temperature. A schematic diagram indicating the axial location of the XX08 instrumentation is shown in Fig. 2. Additional details on XX08 are available in [8].

The general plant instrumentation is calibrated on a periodic basis. However, special calibration efforts were undertaken for these tests. The temperature sensors and their associated signal conditioning equipment were checked for off-sets by operating the plant at full (100 percent) flow and extremely low decay power. This resulted in a nearly isothermal primary system, and all of the signals from the temperature sensors could thereby be corrected. With only a few exceptions, the corrections obtained were less than 1°C, and therefore, it is felt that all of the temperature measurements have uncertainties of less than about ±0.5°C. Although the flowmeters were not calibrated in-place, extensive out-of-pile calibration tests were performed for those units within XX08. Based on these tests we estimate the overall uncertainty to be about ±0.4 percent for flow rates greater than about 6×10^{-4} m^3/s (about 25 percent of full flow), about ±2 percent for flow rates between 0.3×10^{-4} and 6×10^{-4} m^3/s, and about ±10 percent for lower flow rates.

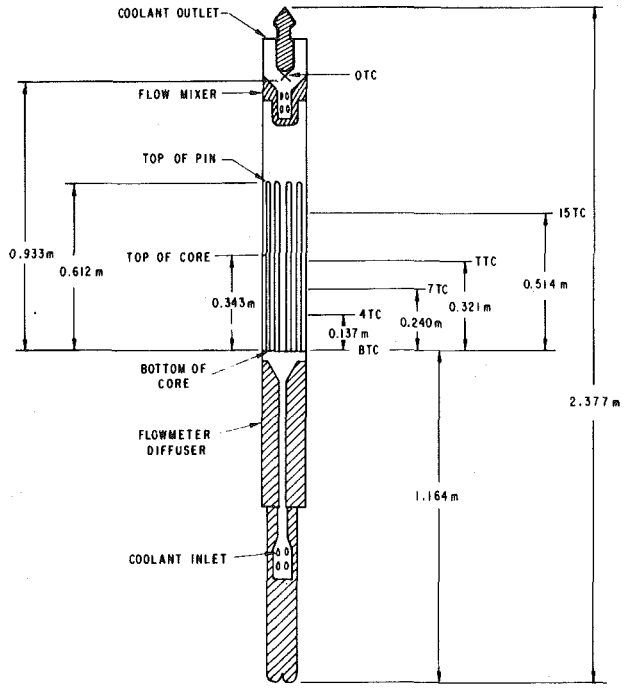

Fig. 2 Schematic of the instrumented fueled subassembly, XX08, including sensor locations

General Experimental Procedures. The series of transients described in this paper was limited to relatively low initial reactor powers and flow rates. The rationale for conducting this first series of tests under these conditions was primarily one of conservatism, i.e., the desire to produce relatively low maximum temperatures. As these tests progressed, the experience gained in conducting them and the concurrent development of an appropriate analytical model provided a sound basis for steadily increasing the severity of the transients.

To accomplish the test objectives while still satisfying the conservatism as described above, the following general experimental procedure was followed. (1) At the end of a normal full power operating run, the reactor was shut down; (2) a wait period ranging from about one hour to seven days was used to permit the decay heat to drop to the desired level; (3) the primary pumps were shut down and the secondary pump adjusted to the specified value (primary forced flow now being provided only by the primary auxiliary pump); and (4) the actual transient was initiated by disconnecting the electrical power supply to the auxiliary pump. Electrical power to the secondary pump was either continued or disconnected according to the specific test requirements. Thus, all of these tests were initiated from an initial condition of approximately 5–6 percent of the normal primary forced flow (100 percent primary flow equals 0.516 m^3/s), secondary forced flow of 2.6 to 10.4 percent of rated flow (100 percent secondary flow equals 0.379 m^3/s), and a reactor decay power level of 0.16 percent of normal (100 percent power equals 60.0 MWt).

Experimental Results

Five separate transient natural circulation tests were conducted with most of them consisting of multiple pump trips and coastdowns (referred to as phases). A summary of the initial conditions is shown in Table 1. The test described as F was conducted as part of an earlier EBR-II experiment and utilized a similar instrumented subassembly (XX07) to obtain local in-core temperature and flow rate data. The following sections of this paper will discuss the details of these tests

Table 1 Initial conditions for natural circulation transients

Test-Phase	Reactor Decay Power (percent)[1]	Reactor Primary Flow (percent)[2]	OTC Temp Rise (°C)	IHX Primary Inlet Temp (°C)	Sec. System Flow (percent)[3]	IHX Sec. Inlet Temp (°C)
1A-1	0.16	5.40	1.8	374	3.3	261
1A-2	0.16	5.60	1.3	374	5.1	267
1A-3	0.16	5.77	1.4	370	7.0	274
1A-4	0.16	5.99	1.6	364	10.4	292
1B-1	0.34	5.47	7.4	374	3.3	267
1B-2	0.34	5.68	6.7	375	7.8	278
1C	0.34	5.91	6.3	370	7.8	297
1D-1	0.68	5.87	15.0	379	9.8	294
1D-2	0.66	6.04	14.2	380	7.3	300
1D-3	0.64	5.67	14.3	378	3.1	299
1E-1	0.19	5.48	4.3	374	2.6	264
1E-2	0.19	5.58	4.1	370	5.8	278
1E-3	0.19	5.71	3.9	366	6.6	289
1E-4	0.19	5.95	4.1	361	9.0	298
F	1.60	5.30	32.5	370	2.0	—

[1] The values are expressed in percent of full reactor power of 60.0 MWt.
[2] The values are expressed in percent of full reactor flow of 0.516 m^3/s.
[3] The values are expressed in percent of full secondary flow of 0.379 m^3/s.

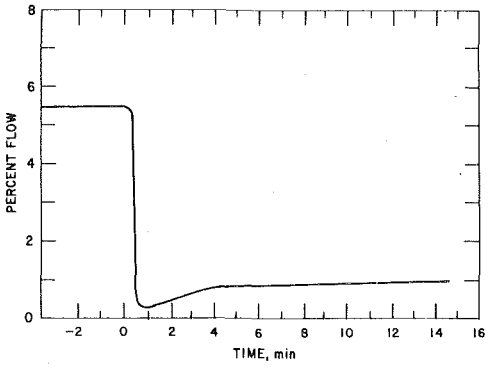

Fig. 3 Transient coolant flow rate in XX08 during Test 1E-1

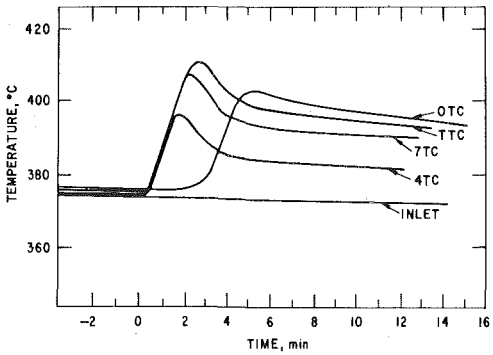

Fig. 4 Transient coolant temperatures in XX08 during Test 1E-1

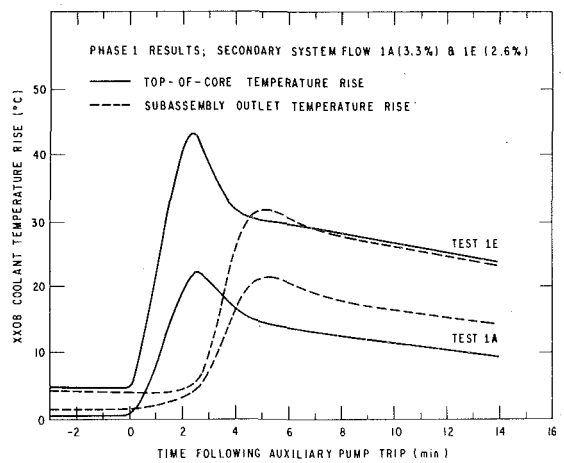

Fig. 5 Comparison of top-of-core and subassembly outlet temperature transients in XX08 during Tests 1A-1 and 1E-1

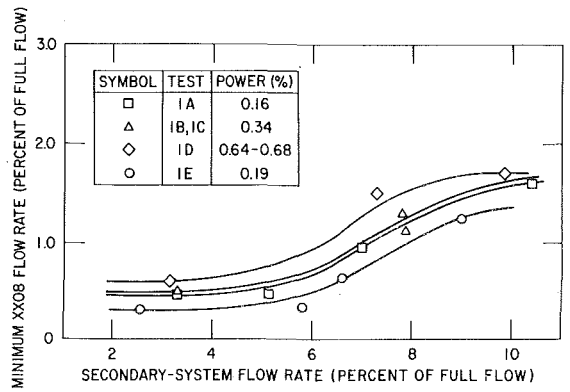

Fig. 6 Effect of secondary coolant flow rate on the minimum natural circulation flow rate in XX08

in terms of the major parametric effects of plant operation upon the extrema of core temperatures and flow rates.

General Characteristics of Transient Behavior. Although this test series was conducted over a range of reactor decay power levels and secondary system flow rates, the general characteristics of the in-core transient behavior were similar from test to test. A typical relationship is that in Fig. 3 where the XX08 in-core flow rate is shown versus time for transient 1E-1. The in-core flow decreases very rapidly when the power to the auxiliary pump is turned off. A turbulent-to-laminar transition occurs during the coastdown and the flow remains laminar throughout the remainder of the transient. The minimum value (the flow "undershoot") is reached as buoyancy forces develop sufficiently to establish natural circulation flow. Later sections of this paper will show the dependence of the minimum flow rate on the decay power level and on the secondary system flow rate.

Figure 4 shows the in-core temperatures at various axial locations in XX08 for the same transient. These data show the peaking of the coolant temperatures at each level and that the time required to reach the maximum temperatures increases with increasing axial distance. The magnitude of the peak coolant temperatures as functions of decay power level and secondary system flow is discussed in subsequent sections of this paper.

Effect of Intersubassembly Heat Transfer. The importance of intersubassembly heat transfer in reducing radial temperature gradients during natural circulation events has been reported in [9]. Those data showed that coolant temperature differences from subassembly-to-subassembly are significantly reduced when an LMFBR changes from a condition of high power and high forced flow to low power and natural circulation flow. This section presents experimental data, obtained under different irradiation conditions, which further indicate the importance of intersubassembly heat transfer during natural circulation transients. These data were obtained by conducting two nearly identical tests with subassembly XX08 in the EBR-II core. One significant difference in these tests was that for the first test (1A), XX08 had not been previously irradiated whereas it had been irradiated prior to the second test (1E).

Test 1A was initiated approximately 6-3/4 days after the shutdown of the preceding reactor run. At this time the overall fission product decay power was 0.16 percent of the full operational power. Although the XX08 subassembly had not been irradiated prior to Test 1A and therefore did not constitute a fission product decay source, it was a susceptor of gamma and beta activity emitted by the surrounding subassemblies which had been irradiated. Calculations done for these conditions yielded a value of 145 W for the XX08 power. Test 1E was conducted five days after a reactor shutdown when the decay power was 0.19 percent. For XX08 this value corresponds to a power of approximately 750 W. Therefore, the power deposited in XX08 for Test 1A was only 19 percent of that for Test 1E. As indicated in Table 1, the flow rates for the initial portion of each test were approximately the same for the respective phases. In each case, 100 percent flow through XX08 was equal to about 2.7×10^{-3} m^3/s.

The initial XX08 temperature rises listed in Table 1 are indicative of the different powers. It is somewhat tempting to say that intersubassembly heat transfer has already begun to reduce the factor of five difference in adiabatic temperature rise; but because of the small rises and the associated ± 1°C uncertainty, this effect can not be readily quantified under these steady-state conditions.

The coolant temperatures for the first phase of each test are shown in Fig. 5 for the top-of-core (TTC) and subassembly outlet (OTC) thermocouples. An examination of these curves provides some insight to the importance of intersubassembly heat transfer during a natural circulation event. Following the pump trip, the TTC temperature rise reached peaks of about 22°C during Test 1A and about 43°C during Test 1E. Thus the maximum TTC temperature rises for these two tests differed by only 95 percent, even though the power deposited in XX08 is about five times greater for Test 1E than for Test 1A. The same effect can be seen with the OTC data where the peak values of 22 and 32°C differed by only about 45 percent. The temperature measurements obtained under the quasi-steady-state natural circulation flow at the end of the transients also indicated the same basic

phenomenon with TTC values of about 10°C for Test 1A and 23°C for Test 1E (a difference of 130 percent) and OTC values of 14 and 23°C, respectively (a difference of 64 percent). Again, these differences are significantly reduced from the factor of 5 which would be expected under adiabatic conditions and the respective power depositions in XX08.

The data presented above further substantiate the importance of intersubassembly heat transfer in reducing local temperature gradients in an LMFBR under natural circulation conditions. Data such as these can be used to reduce calculated local hot channel factors used in the safety analyses of loss-of-forced-flow transients. Any such reductions in these hot channel factors could result in more efficient and economical design and operation of future LMFBRs while still maintaining a reasonable margin of safety.

Effect of Secondary/Primary System Thermal Interactions. The secondary and primary heat transport circuits in EBR-II are thermally connected by an intermediate heat exchanger (IHX). In the IHX, the primary sodium flows downward, so that the net buoyancy of the primary heat transport circuit is aided by the cooling of the sodium in this component. Since the average density of the primary sodium in the IHX is determined by its axial temperature gradient, the dynamics of the heat transfer between the counterflowing primary and secondary sodium will have a direct effect upon the contribution of the IHX to the circuit buoyancy pressure forces. At steady-state full power operating conditions, the primary and secondary flow rates are balanced so that the axial temperature gradient within the IHX is approximately linear. However, during situations where the ratio of the secondary-to-primary flow rates is quite large, most of the heat transfer occurs at the top of the IHX. This results in most of the primary side temperature drop occurring near the IHX top, and thus in a higher average density of the primary sodium in the IHX than under balanced flows.

Conversely, when the secondary-to-primary flow rate ratio is quite small, most of the heat transfer occurs near the bottom of the IHX, resulting in most of the primary side temperature drop existing near the bottom. This yields a lower average density of the primary sodium in the IHX than under balanced flow. The effect of increased secondary flow rate relative to primary flow rate, then, is to cause an increase in the net buoyancy of the primary heat transport circuit, while a decrease in secondary flow rate has an opposite effect.

During loss of flow transients the ratio of secondary-to-primary flow rates will change considerably and will affect core temperatures through its influence on the net buoyancy. In this section, the experimentally measured effect of secondary flow rate upon the transient core temperatures and flow rates is discussed.

In all but one test, the secondary flow rate was held essentially constant during the primary system flow coastdown. Thus, the thermal transient in the IHX was driven only by the primary system coastdown. Since the initial primary forced flow rate was always about 5 to 6 percent of full, and the secondary flow rate varied from about 2 to 10 percent, ratios of secondary-to-primary flow rates of less than to greater than one were investigated.

A summary of the effect of secondary system flow on the minimum primary system flow rate is shown in Fig. 6. The primary system flow rates shown are the minimum values measured in XX08 and thus represent the flow rate at the onset of natural circulation. These data indicate a strong effect of secondary system flow on the minimum in-core flows. This effect is particularly evident in the approximate 5–8 percent range with asymptotic behavior on either side of this range. The 5–8 percent range represents a flow rate of 0.019–0.030 m^3/s in the secondary system, which is roughly comparable to the approximately 0.028 m^3/s primary system flow prior to the initiation of the transient.

The effect of secondary system flow on the maximum coolant temperature rises at the outlet of XX08 is shown in Fig. 7. Although no sharp break points are noted such as was seen with the minimum flow rates, the strong effect of secondary system flow can be seen. Figure 8 shows the same effect with the temperature rises being the average values of the maximum measured temperature rises at the outlet of several different incore subassemblies. All of these experimental observations indicated the important role played by the buoyancy of the primary sodium in the IHX and the strong influence of the secondary flow rate thereupon.

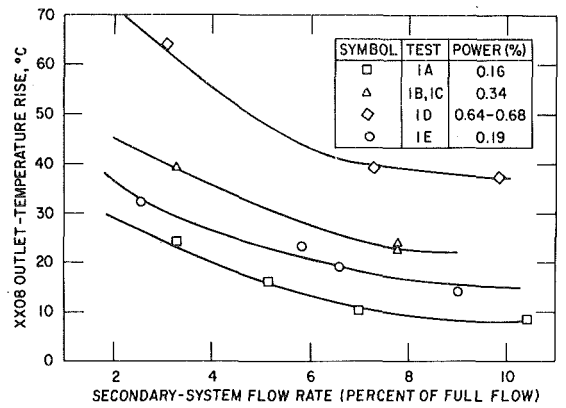

Fig. 7 Effect of secondary coolant flow rate on the maximum subassembly outlet coolant temperature in XX08

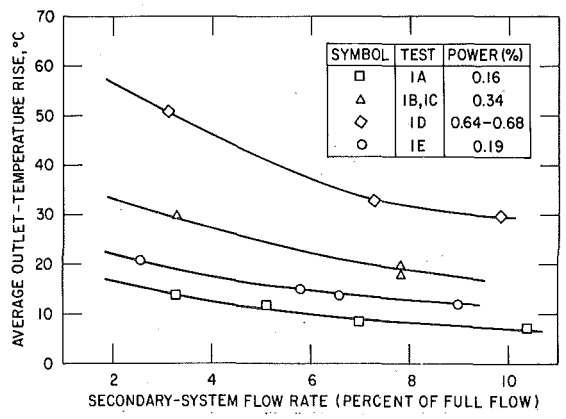

Fig. 8 Effect of secondary coolant flow rate on the peak subassembly outlet coolant temperature (average of 17 subassemblies)

As was noted earlier, one of these transients was conducted with a changing secondary system flow rate. For Test 1C, the primary auxiliary pump and the secondary electromagnetic pump were simultaneously tripped. The secondary system flow therefore coasted down to its natural circulation level of approximately 5 percent in about 1 min. Comparisons of the results from Test 1C with those from Test 1B-2 which had the same initial conditions except for the IHX secondary inlet temperature, show that the minimum in-core flow rates and maximum temperature rises are very nearly equal. These results indicate that the dynamics of the secondary system coastdown were too slow to affect in-core conditions during the first minutes of the transient. The quasi-steady-state in-core flow rates obtained after several minutes did, however, show the effect of decreased secondary system flow with values of approximately 2.0 and 1.5 percent for Test 1B-2 and Test 1C, respectively. This relative independence of primary and secondary system convective flow transients is caused by a combination of factors including the very rapid primary flow coastdown rate, a long fluid transport time from the reactor core to the IHX, and the thermal inertia of the IHX itself. For the much longer primary flow coastdowns resulting from trips of the primary centrifugal pumps, a stronger interaction between the primary and secondary systems exists.

Effect of Reactor Power Level. For the type of transients described in this paper, the reactor power level affects the core temperatures and the natural circulation flow in a similar, but somewhat more complex manner than the IHX thermal conditions. When the reactor power is increased at initially steady natural convective conditions, the coolant axial temperature gradient in the core will correspondingly increase. However, this causes the coolant density to decrease, i.e., the buoyancy forces to increase. This causes an increased convective flow rate and a lowered coolant axial temperature profile. The net effect, however, is for the coolant temperatures to rise with

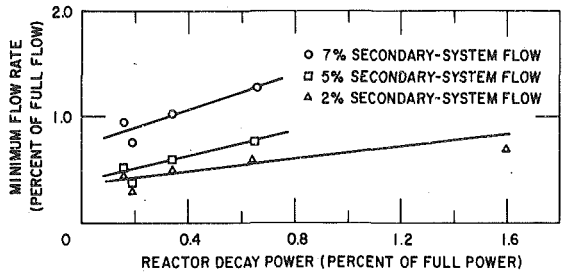

Fig. 9 Effect of power level on the minimum natural convection flow rate in XX08

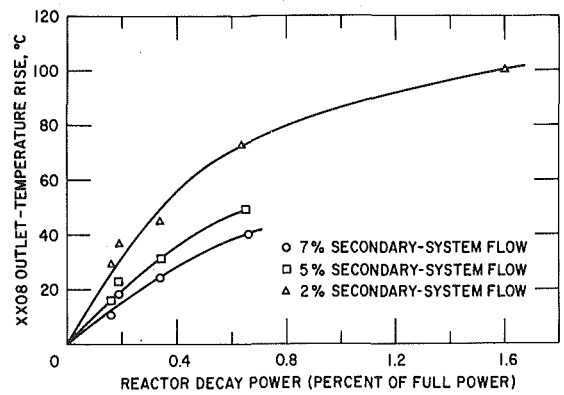

Fig. 10 Effect of power level on the maximum subassembly outlet coolant temperature in XX08

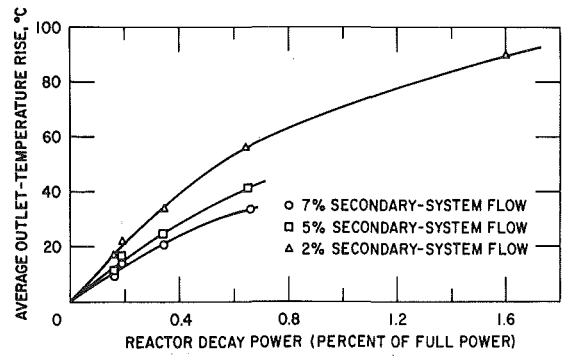

Fig. 11 Effect of power level on the maximum subassembly outlet coolant temperature (average of 17 subassemblies)

increasing reactor power. During a loss of forced flow transient at constant decay power, a similar interaction occurs. For higher initial power levels, the initial buoyancy forces are larger due to the increased axial temperature gradient, so that the transition from forced to natural convective flow will occur at a greater minimum flow rate. However, due to the higher power level, the rate of heat input to the coolant is also larger. Thus, the net effect of power level upon peak transient coolant temperatures is dependent upon the relative dynamics of the flow de- and acceleration and energy storage and transfer.

These tests were designed so that a number of decay power levels at a given secondary flow rate could be attained and their affect upon the minimum coolant flow rate and peak coolant temperature during the loss-of-forced-flow transients studied. To illustrate the effects of decay power on the minimum flow rate at the transition from forced to natural circulation flow, the data of Fig. 6 are cross plotted in Fig. 9 with secondary system flow as a parameter. These data indicate a near linear relationship between decay power and minimum in-core flow rates. Each of the curves appears to have a different intercept for zero decay power. These different intercepts reflect the contribution of the buoyancy forces in the IHX to the minimum in-core flow. The data point at 1.6 percent decay power and 2 percent secondary system flow was obtained in 1974 as part of the XX07 instrumented subassembly natural circulation test program [1]. The measured minimum flow rate of 0.68 percent is seen to be consistent with the values obtained in the current XX08 test program.

The maximum coolant temperature rises at the outlet of XX08 are shown in Fig. 10 as a function of decay power. Each curve in Fig. 10 appears to indicate a zero temperature rise at zero decay power which is the expected result. As with the minimum flow curve, the temperature rise obtained during the earlier XX07 test appears to be reasonably consistent with the XX08 data.

Figure 11 shows the average values of the maximum temperature rises at the outlet of several in-core subassemblies versus decay power. These data show the same relationship as did the XX08 outlet temperature data. The point at 90°C at 1.6 percent decay power represents the XX07 Test F result. Although this test was terminated before all of the outlet temperatures had reached their maximum values, the 90°C value is believed to be approximately the average maximum value which would have been reached if the test had not been terminated.

All these data indicate that the slope of the maximum coolant temperature versus decay power curve is positive, but decreases with increasing power. Thus, although increased power levels increase the peak transient temperature, the increased buoyancy caused by the resulting larger axial temperature gradients somewhat reduces the magnitude of this effect through increased convective flow rates. This same phenomenon is responsible for the redistribution of coolant flow rates across a reactor core and the resultant reduced transverse temperature gradients observed during natural circulations events in LMFBRs [9].

Conclusions

Each of the tests in the XX08 natural circulation test program resulted in a smooth transition from forced to natural circulation flow following an abrupt loss of pumping power. The minimum in-core flow rate has been shown to be a nearly linear function of decay power level. The effect of secondary system flow through the IHX (a parameter representative of the buoyant driving forces in the IHX) was observed to have a very strong effect, particularly over the range where initial primary flow and secondary flow were reasonably closely matched. The data on flows and temperature rises obtained in this test program appear to be consistent with data from an earlier test done as part of the XX07 program.

The data obtained from these tests are being used in the development of computer models for analytical studies of flow coastdown/natural circulation events. These models will provide the link between the data obtained in EBR-II and the expected flows and temperatures in larger LMFBRs having different fuel pin sizes and compositions. The data have also been used as a basis for planning and conducting additional tests which will further enhance our understanding of natural circulation phenomena. The results of these measurements and the analytical predictions will be presented in a forthcoming paper.

Acknowledgments

These whole plant transients could not have been successfully conducted without the direct technical support of many EBR-II personnel. We would like to especially acknowledge Roland Smith, William Perry, Gary Lentz, and all of the reactor operating crews for their efforts related to the many operational problems involved with these tests, William Booty for his work in developing the data acquisition program, Nadine Allen and Lavar Welker for their work in procedures and scheduling, and the many EBR-II experimenters who agreed to having their experimental irradiation subassemblies experience these thermal-hydraulic transients.

References

1 Gillette, J. L., et al., "A Flow Coastdown Transient to Natural Convective Conditions in EBR-II," *Transactions of American Nuclear Society*, Vol. 22, 1975, pp. 594–596.

2 Unpublished document, "Natural Circulation Testing of the SEFOR Reactor Coolant System."
3 Sunderman, I. O., "Hallam Nuclear Power Facility Post Critical Test Completion Report, Scram, and Loss-of-Load," Atomics International Report A1-PC-660, Feb. 1964.
4 Chenal, J. C., Pointer, R., and Delisk, J. P., "Emergency Cooling of the Rapsodie-Fortissimo Core," ASME Paper No. 74-WA/HT-51, 1974. Presented at the 1974 Winter Annual Meeting of the ASME, New York.
5 Guillemard, B., "Start-up of Phenix," *Nuclear Engineering International*, Vol. 19, No. 216, May 1974, pp. 411–414.
6 Gregory, C. V., et al., "Natural Circulation Studies in Support of the Dounreay PFR," Presented at the International Meeting on Fast Reactor Safety Technology, Seattle, Wash., Aug. 19–23, 1979.
7 Koch, L. J., et al., "Hazard Summary Report: Experimental Breeder Reactor II (EBR-II)," Argonne National Laboratory Report No. ANL-5719, May 1957, and ANL-5719 (Addendum), June 1962.
8 Smaardyk, A., et al., "EBR-II Environmental Instrumented Subassembly XX08: Engineering and Assembly," Argonne National Laboratory Report ANL-78-9, May 1978.
9 Singer, R. M., and Gillette, J. L., "Measurements of Subassembly and Core Temperature Distributions in an LMFBR," *AIChE Symposium Series*, Vol. 73, No. 164, 1977, p. 97.

A. A. Emara[1]
F. A. Kulacki
Associate Professor, Mem. ASME

Department of Mechanical Engineering, Ohio State University, Columbus, Ohio 43210

A Numerical Investigation of Thermal Convection in a Heat-Generating Fluid Layer

Finite difference solutions of the equations governing thermal convection driven by uniform volumetric energy sources are presented for two-dimensional flows in a rectangular domain. The boundary conditions are a rigid, (i.e., zero slip), zero heat-flux lower surface, rigid adiabatic sides, and either a rigid or free (i.e., zero shear) isothermal upper surface. Computations are carried out for Prandtl numbers from 0.05 to 20 and Rayleigh numbers from 5×10^4 to 5×10^8. Nusselt numbers and average temperature profiles within the layer are in good agreement with experimental data for rigid-rigid boundaries. For rigid-free boundaries, Nusselt numbers are larger than in the former case. The structure of the flow and temperature fields in both cases is dominated by rolls, except at larger Rayleigh numbers where large-scale eddy transport occurs. Generally, low velocity upflows over broad regions of the layer are balanced by higher velocity downflows when the flow exhibits a cellular structure. The hydrodynamic constraint at the upper surface and the Prandtl number are found to influence only the detailed nature of flow and temperature fields. No truly steady velocity and temperature fields are found despite the fact that average Nusselt numbers reach steady values.

Introduction

This paper presents the results of a numerical investigation, via finite-difference methods, of two-dimensional thermal convection in a horizontal layer of fluid containing uniformly distributed volumetric energy sources. These calculations have been carried out, in part, owing to the possible importance of this heat transfer process in geophysics [1–4], astrophysics [5, 6], and nuclear power reactor safety—specifically, heat removal from a molten pool of fuel and reactor material following a core-melt accident [7]. The heat transfer problem fundamental to all of these areas as a prototypic model is the computation of the convective heat transfer coefficient at the surface of a horizontally infinite, or shallow ($L/X \ll 1$), layer bounded from below by a perfectly insulating surface and from above by a constant temperature surface. In such a system, there is no downward heat transfer, and edge effects are either nonexistent or of negligible influence on the vertical transport processes within the layer. Although several experimental and theoretical investigations [8–14] of this problem have appeared in the open literature, none have presented detailed information on the nature of the velocity and temperature fields of steady convection for finite Prandtl-number fluids and Rayleigh numbers greater than about 30 times the value at the onset of convection. The present study is aimed at providing such information, as well as the calculation of the convective heat transfer coefficient at the upper surface of the layer in a form suitable for engineering applications.

For the present study, it is assumed that the fluid satisfies the Boussinesq equation of state and is a normal fluid in the sense that $\beta > 0$. The layer is bounded from below by a rigid (zero slip), zero heat-flux surface. The upper boundary is held at a constant temperature and, for one series of calculations, is taken as a rigid surface (rigid-rigid case). In another series of calculations, the upper boundary is taken as a free (zero shear) surface (rigid-free case). The vertical boundaries of the layer are taken as rigid and perfectly insulating in both cases.

The computational approach taken is to cast the governing time-dependent, nonlinear partial differential equations in the stream function-vorticity form and to seek quasi-steady solutions for laminar convection in terms of a convergence criterion placed on the horizontally averaged temperature distribution within the layer. This approach is followed in recognition of the previous studies [15–17] which showed both experimentally and theoretically that in thermal convection with uniform volumetric energy sources in a layer with two constant temperature boundaries, horizontally averaged temperature and flow fields exhibit no truly steady pattern despite the fact that average Nusselt numbers at the boundaries reach steady values. It was expected that the same behavior would be found in the present study because the convective momentum and energy transport process within the core region of the layer are not much affected by the substitution of a zero heat flux surface at the lower boundary, at least for Rayleigh numbers greater than several times the value at the onset of convection.

Governing Equations

The familiar Boussinesq equations govern the velocity and temperature fields: the Navier-Stokes equations, the continuity equation, and the energy equation with the body force related linearly to temperature. For the present work, the physical quantities L, α/L, and $HL^2/2k$ are used to scale the length, velocity, and temperature, respectively. These scalings bring out the Rayleigh number and Prandtl number as the governing dimensionless groups.

If one eliminates the pressure from the momentum equation by taking its curl, the Boussinesq equations may be written in the conservative stream function-vorticity form as

$$\frac{1}{\mathrm{Pr}}\frac{\partial \omega}{\partial t} + \frac{\partial (u\omega)}{\partial x} + \frac{\partial (v\omega)}{\partial y} = -\mathrm{Ra}\frac{\partial \theta}{\partial x} + \frac{\partial^2 \omega}{\partial x^2} + \frac{\partial^2 \omega}{\partial y^2}, \tag{1}$$

$$\frac{\partial \theta}{\partial t} + \frac{\partial (u\theta)}{\partial x} + \frac{\partial (v\theta)}{\partial y} = \frac{\partial^2 \theta}{\partial x^2} + \frac{\partial^2 \theta}{\partial y^2} + 2, \tag{2}$$

where the vorticity, ω, is now a scaler quantity owing to the two-dimensional nature of the present problem. The vorticity and stream function are related by the Poisson equation

$$\omega = \frac{\partial^2 \psi}{\partial x^2} + \frac{\partial^2 \psi}{\partial y^2}. \tag{3}$$

Boundary conditions which accompany equations (1–3) are shown in Fig. 1, along with the grid system used in their solution by finite differences. The initial condition taken in all cases is a motionless constant temperature fluid, i.e., $u = v = \theta = \psi = \omega = 0$ at $t = 0$, everywhere within the layer.

[1] Presently with United Technologies, Pratt and Whitney Aircraft Group, East Hartford, Connecticut 06108

Contributed by the Heat Transfer Division and presented at the 18th AIChE/ASME National Heat Transfer Conference, San Diego, Calif., August 6–8, 1979. Revised manuscript received by the Heat Transfer Division, December 28, 1979. Paper No. 79-HT-103.

Solution

The grid sizes used in the present study, $\Delta x = \Delta y = 1/30$ and $1/20$, have been selected on the basis of convergence and accuracy for a test case at $\mathrm{Ra} = 6.3 \times 10^5$. Details of the choice of the difference scheme and the development of the finite-difference equations are given by Emara [18]. Here, only a few remarks on each of these aspects of the solution will be presented.

In the work of Barakat and Clark [19], the nonlinear terms in the energy and vorticity equations were approximated with two-point backward or forward differences according to whether the velocity components u and v were either positive or negative, respectively. This was termed the "first upwind differencing method." Torrance [20] developed a modified form of the first upwind differencing method in which, for example, the mean x-component of velocity, $u = u_{i,j} + u_{i+1,j}/2$, in the nonlinear term $\partial(u\theta)/\partial x$ was multiplied by $\theta_{i,j}$ or $\theta_{i+1,j}$, according to whether u was positive or negative, respectively. This method was termed the "second upwind differencing method" and preserves the conservative and transportive properties of the energy and vorticity equations. All methods which use the central difference approximation for the advective terms do not possess this property [21]. Also, it was shown by Torrance that the finite-difference representation of the energy and vorticity equations using central differences to approximate the advective terms (e.g., in the work of Fromm [22]) leads to numerically induced oscillations in the results. However, the modified scheme for forward or backward differences developed by Torrance retains some features of central differences, in particular, second-order accuracy [21]. Owing to these factors, the second upwind differencing method appears to be the most suitable approximation for the nonlinear terms in equations (5) and (6) and has been adopted in the present work.

Finite difference methods for solving parabolic partial differential equations, such as those of the present study, can be classified as either explicit or implicit. Use of the explicit method, however, may require small time increments, i.e., large computation time, in order to satisfy stability requirements. To avoid severe restrictions on the time increment, implicit methods are usually recommended. In the implicit method, iterative techniques are generally used for the solution of the resulting system of algebraic equations. The Gauss-Seidel procedure is appropriate for this purpose but may require a large number of iterations per time step. On the other hand, increasing the size of the time step would increase the number of iterations required to achieve any reasonable degree of accuracy. The use of the implicit method from the standpoint of realizing a savings of computation time, thus, may be of marginal benefit. Furthermore, the use of the implicit method for the solution of the vorticity equation may have a limited advantage over the explicit method owing to the lack of a way to directly evaluate the vorticity at rigid boundaries. The boundary value of vorticity at time level $n + 1$ is not known, and therefore, the value of the vorticity at the wall at time level n must be used to approximate that at time level $n + 1$. Such a linearization of the vorticity boundary condition requires the use of small time increments so that $\omega_{i,j}{}^n$ at the boundary will be a good approximation for $\omega_{1,j}{}^{n+1}$. With all of these factors taken into consideration, the explicit formulation of the finite-difference equations has been adopted for the present study.

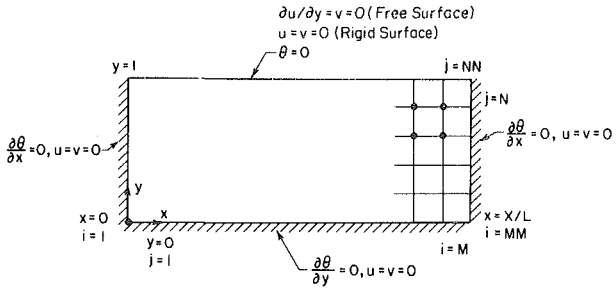

Fig. 1 Domain, coordinate system, grid network and boundary conditions for the finite-difference computations

With regard to the determination of the vorticity at the boundaries, the following procedure has been adopted. Equation (1) is used to solve for the vorticity at the interior grid points, with boundary values of vorticity held constant. After the vorticity at the interior grid points is calculated for the new time step and the stream function has been computed from it at the same time step using equation (3), the values for the vorticity at, say $y = 0$ are evaluated from

$$\omega_{i,1}^{n+1} = \frac{8\psi_{i,2}^{n+1} - \psi_{i,3}^{n+1}}{2(\Delta y)^2} + 0((\Delta y)^2). \tag{4}$$

Stability criteria have been developed for the time step and grid size in the finite difference equations using the analysis of Lax and Richtmeyer [23]. Their analysis guarantees both numerical stability and convergence of the calculations. The specific stability criteria depend on sign of u and v. These have been derived and are tabulated by Emara [18].

As previously indicated, the computations are begun with a motionless, isothermal layer. Horizontally averaged temperature distributions are computed at each time step. When mean temperature profiles for two successive time steps differ by less than 10^{-3} over $0 \leq y \leq 1$, steady state is assumed. At the approach to the steady state, this criterion produces a maximum variation in the Nusselt number at the upper surface of approximately 5 percent between successive time steps. Most of this variation is a result of the order of the approximation for the temperature gradient at the upper boundary.

The local Nusselt number at the upper boundary is defined in terms of the local maximum temperature difference within the layer, θ_0, and the local gradient of temperature at the upper surface. The latter is evaluated by using a Taylor's series expansion of the temperature at $j = N$, $N - 1$ and $N - 2$. This results in an approximation of order $(\Delta y)^3$ for the temperature gradient but does not correct for convection near the surface. Thus, while the numerical methods used in the present work are globally conservative to within round-off errors, the method of estimating the temperature gradient at $y = 1$ produces an error in the gross energy balance over the layer. For $10^5 \leq \mathrm{Ra} \leq 10^8$, such an energy balance is satisfied to within 5 to 10 per cent, where greater accuracy is obtained at the lower Rayleigh numbers. The average Nusselt number at the upper boundary is obtained by numerical

Nomenclature

C, m = constants of correlation, equation (15)
H = volumetric heat generation rate
$\mathbf{j}$ = unit vector in y-direction, (0,1)
k = thermal conductivity
L = vertical depth of fluid layer
P = pressure
Pr = Prandtl number, ν/α
Ra = Rayleigh number, $(g\beta/\alpha\nu)(HL^5/2k)$
t = time
T = temperature
$\mathbf{u}$ = velocity, (u,v)
x = horizontal coordinate
X = horizontal extent of layer
Δx = grid size in x-direction
y = vertical coordinate
Δy = grid size in y-direction
α = thermal diffusivity
β = isobaric coefficient of thermal expansion, $(-1/\rho)(\partial\rho/\partial T)_p$
θ = nondimensional temperature difference, $(T - T_1)/(HL^2/2k)$
ρ = density
ν = kinematic viscosity
ψ = streamfunction, $u = \dfrac{\partial\psi}{\partial y}$ and $v = -\dfrac{\partial\psi}{\partial x}$
ω = vorticity, $\partial v/\partial x - \partial u/\partial y$

Subscripts

i = node location in x-axis, Fig. 1
j = node location in y-axis, Fig. 1
1 = upper surface
0 = lower surface

Superscripts

n = point in time
$*$ = physical quantity

integrations of local values using the trapezoidal rule.

Results

Comparison with Previous Studies. In order to test the precision and accuracy of the numerical scheme of the present study, a series of computations were run for a layer with two rigid, constant temperature boundaries. Measurements of horizontally averaged temperature fields and convective heat transfer coefficients in this system have been reported by Kulacki and Goldstein [15], and Mayinger, et al. [16] have presented both finite-difference solutions and measurements. In Fig. 2, horizontally averaged temperature profiles computed with the present numerical formulation are presented with the measurements of Kulacki and Goldstein for Rayleigh numbers of 2.57×10^4 and 2.02×10^6. The agreement is considered very good. Computed streamline and isotherm patterns of the present study are also in good agreement with those computed by Mayinger, et al. (see Emara [18] for a comparison of these results).

Convective heat transfer coefficients at the upper and lower boundaries of the layer are defined in terms of the maximum temperature difference within the layer. They are conveniently correlated in terms of the Nusselt number versus the Rayleigh number in the form

$$\mathrm{Nu} = C \cdot \mathrm{Ra}^m. \tag{5}$$

The constants of correlation obtained in the present work are listed in Table 1 with those obtained in the experiments of Kulacki and Goldstein [15] and in the calculations and experiments of Mayinger, et al. [16]. Despite the difference in Prandtl number ranges and/or experimental apparata, the several correlations are in good agreement.

The Present Study. Flow fields, temperature fields and average heat transfer coefficients at the upper surface have been computed for both the rigid-rigid and rigid-free cases. The majority of the computations have been done for layer aspect ratios of one-half and unity. The results reviewed here are typical streamline and isotherm patterns of fully developed convection for several Prandtl numbers. They have been selected so that a more general exposition of the convective processes within the layer can be developed than by a review of the computations at only one Prandtl number.

In Figs. 3 to 8, streamline and isotherm patterns are presented for Pr = 6.5 and several values of the Rayleigh number for the rigid-rigid and rigid-free cases. For each Rayleigh number, the streamlines and isotherms are *not* steady even though the horizontally averaged temperature distributions, particularly θ_0, become time-invariant. Despite this quasi-steady nature, the overall features of the velocity and temperature fields change rather slowly with time, and only slight differences can be attributed to the hydrodynamic constraint at the upper surface.

At a Rayleigh number of 5×10^4 ($\mathrm{Ra/Ra}_c = 36$, where $\mathrm{Ra}_c = 1386$ [24]), it can be seen in Fig. 3 that two vortex-like flows, or rolls, carry warm fluid upward across a broad region at the center of the layer in the rigid-rigid case. Cool fluid is carried along the upper boundary and down the sides, and up-flow and down-flow occupy about equal fractions of the horizontal extent of the layer. This indicates that average up-flow and down-flow velocities are approximately equal. These features of the flow and temperature fields remain almost the same (Fig. 7) for the rigid-free case as the Rayleigh number is increased to 10^5 ($\mathrm{Ra/Ra}_c = 72$). The flow field for the rigid-rigid case at $\mathrm{Ra} = 10^5$, however, undergoes a reversal in the center of the layer, and four center-rotating rolls are formed (Fig. 4). The regions of down-flow and up-flow still occupy about equal fractions of the horizontal extent of the layer, with the up-flow occupying a relatively broad region for each pair of recirculating flows. The regions of down-flow become thinner at a Rayleigh number of 5×10^6 ($\mathrm{Ra/Ra}_c = 3608$), with four rolls yet characterizing the streamline pattern for the rigid-rigid case (Fig. 5). In addition, the streamline and isotherm patterns of the rigid-free case at $\mathrm{Ra} = 10^6$ (Fig. 8) have undergone a change to resemble those of the rigid-rigid case.

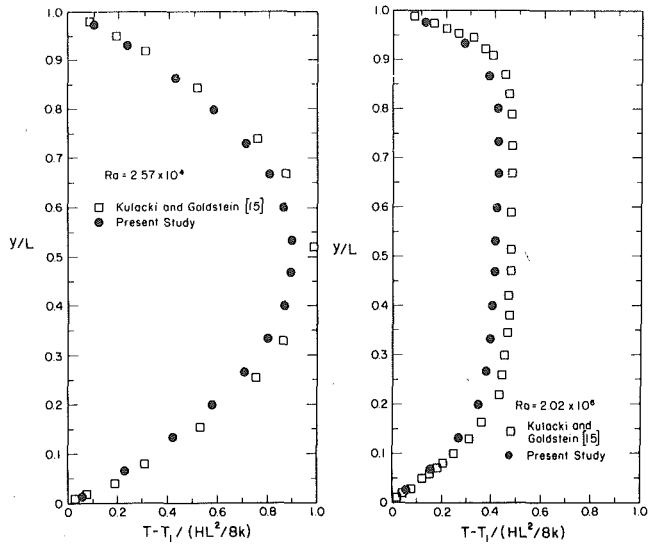

Fig. 2 Calculated and measured horizontally averaged temperature distributions in a layer with two rigid, constant temperature boundaries

For both the rigid-rigid and rigid-free cases, further increases of the Rayleigh number result in the formation of a thin thermal boundary layer on the upper surface, very broad regions of up-flow with corresponding narrow, jet-like down-flows, and the release of large-scale thermals from the upper surface. Streamline patterns at $\mathrm{Ra} = 5 \times 10^6$ and 10^7 (Figs. 5 and 6) have lost the regularity observed at lower Rayleigh numbers. Isotherm patterns at these Rayleigh numbers indicate that thermals released from the thermal boundary layer at the upper surface can have a length scale of the order of the layer depth and can penetrate almost the entire depth of the layer (Fig. 6). Such a large scale eddy disrupts the generally low speed-up flows which are separated by relatively narrow regions of much higher speed down-flow (Figs. 5 and 8). At larger Rayleigh numbers, these features of the streamline and isotherm patterns become more pronounced, and the hydrodynamic boundary condition at the upper surface has minimal influence on the large-scale motion within the layer.

In Figs. 9 and 10, streamline and isotherm patterns are presented for the rigid-rigid case for Pr = 1.0 and Rayleigh numbers of 10^5 and 5×10^6, respectively. At $\mathrm{Ra} = 10^5$, the flow and temperature fields exhibit practically the same features as are observed for Pr = 6.5 (Fig. 4). This similarity in the streamline and isotherm patterns for Pr = 6.5 and 1.0 persists until the Rayleigh number is increased to 5×10^6 (Fig. 10). At this Rayleigh number, two recirculating flows are observed for the Pr = 1.0 case. At this Prandtl number, up-flow in the layer exists over a very broad region, and rapid down-flows are observed at the vertical walls. Comparison of Figs. 5 and 10 reveals that for both Pr = 6.5 and 1.0, any type of regularity in the flow structure begins to diminish, and local transient distortions can be observed in the streamline and isotherm patterns. This is evident in Fig. 10 at

Table 1 Coefficients of correlation for equation (5) for Nusselt numbers in an internally heated layer with two constant temperature boundaries

	Upper Surface		Lower urface			
	C	m	C	m	Ra	Pr
Kulacki and Goldstein [15]	0.436	0.228	1.503	0.095	3.52×10^4 -1.21×10^7	5.76–6.09
Mayinger, et al. [16]* (Calculations)	0.399	0.23	1.163	0.107	$\sim 10^5$–10^8	6.5
Mayinger, et al. [16] (Experiments)	0.405	0.233	1.484	0.095	8×10^4–10^{11}	~7
Present Study	0.385	0.23	1.131	0.119	10^5–10^8	6.5

* Results were originally given as $\mathrm{Nu}_1 = 0.34\mathrm{Ra}^{0.23}\mathrm{Pr}^{0.085}$, $0.04 \leq \mathrm{Pr} \leq 10$.

the upper left and in Fig. 5 to the left of the centerline and can be attributed to the release of thermals at the upper surface. It is also evident from Fig. 10 that the formation and release of large-scale thermals is well established at Ra = 5×10^6 and Pr = 1.0. For the rigid-free case and Pr = 1.0, the flow and temperature fields are generally the same as in the rigid-rigid case, and increases in the Rayleigh number from 10^5 to 5×10^6 result in very similar alterations to the streamline and isotherm patterns.

To gain further insight on the influence of the Prandtl number on the streamline and isotherm patterns, calculations were done for the rigid-rigid and rigid-free cases and Pr = 20. The results have been graphically summarized by Emara [18], and a brief summary of them will be included here. For the rigid-rigid case at Ra = 5×10^6, the convective process exhibits well-defined narrow regions of down-flow

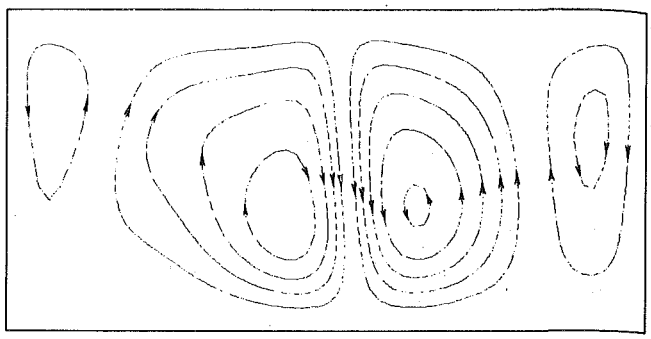

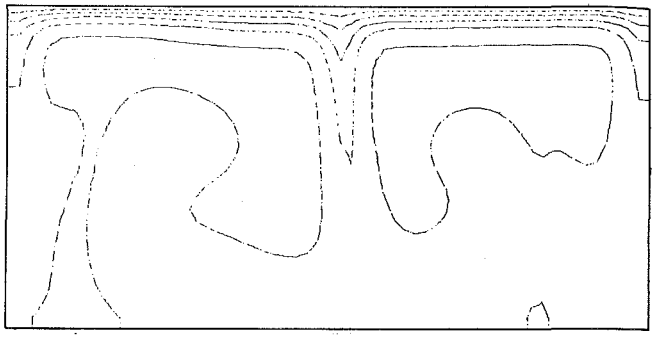

Fig. 5 Streamline and isotherm patterns for rigid-rigid boundaries for Ra = 5×10^6, Pr = 6.5, $\Delta\theta = 0.028$ and $\Delta\psi = 13$

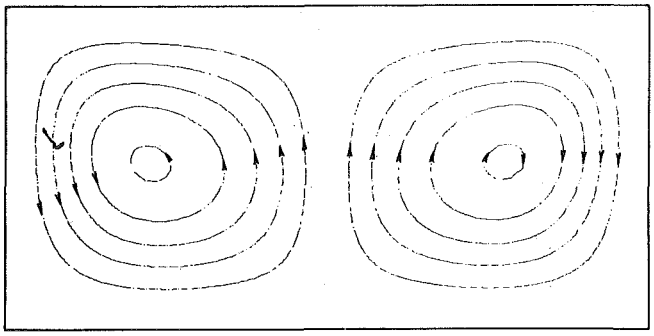

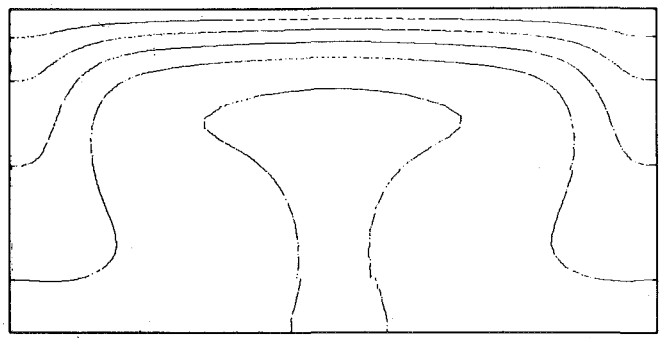

Fig. 3 Streamline and isotherm patterns for rigid-rigid boundaries for Ra = 5×10^4, Pr = 6.5, $\Delta\theta = 0.065$ and $\Delta\psi = 2$

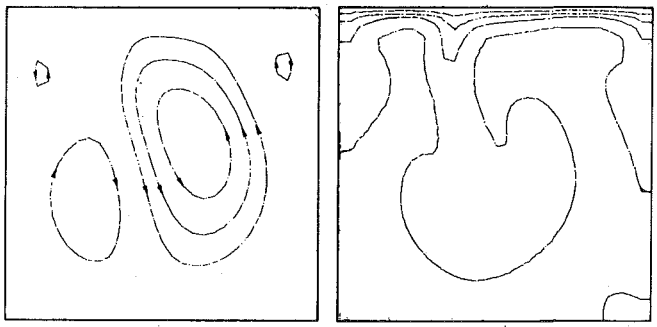

Fig. 6 Streamline and isotherm patterns for rigid-rigid boundaries for Ra = 10^7, Pr = 6.5, $\Delta\theta = 0.03$ and $\Delta\psi = 20$

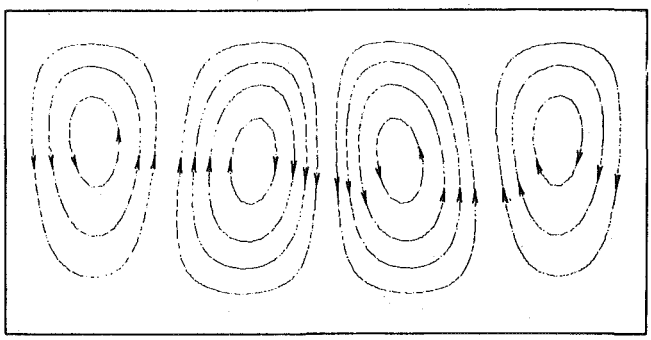

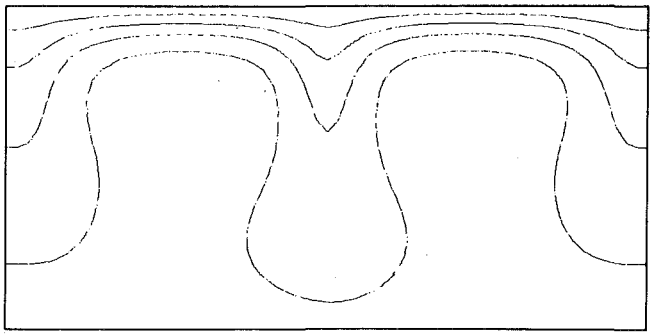

Fig. 4 Streamline and isotherm patterns for rigid-rigid boundaries for Ra = 10^5, Pr = 6.5, $\Delta\theta = 0.06$ and $\Delta\psi = 2.2$

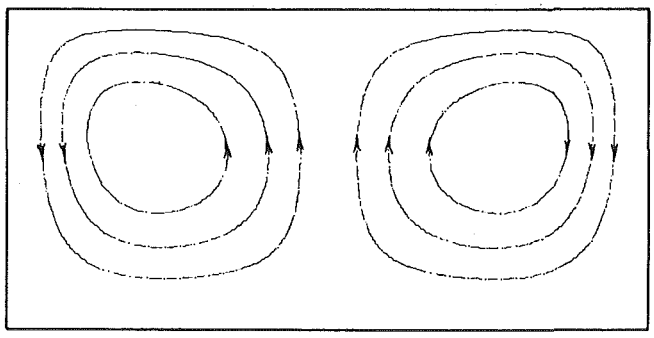

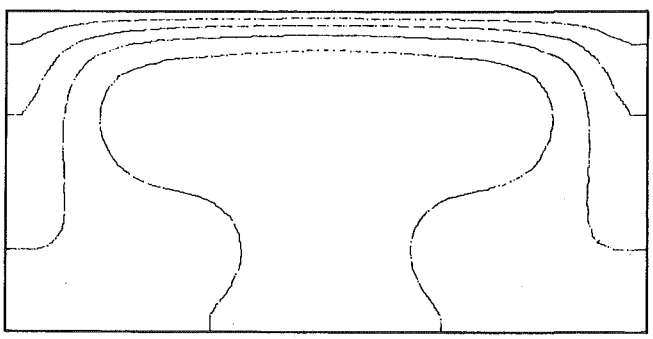

Fig. 7 Streamline and isotherm patterns for rigid-free boundaries for Ra = 10^5, Pr = 6.5, $\Delta\theta = 0.06$ and $\Delta\psi = 2.2$

and fairly broad regions of low velocity up-flow. In comparison to the streamline and isotherm patterns at Pr = 6.5 (Fig. 5) and Pr = 1 (Figs. 9 and 10), the thermal boundary layer for Pr = 20 is much thinner than at the lower Prandtl numbers, and the locally unsteady nature of the flow field at the lower Prandtl numbers is somewhat suppressed. The downflow in the center of the layer at Pr = 20 appears first at a lower Rayleigh number, Ra $\lesssim 10^6$, where the transition from up-flow in the center occurs. At Pr = 6.5, this transition occurs at Ra $\gtrsim 5 \times 10^4$ and, thus the larger Prandtl number has apparently delayed this transition. The transition to down-flow in the center is similarly delayed until Ra $\gtrsim 10^6$ in the rigid-free case. For this case, both the Prandtl number and the hydrodynamic constraint at the upper surface result in a larger Rayleigh number for the flow transition. At Ra $= 10^6$, the low velocity up-flow in the center of the layer is balanced by high-velocity, boundary layer-like down-flows on the vertical boundaries. Between Ra = 10^6 and 10^7, the double-roll streamline pattern at the lower Rayleigh number breaks up into four recirculating flows, and a very narrow down-flow exists at the centerline. At the larger Rayleigh number, the boundary layer structure of the down-flows becomes more established, and the horizontally-averaged temperature profile becomes nearly isothermal in the core of the layer. The formation and release of thermals at the upper boundary, as was previously observed at Pr = 1 and 6.5, does not appear in the streamline and isotherm patterns for Pr = 20 at the Rayleigh numbers accessible with the present solution.

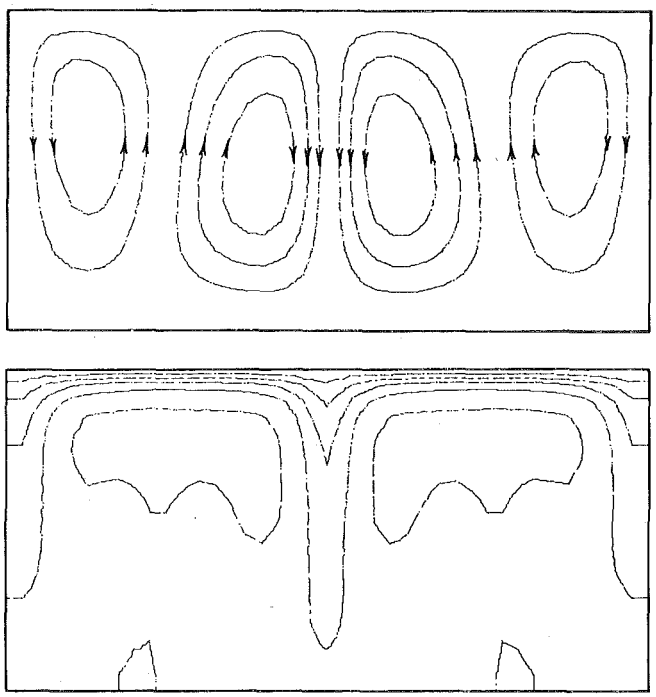

Fig. 8 Streamline and isotherm patterns for rigid-free boundaries for Ra = 10^6, Pr = 6.5, $\Delta\theta = 0.028$ and $\Delta\psi = 13$

Average heat transfer coefficients at the upper boundary of the layer have been computed using equation (5) as a practical relation for engineering purposes. Correlations for the rigid-rigid and rigid-free cases are summarized in Table 2. These are presented graphically in Fig. 11, along with the correlation of Kulacki and Emara [14] for the rigid-rigid case based on measurements on a layer of water (Pr $\simeq$ 6.5) over the range $1.89 \times 10^3 \leq$ Ra $\leq 2.17 \times 10^{12}$. The agreement between the experimental correlation and the results of the present study is excellent over the entire range of the calculations. In addition, an extension of the calculated correlation to low Rayleigh number (Fig. 12) produces equally good agreement with measured Nusselt numbers over the range $1 \leq$ Ra/Ra$_c \leq 2.5$, where convection is quite feeble. A similar comparison to the calculated correlation for the rigid-free case cannot be made at the present owing to the lack of published measurements. However, it may be noted that Mayinger, et al. [16] have found calculated Nusselt numbers at a free upper surface in a layer with two constant temperature boundaries to be larger than those for a rigid upper surface. This is generally the case with the present results except at Ra $\geq 10^8$, where few calculations were made. The extension of the correlation for the rigid-free case to high Rayleigh number, thus, should be done with caution until experimental data are available to better establish the relation between the Nusselt number and the Rayleigh number.

That a zero-shear upper surface results in a larger average Nusselt number than in the case of a rigid upper surface is reasonable on physical grounds. When the upper surface is rigid, i.e., zero-slip, heat transfer must be by conduction at $y = 1$. The tangential velocity permitted by a zero-shear upper surface permits convection to play a role in the heat transfer process. Despite the use of a finite difference

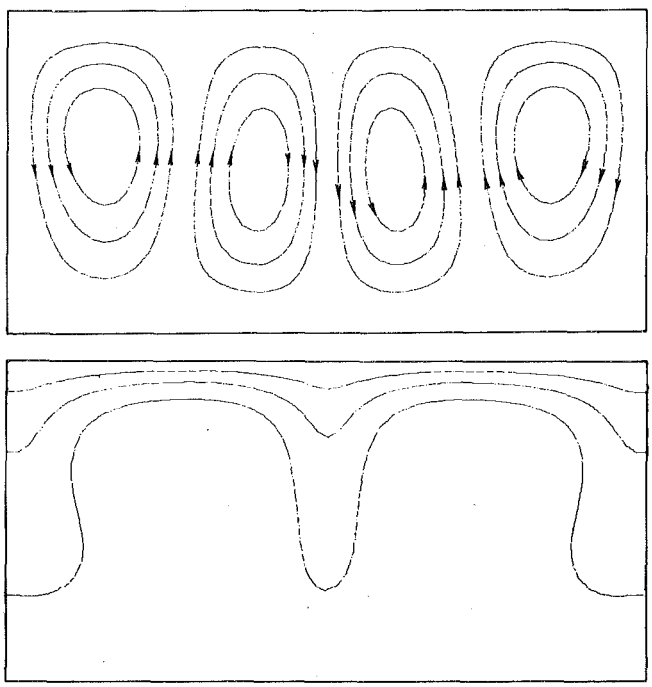

Fig. 9 Streamline and isotherm patterns for rigid-rigid boundaries for Ra = 10^5, Pr = 1, $\Delta\theta = 0.077$ and $\Delta\psi = 2$

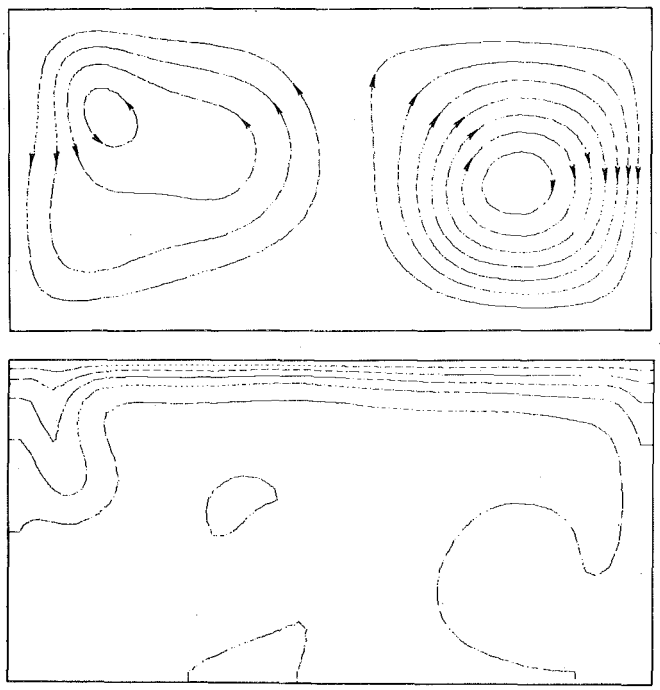

Fig. 10 Streamline and isotherm patterns for rigid-rigid boundaries for Ra = 5×10^6, Pr = 1, $\Delta\theta = 0.035$ and $\Delta\psi = 2$

Table 2 Heat transfer correlations for steady convection in an internally heated horizontal layer with an insulated lower boundary and isotherm upper boundary

Case	$Nu = CRa^m$				$Nu = CRa^mPr^n$				
	C	m	Ra	Pr	C	m	n	Ra	Pr
Rigid-Rigid	0.420	0.223	5×10^3–5×10^8	6.5	0.477	0.210	0.041	5×10^3–5×10^8	0.05–20
Rigid-Free	0.939	0.182	5×10^4–5×10^8	6.5	0.859	0.178	0.059	5×10^4–5×10^8	0.05–20

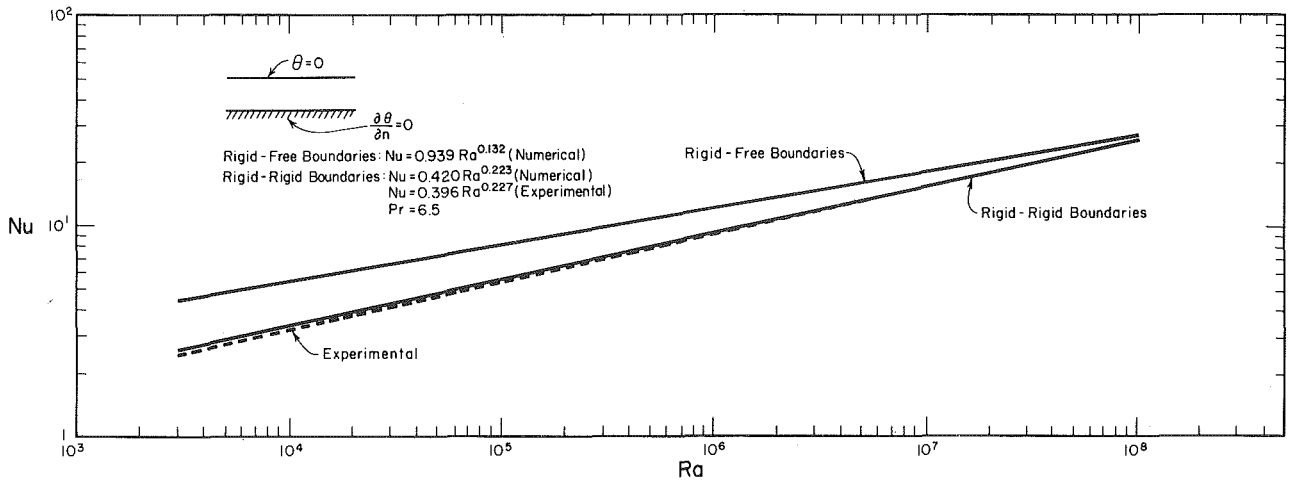

Fig. 11 Heat transfer correlations for rigid-rigid and rigid-free boundaries

calculation of the temperature gradient which does not explicitly account for convection, the presence of non-zero velocity components near the upper surface are taken into account in the temperature field.

It may be noted that the differences between the present results and those of Roberts [9] and Thirlby [10], shown in Fig. 12, arise because of differences in both computational approach and the assumptions on the plan form of motion. Roberts used the globally averaged conservation equations and scaled the velocity and temperature to values at the onset of motion predicted by linear stability theory. This implies a fixed wave number for the convective plan form, which is true even for very low values of the layer aspect ratio, L/X [8]. Thirlby employed the compressible form of the continuity equation with the otherwise incompressible momentum and energy equation. He assumed that steady state was reached when the pressure field, which was related to the density via the simple equation of state p = Constant·ρ, showed no change for two successive time steps. His two-dimensional solutions assumed rolls with a wave number set at the value given by linear stability theory. In the present study, none of these constraints are applied, except for the restriction to two-dimensionality. Of course, the experimental data of Kulacki and Emara [14] are for a full three-dimensional flow, albeit in a low aspect ratio layer.

Horizontally averaged temperature distributions across the layer obtained in the present study for rigid-rigid boundaries are compared to the measurements of Kulacki and Emara [14] in Fig. 13. Good to fair agreement is seen between the numerical and experimental results. The deviations between the calculated temperature distributions and measurements in the core region are believed, in part, a result of disturbances introduced by the thermocouple probe used to obtain time-averaged measurements of temperature. This probe (see reference [14] for details of its construction) was used to record temperatures at all elevations in the layer, including values at the lower boundary.

Concluding Remarks

The finite-difference solution of the equations governing laminar convection in a fluid layer with uniform volumetric energy sources has enabled the calculation of temperature fields and heat transfer

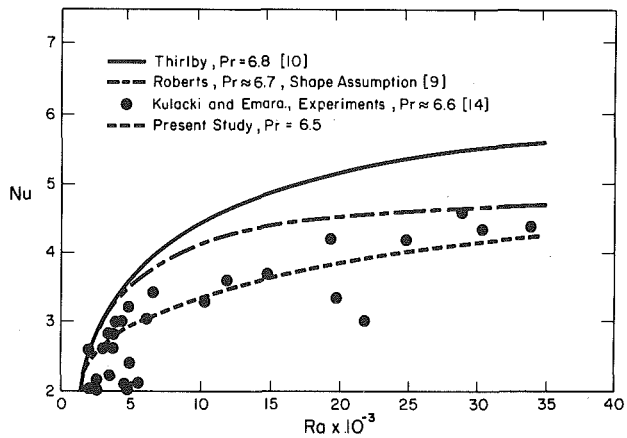

Fig. 12 Calculated and measured Nusselt numbers in the vicinity of the conduction region for rigid-rigid boundaries

coefficients for rigid-free and rigid-rigid boundaries, the latter being in very good agreement with measurements for Rayleigh numbers from near the conduction region to approximately 360,000·Ra_c. Mean temperature profiles in the layer are also in good agreement with time-averaged measurements. However, the structure of the flow and temperature fields is dependent in a complex manner on the Prandtl number and the hydrodynamic boundary condition at the upper surface. Owing to the restriction of the calculations to two-dimensional flows, convection is generally dominated by counter-rotating rolls. This roll convection breaks down, however, at moderately large Rayleigh numbers for $Pr \leq 6.5$ as the release of thermals from the upper boundary becomes an important mechanism of heat transfer.

The results of the present study are formally restricted to laminar convection. No turbulence models for the eddy exchange process at the upper boundary have been considered in the present calculations. However, it should be noted that the present range of Rayleigh numbers overlaps the regime of turbulent convection. The early experiments of Tritton and Zarraga [8] on the planform of the motion in a layer with boundary conditions similar to those of the present

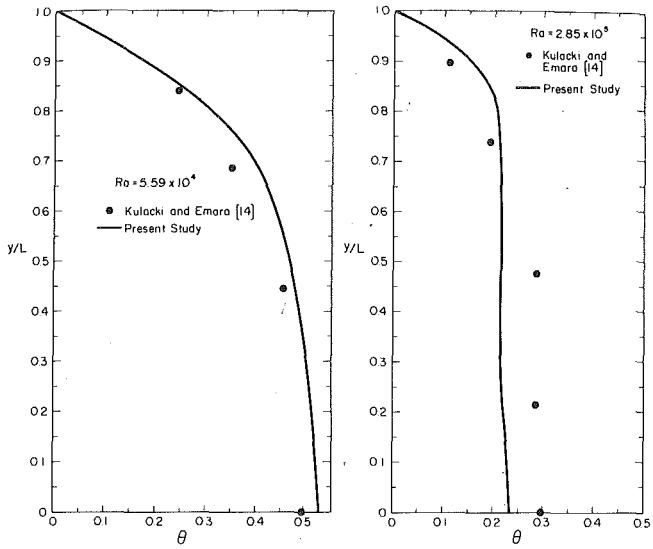

Fig. 13 Horizontally averaged temperature profiles of the present study and the time averaged measurements of Kulacki and Emara [14] for rigid-rigid boundaries

study show that turbulent motion begins at approximately $80 \cdot Ra_c$. More recent experiments [15] on a layer with two isothermal boundaries indicates that turbulent motion begins at a Rayleigh number about $100 \cdot Ra_c$. The work of Tritton and Zarraga, however, is considered as the only substantiated indication of the onset of turbulent convection in the system of interest here. Thus, the general validity of the streamline and isotherm patterns for the larger Rayleigh numbers of the present study can be questioned despite the agreement between computed and measured Nusselt numbers.

It is possible that average heat transfer coefficients are relatively insensitive to the details of the flow field for both turbulent and laminar convection as long as the scale of motion is the order of the layer depth. Recent studies by Cheung [13], who developed a semi-empirical model for turbulent convection, and by Peckover and Hutchinson [25], who numerically investigated laminar convection with internal energy sources in a layer with free-free boundaries, support this contention. On the other hand, numerically induced viscosity effects may inhibit the destabilizing effects of turbulence and, thus, permit reasonably accurate and stable solutions at larger Rayleigh number, at least from the standpoint of an evaluation of the average heat transfer coefficient and the horizontally averaged temperature distribution. These and other issues related to the validity of finite-difference calculations of thermal convection over a wide range of Rayleigh numbers can be resolved only through further analytical and numerical investigation.

Acknowledgment

The authors gratefully acknowledge the support of the National Aeronautics and Space Administration under Grant NGR-36-008-25, the U.S. Nuclear Regulatory Commission under Contract AT-(49-24)-0149, and the Department of Mechanical Engineering.

References

1 Runcorn, S. K., "Convection Currents in the Earth's Mantle," *Nature*, Vol. 195, 1962, p. 1248.

2 Tozer, D. C., "Heat Transfer and Convection Currents," *Proceedings Royal Society*, Vol. A258, London, 1966, pp. 252–271.

3 *The Earth's Mantle*, Gaskell, T. F., ed., Academic Press, New York, 1967.

4 Knopoff, L., "The Upper Mantle of the Earth," *Science*, Vol. 163, No. 3873, 1969, pp. 1277–1287.

5 Bethe, H. A., "Energy Production in Stars," *Science*, Vol. 161, 1958, p. 541.

6 Tritton, D. J., "Internally Driven Heat Convection in the Atmosphere of Venus and in the Laboratory," *Nature*, Vol. 257, 1975, pp. 110–112.

7 Gluekler, E. L. and Baker, L., Jr., "Post-Accident Heat Removal in LMFBR's," *Symposium on the Thermal and Hydraulic Aspects of Nuclear Reactor Safety, Vol. 2: Liquid Metal Fast Breeder Reactors*, Jones, O. C., Jr., and Bankoff, S. G., eds., American Society of Mechanical Engineers, New York, 1977, pp. 285–324.

8 Tritton, D. J. and Zarraga, M. N., "Convection in Horizontal Fluid Layers with Heat Generation, Experiments," *Journal of Fluid Mechanics*, Vol. 30, 1967, pp. 21–32.

9 Roberts, P. H., "Convection in Horizontal Layers with Heat Generation, Theory," *Journal of Fluid Mechanics*, Vol. 30, 1967, pp. 33–41.

10 Thirlby, R., "Convection in an Internally Heated Fluid Layer," *Journal of Fluid Mechanics*, Vol. 44, 1970, pp. 673–693.

11 Fiedler, H. E. and Wille, R., "Turbulante Freie Konvektion in Einer Horizontalen Flussigkeitsschicht mit Volumen-Warmequelle," Paper NC4.5, *Proceedings, Fourth International Heat Transfer Conference*, Paris, Versailles, 1970.

12 Schwiderski, E. W. and Schwab, J. H. A., "Convection Experiments with Electrolytically Heated Fluid Layers," *Journal of Fluid Mechanics*, Vol. 48, 1971, pp. 703–719.

13 Cheung, F. B., "Natural Convection in a Volumetrically Heated Fluid Layer at High Rayleigh Numbers," *International Journal of Heat and Mass Transfer*, Vol. 20, 1977, pp. 499–506.

14 Kulacki, F. A. and Emara, A. A., "Steady and Transient Thermal Convection in a Fluid Layer with Uniform Volumetric Energy Sources," *Journal of Fluid Mechanics*, Vol. 83, 1977, pp. 375–395.

15 Kulacki, F. A. and Goldstein, R. J., "Thermal Convection in a Horizontal Fluid Layer with Uniform Volumetric Energy Sources," *Journal of Fluid Mechanics*, Vol. 55, 1972, pp. 271–287.

16 Mayinger, F. X., Jahn, M., Reineke, H. H., and Steinberner, V., "Examination of Thermohydraulic Processes and Heat Transfer in a Core Melt," Federal Ministry for Research and Technology, Final Report RS48/1, Vols. 1–5 (in German), Hannover, Federal Republic of Germany, July 1975; see also Jahn, M. and Reineke, H. H., "Free Convection Heat Transfer with Internal Heat Sources, Calculations and Measurements," *Proceedings, Fifth International Heat Transfer Conference*, Tokyo, 1974, Vol. 3, pp. 74–78 and "Discussion," Vol. 7, pp. 72–73.

17 Goldstein, R. J., Chu, T. Y., and Kulacki, F. A., "Optical Studies of Thermal Convection," *Engineering Societies Library, Heat Transfer Film Library*, Catalog No. G-5, American Society of Mechanical Engineers, New York, 1977.

18 Emara, A. A., "On Natural Convection with Internal Heating in Fluid Layers," Ph.D. Dissertation in Mechanical Engineering, The Ohio State University, 1977.

19 Barakat, H. Z. and Clark, J. A., "Analytical and Experimental Study of Transient Laminar Natural Convection Flow in Partially Filled Liquid Containers," *Proceedings, Third International Heat Transfer Conference*, Chicago, 1966.

20 Torrance, K. E., "Comparison of Finite-Difference Computations of Natural Convection," *Journal of Research of the National Bureau of Standards, Mathematical Sciences*, Vol. 72B, 1968, pp. 281–301.

21 Roache, P. J., *Computational Fluid Dynamics*, Hermosa Publishers, Albuquerque, 1972.

22 Fromm, J., "The Time Dependent Flow of an Incompressible Viscous Fluid," *Methods in Computational Physics*, Vol. 3, p. 345, Academic Press, New York, 1964.

23 Lax, P. D. and Richtemeyer, R. D., "Survey of the Stability of Linear Finite-Difference Equations," *Communications on Pure and Applied Mathematics*, Vol. 9, 1956, p. 267.

24 Kulacki, F. A. and Goldstein, R. J., "Hydrodynamic Instability in Fluid Layers with Uniform Volumetric Energy Sources," *Applied Scientific Research*, Vol. 31, 1975, pp. 81–109.

25 Peckover, R. S. and Hutchinson, I. H., "Convective Rolls Driven by Internal Heat Sources," *Physics of Fluids*, Vol. 17, 1974, pp. 1369–1371.

Combined Heat and Mass Transfer in Mixed Convection over a Horizontal Flat Plate

T. S. Chen
Mem. ASME

F. A. Strobel[1]

Department of Mechanical and Aerospace Engineering, University of Missouri-Rolla, Rolla, MO 65401

The combined effects of buoyancy forces from thermal and species diffusion on the heat and mass transfer characteristics are analyzed for laminar boundary layer flow over a horizontal flat plate. The analysis is restricted to processes with low concentration levels such that the interfacial velocities due to mass diffusion and the diffusion-thermo/thermo-diffusion effects can be neglected. Numerical results for friction factor, Nusselt number, and Sherwood number are presented for gases having a Prandtl number of 0.7, with Schmidt numbers ranging from 0.6 to 2.0. In general, it is found that, for the thermally assisting flow, the surface heat and mass transfer rates as well as the wall shear stress increase with increasing thermal buoyancy force. These quantities are further enhanced when the buoyancy force from species diffusion assists the thermal buoyancy force, but are reduced when the two buoyancy forces oppose each other. While a higher heat transfer rate is found to be associated with a lower Schmidt number, a higher mass transfer rate occurs at a higher Schmidt number.

Introduction

In studying forced convective heat transfer over horizontal surfaces, the buoyancy effect may become significant if the flow velocities are relatively low and the temperature and/or concentration differences between the surface and the free stream are large. This is because the buoyancy forces induce a streamwise pressure gradient which modifies the flow field and hence the heat and mass transfer rates. Thus, it is of practical interest to study the heat and mass transfer characteristics in flow situations in which the buoyancy effects from both thermal and species diffusions are significant. Even in processes with very low concentration levels, such as terrestrial processes in air and in water, the buoyancy effect from species diffusion can play a role as important as the thermal buoyancy effect. Atmospheric flows, for example, are not only influenced by the temperature difference between the surface of the earth and the ambient air, but also by the amount of water vapor that is diffused from the ground into the air. If the concentration level is low, the analysis of the problem can be greatly simplified by neglecting the interfacial velocities due to species diffusion as well as the diffusion-thermo and thermo-diffusion effects (i.e., the Soret and Dufour effects).

Thermal buoyancy effects in laminar forced convection flow over a horizontal flat plate have been analyzed rather extensively (see, for example, [1–3]). An analysis dealing with the combined heat and mass transfer in natural convection flow over a horizontal plate has also been reported [4]. However, a study of mixed forced and natural convection flow over a horizontal plate under the combined buoyancy effects of thermal and mass diffusion seems not to have been reported in the literature. This has motivated the present investigation. In the analysis, consideration is given to processes with low concentration levels. The conservation equations of the boundary layer are reduced to a dimensionless form by a nonsimilarity transformation, and the resulting system of equations are then solved by the local nonsimilarity method (see, for example, [5, 6]).

Numerical results are obtained for a Prandtl number of 0.7, which is representative of air, and Schmidt numbers Sc of 0.6, 1.0, and 2.0. The parameter N which measures the relative effect of mass and thermal diffusion ranges from −0.5 to 2.0 for Schmidt number of 0.6 and from −0.5 to 1.0 for Sc = 1.0 and 2.0. For each case the thermal buoyancy parameter $\mathrm{Gr}_x/\mathrm{Re}_x^{5/2}$ is varied from 0 to 1.0. The Schmidt number range covers diffusion into air of water vapor (Sc = 0.6), carbon dioxide (Sc = 0.94), methanol (Sc = 0.97), benzene (Sc = 1.76), and ethyl benzene (Sc = 2.01), etc. under one atmospheric pressure and room temperature.

Analysis

Consider a horizontal flat plate which is placed parallel to a uniform free stream with velocity u_∞, temperature T_∞, and mass fraction C_∞. The plate is maintained at a uniform temperature T_w and uniform mass fraction C_w. Let x represent the streamwise distance from the leading edge of the plate and y the distance normal to the plate. Positive y is taken vertically upward for flow above the plate and vertically downward for flow below the plate.

With the assumption of constant fluid properties, the Boussinesq approximation, and in the absence of Soret and Dufour effects, the conservation equations of the laminar boundary layer can be written as

$$\frac{\partial u}{\partial x}+\frac{\partial v}{\partial y}=0 \tag{1}$$

$$u\frac{\partial u}{\partial x}+v\frac{\partial u}{\partial y}=\nu\frac{\partial^2 u}{\partial y^2}\pm g\beta\frac{\partial}{\partial x}\int_y^\infty (T-T_\infty)dy \pm g\beta^*\frac{\partial}{\partial x}\int_y^\infty (C-C_\infty)dy \tag{2}$$

$$u\frac{\partial T}{\partial x}+v\frac{\partial T}{\partial y}=\alpha\frac{\partial^2 T}{\partial y^2} \tag{3}$$

$$u\frac{\partial C}{\partial x}+v\frac{\partial C}{\partial y}=D\frac{\partial^2 C}{\partial y^2} \tag{4}$$

The second and third terms on the right-hand side of equation (2) are, respectively, the pressure gradients induced by the buoyancy forces due to thermal and mass diffusion. The plus and minus signs preceding these terms pertain to flows above and below the plate, respectively. Equations (1–3) are subject to the following boundary conditions.

$$u=0,\ v=v_w,\ T=T_w,\ C=C_w \text{ at } y=0$$

$$u\to u_\infty,\ T\to T_\infty,\ C\to C_\infty \text{ as } y\to\infty \tag{5}$$

To solve equations (1–4) by the local nonsimilarity method, it is necessary to make a transformation from the (x, y) coordinates to the $(\xi(x), \eta(x, y))$ coordinates by introducing

$$\xi=\xi(x),\ \eta=y(u_\infty/\nu x)^{1/2} \tag{6}$$

[1] Presently with Naval Weapons Center, China Lake, Calif.

Contributed by The Heat Transfer Division and presented at the Winter Annual Meeting, New York, NY. December 2–7, 1979 of THE AMERICAN SOCIETY OF MECHANICAL ENGINEERS. Revised manuscript received by the Heat Transfer Division October 19, 1979.

In addition, one introduces a reduced stream function $F(\xi, \eta)$, a dimensionless temperature $\theta(\xi, \eta)$, and a dimensionless mass fraction $\lambda(\xi, \eta)$ defined, respectively, as

$$F(\xi, \eta) = \psi(x, y)/(\nu u_\infty x)^{1/2},\ \theta(\xi, \eta) = (T - T_\infty)/(T_w - T_\infty),$$
$$\lambda(\xi, \eta) = (C - C_\infty)/(C_w - C_\infty) \quad (7)$$

where the stream function $\psi(x, y)$ satisfies the continuity equation (1) with

$$u = \partial\psi/\partial y,\ v = -\partial\psi/\partial x \quad (8)$$

By substituting equations (6) and (7) into equations (2–5), one obtains the following system of equations.

$$F''' + \frac{1}{2}FF'' \pm \frac{1}{2}\xi\left[\eta\theta + \int_\eta^\infty \theta d\eta + \xi\int_\eta^\infty \frac{\partial\theta}{\partial\xi}d\eta\right] \pm \frac{1}{2}N\xi$$
$$\times\left[\eta\lambda + \int_\eta^\infty \lambda d\eta + \xi\int_\eta^\infty \frac{\partial\lambda}{\partial\xi}d\eta\right] = \frac{1}{2}\xi\left[F'\frac{\partial F'}{\partial\xi} - F''\frac{\partial F}{\partial\xi}\right] \quad (9)$$

$$\frac{1}{\mathrm{Pr}}\theta'' + \frac{1}{2}F\theta' = \frac{1}{2}\xi\left[F'\frac{\partial\theta}{\partial\xi} - \theta'\frac{\partial F}{\partial\xi}\right] \quad (10)$$

$$\frac{1}{\mathrm{Sc}}\lambda'' + \frac{1}{2}F\lambda' = \frac{1}{2}\xi\left[F'\frac{\partial\lambda}{\partial\xi} - \lambda'\frac{\partial F}{\partial\xi}\right] \quad (11)$$

$$F(\xi, 0) + \xi\partial F(\xi, 0)/\partial\xi = 0,\ F'(\xi, 0) = 0,$$
$$\theta(\xi, 0) = 1,\ \lambda(\xi, 0) = 1 \quad (12a)$$

$$F'(\xi, \infty) = 1,\ \theta(\xi, \infty) = 0,\ \lambda(\xi, \infty) = 0 \quad (12b)$$

In the preceding equations the primes denote partial differentiation with respect to η, the thermal buoyancy parameter $\xi(x)$ is given by

$$\xi(x) = |\mathrm{Gr}_x|/\mathrm{Re}_x^{5/2} \quad (13)$$

and the relative effect between species and thermal diffusion N by

$$N = \beta^*(C_w - C_\infty)/\beta(T_w - T_\infty) = \mathrm{Gr}_{x,c}/\mathrm{Gr}_x \quad (14)$$

in which the local thermal Grashof number Gr_x, the local concentration Grashof number $\mathrm{Gr}_{x,c}$, and the local Reynolds number are defined as

$$\mathrm{Gr}_x = g\beta(T_w - T_\infty)x^3/\nu^2,$$
$$\mathrm{Gr}_{x,c} = g\beta^*(C_w - C_\infty)x^3/\nu^2,\ \mathrm{Re}_x = u_\infty x/\nu \quad (15)$$

The buoyancy force from species diffusion assists the thermal buoyancy force when $N > 0$, whereas it opposes the thermal buoyancy force when $N < 0$. The case of $N = 0$ corresponds to the situation in which there is no buoyancy force from species diffusion.

It is noted here that the absolute value is used in the definition of the thermal buoyancy parameter ξ. Thus, the plus and minus signs on the left-hand side of equation (9) refer, respectively, to thermal buoyancy force assisting and opposing the forced flow. For flow above the plate, the plus sign is associated with the case $T_w > T_\infty$, and the minus sign with the case $T_w < T_\infty$. The opposite is true for flow below the plate.

In writing the boundary condition $F(\xi, 0) + \xi\,\partial F(\xi, 0)/\partial\xi = 0$ in equation (12a), it has been assumed that the normal velocity at the wall v_w due to mass diffusion is negligibly small. This assumption is valid when the condition

$$2(v_w x/\nu)/(u_\infty x/\nu)^{1/2} \ll 1 \quad (16)$$

is fulfilled. Since $v_w = -[D/(1 - C_w)](\partial C/\partial y)_{y=0}$ (see, for example, [7]), the above condition is equivalent to

$$\frac{2}{\mathrm{Sc}}\frac{C_w - C_\infty}{1 - C_w}[-\lambda'(\xi, 0)] \ll 1 \quad (17)$$

Equation (17) will be valid when the ratio $(C_w - C_\infty)/(1 - C_w)$ is very small; that is, when the mass-fraction level is very low. There are many transport processes in which the mass-fraction level is low, but the species diffusion effect is significant. The evaporation of water vapor into an air stream is such an example. Simple calculations for diffusion of water vapor into air at one atmospheric pressure and around room temperature (with Pr = 0.7 and Sc = 0.6) show that $C < 0.04$ for $T < 100°\mathrm{F}$ and that $(C_w - C_\infty) \doteq 0.0057 \sim 0.0294$, $(C_w - C_\infty)/(1 - C_w) \doteq 0.006 \sim 0.03$, and $N \doteq 1 \sim 4$ for $(T_w - T_\infty) = 20 \sim 40°\mathrm{F}$. Thus, even though the mass-fraction C and the mass-fraction difference $(C_w - C_\infty)$ are small, the buoyancy effects from mass diffusion are as significant as the thermal buoyancy effects (i.e., $N > 1$). In addition, for $N \leq 2$ and $\mathrm{Gr}_x/\mathrm{Re}_x^{5/2} = 0 \sim 1.0$, as covered in the present study, the value of $2(C_w - C_\infty)[-\lambda'(\xi, 0)]/[\mathrm{Sc}(1 - C_w)]$ varies from about 0.005 to 0.025, which is indeed very small compared to 1. Thus, the condition for the neglect of interfacial velocity, as given by equation (17), is fully satisfied for such a flow process and can also be satisfied for similar processes with low mass-fraction levels. Furthermore, with the existence of small C and $(C_w - C_\infty)$ values, the neglect of Soret and Dufour effects in the analysis can be justified. The effects of finite and large interfacial velocities (i.e., large values of $(C_w - C_\infty)/(1 - C_w)$) on mass transfer in laminar boundary flows were examined by Acrivos [8, 9].

To solve equations (9–12) by the local nonsimilarity method, it is first necessary to remove the integral terms in equation (9) by differentiating the equation once with respect to η. This yields a fourth order differential equation and necessitates the introduction of an

Nomenclature

C = mass fraction or concentration
C_f = local friction factor
D = mass diffusion coefficient
F = reduced stream function
G = derivative of F with respect to ξ
g = gravitational acceleration
Gr_x = local thermal Grashof number, $g\beta(T_w - T_\infty)x^3/\nu^2$
Gr_L = thermal Grashof number based on L, $g\beta(T_w - T_\infty)L^3/\nu^2$
$Gr_{x,c}$ = local concentration Grashof number, $g\beta^*(C_w - C_\infty)x^3/\nu^2$
h = local heat transfer coefficient
$\overline{h}$ = average heat transfer coefficient
h_m = local mass transfer coefficient
$\overline{h}_m$ = average mass transfer coefficient
k = thermal conductivity
L = length of plate
$\dot{m}_w$ = local surface mass transfer rate per unit area
N = ratio of Grashof numbers, $\mathrm{Gr}_{x,c}/\mathrm{Gr}_x = \beta^*(C_w - C_\infty)/\beta(T_w - T_\infty)$
Nu_x = local Nusselt number, $q_w x/(T_w - T_\infty)k$
$\overline{\mathrm{Nu}}$ = average Nusselt number, $\overline{h}L/k$
Pr = Prandtl number
q_w = local surface heat transfer rate per unit area
Re_x = local Reynolds number, $u_\infty x/\nu$
Re_L = Reynolds number based on L, $u_\infty L/\nu$
Sc = Schmidt number
Sh_x = local Sherwood number, $\dot{m}_w x/\rho D(C_w - C_\infty)$
$\overline{\mathrm{Sh}}$ = average Sherwood number, $\overline{h}_m L/\rho D$
T = fluid temperature
u = axial velocity component
v = normal velocity component
x = axial coordinate
y = transverse coordinate
α = thermal diffusivity
β = volumetric coefficient of thermal expansion
β^* = volumetric coefficient of expansion with mass fraction
η = pseudo-similarity variable
θ = dimensionless temperature
λ = dimensionless mass fraction
μ = dynamic viscosity
ν = kinematic viscosity
ξ = thermal buoyancy parameter
ξ_L = thermal buoyancy parameter based on L
ρ = density of fluid
τ_w = wall shear stress
ϕ = derivative of θ with respect to ξ
ψ = stream function
ω = derivative of λ with respect to ξ

Subscripts

w = condition at wall
∞ = condition at free stream

additional boundary condition, which can be obtained by evaluating equation (9) at $\eta = 0$. If, in addition, one introduces the dependent variables

$$G = \partial F/\partial \xi,\ \phi = \partial \theta/\partial \xi,\ \omega = \partial \lambda/\partial \xi \tag{18}$$

the resulting system of equations can be written as

$$F'''' + \frac{1}{2}(FF''' + F'F'') \pm \frac{1}{2}\xi\eta(\theta' + N\lambda') \mp \frac{1}{2}\xi^2(\phi + N\omega) = \frac{1}{2}\xi(F'G'' - F'''G) \tag{19}$$

$$\frac{1}{\mathrm{Pr}}\theta'' + \frac{1}{2}F\theta' = \frac{1}{2}\xi(F'\phi - \theta'G) \tag{20}$$

$$\frac{1}{\mathrm{Sc}}\lambda'' + \frac{1}{2}F\lambda' = \frac{1}{2}\xi(F'\omega - \lambda'G) \tag{21}$$

$$F(\xi, 0) + \xi G(\xi, 0) = F'(\xi, 0) = 0,\ \theta(\xi, 0) = \lambda(\xi, 0) = 1 \tag{22a}$$

$$F'''(\xi, 0) = \mp\frac{1}{2}\xi\left[\int_0^\infty \theta d\eta + N\int_0^\infty \lambda d\eta\right] \mp \frac{1}{2}\xi^2\left[\int_0^\infty \phi d\eta + N\int_0^\infty \omega d\eta\right] \tag{22b}$$

$$F'(\xi, \infty) = 1,\ \theta(\xi, \infty) = \lambda(\xi, \infty) = 0 \tag{22c}$$

Equations (19–21) are three coupled equations with six unknown functions $F, \theta, \lambda, G, \phi$, and ω. In order to solve these equations by the local nonsimilarity method, it is necessary to obtain subsidiary equations by differentiating equations (19–21) with respect to ξ. In the present investigation, this differentiation is carried out once and the analysis corresponds therefore to the second level of truncation [5, 6]. For the second level of truncation, the transformed conservation equations are left intact, but terms containing $\partial G/\partial\xi$, $\partial\phi/\partial\xi$, $\partial\omega/\partial\xi$ and their η derivatives are neglected in the subsidiary equations. With this operation, the system of equations for the second level of truncation can be summarized as follows.

(a) Equations (19–21)

(b) The truncated equations for G, ϕ, and ω given by

$$G'''' + \frac{1}{2}(FG''' + F''G') + F'''G \pm \frac{1}{2}\eta[\theta' + \xi\phi' + N(\lambda' + \xi\omega')] \mp \xi(\phi + N\omega) + \frac{1}{2}\xi(GG''' - G'G'') = 0 \tag{23}$$

$$\frac{1}{\mathrm{Pr}}\phi'' + \frac{1}{2}F\phi' - \frac{1}{2}F'\phi + G\theta' + \frac{1}{2}\xi(G\phi' - G'\phi) = 0 \tag{24}$$

$$\frac{1}{\mathrm{Sc}}\omega'' + \frac{1}{2}F\omega' - \frac{1}{2}F'\omega + G\lambda' + \frac{1}{2}\xi(G\omega' - G'\omega) = 0 \tag{25}$$

(c) The boundary conditions

$$F(\xi, 0) = F'(\xi, 0) = G(\xi, 0) = G'(\xi, 0) = \phi(\xi, 0) = \omega(\xi, 0) = 0$$
$$\theta(\xi, 0) = \lambda(\xi, 0) = 1 \tag{26a}$$

$$F'''(\xi, 0) = \mp\frac{1}{2}\xi\left[\int_0^\infty \theta d\eta + N\int_0^\infty \lambda d\eta\right] \mp \frac{1}{2}\xi^2\left[\int_0^\infty \phi d\eta + N\int_0^\infty \omega d\eta\right] \tag{26b}$$

$$G'''(\xi, 0) = \mp\frac{1}{2}\left[\int_0^\infty \theta d\eta + N\int_0^\infty \lambda d\eta\right] \mp \frac{3}{2}\xi\left[\int_0^\infty \phi d\eta + N\int_0^\infty \omega d\eta\right] \tag{26c}$$

$$F'(\xi, \infty) = 1,\ G'(\xi, \infty) = \theta(\xi, \infty) = \phi(\xi, \infty) = \lambda(\xi, \infty) = \omega(\xi, \infty) = 0 \tag{26d}$$

It can be seen that equations (19–21) and (23–25) are coupled and must be solved simultaneously to obtain solutions for the unknown functions of $F, \theta, \lambda, G, \phi$, and ω. This will be described later.

The physical quantities of greatest interest are the local and average Nusselt numbers Nu_x and $\overline{\mathrm{Nu}}$, the local and average Sherwood numbers Sh_x and $\overline{\mathrm{Sh}}$, and the local friction factor C_f. The local quantities are defined, respectively, by

$$\mathrm{Nu}_x = \frac{q_w}{T_w - T_\infty}\frac{x}{k},\ \mathrm{Sh}_x = \frac{\dot{m}_w}{C_w - C_\infty}\frac{x}{\rho D},\ C_f = \frac{\tau_w}{\rho u_\infty{}^2/2} \tag{27}$$

With the use of Fourier's law $q_w = -k(\partial T/\partial y)_{y=0}$, Fick's law $\dot{m}_w = -\rho D(\partial C/\partial y)_{y=0}$, and the definition of wall shear stress $\tau_w = \mu(\partial u/\partial y)_{y=0}$ along with equations (6) and (7), the following expressions for the local Nusselt number, the local Sherwood number, and the local friction factor are obtained.

$$\mathrm{Nu}_x\mathrm{Re}_x{}^{-1/2} = -\theta'(\xi, 0),\ \mathrm{Sh}_x\mathrm{Re}_x{}^{-1/2} = -\lambda'(\xi, 0),\ C_f\mathrm{Re}_x{}^{1/2} = 2F''(\xi, 0) \tag{28}$$

The average Nusselt and Sherwood numbers are defined, respectively, by

$$\overline{\mathrm{Nu}} = \bar{h}L/k,\ \overline{\mathrm{Sh}} = \bar{h}_m L/\rho D \tag{29}$$

where the average heat transfer and mass transfer coefficients are determined from the following expressions

$$\bar{h} = \frac{1}{L}\int_0^L h(x)dx,\ \bar{h}_m = \frac{1}{L}\int_0^L h_m(x)dx \tag{30}$$

When the axial coordinate x in equation (30) is replaced by the thermal buoyancy parameter ξ, the average Nusselt and Sherwood numbers are found to be

$$\overline{\mathrm{Nu}}\mathrm{Re}_L{}^{-1/2} = \frac{2}{\xi_L}\int_0^{\xi_L}[-\theta'(\xi, 0)]d\xi \tag{31}$$

$$\overline{\mathrm{Sh}}\mathrm{Re}_L{}^{-1/2} = \frac{2}{\xi_L}\int_0^{\xi_L}[-\lambda'(\xi, 0)]d\xi \tag{32}$$

wherein the thermal buoyancy parameter ξ_L, the Reynolds number Re_L, and the Grashof number Gr_L are based on the plate length and are expressed, respectively, by

$$\xi_L = \mathrm{Gr}_L/\mathrm{Re}_L{}^{5/2},\ \mathrm{Re}_L = u_\infty L/\nu,\ \mathrm{Gr}_L = g\beta(T_w - T_\infty)L^3/\nu^2 \tag{33}$$

Also of interest are the velocity, temperature, and concentration distributions. They are determined, respectively, from the following expressions.

$$u/u_\infty = F'(\xi, \eta),\ (T - T_\infty)/(T_w - T_\infty) = \theta(\xi, \eta),\ (C - C_\infty)/C_w - C_\infty) = \lambda(\xi, \eta) \tag{34}$$

Numerical Solutions

Equations (19–21) and (23–25) can be treated as a system of coupled ordinary differential equations for a prescribed value of ξ. These equations were solved by the Runge-Kutta integration scheme in conjunction with Newton-Raphson shooting method to fulfill the conditions at the edge of the boundary layers. A predictor-corrector integration scheme was employed to improve the accuracy of the numerical integration.

The procedure for solving the system of equations for a prescribed value of ξ is similar to that described in [1]. The initial values which must be guessed are $F''(\xi, 0)$, $G''(\xi, 0)$, $\theta'(\xi, 0)$, $\phi'(\xi, 0)$, $\lambda'(\xi, 0)$, $\omega'(\xi, 0)$ as well as the θ, ϕ, λ, and ω integrals. The integrals were considered converged when the differences in the values of $F'''(\xi, 0)$ and $G'''(\xi, 0)$ between the two successive iterations became less than 10^{-4} and 10^{-3}, respectively. A solution was considered converged when the conditions $|F' - 1.0, F''| \le 3 \times 10^{-3}$, $|\theta, \theta', \lambda, \lambda', \phi, \phi', \omega, \omega'| \le 5 \times 10^{-3}$, and $|G', G''| \le 10^{-2}$ at the edge of the boundary layers were fulfilled simultaneously.

Results and Discussion

Numerical results were obtained for a Prandtl number of 0.7 and Schmidt numbers of 0.6, 1.0, and 2.0. For a Schmidt number of 0.6, the values of N cover 2.0, 1.0, 0.5, 0, −0.5 and for Schmidt numbers of 1.0 and 2.0 they cover 1.0, 0.5, 0, −0.5. For each case the thermal buoyancy parameter $\mathrm{Gr}_x/\mathrm{Re}_x{}^{5/2}$ was varied from 0 to 1.0; that is, the

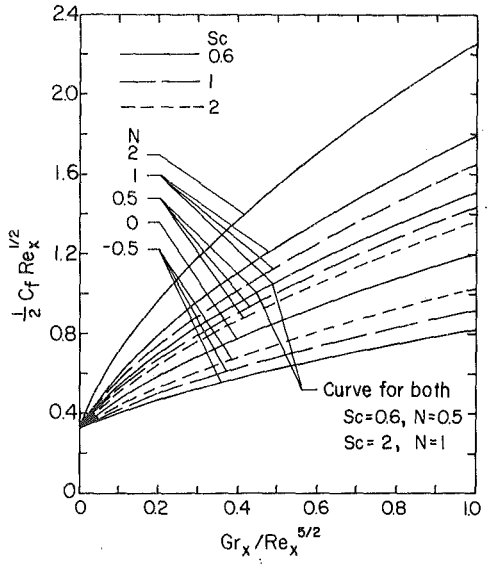

Fig. 1 Local friction factor results

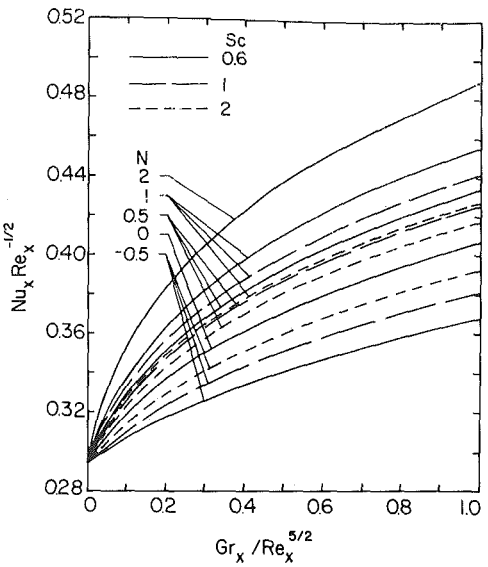

Fig. 2 Local Nusselt number results

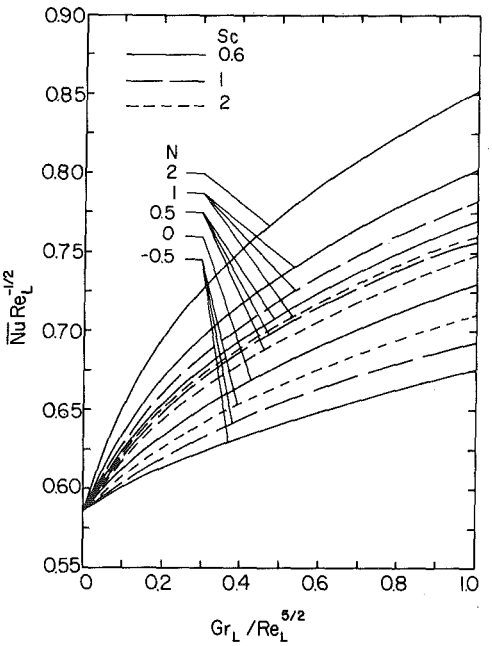

Fig. 3 Average Nusselt number results

results are for thermal buoyancy force assisting the forced flow. These results will now be presented.

The effects of buoyancy forces on the local friction factor, the local Nusselt number, and the average Nusselt number are shown, respectively, in Figs. 1–3. As can be seen from the figures, the local friction factor and the local Nusselt number increase with increasing value of $Gr_x/Re_x^{5/2}$, whereas the average Nusselt number increase with increasing $Gr_L/Re_L^{5/2}$. This trend is to be expected, because the favorable pressure gradient caused by the buoyancy forces increases the flow velocity near the wall, which results in an increase in the wall shear stress and hence the rate of surface heat transfer. By comparing the curves with that for $N = 0$ (i.e., no buoyancy effect from mass diffusion), it is possible to measure the relative effect between the buoyancy forces from mass and thermal diffusion. For a given Schmidt number, the friction factor and the Nusselt numbers increase beyond those for $N = 0$ when $N > 0$; that is, when the buoyancy force from mass diffusion acts in the same direction as the thermal buoyancy force, thereby resulting in additive buoyancy effects. On the other hand, the two buoyancy forces oppose each other when $N < 0$. The net effect is a decrease in the combined buoyancy forces below that for $N = 0$ and hence a decrease in the friction factor and the Nusselt numbers. It is also of interest to note from Figs. 1 and 2 that a lower Schmidt number yields larger local friction factor and local Nusselt number than those for $N = 0$ when $N > 0$ and smaller local friction factor and local Nusselt number when $N < 0$. The reason for the larger departure of these two quantities from $N = 0$ is that a diffusing species with a smaller Schmidt number has a larger diffusion coefficient which exerts a larger effect on the flow and thermal fields.

The local Sherwood numbers are shown in Fig. 4 as a function of the thermal buoyancy parameter $Gr_x/Re_x^{5/2}$ and the average Sherwood numbers in Fig. 5 as a function of $Gr_L/Re_L^{5/2}$. Again, the curves for $N = 0$ correspond to the situation in which buoyancy effect from species diffusion does not exist. As expected, the effect of the buoyancy forces is to increase the flow velocity which in turn enhances the Sherwood number and hence the mass transfer rate. As in the local friction factor and Nusselt number results, the Sherwood numbers increase when $N > 0$ and decrease when $N < 0$. In addition, a larger Schmidt number is seen to provide a larger Sherwood number. This is because as the Schmidt number increases, the concentration boundary layer thickness decreases, thus resulting in a larger surface concentration gradient (see Fig. 8) and hence a higher rate of mass transfer from the surface.

It must be pointed out that as the value of N becomes more negative, the buoyancy effect due to mass diffusion may outweigh that due to thermal diffusion and the net effect of the buoyancy forces is to oppose the forced flow. To determine if the net buoyancy force effect will assist or oppose the forced flow, it is necessary to examine the last two terms on the left-hand side of equation (9),

$$\frac{1}{2}\xi\left[\eta\theta + \int_\eta^\infty \theta d\eta + \xi\int_\eta^\infty \frac{\partial\theta}{\partial\xi}d\eta\right]$$

and

$$\frac{1}{2}N\xi\left[\eta\lambda + \int_\eta^\infty \lambda d\eta + \xi\int_\eta^\infty \frac{\partial\lambda}{\partial\xi}d\eta\right].$$

For the case of Sc = Pr, the θ and λ solutions are identical. Thus, if $N = -1$, these terms will add up to zero and the buoyancy forces cancel each other, yielding results identical to those for pure forced convection. In general, for a given thermal buoyancy force, if the sum of the two terms is positive, the net buoyancy force will assist the forced flow. On the other hand, if it is negative, the net buoyancy force will oppose the forced flow. These outcomes depend on the Schmidt and Prandtl numbers as well as on the relative species-thermal buoyancy parameter N.

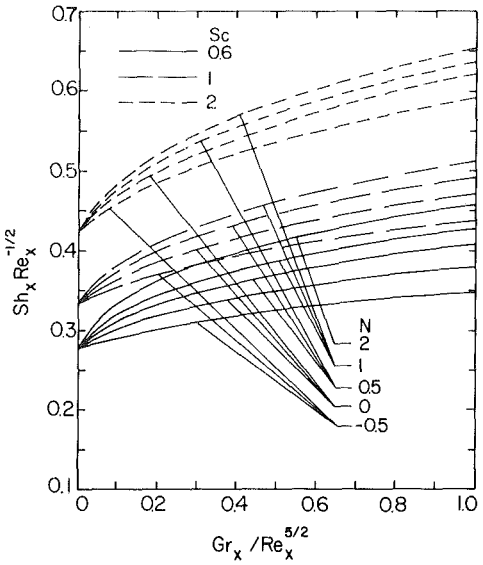

Fig. 4 Local Sherwood number results

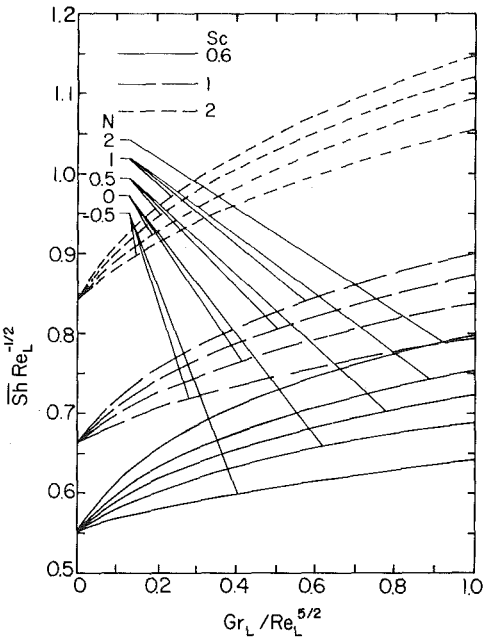

Fig. 5 Average Sherwood number results

It is interesting to examine how the buoyancy forces affect the velocity, temperature, and concentration fields in the boundary layers. Figure 6 shows representative velocity profiles for Schmidt numbers of 0.6 and 2.0. It is seen that for a given Schmidt number the velocity gradient at the wall increases as either $Gr_x/Re_x^{5/2}$ or N increases. In addition, for the same values of N and $Gr_x/Re_x^{5/2}$, a lower Schmidt number is seen to provide a larger wall velocity gradient. When the net buoyancy force becomes relatively large, the velocity profile exhibits an overshoot beyond the free stream velocity. This overshoot is more pronounced when the Schmidt number becomes smaller. For example, when $N = 1.0$ and $Gr_x/Re_x^{5/2} = 1.0$, the overshoot is about 37 percent for Sc = 0.6 as compared to about 20 percent for Sc = 2.0.

Representative temperature profiles are shown in Fig. 7 for Schmidt numbers of 0.6 and 2. The most noteworthy trends for a given Schmidt number are an increase in the temperature gradient at the wall and a decrease in the thermal boundary layer thickness as either N or $Gr_x/Re_x^{5/2}$ increases. In addition, the temperature gradient at the wall is seen to increase as the Schmidt number decreases.

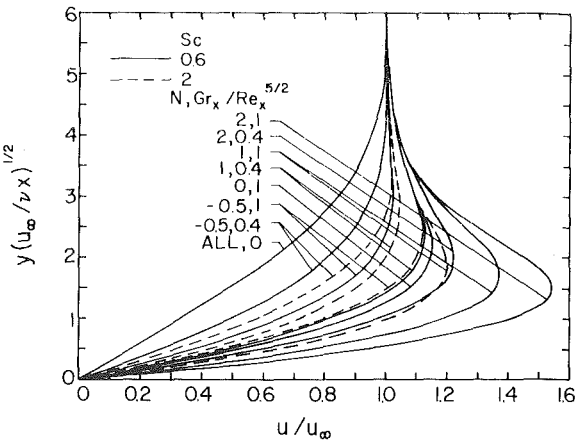

Fig. 6 Representative velocity profiles

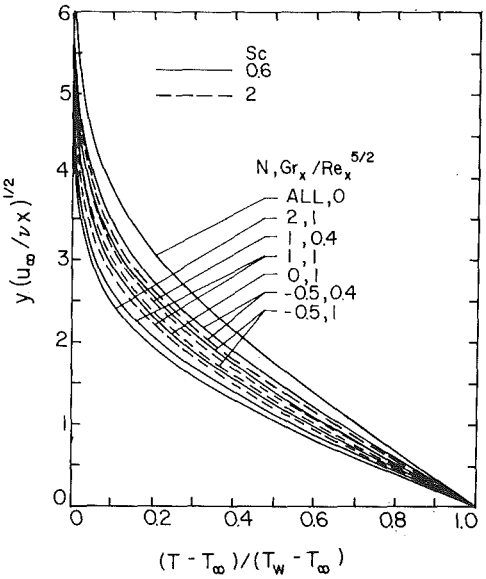

Fig. 7 Representative temperature profiles

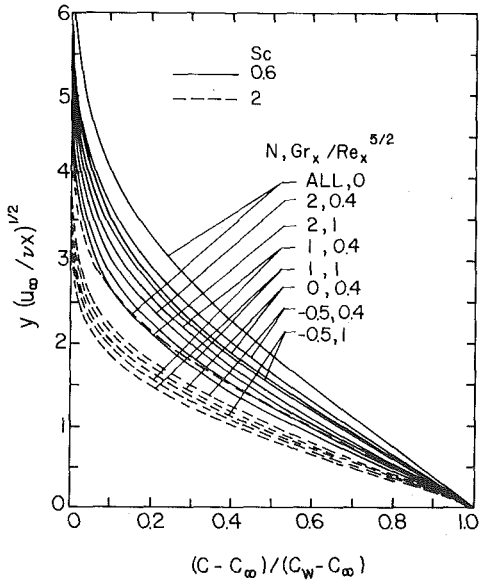

Fig. 8 Representative mass-fraction profiles

The mass fraction profiles (Fig. 8) exhibit trends similar to those of the temperature profiles. That is, the concentration gradient at the wall increases and the concentration boundary layer thickness decreases as the net buoyancy force increases. Also evident from the figure is that a larger wall gradient and a smaller boundary layer thickness are associated with a larger Schmidt number.

Conclusion

Laminar mixed convection flow over a horizontal flat plate under the combined buoyancy effects of thermal and mass diffusion has been studied analytically. The analysis is restricted to mass diffusion processes with low concentration levels, and numerical results are presented for a Prandtl number of 0.7, with Schmidt numbers of 0.6, 1.0, and 2.0. In general, it has been found that as the thermal buoyancy force increases (i.e., $Gr_x/Re_x^{5/2} > 0$ increases), the local surface heat and mass transfer rates as well as the local wall shear stress increase. When the buoyancy force from mass diffusion assists the thermal buoyancy force (i.e., when $N > 0$), these quantities increase further with an increasing value of N. On the other hand, they decrease with N when the two buoyancy forces oppose each other (i.e., when $N < 0$). While a higher heat transfer rate and a higher wall shear stress are associated with a lower Schmidt number, a higher mass transfer rate occurs at a higher Schmidt number. For relatively large net buoyancy forces that assist the forced flow, the velocity profiles exhibit an overshoot beyond the free stream velocity. This overshoot becomes more pronounced as the Schmidt number decreases.

Acknowledgment

This work was supported by a grant from the National Science Foundation (NSF ENG 75-15033 A01).

References

1 Chen, T. S., Sparrow, E. M. and Mucoglu, A., "Mixed Convection in Boundary Layer Flow on a Horizontal Plate," ASME JOURNAL OF HEAT TRANSFER, Vol. 99, 1977, pp. 66–71.

2 Sparrow, E. M., and Minkowycz, W. J., "Buoyancy Effects on Horizontal Boundary-Layer Flow and Heat Transfer," *International Journal of Heat and Mass Transfer*, Vol. 5, 1962, pp. 505–511.

3 Heiber, C. A., "Mixed Convection Above a Heated Horizontal Surface," *International Journal of Heat and Mass Transfer*, Vol. 16, 1973, pp. 769–785.

4 Pera, L., and Gebhart, B., "Natural Convection Flows Adjacent to Horizontal Surfaces Resulting from the Combined Buoyancy Effects of Thermal and Mass Diffusion," *International Journal of Heat and Mass Transfer*, Vol. 15, 1972, pp. 269–278.

5 Sparrow, E. M., and Yu, H. S., "Local Nonsimilarity Thermal Boundary-Layer Solutions," ASME JOURNAL OF HEAT TRANSFER, Vol. 93, 1971, pp. 328–334.

6 Chen, T. S., and Mucoglu, A., "Buoyancy Effects on Forced Convection Along a Vertical Cylinder," ASME JOURNAL OF HEAT TRANSFER, Vol. 97, 1975, pp. 198–203.

7 Eckert, E. R. G., and Drake, Jr., R. M., "*Heat and Mass Transfer*," Second Edition, Chapter 16, McGraw-Hill, New York, 1959.

8 Acrivos, A., "Mass Transfer in Laminar-Boundary-Layer Flows with Finite Interfacial Velocities," *AIChE Journal*, Vol. 6, 1960, pp. 410–414.

9 Acrivos, A., "The Asymptotic Form of the Laminar Boundary-Layer Mass-Transfer Rate for Large Interfacial Velocities," *Journal of Fluid Mechanics*, Vol. 12, 1962, pp. 337–357.

C. T. Hsu

Fluid Mechanics Department,
TRW Systems and Energy,
Redondo Beach, Calif. 90278

P. Cheng

Department of Mechanical Engineering,
University of Hawaii,
Honolulu, Hawaii 96822

The Onset of Longitudinal Vortices in Mixed Convective Flow over an Inclined Surface in a Porous Medium

The conditions marking the onset of vortex instability in mixed convective flow over an inclined surface in a saturated porous medium are investigated by means of a linear stability analysis. The basic state is assumed to be the steady two-dimensional boundary layer flow. The three-dimensional perturbation equations are simplified on the basis of a scaling argument whereby most of the streamwise derivatives of the disturbances are found to be negligible. For vortex disturbances, the resulting simplified equations in terms of the amplitude are solved approximately by the local similarity method. The eigenvalue problem is solved numerically for the cases of (1) an inclined surface at constant wall temperature with free stream velocity at zero angle of incidence with the inclined surface and (2) an inclined surface with constant heat flux with free stream velocity at 45 deg with respect to the inclined surface. Both aiding and opposing external flows are considered. The critical parameters and the critical wave numbers of disturbances for the two cases are obtained. It is found that the effect of the external flow is to suppress the growth of vortex disturbances in both aiding and opposing flows. At the same value of the mixed convection parameter, the opposing flow is found to be more unstable than the aiding flow.

Introduction

The study of mixed convection in a porous medium has important applications to the transport processes occurring in a geothermal reservoir. The imposed external pressure gradients in a geothermal system are usually generated either due to natural recharge and discharge of groundwater, or man-made withdrawal and reinjection of geothermal fluids. In a recent paper, Cheng [1] obtained similarity solutions for mixed convection in a porous medium adjacent to inclined surfaces wherein steady two-dimensional boundary layer flow is assumed. Because of the destabilized effect of the component of the buoyancy force normal to the inclined surface, secondary flow in the form of longitudinal vortex (or rolls) will appear downstream. The conditions marking the onset of longitudinal vortex downstream adjacent to the inclined surface in a porous medium are the subject of investigation in the present paper.

A linear stability analysis is performed where the basic state is assumed to be steady two-dimensional boundary layer flows. As in the previous papers by Hsu, et al. [2–4], the three-dimensional disturbances equations are simplified based on a scaling argument. The resulting equations for the amplitude of disturbances are solved approximately based on the local similarity model. The final eigenvalue problem is solved numerically for an inclined surface with isothermal wall temperature distribution as well as with constant surface heat flux. The critical parameters and the critical wave numbers of disturbances for both aiding flow (where the buoyancy force has a component in the direction of free stream velocity) and opposing flow (where the buoyancy force has a component opposite to the free stream velocity) are obtained. It is found that disturbances in the form of longitudinal vortex will not manifest itself in mixed convection in a porous medium adjacent to a vertical surface. For other inclination angles, the effect of external flow is to suppress vortex instability in both aiding and opposing flows.

Linear Stability Analysis

Consider the problem of mixed convection in a porous medium adjacent to a surface with an inclination angle α_0 (with respect to the vertical where $0 \leq \alpha_0 < \pi/2$) as shown in Fig. 1, where x is the coordinate along the bounding surface in the streamwise direction, z is the coordinate tangent to the bounding surface, and y is the coordinate normal to the surface. The wall temperature distribution is given by $T_w = T_\infty + Ax^m$ (where T_∞ is the temperature outside the thermal boundary layer and A is a positive constant) and the velocity outside the boundary layer is given by $u_\infty = Bx^n$ where n is related to the angle of incidence β_0 ($0 \leq \beta_0 \leq \pi/2$) by $n = \beta_0/(\pi - \beta_0)$. Cheng [1] has shown that similarity solutions exist for the problem if $m = n$, and has presented numerical results for the special case of $\alpha_0 = \beta_0$, although similarity solutions also exist for $\alpha_0 \neq \beta_0$. Thus, in this paper, α_0 and β_0 are regarded as two independent variables with α_0 related to the gravitational force term and β_0 related to the direction of free stream velocity with respect to the surface.

A linear stability analysis will now be performed to study the onset of vortex instability downstream adjacent to an inclined surface in a porous medium. Both aiding flow and opposing flow will be considered. The first step in a linear stability analysis is to decompose

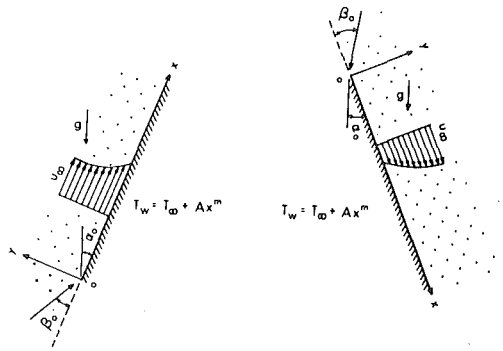

Fig. 1(*a*) Aiding flow Fig. 1(*b*) Opposing flow

Fig. 1 Coordinate systems

Contributed by the Heat Transfer Division for publication in the JOURNAL OF HEAT TRANSFER. Manuscript received by the Heat Transfer Division February 4, 1980.

the variables in the flow and temperature fields into a basic flow and infinitesimal disturbances as

$$T(x, y, z, t) = T_0(x, y) + T_1(x, y, z, t),$$
$$p(x, y, z, t) = p_0(x, y) + p_1(x, y, z, t),$$
$$u(x, y, z, t) = u_0(x, y) + u_1(x, y, z, t),$$
$$v(x, y, z, t) = v_0(x, y) + v_1(x, y, z, t),$$
$$w(x, y, z, t) = \quad w_1(x, y, z, t), \tag{1}$$

where the subscript 0 denotes the basic undisturbed flow and the subscript 1 denotes the three-dimensional disturbances. The solution for the basic undisturbed flow has been given by Cheng [1] as

$$\psi_0 = \alpha\sqrt{\text{Pe}}\, f_0(\eta), \tag{2a}$$
$$\theta_0(\eta) = \frac{T_0 - T_\infty}{T_w - T_\infty}, \tag{2b}$$
$$\eta = \sqrt{\text{Pe}}\, y/x, \tag{2c}$$

where f_0 and θ_0 are determined from

$$f_0'' = \pm M\theta_0', \tag{3}$$
$$\theta_0'' = m\theta_0 f_0' - \frac{m+1}{2} f_0\theta_0', \tag{4}$$

subject to the boundary conditions

$$f_0(0) = 0, \quad \theta_0(0) = 1, \tag{5a, b}$$
$$f_0'(\infty) = 1, \quad \theta_0(\infty) = 0, \tag{6a, b}$$

where the positive and negative signs in equation (3) indicate aiding or opposing flows, and the primes on basic flow quantities indicate derivatives with respect to η. The parameter M = Ra/Pe where Ra and Pe are, respectively, the Rayleigh number and the Peclet number defined as $\text{Ra} \equiv K\beta q \cos\alpha_0 |T_w - T_\infty| x/\nu\alpha$ and $\text{Pe} = u_\infty x/\alpha$ with α denoting the equivalent thermal diffusivity, K the permeability of the saturated porous medium, and β and ν the thermal expansion coefficient and the kinematic viscosity of the fluid. Note that $M = g \cos\alpha_0 A\beta\nu/B$ is a constant independent of x and that M = Ra/Pe = Gr/Re (since Ra = Gr Pr and Pe = Re Pr) where Gr and Re are, respectively, the Grashoff number and the Reynolds number defined as $\text{Gr} \equiv K\beta g \cos\alpha_0 |T_w - T_\infty| x/\nu^2$ and $\text{Re} = u_\infty x/\nu$. The quantity M is a parameter which measures the relative importance of free to forced convection in the porous medium adjacent to an inclined surface. For the case of forced convection, i.e., $M = 0$, equations (3) and (4) with boundary conditions, equation (5) and (6), have the exact solution of the form

$$f_0 = \eta, \tag{7}$$
$$\theta_0 = \frac{\Gamma\left(\frac{1-\nu}{2}\right)}{2^{\nu/2}\Gamma\left(\frac{1}{2}\right)} e^{-\tilde{\xi}^2/4} D_\nu(\tilde{\xi}), \tag{8}$$

where $\tilde{\xi} \equiv \sqrt{(m+1)/2}\,\eta$, $D_\nu(\tilde{\xi})$ is the parabolic cylinder function [5] of order ν with $\nu = -(3m+1)/(m+1)$ and Γ is the Gamma function.

To obtain the governing equations for disturbances, we substitute equations (1) into the governing equations for convective flow in a porous medium and subtract the boundary layer equations to get

$$\frac{\partial u_1}{\partial x} + \frac{\partial v_1}{\partial y} + \frac{\partial w_1}{\partial z} = 0, \tag{9}$$
$$\frac{\partial p_1}{\partial x} = -\frac{\mu u_1}{K} \pm \rho_\infty \beta g \cos\alpha_0 T_1, \tag{10}$$
$$\frac{\partial p_1}{\partial y} = -\frac{\mu v_1}{K} + \rho_\infty \beta g \sin\alpha_0 T_1, \tag{11}$$
$$\frac{\partial p_1}{\partial z} = -\frac{\mu w_1}{K}, \tag{12}$$
$$\alpha\left(\frac{\partial^2 T_1}{\partial x^2} + \frac{\partial^2 T_1}{\partial y^2} + \frac{\partial^2 T_1}{\partial z^2}\right) = \lambda\frac{\partial T_1}{\partial t} + u_0\frac{\partial T_1}{\partial x} + v_0\frac{\partial T_1}{\partial y} + u_1\frac{\partial T_0}{\partial x} + v_1\frac{\partial T_0}{\partial y}, \tag{13}$$

Nomenclature

a = dimensional spanwise wave number
A = constant in wall temperature relation
A_0 = integration constant in equation (29)
B = constant in free stream velocity
B_0 = integration constant in equation (27)
C_i = superposition constant in equation (36)
D = differentiation with respect to disturbances
D_ν = parabolic cylinder function of order ν
f = dimensionless base state stream function
F = dimensionless disturbance stream function
g = acceleration due to gravity
G = dimensionless disturbance velocity in the x-direction
Gr = local Grashoff number based on x
i = complex number
k = dimensionless wave number for mixed convection
k_f = dimensionless wave number for free convection
K = Darcy permeability
m = exponent on wall temperature relation
M = mixed convection parameter
n = exponent on free stream velocity
p = pressure
Pe = local Peclet number based on x
Ra = local Rayleigh number based on x
t = time
T = temperature
u = Darcy's velocity in x-direction
v = Darcy's velocity in y-direction
w = Darcy's velocity in z-direction
x = dimensional coordinate in downstream direction
y = dimensional coordinate normal to bounding surface
z = dimensional coordinate tangent to bounding surface
α = effective thermal diffusivity
α_0 = inclination angle with respect to vertical
β = coefficient of thermal expansion
β_0 = angle of incidence of the free stream with respect to the surface
λ = volumetric heat capacity of the fluid to that of the saturated porous medium
Γ = Gamma function
Δ = function defined in equation (39)
μ = fluid viscosity
ξ = independent variable in equation (28)
η = similarity variable
θ = dimensionless base state temperature
Θ = dimensionless disturbance temperature
ψ = stream function
ρ = fluid density
τ = dimensionless time

Superscripts

$\hat{}$ = amplitude function for disturbances
$*$ = critical values
$\tilde{}$ = dimensionless quantities

Subscripts

0 = basic undisturbed quantities
1 = disturbed quantities
∞ = condition away from the bounding surface
w = condition at the wall

where the positive and negative signs in equation (10) indicate the coordinate systems in Figs. 1(*a*) and 1(*b*), respectively. Note that in equation (13), $u_0 = \alpha/x \text{ Pe } f_0'(\eta)$ and $v_0 = \alpha/2x \sqrt{\text{Pe}}\,[(1-m)\eta f_0' - (1+m)f_0]$ which follow from equation (2*a*).

Using a procedure similar to that of reference [3], it can be shown that the first term in equations (9, 10), and (13) is the smallest term in their respective equations and can therefore be neglected. Note that the omission of $\partial u_1/\partial x$ in equation (9) implies the existence of a stream function ψ_1 for the secondary flow such that

$$w_1 = \frac{\partial \psi_1}{\partial y} \quad \text{and} \quad v_1 = -\frac{\partial \psi_1}{\partial z}. \tag{14}$$

The elimination of p_1 from equations (11) and (12) with the aid of equation (14) and the omission of $\partial p_1/\partial x$ and $\alpha\,\partial^2 T_1/\partial x^2$ in equations (10) and (13) lead to

$$u_1 = \pm \frac{K}{\mu} \rho_\infty \beta g \cos \alpha_0 T_1, \tag{15}$$

$$\frac{\partial^2 \psi_1}{\partial y^2} + \frac{\partial^2 \psi_1}{\partial z^2} = -\frac{K \rho_\infty \beta g \sin \alpha_0}{\mu} \frac{\partial T_1}{\partial z}, \tag{16}$$

$$\alpha \left(\frac{\partial^2 T_1}{\partial y^2} + \frac{\partial^2 T_1}{\partial z^2} \right) = \lambda \frac{\partial T_1}{\partial t} + u_0 \frac{\partial T_1}{\partial x} + v_0 \frac{\partial T_1}{\partial y} + u_1 \frac{\partial T_0}{\partial x} - \frac{\partial \psi_1}{\partial z} \frac{\partial T_0}{\partial y}, \tag{17}$$

which are the simplified equations for the disturbances. To investigate vortex mode of instability, the secondary flow at neutral condition is assumed to be of the form [4]

$$\psi_1(x, y, z) = i\alpha \sqrt{\text{Pe}}\, F(\eta, x) \exp [iaz],$$

$$u_1(x, y, z) = \frac{\alpha}{x} \text{Pe } G(\eta, x) \exp [iaz],$$

$$T_1(x, y, z) = A x^m \Theta(\eta, x) \exp [iaz], \tag{18}$$

where a is a spanwise periodic wave number of the disturbances while the functions $F(\eta, x)$, $G(\eta, x)$ and $\theta(\eta, x)$ can be determined by substituting equations (18) into equations (15–17) which yields

$$G = \pm M \Theta, \tag{19}$$

$$\frac{\partial^2 F}{\partial \eta^2} - k^2 F = -M \tan \alpha_0 k \Theta, \tag{20}$$

$$\frac{\partial^2 \Theta}{\partial \eta^2} - k^2 \Theta - m f_0 \Theta + \left(\frac{m+1}{2} \right) f_0 \frac{\partial \Theta}{\partial \eta} - \left[m\theta_0 + \frac{m-1}{2} \eta \theta_0' \right] G - \sqrt{\text{Pe}}\, \theta_0 k F = f_0' x \frac{\partial \Theta}{\partial x}, \tag{21}$$

subject to boundary conditions

$$F(0, x) = F(\infty, x) = 0, \tag{22}$$

$$\Theta(0, x) = \Theta(\infty, x) = 0, \tag{23}$$

where $k = ax/(\text{Pe})^{1/2}$ is the dimensionless wave number. Depending on the accuracy required, equations (19–23) can be solved approximately either by the local nonsimilarity method or the local similarity method, where x can be regarded as a parameter in both cases [7–9]. In the former method the term $\partial\Theta/\partial x$ in equation (21) is regarded as a new variable and additional equations are introduced to complete the mathematical formulation. In the latter method, it is assumed that the x-dependence of the variables is weak such that $\partial/\partial x \ll \partial/\partial\eta$ and therefore the last term of equation (21) can be dropped. As a result equations (19–23) would contain only η-derivatives with x being regarded as a parameter, and the results are called the local similarity solutions. Since the local similarity solutions are known to be accurate enough for most of the problems in boundary layer flow, we shall proceed to obtain local similarity solutions for this problem. To this end, we substitute G and Θ from equations (19) and (20) into equation (21) and invoke the local similarity approximation to yield

$$(D^2 - k^2)^2 F = m f_0' (D^2 - k^2) F - \left(\frac{m+1}{2} \right) f_0 D (D^2 - k^2) F \pm M [m\theta_0 + \left(\frac{m-1}{2} \right) \eta \theta_0'] (D^2 - k^2) F - M (\text{Pe} \tan^2 \alpha_0)^{1/2} \theta_0' k^2 F, \tag{24}$$

where $D \equiv d/d\eta$ is the derivative with respect to disturbances. The boundary conditions for equation (24) are

$$F(0) = D^2 F(0) = 0, \tag{25}$$

$$F(\infty) = D^2 F(\infty) = 0. \tag{26}$$

Equations (24–26) constitute an eigenvalue problem for which $\text{Pe} \tan^2 \alpha_0$ can be regarded as the eigenvalue which depends on M, k and m. The product of Pe and $\tan \alpha_0$ as an eigenvalue implies that different inclined angle α_0 and different distance x which result in the same value of $\text{Pe} \tan^2 \alpha_0$ will trigger the vortex instability for the mixed convection flow in a porous medium adjacent to an inclined heated surface.

Numerical Solutions of the Eigenvalue Problem

The eigenvalue problem can best be solved numerically by integrating equation (24) inward from $\eta \to \infty$ (i.e., the edge of the boundary layer of the basic flow) to $\eta = 0$ (at the wall). To start the integration, asymptotic solutions as $\eta \to \infty$ for the basic and disturbed flows are needed.

We consider first the asymptotic behavior for the basic flow. With the aid of equation (6), the first approximation for f_0 as $\eta \to \infty$ can be obtained by integrating equation (3) twice to give

$$f_0 = \eta_\infty + B_0, \tag{27}$$

where B_0 is a measure of the amount of the fluid entrained into the boundary layer by thermally-induced convection. Substituting equation (27) into equation (4) and changing the variable η_∞ to ξ by $\xi = \sqrt{(m+1/2)}\,(\eta_\infty + B_0)$, we have

$$\frac{d^2\theta_0}{d\xi^2} + \xi \frac{d\theta_0}{d\xi} + (\nu + 1)\theta_0 = 0, \tag{28}$$

whose solutions satisfying $\theta_0(\infty) = 0$ is

$$\theta_0 = A_0 e^{-\xi^2/4} D_\nu(\xi), \tag{29}$$

where A_0 is an undetermined coefficient and $D_\nu(\xi)$ is a parabolic cylinder function of order ν as defined earlier. Consequently,

$$\theta_0' = -\sqrt{\frac{m+1}{2}}\, A_0 e^{-\xi^2/4} D_{\nu+1}(\xi). \tag{30}$$

The asymptotic expansions for equations (29) and (30) at $\xi \to \infty$ are

$$\theta_0(\xi) = A_0 e^{-\xi^2/2} \xi^\nu \left\{ 1 - \frac{\nu(\nu-1)}{2\xi^2} + \frac{\nu(\nu-1)(\nu-2)(\nu-3)}{2.4.\xi^4} \pm \ldots \right\}, \tag{31}$$

$$\theta_0'(\xi) = -\sqrt{\frac{m+1}{2}}\, A_0 e^{-\xi^2/2} \xi^{\nu+1} \left\{ 1 - \frac{(\nu+1)\nu}{2\xi^2} + \frac{(\nu+1)\nu(\nu-1)(\nu-2)}{2.4.\xi^4} \pm \ldots \right\}. \tag{32}$$

The improved approximations for f_0 and f_0' as $\eta \to \infty$ can then be obtained by substituting equation (32) into equation (3) and performing the integration [4].

To perform the numerical integration of the basic flow, the values of A_0 and B_0 are first guessed and the values of θ_0, θ_0', f_0 and f_0' at $\eta = \eta_\infty$ are evaluated. Equations (3) and (4) are then integrated backward to $\eta = 0$ by the Runge-Kutta integration procedure. The boundary conditions at $\eta = 0$ given by equations (5) were then tested and the values of A_0 and B_0 are readjusted based on the Newton-Raphson iteration method until equations (5) are satisfied. The numerical results obtained in this way for the basic flow agree with those obtained by Cheng [1] using the straight-forward shooting method for forward integration.

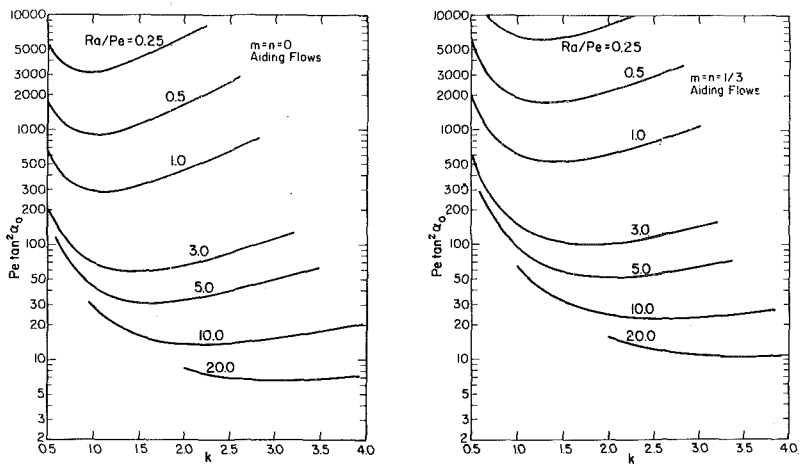

Fig. 2 Neutral stability curves for aiding flows over an inclined surface at (*a*) constant wall temperature ($m = n = \beta_0 = 0$) and (*b*) constant heat flux ($m = n = 1/3$; $\beta_0 = \pi/4$)

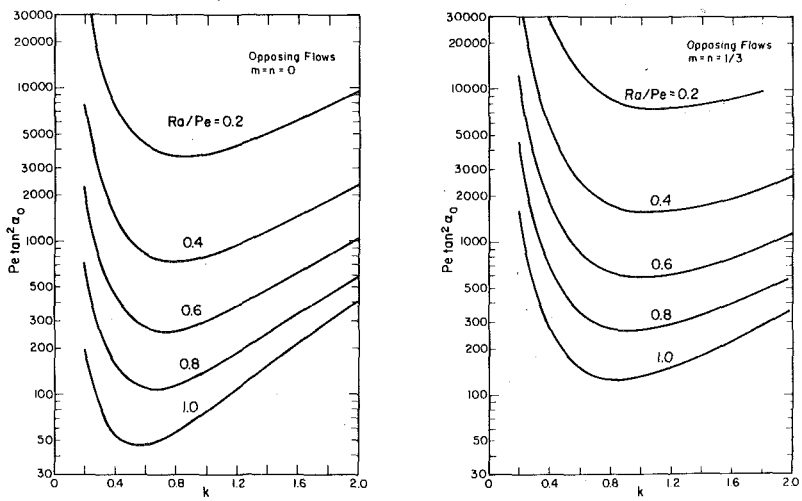

Fig. 3 Neutral stability curves for opposing flows over an inclined surface at (*a*) constant wall temperature ($m = n = \beta_0 = 0$) and (*b*) constant surface heat flux ($m = n = 1/3$; $\beta_0 = \pi/4$)

To obtain the numerical solutions of equation (24), the asymptotic solutions for disturbances will now be sought. As $\eta \to \infty$, equation (24) reduces to

$$(D^2 - k^2)^2 F + \frac{m+1}{2}(\eta_\infty + B_0)D(D^2 - k^2)F - m(D^2 - k^2)F = 0, \tag{33}$$

where $\theta_0 \to 0$, $\theta_0' \to 0$, $f_0 \to \eta_\infty + B_0$ and $f_0' \to 1$ are invoked. Hence, from the boundary condition (26), we have

$$(D^2 - k^2)F = Ce^{-\xi^2/4}D_{\tilde{\nu}}(\xi), \tag{34}$$

where $\tilde{\nu} = -(3m + 1 + 2k^2)/(m + 1)$. The decaying homogeneous solution to equation (34) with $C = 0$ is

$$F_1(\eta_\infty) = e^{-k\eta_\infty}. \tag{35}$$

The particular solution $F_2(\eta_\infty)$ to equation (34) can be found by arbitrarily setting $C = 1$ and integrating twice. The two eigenfunctions for equations (24–26) are $F_1(\eta)$ and $F_2(\eta)$ whose linear combination is

$$F(\eta) = C_1F_1(\eta) + C_2F_2(\eta), \tag{36}$$

where the asymptotic functions for $F_1(\eta)$ and $F_2(\eta)$ are the homogeneous and the particular solutions to equation (34). The values of $F_1(\eta)$, $DF_1(\eta)$, $D^2F_1(\eta)$ and $D^3F_1(\eta)$ at $\eta = \eta_\infty$ can now be found from equation (35). Without losing the generality, we can set $F_2(\eta) = DF_2(\eta) = 0$ at $\eta = \eta_\infty$ so that $D^2F_2(\eta)$ and $D^3F_2(\eta)$ at $\eta = \eta_\infty$ are given by

$$D^2F_2(\eta_\infty) = e^{-\xi^2/4}D_{\tilde{\nu}}(\xi), \tag{37}$$

and

$$D^3F_2(\eta_\infty) = -\sqrt{\frac{m+1}{2}}\,e^{-\xi^2/4}D_{\tilde{\nu}+1}(\xi), \tag{38}$$

which have similar asymptotic expansions as θ_0 and θ_0' as given by equations (31) and (32).

Substituting equation (36) into equation (25) yields

$$\Delta(\text{Pe tan}^2\,\alpha_0;\, m, M, k) = F_1(0)D^2F_2(0) - F_2(0)D^2F_1(0) = 0. \tag{39}$$

For a given set of m, M and K, condition (39) in general is not compatible unless Pe tan^2 α_0 is the eigenvalues of the problem. Using $F_i(\eta_\infty)$, $DF_i(\eta_\infty)$ and $D^3F_i(\eta_\infty)$ with $i = 1, 2$ as the starting values for integration, the numerical procedure to search for the eigenvalue Pe tan^2 α_0 is proceeded as in our previous work [2–4] and will not be elaborated here.

Results and Discussions

Computations were carried out for both aiding and opposing flows over inclined surfaces with constant wall temperature and with constant surface heat flux. As shown in reference [1], the former corresponds to $m = n = \beta_0 = 0$ while the latter corresponds to $m = n = 1/3$ and $\beta_0 = \pi/4$.

Figures 2 and 3 are the neutral stability curves for aiding and opposing flows respectively where the eigenvalues Pe tan^2 α_0 are plotted

against the dimensionless wave numbers at selected values of M. At a given value of M the minimum value of Pe $\tan^2 \alpha_0$ is the critical value for the onset of vortex instability. It is noted in these figures that the value of critical parameter decreases as M is increased. In other words the effect of velocity outside the boundary layer is to suppress the onset of vortex instability in both aiding and opposing flows. The fact that the critical value Pe* $\tan^2 \alpha_0$ is finite implies that the critical Peclet number Pe* becomes infinite when $\alpha_0 = 0$, i.e., for a vertical surface. It follows that vortex mode of instability would not manifest itself in mixed convection in a porous medium adjacent to vertical surfaces. This is due to the fact that the vortex instability is triggered by the buoyancy force in the direction normal to the heated plate, and this force is absent for the case of a vertical plate. The same figures show that the effect of M on the dimensionless wave number k^* are different for aiding and opposing flows. As M is increased, the value of k^* increases for aiding flows while that for opposing flows decreases. This is because the effect of increasing the thermally-induced flow has opposite effects on the boundary layer thickness (and consequently the wave length and wave number of the vortex as implied by the bottling effect) of the aiding and opposing flows. The values of Pe* $\tan^2 \alpha_0$ and k^* at selected values of M for the two cases are also tabulated in Table 1 for future reference.

The variations of the critical parameter and dimensionless critical wave number for aiding flow from nearly pure free convection to nearly pure forced convection are presented in Figs. 4 and 5. For the convenience of presentation, the ordinate in Fig. 4 is chosen to be Ra* $\tan^2 \alpha_0$ while that in Fig. 5 is $k^*/M^{1/2}$ which are respectively the critical parameter and the associated dimsionless wave number for the onset of vortex instability in *free* convection flow in a porous medium adjacent to an inclined surface. The free convection asymptotes which appear as horizontal lines in these plots are obtained from the authors' previous work [3] which gives

$$\text{Ra}^* \tan^2 \alpha_0 = 120.7 \text{ and } k_f^* = 0.636 \text{ for } m = 0 \text{ (isothermal)},$$

and

$$\text{Ra}^* \tan^2 \alpha_0 = 195.1 \text{ and } k_f^* = 0.717 \text{ for } m = 1/3 \text{ (constant heat flux)},$$

where k_f^* is the dimensionless wave number for free convection and is related to k^* for mixed convection by $k_f^* = k^*/M^{1/2}$ which is the ordinate chosen for Fig. 5. The forced convection asymptotes are obtained by letting $M = 0$ in equation (24) while regarding M^2(Pe $\tan^2 \alpha_0$) as the eigenvalues of the problem. This is equivalent to neglecting the component of the buoyancy force in the streamwise direction in equation (15) and consequently $u_1 = 0$; i.e., the thermally-induced streamwise velocity is zero. The numerical results for this case are (1) for isothermal wall ($m = n = 0$)

$$\text{Ra}^* \tan^2 \alpha_0 = \frac{167.6}{M} \quad \text{and} \quad k_f^* = \frac{0.903}{\sqrt{M}}$$

Table 1 Critical values of Pe*tan$^2\alpha_0$ and their associated wave numbers

		inclined plate with isothermal wall temperature ($m = n = \beta_0 = 0$)		inclined plate with constant surface heat flux ($m = n = 1/3$; $\beta_0 = \pi/4$)	
	M	Pe*tan$^2\alpha_0$	k^*	Pe*tan$^2\alpha_0$	k^*
Aiding Flows	0.25	3164.1	0.96	6126.0	1.23
	0.50	911.42	1.01	1729.8	1.29
	1.00	288.02	1.11	531.10	1.40
	3.00	58.73	1.44	102.52	1.75
	5.00	30.77	1.70	52.50	2.03
	10.0	13.73	2.22	22.87	2.59
	20.0	6.67	3.10	10.73	3.51
Opposing Flows	0.20	3588.0	0.84	7321.5	1.12
	0.40	746.03	0.79	1577.1	1.06
	0.60	264.34	0.73	586.97	1.00
	0.80	110.76	0.65	264.79	0.92
	1.00	46.61	0.55	126.20	0.84

and (2) for constant surface heat flux ($m = n = 1/3$)

$$\text{Ra}^* \tan^2 \alpha_0 = \frac{333.0}{M} \quad \text{and} \quad k_f^* = \frac{1.17}{\sqrt{M}}$$

The finite value of M^2(Pe $\tan^2 \alpha_0$) implies that Pe $\tan^2 \alpha_0 \to \infty$ as $M \to 0$; consequently a pure forced convective flow (i.e., the buoyancy force terms are neglected) about an inclined surface in a porous medium is stable to any vortex disturbances. It is also of interest to note that in Fig. 4, the critical values Ra* $\tan^2 \alpha_0$ for opposing flow lay below the forced asymptotes while those for aiding flow lay above. This means that if the thermally-induced streamwise velocity is in the same direction of the forced flow it would stabilize any vortex disturbances. On the other hand, if the thermally-induced streamwise velocity is in opposite direction to that of the forced flow, it would enhance the growth of the vortex disturbances. Figure 4 also shows that the critical value Ra* $\tan^2 \alpha_0$ decreases very rapidly near $M = 1$ for opposing flow; i.e., the neutral condition for the opposing flow near $M = 1$ is very sensitive to the value of the mixed convection parameter. In fact, Cheng's results [1] for the basic flow with opposing thermally-induced flow indicate that a flow reversal may occur near the heated surface when $M > 1$.

The variation of $k^*/\sqrt{M}$ versus M is plotted in Fig. 5 where it is shown that at a fixed value of M the values of $k^*/\sqrt{M}$ lie above the free and forced convection asymptotes for aiding flow, while they lie below the forced convection asymptotes for opposing flow. This is because when the buoyancy-induced streamwise velocity is in the same direction of the forced flow as in the case of aiding flow, the effect of the induced velocity is to decrease the boundary layer thickness and consequently the wave length of the vortex is also decreased. On the other hand, for opposing flow where the buoyancy-induced streamwise velocity is in a direction opposite to the forced flow, the effect of the induced velocity is to increase the boundary layer thickness and consequently the wave length of the vortex. The same figure shows that the values of $k^*/\sqrt{M}$ decreases as M increases for both aiding and opposing flows. This is because the effect of decreasing free stream velocity is to increase the boundary layer thickness for both aiding and opposing flows.

Concluding Remarks

The conditions marking the onset of vortex instability in mixed convection over an inclined surface embedded in a saturated porous medium are investigated on the basis of a linear stability analysis. The solution for the base flow is obtained by Cheng [1] based on boundary layer simplifications which consist of (1) the streamwise pressure

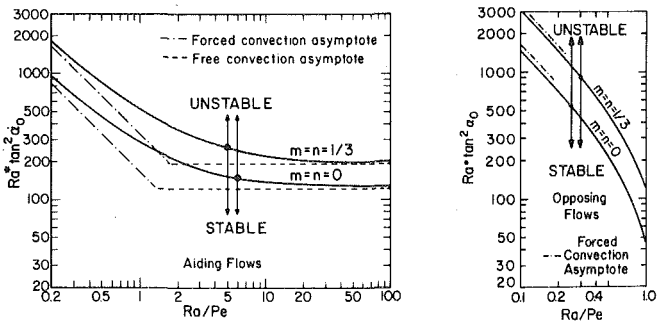

Fig. 4 Ra*tan$^2\alpha_0$ versus mixed convection parameter Ra/Pe for aiding and opposing flows

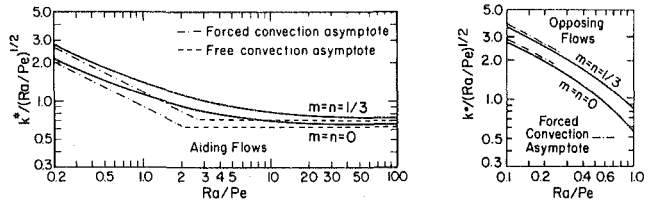

Fig. 5 Critical wave numbers versus mixed convection parameter Ra/Pe for aiding and opposing flows

gradient is small in comparison with the component of the buoyancy force in the streamwise direction which is valid only for small inclination angles, (2) Darcy's friction force in the direction normal to the surface is small in comparison with the component of the buoyancy force in the same direction; the latter gives rise to the vortex instability, and (3) the heat conduction in the streamwise direction is small in comparison with that in the direction normal to the surface.

The three-dimensional disturbances equations are simplified on the basis of a scaling argument whereby most of the streamwise derivatives of the disturbances (except one term in the energy equation) are found to be negligible. The simplified equations are solved approximately based on the local similarity concept in which the disturbances are assumed to have a weak dependence in the streamwise direction. The eigenvalue problem is solved numerically by the Runge-Kutta method incorporate with the Kaplan filtering technique [10] to maintain linear independence of the two eigenfunctions. It is found that yortex instability will not manifest itself in forced convection over an inclined surface or mixed convection along a vertical surface. This is as expected since the component of the buoyancy force normal to the surface (which gives rise to vortex instability) does not exist in both cases. The critical parameters and the critical wave numbers of vortex disturbances for mixed convection over inclined surfaces with constant wall temperature and constant surface heat flux are obtained. The effect of external flow is found to suppress the growth of vortex disturbances. It should be noted that, for mixed convection over nearly vertical surfaces, instability will be characterized by wave disturbances [11]. This problem will be investigated by the present authors.

Acknowledgments

This work was supported by the National Science Foundation through Grant No. ENG 77-27527.

References

1 Cheng, P., "Combined Free and Forced Convection Flow About Inclined Surfaces in Porous Media," *International Journal of Heat Mass Transfer,* Vol. 20, 1977, pp. 807–814.

2. Hsu, C. T., Cheng, P., and Homsy, G. M., "Instability of Free Convection Flow Over a Horizontal Impermeable Surface in a Porous Medium," *International Journal of Heat Mass Transfer,* Vol. 21, 1978, pp. 1221–1228.

3 Hsu, C. T., and Cheng, P., "Vortex Instability in Buoyancy-Induced Flow Over Inclined Heated Surfaces in Porous Media," ASME JOURNAL OF HEAT TRANSFER, Vol. 101, 1979, pp. 660–665.

4 Hsu, C. T., and Cheng, P., "Vortex Instability of Mixed Convective Flow in a Semi-Infinite Porous Medium Bounded by a Horizontal Surface," to appear in *International Journal of Heat Mass Transfer.*

5 Magnus, W., and Oberthettinger, F., *Functions of Mathematical Physics,* translated by J. Wermer, Chelsea Publishing, New York, 1949, pp. 91–94.

6 Haaland, S. E., and Sparrow, E. M., "Vortex Instability of Natural Convection Flow on Inclined Surfaces," *International Journal of Heat Mass Transfer,* Vol. 16, 1973, pp. 2355–2367.

7 Moore, F. K., *Theory of Laminar Flows,* Princeton University Press, 1964, pp. 486–490.

8 Sparrow, E. M. and Yu, H. S., "Local Non-Similarity Thermal Boundary Layer Solutions," ASME JOURNAL OF HEAT TRANSFER, Vol. 93, 1971, pp. 328–334.

9 Sparrow, E. M., Quack, H., and Boerner, C. J., "Local Nonsimilarity Boundary Layer Solutions," *AIAA Journal,* Vol. 8, 1970, pp. 1936–1942.

10 Kaplan, R. E., "The Stability of Laminar Incompressible Boundary Layers in the Presence of Compliant Boundaries," M.I.T. Aero-Elastic and Structures Research Laboratory, ASRL-TR 116-1, 1964.

11 Chen, T. S. and Moutsoglo, A., "Wave Instability of Mixed Convection Flow on Inclined Surfaces," presented at the 1978 National Heat Transfer Conference, Paper No. 79-HT-105.

Yin-Chao Yen[1]
Supervisory Research Physical Scientist,
U.S. Army Cold Regions Research
and Engineering Laboratory,
Hanover, NH 03755

Free Convection Heat Transfer Characteristics in a Melt Water Layer

An experimental study was conducted on the formation of a water layer containing a maximum density, its effect on the onset of convection, and the heat transfer characteristics of such a system. This water layer was formed by one-dimensional melting (either from below or above) of a cylinder of bubble-free ice. For melting from above, with a melting rate measurement, the warm plate temperature T_h varied from 4.16 to 13.09°C with initial ice temperatures T_0 of −6.5 and −13°C, respectively. For experiments with a measurement of temperature profile, T_h varied from 11.75 to 39.90°C with T_0 at −12 and −15°C. For melting from below with a melting rate measurement, T_h ranged from 7.70 to 25.50°C with four T_0's from −4.8 to −22°C. The layer depth at the onset of convection was determined by locating the inflection point on the water layer depth versus time curve, and was compared with layer depth calculated from a linear stability analysis of an identical problem. The results were compared with the analytical work of Veronis and were found to be in excellent agreement. Formation of a constant temperature layer was observed by measuring the water temperature distribution as melting progressed. The constant temperature was found to be dependent on T_h for melting from below but was a constant for melting from above. The heat flux to the melting surface increased linearly with T_h for melting from below, but had a weaker dependence for melting from above. Non-dimensional mean temperature profiles of the water layer were found to be in good agreement with those by Adrian for melting from above. In the case of melting from below, the mean temperature profile also fell into a single line with a somewhat higher value in the convection layer.

Introduction

The phenomenon of convection in a water layer when the lower boundary is between 0 and 3.98°C and the upper boundary is warmer than 3.98°C, is of special interest because the system divides itself into a convection layer lying under a stable layer. Veronis [1] dealt with this problem analytically for the case where the upper boundary is a free surface. He showed that this system is subject to finite amplitude instability and that motions in the convection layer can penetrate a finite distance into the region of stably stratified fluid. The penetrative convection observed over melting ice provides a simple means of analytically and experimentally studying similar phenomena which occur in geophysical flows.

Townsend [2], and later Myrup, et al. [3], reported on the first experimental studies of natural convection in water over an ice surface since Veronis's pioneer work. In both investigations, the layer depths were much larger (~10–15 cm) than in [1], and the convection was turbulent. They observed that intermittent narrow plumes that extended across the convection layer were the prevalent structures rather than roll cells. Townsend found that sudden cooling of the lower plate in his box experiment created a convection layer that grew upward and eventually reached a constant depth. This depth was determined by the condition that the conductive heat flux through the stable layer be equal to the turbulent heat flux in the convection layer. The latter quantity was independent of the convection layer depth, as in Rayleigh convection, where the heat flux is controlled by the conduction layer. Townsend's most interesting observation was of the large magnitude of temperature fluctuations near the interface between the convection layer and the stable layer. He attributed this to breaking internal gravity waves generated in the stable layer by the impact of rising fluid on its base. Wavelike motions have also been observed in convection in water over ice by Myrup, et al. [3], Moore and Weiss [4], and in unsteady convection under a stable layer by Deardorff, et al. [5].

More detailed analyses of convection in water over ice were reported by Musman [6] and Moore and Weiss [4]. In these studies, two-dimensional flows with free boundaries were assumed while the maximum Rayleigh numbers were less than those required for transition to the turbulent flow regime. Both analyses predicted horizontally periodic cells. At large Rayleigh numbers, Moore and Weiss observed cellular oscillations that were coupled to waves in the stable layer. Tankin and Farhadieh [7] reported an experimental study of convection in thin layers of water over ice. They indicated the flows were laminar, and interferograms suggested periodic roll cells similar to those predicted by Musman [6] and Moore and Weiss [4] at low Rayleigh numbers. Tien [8] and Sun, et al. [9], using linear stability analysis, also reported the conditions for instability in terms of a critical Rayleigh number.

The work of Adrian [10] was, in essence, an extension of the experiments of Townsend [2] and Myrup, et al. [3] in which attention was limited to the statistically steady case. In his study, vertical velocity and simultaneous temperature flucutations at fixed points in turbulent, statistically steady convection were measured. He concluded that 80 percent of the mean-square fluctuations in temperature and velocity occurring in the unstable layer were associated with large scale coherent motions.

The first experimental work on the effect of maximum density on convection in a water layer, either above or below an ice surface, were reported by Yen, et al. [11], Yen [12] and Yen and Galea [13]. The fundamental difference between these works and the studies mentioned above was that the water layers were formed by melting which increased the depth of the layer (beginning at zero) as the experiment progressed. The onset of convection was found to be dependent on boundary temperatures and was in close agreement with the predicted results given in Sun, et al. [9].

Most recently, Legros, et al. [14] studied the Bernard problem in water near 4°C. In their experiments, a 4.67-mm-deep water layer was heated from below while the top was maintained at temperatures between 0.54 and 20.4°C. For upper boundary temperatures greater than 4°C, the observed critical temperature difference T_c was compared with those computed from the classical Rayleigh number with

[1] Also Adjunct Professor, Department of Chemical Engineering, University of New Hampshire, Durham, NH 03824.

Contributed by The Heat Transfer Division for publication in The JOURNAL OF HEAT TRANSFER. Manuscript received by The Heat Transfer Division January 31, 1980.

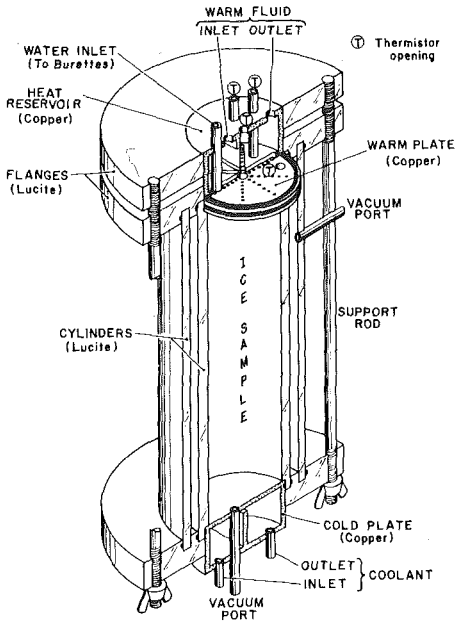

Fig. 1 Schematic of the experimental apparatus

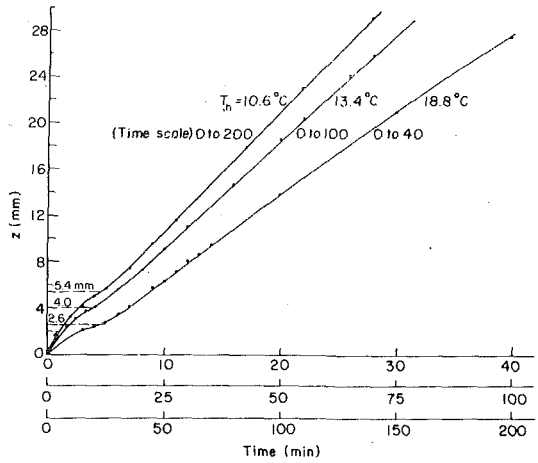

Fig. 2 Typical water layer depth versus time curve for melting from below

fixed boundaries. For upper boundary temperatures lower than 4°C, they compared their results using an analogy, pointed out first by Veronis [1], between the eigenvalues for the Bernard problem with a maximum density and the eigenvalues for the stability of viscous flow between two cylinders rotating at almost the same angular velocity. They found an excellent agreement.

In a recent analytical study, Merker, et al. [15] investigated the onset of convection in a water layer at temperatures where the density anomaly cannot be neglected. Linear stability analysis was used. The resulting perturbation equations were solved with the aid of Galerkin's method. Merker, et al. defined the Rayleigh number in terms of the height of the total water layer, rather than the height of the unstable layer which is used by most investigators.

The present study extends the work reported by Yen [12] and Yen and Galea [13]. The experimentally determined critical water layer depth was used to confirm Legros, et al.'s findings and to extend the comparison with Veronis' [1] analytical work. The developing thermal profile in the continuously forming water layer for the case of melting from above was compared with those reported by Adrian [10] and Townsend [2] from their rather deep but constant depth water-layer experiments. Thermal profiles for melting from below were also obtained which show quite different characteristics in comparison with those for melting from above.

Experimental Apparatus and Procedure

The apparatus is shown schematically in Fig. 1. The test chamber was a double-walled Lucite cylinder with walls of 0.125 and 0.150 m dia, fitted on both ends with copper warm and cold plates. It was designed so that after the ice sample was assembled and connected to the warm and cold circulating fluids, it could be inverted to produce melting from above. The warm plate maintained the desired temperature and provided the water needed to compensate for the volume decrease resulting from the transition from ice to water. This was accomplished by injecting the water through the outer, warm circulating chamber, distributing it over the warm plate, and passing it through the drilled holes before diffusing it into the test chamber. Both the warm and cold plate temperatures could be maintained within ±0.02°C.

The volume of water flowing in was periodically recorded and was used to calculate the mean water/ice interface position. Thermistors with a bead diameter of 0.8 mm were mounted in Bakelite tubing of 3.0 mm dia (130 mm in length with 2.5-mm graduations) and secured in place by means of RTV Silastic with the beads just outside the tubing opening. The thermistor response time was about 2 s.

Before the experiment, the thermistors were inserted through the openings in the heat reservoir and were installed with one in the center and the other three on radii 60 deg apart and 20, 30 and 40 mm from the center to minimize the effect of fluid disturbance. The ends of the thermistors were kept level with the surface of the warm plate. When a temperature profile of the melted layer was desired, however, they were gently moved upward at 2.5-mm intervals. The sampling time was about 1 min for recording four readings at the same level. The total time needed to complete a temperature profile depended on the depth of the liquid layer.

The preparation of bubble-free ice using deaerated distilled water

Nomenclature

A = a parameter defined as $T_\ell - T_{\max}/T_\ell - T_u$ and cross-sectional area of the sample
c_i = specific heat of ice
c_w = specific heat of water
d_c = layer depth at onset of convection
g = gravitational constant
h = layer depth of unstable region
H = total heat flux
k_i = thermal conductivity of ice
k_w = thermal conductivity of water
L = latent heat of fusion
Q = kinematic heat flux defined by $Q = H/\rho_w c_w$
R = defined as $g\alpha(\Delta T)^2 h^3/\alpha_w \nu_w$
t = time
T = temperature
T_c = temperature of the constant temperature layer
T_h = warm plate temperature
T_m = melting temperature
$T_{\max}$ = temperature of maximum density
T_0 = initial ice temperature
V = volume of water added
w_0 = defined by equation (13)
w_* = defined by equation (14)
z = water layer depth
z_0 = defined by equation (13)
z_* = characteristic length of convection scale
α_i = thermal diffusivity of ice
α_w = thermal diffusivity of water
β = constant defined in equations (10) and (15)
β_1, β_2 = constants defined in equation (3)
λ = defined as d_c/h $(= 1 - \mu)$
λ_1, λ_2 = parameters defined in equations (4) and (5)
μ = ratio of rotation rates of outer to inner cylinder
ρ_i = ice density
$\rho_{\max}$ = water density at $T_{\max}$
ρ_w = water density
ν_w = kinematic viscosity of water
$\bar{\theta}$ = mean temperature
θ_0, θ_* = defined in equations (13) and (14)

has been described in great detail [11]. The ice sample was conditioned to a desired intial temperature T_0 and maintained at T_0 at one end during the course of the experimentation. The coupling of the test chamber and the heat reservoir was done in such a manner that no air was trapped between the bottom of the warm plate and the top of the reservoir. This was accomplished by allowing the water to fill the groove on the top of the reservoir prior to the coupling.

Results and Discussion

Experiments were conducted for both cases, i.e., the water layer was formed either over the ice (melting from above) or under the ice (melting from below). When the temperature profile of the melted layer at the various stages of melting was taken the rate at which water flowed in to compensate for the volume of shrinkage was not recorded.

Figure 2 shows a typical layer depth versus time curve for the case of melting from below. For T_h higher than 18.8°C, the melting is so rapid that the transition of the heat transfer mode from conduction to convection is almost instantaneous. It can also be seen that the melting rate, after the onset of convection, remains essentially constant at all values of T_h, and is strongly dependent on T_h. Before the critical number is exceeded, the water/ice interface is always flat, indicating a negligible importance of radial heat gain or loss.

After the transition to convection, cells started to form. These cells were hemispherical and higher in the center (for the case of melting from below). They had a circular cross section and were different from the hexagonal Bernard cells. They were distributed uniformly over the whole interface without any disturbance from the holes drilled in the warm plate.

Figure 3 is a schematic representation of the water/ice interface after the onset of convection for melting from below. It is interesting to note that in the case of melting from above, as soon as a melted water layer was formed, a stable region would form over the unstable region near the water/ice interface. At the onset of convection, the interface became covered with a series of circular concentric ridges equally spaced from each other. This phenomenon was not observed in the case of melting from below. The case of melting from above is equivalent to most of the work cited in the references.

Figure 4 is a schematic drawing of the water/ice interface in the beginning stages of the convective motion for melting from above. The height between crest and trough increases with time. It can reach a value as large as 5.0 mm. However, this pattern was replaced by that of small inverted hemispherical cells which gradually enlarged in size and finally formed an irregular and unsymmetrical surface as the melting progressed (as in the case of melting from below).

In all, a total of 51 experiments were conducted. Melting rates were determined in 38 of them (22 were melting from below and 16 were melting from above) and in the remaining 13, temperature profiles of the water layer were measured (11 of these were melting from above and 2 melting from below). For melting from below with melting rate measurements, T_h ranged from 7.7 to 25.5°C with initial ice temperature T_0 from −4.8 to −22°C; for the two experiments with temperature measurements, T_h was 7.46 and 9.16°C, respectively. For melting from above with melting rate measurement, T_h ranged from 4.16 to 13.9°C with T_0 at −12 and −15°C.

The water layer depth d_c (determined from experiments with melting rate measurement) at onset of convection was defined by locating the inflection point on the water-layer depth versus time curve and was found to be dependent on the direction of melting and to be a sole function of T_h. For melting from below, the value of d_c obtained can be expressed by

$$d_c = 152(T_h)^{-1.36} \quad (1)$$

with d_c varying from 2.0 to 10.2 mm and with $7.7°C \leq T_h \leq 25.5°C$. On the other hand, for the case of melting from above, d_c can be fairly well represented by a linear relation:

$$d_c = 1.75 + T_h \quad (2)$$

with d_c ranging from 6.4 to 15.0 mm and with $4.16°C \leq T_h \leq 13.09°C$.

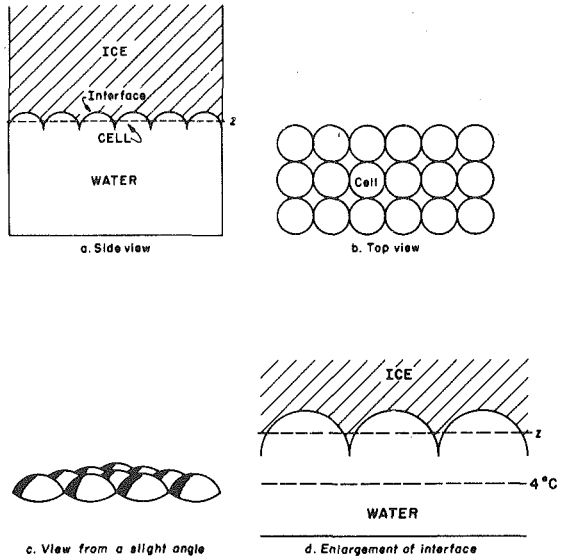

Fig. 3 Schematic of water/ice interface shortly after onset of convection for melting from below

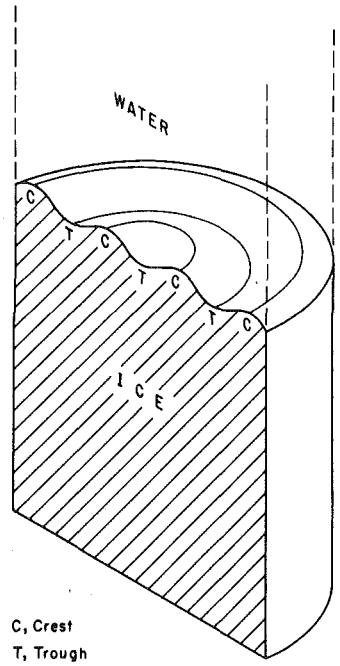

Fig. 4 Schematic of water/ice interface after the onset of convection for melting from above

It is evident that for melting from below, the values of d_c decrease as T_h increase and vice versa. At $T_h = 4°C$, the water is at its maximum density and therefore the system is always stable, thus d_c theoretically has a value of infinity (equation (1) shows this trend). Contrary to the case of melting from below, the instability region in melting from above is limited to temperatures between 0 and 4°C in the adjacent water layer over the water/ice interface. The value of d_c increases at T_h increases.

These experimentally determined values of d_c provide a concrete verification of the findings, given in [9], that in water layers formed by phase transition (either melting from below or above), or in water layers containing the temperature of maximum density, the onset of convection is no longer at a constant value as in the classic Bernard problem, but is dependent on direction of melting, boundary temperature, and conditions and physical properties of the fluid medium.

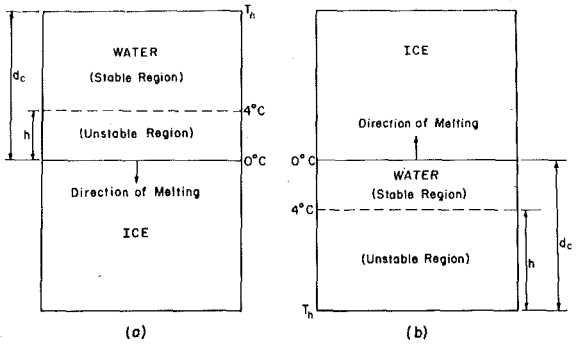

(a) (b)

Fig. 5(*a*) Melting from above **Fig. 5(*b*) Melting from below**

Fig. 5 Schematics of unstable layer and temperature conditions at onset of convection

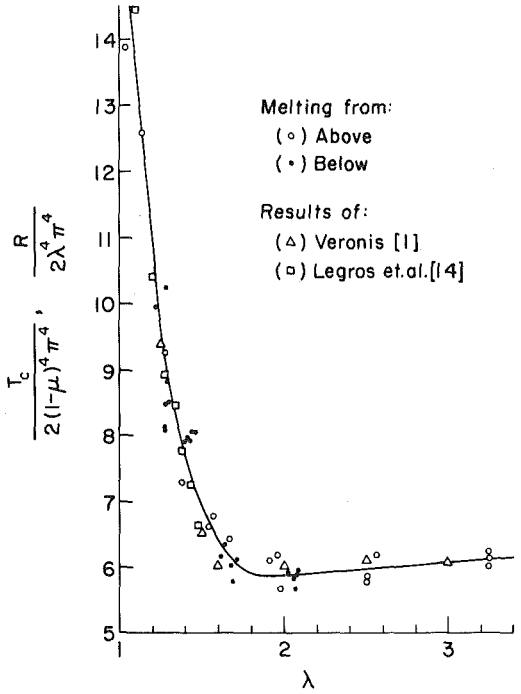

Fig. 6 Relations of $R/2\lambda^4\pi^4$ and $T_c/2(1-\mu)^4\pi^4$ and λ

The aspect ratio (defined as the ratio of the diameter of the ice container to the water layer depth at onset of convection d_c) included both types of melting experiments and ranged from 8.33 to 62.50. However, in a great majority of the experiments, aspect ratios were skewed toward the higher value; thus the effect of the circular boundary on the onset of convection is considered to be insignificant.

In reference [9] a linear stability analysis for a horizontal layer of water containing a maximum density was made for a density and temperature relationship in the form

$$\rho = \rho_{\max}[1 - \beta_1(T - T_{\max})^2 - \beta_2(T - T_{\max})^3]. \tag{3}$$

The Rayleigh number was found to be dependent on two parameters containing the lower, T_ℓ, and upper, T_u, boundary temperatures.

$$\lambda_1 = \left(-\frac{1}{A}\right)\left[1 + 3\frac{\beta_2}{\beta_1}A\Delta T\right)\Big/\left(1 + \frac{3}{2}\frac{\beta_2}{\beta_1}A\Delta T\right)\Big] \tag{4}$$

and

$$\lambda_2 = \frac{1}{A^2}\left[\frac{3}{2}\frac{\beta_2}{\beta_1}A\Delta T\Big/\left(1 + \frac{3}{2}\frac{\beta_2}{\beta_1}A\Delta T\right)\right], \tag{5}$$

where $A = T_\ell - T_{\max}/T_\ell - T_u$, and $\Delta T = T_\ell - T_u$. The Rayleigh number was derived by

$$N_{\mathrm{Ra}} = \frac{2\beta_1 g A(\Delta T)^2 d^3\left(1 + \frac{3}{2}\frac{\beta_2}{\beta_1}A\Delta T\right)}{\alpha\nu} \tag{6}$$

and it was found to be applicable to either $T_\ell > T_u$ (melting from below) or $T_\ell < T_u$ (melting from above). Using the notation in this paper, we have, for melting from below, $A = T_h - T_{\max}/T_h$ and $\Delta T = T_h$. For melting from above, $A = T_{\max}/T_h$ and $\Delta T = -T_h$. By substituting experimentally determined values of d_c, A and ΔT into equation (6), the critical Rayleigh numbers, N_{Ra_c}, were computed and compared with those reported in [9] with corresponding values of λ_1 and λ_2 as defined in equations (4) and (5). The maximum deviation was found to be 18 percent. Since $N_{\mathrm{Ra}_c} \propto d_c{}^3$, the deviation of d_c is therefore only about 6 percent.

The d_c values were also used in deriving a comparison with the analytical work of Veronis [1] and the experimental results of Legros, et al. [14]. Veronis considered the case equivalent to melting from above while Legros, et al. studied the case equivalent to melting from below. In both cases, however, the layer was at a fixed depth while in the present case the water layer depth was formed (initially at zero) continuously as a result of phase transition. The results of Veronis were plotted in terms of $T_c/2(1-\mu)^4\pi^4$ versus λ, in which T_c is the critical Taylor number for a Couette flow problem, μ is the ratio of the rotation rate of the outer cylinder to that of the inner cylinder, and $\lambda(\equiv 1 - \mu)$ is the ratio of d_c/h, where h is the depth of the unstable region at the onset of convection. The work of [14] was plotted in terms of $R/2\lambda^4\pi^4$ versus λ in which R is defined as $R = g\gamma(\Delta T)^2h^3/\alpha_w\nu_w$. The value of ΔT is the temperature difference across the unstable layer.

Figure 5 shows schematically the relative depths of the unstable layers and the temperatures at the onset of convection for both melting from above and below. In the present study of melting from above, the unstable region is between 0 and 4°C. For total layer depth at the onset of convection d_c and total temperature differential T_h, the depth of the unstable region is $h = (4/T_h)d_c$; similarly, for melting from below, the unstable region is between 4°C and T_h; the temperature differential is T_h. The depth of the unstable region is $h = [(T_h - 4)/T_h]d_c$. The values of α_w and ν_w are evaluated at $T_h/2$. Figure 6 shows the comparison. Agreement was found to be exceptionally good. The range of comparison with Veronis's work has also been extended from $\lambda \simeq 1.5$ to 3.25.

Mean Temperature Profiles. Typical mean temperature profiles are shown in Figs. 7 and 8 for both melting from below and above; each data point represents the average of the four thermistor readings from the same level. It should be noted that for both cases the thermistor readings contained a random component associated with the fluctuating temperature fields in the convection region. Thus, the convective motions were unsteady, in contrast to the steady-state model assumed by Musman [6].

In the case of melting from below (Fig. 7), it can be seen that a nearly constant temperature layer formed and expanded as the experiment progressed and finally occupied a great portion of the layer. The temperature readings are more scattered than the case for melting from above, especially near the lower warm plate and the upper water/ice interface. The constant temperature of the convective layer T_c is dependent on T_h. T_c was observed to be at 5.2 and 6.5°C for T_h = 7.46 and 9.16°C, respectively. The degree of random fluctuation of the thermistor readings was also observed to be intensified as T_h increased.

Contrary to melting from below, in the case of melting from above (Fig. 8), a constant temperature layer of approximately 4°C forms initially with a lesser degree of scattering. As time goes on, a layer of much more uniform temperature forms and occupies most of the total layer depth with much greater temperature scatter at the juncture of the upper, stable layer and the underlying convective layer, and at the water/ice interface.

However, for a variation of T_h from 11.75 to 39.90°C, the convective layer has a temperature of about 3.2°C as reported by Townsend [2], Myrup, et al. [3] and Adrian [10]. In these studies, the water layer

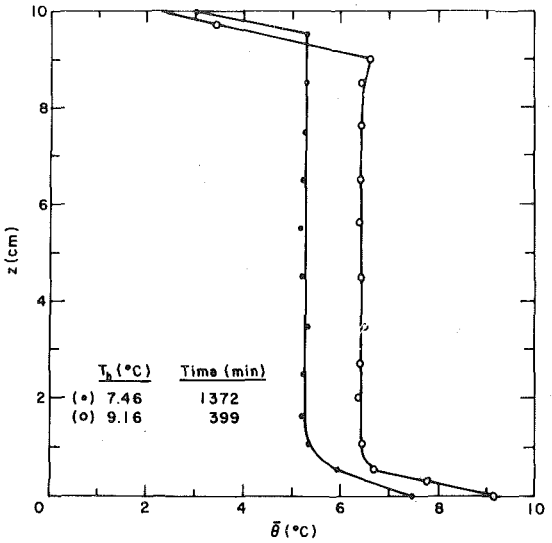

Fig. 7 Mean temperature profiles for melting from below

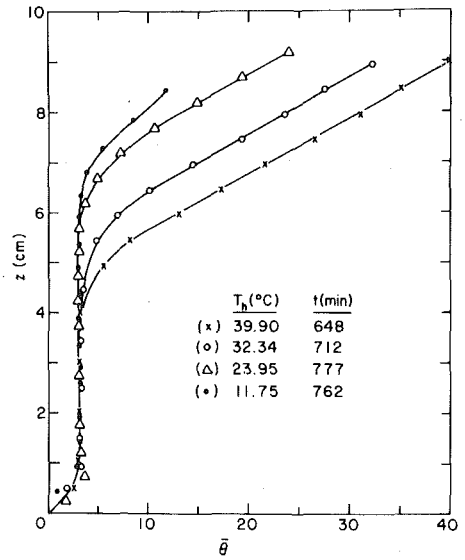

Fig. 8 Mean temperature profile for melting from above

depths were invariant which is contrary to the continuously deepening layer depth in the present study. It appeared that the unsteadiness is dynamically insignificant in the present problem.

Figure 9 shows a typical plot of temperature versus layer depth at 608 min after initiation of the experiment. At each level, four thermistor readings were taken. It can be seen that with the exception of the neighborhood of the two interfaces, where the temperature fluctuations were much greater, the temperature variations were rather small in the convective layer. It can easily be seen that there is a temperature reversal from about 1 cm to approximately 5 cm above the ice surface. The temperature of the convective layer decreases (instead of increases) from about 3.3 to 2.7°C. Slight temperature reversals can also be observed in Figs. 10 and 11, based on mean temperature readings of each level. Overshoots were observed in all the temperature traverses (whether the melting was from above or below) in the pseudo-steady conditions. Although they were somewhat larger when the depth of the constant-temperature region was small, this temperature reversal clearly demonstrated the findings of Townsend [2].

Heat Flux. The total downward or upward heat flux for melting from above or below can be expressed by

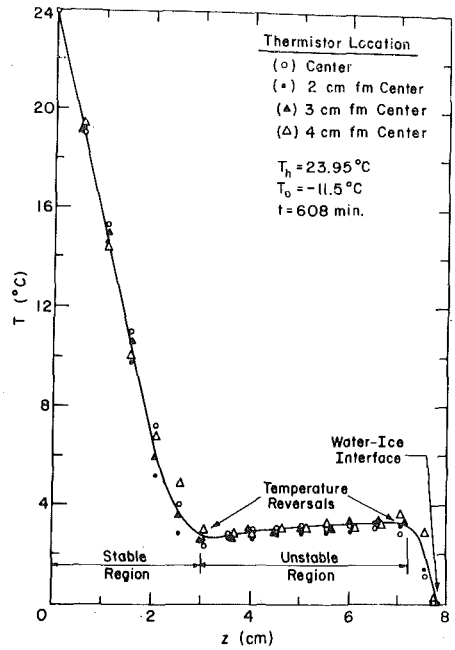

Fig. 9 Typical temperature readings in a well-formed convective water layer

$$H = \rho_w \frac{dz}{dt}[L + c_i(T_m - T_0)] - k_i \left.\frac{dT_i}{dz}\right|_{z=d_c} \tag{7}$$

Since the average value of dz/dt remained nearly constant as soon as the onset of convection occurred, the value of dT_i/dz was evaluated when $z = d_c$.

The value of z is found from the relation

$$z = V\rho_w/(\rho_w - \rho_i)A \tag{8}$$

Where V is the volume of water added at T_h; and ρ_w and ρ_i are the densities of water and ice, respectively; c_i is the specific heat of ice; k_i the thermal conductivity of ice; and T_m and T_0 are the temperature of melting and the initial ice temperature. The value of dT_i/dz is evaluated from the expression describing the temperature distribution in ice [16] by

$$T_i = T_0[1 - \text{erfc}\,(z/2\sqrt{\alpha_i t})/\text{erfc}\,(\beta\sqrt{\alpha_w/\alpha_i})] \tag{9}$$

with β from

$$\frac{\exp(-\beta^2)}{\text{erf}\,\beta} + \left(\frac{k_i/\alpha_w T_0}{k_w\sqrt{\alpha_i} T_h}\right)\frac{\exp(-\beta^2\alpha_w/\alpha_i)}{\text{erfc}(\beta\sqrt{\alpha_w/\alpha_i})} = \frac{\beta L/\pi}{c_w T_h}. \tag{10}$$

With a given set of T_0 and T_h, β can be calculated from equation (10), and then the gradient dT_i/dz at $z = d_c$ with the corresponding experimental duration $t = t_c$ can be calculated.

The heat flux for the case of melting from below was found to be a strong function of T_h. For the range of T_h varying from 7.7 to 25.5°C, the heat flux can be expressed linearly by

$$H = -1900 + 315(T_h) \tag{11}$$

where H is expressed in W/m^2. The higher the value of T_h, the more extensive the convective motion in the unstable region; thus the thickness of the stable layer adjacent to the ice surface is reduced and the heat transfer rate is promoted.

For the case of melting from above, the heat flux was not found to be a strong function of T_h. The heat transfer rate is controlled by the convective layer over the ice with a driving potential of a mere 4°C. In those experiments with T_h ranging from 11.75 to 39.9°C (as shown in Table 1) the heat flux H was evaluated from the mean temperature gradients at the uppermost stable region (i.e., near the warm plate) starting immediately after the onset of convection. An arithematic mean value of the temperature gradients at times t_1 and t_2 was evaluated as the mean temperature gradient during the period $(t_2 - t_1)$.

For a typical run, at least a dozen or more of these periods (with varying durations) were used to obtain an overall heat flux, i.e.,

$$H = \sum \frac{k_w}{2}\left[\left(\frac{dT}{dx}\right)_2 + \left(\frac{dT}{dx}\right)_1\right](t_2 - t_1)/\Delta t$$

where subscripts 1 and 2 indicate the beginning and end of each period, and Δt is the total time period. Each value of H shown in Table 1 was calculated in such a manner, and can be represented fairly well by

$$H = 177(T_h)^{0.303} \tag{12}$$

with an average value of $H = 474$ W/m^2. This value is very close to the average H obtained from equation (7) for similar melting experiments but with the melting rate measurement (i.e., $H \approx 505$ W/m^2).

It should be pointed out that for both techniques used in evaluating H, there were uncertainties in determining the temperature gradients and the melting rates. For the temperature gradient evaluation, difficulty was especially encountered immediately following and shortly after the formation of the convective layer (i.e., a shallow layer depth). During this period the temperature distribution in the stable region was somewhat scattered, making it impossible to obtain an accurate temperature gradient. For the melting rate measurement, and subsequently in calculating the heat flux H, the difficulty rested in the determination of the slope of the layer depth versus time curve after the onset of convection (because of the rather small melting rate in this type of experiment).

In Townsend's [2] experiment, with a constant water layer depth of about 15 cm and without any consideration of the phase change at the bottom of the tank, the downward heat flux was calculated from the rate of change of heat content below some fixed level in the stable region and the vertical gradient of temperature at that level. He reported that the heat flux decreased from 340 W/m^2 in the early stages to about 260 W/m^2 as the temperature distribution approached equilibrium. He indicated that the most probable cause of the heat flux decrease is the increasing heat flow into the tank by conduction through the side walls as the layer of cold fluid forming the constant temperature region becomes thicker. Since observations of temperature distribution showed no corresponding changes in the pattern of convection, he concluded that the equilibrium heat flux in a horizontally homogeneous system would be close to 340 W/m^2.

The work of Adrian [10] was similar to that of Townsend [2]. He also calculated the heat flux from the mean temperature gradients at the upper plate and found it to be in good agreement with Townsend's value. It is reasonable to assume that the cause of the discrepancy in H values between this investigation and those of Townsend [2] and Adrian [10] is probably the real difference in the processes involved in the experimental system. The present investigation studied the heat transfer characteristics of a continuously forming layer while Townsend and Adrian's studied the temperature behavior of an invariant and rather large layer depth.

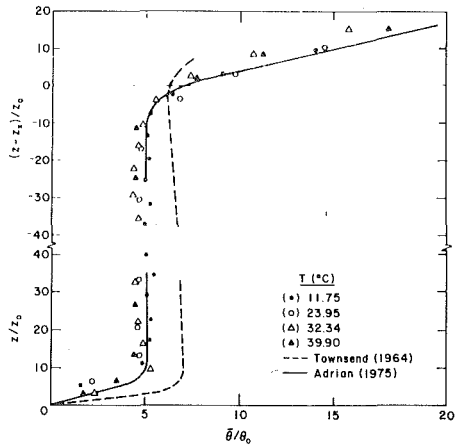

Fig. 10 Nondimensional mean temperature profile for melting from above

Nondimensionalization. Typical data on temperature measurements have been made dimensionless by use of the molecular scales of velocity, length, and temperature for convection in water over ice given by Townsend [2]

$$w_0 = (\alpha\beta g Q^2)^{1/5},\ z_0 = \alpha/w_0,\ \theta_0 = Q/w_0 \tag{13}$$

or the convection scales defined as

$$w_* = (\beta g z_* Q^2)^{1/4},\ z_*,\ \theta_* = Q/w_* \tag{14}$$

which are analogous to the scales proposed by Deardorff [17] for convection in air. In these formulae, α is the thermal diffusivity, β is defined in

$$\rho_w = \rho_{\max}[1 - \beta(T - T_{\max})^2], \tag{15}$$

where $\rho_{\max}$ is the density corresponding to temperature at $T_{\max} = 3.98$°C, g is acceleration due to gravity, and Q is the kinematic heat flux ($= H/\rho_w c_w$). The convection length scale z_* is taken as the depth of the convection layer, and for the present study, as indicated by Adrian [10], it has been defined as the height at which the mean temperature reached 3.98°C. Values of the scales are given in Table 1 along with reported values by Adrian.

The molecular scales are based on the assumption that in certain regions of the flow the convection-layer depth is not dynamically significant, but molecular diffusion is important. Hence, the molecular scales are expected to be appropriate in boundary regions such as the

Table 1 Summary of experimental parameters and computed characteristics scale values of length, velocity and temperature

Run	T_h(°C)	t(min)	z(cm)	H(W/m^2)	z_*(cm)	w_*(cm/s)	θ_*(°C)	z_0(cm)	w_0(cm/s)	θ_0(°C)
					(a) Melting from above					
3	17.60	755	9.00	450	6.5	0.0493	0.217	0.0793	0.0164	0.652
4	23.95	777	9.25	470	6.5	0.0504	0.222	0.0779	0.0167	0.671
5	24.01	757	9.25	468	6.2	0.0499	0.225	0.0779	0 0167	0.671
6	11.75	762	8.25	387	7.0	0.0468	0.199	0.0839	0.0155	0.600
7	32.34	712	9.00	519	5.7	0.0514	0.242	0.0747	0.0174	0.713
8	32.33	726	9.00	509	5.5	0.0504	0.242	0.0754	0.0173	0.706
9	11.92	737	8.50	358	6.5	0.0444	0.193	0.0867	0.0150	0.571
10	17.98	761	8.50	472	6.0	0.0497	0.227	0.0778	0.0167	0.677
11	39.90	648	9.00	530	4.8	0.0498	0.255	0.0743	0.0175	0.726
12	39.75	651	9.25	564	4.5	0.0505	0.267	0.0722	0.0180	0.756
13	28.40	728	8.75	489	5.0	0.0483	0.242	0.0765	0.0170	0.688
					(b) Results of Adrian [10]					
A				354	14.15	0.0521	0.155	0.0897	0.0148	0.548
B				360	13.95	0.0524	0.157	0.0902	0.0148	0.550
C				342	11.80	0.0490	0.160	0.0915	0.0146	0.539
					(c) Melting from below					
14	7.46	1372	10.60	523	9.5	0.0589	0.2122	0.0747	0.0174	0.718
15	9.16	399	10.40	1025	9.5	0.0820	0.2987	0.0461	0.0282	0.869

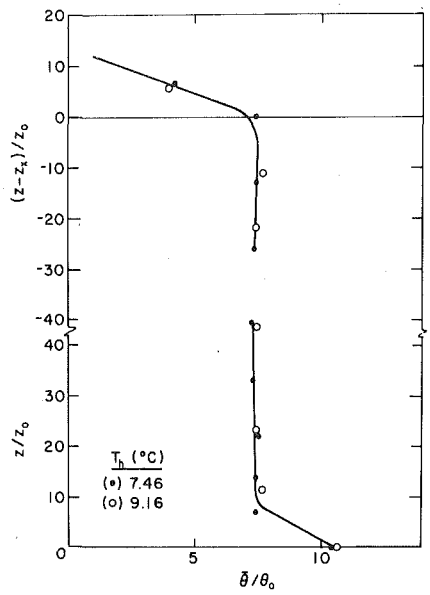

Fig. 11 Nondimensional mean temperature profile for melting from below

conduction layer and the interfacial layer. On the other hand, the convection scales are intended to apply in the core of the convection layer where the length scale of the convection motion is on the order of the layer depth, and molecular diffusion is not important.

Figure 10 shows the typical non-dimensional mean temperature profiles for the case of melting from above. The works of Adrian [10] and Townsend [2] on convection of water over ice are also shown (the results of Myrup, et al. were hard to reproduce for comparison). However, it should be noted that in all their work no actual phase change was taking place. Instead, a constant but rather deep water layer (~15 cm) was used. The work of Adrian seems to agree rather well with the present study.

Figure 11 shows the nondimensional mean temperature profile for the case of melting from below. As in the case of melting from above the convection layer occupied a considerable fraction of the water depth. Although the temperature of the convection layer as indicated in Fig. 7 depends on the value of T_h, the nondimensional mean temperature, derived from the limited available data, falls into a single line as in the case of melting from above with a somewhat higher ratio of $\bar{\theta}/\theta_0$ for the convection layer. The only experimental work closely related to the case of melting from below was conducted by Legros, et al. [14] (for those experiments with an upper boundary less than 4°C). However, their basic concern was the determination of the critical temperature difference across the water layer and no attempt was made to measure the temperature profiles within the layer.

Conclusions

From the experimental results reported, the following conclusions can be drawn.

1 For the temperature range T_h studied, the inflection point on the water layer depth versus time curve can be located fairly accurately for determining d_c, the layer depth at onset of convection. These values were compared with those calculated from the linear stability analysis of an identical system [9] and were found to be in excellent agreement.

2 A nearly constant temperature layer forms for both cases of melting. For melting from below, the temperature of the convective layer depends on T_h. On the other hand, the constant temperature layer is always at about 3.2°C regardless of T_h for melting from above.

3 The total heat flux H to the melting surface is found to increase linearly with T_h in the case of melting from below. For melting from above, the values of H are found to be a somewhat weaker function of T_h and independent of initial ice temperature T_0.

4 The present results in terms of $R/2\lambda^4\pi^4$ were compared with those of Legros, et al. [14] and the analytical results of Veronis [1]. The present study has extended the value of λ from nearly 1.5 to 3.25 and the agreement was found to be exceptionally good.

5 Under psuedo-steady conditions, the nondimensional mean temperature profile of the water layer was compared with those presented by Adrian [10] and Townsend [2] from their deep water layer experiments. The work of Adrian's seems to agree well with the present study. It further indicates that the unsteadiness in the melting problem is dynamically insignificant.

References

1 Veronis, G., "Penetrative Convection," *Astrophysics Journal,* Vol. 137, 1963, pp. 641–663.

2 Townsend, A. A., "Natural Convection in Water over an Ice Surface," *Quarterly Journal of the Royal Metals Society,* Vol. 90, 1964, pp. 248–259.

3 Myrup, L., Gross, D., Hoo, L. S., and Goddard, W., "Upside-down Convection," *Weather,* Vol. 25, No. 4, 1970, pp. 150–156.

4 Moore, D. R., and Weiss, N. O., "Non-linear Penetrative Convection," *Journal of Fluid Mechanics,* Vol. 61, part 3, 1973, pp. 553–581.

5 Deardorff, J. W., Willis, G. F., and Lilly, D. K., "Laboratory Investigation of Non-Steady Penetrative Convection, *Journal of Fluid Mechanics,* Vol. 35, part 1, 1969, pp. 7–31.

6 Musman, S. "Penetrative Convection," *Journal of the Fluid Mechanics,* Vol. 31, part 2, 1968, pp. 343–360.

7 Tankin, R. S., and Farhadieh, R., "Effects of Thermal Convection Current on Formation of Ice," *International Journal of Heat Mass Transfer,* Vol. 14, 1971, pp. 953–971.

8 Tien, Chi, "Thermal Instability of a Horizontal Layer of Water Near 4°C, *AIChE Journal,* Vol. 14, No. 4, 1968, pp. 652–653.

9 Sun, An-Shung, Tien, C., and Yen, Yin-Chao, "Thermal Instability of a Horoizontal Layer of Liquid with Maximum Density," *AIChE Journal,* Vol. 15, No. 6, 1969, pp. 910–915.

10 Adrian, R. J., "Turbulent Convection in Water over Ice," *Journal of Fluid Mechanics,* Vol. 69, part 4, 1975, pp. 753–781.

11 Yen, Yin-Chao, Tien, C., and Sander, G., "An Experimental Study of a Melting Problem with Natural Convection," *Proceedings of the 3rd International Heat Transfer Conference,* Vol. 4, 1966, pp. 159–166.

12 Yen, Yin-Chao, "Onset of Convection in a Layer of Water Formed by Melting Ice from Below," *The Physics of Fluids,* Vol. 11, No. 6, 1968, pp. 1263–1270.

13 Yen, Yin-Chao and Galea, F., "Onset of Convection in a Water Layer Formed Continuously by Melting Ice," *The Physics of Fluids,* Vol. 12, No. 3, 1969, pp. 509–516.

14 Legros, J. C., Longree, D., and Thomas, G., "Bernard Problem in Water Near 4°C," *Physics,* Vol. 72, 1974, pp. 410–414.

15 Merker, G. P., Wass, P., and Grigull, U., "Onset of Convection in a Horizontal Water Layer with Maximum Density Effects," *International Journal of Heat and Mass Transfer,* Vol. 22, 1979, pp. 505–515.

16 Carslaw, H. S., and Jaeger, J. C., *Conduction of Heat in Solids,* 2nd ed., Oxford Press, 1959, pp. 285–286.

17 Deardorff, J. W., "Convective Velocity and Temperature Scales for the Unstable Planetary Boundary Layer and for Rayleigh Convection," *Journal of Atmospheric Science,* Vol. 27, 1970, pp. 1211–1213.

Effects of Water Temperature and Salt Concentration on the Characteristics of Horizontal Buoyant Submerged Jets

J. B. Riester[1]
R. A. Bajura
S. H. Schwartz[2]

Department of Mechanical Engineering and Mechanics,
West Virginia University,
Morgantown, WV 26506

This paper summarizes the results of an analytical/experimental study of submerged buoyant fresh water and salt water jets injected horizontally into a quiescent, unstratified reservoir. Fresh water jets of a fixed exit Froude number penetrated to a greater horizontal distance before surfacing as the temperature of the reservoir was lowered. The overall flow characteristics were markedly affected by changes in the reservoir temperature, but were only slightly dependent upon the jet exit temperature for a given reservoir. Salt water jets of a fixed exit Froude number penetrated shorter horizontal distances into the reservoir as the salt concentration was increased. An analytical model was developed for fresh water jets which includes the effect of temperature on the thermal expansion coefficient and the effective buoyancy of the jet. The model successfully predicts the observed temperature dependence in the experiments and is applicable to salt water jets at low concentration levels. A correlation is proposed to minimize the effect of the reservoir temperature on the jet trajectory. The dependence of the flow characteristics on temperature and salt concentration is shown to be a significant factor contributing to the wide discrepancy in the data reported by previous investigators.

1 Introduction

Submerged buoyant jets occur in the discharge from thermal power plants and in the operation of pumped storage hydroelectric plants. Accurate predictions of the jet trajectory and temperature dilution are necessary if discharge structures are to be designed to meet federal and state standards for the effluent streams. A majority of the previously reported analytical models for horizontal buoyant submerged jets employ an integral-type analysis such as was first proposed by Morton, et al. [1]. In Morton's analysis, the profiles of velocity and density deficiency (buoyancy) were assumed to be similar at all elevations within the plume and gaussian in form. An entrainment coefficient was postulated to determine the change in volume flow rate along the trajectory. This technique has been used by several other researchers [2–7]. Abraham [6] determined the velocity and concentration profiles using experimentally obtained constants. Other methods which treat detailed turbulence modeling of the jet mixing characteristics were developed by Schatzmann [8] and Madni and Pletcher [9].

In view of the Reynolds number independence of the flow field in jets and plumes reported by Ungate, et al. [10], it is generally assumed that Froude number scaling is the only requirement to ensure similarity between velocity and temperature profiles along the trajectory for both model and prototype systems. Figure 1 illustrates the analytical predictions of references [2–6] for the trajectories of horizontal submerged buoyant jets having exit Froude numbers of 10 and 20, respectively. The theoretical predictions vary considerably for jets having the same Froude number. Even more perplexing is the fact that each prediction is in agreement with a set of experimental data obtained from tests conducted at the selected Froude number.

Figure 2 summarizes experimental data obtained by various researchers for the trajectories of both positively and negatively buoyant jets. Anwar [2] studied the flow of fresh water into salt water with a specific gravity of 1.028, which is representative of sea water. Fan [5] studied salt water jets with a specific gravity 1.12 injected into fresh

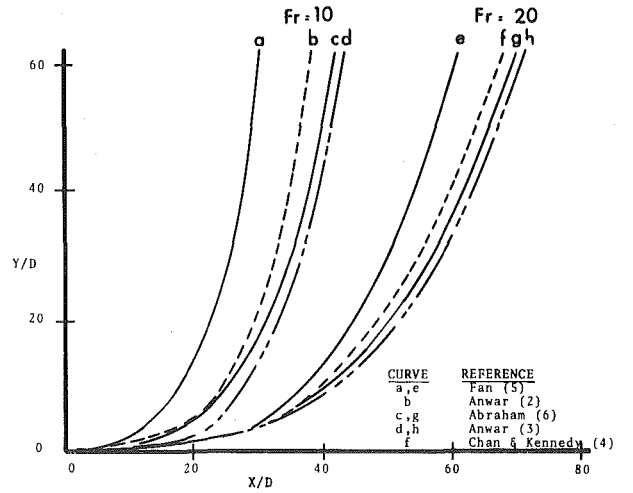

Fig. 1 Analytical predictions for the centerline trajectory of horizontal buoyant submerged jets for exit Froude numbers of 10 and 20

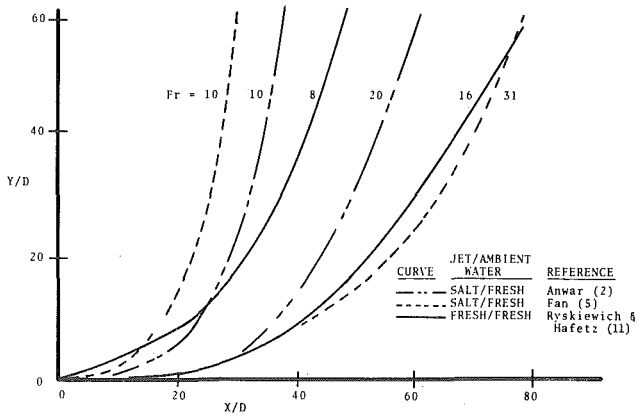

Fig. 2 Illustration of experimentally determined trajectories of horizontal buoyant submerged jets reported by Anwar [2], Fan [5], and Ryskiewich and Hafetz [11]

[1] Present Address: Conoco Research Center, Morgantown, WV 26505.

[2] Present Address: Department of Chemical and Mechanical Engineering, California State University, Northridge, CA 91330.

Contributed by the Heat Transfer Division for publication in the JOURNAL OF HEAT TRANSFER. Manuscript received by the Heat Transfer Division June 7, 1979.

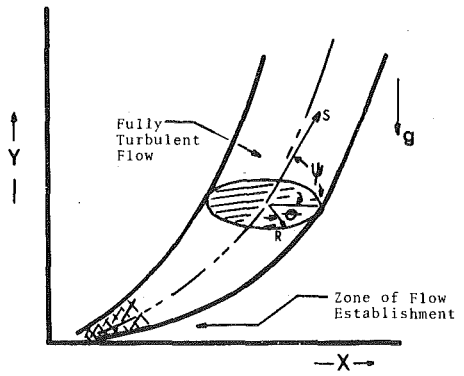

Fig. 3 Jet coordinate system

water. Ryskiewich and Hafetz [11] injected fresh water at 77°C into fresh water at 21°C. A wide variation in the experimental data is observed for tests which are identically scaled according to the Froude number criterion. In the following discussion, the authors will demonstrate that the observed variation in the experimental data is predominantly due to fluid property variations which are not accounted for by the usual Froude number parameter.

2 Analytical Model

Assumptions. The present analytical model for a buoyant submerged jet discharging horizontally into a reservoir is based upon an integral method utilized by Morton, et al. [1]. Figure 3 illustrates the coordinate system. Upon leaving the nozzle, the jet traverses a zone of flow establishment before attaining a fully developed turbulent state that persists until the plume reaches the surface. At the end of the zone of flow establishment, the velocity and temperature profiles are assumed to be gaussian with the following form:

$$U/U_s = \exp(-R^2/B^2) \tag{1}$$

$$(T - T_a)/(T_s - T_a) = \exp(-R^2/\lambda^2 B^2) \tag{2}$$

Anwar [3] and Cardel, et al. [12] have verified the gaussian assumption for jets following curved trajectories. Rouse, et al. [13] suggest the value of 1.16 for the parameter, λ, which is the spreading ratio between the velocity and temperature profiles. Density variations are neglected in the analysis except for the buoyancy term.

The rate of entrainment controls the spreading rate of the jet. Entrainment of the ambient fluid is assumed to be proportional to the centerline velocity and the jet width according to the relation

$$dQ/dS = 2\pi\alpha B U_s \tag{3}$$

Anwar [3] has shown that the rate of entrainment depends upon whether the flow field is characterized as a plume or a free jet. Therefore, the present analytical model utilizes a functional form for the entrainment coefficient, α, which varies with the angle of the trajectory from the horizontal, according to the relation

$$\alpha = [(0.057\cos\psi)^2 + (0.082\sin\psi)^2]^{1/2} \tag{4}$$

As the angle of inclination, ψ, approaches the extremes of zero and 90 deg, the entrainment coefficient assumes the values for the free jet and buoyant plume, respectively.

Governing Equations. The independent parameter for a steady flow analysis is the path length, S. The governing equations for the problem are the conservation of mass, horizontal and vertical momentum, energy, and the (X, Y) coordinates of points on the centerline of the jet trajectory. These equations are, respectively,

$$d/dS\left(\int_0^\infty \int_0^{2\pi} U R d\theta dR\right) = 2\pi\alpha B U_s \tag{5}$$

$$d/dS\left(\int_0^\infty \int_0^{2\pi} \rho U^2 \cos(\psi) R d\theta dR\right) = 0 \tag{6}$$

$$d/dS\left(\int_0^\infty \int_0^{2\pi} \rho U^2 \sin(\psi)\, R d\theta dR\right) = g\int_0^\infty \int_0^{2\pi} (\rho_a - \rho) R d\theta dR \tag{7}$$

$$d/dS\left(\int_0^\infty \int_0^{2\pi} \rho U c_p (T - T_a) R d\theta dR\right) = 0 \tag{8}$$

$$dX/dS = \cos\psi \qquad dY/dS = \sin\psi \tag{9}$$

Equation (8), the conservation of energy relation, is written as a density deficiency equation by some researchers [2–5] by substituting density for temperature according to the relation:

$$T = T_a - (\rho - \rho_a)/\beta\rho_a \tag{10}$$

This formulation assumes a linear relationship between temperature and density (i.e., a constant value of the thermal expansion coefficient, β). When the temperature difference between the jet and the ambient is large, a significant error is introduced in the energy conservation equation by assuming a linear relationship. In the present analysis, β is approximated as

$$\beta = A_1 + A_2 T + A_3 T^2 \tag{11}$$

The fitting coefficients A_1, A_2, and A_3 are evaluated for the range of temperatures pertinent to a given calculation.

Dimensionless Equations. Utilizing the exit velocity, U_e, the nozzle diameter, D, and the initial temperature difference $(T_e - T_a)$, as reference parameters, the governing equations are made nondimensional before further analysis. The dimensionless variables are

$$s = S/D \qquad x = X/D \qquad y = Y/D$$

$$u = U/U_e \qquad b = B/D \qquad \Delta t = (T - T_a)/(T_e - T_a)$$

The conservation equations are integrated over the jet cross section to obtain the following dimensionless equations applicable to the flow in the fully established zone.

$$u_s b^2 \Delta t_s = u_{s0} b_0^2 \Delta t_{s0} \tag{12}$$

$$du_s/ds = K_1 \sin(\psi)/b u_s - 2\alpha u_s/b \tag{13}$$

$$db/ds = 2\alpha - K_1 \sin(\psi)/2u_s^2 \tag{14}$$

Nomenclature

A = constants in equation (11)
B = jet width
b = dimensionless jet width, B/D
c_p = specific heat
D = nozzle exit diameter
Fr = Froude number $U_e/[gD(\rho_a - \rho_e)/\rho_a]^{1/2}$
Fr_a = effective Froude number
g = gravity
Q = volume flow rate in jet
R = radius
Re = Reynolds number $U_e D/\nu$
S = path distance
s = dimensionless path distance, S/D
T = temperature
Δt = dimensionless temperature $(T - T_a)/(T_e - T_a)$
U = velocity
u = dimensionless velocity, U/U_e
X = horizontal coordinate
x = dimensionless horizontal coordinate, X/D
Y = vertical coordinate
y = dimensionless vertical coordinate, Y/D
β = coefficient of expansion of water
Δ = difference between quantities
θ = circumferential coordinate
λ = spreading ratio of heat to momentum
ν = kinematic viscosity
π = 3.14
ψ = angle of inclination from horizontal
(a) = reference to ambient
(e) = reference to exit
(0) = reference to end of zone of flow establishment
(s) = reference to centerline

$$d\psi/ds = K_1 \cos(\psi)/bu_s^2 \tag{15}$$

$$\cos(\psi) = dx/ds \qquad \sin(\psi) = dy/ds, \tag{16}$$

The parameter, K_1, is defined as

$$K_1 = \frac{2A_1\Delta T_0 \lambda^2 b}{\mathrm{Fr}(\rho_a - \rho_e)/\rho_a}\left(\Delta t_s + \frac{A_2\Delta T_0}{4A_1}\Delta t_s^2 + \frac{A_3\Delta T_0^2}{9A_1}\Delta t_s^3\right) \tag{17}$$

In equation (13), the subscript (0) denotes the value of the dimensionless parameters at the end of the zone of flow establishment. The five first order differential equations (14–17) are solved simultaneously to determine the jet properties at any point along the trajectory.

Initial Conditions. The values of the jet centerline velocity, width, location, angle of inclination and the centerline temperature difference at the end of the zone of flow establishment are the initial conditions for the fully turbulent zone of flow. Riester [14] developed a method of determining these initial conditions using previously published data and the following analysis of the zone of flow establishment. Based upon the results of Abraham [6], the length of the zone of flow establishment is approximately 5.3 nozzle diameters (i.e., $s_0 = 5.3$) for all Froude numbers above 3.2. The angle of inclination and the width of the jet at the downstream end of this zone are given by

$$\tan(\psi_0) = 1.417\, s_0/\mathrm{Fr} \tag{18}$$

$$b_0 = s_0/[-304(\psi_0/\pi)^3 + 228(\psi_0/\pi)^2 + 77] \tag{19}$$

Riester approximated the coordinates of the end of the zone of flow establishment from Abraham's results as

$$x_0 = s_0 \cos(\psi_0)/2 \qquad y_0 = s_0 \sin(\psi_0)/2 \tag{20}$$

Mixing in the shear layer reduces the temperature difference between the outer edge of the jet and the ambient and erodes the potential core. The centerline velocity will increase due to the action of buoyancy forces over the vertical displacement, y_0. Riester assumed gaussian profiles for the temperature and velocity distribution in the shear layer and calculated the centerline velocity at the end of the zone of flow establishment as

$$u_{s0} = 1 + y_0\left(\frac{gD}{U_e^2}\right)\left[\frac{\rho_a - \rho_e}{\rho_a} + \beta_{av}(T_e - T_a)\right] \tag{21}$$

The thermal expansion coefficient, β_{av}, is determined at a zonal average temperature equal to $(2T_a + T_e)/3$. Since no mixing occurs on the centerline, the dimensionless temperature, Δt_{s0}, has the value of unity at the beginning of the fully turbulent zone. Additional discussion on the development of the analytical model is presented in reference [14].

3 Experimental Apparatus

All experiments were conducted in a tank 6.2 m long and 1.1 m wide which was filled with water to a depth of 0.8 m. The longer sides of the test facility were made from glass to permit flow visualization. A smoothly contoured nozzle 0.87 cm in diameter was centrally located on the 1.1 m side of the tank and projected approximately 35 cm into the reservoir. For positively buoyant jets, the nozzle was located 10 cm above the bottom; for negatively buoyant jets, the nozzle was located 10 cm from the surface. This arrangement permitted a vertical displacement of the jet trajectory of 75 exit diameters.

Photographs of the dye-colored jet were taken against an illuminated grid background at a distance of 7.6 m from the centerline with a 200 mm lens to reduce parallax errors. Temperature data were obtained from a rake of 21 thermocouples fabricated from 30 gauge copper-constantan wire. Each thermocouple was coated with an epoxy resin to a diameter of approximately 3 mm to increase the response time. The temperature data were reduced by a computer program designed to provide a statistical curve fit for the temperature profile at five different spatial locations along the trajectory. The trajectories were measured photographically and also from the location of the jet centerline as determined from the temperature data. An accuracy of ±0.06°C is estimated for the temperature measurements.

Several test programs were carried out in which the Reynolds number of the jet, $\mathrm{Re} = U_e D/\nu$, was varied from a minimum of 900 to values exceeding 20,000. No Reynolds number effects could be determined for jets which had exit Reynolds numbers greater than 1500. Most tests were conducted at Reynolds numbers of 2000 or higher. Exit velocities were determined with rotameters calibrated over the temperature range of the experiments to an accuracy of less than 2 percent error. Test conditions for a given Froude number grouping vary (typically) over a range of (±) 10 percent; e.g., Fr = 10 ± 1. Based upon an analysis of the photographic data, the uncertainty estimate for the dimensionless distances x, y, and s is (±1.5), and (±0.2) for the dimensionless jet width, b. The uncertainty estimate for the dimensionless temperature, Δt, is (±0.03).

4 Results for Fresh Water Jets

A. Positively Buoyant Jets. A series of 92 tests was conducted with fresh water jets for which the ambient temperature was varied between the limits of 4.5 and 43°C. Only a representative sample of these experiments will be discussed here.

Jet Trajectories. Experimental data and analytical predictions of the trajectory of jets having initial Froude numbers of 8 and 15 are shown in Fig. 4. The analytical solutions are in good agreement with the corresponding set of experimental data. In all tests conducted, the positively buoyant jets penetrated further into the reservoir before surfacing as the ambient temperature was reduced under otherwise similar Froude number test conditions.

Jet Centerline Temperatures. The variation of the dimensionless jet centerline temperature along the trajectory is shown in Fig. 5 for tests at a Froude number of 10. The analytical model predicts that the difference between the jet centerline and the reservoir temperature will be decreased slightly as the temperature of the ambient is decreased. The experimental data for the dimensionless temperature

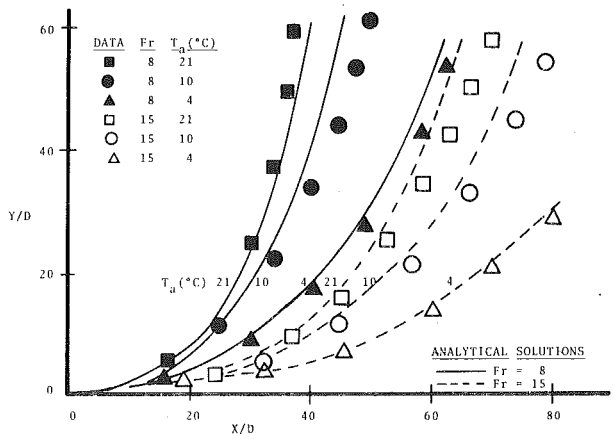

Fig. 4 Variation of the jet centerline trajectory with ambient temperature for jets with positive buoyancy

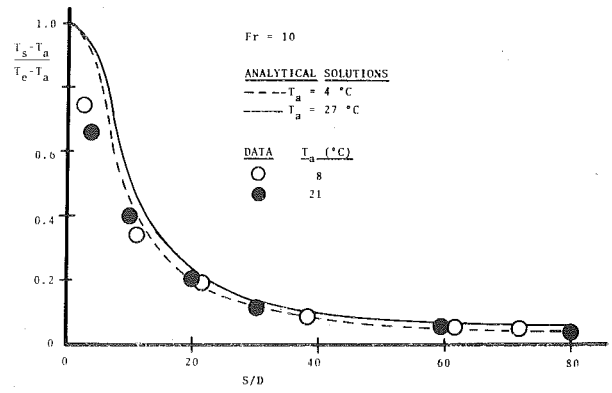

Fig. 5 Variation of temperature dilution with path length for positively buoyant fresh water jets as a function of ambient temperature

difference are fairly insensitive to changes in ambient temperature, however, but are in good agreement with the analytical predictions. Temperature data close to the nozzle are significantly below the predicted curves. At this location, the ratio of the thermocouple bead diameter to the plume diameter is relatively large. Therefore, the thermocouples sense a spatially-averaged temperature rather than a local temperature. Some blockage of the flow also occurs. These conditions contribute to a lower temperature reading on the centerline.

Plume Width and Centerline Velocity. The variation of the jet width as a function of the ambient temperature is illustrated by Fig. 6 for a jet with an initial Froude number of 10. The analytical model predicts that the jet diameter will be greater when the temperature of the reservoir is lowered. A unit temperature change in the reservoir brings about a larger change in the jet width at lower temperatures due to the rapid variation in the value of the thermal expansion coefficient near the critical temperature of 4°C. The trend established by the experimental data is in good agreement with the analytical predictions. Figure 7 illustrates the dependence of the calculated centerline velocity upon the temperature of the reservoir for a case where the Froude number is 10. The centerline velocity decreases as the reservoir temperature is lowered. This effect is consistent with the data in Fig. 6 showing an increased width of the jet to satisfy continuity requirements. Data for the velocity were not obtained in the present study.

Effect of Temperature—Density Relationship on Trajectory. The influence of the ambient temperature and the thermal expansion coefficient upon the trajectory can be explained physically as follows. Figure 5 shows that the jet temperature drops rapidly due to entrainment and approaches the temperature of the ambient close to the nozzle exit. Figure 4 shows that the angle of inclination is relatively shallow in this region such that all jets have a substantial horizontal velocity component. Consider the local environment of the jet at a location, say, 10 diameters from the exit. The temperature difference between the jet and the ambient is now sufficiently small that the thermal expansion coefficient can be considered constant for the remainder of the trajectory. Figure 7 shows that all jets will have essentially the same velocity at this location. For jets injected into a lower temperature reservoir at a given Froude number, the value of the thermal expansion coefficient 10 diameters along the trajectory is much lower than its initial value. Therefore, the jet experiences a lower buoyancy force (higher effective Froude number), which causes it to penetrate further into the reservoir before surfacing than an otherwise equivalent jet injected into a reservoir at a higher temperature.

B Negatively Buoyant Jets. Studies were conducted with fresh water jets having negative buoyancy as an extension of the analytical model and to determine if the direction of the buoyancy force affected the path of the jet. Figure 8 illustrates the results of a comparative study at a fixed ambient temperature of 43° C for jets with Froude numbers of 10 and 15. Both the analytical model and the experimental results demonstrate that the negatively buoyant jets do not penetrate as far into the reservoir as the corresponding positively buoyant jet. Based upon the discussion presented above, it is seen that the negatively buoyant jet, which is initially cooler than the ambient, soon entrains enough fluid to approach the temperature of the environment. The effective value of the thermal expansion coefficient is increasing along the trajectory since the plume is becoming warmer. The apparent buoyancy force is therefore increased, the local Froude number decreases, and the jet descends to the bottom sooner than the corresponding positively buoyant jet reaches the surface.

C Effective Froude Number Correlation. The previous results demonstrate that a temperature parameter is required in addition to the Froude number in order to obtain a satisfactory prediction of the jet characteristics. Correlation studies with our experimental data and analytical model indicate that the effect of the jet and ambient temperatures on the trajectory can be minimized if the buoyancy term is calculated using the actual temperature difference and the value of β at the ambient temperature. This procedure results in a different Froude number for the jet,

$$\mathrm{Fr}_a = U_e/[gD\beta_a(T_e - T_a)]^{1/2}, \tag{22}$$

than if the actual density difference $(\rho_a - \rho_e)/\rho_a$ is used. Figure 9 illustrates two sets of data for which almost identical trajectories were obtained for widely different reservoir conditions and exit Froude numbers. However, the effective Froude number, Fr_a, is essentially the same. It is therefore recommended that the effective Froude number, Fr_a, be used in cases where the temperature difference between the jet and the ambient is large.

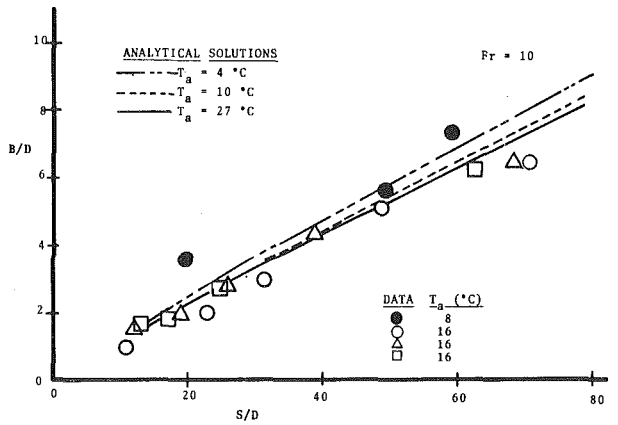

Fig. 6 Variation of jet width with path length as a function of ambient temperature for positively buoyant fresh water jets

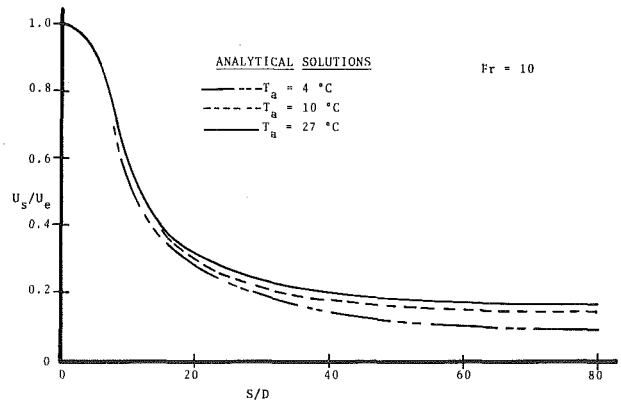

Fig. 7 Analytical predictions for the variation of centerline velocity along the path as a function of the ambient temperature

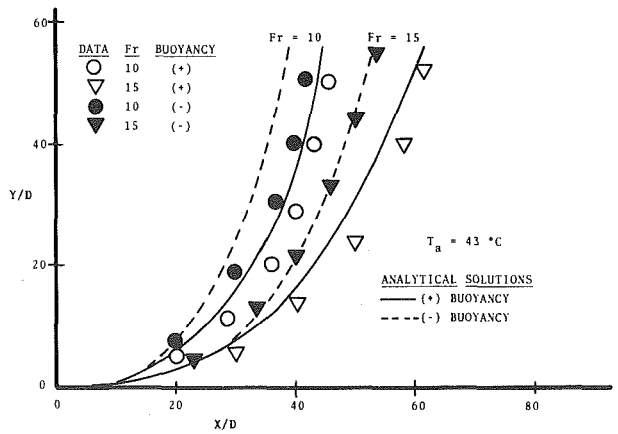

Fig. 8 Comparison of the trajectories of positively and negatively buoyant fresh water jets

5 Salt Water Jets

Buoyant thermal plumes and jets are often simulated using mixtures of salt water and fresh water at room temperature to avoid spurious surface heat transfer effects which may occur in a laboratory model. If the turbulent Prandtl and Schmidt numbers are assumed to be identical, the diffusion of salt in the model should simulate the diffusion of heat in the prototype. This assumption neglects any possible effect of the variation in β upon the thermal plume.

In modeling estuarian flows, the salt solution is usually formulated to have the same density as sea water in an exact simulation of the prototype. However, the density of the salt solution is often determined by other criteria such as maintaining a sufficiently high Reynolds number in the model to ensure turbulent flow. Therefore, the salt solution may vary from test to test in a set of experiments, with relatively dense solutions used for low Froude number cases. Negatively buoyant salt water jets are often used to simulate positively buoyant prototype situations under the assumption that the direction of the buoyancy force and the bottom boundary will not affect the flow characteristics along the trajectory. In view of the different experimental results obtained by Anwar and Fan (Fig. 2), the present experiments with salt (28 cases) were undertaken to determine the effect of concentration and direction of the buoyancy force on the jet trajectories.

Effect of Concentration on Trajectory. A series of experiments was conducted using negatively buoyant salt jets injected into fresh water at the same temperature. The salt concentration was determined by gravimetric analysis. Figure 10 illustrates a set of curves obtained from experiments conducted at a Froude number of 10 using salt solutions of different densities. Actual data points are adjusted for clarity. As the density of the salt solution is increased, the horizontal penetration of the jet is reduced. The data shown by the solid circles is taken from Fan [5] for tests with an initial density difference of 11.8 percent. Each curve in Fig. 10 represents the average result of a series of tests over a range of Reynolds from 2000 to 9000 which showed the trajectories to be Reynolds number independent. It is seen that the concentration significantly affects the mixing and therefore the effective buoyancy of the jet. This observation can be used to explain the different results of Fan and Anwar in view of the different concentrations used in their tests.

Positively and Negatively Buoyant Salt Water Jets. Figure 11 illustrates the results of tests with positively and negatively buoyant jets of the same Froude number with initial density differences ($\Delta\rho/\rho$) ranging from 0.003 to 0.014. Both jets follow the same trajectory in contrast to the results for fresh water. Analytical solutions were obtained from the fresh water model under the assumption that the temperature difference was negligibly small such that the coefficient of expansion was constant. The similarity between the data in Fig. 11 suggest that the nozzle was located far enough away from the walls of the test facility to preclude any boundary effects on the jet trajectory for both the salt and fresh water test programs.

6 Discussion and Concluding Remarks

Effect of Jet Temperature on Trajectory. Figure 12 illustrates the results of a series of computer experiments for a jet with a Froude number of 10 injected into an environment held at a fixed temperature of 16°C. When the initial temperature difference is small, both positively and negatively buoyant jets have essentially the same trajectory as shown by curves (b) and (c). The difference between the trajectories increases as the magnitude of the temperature difference is increased. Experimental data are shown for a test at a jet temperature of 51°C

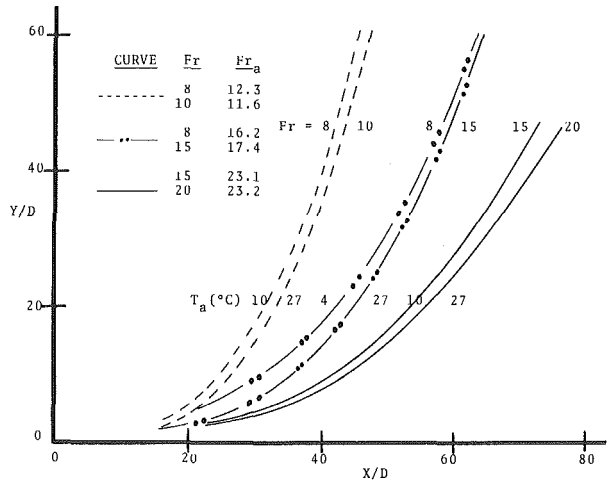

Fig. 9 Correlation of jet trajectories with the effective Froude number Fr_a

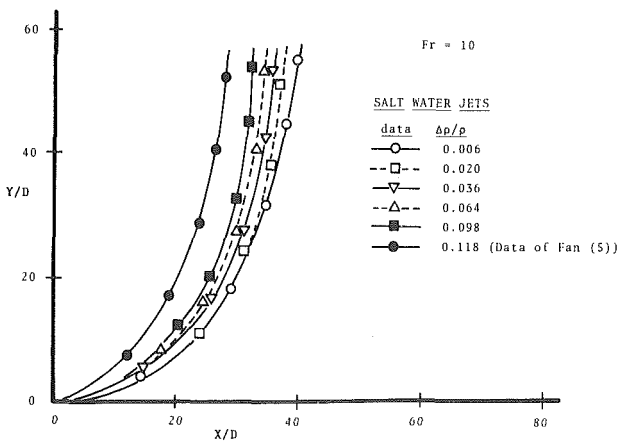

Fig. 10 Variation of trajectory with salt concentration for a negatively buoyant jet

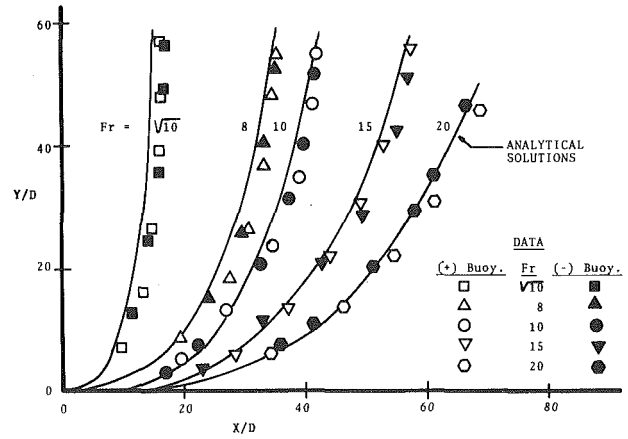

Fig. 11 Comparison of the trajectories of positively and negatively buoyant salt water jets of the same concentration

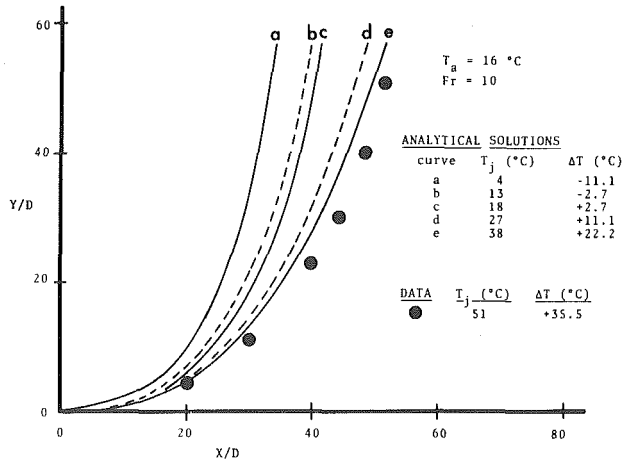

Fig. 12 Illustration of the effect of the jet exit temperature on the trajectory

which are consistent with the trends shown by the analytical solutions.

In view of the flow field characteristics illustrated by Figs. 4 and 12, the following conclusions are formulated concerning the effect of temperature on the jet trajectory. First, if the initial temperature difference between the jet and the ambient is greater than 3°C, the effect of the temperature-density relationship of water on the trajectory must be considered. This result is of particular significance when laboratory models are operated at high temperature differences to simulate a prototype flow characterized by low temperature differences. Second, the practice of using positively buoyant fresh water jets to simulate negatively buoyant fresh water jets (or vice-versa) will yield misleading data due to the divergent paths followed by each type of jet. Third, the effects of temperature on the trajectory can be minimized by using the effective Froude number, Fr_a, instead of the densimetric Froude number, Fr, to define the flow conditions. Otherwise, both the Froude number and a temperature parameter will be required to predict the jet trajectory. Additional work is required to determine the correlation applicable to jet flows which experience reversing buoyancy for cases near 4°C.

Salt Solutions. Salt water jets cannot simulate the characteristics of fresh water jets operating over large temperature differences since the salt models do not duplicate the temperature-density characteristics of the fresh water system. Further, the results obtained with salt solutions are strongly dependent upon the level of concentration. In examining the data of Fig. 10, it is noted that the trajectory obtained experimentally for the lightest salt concentration is in excellent agreement with the curves of Fig. 12 for the case where the temperature difference is small (curves b and c). Therefore, if the concentration of the salt solution is maintained to less than 1 percent, salt models will be useful in simulating fresh water flows with small temperature differences.

Analytical Model. The contributions of the present work to the analysis of horizontal, submerged buoyant fresh water jets are the development of a method for specifying the flow characteristics in the zone of flow establishment, the development of an appropriate functional form for the entrainment coefficient along the trajectory, and the use of a variable temperature-density relationship. The model successfully correlates data for both fresh and salt water jet flows, including data from other investigators, and is expected to be applicable to a wider range of conditions than previous methods which were formulated without incorporating the effects of temperature or concentration in the determination of coefficients for the governing equations.

If it is assumed that the jet issues from a point source and that the velocity, width and density difference vary with (S) raised to a power, then the jet coordinates can be correlated by a relationship of the form

$$(Y/D) = K(X/D)^p/\mathrm{Fr}^2 \tag{23}$$

The exponent (p) is expected to have a value near 3. The data of Figs. 9 and 11 for negligible density differences are adequately correlated using the value of 0.29 for K and 2.6 for p. A more accurate correlation for the trajectory must include a treatment of the zone of flow establishment and a consideration of the virtual origin of the jet.

Acknowledgments

The authors wish to acknowledge the support of the Office of Water Research and Technology under Grant 14-34-0001-6214.

References

1 Morton, B. R., Taylor, G. I., and Turner, J. S., "Turbulent Gravitational Convection from Maintained and Instantaneous Sources," *Proceedings Royal Society London*, A234, 1956, pp. 1–23.

2 Anwar, H. O., "Behavior of Buoyant Jet in Calm Fluid," *Proceedings ASCE, Journal Hydraulics Division*, 95, HY4, July, 1969, pp. 1289–1303.

3 Anwar, H. O., "Measurements on Horizontal Buoyant Jet in Calm Ambient Fluid, with Theory Based on Variable Coefficient of Entrainment Determined Experimentally," *La Houille Blanche*, No. 4, 1972, pp. 311–319.

4 Chan, D. T. L., and Kennedy, J. P., "Submerged Buoyant Jets in Quiescent Fluids," *Proceedings ASCE, Journal Hydraulics Division*, 101, HY6, June, 1975, pp. 733–47.

5 Fan, L. N., "Turbulent Buoyant Jets into Stratified or Flowing Ambient Fluids," Report No. KH-R-15, W. M. Keck Lab of Hydrodyamic and Water Resources, California Institute of Technology, 1967.

6 Abraham, G., "Horizontal Jets in Stagnant Fluid of Other Density," *Proceedings ASCE, Journal Hydraulics Division*, 91, HY4, July, 1965, pp. 138–54.

7 Wright, S. J., "An Entrainment Model for Buoyant Jet Discharges," *Proceedings of the 1978 Heat Transfer and Fluid Mechanics Institute*, C. T. Crowe and W. L. Grosshandler, Editors, Stanford University Press, 1978.

8 Schatzmann, M., "A Methematical Model for the Prediction of Plume Rise in Stratified Flows," Symposium on Turbulent Shear Flows, Pennsylvania State University, 1977, pp. 6.39–6.49.

9 Madni, I. K., and Pletcher, R. H., "Buoyant Jets Discharging Nonvertically into a Uniform, Quiescent Ambient—A Finite-Difference Analysis and Turbulence Modeling," ASME JOURNAL OF HEAT TRANSFER, Vol. 99, 1977, pp. 641–647.

10 Ungate, C. D., Harleman, D. R. F., and Jirka, G. H., "Stability and Mixing of Submerged Turbulent Jets at Low Reynolds Numbers," Energy Lab Report No. MIT-EL 75-014, Massachusetts Institute of Technology, Feb. 1975.

11 Ryskiewich, B. S. and Hafetz, L., "An Experimental Study of the Free Surface Effect on a Buoyant Jet," Report No. 4440-74-103, General Dynamics, 1975.

12 Cardel, G. P., Fletcher, L. S. and Chen, D. F., "Temperature Profiles of Smokestack Plumes Augmented by Aerodynamic Means," Report RU-TR 149-MIAE-F, Department of Mechanical, Industrial and Aerospace Engineering, Rutgers University, Aug. 1976.

13 Rouse, H., Yih, C. S. and Humphreys, H. W., "Gravitational Convection from a Boundary Source," *Tellus*, 4, 1952, pp. 201–210.

14 Riester, J. B., Bajura, R. A. and Schwartz, S. H., "Water Temperature Effects on Horizontal Buoyant Submerged Jets," OWRT Report No. 4, Department of Mechanical Engineering and Mechanics, West Virginia University, (NTIS Publication No. PB 297293/AS) Sept. 1977.

Directional Control of Radiation Heat Transfer by V-Groove Cavities—Collimation of Energy in Direction Normal to Cavity Opening

H. Masuda

Assistant Professor,
Institute of High Speed Mechanics,
Tohoku University, Sendai, Japan

To improve the V-groove cavity devised for directional control of radiation heat transfer, a new model with a black fin provided on the cavity base is proposed. The radiative characteristics of the new model are theoretically offered comparing two typical constitutional forms—symmetrical and asymmetrical. It is evident that the fin helps accelerate radiation heat transfer from the V-groove and promote its collimation. The effects can be further enhanced by carefully choosing the various geometrical parameters. The new V-groove cavity proposed would probably be evaluated as a favorable directional surface. The direction of energy collimation can be altered by using the asymmetrical groove cavity.

1 Introduction

Among the various modes of heat transfer, radiation is known to have several unique characteristics of its own. For instance, the propagation of radiative energy turns its course through a specularly reflecting surface. This characteristic has been used to produce specific distributions of radiation intensity with a directional control of energy transmission. Typical examples are seen in the various devices used to concentrate radiative energy: e.g., concentrating type solar collectors [1–3], thermal control of space vehicles [4], specific radiative heating of an object surface to provide it with a prescribed distribution of radiative heat flux [5, 6], and directional control of radiative heat transfer with the use of cavities varying in shape [7–9]. This paper, which concerns the last of the aforementioned topics, introduces a new type of V-groove, a modification of the simple model studied by Black and Schoenhals [7, 8], with theoretical consideration of its radiative transfer characteristics. Our new V-groove cavities would be appreciated as favorable not only for directional control of emission from surfaces, but for radiative heating of objects in a desired direction, well applicable, for instance, in room heating and the like.

Perlmutter and Howell [10] first pointed out that use of a V-groove with specularly reflecting side surfaces can lead the energy emitted from its base to converge in a specific direction. Based on this principle, Black and Schoenhals [7–9] scrutinized V-groove and rectangular groove cavities in pursuit of their characteristic directionality and strength of emission. Clausen and Neu [4], using many surfaces varying in configuration, conducted studies to identify their directional absorptances. The purpose of the present study is to establish directional surfaces favorable for control of radiation heat transfer.

The V-groove dealt with by Black [9] represents the simplest groove shape able to collimate the emitted energy in the direction normal to the cavity opening area. In an attempt to expand it into a more effective directional surface, we have developed a new model V-groove that has a normal black fin on the base surface of the groove cavity, as shown in Fig. 1. Adjustment of the height of fin may be able to change both the heat-transfer rate of the groove cavity and the degree of energy collimation in a desired direction. To examine their effects and how the direction of energy collimation can be changed by using groove cavities different in shape, calculations have been made on a symmetrical and an asymmetrical V-groove cavity.

Use of curved specular surfaces in a groove cavity as employed in Winston's solar collector [11] is supposedly likely to raise the degree of collimation of emitted energy; but in this study, attaching importance to simple shapes of groove and availability of comparison between our results and Black's, we take up the V-groove as the object.

2 V-Groove Model and Analysis

Radiative energy emitted from a V-groove cavity has been known to collimate ahead of the cavity opening [7–10]. Further investigations are made on a new model (Fig. 1); these differentiate between the effects of the following two cavity shapes. (1) symmetrical V-groove leading to collimation of emitted energy in the direction normal to the cavity opening. (2) asymmetrical V-groove leading to collimation of emitted energy in the direction slanting from normal to the cavity opening.

In the analysis, the following assumptions are provided: The base of the groove and the fin are both blackbody, while the side surfaces are specular reflectors as well as diffuse emittors with emissivity ϵ_s. All surfaces, including the fin, are maintained at a constant temperature. The V-groove cavity is infinite in length, as it represents a two-dimensional radiation transfer system. The incident radiation from the outside is disregarded.

Various dimensionless quantities are defined mainly following those used by Black and Schoenhals [7, 9] for the convenience of available comparison.

2.1 Symmetrical V-Groove. A symmetrical V-groove cavity with a normal black fin in the center of the base is taken up (Fig. 2); this seems to make energy collimation more favorable. The opening half angle is denoted by θ, the height from the apex to the cavity opening by L, the distance between the apex and the cavity base by B, and the height of the fin is shown by T. Coordinates of x and y and angles of η and β are taken as shown in Fig. 2. The term x_0 is the width of the cavity opening (dotted line in the figure); and y_0 is the length

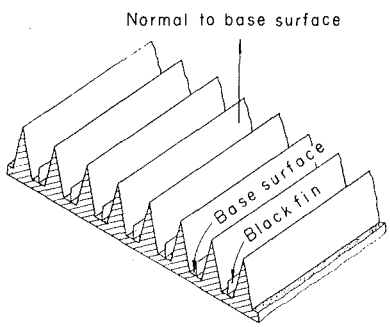

Fig. 1 Configuration of V-groove-arranged surface

Contributed by the Heat Transfer Division for publication in The JOURNAL OF HEAT TRANSFER. Manuscript received by the Heat Division September 24, 1979.

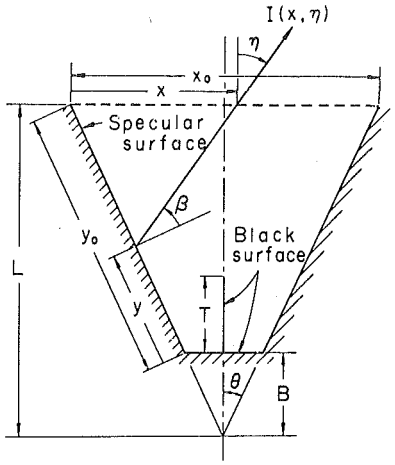

Fig. 2 Coordinate system and symbols for symmetrical V-groove

of the side surface measured along the y-axis. By using the dimensionless expressions

$$b = \frac{B}{L}, t = \frac{T}{L}, \zeta = \frac{x}{L}, \zeta_0 = \frac{x_0}{L},$$

$$\xi = \frac{y}{L}, \xi_0 = \frac{y_0}{L}, \tag{1}$$

the intensity of radiation across the position ζ on the cavity opening area can generally be expressed as a function of ζ and η [12], $I(\zeta, \eta)$, because the system of radiation transfer is two-dimensional with a groove infinite in length. If the radiation ray is from the side surface as shown in Fig. 2, the intensity $I(\zeta, \eta)$ can be replaced by $I(\xi, \beta)$ on the side surface, while if it is not from the side surface but from the base surface or the fin, the intensity can be replaced by I_b as the black intensity at the wall temperature. Local directional emissivity is defined as

$$\epsilon(\zeta, \eta) = \frac{I(\zeta, \eta)}{I_b} \tag{2}$$

The apparent directional emissivity on the cavity opening area, $\epsilon_a(\eta)$, is defined, similar to Black's, as

$$\epsilon_a(\eta) = \frac{1}{\zeta_0} \int_0^{\zeta_0} \epsilon(\zeta, \eta) d\zeta \tag{3}$$

From equation (3), the hemispherical emissivity, $\epsilon_{a,h}$, can be expressed as

$$\epsilon_{a,h} = \frac{1}{2} \int_{-\pi/2}^{\pi/2} \epsilon_a(\eta) \cos \eta \, d\eta \tag{4}$$

The limiting angle, η_L, indicative of the degree of energy collimation, is defined following Black [9] as

$$0.9\epsilon_{a,h} = \int_0^{\eta_L} \epsilon_a(\eta) \cos \eta \, d\eta \tag{5}$$

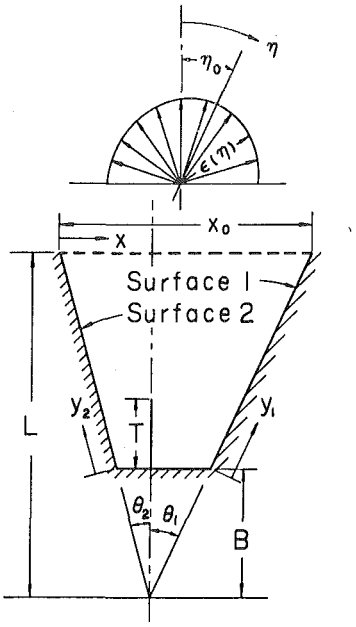

Fig. 3 Coordinate system and symbols for asymmetrical V-groove

If $\epsilon_a(\eta)$ is not directional at all, as in the case of black side surfaces, $\epsilon_a(\eta)$ being unity, η_L will take the following value.

$$\eta_L = \sin^{-1} 0.9 = 64.2 \text{ deg} \tag{6}$$

The value 64.2 deg serves as a standard showing that values less than that indicate higher degrees of energy collimation.

2.2 Asymmetrical V-Groove. For a model capable of turning the direction of energy collimation from normal toward the cavity opening area, we adopt an asymmetrical V-groove cavity. As shown in Fig. 3, the side surfaces are denoted by surface 1 and 2, and the opening angles of right and left sides by θ_1 and θ_2, respectively. The opening area is parallel to the base, and a fin on the base is set along the normal to the base from the apex. The definitions expressed in equations (2–4) are also used in this model, while the two limiting angles are redefined with the aid of angle η_0 (Fig. 3) which is expressive of the direction of energy collimation as given by

$$\epsilon_{a,h} = \int_{-\pi/2}^{\eta_0} \epsilon_a(\eta) \cos\eta \, d\eta = \int_{\eta_0}^{\pi/2} \epsilon_a(\eta) \cos\eta \, d\eta \tag{7}$$

The angle η_0, as it will be described later, becomes positive for $\theta_1 > \theta_2$. The limiting angles are then defined for two ranges—$\eta_0 < \eta < \pi/2$ and $-\pi/2 < \eta < \eta_0$—with respective symbols of $\eta_L +$ and $\eta_L -$.

$$0.9\epsilon_{a,h} = \int_{\eta_0}^{\eta_L^+} \epsilon_a(\eta) \cos\eta \, d\eta \tag{8a}$$

$$0.9\epsilon_{a,h} = \int_{\eta_L^-}^{\eta_0} \epsilon_a(\eta) \cos\eta \, d\eta \tag{8b}$$

Nomenclature

B = distance from apex to base of cavity
b = dimensionless base level, equation (1)
I = radiation intensity
I_b = radiation intensity of blackbody
L = height from apex to cavity opening
T = height of normal black fin
t = dimensionless height of fin, equation (1)
x = position coordinate across cavity opening (Fig. 2)
x_0 = width of the cavity opening
y = position coordinate across side surface of cavity (Fig. 2)
y_0 = width of the side surface of cavity
β = angle between the projection of a ray leaving the side surface on the plane of Fig. 2 and the normal to the side surface
ϵ = emissivity
$\epsilon(\zeta,\eta)$ = local directional emissivity
$\epsilon_a(\eta)$ = apparent directional emissivity
$\epsilon_{a,h}$ = apparent hemispherical emissivity
ϵ_s = side surface emissivity of cavity
ζ = dimensionless coordinate, equation (1)
ζ_0 = dimensionless width, equation (1)
η = angle between the projection of a ray leaving the cavity opening on the plane of Fig. 2 and the normal to the cavity opening
η_L = limiting angle expressing the degree of energy collimation, equation (5)
η_L^+, η_L^- = limiting angles expressing the degree of energy collimation, equation (8)
η_0 = angle expressing the center of the propagation direction of energy emitted from cavity, equation (7)
θ = opening half angle of symmetrical groove (Fig. 2)
θ_1, θ_2 = opening angles of asymmetrical groove (Fig. 3)
ξ = dimensionless coordinate, equation (1)
ξ_0 = dimensionless width, equation (1)

2.3 Solution Procedure. To obtain the aforementioned quantities, the unknown function, $I(\zeta, \eta)$, that is, the intensity of radiation $I(\xi, \beta)$, must be solved. Although the usual image method [7, 10, 13] can be applied to solve $I(\xi, \beta)$, use of the method analyzed in [12] would prove more convenient as it can obtain the solutions independent of the reflection times of radiation rays varying with groove shape, the position ξ, or the direction β. In the present study, the numerical solutions of $I(\xi, \beta)$ were obtained by applying the equations for the two-dimensional radiation transfer system [12] (equations (7) and (8) in [12]). In fact, the calculations were performed with step sizes of $\Delta\xi = \xi_0/100$ and $\Delta\beta = \pi/200$. Once the values of $I(\zeta, \eta)$ have been determined from the solutions of $I(\xi, \beta)$, the values of $\epsilon(\zeta, \eta)$, $\epsilon_a(\eta)$, $\epsilon_{a,h}$, η_0 and η_L ($\eta_L{}^+$ and $\eta_L{}^-$ for an asymmetrical V-groove) can in turn be obtained from their respective expressions.

3 Results and Discussions

3.1 Symmetrical V-Groove. The results obtained by Black and Schoenhals [7–9] for the V-groove with no fin (henceforth referred to as the simple V-groove) are reviewed to feature the radiative characteristics of the present V-groove.

Figure 4(a) shows an example of the values of $\epsilon_a(\eta)$ obtained with the black fin different in height for $\theta = 30$ deg, $\epsilon_s = 0.1$, and $b = 0.2$. These values of θ and ϵ_2, which will be detailed later, are a set of the values favorable for energy collimation. As can be seen in the figure, with an increase in t, the value of $\epsilon_a(\eta)$ becomes greater in a certain range of η around $\eta = 0$. The change in angular distribution of $\epsilon_a(\eta)$ with the height of fin means a change in the heat-transfer rate from the groove and in the degree of energy collimation (Fig. 5(a,b)). Figure 4(b) shows the values of $\epsilon_a(\eta)$ varying with the difference in base level b in the simple V-groove. Comparison of Fig. 4(a) with Fig. 4(b) shows that the effect of the change in height of the black fin is nearly equivalent to that of the change in level of the cavity base in the simple V-groove.

Figure 5(a) shows, in relation to b, how the height of fin affects the apparent hemispherical emissivity, $\epsilon_{a,h}$, which also represents the heat-transfer rate from the groove to the surroundings. The dotted line in the figure indicates the case with the simple V-groove ($t = 0$). The value of $\epsilon_{a,h}$ increases with b in the simple V-groove, while in the V-groove with a black fin it increases with t when b is constant. Each curve with b as a parameter tends to asymptotically approach the limiting curve for $b = 0$. Figure 5(b) shows the changes with t in the limiting angle η_L. In the simple V-groove, according to Black [9], an optimum value of b exists which produces the strongest energy collimation for given values of θ and ϵ_s; while in the V-groove with a fin an optimum height $(b + t)_{opt}$ exists when b is small as seen in the curves for $b = 0$ and 0.2, underscoring a significant influence of t on η_L. The minimum value of η_L for the optimum height, $\eta_{L,min}$, is almost equivalent to that of the simple V-groove under the same conditions for θ and ϵ_s. This substantiates the influence of black fin in promoting energy collimation or altering its degree. For larger b, the values of η_L increase monotonously with t as seen in the curves for $b \geq 0.4$. In Fig. 5(b), by comparing the values of η_L at an arbitrary $b + t$ between the present and the simple V-groove, we can see the values of η_L considerably lower in the former in the range where $b + t$ is comparatively larger. This means that the effect of energy collimation is better with the present groove in the range where $b + t$ is relatively large but b is small. The reason for the excellent effect in the present model can be partially explained as follows.

As Fig. 6 shows, the radiation rays in a specific direction can be compared for the V-groove with a black fin and the simple V-groove in which the base (dotted line) is placed at the position of the black fin tip. On the plane of the figure, take a point P on one side surface a little below the dotted line, and draw a line PN normal to the side surface. Let Q be the intersection of the extension of the line connecting P with the fin tip and the opposite surface, and β_p be the angle QPN. Draw a line PR symmetrical to PQ with respect to the axis PN. Let I_p be the intensities of radiation within the angle NPR originating from P. For the V-groove with a fin, under the situation shown in the figure, we find that i_p ($= I_p/I_b$) $\ll 1$ for $\epsilon_S \ll 1$, because they include no reflection component of emission from black surfaces. By contrast,

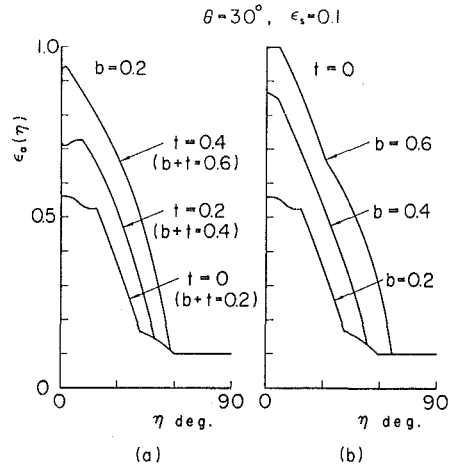

Fig. 4 Apparent directional emissivity for symmetrical V-groove, (a) V-groove with a black fin, (b) simple V-groove

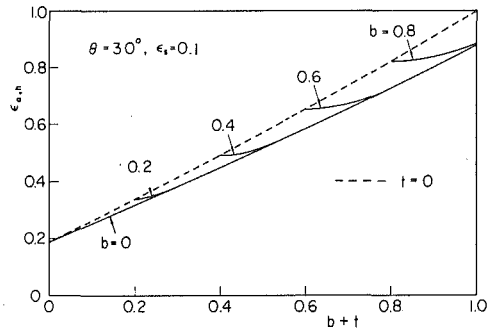

Fig. 5(a) Variation of $\epsilon_{a,h}$ with fin height (symmetrical V-groove)

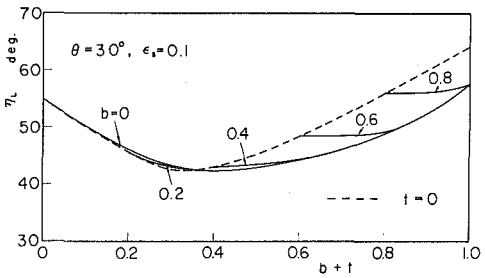

Fig. 5(b) Directionality varying with fin height (symmetrical V-groove)

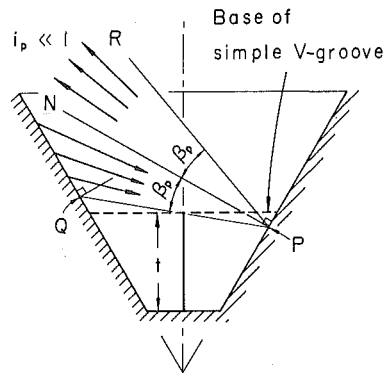

Fig. 6 Weak intensities of radiation in slanting direction

for the simple V-groove, the intensities within the same angle are $i_p = 1$, as they are black ones from the base and much larger than those of the V-groove with a fin. Such large differences in the intensities of radiation rays between the two types of V-groove are made predominantly when they cross the opening area slantwise. After all, the V-groove with a fin enhances the degree of energy collimation in the normal direction by reducing radiative energy leaving slantwise. This fact may also be understood by inspecting Fig. 4(a) and (b).

The radiative characteristics of a V-groove can also be considerably influenced by the side surface emissivity ϵ_s [9]. Figure 7 shows the effect of ϵ_s on η_L for the limit of $b = 0$. Similar to the case of the simple V-groove, the minimum value of η_L becomes smaller with lower ϵ_s, and the value of $(b + t)_{\text{opt}}$ in each curve becomes smaller with lower ϵ_s, approaching zero for $\epsilon_s = 0$.

These results have all been obtained for $\theta = 30$ deg. It is also important to discuss the radiative characteristics in relation to the remaining parameter—the angle θ. The variation of η_L with θ are compared in Fig. 8(a) for the V-groove with a fin ($b = 0, t = 0.4$) and Fig. 8(b) for the simple V-groove ($b = 0.4$). In the present model (Fig. 8(a)), an optimum θ to produce the strongest collimation exists in each curve with ϵ_s as a parameter, similar to the case with the simple V-groove in Fig. 8(b). The minimum values of η_L for the optimum opening angle are smaller with lower ϵ_s. Under the condition of this figure, the value of η_L in each curve is 64.2 deg at $\theta = 70$ deg regardless of the value of ϵ_s, and in the range of θ between 70 and 90 deg each curve has its peak as shown by the dotted lines in Fig. 8(a).

The most interesting finding in the V-groove with a black fin is that a mere adjustment of the height of fin can widely alter the heat-transfer rate from the groove and the degree of energy collimation. Thus, the new model of V-groove can be justified as a promising device favorable for controlling radiation transfer. Furthermore, adequate selection of the geometrical parameters can bring about a higher heat-transfer rate than with the simple V-groove for a given value of η_L. For example, if the heat-transfer rate is intended to rise for $\eta_L = 45$ deg under the conditions of $\theta = 30$ deg and $\epsilon_s = 0.1$, the present model can attain $\epsilon_{a,h} = 0.62$ with $b = 0.4$, $t = 0.24$, against $\epsilon_{a,h} = 0.57$, the highest possible level with the simple V-groove at $b = 0.5$, showing about 10 percent greater $\epsilon_{a,h}$ obtainable by the former (see Figs. 5(a) and (b)).

3.2 Asymmetrical V-Groove. Comparison of the asymmetrical with the symmetrical V-groove is made to ascertain how and to what extent the difference between θ_1 and θ_2 (asymmetrical degree) can influence the value of η_0, affecting the heat-transfer rate and the degree of energy collimation. In the present study, calculations were made for the case $\theta_1 > \theta_2$. With values of θ_2 in the range of $0 \le \theta_2 \le \theta_1$ for a cavity with a fixed value of θ_1, the angle η_0 may change in the range of about $0 < \eta_0 < \theta_1/2$.

Figure 9 shows the angular distributions of $\epsilon_a(\eta)$ for several values of θ_2 at $\theta_1 = 30$ deg and $\epsilon_s = 0.1$. Reduction of θ_2 from 30 (symmetrical V-groove) to 0 deg leads η_0 to change from 0 to 10.8 deg. The degree of energy collimation undergoes no appreciable change with θ_2 in this range, disclosing the sum of the two limiting angles $(\eta_L{}^+ - \eta_0) + (\eta_0 - \eta_L{}^-) \approx 88$ deg. Figure 10 shows η_0 varying with θ_2 with ϵ_s as a parameter. As θ_2 decreases, η_0 increases monotonously up to its maximum at $\theta_2 = 0$ deg, the changes greater with lower ϵ_s. In the asymmetrical groove, η_0 thus becomes largest at $\theta_2 = 0$ deg. Let us then pursue the characteristics of the asymmetrical V-groove for $\theta_2 = 0$ deg as a limiting case.

The hemispherical emissivity and the angle η_L identified in the asymmetrical V-groove are shown in Figs. 11(a) and (b), respectively, to descriminate them from those in the symmetrical V-groove shown in Figs. 5(a) and (b). The variations of $\epsilon_{a,h}$ and η_L are comparable in Fig. 11(a) and Fig. 5(a), and in Fig. 11(b) and Fig. 5(b), respectively. In these figures, the dotted lines for $t = 0$ show the corresponding variations in the simple V-groove. In the asymmetrical V-groove for $\theta_2 = 0$ deg, although the black fin is contiguous to the side surface, changes in its height considerably affect the radiative transfer and the degree of energy collimation similar to the case of symmetrical V-groove. Values of $\epsilon_{a,h}$ are generally higher in Fig. 11(a) than in Fig. 5(a). This indicates an instance of the so-called cavity effect arising

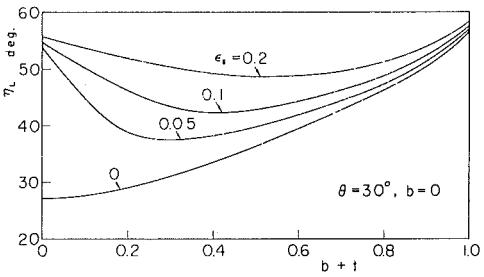

Fig. 7 Effect of side surface emissivity on directionality (symmetrical V-groove, $b = 0$)

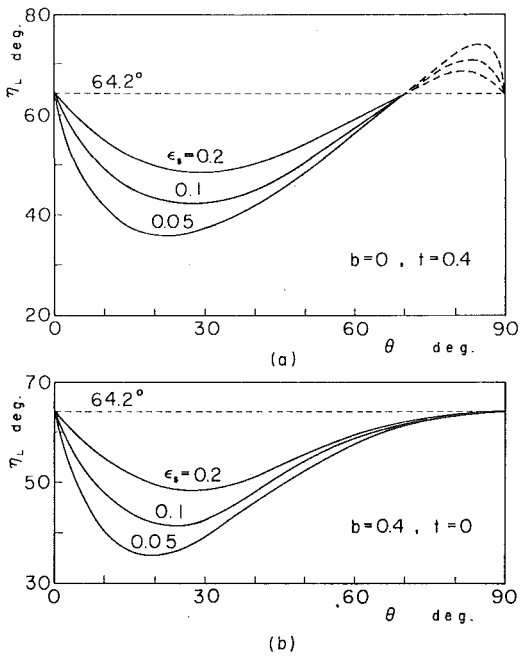

Fig. 8 Effect of opening angle on directionality (symmetrical V-groove), (a) V-groove with a black fin, (b) simple V-groove

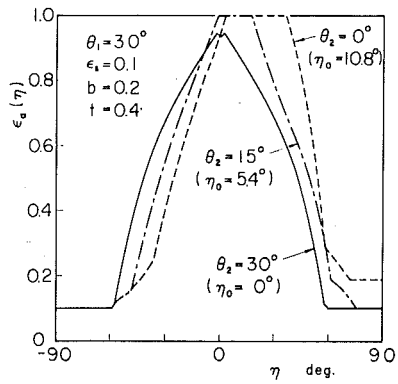

Fig. 9 Apparent directional emissivity for asymmetrical V-groove

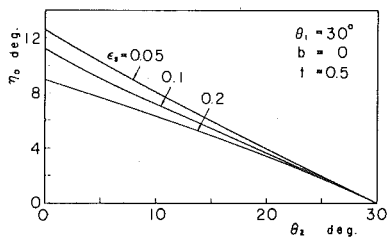

Fig. 10 Variation of η_0 with θ_2

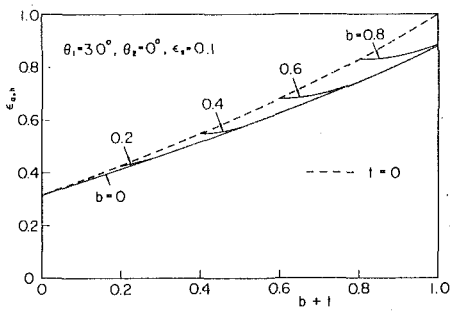

Fig. 11(*a*) Variation of $\epsilon_{a,h}$ with fin height (asymmetrical V-groove)

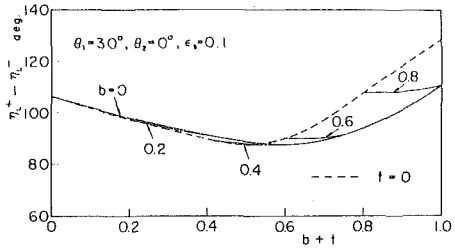

Fig. 11(*b*) Directionality varying with fin height (asymmetrical V-groove)

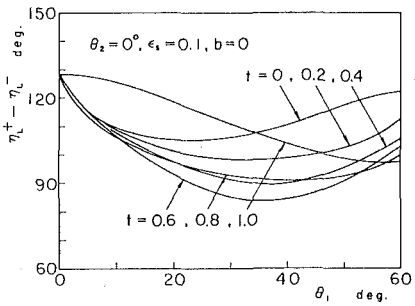

Fig. 12(*a*) Effect of opening angle on directionality (asymmetrical V-groove, $b = 0$)

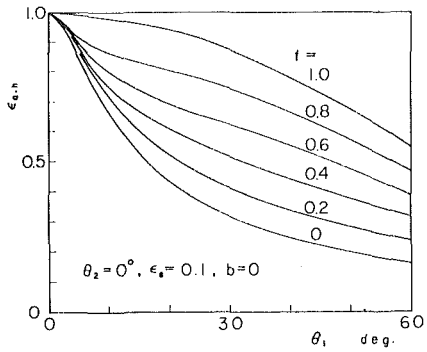

Fig. 12(*b*) Effect of opening angle on $\epsilon_{a,h}$ (asymmetrical V-groove, $b = 0$)

from the decrease in the cavity opening area to 1/2. In Fig. 11(*b*), as a representative result, the optimum values, $(b + t)_{opt}$, appear in all the curves for $b \leq 0.4$ consistently at $b + t \approx 0.6$. This is appreciably greater than for the symmetrical V-groove with $\theta = 30$ deg.

Even in the asymmetrical V-groove, the opening angle exerts a great influence on the radiative transfer characteristics. Figure 12(*a*) shows the variation of the limiting angle η_L with the angle θ_1. As is the case with the symmetrical V-groove (Fig. 8(*a*)), neither curve has directionality at $\theta_1 = 0$ and 90 deg (graphical indication partly omitted), showing $|\eta_L{}^+| + |\eta_L{}^-| = 128.3$ deg, within which each has a minimum value. The curves with t as a parameter are not consistent in shifting trend, but suggest the existence of a value of t favorable for collimation of energy. From the figure, this optimum fin height appears to be $t \approx 0.6$. Figure 12(*b*) shows the relation between $\epsilon_{a,h}$ and θ_1. The hemispherical emissivity, expressive of the radiative heat transfer from the cavity, is always greater with smaller θ_1 and a higher fin, due to the cavity effect.

4 Conclusions

On a V-groove cavity with a black fin on its base as a directional surface, the characteristics of radiative transfer were theoretically made clear. The results obtained are summarized as follows.

1 The black fin in a symmetrical V-groove promotes both radiative heat transfer and collimation of energy in the direction normal to the base surface. Changes in the height of fin can widely alter the heat-transfer rate of the groove cavity and the degree of energy collimation.

2 An optimum height of the fin exists which produces the maximum directional effect for given values of the V-groove opening angle and the base level.

3 The influence of the V-groove opening angle on the radiative transfer characteristics is also great. Therefore, by carefully selecting the geometrical parameters—the base level, the height of fin and the opening angle—it is possible to design a V-groove cavity as a still better directional surface.

4 The direction of energy collimation can be turned by using an asymmetrical V-groove cavity with a black fin. In this case, the effects of the black fin on the radiative transfer characteristics remain almost unaltered from the case of symmetrical V-groove.

Acknowledgments

The author wishes to express his sincere thanks to Professor Emeritus T. Tsubouchi of Tohoku University for his useful advice in completing this study. He also extends thanks to Miss K. Akiyama of the staff of the Institute of High Speed Mechanics, Tohoku University, for her assistance throughout this study.

References

1 Mills, D. R., and Giutronich, J. E., "Asymmetrical Non-Imaging Cylindrical Solar Concentrators," *Solar Energy*, Vol. 20, No. 1, 1978, pp. 45–55.

2 Grimmer, D. P., "A Comparison of Compound Parabolic and Simple Parabolic Concentrating Solar Collectors," *Solar Energy*, Vol. 22, No. 1, 1979, pp. 21–25.

3 Rabl, A., et al., "Practical Design Considerations for CPC Solar Collectors," *Solar Energy*, Vol. 22, No. 4, 1979, pp. 373–381.

4 Clausen, O. W., and Neu, J. T., "The Use of Directionally Dependent Radiation Properties for Spacecraft Thermal Control," *Astronautica Acta*, Vol. 11, No. 5, 1965, pp. 328–339.

5 Horton, T. E., and McDermit, J. H., "Design of a Specular Aspheric Surface to Uniformly Radiate a Flat Surface using a Nonuniform Collimated Radiation Source," ASME JOURNAL OF HEAT TRANSFER, Vol. 94, No. 4, Nov. 1972, pp. 453–458.

6 Pfahl, R.C., Jr., "Specular Reflectors for Prescribed Disturbed Radiant Heating from a Point Energy Source," ASME JOURNAL OF HEAT TRANSFER, Vol. 95, No. 1, Feb. 1973, pp. 25–30.

7 Black, W. Z., and Schoenhals, R. J., "A Study of Directional Radiation Properties of Specially Prepared V-Groove Cavities," ASME JOURNAL OF HEAT TRANSFER, Vol. 90, No. 4, Nov. 1968, pp. 420–428.

8 Black, W. Z., and Schoenhals, R. J., "An Experimental Study of Radiation Heat Transfer From Parallel Plates With Direction-Dependent Properties," ASME JOURNAL OF HEAT TRANSFER, Vol. 92, No. 4, Nov. 1970, pp. 610–615.

9 Black, W. Z., "Optimization of the Directional Emission from V-Groove and Rectangular Cavities," ASME JOURNAL OF HEAT TRANSFER, Vol. 95, No. 1, Feb. 1973, pp. 31–36.

10 Perlmutter, M., and Howell, J. R., "A Strongly Directional Emitting and Absorbing Surface," ASME JOURNAL OF HEAT TRANSFER, Vol. 85, No. 3, Aug. 1963, pp. 282–283.

11 Winston, R., "Principles of Solar Concentrators of a Novel Design," *Solar Energy*, Vol. 16, No. 2, Oct. 1974, pp. 89–95.

12 Masuda, H., "Radiation Heat Transfer Between Specularly and Diffusely Reflecting Surfaces," *Journal of Quantitative Spectroscopy and Radiative Transfer*, Vol. 16, No. 12, Dec. 1976, pp. 997–1009.

13 Eckert, E. R. G., and Sparrow, E. M., "Radiative Heat Exchange Between Surfaces with Specular Reflection," *International Journal of Heat and Mass Transfer*, Vol. 3, No. 1, Aug. 1961, pp. 42–54.

Journal of Heat Transfer

Technical Notes

Heat Transfer in a Tube Downstream of a Tee in which Airstreams of Different Temperature are Mixed

E. M. Sparrow,[1] N. Cur,[1] and R. G. Kemink[1]

Nomenclature

D = diameter of test section tube
$\bar{h}_x$ = circumferential average heat transfer coefficient at x
$h_x(\theta)$ = local heat transfer coefficient at x,θ
k = thermal conductivity
$\dot{m}$ = mass flow rate in test section
$\dot{m}_1$ = mass flow rate entering side port
$\dot{m}_2$ = mass flow rate entering center port
Nu_{fd} = fully developed Nusselt number
$\overline{\mathrm{Nu}}_x$ = circumferential average Nusselt number at x, $\bar{h}_x D/K$
$\mathrm{Nu}_x(\theta)$ = local Nusselt number at x,θ, $h_x(\theta)D/k$
Re = test section Reynolds number, $4\dot{m}/\mu\pi D$
T_b = bulk temperature
T_{b1} = bulk temperature of airstream entering side port
T_{b2} = bulk temperature of airstream entering center port
T_w = wall temperature
x = axial coordinate
θ = angular coordinate
μ = viscosity
Φ = bulk temperature imbalance ratio, $|T_{b2} - T_{b1}|/(T_w - T_b)_{fd}$

Introduction

It was demonstrated experimentally in [1] that the mixing of two air streams in a tee gives rise to enhanced heat transfer in a tube situated downstream of the tee. In those experiments, air was ducted to the center port and one of the side ports of a tee. The discharge from the other side port passed through a uniformly heated tube which served as the test section for heat transfer measurements. In the test setup used in [1], the temperatures of the two air streams entering the tee were the same. Under such conditions, the heat transfer results in the downstream tube reflect the numerous and complex hydrodynamic processes which are induced by the mixing of the streams.

The present experiments were undertaken as a sequel to those of [1] with the aim of investigating the mixing of air streams of different temperatures. Thus, compared with [1], the present results will reflect not only mixing-related hydrodynamic processes but also the effects of the thermal imbalance of the component air streams.

The Experiments

The mixing arrangement is pictured schematically in the inset of Fig. 1. As shown there, the air stream entering the side port of the tee has a bulk temperature T_{b1}, while that entering the center port has a bulk temperature T_{b2}. The respective mass flow rates are $\dot{m}_1$ and $\dot{m}_2$, and $\dot{m} = \dot{m}_1 + \dot{m}_2$ is the mass flow rate of the merged flow which passes from the other side port into the uniformly heated test section tube.

Both the $\dot{m}_1$ and $\dot{m}_2$ air streams were supplied from a central compressor. The $\dot{m}_2$ stream was ducted through a 100-diameters-long electrically heated circular tube en route to the center port of the tee. On the other hand, the $\dot{m}_1$ stream passed through an adiabatic-walled tube of similar length which delivered the air to the side port. Thus, the heating of the $\dot{m}_2$ stream coupled with the nonheating of the $\dot{m}_1$ stream gave rise to a difference $|T_{b2} - T_{b1}|$ in the bulk temperatures of the entering streams.[2]

To obtain a dimensionless characterization which will reflect whether $|T_{b2} - T_{b1}|$ is large or small compared with a representative temperature difference in the flow in the test section tube, the ratio

$$\Phi = |T_{b2} - T_{b1}|/(T_w - T_b)_{fd} \tag{1}$$

was employed. The quantity $(T_w - T_b)_{fd}$ is the wall-to-bulk temperature difference in the fully developed regime which is attained in the downstream portion of the tube. During the course of the experiments, the Φ ratio was varied from zero to three.

Aside from the bulk temperature imbalance as reflected by Φ, the conduct of the experiments and the data reduction procedure were similar to that of [1], and [1] may be consulted for details. For a given test section Reynolds number

$$\mathrm{Re} = 4\dot{m}/\mu\pi D \tag{2}$$

data runs were carried out for parametric values of the flow mixing ratio $\dot{m}_1/\dot{m}$. The extreme values of $\dot{m}_1/\dot{m}$, namely, $\dot{m}_1/\dot{m} = 0$ and 1, are irrelevant to the present study of temperature imbalance effects since they represent single stream inflows. Data runs corresponding to values of $\dot{m}_1/\dot{m} = 0.25$, 0.50, and 0.75 were made for each Reynolds number.

The original research plan included a parametric study involving several Reynolds numbers. However, with increasing Reynolds number and at higher Φ values, it was not possible to null out radial heat flows in the bus bars used to deliver current to the upstream end of the electrically heated test section. The bus bars were fitted with guard heaters and differential thermocouples, but under the afore-

[1] Department of Mechanical Engineering, University of Minnesota, Minneapolis, Minn. 55455.

Contributed by the Heat Transfer Division for publication in the JOURNAL OF HEAT TRANSFER. Manuscript received by the Heat Transfer Division January 4, 1980.

[2] The absolute value of the difference between T_{b2} and T_{b1} will be used here because the results should be applicable both for $T_{b2} > T_{b1}$ and $T_{b2} < T_{b1}$.

mentioned conditions the guard heaters were unable to reduce the readings of the differential thermocouples to zero. Satisfactory operation was obtained for the data runs corresponding to a Reynolds number of 20,000, but the Re = 30,000 results contain some uncertainty. Fortunately, all of the trends in evidence for Re = 20,000 also appear in the results for Re = 30,000. Because of their greater certainty and owing to journal space constraints, only the Re = 20,000 results are presented here. Those for Re = 30,000 may be found in [2].

Owing to the right-angle intersection of the two streams entering the tee, circumferential variations of the test-section heat transfer coefficients are encountered in addition to axial variations. In view of this, two types of heat transfer coefficients are employed in the presentation of the results. One of these is the circumferential average heat transfer coefficient $\bar{h}_x$ corresponding to an axial station x. If $\bar{q}_x$ is the circumferential average rate of heat transfer per unit area at x and $\overline{T}_{wx}$ is the circumferential average wall temperature, also at x, then

$$\bar{h}_x = \bar{q}_x/(\overline{T}_{wx} - T_{bx}) \tag{3}$$

where T_{bx} is the local bulk temperature of the air. The data reduction methods used in the evaluation of equation (3) may be found in [1] or [2]. The local Nusselt number corresponding to $\bar{h}_x$ is

$$\overline{\mathrm{Nu}}_x = \bar{h}_x D/k \tag{4}$$

in which k was evaluated at T_{bx}.

The other heat transfer coefficient used in the presentation of results is the local angular coefficient $h_x(\theta)$, which pertains to an angular position θ at an axial station x. The defining equations for $h_x(\theta)$ and its dimensionless counterpart $\mathrm{Nu}_x(\theta)$ are

$$h_x(\theta) = q_x(\theta)/(T_{wx}(\theta) - T_{bx}), \quad \mathrm{Nu}_x(\theta) = h_x(\theta)D/k \tag{5}$$

where, again, k corresponds to the local bulk temperature. For the evaluation of equation (5), the local wall temperature $T_{wx}(\theta)$ is determined by direct measurement while $q_x(\theta)$ is obtained from a data reduction procedure which accounts for internal heat generation and circumferential conduction in the tube wall and for heat losses to the surroundings [1, 2].

Results and Discussion

The circumferential average heat transfer results for Re = 20,000 are presented in Figs. 1–3, respectively for $\dot{m}_1/\dot{m} = 0.25, 0.5$, and 0.75. In each figure, the Nusselt number ratio $\overline{\mathrm{Nu}}_x/\mathrm{Nu}_{fd}$ is plotted as a function of the dimensionless axial coordinate x/D, where x is measured from the geometric center of the tee and the heated tube begins at $x/D = 0.76$. The quantity Nu_{fd} is the fully developed Nusselt number. The data appearing in each figure are parameterized by the inlet bulk-temperature imbalance ratio $|T_{b2} - T_{b1}|/(T_w - T_b)_{fd}$. The limited case $|T_{b2} - T_{b1}|/(T_w - T_b)_{fd} = 0$, which corresponds to identical temperatures of the two streams entering the tee, serves as a baseline case against which to compare the results for the cases with temperature imbalance.

Examination of the figures shows that the expected trend of $\overline{\mathrm{Nu}}_x/\mathrm{Nu}_{fd}$ decreasing with x/D is preserved for all of the inlet temperature imbalances investigated here. Aside from a few exceptions at the smaller x/D, there is a trend toward lower values of $\overline{\mathrm{Nu}}_x/\mathrm{Nu}_{fd}$ as the inlet temperature imbalance increases. Thus, it appears that the effect of temperature imbalance is to decrease the circumferential average Nusselt number. The influence of the imbalance is greatest at small x/D and diminishes as the fully developed region is approached.

Further inspection of the figures suggests that there is an overall trend for the results to be more sensitive to the inlet temperature imbalance as $\dot{m}_1/\dot{m}$ increases. Indeed, aside from the most upstream station, the Nusselt numbers for $\dot{m}_1/\dot{m} = 0.25$ are nearly independent of the imbalance. Even for $\dot{m}_1/\dot{m} = 0.5$, there is only a small spread in the data for different $|T_{b2} - T_{b1}|/(T_w - T_b)_{fd}$. The greatest sensitivity of the results to the imbalance is for $\dot{m}_1/\dot{m} = 0.75$.

To rationalize the aforementioned trend with $\dot{m}_1/\dot{m}$, attention may be called to the fact that the smaller the $\dot{m}_1/\dot{m}$, the larger are the values of $\overline{\mathrm{Nu}}_x/\mathrm{Nu}_{fd}$. This is entirely reasonable since small $\dot{m}_1/\dot{m}$ signifies a relatively large inflow through the center port of the tee. The fluid entering via the center port experiences a complex and chaotic turning process (replete with impingement on the wall of the tee) en route to the exit (side) port of the tee. This process generates highly intense turbulence, mixing, and three-dimensional motions, the totality of which contributes to the heat transfer enhancement that is in evidence when $\dot{m}_1/\dot{m}$ is small (i.e., when $\dot{m}_2/\dot{m}$ is large). When $\dot{m}_1/\dot{m}$ is large, the turning process is relatively placid, and the enhancement is small.

These ideas can now be used to explain why a flow with small $\dot{m}_1/\dot{m}$ is less sensitive to the inlet bulk-temperature imbalance than is a flow with large $\dot{m}_1/\dot{m}$. First, it should be noted that if perfect thermal mixing of the $\dot{m}_1$ and $\dot{m}_2$ streams were to occur before the merged flow enters the heated test section tube, the Nusselt number results would be completely unaffected by the difference between T_{b2} and T_{b1}. It is also reasonable to expect that if no thermal mixing were to occur before the merged flow enters the test section, there would be high sensitivity of the Nusselt number results to the imbalance between T_{b2} and T_{b1}. On the basis of the preceding paragraph, it can be expected that much greater thermal mixing will occur for $\dot{m}_1/\dot{m} = 0.25$ than for $\dot{m}_1/\dot{m} = 0.75$, thereby explaining the trend in the results of Figs. 1–3.

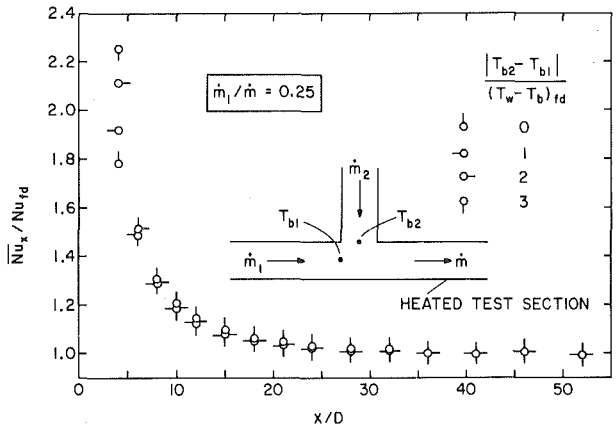

Fig. 1 Circumferential average Nusselt numbers, Re = 20,000 and $\dot{m}_1/\dot{m}$ = 0.25. The inset is a schematic of the mixing arrangement.

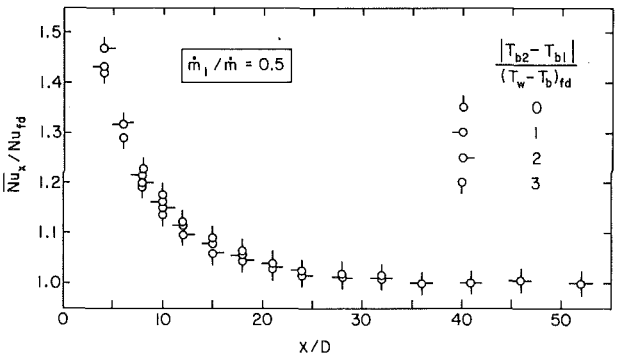

Fig. 2 Circumferential average Nusselt numbers, Re = 20,000 and $\dot{m}_1/\dot{m}$ = 0.5

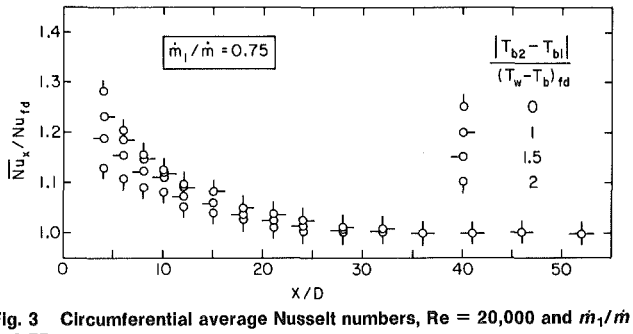

Fig. 3 Circumferential average Nusselt numbers, Re = 20,000 and $\dot{m}_1/\dot{m}$ = 0.75

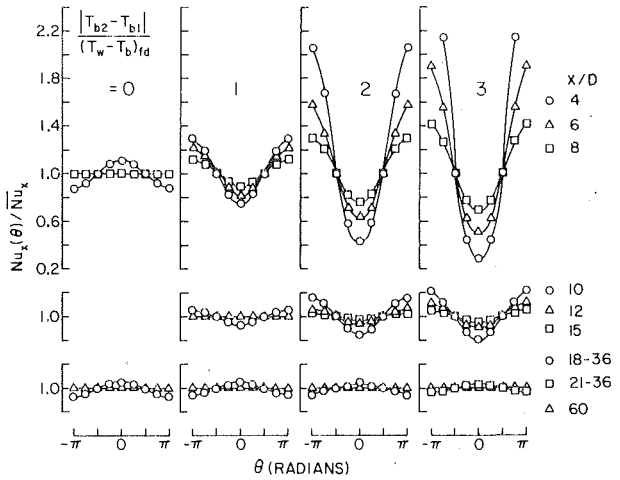

Fig. 4 Angular distributions of the local Nusselt number, Re = 20,000 and $\dot{m}_1/\dot{m} = 0.5$

There are isolated axial stations in evidence in Figs. 1–3 at which the general trends identified in the foregoing paragraphs are not in force. This is especially true at the first axial station in Fig. 1. These deviations may be true reflections of the participating physical phenomena or, alternatively, they may reflect extraneous effects such as bus bar heat losses (or gains). It appears that this issue cannot be conclusively settled with the information at hand.

Attention is now turned to the angular distributions of the local heat coefficient $h_x(\theta)$. Representative results, corresponding to Re = 20,000 and $\dot{m}_1/\dot{m} = 0.5$, are presented in Fig. 4 (other angular distributions are available in [2]). The figure contains four columns of graphs, with each column conveying data for a specific value of $|T_{b2} - T_{b1}|/(T_w - T_b)_{fd}$. In each graph, the ratio $Nu_x(\theta)/\overline{Nu}_x$ is plotted as a function of the angular coordinate θ. The $\theta = 0$ position corresponds to the top of the tube as it is pictured in the inset of Fig. 1 (i.e., $\theta = 0$ lies along the centerline of the center port), while $\theta = \pi$ is at the bottom of the tube. Angular distributions are presented at a number of axial stations for which the x/D values are indicated in the graphs.

The main message of the figure relates to the different nature of the angular variations at the first several stations for $|T_{b2} - T_{b1}| = 0$ and $|T_{b2} - T_{b1}| > 0$. For the former, the highest heat transfer coefficients occur at $\theta = 0$ and the lowest at $\theta = \pi$. An opposite relationship is in force for the latter, and the deviation between the bottom and top coefficient values increases as $|T_{b2} - T_{b1}|/(T_w - T_b)_{fd}$ increases. With increasing downstream distance, the angular variations ultimately die away, but residual variations are still present as far downstream as $x/D = 36$.

Acknowledgment

The research reported here was performed under the auspices of the Office of Naval Research (contract No. N00014-79-C-0621).

References

1 Sparrow, E. M., and Kemink, R. G., "The Effect of a Mixing Tee on Turbulent Heat Transfer in a Tube," *International Journal of Heat and Mass Transfer*, Vol. 22, 1979, pp. 909–917.

2 Cur, N., "Heat Transfer Downstream of a Tee which Mixes Airstreams of Different Temperature," M.S. Thesis, Department of Mechanical Engineering, University of Minnesota, Minneapolis, Minn. 1980.

Further Studies on the Delayed Hot Water Problem[1]

P. C. Lu[2]

Nomenclature

$A = \alpha_2/\alpha_1$, dimensionless
a = radius of fluid passage, m
B = interphase Biot number ah/k_1, dimensionless
b = outer radius of solid wall, m
$b_1 = (2\alpha_1/a^2)$B, s^{-1}
$b_1' = 2(L^2/a^2)$FB, dimensionless
$b_2 = 2(k_1/k_2)\alpha_2 B/(b^2 - a^2)$, s^{-1}
$b_2' = b_1'(\rho_1 c_1/\rho_2 c_2)a^2/(b^2 - a^2)$, dimensionless
$C = (\rho_1 c_1/\rho_2 c_2)a^2/(b^2 - a^2)$, dimensionless
c_1 = specific heat capacity of fluid, J/K-kg
c_2 = specific heat capacity of solid, J/K-kg
erfc = complementary error function of
F = Fourier number, $\alpha_1 \tilde{t}/L^2 (= \alpha_1/LV)$, dimensionless
$F' = (A + C)$F$/(1 + C)$, dimensionless
h = equivalent interphase heat-transfer coefficient, W/m^2-K
k_1 = thermal conductivity of fluid, W/m-K
k_2 = thermal conductivity of solid, W/m-K
L = length of pipe, m
T = dimensionless temperature difference of solid, ((solid temperature)-(initial temperature))/(rise in temperature at inlet)
$T_{(0)}$ = zeroth-order solution for T, dimensionless
$T_{(0)}{}^i$ = inner limit of $T_{(0)}$, dimensionless
$T_{(0)}{}^o$ = outer limit of $T_{(0)}$, dimensionless
t = time, s
$\tilde{t} = L/V$, representative time, s
$t' = t/\tilde{t}$, dimensionless
V = constant flow speed, m/s
$V'' = 1/(1 + 1/C)$, dimensionless
$V''/F' = [C/(A + C)](LV/\alpha_1)$
V^* = propagational speed of thermal front, $V/[1 + \rho_2 c_2(b^2 - a^2)/\rho_1 c_1 a^2]$, m/s
x = distance along the flow direction, measured from the inlet, m
$x' = x/L$, dimensionless
α_1 = thermal diffusivity of solid, m^2/s
α_2 = thermal diffusivity of solid, m^2/s
$\alpha^* = \alpha_1(A + C)/(1 + C)$, m^2/s
ρ_1 = density of fluid, kg/m^3
ρ_2 = density of solid, kg/m^3
θ = dimensionless temperature difference of fluid, ((fluid temperature)-(initial temperature))/(rise in temperature at inlet)
$\theta_{(0)}$ = zeroth-order solution for θ, dimensionless
τ = same as t', dimensionless
$\zeta = x' - \bar{V}''t'$, dimensionless
$\zeta' = \zeta/\sqrt{F'}$, dimensionless

Introduction

The delayed arrival of a hot or cold front (relative to the flow speed) in a fluid flowing through a pipe was first explained in a preliminary Note by Munk [1] in terms of the daily life experience of waiting for the hot water after turning on the faucet. This "delayed hot water problem" has recently been examined very carefully by Comstock, et al. [2] who displayed matched perturbation solutions based on large flow speed. The important conclusions arrived at in [2] are as follows: After the flow (with large speed) is turned on, there is, at first, a front travelling as fast as the flow, carrying a jump in the water temperature and there is another front propagating at a slower speed, as predicted by Munk [1], carrying "relative minima" of the wall and fluid temperatures. While these conclusions are undoubtedly correct within the framework of [2], they are not as directly linked to the work of Munk [1] as one would like to see; and it is felt that large flow speed

[1] Work performed under NSF Grant ENG78-04060 and presented in a more detailed form before the 1979 Winter Annual Meeting of ASME as Paper No. 79-WA/HT-57.

[2] Professor, Department of Mechanical Engineering, University of Nebraska, Lincoln, Neb. Mem ASME.

Contributed by the Heat Transfer Division for publication in the JOURNAL OF HEAT TRANSFER. Manuscript received by the Heat Transfer Division February 28, 1980.

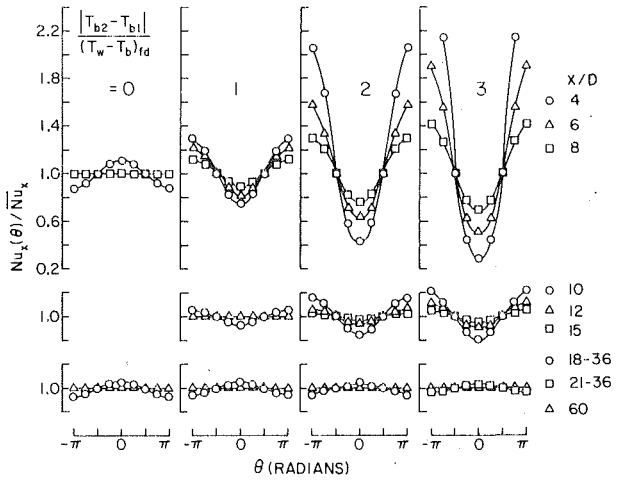

Fig. 4 Angular distributions of the local Nusselt number, Re = 20,000 and $\dot{m}_1/\dot{m} = 0.5$

There are isolated axial stations in evidence in Figs. 1–3 at which the general trends identified in the foregoing paragraphs are not in force. This is especially true at the first axial station in Fig. 1. These deviations may be true reflections of the participating physical phenomena or, alternatively, they may reflect extraneous effects such as bus bar heat losses (or gains). It appears that this issue cannot be conclusively settled with the information at hand.

Attention is now turned to the angular distributions of the local heat coefficient $h_x(\theta)$. Representative results, corresponding to Re = 20,000 and $\dot{m}_1/\dot{m} = 0.5$, are presented in Fig. 4 (other angular distributions are available in [2]). The figure contains four columns of graphs, with each column conveying data for a specific value of $|T_{b2} - T_{b1}|/(T_w - T_b)_{fd}$. In each graph, the ratio $Nu_x(\theta)/\overline{Nu}_x$ is plotted as a function of the angular coordinate θ. The $\theta = 0$ position corresponds to the top of the tube as it is pictured in the inset of Fig. 1 (i.e., $\theta = 0$ lies along the centerline of the center port), while $\theta = \pi$ is at the bottom of the tube. Angular distributions are presented at a number of axial stations for which the x/D values are indicated in the graphs.

The main message of the figure relates to the different nature of the angular variations at the first several stations for $|T_{b2} - T_{b1}| = 0$ and $|T_{b2} - T_{b1}| > 0$. For the former, the highest heat transfer coefficients occur at $\theta = 0$ and the lowest at $\theta = \pi$. An opposite relationship is in force for the latter, and the deviation between the bottom and top coefficient values increases as $|T_{b2} - T_{b1}|/(T_w - T_b)_{fd}$ increases. With increasing downstream distance, the angular variations ultimately die away, but residual variations are still present as far downstream as $x/D = 36$.

Acknowledgment

The research reported here was performed under the auspices of the Office of Naval Research (contract No. N00014-79-C-0621).

References

1 Sparrow, E. M., and Kemink, R. G., "The Effect of a Mixing Tee on Turbulent Heat Transfer in a Tube," *International Journal of Heat and Mass Transfer*, Vol. 22, 1979, pp. 909–917.

2 Cur, N., "Heat Transfer Downstream of a Tee which Mixes Airstreams of Different Temperature," M.S. Thesis, Department of Mechanical Engineering, University of Minnesota, Minneapolis, Minn. 1980.

Further Studies on the Delayed Hot Water Problem[1]

P. C. Lu[2]

Nomenclature

$A = \alpha_2/\alpha_1$, dimensionless
a = radius of fluid passage, m
B = interphase Biot number ah/k_1, dimensionless
b = outer radius of solid wall, m
$b_1 = (2\alpha_1/a^2)$B, s^{-1}
$b_1' = 2(L^2/a^2)$FB, dimensionless
$b_2 = 2(k_1/k_2)\alpha_2 B/(b^2 - a^2)$, s^{-1}
$b_2' = b_1'(\rho_1 c_1/\rho_2 c_2)a^2/(b^2 - a^2)$, dimensionless
$C = (\rho_1 c_1/\rho_2 c_2)a^2/(b^2 - a^2)$, dimensionless
c_1 = specific heat capacity of fluid, J/K-kg
c_2 = specific heat capacity of solid, J/K-kg
erfc = complementary error function of
F = Fourier number, $\alpha_1 \tilde{t}/L^2 (= \alpha_1/LV)$, dimensionless
$F' = (A + C)$F$/(1 + C)$, dimensionless
h = equivalent interphase heat-transfer coefficient, W/m^2-K
k_1 = thermal conductivity of fluid, W/m-K
k_2 = thermal conductivity of solid, W/m-K
L = length of pipe, m
T = dimensionless temperature difference of solid, ((solid temperature)-(initial temperature))/(rise in temperature at inlet)
$T_{(0)}$ = zeroth-order solution for T, dimensionless
$T_{(0)}{}^i$ = inner limit of $T_{(0)}$, dimensionless
$T_{(0)}{}^o$ = outer limit of $T_{(0)}$, dimensionless
t = time, s
$\tilde{t} = L/V$, representative time, s
$t' = t/\tilde{t}$, dimensionless
V = constant flow speed, m/s
$V'' = 1/(1 + 1/C)$, dimensionless
$V''/F' = [C/(A + C)](LV/\alpha_1)$
V^* = propagational speed of thermal front, $V/[1 + \rho_2 c_2(b^2 - a^2)/\rho_1 c_1 a^2]$, m/s
x = distance along the flow direction, measured from the inlet, m
$x' = x/L$, dimensionless
α_1 = thermal diffusivity of solid, m^2/s
α_2 = thermal diffusivity of solid, m^2/s
$\alpha^* = \alpha_1(A + C)/(1 + C)$, m^2/s
ρ_1 = density of fluid, kg/m^3
ρ_2 = density of solid, kg/m^3
θ = dimensionless temperature difference of fluid, ((fluid temperature)-(initial temperature))/(rise in temperature at inlet)
$\theta_{(0)}$ = zeroth-order solution for θ, dimensionless
τ = same as t', dimensionless
$\zeta = x' - V''t'$, dimensionless
$\zeta' = \zeta/\sqrt{F'}$, dimensionless

Introduction

The delayed arrival of a hot or cold front (relative to the flow speed) in a fluid flowing through a pipe was first explained in a preliminary Note by Munk [1] in terms of the daily life experience of waiting for the hot water after turning on the faucet. This "delayed hot water problem" has recently been examined very carefully by Comstock, et al. [2] who displayed matched perturbation solutions based on large flow speed. The important conclusions arrived at in [2] are as follows: After the flow (with large speed) is turned on, there is, at first, a front travelling as fast as the flow, carrying a jump in the water temperature and there is another front propagating at a slower speed, as predicted by Munk [1], carrying "relative minima" of the wall and fluid temperatures. While these conclusions are undoubtedly correct within the framework of [2], they are not as directly linked to the work of Munk [1] as one would like to see; and it is felt that large flow speed

[1] Work performed under NSF Grant ENG78-04060 and presented in a more detailed form before the 1979 Winter Annual Meeting of ASME as Paper No. 79-WA/HT-57.

[2] Professor, Department of Mechanical Engineering, University of Nebraska, Lincoln, Neb. Mem ASME.

Contributed by the Heat Transfer Division for publication in the JOURNAL OF HEAT TRANSFER. Manuscript received by the Heat Transfer Division February 28, 1980.

is by no means the only possible (or the most realistic) starting point in searching for perturbation solutions.

In the present work, the problem is examined from another point of view. Perturbation solutions based on strong thermal link (essentially, large interphase Biot number and slender passage for the fluid) are sought. The zeroth-order solutions turn out to be identical for the fluid and the solid. These solutions also furnish direct substantiation of Munk's preliminary prediction that a temperature front propagates at a slower speed than the flowing fluid, for small values of the Fourier number (mainly small thermal diffusivity and long flow passage). The present study also exhibits a diffusive region "softening" the moving front with an effective diffusivity exactly as reported in [2]. It must be emphasized that, in contrast to [2], the present investigation is made against a background of long but finite length of the flow passage, without any specific importance attached to the order of magnitude of the flow speed.

The Problem

Consider a pipe with radii a (inner) and b (outer), extending from $x = 0$ to $x = L$, filled completely with a fluid. At time $t < 0$, the fluid is at rest and the temperature is uniform throughout the fluid and the solid wall. Then, at $t = 0$, the fluid is suddenly driven in the x-direction with a uniform and constant speed V. For simplicity, both the fluid and the wall temperatures at $x = 0$ are raised to and maintained at the same constant temperature for $t \geq 0$; the exit ($x = L$) is perfectly insulating for both phases. The governing equations and conditions can then be shown [2] to be as follows (with the outer surface of the pipe insulated).

$$\alpha_1 \frac{\partial^2 \theta}{\partial x^2} - V \frac{\partial \theta}{\partial x} = \frac{\partial \theta}{\partial t} + b_1 (\theta - T) \tag{1}$$

$$\alpha_2 \frac{\partial^2 T}{\partial x^2} = \frac{\partial T}{\partial t} - b_2 (\theta - T) \tag{2}$$

$$t = 0 : \theta, T = 0 \tag{3}$$

$$x = 0 : \theta, T = 1 \tag{4}$$

$$x = L : \frac{\partial \theta}{\partial x}, \frac{\partial T}{\partial x} = 0 \tag{5}$$

where θ and T are the dimensionless temperature differences of the fluid and the solid, respectively, above the initial temperature, with the difference of the temperature at $x = 0$ above the initial value serving as the characteristic quantity; α_1 and α_2 are the thermal diffusivities for the fluid and solid, respectively. The parameters b_1 and b_2 are related to the interphase Biot number $\mathrm{B} = ah/k_1$: $b_1 = (2\alpha_1/a^2)\mathrm{B}$, $b_2 = (k_1/k_2)\mathrm{B}(2\alpha_2)/(b^2 - a^2)$, where k_1 and k_2 are the thermal conductivities of the fluid and solid, respectively, and h is the equivalent interphase heat-transfer coefficient.

Using the representative time $\tilde{t} = L/V$, we may further nondimensionalize the problem thus.

$$\mathrm{F} \frac{\partial^2 \theta}{\partial x'^2} - \frac{\partial \theta}{\partial x'} = \frac{\partial \theta}{\partial t'} - b_1' (\theta - T) \tag{6}$$

$$\left(\frac{\alpha_2}{\alpha_1}\right) \mathrm{F} \frac{\partial^2 T}{\partial x'^2} = \frac{\partial T}{\partial t'} - b_2' (\theta - T) \tag{7}$$

$$t' = 0 : \theta, T = 0 \tag{8}$$

$$x' = 0 : \theta, T = 1 \tag{9}$$

$$x' = 1 : \frac{\partial \theta}{\partial x'}, \frac{\partial T}{\partial x'} = 0 \tag{10}$$

where

$$t' = t/\tilde{t}, x' = x/L \tag{11}$$

$$b_1' = 2\left(\frac{L^2}{a^2}\right)\mathrm{FB} \tag{12}$$

$$b_2' = 2\left(\frac{L^2}{b^2 - a^2}\right)\left(\frac{\rho_1 c_1}{\rho_2 c_2}\right)\mathrm{FB} = b_1'\left(\frac{a^2}{b^2 - a^2}\right)\left(\frac{\rho_1 c_1}{\rho_2 c_2}\right) \tag{13}$$

and the Fourier number F is defined as $\mathrm{F} = \alpha_1 \tilde{t}/L^2 = \alpha_1/LV$. (The products $\rho_1 c_1$ and $\rho_2 c_2$ are the heat capacities per unit volume of the fluid and solid, respectively.)

The Outer Limit

When the flow passage of the fluid is very slender, and the thermal link between the fluid and solid (as measured by the interphase heat transfer coefficient) is very strong, we have $(L^2/a^2)\mathrm{B} \gg 1$. Since we plan to investigate later the case with $\mathrm{F} \ll 1$, let us also stipulate that

$$(L^2/a^2)\mathrm{B} \gg 1/\mathrm{F} \tag{14}$$

Then, $b_1' \gg 1$ even for small values of F. Perturbation solutions for θ and T can then be sought as power series of $1/b_1'$.

Using the abbreviations $A = \alpha_2/\alpha_1$ and $C = b_2'/b_1'$, it can be easily shown that the zeroth-order solutions $\theta_{(0)}$ and $T_{(0)}$ are governed by the following system.

$$(1 + C)\frac{\partial T_{(0)}}{\partial t'} + C\frac{\partial T_{(0)}}{\partial x'} = (A + C)\mathrm{F}\frac{\partial^2 T_{(0)}}{\partial x'^2} \tag{15}$$

$$\theta_{(0)} = T_{(0)} \tag{16}$$

$$t' = 0 : T_{(0)}, \theta_{(0)} = 0 \tag{17}$$

$$x' = 0 : T_{(0)}, \theta_{(0)} = 1 \tag{18}$$

$$x' = 1 : \frac{\partial T_{(0)}}{\partial x'}, \frac{\partial \theta_{(0)}}{\partial x'} = 0 \tag{19}$$

It is noted that, to the zeroth order, the temperature variation is the same in the two phases.[3] This is exactly one of the items *assumed* by Munk in starting his preliminary study [1].

Before equation (15) is solved together with the initial-boundary conditions, some interesting aspects of its behavior as $\mathrm{F} \to 0$ (still under the stipulation (14)) can be discussed qualitatively by way of the matched inner-outer limits ([3]). It must be emphasized here once again that $\mathrm{F} \to 0$ is physically tied in with $\alpha_1/L \to 0$, *not* with $V \to \infty$ as in [2].

A straightforward limiting process as $\mathrm{F} \to 0$ yields

$$\frac{\partial T_{(0)}{}^o}{\partial t'} + \frac{1}{(1 + 1/C)}\frac{\partial T_{(0)}{}^o}{\partial x'} = 0 \tag{20}$$

with the second-order derivative dropped. Equation (20) is precisely the starting point of Munk's preliminary analysis [1]; its classical solution is

$$T_{(0)}{}^o = 1, x' \leq V''t' \tag{21}$$

$$= 0, x' > V''t' \tag{22}$$

where $V'' = 1/[1 + 1/C]$. This limiting process is singular at $x' = V''t'$ (although all initial-boundary conditions, (17–19), are enforceable), since the solution exhibits a jump there. This jump obviously renders the omission of the second-order derivative unjustifiable in the neighborhood of $x' = V''t'$. In the language of modern formalism of singular perturbation, this is exactly the outer limit of the problem; therefore, a superscript o is added to $T_{(0)}$.

Physically, the outer limit as shown by equations (21) and (22) represents a moving front carrying the full amount of temperature jump (from the initial value to the applied value of $x = 0$). The front is seen to propagate at a dimensionless speed V'', or a *dimensional* speed

$$V^* = VV'' = V\Big/\left[1 + \frac{\rho_2 c_2 (b^2 - a^2)}{\rho_1 c_1 a^2}\right] \tag{23}$$

Relative to the flow speed V, this propagational speed is seen to be slower. Furthermore, since

$$\frac{\rho_2 c_2 (b^2 - a^2)}{\rho_1 c_1 a^2} = \frac{\text{(heat capacity of solid per unit length)}}{\text{(heat capacity of fluid per unit length)}} \tag{24}$$

[3] This conclusion holds also for other types of the boundary condition at $x' = 1$, as long as it is the same for both θ and T.

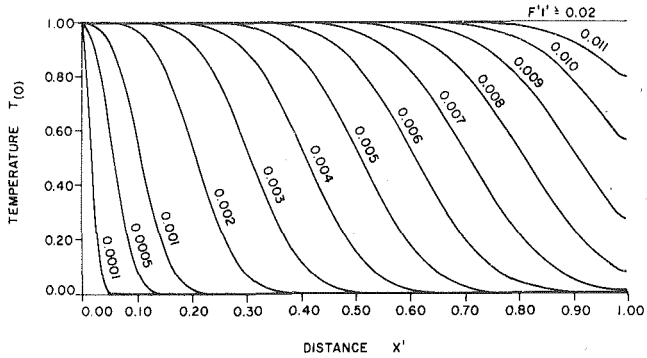

Fig. 1 Evolution of temperature for $V''/F' = 100$

is the ratio of the (thermal) storage capabilities of the solid to the fluid, the delay of the arrival of the front is physically due to the fact that the pipe wall must store up (thermal) energy first. If the pipe could not store any energy, V^* would be the same as V, and the front would arrive together with the fluid stream. On the other hand, should the storing capability of the solid phase be enormous, $V^* \to 0$; and the delay would be very dramatic. We have thus substantiated Munk's conclusions in a direct and unambiguous manner, for small F and large b_1'.

The Inner Limit

To remedy the singularity (at $x' = V''t'$) involved in $T_{(0)}{}^o$, we must "magnify" the narrow region around $x' = V''t'$ so that the second-order derivative in equation (15) is retained in letting $F \to 0$. To this end, we first transform the independent variables from (x', t') to (ζ, τ) where $\zeta = x' - V''t'$, and $\tau = t'$. Equation (2) then becomes

$$\frac{\partial T_{(0)}}{\partial \tau} = F' \frac{\partial^2 T_{(0)}}{\partial \zeta^2} \tag{25}$$

where $F' = (A + C)F/(1 + C)$. Now, introducing $\zeta' = \zeta/\sqrt{F'}$, and letting $F' \to 0$ while holding ζ' constant, equation (25) reduces to

$$\frac{\partial T_{(0)}{}^i}{\partial \tau} = \frac{\partial^2 T_{(0)}{}^i}{\partial \zeta'^2} \tag{26}$$

where superscript i is introduced to indicate that this result is the inner limit of $T_{(0)}$. The matching principle ([3]) demands that $T_{(0)}{}^i$ match with $T_{(0)}{}^o$ as expressed by equations (21) and (22), respectively, as $\zeta' \to -\infty$ and $+\infty$. The classical solution here is

$$T_{(0)}{}^i = \frac{1}{2}\operatorname{erfc}\left(\frac{\zeta'}{2\sqrt{\tau}}\right), \quad -\infty < \zeta' < \infty \tag{27}$$

where the initial condition is also satisfied. In terms of a single diffusivity, equation (27) implies an equivalent value

$$\alpha^* = \alpha_1\left(\frac{A + C}{1 + C}\right) = \alpha_1\left[1 + \frac{k_2(b^2 - a^2)}{k_1 a^2}\right] \Big/ \left(1 + \frac{b_1'}{b_2'}\right) \tag{28}$$

exactly as reported in [2]. Physically, the inner limit softens the finite jump in $T_{(0)}{}^o$ around the moving front, as if a layer of heat conducting material with thermal diffusivity α^* were present. The thickness of the layer is small of order $\sqrt{F'}$. (From equation (27)), it is also seen that this layer thickens like $\sqrt{t}$.)

Thus, the propagation of the softening front along the *characteristic* of the problem, $x = V^*t$, is demonstrated. However, the instant of observation t must be small (or moderate) compared to L/V^*; otherwise, the front will be close to the exit $x = L$, and its interaction with the exit will have to be considered with the result that the front will no longer be recognizable.

Numerical Substantiation

Finally, Fig. 1 is offered as a numerical substantiation. The *exact* solution of equation (15), with initial-boundary conditions (17–19), is presented graphically for $V''/F' = 100$ on the basis of a generalized Fourier series expansion. The formation, propagation, and interaction with the exit of the front are clearly recognizable.

Conclusion

It has been demonstrated, both numerically and by perturbation, that the (almost) identical temperature for the fluid steam and the solid wall, with very fast thermal link between the two phases, evolves from its initial value in three stages. First, the suddenly applied new value at the entrance is diffused slightly in the flow direction. In the last stage, the evolving temperature profile reaches and interacts with the exit, and thereby raises the exit temperature at various rates. These two stages are there for all values of F (which is proportional to the thermal diffusivity of the fluid, and inversely proportional to the length of the flow passage, for any given flow speed). For smaller values of F, an intermediate stage appears in which the temperature profile assumes the form of a propagating front carrying a rather steep change of temperature from the initial value before to the new value after the front. The front diffuses forward and backward as it propagates.

As $F \to 0$, the front in the intermediate stage approaches a jump. This jump is then seen to propagate at a speed V^* expressed by equation (23), which is slow compared to the flow speed because of large heat capacity of the solid phase. The slight diffusion around this jump is effected through an equivalent diffusivity α^* as expressed in equation (28).

It is thus suggested that Munk's prediction and explanation [1] of the phenomenon of delayed hot water, although preliminary, are correct when viewed from the angle of fast interphase (thermal) link, long flow passage, and small (thermal) diffusivity. Together with the interpretation, based on massive blowing, by Comstock, et al. [2], we feel that the problem has now been completely covered.

References

1 Munk, W., "The Delayed Hot Water Problem," ASME JOURNAL OF APPLIED MECHANICS, Vol. 76, 1954, p. 193.

2 Comstock, C., Zargary, A., and Brock, J. E., "On the Delayed Hot Water Problem" ASME JOURNAL OF HEAT TRANSFER, Vol. 96, 1974, pp. 166–171.

3 Van Dyke, M., *Perturbation Methods in Fluid Mechanics*, Academic Press, New York, 1964.

Effect of Interstitial Fluid Heat Capacity on Regenerator Performance

I. L. Maclaine-cross[1]

Nomenclature

A = heat transfer surface area associated with h(m^2)
c_f, c_m = specific heat at constant pressure of fluid or matrix (J kg^{-1} K^{-1})
E_i = regenerator parameters $E_1 = h_1A_1\theta_1/(c_{f1}m_{n1}\ (1 + E_4))$, $E_2 = c_{f1}m_{n1}/(c_{f2}m_{n2})$, $E_3 = c_m m_m/(c_{f1}m_{n1})$ and $E_4 = h_1A_1/h_2A_2$
h = heat transfer coefficient (W m^{-2} K^{-1})
m_f, m_m = mass of interstitial fluid or of matrix (kg)
m_n = net fluid mass flow during period (kg)
T_1, T_2 = inlet fluid temperature for period one or two (K)
T_{1out} = bulk mean outlet temperature for period one (K)
v = mean velocity of fluid in matrix interstices or passages (m s^{-1})
x = distance from matrix fluid inlet in flow direction (m)
$\eta_1 = (T_{1out} - T_1)/(T_2 - T_1)$ temperature efficiency for period one
η_{1a} = η_1 calculated using literature approximations [1, 2]
η_{1e} = η_1 calculated using author's exact numerical solution
θ = time from beginning of period (s)
θ_1 = duration of period one (s)
$\mu = m_m/m_f$ ratio of matrix to interstitial fluid mass
$\sigma = c_m/c_f$ ratio of matrix to fluid specific heat

[1] University of New South Wales, Broken Hill, Australia.

Contributed by the Heat Transfer Division for publication in the JOURNAL OF HEAT TRANSFER. Manuscript received by The Heat Transfer Division September 5, 1979.

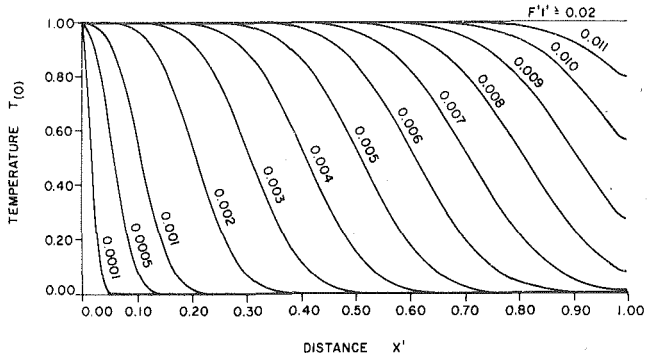

Fig. 1 Evolution of temperature for $V''/F' = 100$

is the ratio of the (thermal) storage capabilities of the solid to the fluid, the delay of the arrival of the front is physically due to the fact that the pipe wall must store up (thermal) energy first. If the pipe could not store any energy, V^* would be the same as V, and the front would arrive together with the fluid stream. On the other hand, should the storing capability of the solid phase be enormous, $V^* \to 0$; and the delay would be very dramatic. We have thus substantiated Munk's conclusions in a direct and unambiguous manner, for small F and large b_1'.

The Inner Limit

To remedy the singularity (at $x' = V''t'$) involved in $T_{(0)}{}^o$, we must "magnify" the narrow region around $x' = V''t'$ so that the second-order derivative in equation (15) is retained in letting $F \to 0$. To this end, we first transform the independent variables from (x', t') to (ζ, τ) where $\zeta = x' - V''t'$, and $\tau = t'$. Equation (2) then becomes

$$\frac{\partial T_{(0)}}{\partial \tau} = F' \frac{\partial^2 T_{(0)}}{\partial \zeta^2} \tag{25}$$

where $F' = (A + C)F/(1 + C)$. Now, introducing $\zeta' = \zeta/\sqrt{F'}$, and letting $F' \to 0$ while holding ζ' constant, equation (25) reduces to

$$\frac{\partial T_{(0)}{}^i}{\partial \tau} = \frac{\partial^2 T_{(0)}{}^i}{\partial \zeta'^2} \tag{26}$$

where superscript i is introduced to indicate that this result is the inner limit of $T_{(0)}$. The matching principle ([3]) demands that $T_{(0)}{}^i$ match with $T_{(0)}{}^o$ as expressed by equations (21) and (22), respectively, as $\zeta' \to -\infty$ and $+\infty$. The classical solution here is

$$T_{(0)}{}^i = \frac{1}{2}\,\mathrm{erfc}\left(\frac{\zeta'}{2\sqrt{\tau}}\right), \quad -\infty < \zeta' < \infty \tag{27}$$

where the initial condition is also satisfied. In terms of a single diffusivity, equation (27) implies an equivalent value

$$\alpha^* = \alpha_1 \left(\frac{A + C}{1 + C}\right) = \alpha_1 \left[1 + \frac{k_2(b^2 - a^2)}{k_1 a^2}\right] \Big/ \left(1 + \frac{b_1'}{b_2'}\right) \tag{28}$$

exactly as reported in [2]. Physically, the inner limit softens the finite jump in $T_{(0)}{}^o$ around the moving front, as if a layer of heat conducting material with thermal diffusivity α^* were present. The thickness of the layer is small of order $\sqrt{F'}$. (From equation (27)), it is also seen that this layer thickens like $\sqrt{t}$.)

Thus, the propagation of the softening front along the *characteristic* of the problem, $x = V^*t$, is demonstrated. However, the instant of observation t must be small (or moderate) compared to L/V^*; otherwise, the front will be close to the exit $x = L$, and its interaction with the exit will have to be considered with the result that the front will no longer be recognizable.

Numerical Substantiation

Finally, Fig. 1 is offered as a numerical substantiation. The *exact* solution of equation (15), with initial-boundary conditions (17–19), is presented graphically for $V''/F' = 100$ on the basis of a generalized Fourier series expansion. The formation, propagation, and interaction with the exit of the front are clearly recognizable.

Conclusion

It has been demonstrated, both numerically and by perturbation, that the (almost) identical temperature for the fluid steam and the solid wall, with very fast thermal link between the two phases, evolves from its initial value in three stages. First, the suddenly applied new value at the entrance is diffused slightly in the flow direction. In the last stage, the evolving temperature profile reaches and interacts with the exit, and thereby raises the exit temperature at various rates. These two stages are there for all values of F (which is proportional to the thermal diffusivity of the fluid, and inversely proportional to the length of the flow passage, for any given flow speed). For smaller values of F, an intermediate stage appears in which the temperature profile assumes the form of a propagating front carrying a rather steep change of temperature from the initial value before to the new value after the front. The front diffuses forward and backward as it propagates.

As $F \to 0$, the front in the intermediate stage approaches a jump. This jump is then seen to propagate at a speed V^* expressed by equation (23), which is slow compared to the flow speed because of large heat capacity of the solid phase. The slight diffusion around this jump is effected through an equivalent diffusivity α^* as expressed in equation (28).

It is thus suggested that Munk's prediction and explanation [1] of the phenomenon of delayed hot water, although preliminary, are correct when viewed from the angle of fast interphase (thermal) link, long flow passage, and small (thermal) diffusivity. Together with the interpretation, based on massive blowing, by Comstock, et al. [2], we feel that the problem has now been completely covered.

References

1 Munk, W., "The Delayed Hot Water Problem," ASME JOURNAL OF APPLIED MECHANICS, Vol. 76, 1954, p. 193.

2 Comstock, C., Zargary, A., and Brock, J. E., "On the Delayed Hot Water Problem" ASME JOURNAL OF HEAT TRANSFER, Vol. 96, 1974, pp. 166–171.

3 Van Dyke, M., *Perturbation Methods in Fluid Mechanics*, Academic Press, New York, 1964.

Effect of Interstitial Fluid Heat Capacity on Regenerator Performance

I. L. Maclaine-cross[1]

Nomenclature

A = heat transfer surface area associated with h(m^2)
c_f, c_m = specific heat at constant pressure of fluid or matrix (J kg^{-1} K^{-1})
E_i = regenerator parameters $E_1 = h_1A_1\theta_1/(c_{f1}m_{n1}\,(1 + E_4))$, $E_2 = c_{f1}m_{n1}/(c_{f2}m_{n2})$, $E_3 = c_m m_m/(c_{f1}m_{n1})$ and $E_4 = h_1A_1/h_2A_2$
h = heat transfer coefficient (W m^{-2} K^{-1})
m_f, m_m = mass of interstitial fluid or of matrix (kg)
m_n = net fluid mass flow during period (kg)
T_1, T_2 = inlet fluid temperature for period one or two (K)
T_{1out} = bulk mean outlet temperature for period one (K)
v = mean velocity of fluid in matrix interstices or passages (m s^{-1})
x = distance from matrix fluid inlet in flow direction (m)
$\eta_1 = (T_{1out} - T_1)/(T_2 - T_1)$ temperature efficiency for period one
η_{1a} = η_1 calculated using literature approximations [1, 2]
η_{1e} = η_1 calculated using author's exact numerical solution
θ = time from beginning of period (s)
θ_1 = duration of period one (s)
$\mu = m_m/m_f$ ratio of matrix to interstitial fluid mass
$\sigma = c_m/c_f$ ratio of matrix to fluid specific heat

[1] University of New South Wales, Broken Hill, Australia.

Contributed by the Heat Transfer Division for publication in the JOURNAL OF HEAT TRANSFER. Manuscript received by The Heat Transfer Division September 5, 1979.

Subscripts

1 = period one
2 = period two
c = corrected for interstitial fluid heat capacity

1 Introduction

In sensible heat regenerators or regenerative heat exchangers, heat is transferred to a porous matrix from fluid flowing through its voids or interstices and later from the matrix to another interstitial fluid stream. This cycle consisting of two periods may be repeated indefinitely. The interstitial fluid remaining in the matrix at the end of a period will leave during the following period and is called carryover. The effect of carryover depends on interstitial fluid heat capacity. This effect is negligible if the ratio of matrix heat capacity to interstitial fluid heat capacity $\mu\sigma > 100$. However the analogy theory of combined heat and mass regenerators [1, 2] requires consideration of analogous sensible heat regenerators with $\mu\sigma < 100$. Even for sensible heat regenerators, very low values of $\mu\sigma$ may be used in the future. The author has estimated $\mu\sigma$ approximately two for the rock bed heat stores with liquid hydrocarbon heat transfer fluid recently proposed for solar thermal electric power stations [3].

Design tables and charts neglecting interstitial fluid heat capacity have been given by Kays and London [4] for effectiveness ϵ, which equals temperature efficiency η_1 here, as a function of the four dimensionless parameters E_1, E_2, E_3, E_4. Kays and London's symbols for these parameters are $N_{tu,0}$, $C_{\min}/C_{\max}$, $C_r/C_{\min}$ and $(hA)^*$, respectively. These tables and charts are based on finite difference solutions obtained by Lambertson [5] and later authors using Dusinberre's equations [6] which are accurate, reliable and efficient when properly applied [2].

Approximate corrections to these tables and charts for interstitial fluid heat capacity were derived by Maclaine-cross and Banks [1]. These corrections are equivalent to replacing uncorrected values of matrix specific heat c_m and matrix fluid heat transfer coefficient h wherever they occur in the dimensionless parameters by corrected values c_{mc}, h_c calculated using equations (1, 2)

$$c_{mc} = c_m(1 + \mu\sigma)/(\mu\sigma) \tag{1}$$

$$h_c = h(1 + \mu\sigma)/(\mu\sigma) \tag{2}$$

$(1 + \mu\sigma)/\mu\sigma$ is the ratio of matrix and interstitial fluid heat capacity to matrix heat capacity. Using a similar approximate argument to [1], Maclaine-cross [2] showed that greater accuracy could be expected using equations (1, 3)

$$h_c = h((1 + \mu\sigma)/(\mu\sigma))^2 \tag{3}$$

Finite difference solutions for the effect of interstitial fluid heat capacity have been obtained by Heggs and Carpenter [7]. Such solutions are considerably more complex than the use of Kays and London's [4] tables and charts with the parameters corrected using equations (1, 3). In some design problems interstitial fluid heat capacity is one of many effects for which Lambertson's model [5] must be corrected, making finite difference solutions very expensive. The interstitial fluid heat capacity effect adds an additional dimensionless parameter, $\mu\sigma$, making it impossible to cover the whole range of practical parameter values with a small number of tables or charts unless equations (1, 3) are used. Finite difference solutions may be used to investigate the range of validity of equations (1, 3). The charts and table of Heggs and Carpenter [7] cover only part of the practical range of parameters and for the part covered high accuracy is expected of equations (1, 3). Thus they are of limited use in investigating these equations.

The accuracy of equations (1, 3) for regenerator design will be tested here by comparison (Section 3) with a new finite difference solution (Section 2). In this comparison emphasis is placed on air conditioning regenerators.

2 A New Finite Difference Solution

The author's FORTRAN IV subroutine EFFSH uses Dusinberre's finite difference equations [6] and the Anzelius [8] transformed time variable, $\theta - x/v$, to calculate on a digital computer the temperature efficiency η_1 including the interstitial fluid heat capacity effect. All Lambertson's other assumptions [5] were assumed to apply. Fluid and matrix temperatures at the end of a period were assumed equal to those at the beginning of the next period. This assumption is conservative as conduction heat transfer between fluid and matrix during any interval of zero flow between periods improves the overall heat transfer.

A discontinuity in fluid temperature at the beginning of a period occurs because the outlet fluid temperature at the end of the previous period does not equal the inlet fluid temperature to the next. Half the fluid entering the inlet element at the beginning of a period in the author's finite difference grid came from the outlet of the previous period and half from the current period inlet. Thus, the inlet temperature to this grid element was chosen as the average of the fluid outlet temperature at the end of the previous period and the inlet temperature of the current period. This value minimized the error and maintained the second order accuracy of the finite difference method.

3 Comparison of Equations (1, 3) With Finite Difference Solutions

Air conditioning regenerators are mostly operated counterflow with

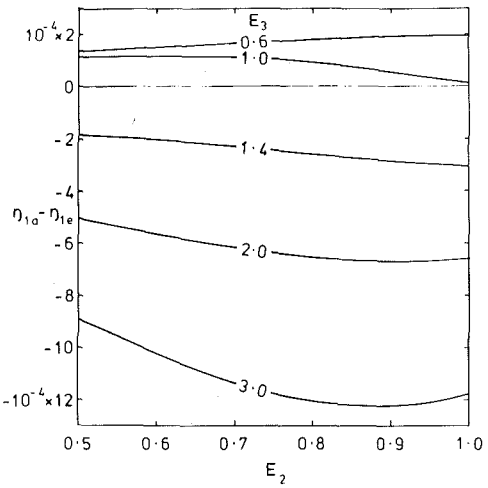

Fig. 1 Difference in temperature efficiency $\eta_{1a} - \eta_{1e}$ between two approximate solutions [1, 2] and the author's exact numerical solution including interstitial fluid heat capacity with $E_2 = E_4 = 1$

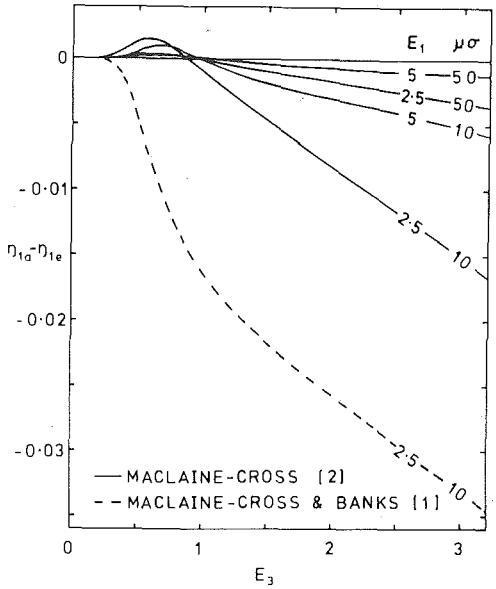

Fig. 2 Difference in temperature efficiency $\eta_{1a} - \eta_{1e}$ between an approximate solution [2] and the author's exact numerical solution including interstitial fluid heat capacity with $\mu\sigma = 50$, $E_4 = 1$ and $E_1 = 5$

Table 1 Temperature efficiency η_1 including interstitial fluid heat capacity

Dimensionless Parameters $E_2 = E_4 = 1$			Literature Solutions		Author's Solution	
E_1	E_3	$\mu\sigma$	η_{1a} [2]	η_1 [7]	η_{1e} EFFSH	Error in η_{1e} [2, p. 90]
2.5	1.0	10	0.6823	0.6735	0.683 237	1.1×10^{-5}
5.0	2.0	10	0.8373	0.8407	0.840 314	2.3×10^{-5}
10.0	1.0	1.25	0.9533	0.9526	0.954 780	2.4×10^{-5}

$E_1 > 2.5$, $0.5 < E_2 < 2$, $E_3 < 0.1\ \mu\sigma$ and $\mu\sigma > 10$. These conditions insure that regenerators have high temperature efficiency with minimum fan power and carryover within the mechanical and physical limitations of practical matrices. Usually $E_4 \simeq 1$ but its effect on performance is small [4, 5] so $E_4 = 1$ will be used here.

The solid lines in Fig. 1 are the difference between the temperature efficiency predicted by the approximate solution [2] using equations (1, 3), η_{1a}, and by the author's finite difference method (Section 2), η_{1e}. It may be seen that the magnitude of the difference $|\eta_{1a} - \eta_{1e}|$ decreases as E_1 increases from 2.5 or $\mu\sigma$ from 10 except for $E_3 \simeq 1$ where $|\eta_{1a} - \eta_{1e}|$ is very small. Also $|\eta_{1a} - \eta_{1e}|$ increases with E_3 for $E_3 > 1$. The condition that $E_3 < 0.1\ \mu\sigma$ limits E_3 to values where $|\eta_{1a} - \eta_{1e}|$ is less than 1 percent of η_{1e} for $E_1 > 2.5$ and $\mu\sigma > 10$. Figure 2 shows that $|\eta_{1a} - \eta_{1e}|$ is only slightly affected by E_2 for $0.5 < E_2 < 1$. With conservation of energy this may be used to show that the effect of E_2 is slight for $1 < E_2 < 2$ also. Thus for air conditioning regenerators the error in the temperature efficiency predicted by the approximate solution using equations (1, 3) is less than 1 percent.

For high performance air conditioning regenerators E_1 and E_3 may be further restricted to $E_1 > 5$ and $E_3 < 0.03\ \mu\sigma$. The above argument and figures then support the conclusion that the error in the approximate solution is less than 0.1 percent.

The conclusions in the previous two paragraphs are also supported by the author's results not given here. The approximate solution also agrees with Heggs and Carpenter [7] within their 2 percent accuracy (e.g., Table 1).

For rock bed heat stores with liquid heat transfer fluid, the operating parameter range is not yet clearly established. The minimum value of E_1 will be greater and maximum value of E_3 less than for air conditioning regenerators increasing the accuracy of the approximate solution. The minimum value of $\mu\sigma$ will be less, reducing the accuracy of the approximate solution. The third set in Table 1 shows possible parameter values for a low performance heat store for which the error in the approximate solution is less than 0.2 percent. This suggests that the accuracy is similar to that for air conditioning regenerators. Comparison with Heggs and Carpenter [7] supports this. Higher performance heat stores with higher E_1 and $\mu\sigma$ would be predicted with greater accuracy.

4 Conclusion

The effect of interstitial fluid heat capacity on regenerator performance is almost the same as the effect of an increase in matrix specific heat given by equation (1) together with an increase in heat transfer coefficient given by equation (3). Equations (1, 3) may be used to include the effect approximately in published tables and charts [2, 4, 5] which neglect it. For counterflow air conditioning regenerators with $E_1 > 2.5$, $0.5 < E_2 < 2$, $E_3 < 0.1\ \mu\sigma$, $E_4 \simeq 1$ and $\mu\sigma > 10$ the error in temperature efficiency using this approximate solution is less than 1 percent. For high performance counterflow air conditioning regenerators with $E_1 > 5$, $0.5 < E_2 < 2$, $E_3 < 0.03\ \mu\sigma$, $E_4 \simeq 1$ and $\mu\sigma > 10$ the error is less than 0.1 percent. For rock bed heat stores with liquid heat transfer fluid the error is expected to be similar to that for air conditioning regenerators.

References

1 Maclaine-cross, I. L., and Banks, P. J., "Coupled Heat and Mass Transfer in Regenerators-Prediction Using an Analogy with Heat Transfer," *International Journal of Heat and Mass Transfer*, Vol. 15, 1972, pp. 1225–1242.

2 Maclaine-cross, I. L. "A Theory of Combined Heat and Mass Transfer in Regenerators," Ph.D. thesis, Department of Mechanical Engineering, Monash University, Australia, 1974.

3 "Three Companies Compete in Designing 10-MW Pilot Plant," *Machine Design*, Vol. 49, No. 3, Feb. 10th 1977, pp. 30–32.

4 Kays, W. M., and London, A. L., *Compact Heat Exchangers*, 2nd ed. McGraw-Hill, New York, 1964.

5 Lambertson, T. J., "Performance Factors of a Periodic-Flow Heat Exchanger," *Trans ASME*, Vol. 80, 1958, pp. 586–592.

6 Dusinberre, G. M., *Trans ASME* Vol. 75, 1953, p. 785.

7 Heggs, P. J., and Carpenter, K. J., "The Effect of Fluid Hold-Up on the Effectiveness of Contraflow Regenerators," *Transactions of the Institution of Chemical Engineers*, Vol. 54, 1976, pp. 232–238.

8 Anzelius, A., "Über Erwärmung Vermittels Durchströmender Medien," *Zeitschrift für angewandte Mathematik und Mechanik*, Vol. 6, 1926, pp. 291–294.

Approximate Treatment of Transverse Conduction in Regenerators

F. E. Romie[1]

Nomenclature

a = thermal diffusivity of matrix material
A = heat transfer area of matrix
b = first zero of characteristic equation
Bi = Biot number, $h\Delta/k$
c = specific heat of gas
c_e = heat capacity per unit heat transfer area
C = specific heat of matrix material
Δ = dimension, defined in text
G = conductance factor, equation (4)
h = convective conductance per unit area
h_i = conductive conductance per unit area
k = thermal conductivity of matrix material
K = constant, defined following equation (6)
r = radius
t = time
t_a = regenerator blow period for gas a
T_s = surface temperature
w = mass rate of gas
W = mass of matrix

Introduction

Most numerical descriptions [1–4] of regenerator operation are obtained from analyses which incorporate the idealization that the thermal conductivity of the regenerator solid is infinite in the direction transverse to the fluid flows. An approximate method of accounting for finite transverse conductivity has been presented by Hausen [5]; and several authors [6–8] have written finite difference computer programs which describe regenerator operation with transverse conduction.

The purpose of this note is to present a simple method of approximating the effects of transverse conduction and to indicate the conditions for which the method should be applicable with good accuracy.

Analysis

The usual idealizations used in regenerator analyses include, in addition to infinite transverse thermal conductivity, zero axial thermal conduction in the matrix composing the regenerator. Consequently,

[1] Palos Verdes Estates, Calif. 90274.

Contributed by The Heat Transfer Division for publication in the JOURNAL OF HEAT TRANSFER. Manuscript received by the Heat Transfer Division August 25, 1979.

Table 1 Temperature efficiency η_1 including interstitial fluid heat capacity

Dimensionless Parameters $E_2 = E_4 = 1$			Literature Solutions		Author's Solution	
E_1	E_3	$\mu\sigma$	η_{1a} [2]	η_1 [7]	η_{1e} EFFSH	Error in η_{1e} [2, p. 90]
2.5	1.0	10	0.6823	0.6735	0.683 237	1.1×10^{-5}
5.0	2.0	10	0.8373	0.8407	0.840 314	2.3×10^{-5}
10.0	1.0	1.25	0.9533	0.9526	0.954 780	2.4×10^{-5}

$E_1 > 2.5$, $0.5 < E_2 < 2$, $E_3 < 0.1\ \mu\sigma$ and $\mu\sigma > 10$. These conditions insure that regenerators have high temperature efficiency with minimum fan power and carryover within the mechanical and physical limitations of practical matrices. Usually $E_4 \simeq 1$ but its effect on performance is small [4, 5] so $E_4 = 1$ will be used here.

The solid lines in Fig. 1 are the difference between the temperature efficiency predicted by the approximate solution [2] using equations (1, 3), η_{1a}, and by the author's finite difference method (Section 2), η_{1e}. It may be seen that the magnitude of the difference $|\eta_{1a} - \eta_{1e}|$ decreases as E_1 increases from 2.5 or $\mu\sigma$ from 10 except for $E_3 \simeq 1$ where $|\eta_{1a} - \eta_{1e}|$ is very small. Also $|\eta_{1a} - \eta_{1e}|$ increases with E_3 for $E_3 > 1$. The condition that $E_3 < 0.1\ \mu\sigma$ limits E_3 to values where $|\eta_{1a} - \eta_{1e}|$ is less than 1 percent of η_{1e} for $E_1 > 2.5$ and $\mu\sigma > 10$. Figure 2 shows that $|\eta_{1a} - \eta_{1e}|$ is only slightly affected by E_2 for $0.5 < E_2 < 1$. With conservation of energy this may be used to show that the effect of E_2 is slight for $1 < E_2 < 2$ also. Thus for air conditioning regenerators the error in the temperature efficiency predicted by the approximate solution using equations (1, 3) is less than 1 percent.

For high performance air conditioning regenerators E_1 and E_3 may be further restricted to $E_1 > 5$ and $E_3 < 0.03\ \mu\sigma$. The above argument and figures then support the conclusion that the error in the approximate solution is less than 0.1 percent.

The conclusions in the previous two paragraphs are also supported by the author's results not given here. The approximate solution also agrees with Heggs and Carpenter [7] within their 2 percent accuracy (e.g., Table 1).

For rock bed heat stores with liquid heat transfer fluid, the operating parameter range is not yet clearly established. The minimum value of E_1 will be greater and maximum value of E_3 less than for air conditioning regenerators increasing the accuracy of the approximate solution. The minimum value of $\mu\sigma$ will be less, reducing the accuracy of the approximate solution. The third set in Table 1 shows possible parameter values for a low performance heat store for which the error in the approximate solution is less than 0.2 percent. This suggests that the accuracy is similar to that for air conditioning regenerators. Comparison with Heggs and Carpenter [7] supports this. Higher performance heat stores with higher E_1 and $\mu\sigma$ would be predicted with greater accuracy.

4 Conclusion

The effect of interstitial fluid heat capacity on regenerator performance is almost the same as the effect of an increase in matrix specific heat given by equation (1) together with an increase in heat transfer coefficient given by equation (3). Equations (1, 3) may be used to include the effect approximately in published tables and charts [2, 4, 5] which neglect it. For counterflow air conditioning regenerators with $E_1 > 2.5$, $0.5 < E_2 < 2$, $E_3 < 0.1\ \mu\sigma$, $E_4 \simeq 1$ and $\mu\sigma > 10$ the error in temperature efficiency using this approximate solution is less than 1 percent. For high performance counterflow air conditioning regenerators with $E_1 > 5$, $0.5 < E_2 < 2$, $E_3 < 0.03\ \mu\sigma$, $E_4 \simeq 1$ and $\mu\sigma > 10$ the error is less than 0.1 percent. For rock bed heat stores with liquid heat transfer fluid the error is expected to be similar to that for air conditioning regenerators.

References

1 Maclaine-cross, I. L., and Banks, P. J., "Coupled Heat and Mass Transfer in Regenerators-Prediction Using an Analogy with Heat Transfer," *International Journal of Heat and Mass Transfer*, Vol. 15, 1972, pp. 1225–1242.

2 Maclaine-cross, I. L. "A Theory of Combined Heat and Mass Transfer in Regenerators," Ph.D. thesis, Department of Mechanical Engineering, Monash University, Australia, 1974.

3 "Three Companies Compete in Designing 10-MW Pilot Plant," *Machine Design*, Vol. 49, No. 3, Feb. 10th 1977, pp. 30–32.

4 Kays, W. M., and London, A. L., *Compact Heat Exchangers*, 2nd ed. McGraw-Hill, New York, 1964.

5 Lambertson, T. J., "Performance Factors of a Periodic-Flow Heat Exchanger," *Trans ASME*, Vol. 80, 1958, pp. 586–592.

6 Dusinberre, G. M., *Trans ASME* Vol. 75, 1953, p. 785.

7 Heggs, P. J., and Carpenter, K. J., "The Effect of Fluid Hold-Up on the Effectiveness of Contraflow Regenerators," *Transactions of the Institution of Chemical Engineers*, Vol. 54, 1976, pp. 232–238.

8 Anzelius, A., "Über Erwärmung Vermittels Durchströmender Medien," *Zeitschrift für angewandte Mathematik und Mechanik*, Vol. 6, 1926, pp. 291–294.

Approximate Treatment of Transverse Conduction in Regenerators

F. E. Romie[1]

Nomenclature

a = thermal diffusivity of matrix material
A = heat transfer area of matrix
b = first zero of characteristic equation
Bi = Biot number, $h\Delta/k$
c = specific heat of gas
c_e = heat capacity per unit heat transfer area
C = specific heat of matrix material
Δ = dimension, defined in text
G = conductance factor, equation (4)
h = convective conductance per unit area
h_i = conductive conductance per unit area
k = thermal conductivity of matrix material
K = constant, defined following equation (6)
r = radius
t = time
t_a = regenerator blow period for gas a
T_s = surface temperature
w = mass rate of gas
W = mass of matrix

Introduction

Most numerical descriptions [1–4] of regenerator operation are obtained from analyses which incorporate the idealization that the thermal conductivity of the regenerator solid is infinite in the direction transverse to the fluid flows. An approximate method of accounting for finite transverse conductivity has been presented by Hausen [5]; and several authors [6–8] have written finite difference computer programs which describe regenerator operation with transverse conduction.

The purpose of this note is to present a simple method of approximating the effects of transverse conduction and to indicate the conditions for which the method should be applicable with good accuracy.

Analysis

The usual idealizations used in regenerator analyses include, in addition to infinite transverse thermal conductivity, zero axial thermal conduction in the matrix composing the regenerator. Consequently,

[1] Palos Verdes Estates, Calif. 90274.

Contributed by The Heat Transfer Division for publication in the JOURNAL OF HEAT TRANSFER. Manuscript received by the Heat Transfer Division August 25, 1979.

an elemental length of a matrix element can be treated as a thermal capacitor connected through a constant and uniform convective resistance, $1/h$, to the varying gas temperature. If a single internal resistance, $1/h_i$, is assigned to the capacitor then the surface temperature response to a unit step change in gas temperature is

$$Ts = \frac{h_i}{h + h_i} \exp\left(\frac{-thh_i}{c_e(h + h_i)}\right) \tag{1}$$

in which c_e is the thermal capacity of the element per unit heat transfer area.

Transient surface temperature responses to a unit step change in fluid temperature are well known [9, 10] for several simple geometries and are given in series form. The first term of the series solution which gives the surface temperature response of a slab to a unit step change in fluid temperature is

$$T_s = \frac{2 \sin b \cos b}{b + \sin b \cos b} \exp\left(-b^2 \frac{at}{\Delta^2}\right) \tag{2}$$

in which b is the first zero of the characteristic equation $h\Delta/k - b \tan b = 0$ and Δ is the half thickness of the slab. This first term adequately describes the surface temperature response when the Biot number, $h\Delta/k$, is not large and the exponential function is somewhat less than unity. Therefore, as a first approximation to transverse conduction in the element, the factors of the exponential functions in equations (1) and (2) can be equated to obtain, for the slab,

$$G = \frac{2 \sin b \cos b}{b + \sin b \cos b} \tag{3}$$

where G in a conductance factor defined, for all geometries, by the equation

$$G = \frac{h_i}{h + h_i} \tag{4}$$

When the factors of equations (1) and (2) are equated, the absolute value of the argument of the exponential function in equation (1) is smaller than that of equation (2) by less than 5 percent for a Biot number of 2, by less than 1.6 percent for Bi = 1 and by less than ½ percent for Bi = 0.5. The effect of this lack of equality is small and will be ignored.

The product of G and the convective conductance per unit area, h, is

$$Gh = \left(\frac{1}{h} + \frac{1}{h_i}\right)^{-1} \tag{5}$$

and this product can be used, subject to conditions to be discussed, in place of h alone to approximate the effect of transverse conduction in the regenerator.

Figure 1 shows the factor G as a function of the Biot number for the slab, cylinder, sphere, and tube thermally insulated on its external surface. The dimension, Δ, is the half thickness of the slab (exposed on both surfaces to the fluid), the radius of the cylinder, the radius of the sphere, and the tube wall thickness. The curve shown for the tube is for an outer radius to inner radius ratio of three. The curve for the slab applies to the tube with a radius ratio of unity. The value of G for tubes with intermediate values of the radius ratio can be found by interpolation between the two curves.

In a regenerator two gases, which enter at constant but different temperatures, flow sequentially and counter-currently through the same flow passages for time periods t_a and t_b. In the following discussion it is assumed, for simplicity, that the flow periods are equal.

Use of the factor G requires that the Fourier number, at_a/Δ^2, be sufficiently large. This requirement is illustrated by the curves on Fig. 2 which show the steady periodic surface temperature responses of a slab element exposed, as an approximation to conditions in the matrix, to a square wave variation of gas temperature. The surface temperature responses are shown during the trough of the wave (e.g., during the flow period, t_a) and for a Biot number of 0.7.

In both panels of Fig. 2, the top curve is the response that would obtain with zero internal resistance; the bottom curve is the response

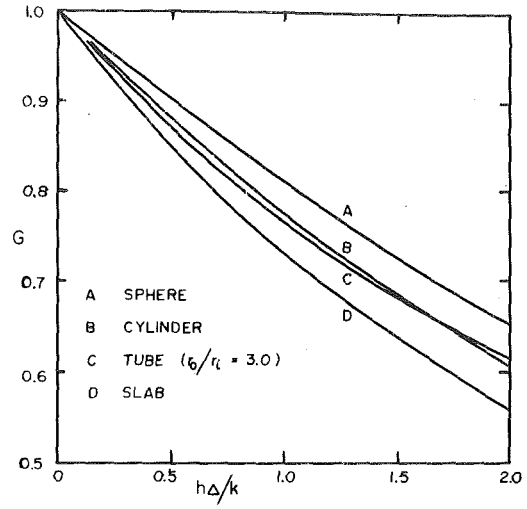

Fig. 1 The conductance factor G as a function of the Biot number

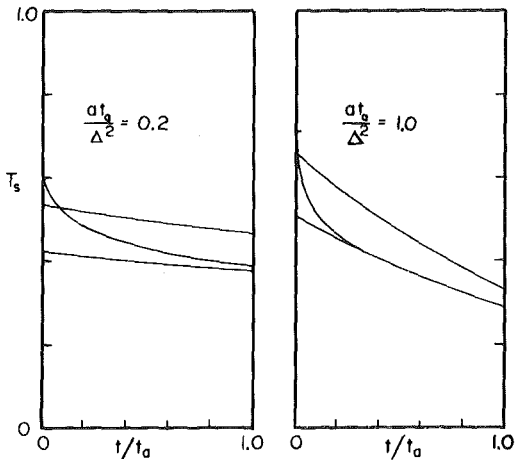

Fig. 2 Square wave responses of the surface temperature of a slab for two values of the Fourier number. The Biot number is 0.7 for both panels.

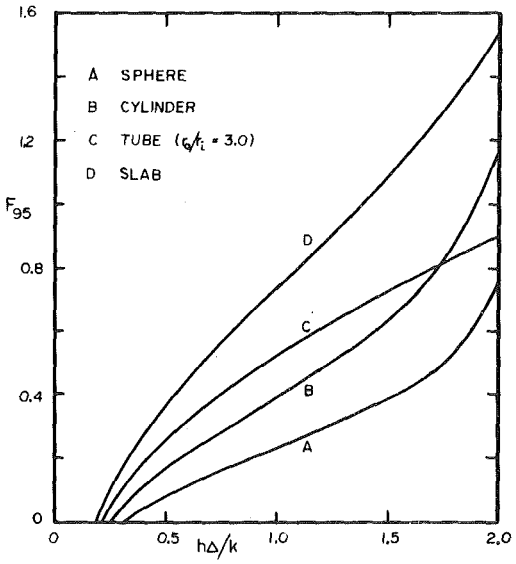

Fig. 3 The value of F_{95} as a function of the Biot number

with a single internal resistance (selected in accordance with Fig. 1); and the central curve is the actual response calculated for distributed resistance and capacitance. It will be observed that the curve for the single internal resistance approximates the actual temperature response with increasing accuracy as the Fourier number increases.

The area under each curve in a panel of Fig. 2 is proportional to the heat transfered from the slab to the gas. Figure 3 shows the Fourier

number, F_{95}, for which the area under the single internal resistance curve is 95 percent of the area under the distributed resistance-capacitance curve. The larger the value of at_a/Δ^2, the better will be the accuracy in the use of the factor G. Figure 3 can be used to give a reference value against which the "largeness" of the Fourier number can be established.

The use of a square-wave variation of gas temperature represents a simple condition for determining a value for F_{95}. However, the information given Fig. 1 is not dependent on the shape assumed for the gas temperature variation. When the operating parameters of the regenerator are asymmetric (e.g., $t_a \neq t_b$, $h_a \neq h_b$) it seems reasonable, in the absence of further analysis, to determine values of G_a and G_b independently. Specifically, using Fig. 1, $G_a = f(h_a\Delta/k)$ and $G_b = f(h_b\Delta/k)$. Thus, h_a would be replaced by $G_a h_a$ and h_b by $G_b h_b$. The test for applicability (Fig. 3) of the conductance factors can also be carried out independently.

The Fourier number, at_a/Δ^2, can be expressed in terms of regenerator parameters by the equation

$$\frac{at_a}{\Delta^2} = \frac{K}{\mathrm{Bi}}\left[\left(\frac{hA}{wc}\right)\left(\frac{wct}{WC}\right)\right]_a \tag{6}$$

The constant, K, is 1.0 for the slab, ½ for the cylinder, ⅓ for the sphere and $(r_0/r_i + 1)/2$ for the tube. The terms within brackets are regenerator parameters used in [1] and can be readily deduced from nomenclatures used in other sources.

References

1 Romie, F. E., "Periodic Thermal Storage: The Regenerator," ASME JOURNAL OF HEAT TRANSFER, Vol. 101, 1979, pp. 726–731.

2 Kays, W. M., and London, A. L., *Compact Heat Exchangers,* 2nd Edition, McGraw-Hill, New York, 1964, pp. 44–49.

3 Lambertson, T. J., "Performance Factors of a Periodic-flow Heat Exchanger," *Trans. ASME,* Vol. 80, 1958, pp. 586–592.

4 Mondt, J. R., "Vehicular Gas Turbine Periodic-flow Heat Exchanger Solid and Fluid Temperature Distributions," ASME *Journal of Engineering for Power,* Vol. 86, 1964, pp. 121–126.

5 Hausen, H., "Survey of the Heat Transfer Theories in Regenerators," *Heat Exchangers: Design and Theory Source Book,* McGraw-Hill, New York, 1974, pp. 207–222.

6 Willmott, A. J., "Developments in Regenerator Theory Since the Advent of the Digital Computer," *Heat Exchangers: Design and Theory Source Book,* McGraw-Hill, New York, 1974, pp. 223–237.

7 Reihman, T. C., Townes, H. W., and Mozer, C. J., "Thermal Analysis Techniques for Regenerative Heat Exchanger Simulation," ASME Paper No. 76-WA/HT-7.

8 Edwards, J. V., Evans, R., Probert, S. D., "Computation of Transient Temperatures in Regenerators," *International Journal of Heat and Mass Transfer,* Vol. 14, 1971, pp. 1175–1202.

9 Jacob, M., *Heat Transfer,* Vol. 1, 1st Ed., John Wiley and Sons, New York, 1949, pp. 270–280.

10 Carslaw, H. S., and Jaeger, J. C., *Conduction of Heat in Solids,* 2nd ed., Oxford Clarendon Press, 1959, pp. 332–334.

An Instrument for the Measurement of Heat Flux from a Surface with Uniform Temperature

J. S. Kraabel,[1] J. W. Baughn,[2] and A. A. McKillop[2]

Nomenclature

A = surface area
C_e = thermal conductance
E = voltage
h = heat transfer coefficient
I = current
Nu = Nusselt number
P = power
q = heat rate
q'' = heat flux
Re = Reynolds number
R = resistance
T = temperature
x_i = general independent variable
ϵ = emissivity
θ = circumferential angle
σ = Stefan-Boltzmann constant

Subscripts

aw = adiabatic wall
c = convective heat rate loss
lw = leadwire
o = stagnation point
rad = radiation
s = sensor
w = wall
∞ = free stream

Introduction

The design and testing of a low convective heat flux instrument is described. An error analysis shows that convective heat fluxes measured with this instrument have an uncertainty of ±2 percent in the range of 420–1670 W/m^2. Measurements of the heat transfer from a heated cylinder in normal air flow showed a circumferential Nusselt number distribution which agrees well with other data.

In many heat transfer experiments it is desirable to measure local heat fluxes from a surface with a uniform temperature. An instrument for this purpose may alter the local surface temperature and thereby change the rate of heat transfer. The instrument described in this paper has the following characteristics (see reference [1] for more details): preservation of a nearly isothermal surface and minimal perturbation of the local convective heat transfer, small surface area, flush mounted with the surface, and an accuracy of ±2 percent for low heat flux measurements.

Descriptions of many heat flux sensors appear in the literature. For example, the Gardon gage [2, 3] makes use of a circular foil in which the temperature difference between the center and the edge of the foil is measured. For high sensitivity with this gage it is necessary to make it very thin. Newman, et al., [4] developed such a thin Gardon gage for measurement of convective heat transfer from a sphere at low heat fluxes. He did not calibrate his instrument, but instead presented his results in the form of the ratio $(\mathrm{Nu}/\mathrm{Re}^{1/2})/(\mathrm{Nu}/\mathrm{Re}^{1/2})_0$.

In the paper by Achenbach [5] a sensor is described which is conceptually similar to the design discussed in this paper. The sensor consists of a copper plug which is thermally insulated from the surrounding cylinder wall and is separately heated, thereby permitting nearly isothermal conditions to prevail. Unfortunately, details of that design and an error analysis are not presented. Unlike the instrument described herein, Achenbach separately measures the temperature of the sensor and of the surrounding wall. The heater power of the sensor is then adjusted until isothermal wall conditions, as determined by these separate readings, are obtained. A small error in either or both thermocouples, therefore, can result in a larger error in the difference between the two surface temperatures, a serious problem for low heat flux measurements. This problem is surmounted in the present instrument by making a differential temperature measurement between the sensor and the wall. Another point of concern is Achenbach's measured value of $\mathrm{Nu}/\mathrm{Re}^{1/2}$ at the forward stagnation point; this was at least 6 percent higher than the theoretical value by Frossling [6]. Achenbach does not discuss this discrepancy nor state the conditions (turbulence level and cylinder to air temperature difference) for the results shown in his figures.

Design and Operation of Sensor

A diagram of our sensor is shown in Fig. 1. It is a copper cone em-

[1] Sandia Laboratories, Livermore, Calif.

[2] Department of Mechanical Engineering, University of California, Davis, Calif. 95616

Contributed by the Heat Transfer Division for publication in the JOURNAL OF HEAT TRANSFER. Manuscript received by the Heat Transfer Division May 2, 1979.

number, F_{95}, for which the area under the single internal resistance curve is 95 percent of the area under the distributed resistance-capacitance curve. The larger the value of at_a/Δ^2, the better will be the accuracy in the use of the factor G. Figure 3 can be used to give a reference value against which the "largeness" of the Fourier number can be established.

The use of a square-wave variation of gas temperature represents a simple condition for determining a value for F_{95}. However, the information given Fig. 1 is not dependent on the shape assumed for the gas temperature variation. When the operating parameters of the regenerator are asymmetric (e.g., $t_a \neq t_b$, $h_a \neq h_b$) it seems reasonable, in the absence of further analysis, to determine values of G_a and G_b independently. Specifically, using Fig. 1, $G_a = f(h_a\Delta/k)$ and $G_b = f(h_b\Delta/k)$. Thus, h_a would be replaced by $G_a h_a$ and h_b by $G_b h_b$. The test for applicability (Fig. 3) of the conductance factors can also be carried out independently.

The Fourier number, at_a/Δ^2, can be expressed in terms of regenerator parameters by the equation

$$\frac{at_a}{\Delta^2} = \frac{K}{\mathrm{Bi}}\left[\left(\frac{hA}{wc}\right)\left(\frac{wct}{WC}\right)\right]_a \tag{6}$$

The constant, K, is 1.0 for the slab, ½ for the cylinder, ⅓ for the sphere and $(r_0/r_i + 1)/2$ for the tube. The terms within brackets are regenerator parameters used in [1] and can be readily deduced from nomenclatures used in other sources.

References

1 Romie, F. E., "Periodic Thermal Storage: The Regenerator," ASME JOURNAL OF HEAT TRANSFER, Vol. 101, 1979, pp. 726–731.

2 Kays, W. M., and London, A. L., *Compact Heat Exchangers,* 2nd Edition, McGraw-Hill, New York, 1964, pp. 44–49.

3 Lambertson, T. J., "Performance Factors of a Periodic-flow Heat Exchanger," *Trans. ASME,* Vol. 80, 1958, pp. 586–592.

4 Mondt, J. R., "Vehicular Gas Turbine Periodic-flow Heat Exchanger Solid and Fluid Temperature Distributions," ASME *Journal of Engineering for Power,* Vol. 86, 1964, pp. 121–126.

5 Hausen, H., "Survey of the Heat Transfer Theories in Regenerators," *Heat Exchangers: Design and Theory Source Book,* McGraw-Hill, New York, 1974, pp. 207–222.

6 Willmott, A. J., "Developments in Regenerator Theory Since the Advent of the Digital Computer," *Heat Exchangers: Design and Theory Source Book,* McGraw-Hill, New York, 1974, pp. 223–237.

7 Reihman, T. C., Townes, H. W., and Mozer, C. J., "Thermal Analysis Techniques for Regenerative Heat Exchanger Simulation," ASME Paper No. 76-WA/HT-7.

8 Edwards, J. V., Evans, R., Probert, S. D., "Computation of Transient Temperatures in Regenerators," *International Journal of Heat and Mass Transfer,* Vol. 14, 1971, pp. 1175–1202.

9 Jacob, M., *Heat Transfer,* Vol. 1, 1st Ed., John Wiley and Sons, New York, 1949, pp. 270–280.

10 Carslaw, H. S., and Jaeger, J. C., *Conduction of Heat in Solids,* 2nd ed., Oxford Clarendon Press, 1959, pp. 332–334.

An Instrument for the Measurement of Heat Flux from a Surface with Uniform Temperature

J. S. Kraabel,[1] J. W. Baughn,[2] and A. A. McKillop[2]

Nomenclature

A = surface area
C_e = thermal conductance
E = voltage
h = heat transfer coefficient
I = current
Nu = Nusselt number
P = power
q = heat rate
q'' = heat flux
Re = Reynolds number
R = resistance
T = temperature
x_i = general independent variable
ϵ = emissivity
θ = circumferential angle
σ = Stefan-Boltzmann constant

Subscripts

aw = adiabatic wall
c = convective heat rate loss
lw = leadwire
o = stagnation point
rad = radiation
s = sensor
w = wall
∞ = free stream

Introduction

The design and testing of a low convective heat flux instrument is described. An error analysis shows that convective heat fluxes measured with this instrument have an uncertainty of ±2 percent in the range of 420–1670 W/m^2. Measurements of the heat transfer from a heated cylinder in normal air flow showed a circumferential Nusselt number distribution which agrees well with other data.

In many heat transfer experiments it is desirable to measure local heat fluxes from a surface with a uniform temperature. An instrument for this purpose may alter the local surface temperature and thereby change the rate of heat transfer. The instrument described in this paper has the following characteristics (see reference [1] for more details): preservation of a nearly isothermal surface and minimal perturbation of the local convective heat transfer, small surface area, flush mounted with the surface, and an accuracy of ±2 percent for low heat flux measurements.

Descriptions of many heat flux sensors appear in the literature. For example, the Gardon gage [2, 3] makes use of a circular foil in which the temperature difference between the center and the edge of the foil is measured. For high sensitivity with this gage it is necessary to make it very thin. Newman, et al., [4] developed such a thin Gardon gage for measurement of convective heat transfer from a sphere at low heat fluxes. He did not calibrate his instrument, but instead presented his results in the form of the ratio $(\mathrm{Nu}/\mathrm{Re}^{1/2})/(\mathrm{Nu}/\mathrm{Re}^{1/2})_0$.

In the paper by Achenbach [5] a sensor is described which is conceptually similar to the design discussed in this paper. The sensor consists of a copper plug which is thermally insulated from the surrounding cylinder wall and is separately heated, thereby permitting nearly isothermal conditions to prevail. Unfortunately, details of that design and an error analysis are not presented. Unlike the instrument described herein, Achenbach separately measures the temperature of the sensor and of the surrounding wall. The heater power of the sensor is then adjusted until isothermal wall conditions, as determined by these separate readings, are obtained. A small error in either or both thermocouples, therefore, can result in a larger error in the difference between the two surface temperatures, a serious problem for low heat flux measurements. This problem is surmounted in the present instrument by making a differential temperature measurement between the sensor and the wall. Another point of concern is Achenbach's measured value of $\mathrm{Nu}/\mathrm{Re}^{1/2}$ at the forward stagnation point; this was at least 6 percent higher than the theoretical value by Frossling [6]. Achenbach does not discuss this discrepancy nor state the conditions (turbulence level and cylinder to air temperature difference) for the results shown in his figures.

Design and Operation of Sensor

A diagram of our sensor is shown in Fig. 1. It is a copper cone em-

[1] Sandia Laboratories, Livermore, Calif.

[2] Department of Mechanical Engineering, University of California, Davis, Calif. 95616

Contributed by the Heat Transfer Division for publication in the JOURNAL OF HEAT TRANSFER. Manuscript received by the Heat Transfer Division May 2, 1979.

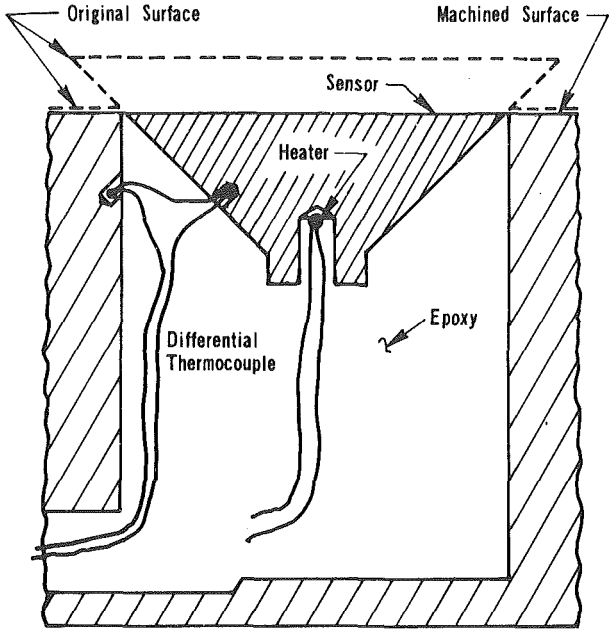

Fig. 1 Diagram of the neat flux sensor

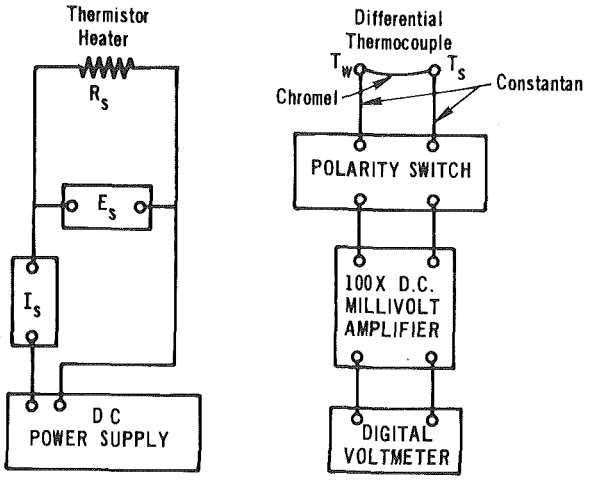

Fig. 2 Sensor instrumentation diagram

bedded in, but insulated from, the heat-emitting surface, in this case a thick-walled (5.1 mm) copper cylinder 48.2 mm in diameter.

To heat the sensor, a glass-coated bead thermistor was used (5000 Ω at 25°C, 0.28 mm in diameter, with 50 gauge lead wires). After it was inserted into the hole in the base of the sensor, a high thermal conductivity (0.63 W/m K) silicon grease filled the remaining volume to insure that the heat conducted into the lead wires would be dissipated into the sensor. An analytical approximation in which the lead wires were assumed to be infinite fins in a conducting medium, showed that heat loss down such wires would be less than 0.1 percent. To insure that the heat loss would not exceed this figure, the lead wires were wrapped around the stem of the sensor several times. As a result heat loss by conduction down the lead wires can be neglected.

A chromel-constantan differential thermocouple was used to measure the temperature difference between the cone and the wall. A chromel wire 18 mm long and 0.76 mm dia was used to further minimize heat conduction between the cone and wall.

Once the heater and the thermocouples were installed, the sensor was set into the wall using epoxy glue. The conical shape of the upper portion was chosen to minimize the area of the epoxy exposed to the environment while allowing for a greater degree of insulation below the surface. The entire cylindrical assembly was then turned in a lathe to remove excess sensor material (dashed lines. Fig. 1) and any out-of-roundness of the cylinder. Finally the entire cylindrical assembly surface was polished.

The surface areas of the sensor and of the epoxy were measured with the aid of a traveling microscope; the areas measured were 13.82 mm^2 and 0.91 mm^2, respectively. Because of the curvature of the surface, the thickness of the epoxy ring varied from 0.036 to 0.10 mm. The sensor subtended an arc of 9.5 deg. Since heat convected away from the epoxy surface area can come from both the sensor and the cylinder, the effective area of the sensor had to be defined. An analysis of this conduction problem was done by computer. The wall temperatures of the cylinder and the sensor were assumed to be constant and equal; the boundary condition at the exposed surface of the epoxy ring was taken to be convective (constant h and T). The computations showed that the minimum surface temperature of the epoxy ring was approximately 0.3°C lower than the temperature of the sensor and the cylinder for a cylinder-to-air temperature difference of 10°C and a local heat flux of 1680 W/m^2. The effective area of the sensor was taken to be its measured area (13.82 mm^2) plus the area of the epoxy out to the minimum temperature location (0.48 mm^2).

The instrumentation is shown in Fig. 2. Because the desired output of the differential thermocouple is a null signal, the circuit was designed to attain the maximum resolution of this signal. This resolution was accomplished by use of a high quality thermocouple switch to reverse the polarity of the signal and thereby eliminate the need to zero the amplifier and the digital voltmeter. The voltage into the sensor heater was adjusted until the amplifier output was the same for both polarities. The circuit provides a resolution of ±0.5 μV (approximately ±0.008°C).

Whenever sensor power is adjusted to give a null reading, heat trasnfer should no longer occur between the sensor and the adjacent wall. Under this condition the electrical power into the sensor is equal to the heat rate out of the sensor surface. Thus, the sensor heat flux is simply $q_s'' = P_s/A_s$.

Error Analysis

To perform an error analysis on any measurement device, we must know the physical equations that model its behavior. For this sensor the basic equation is the First Law of Thermodynamics.

$$\underset{(a)}{\text{Heat rate into sensor,}} = \underset{(b)}{\text{Heat loss out the surface}} + \underset{(c)}{\text{Conduction loss through epoxy}}$$

We express each term as follows.

$$(a)\quad P_s = I_s E_s - I_s^2 R_{\ell w}$$

$$(b)\quad q_S = q_s'' A_s$$

$$(c)\quad q_{\text{cond}} = C_e(T_s - T_w)$$

Table 1 Stagnation point data

x_i	Value of x_i	δx_i	$\frac{\partial q''}{\partial x_i}\delta x_i$ (W/m^2)	$\frac{1}{q''}\frac{q''}{x_i}\delta x_i$ (percent)
E_s	7.690 V	0.0087 V	2.38	0.14
I_s	3.093 mA	0.0051 mA	2.74	0.16
A_s	14.22 mm^2	0.13 mm^2	15.70	0.92
R_{1w}	5.6 Ω	1.0 Ω	0.68	0.04
$T_w - T_s$	0°C	0.008°C	6.43	0.45

The thermal conductance, C_e, accounts for conduction in axial, circumferential, and radial directions between the sensor and the cylinder. It must be determined experimentally. In our case, it was determined by placing insulation over the sensor surface and then heating the sensor. In this manner, the sensor heater power equals the sensor conduction losses to the cylinder. Thus, $C_e = P_s/(T_s - T_w)$ for the sensor geometry and epoxy used in this study, we found C_e = 11.55 mW/°C.

Using terms (*a, b*), *and* (*c*) and dividing by A_s, we arrive at the analytical expression for the performance of the sensor

$$q_s'' = \frac{1}{A_s}\left[I_s E_s - I_s^2 R_{\ell w} - C_e(T_s - T_w)\right] \quad (1)$$

The uncertainty in the heat flux measurement associated with each measured x_i is $(\partial q_s''/\partial x_i)\delta x_i$ where δx_i is the uncertainty in x_i. The measurements involved in this analysis are shown in Table 1 along with the numerical values of δx_i and x_i for stagnation point heat transfer from a cylinder in normal flow.

The total rms error is, then,

$$\delta q_s'' = \sqrt{\sum_{i=1}^{n}\left[\left(\frac{\partial q_s''}{\partial x_i}\right)\delta x_i\right]^2} \quad (2)$$

The results of the application of equation (2) to the data given are shown in Table 1. For this example $\delta q''/\delta q_s'' = 0.0104$. The value of the surface heat flux can be calculated from equations (1) and (2); it is $q_s'' = 1671 \pm 17.4$ W/m^2 (±1.04 percent). A similar analysis for the separation point on the cylinder yields $q_s'' = 419 + 7.6$ W/m^2 (1.8 percent).

An examination of Table 1 shows that the sensor surface area is the primary source of error in the heat flux measurement. This systematic error is constant, that is, it contributes 0.92 percent uncertainty regardless of the heat flux.

Convective Heat Flux Measurement

The above error analysis gives typical uncertainties in the *total* heat flux, q_s''. For the uncertainty in the convective heat transfer, we write an energy balance for the sensor

$$h(T_s - T_{aw}) = q_s'' - q_{\text{rad}}'' \quad (3)$$

where T_{aw} (the adiabatic wall temperature) is used to include the compressibility effects. Although this is usually negligible, the high accuracy of this instrument requires its use here.

Since we used $T_w - T_\infty \simeq 10°$C, we can approximate the radiation loss by

$$q_{\text{rad}}'' = \epsilon\sigma(T_s^4 - T_\infty^4), \quad (4)$$

The desired convective heat flux, however, is given by

$$q_c'' = h(T_w - T_{aw}) = h(T_s - T_{aw}) + h(T_w - T_s) \quad (5)$$

If we combine equations (1, 3, 4), and (5), we obtain the analytical expression from which an error analysis can be made for the convective heat flux

$$q_c'' = h(T_w - T_{aw}) = \frac{1}{A_s}\left[I_s E_s - I^2 R_{lw} - \epsilon\sigma A_s(T_s^4 - T_\infty^4) + (C_e + hA_s)(T_w - T_s)\right]. \quad (6)$$

In this equation $(C_e + hA_s)$ is the static sensitivity of the sensor. An error analysis (not shown) performed using equation (6) for the stagnation and separation points yields $q_c'' = 1669 \pm 18$ w/m^2 (± 1.1 percent) and $q_c'' = 417 \pm 8.7$ W/m^2 (±2 percent), respectively.

In this analysis the uncertainty in the differential temperature contributes a nearly constant error of 6.43 W/m^2 regardless of the value of the heat flux; this error is random in nature. For instance, at the separation point, where $q_c'' = 417$ W/m^2, this term accounts for 90 percent of the uncertainty.

Application

For our particular application of heat transfer from a heated cylinder in normal flow, the apparatus consisted of an internally heated cylinder mounted horizontally in a wind tunnel. The test section of this tunnel was less than 1.02 m by 0.91 m. Blockage was 8 percent and free stream turbulence was 0.4 percent. The copper test assembly (shown partly in Fig. 1) was located in the center of a 0.6 m aluminum section. On each side of the test section were 0.93 m aluminum cylinders that were independently heated and that thereby prevented heat losses from the ends of the test section. Cylinder temperature measurements showed circumferential variations of ±0.07°C for $T_w - T_\infty = 10°C$.

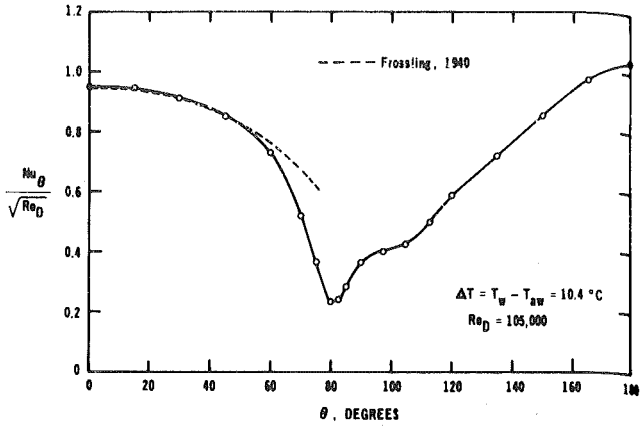

Fig. 3 Results for the circumferential distribution of the Nusselt number

From these experiments we show, in Fig. 3, a typical Nu distribution. At the stangation point our data gives $Nu_\theta/\sqrt{Re_D}^{1/2} = 0.955$ (standard deviation = 0.008) while Frossling calculates it to be 0.9445. This difference may be due to our experimental conditions, which involve blockage and free stream turbulence [4]. Our results were reproduced many times under identical conditions.

Our circumferential distribution, over the leading part of the cylinder, agrees well with Frossling (see Fig. 3). The agreement with Achenbach is less satisfactory; 5 percent at the forward stagnation point and approximately 20 percent at the rear stagnation point. His results may show the effects of a non-uniform circumferential temperature distribution and of greater blockage, for the latter a higher value of Nu_θ/Re_D occurs at the stagnation point and separation (θ = 85 deg) is delayed [1].

Acknowledgment

This research was supported under NSF Grant 75-19046 which is gratefully acknowledged.

References

1 Kraabel, J. S., "An Isothermal Heat Flux Sensor," M.S. Thesis, University of California, Davis, 1977.

2 Gardon, R., "An Instrument for the Direct Measurement of Intense Thermal Radiation," *The Review of Scientific Instruments*, Vol. 24, No. 5, 1953, p. 366.

3 Gardon, R., "A Transducer for the Measurement of Heat-Flow Rate," ASME JOURNAL OF HEAT TRANSFER, Vol. 82, 1960, p. 396.

4 Newman, L. B., Sparrow, E. M., Eckert, E. R. G., "Free Stream Turbulence Effects on Local Heat Transfer from a Sphere," ASME JOURNAL OF HEAT TRANSFER, Vol. 94., 1972, p. 7.

5 Achenbach, E., "Total and Local Heat Transfer from a Smooth Circular Cylinder in Crossflow at High Reynolds Number," *International Journal of Heat and Mass Transfer*, Vol. 18, 1975, p. 1387.

6 Frossling, N., "Verdunstung, Warmeubergang und Geschwindigkeitsverteilung bei Zweidimensionaler und Rotationssymmetrischer Grenzschicht Stromung," English translation in NACA TM 1432, 1958.

7 Kestin, J., and Wood, R. T., "The Influence of Turbulence on Mass Transfer From Cylinders," ASME JOURNAL OF HEAT TRANSFER, Vol. 93, 1971, p. 321.

8 Zukauskas, A., "Heat Transfer from Tubes in Crossflow," *Advances in Heat Transfer*, Vol. 8, 1972, Academic Press, N.Y.

Analytic Solution to Inverse Heat Conduction Problems with Periodicity

D. M. France[1] and T. Chiang[1]

Nomenclature

A_n $n = 0, 1, 2 \ldots$ = Fourier series coefficients, °C
α = thermal diffusivity, m^2/s
f_0 = fundamental frequency, Hz
h = heat transfer coefficient, $kW/m^2 \cdot K$
$i = [-1]^{1/2}$
k = thermal conductivity, kW/m·K
r = radial coordinate, m
R_A, R_B, R_c = values of r (see Fig. 1), m
re = real part
t = time, s
T = temperature, °C
T_m = temperature measured at $r = R_B$, °C
T_F = fluid temperature, °C
ω = frequency, rad/s

Introduction

A class of ill-posed, transient heat conduction problems has, in recent years, been termed inverse heat conduction. This class of problems is graphically displayed in cylindrical coordinates in one space dimension in Fig. 1. In general, a solution to the energy equation is sought in the region $R_c \le r \le R_A$. If boundary conditions were specified at $r = R_A$ and $r = R_c$, then a solution to either the transient or steady state energy equation could be obtained by various analytical and/or numerical methods, depending on the particular problem of interest. If, however, boundary conditions were specified at $r = R_A$ and $r = R_B$, the problem is ill-posed for solutions in the entire region $R_c \le r \le R_A$. In this case, solutions are obtainable to either the transient or steady state conduction energy equation on the interval $R_B \le r \le R_A$. The steady state solution can be accurately extrapolated to include the remainder of the region, $R_c \le r \le R_B$, but, in general, the transient solution cannot be so extrapolated. Attempts to obtain a solution to the transient problem in the region $R_c \le r \le R_B$ by standard methods usually produce inaccuracies, and in many cases, no solution at all. This transient problem is defined as the inverse type.

There is considerable interest in solutions to inverse heat conduction problems, and one important application is found in the area of transient heat transfer experimentation. In terms of Fig. 1 and the example of the previous paragraph, a temperature measurement as a function of time is made at $r = R_B$ within a solid material in the region $R_c \le r \le R_A$. This temperature measurement provides a known boundary condition at $r = R_B$, and a second boundary condition is known at $r = R_A$. In general, a solution to the energy equation may be obtained in the region $R_B \le r \le R_A$, but it is desirable to obtain a solution in region $R_c \le r \le R_B$ as well. Often the impetus is to predict the temperature at $r = R_c$, where no measurement was made, from the information gained from a measurement at $r = R_B$ (plus a boundary condition at $r = R_A$). Such a problem is of the inverse type and has contributed significantly to the interest in inverse heat conproblems, it is not surprising that several techniques for solving these problems have been published in the engineering literature in recent years. These methods are of both analytical and numerical types, the latter being more general in character. Some of these methods were compared to each other in an article by Beck [1], including a numerical treatment by Beck [2], and an analytical treatment by Sparrow, et al. [3]. These methods attempt to be as general as possible but still include various restrictions on their application, e.g., solution stability criteria.

In the present work, a method for obtaining an analytic solution to a specific class of heat conduction problems is presented. This class of problems is characterized by boundary conditions with periodicity. Solutions to such problems are possible using other methods, including Beck's general numerical scheme [2]. However, the present method incorporates the advantages of simplicity and accuracy (at the expense of generality). There is no loss of resolution or solution stability as a function of the time constant of the transient using the present method, and other useful features of continuous (analytical) versus discrete (numerical) solutions are inherent in this method.

Returning to the example of Fig. 1, assume that one desires to calculate the temperature at $r = R_c$ when the boundary conditions are known at $r = R_B$ and $r = R_A$, and the time dependent boundary condition is periodic. As an example, a periodic temperature might be measured at $r = R_B$ and convection to a fluid of a known temperature exists at $r = R_A$. The present method of solution takes advantage of the special circumstance of the problem, the periodicity. Using the principle of superposition, particular solutions to the steady periodic problem in the region $R_B \le r \le R_A$ are summed to produce the general solution in that region. Then, as in the case of a steady-state solution (and different from the strictly transient case), the solution can be accurately extrapolated to include the remainder of the region, $R_c \le r \le R_B$. The mechanics of applying this method of solution are presented for the sample problem of Fig. 1, and the validity is delineated.

Analytical Method

The energy equation for a constant property material in the region $R_c \le r \le R_A$ may be written as

$$\frac{1}{\alpha}\frac{\partial T(t, r)}{\partial t} = \frac{\partial^2 T}{\partial r^2} + \frac{1}{r}\frac{\partial T}{\partial r} \tag{1}$$

Addressing the sample problem previously discussed, there is a measured temperature, $T_m(t)$, at $r = R_B$, and convection to a fluid at constant temperature at $r = R_A$. The corresponding boundary conditions are

$$T(t, R_B) = T_m(t) \tag{2}$$

$$-k\frac{\partial T}{\partial r}\bigg|_{r = R_A} = h(T(t, R_A) - T_F) \tag{3}$$

Temperature $T_m(t)$ was then expanded into a Fourier series.

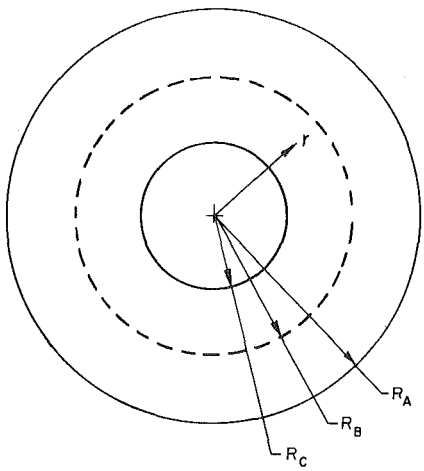

Fig. 1 Geometrical schematic

[1] Components Technology Division, Argonne National Laboratory, Argonne, Ill. 60439

Contributed by the Heat Transfer Division for publication in the JOURNAL OF HEAT TRANSFER. Manuscript received by the Heat Transfer Division February 21, 1980.

$$T_m(t) = A_0 + re \sum_{n=1}^{N} A_n e^{i\omega_n t} \tag{4}$$

where

$$A_n = \frac{2}{\tau}\int_0^{\tau} T_m(t)e^{-i\omega_n t}dt \quad n = 1, 2, 3, \ldots \tag{5}$$

$$A_0 = \frac{1}{\tau}\int_0^{\tau} T_m(t)dt \tag{6}$$

The symbol τ denotes the period of time over which the analysis is performed. Thus, the fundamental frequency $f_0 = 1/\tau$, and $\omega_n = 2\pi f_0 n$, $n = 1, 2, 3, \ldots$

Taking advantage of the periodic nature of the boundary condition, $T_m(t)$, a steady periodic solution is sought in the form

$$T(t, r) = u(r) + re \sum_{n=1}^{N} v_n(r)e^{i\omega_n t} \tag{7}$$

where $v_n(r)$ are complex, In choosing the form of equation (7), the principle of superposition was utilized in summing particular solutions for each term in the Fourier series expansion of the boundary condition, equation (4). Substituting the assumed solution, equation (7), into the energy equation, equation (1), and boundary conditions, equations (2) and (3), the problem was divided into steady-state and oscillating portions

$$\frac{d^2u}{dr^2} + \frac{1}{r}\frac{du}{dr} = 0 \tag{8}$$

$$u(R_B) = A_0 \tag{9}$$

$$-k\left.\frac{du}{dr}\right|_{r=R_A} = h(u(R_A) - T_F) \tag{10}$$

$$\frac{d^2v_n}{dr^2} + \frac{1}{r}\frac{dv_n}{dr} - \frac{i\omega_n}{\alpha}v_n = 0 \tag{11}$$

$$v_n(R_B) = A_n \tag{12}$$

$$-k\left.\frac{dv_n}{dr}\right|_{r=R_A} = hv_n(R_A) \tag{13}$$

The solution to the steady-state portion of the problem is

$$u(r) = \frac{A_0\left(\ell n\frac{r}{R_A} - \frac{k}{R_A h}\right) + T_F \ell n\frac{R_B}{r}}{\ell n\frac{R_B}{R_A} - \frac{k}{R_A h}} \tag{14}$$

The general solution to the oscillating portion of the problem, equation 11, is

$$v_n(r) = P_n I_0(i^{1/2}\beta_n r) + Q_n K_0(i^{1/2}\beta_n r) \tag{15}$$

(See, for example, the treatment of steady periodic solutions in reference [4]) where P_n and Q_n are complex constants, I_0 and K_0 are zero-order, modified Bessel functions of the first and second kinds, respectively, and

$$\beta_n = (\omega_n/\alpha)^{1/2} \tag{16}$$

Applying the boundary conditions, equations (12) and (13) to equation (15) yields the final solution for $v_n(r)$, which leads to the temperature, $T(t, r)$, via equation (7).

Results and Discussion

Equations (7, 14, 15, 17) and (18) are the solution to the conduction energy equation, equation (1), in the region $R_B \le r \le R_A$. The solution was then extrapolated (i.e., evaluated) to $r = R_c$ to obtain the temperature there. The accuracy of the extrapolation was determined by comparison with an independent calculation. Starting with an arbitrarily chosen temperature at $r = R_B$, $T_m(t)$, and a fluid temperature, T_F, the temperature at $r = R_c$, $T(t, R_c)$ was calculated from equations (7, 14, 15, 17) and (18). Then, using $T(t, R_c)$ and T_F as boundary conditions, the temperature at $r = R_B$ was calculated from a standard, transient, finite difference, heat conduction computer code. Good agreement was obtained between $T_m(t)$ and the temperature $T(t, R_B)$ calculated from the computer code, thus verifying the validity of the original extrapolation. (The two temperatures were nearly coincidental.)

As an example, the results of equations (7, 14, 15, 17) and (18) were applied to a set of experimental data obtained at Argonne National Laboratory and discussed in reference [5]. A tube with $R_c = 5$ mm, $R_A = 7.95$ mm, and made of $2\frac{1}{4}$ Cr − 1 Mo steel was tested with an unstable, boiling fluid on the inside, giving rise to temperature fluctuations in the tube. A second fluid on the outside of the tube had a constant and known temperature, $T_F = 431°C$, and heat transfer coefficient, $h = 28.7 kW/m^2{\cdot}K$. A thermocouple was embedded in the tube with its junction located at $R_B = 6.73$ mm. During the test, the temperature at R_B was recorded as a function of time. A segment of the measured temperature, $T_m(t)$, is shown in Fig. 2. It was desired to calculate the temperature at R_c, where no measurement was made. First, a time period, $\tau = 25.6$ s, was chosen, and the temperature, $T_m(t)$, was represented by a Fourier series, equation (4) with $N = 64$ and fundamental frequency $f_0 = 0.03906$ Hz. As a consequence of the number of terms in the series required to achieve good representation of the measurement, determination of the Fourier series coefficients, A_n, was facilitated by use of a Fast Fourier Transform (FFT) algorithm on a digital computer. Subsequently, equation (7) was evaluated at R_c using equations (14, 15, 17) and (18) producing the desired temperature at $r = R_c$. This result is also plotted in Fig. 2.

In applying the present solution method to an engineering problem of the type discussed above, several practical considerations require some attention. The time period for analysis, τ, must be chosen to include several periods of the lowest frequency present in the measured signal. The number of terms, N, in the Fourier series expansion of the measured signal must be chosen large enough to accurately represent the highest frequency present. The power spectral density of the signal (which may be calculated from the Fourier series coefficients, A_n) is a useful indicator of the adequacy of the values of τ and N employed. The analysis may be performed with various values of these parameters using the power spectral density and measured time signal as criteria for selection of the smallest values that retain high accuracy. Further, the time response of the temperature measuring sensor must be fast relative to the highest frequency present in the system. In the problem discussed above, this time response was controlled by the distance $R_B - R_c$. The thermocouple must be placed close enough to the signal source such that the highest frequency present at the source is not excessively attenuated at the location of the sensor. Although all of these practical considerations are important to the accuracy of the final solution they differ from the accuracy and stability problems inherent in the mathematics of the more general inverse heat transfer solution methods.

As a final point of interest, the present solution method does not require the boundary conditions to be separated. Thus, two boundary

$$P_n = \frac{A_n[K_0(i^{1/2}\beta_n R_A) - i^{1/2}\beta_n k K_1(i^{1/2}\beta_n R_A)/h]/K_0(i^{1/2}\beta_n R_B)}{\frac{-i^{1/2}\beta_n k}{h}\left[I_1(i^{1/2}\beta_n R_A) + \frac{K_1(i^{1/2}\beta_n R_A)I_0(i^{1/2}\beta_n R_B)}{K_0(i^{1/2}\beta_n R_B)}\right] - I_0(i^{1/2}\beta_n R_A) + \frac{K_0(i^{1/2}\beta_n R_A)I_0(i^{1/2}\beta_n R_B)}{K_0(i^{1/2}\beta_n R_B)}} \tag{17}$$

$$Q_n = \frac{A_n - P_n I_0(i^{1/2}\beta_n R_B)}{K_0(i^{1/2}\beta_n R_B)} \tag{18}$$

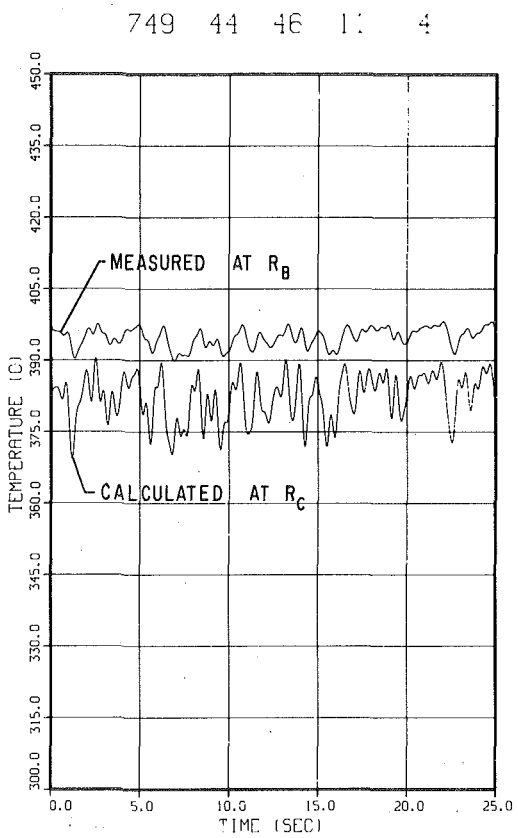

Fig. 2 Temperature in the solid: boundary conditions at R_A and R_B

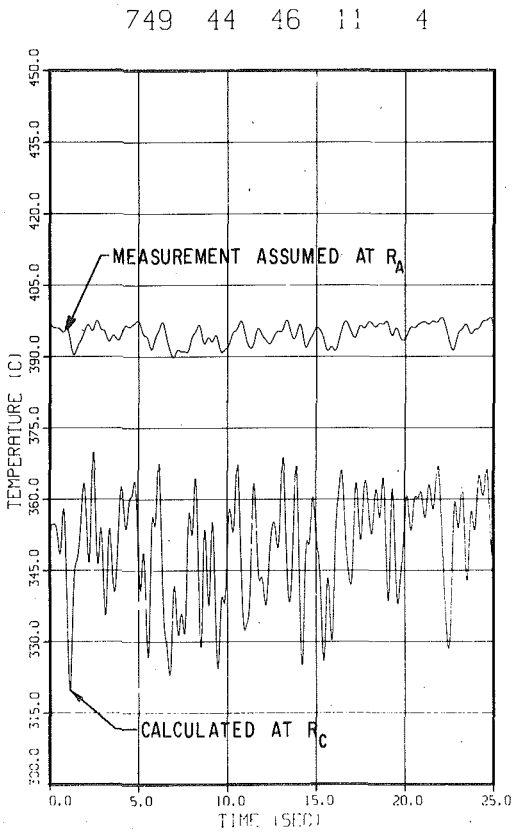

Fig. 3 Temperature in the solid: both boundary conditions at R_A

conditions may be specified at the same spatial location. For example, it was assumed that the measured temperature, $T_m(t)$, shown in Fig. 2 was measured at $r = R_A$ instead of $r = R_B$ (where the measurement was actually made). This assumption resulted in both boundary conditions specified at $r = R_A$. As seen in Fig. 3, there was no problem associated with calculating the temperature at $r = R_c$.

Conclusion

It was demonstrated that a steady periodic solution to a heat conduction problem can be extrapolated to give the solution to a problem of the inverse type. The principle of superposition of solutions was used to include problems wherein the boundary conditions are arbitrary functions of time with the one constraint that they are periodic in nature.

References

1 Beck, J. V., "Criteria for Comparison of Methods of Solution of the Inverse Heat Conduction Problem," ASME Paper No. 75-WA/HT-82, 1975.

2 Beck, J. V., "Nonlinear Estimation Applied to the Nonlinear Inverse Heat Conduction Problem," *International Journal of Heat Mass Transfer*, Vol. 13, 1970, pp. 703–716.

3. Sparrow, E. M., Hadji-Sheikh, A., and Lundgren, T. S., "The Inverse Problem in Transient Heat Conduction," *Journal of Applied Mechanics*, Vol. 86, 1964, pp. 369–375.

4. Carslaw, H. S., and Jaeger, J. C., *Conduction of Heat in Solids*, Second Edition, Oxford University Press, 1959.

5. France, D. M., Chiang, T., and Carlson, R. D., "Large-Amplitude Thermal Oscillations Measured in an LMFBR Steam Generator Tube," *Transactions of The American Nuclear Society*, Vol. 27, Nov. 1977, pp. 734–735.

Thermal Instability in Liquid Droplets on a Heated Surface[1]

J. C. Han[2] and Wen-Jei Yang[3]

Nomenclature

D_ℓ = operator defined by equation (11)
f,g = functions defined by equation (7)
m = integer
n = integer, 1, 2, . . .
$p = \partial/\partial r$
Q = heat flux across droplet surface, W/m^2; Q_0, at steady state
R = radius of hemispherical droplet, m
S = surface tension of liquid, N/m; S_0, at steady state
T = liquid temperature = $T_0 + T'$, °C; T_0, at steady state; T_{c0}, at droplet center under steady state
T_S = liquid surface temperature, °C; T_{s0}, at steady state
T_∞ = ambient temperature, °C
T' = perturbed temperature of liquid, °C; T_s'; at liquid surface

Introduction

The Benards problem, the phenomenon of cellular convection in a horizontal layer of fluid heated from below [1], was described as a result of buoyancy [2], a surface-tension effect [3] or their combination [4]. The onset of instability is indicated by a critical value of the Rayleigh number, Marangoni number or both, depending on its mechanism. Pearson's analysis [3] concluded that for liquid thickness less than the order of 1 cm, surface tension forces are more effective than buoyancy forces in producing instability. For thickness as small as 1 mm, the onset of cellular motion could confidently be attributed to surface tension rather than to buoyancy. Acriovs, et al. [5] experimentally determined convective patterns as a function of the depth

[1] This work was supported by a National Science Foundation, under ID No. ENG 7816972.

[2] Ex-Cell-O Corporation, Walled Lake, Mich. 48088. Also visiting scholar at the University of Michigan.

[3] Department of Mechanical Engineering, University of Michigan, Ann Arbor, Mich. 48109.

Contributed by the Heat Transfer Division for publication in the JOURNAL OF HEAT TRANSFER. Manuscript received by the Heat Transfer Division January 7, 1980

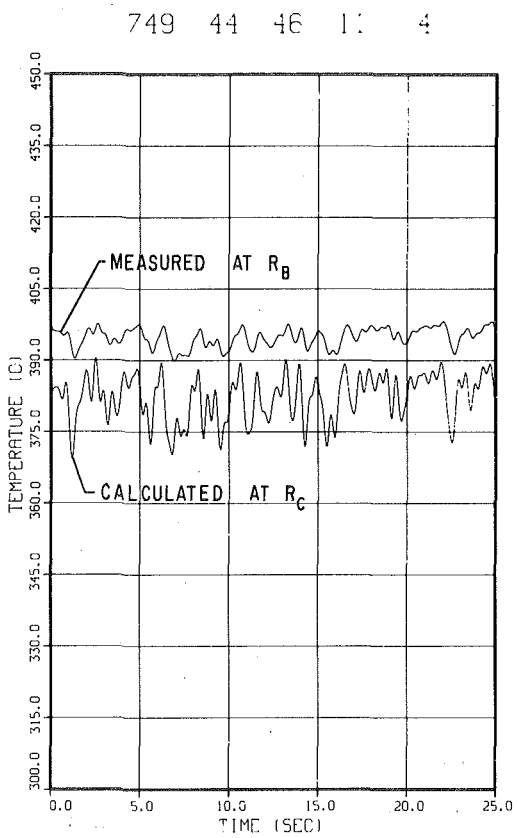

Fig. 2 Temperature in the solid: boundary conditions at R_A and R_B

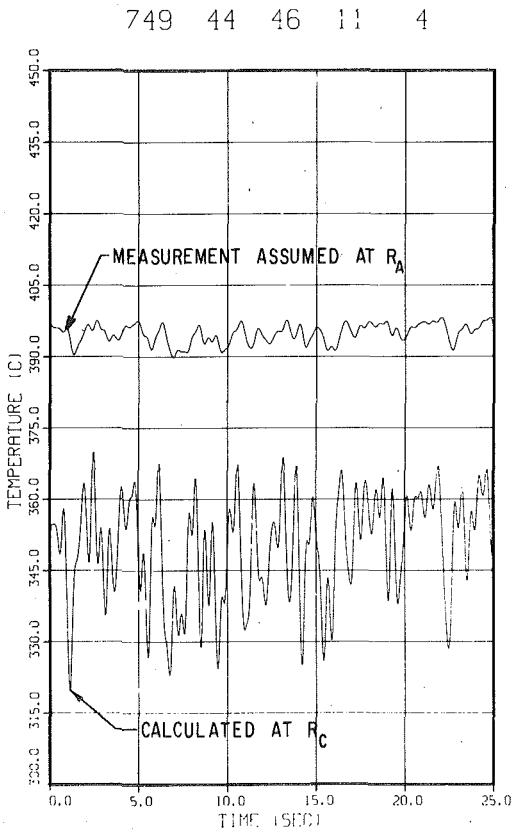

Fig. 3 Temperature in the solid: both boundary conditions at R_A

conditions may be specified at the same spatial location. For example, it was assumed that the measured temperature, $T_m(t)$, shown in Fig. 2 was measured at $r = R_A$ instead of $r = R_B$ (where the measurement was actually made). This assumption resulted in both boundary conditions specified at $r = R_A$. As seen in Fig. 3, there was no problem associated with calculating the temperature at $r = R_c$.

Conclusion

It was demonstrated that a steady periodic solution to a heat conduction problem can be extrapolated to give the solution to a problem of the inverse type. The principle of superposition of solutions was used to include problems wherein the boundary conditions are arbitrary functions of time with the one constraint that they are periodic in nature.

References

1 Beck, J. V., "Criteria for Comparison of Methods of Solution of the Inverse Heat Conduction Problem," ASME Paper No. 75-WA/HT-82, 1975.

2 Beck, J. V., "Nonlinear Estimation Applied to the Nonlinear Inverse Heat Conduction Problem," *International Journal of Heat Mass Transfer*, Vol. 13, 1970, pp. 703–716.

3. Sparrow, E. M., Hadji-Sheikh, A., and Lundgren, T. S., "The Inverse Problem in Transient Heat Conduction," *Journal of Applied Mechanics*, Vol. 86, 1964, pp. 369–375.

4. Carslaw, H. S., and Jaeger, J. C., *Conduction of Heat in Solids*, Second Edition, Oxford University Press, 1959.

5. France, D. M., Chiang, T., and Carlson, R. D., "Large-Amplitude Thermal Oscillations Measured in an LMFBR Steam Generator Tube," *Transactions of The American Nuclear Society*, Vol. 27, Nov. 1977, pp. 734–735.

Thermal Instability in Liquid Droplets on a Heated Surface[1]

J. C. Han[2] and Wen-Jei Yang[3]

Nomenclature

D_ℓ = operator defined by equation (11)
f,g = functions defined by equation (7)
m = integer
n = integer, 1, 2, . . .
$p = \partial/\partial r$
Q = heat flux across droplet surface, W/m^2; Q_0, at steady state
R = radius of hemispherical droplet, m
S = surface tension of liquid, N/m; S_0, at steady state
T = liquid temperature = $T_0 + T'$, °C; T_0, at steady state; T_{c0}, at droplet center under steady state
T_S = liquid surface temperature, °C; T_{s0}, at steady state
T_∞ = ambient temperature, °C
T' = perturbed temperature of liquid, °C; T_s'; at liquid surface

Introduction

The Benards problem, the phenomenon of cellular convection in a horizontal layer of fluid heated from below [1], was described as a result of buoyancy [2], a surface-tension effect [3] or their combination [4]. The onset of instability is indicated by a critical value of the Rayleigh number, Marangoni number or both, depending on its mechanism. Pearson's analysis [3] concluded that for liquid thickness less than the order of 1 cm, surface tension forces are more effective than buoyancy forces in producing instability. For thickness as small as 1 mm, the onset of cellular motion could confidently be attributed to surface tension rather than to buoyancy. Acriovs, et al. [5] experimentally determined convective patterns as a function of the depth

[1] This work was supported by a National Science Foundation, under ID No. ENG 7816972.

[2] Ex-Cell-O Corporation, Walled Lake, Mich. 48088. Also visiting scholar at the University of Michigan.

[3] Department of Mechanical Engineering, University of Michigan, Ann Arbor, Mich. 48109.

Contributed by the Heat Transfer Division for publication in the JOURNAL OF HEAT TRANSFER. Manuscript received by the Heat Transfer Division January 7, 1980

of the evaporating liquid pool. In evaporating binary solutions, surface tension mechanism was obtained at 1 and 2 mm. Cellular patterns changed as the depth increased. As the depth reached about 1 cm and beyond, no further change was detected. In contrast, no convection by buoyancy mechanism was observed until the liquid depth reached about 1 cm. Scriven and Sternling [6] developed a criterion for visually distinguishing the dominant force in cellular convection in liquid pools: In steady cellular convection by surface tension, there is upflow beneath depressions (shallow sections) and downflow beneath elevations (deeper sections) of the free surface. The relationship is just the converse in buoyancy-driven flows. Bupara [7] derived the general solutions for the onset of surface-tension driven convection in a fluid sphere and in a spherical fluid layer with a free surface. Kenning [8] gave a survey of cellular convection in thin liquid layers.

This work deals with cellular convection in minute droplets on a solid surface. To the author's knowledge, there is no previous study on this problem, obviously due to the mathematical complexity of the analysis. For droplet size on the order of a few mm or less, the onset of cellular convection is attributed to surface tension, as in the case of thin liquid layers. In order to make the problem tractable mathematically, the droplet on the surface is assumed to be hemispherical and two types of thermal distribution are imposed within the liquid:linear and parabolic profiles. Pearson's analysis on cellular convection in thin liquid layers is then applied to determine the criterion for the onset of cellular motion in the droplet.

Analysis

Consider a hemispherical liquid droplet of the radius R on a flat surface. There is a finite heat transfer coefficient, h, between the ambient gas at temperature T_∞ and the liquid-gas interface at temperature T_{s0}. Let the origin of spherical coordinates (r, θ, φ) be fixed at the droplet center. Under steady-state conditions, the solid temperature varies linearly with the radial distance from the center to the surface of the droplet as

$$T_0(r) = T_{c0} - \beta r \tag{1}$$

in which $\beta = Q_0/k$. k denotes the liquid thermal conductivity and Q_0 is the heat flux across the droplet surface at steady state. Let the liquid temperature variation take the form of equation (1) with T_{c0} as the unperturbed temperature at the droplet center.

When an infinitesimal disturbance is imposed on the system, the linearized equations of motion and heat conduction in the liquid read

$$\left(\frac{\partial}{\partial t} - D\nabla^2\right)\nabla^2 v = 0; \qquad \left(\frac{\partial}{\partial t} - \alpha\nabla^2\right)T' = \beta v \tag{2}$$

respectively. Here, t represents the time, ν, kinematic viscosity, v, velocity in the r-direction, α, thermal diffusivity, and T', perturbed temperature. Let the surface tension of the liquid S and the heat flux across the droplet surface vary linearly with the perturbed droplet surface temperature T' as

$$S = S_0 - \sigma T_s'; \quad Q = Q_0 + hT_s' \tag{3}$$

Here, $-\delta = (\partial S/\partial T)$ and $h = (\partial Q/\partial T)$ both evaluated at temperature, T_{s0}. S_0 varies with the droplet surface temperature T_{s0}, while σ depends on the liquid itself. T, the liquid temperature, is equal to $T' + T_0$. h is the heat transfer coefficient between droplet surface and the ambient.

Equation (2) is subject to the following boundary conditions.

$$\text{at } r = 0, \qquad v = \partial v/\partial r = 0; \partial T'/\partial r = 0 \tag{4}$$

$$\text{at } r = R, \qquad v = 0; -\frac{\rho\nu}{r^2}\frac{\partial}{\partial r}\left(r^2\frac{\partial v}{\partial r}\right) = \sigma\nabla_1{}^2T'; -T' = \frac{k}{h}\frac{\partial T'}{\partial r} \tag{5}$$

Here,

$$\nabla_1{}^2 = \frac{1}{r^2}\left[\frac{1}{\sin\theta}\frac{\partial}{\partial\theta}\left(\sin\theta\frac{\partial}{\partial\theta}\right) + \frac{1}{\sin^2\theta}\frac{\partial^2}{\partial\varphi^2}\right] \tag{6}$$

and its characteristic values are $n(n+1)$ where n is an integer. The second expression of equation (4) follows directly from the continuity equation. In the second relation of equation (5), the change in surface tension due to temperature variations across the droplet surface is equated to the shear stress experienced by the fluid at the droplet surface, making use of the continuity condition. The third expression of equation (5) describes the general thermal condition on the droplet surface. Its two limiting cases correspond to (2) $h = 0$ or insulating and (2) $h = \infty$ or conducting. Let

$$Rv = \alpha Y_n{}^m(\theta, \varphi)f(\eta)e^{p\tau}; \; T' = \beta R Y_n{}^m(\theta, \varphi)g(\eta)e^{p\tau} \tag{7}$$

wherein

$$\tau = \frac{\nu t}{R^2}; \; \eta = \frac{r}{R}; \; p = \frac{\partial}{\partial\tau} \tag{8}$$

and the spherical harmonics $Y_n{}^m(\theta, \phi)$ are the eigen functions. With the substitution of equation (7) followed by the separation of variables, equation (2) can be reduced to

$$(D_\ell - p)D_\ell f = 0; \; (p\mathrm{Pr} - D_\ell)g = f \tag{9}$$

respectively, and

$$\frac{1}{\eta^2}\left[\frac{1}{\sin\theta}\frac{\partial}{\partial\theta}\left(\sin\theta\frac{\partial Y_n{}^m}{\partial\theta}\right) + \frac{1}{\sin^2\theta}\frac{\partial^2 Y_n{}^m}{\partial\varphi^2}\right] + \lambda Y_n{}^m = 0 \tag{10}$$

Here, Pr denotes the Prandtl number, λ is the eigen value, i.e., wave number, and is equal to $\lambda = n(n+1)$ where n is an integer $1, 2, \ldots$. The operator D_ℓ is defined as

$$D_\ell = \frac{1}{\eta^2}\left[\frac{d}{d\eta}\left(\eta^2\frac{d}{d\eta}\right) - \lambda\right] \tag{11}$$

It can be proved that, with respect to functions which vanish at the ends of an interval, (0, 1), the operator $\eta^2 D_\ell$ is Hermitian [9]. The boundary conditions (4) and (5) are reduced to

$$f(0) = f'(0) = 0; \qquad f(1) = 0 \tag{12}$$

$$g'(1) = -\mathrm{Big}(1); \qquad g'(0) = 0 \tag{13}$$

$$f''(1) = -\lambda\mathrm{Ma}g(1) \tag{14}$$

where

$$\mathrm{Ma} = \frac{\sigma\beta R^2}{\rho\nu\alpha}; \; \mathrm{Bi} = \frac{hR}{k}.$$

Ma is the Marangoni number which expresses the relative importance of surface tension forces (due to temperature variation) and viscous forces. Bi denotes the Biot number. For marginal stability corresponding to $p = 0$, the solutions of equation (9) satisfying the boundary conditions (12) and (13) are found to be

$$f = C_1(\eta^n - \eta^{n+2}); \; g = C_1\left(A - \frac{1}{4n+6}\eta^2 + \frac{1}{8n+20}\eta^4\right)\eta^n \tag{15}$$

where C_1 is a constant and

$$A = \frac{\mathrm{Bi}(2n+7) + (2n^2+7n+8)}{4(2n+3)(2n+5)(n+\mathrm{Bi})} \tag{16}$$

The substitution of equation (15) into the boundary condition (14) yields the characteristic equation, a relationship between Ma, Bi and n. This is

$$\mathrm{Ma} = \frac{(2n+1)(2n+3)(2n+5)(n+\mathrm{Bi})}{n(n+1)} \tag{17}$$

at which disturbances will become marginally stable. In other words, instability will set in with that value of n which leads to the lowest value for Ma. Equation (17) indicates that for any value of Bi, the easiest modes to excite are those belonging to $n = 1$.

Results and Discussion

Equation (17) is plotted in Fig. 1 for the various values of Bi. These curves are neutral stability curves; the regions embraced by the curves correspond to unstable disturbances and those outside them contain stable points. It is important to note that n has to be an integer. All the curves asymptote to $\mathrm{Ma} = 8\lambda^2$ for large values of n and all display

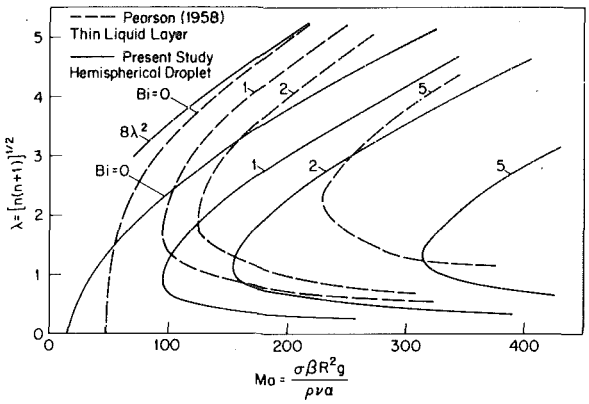

Fig. 1 Neutral stability curves, insulating case

a critical (minimum) value of Ma at λ of nearly unity, for which the closest value of n is unity. In other words, stable disturbances are first possible at $n = 1$. The special case Bi = 0 corresponds to the insulated droplet surface with the critical Ma of 52.5 at $n = 1$. In general, larger values of Bi lead to larger critical Ma, i.e., greater stability. The values of Bi depend on the droplet radius and would tend to zero for very small droplets. It is interesting to note that the condition (17) applies to both $\partial T'/\partial r = 0$ and $T' = 0$ at the droplet center, which were referred to as "insulating" and "conducting" cases, respectively, in reference [3].

Superimposed on Fig. 1 are Pearson's neutral stability curves, insulating case, for thin liquid layers [3]. In this case, the thickness of liquid layers is employed as the characteristic length in both Bi and Ma. All curves are also asymptotic to $\text{Ma} = 8\lambda^2$ for large values of λ. The case Bi = 0 is special in that the critical wave number is zero, at which the critical Ma is 48. At the same Bi, the critical Ma for a liquid layer is lower than that of a hemispherical droplet at $n = 1$ mode, indicating that a hemispherical geometry is more stable to surface tension induced mechanism than a flat layer geometry. The difference in the critical Marangoni numbers between the two distinct geometries grows larger with an increase in the Biot number. This observation is also applicable to the other extreme case of conducting boundary condition, as may be concluded by comparing our Fig. 1 with Fig. 1 in reference [3]. In reality, a liquid droplet on a heated surface takes a form between a hemispheric shape and a flat layer.

Another thermal condition under which the critical Marangoni number for the onset of cellular convection can be obtained in closed form is for the steady temperature profile to take a parabolic form. That is

$$T_0(r) = T_{c0} - \beta_*{}^2 r^2 \tag{18}$$

where β_* is a constant. Equation (2) remains unchanged with β replaced by $2\beta_*\gamma$. Both equations are subject to the same boundary conditions (4) and (5). In the solutions, R in equation (7) must be replaced by r, while βR becomes $\beta_* R^2$. Ma on the *RHS* of equation (14) reduces to $2\text{M}_a{}^* = 2\sigma\beta_* \text{R}^4/\rho\nu\alpha$. The critical Marangoni number then reads

$$2\text{M}_a{}^* = \text{Ma} \tag{19}$$

and the neutral stability curves in Fig. 1 can be applied accordingly. The result suggests that under the same values of n and Bi, a linear steady temperature profile in twice more stable than a parabolic one.

Conclusions

A linear small-perturbation method is applied which yields a closed-form expression for the criterion for marginal stability in a hemispherical liquid droplet on a heated surface induced by surface tension mechanism: Equation (17) predicts Ma and $2\text{M}_a{}^*$ for the steady temperature distributions of the linear and parabolic profiles, respectively. Due to the nature of the boundary conditions, (4) and (5), the results can be also applied to a spherical droplet suspended in a warm environment. It is concluded that (1) larger values of the Biot number lead to greater stability; (2) a hemispherical droplet is more stable under surface tension variations than a flat liquid layer; and (3) a parabolic steady thermal profile is more susceptable than a linear one to thermal disturbances due to surface tension force.

References

1 Benard, H., "Les Tourbillons Cellulaires dan une Nappe Liquide Transportant de la Chaleur par Convection en Regime Permanent," *Annales Chimie et Physique,* Vol. 23, 1901, pp. 62–144.

2 Rayleigh, Lord, "On Convection Currents in a Horizontal Layer of Fluid, when the Higher Temperature is on the Under Side," *Phil. Magazine,* Vol 32, 1916, p. 529.

3 Pearson, J. R. A., "On Convection Cells Induced by Surface Tension," *Journal of Fluid Mechanics,* Vol. 4, 1958, p. 489.

4 Nield, D. A., "Surface Tension and Buoyancy Effects on Cellular Convection," *Journal of Fluid Mechanics,* Vol. 19, 1964, p. 341.

5 Berg, J. C., Boudart, M., and Acrivos, A., "Natural Convection in Pools of Evaporating Liquids," *Journal of Fluid Mechanics,* Vol. 24, 1966, p. 721.

6 Scriven, L. E., and Sternling, C. V., "On Cellular Convection Driven by Surface Tension Gradients: Effects of Mean Surface Tension and Surface Viscosity," *Journal of Fluid Mechanics,* Vol. 19, 1964, p. 321.

7. Bupara, S. S., "Spontaneous Movements of Small Round Bodies in Viscous Fluids," Doctoral Thesis, Department of Chemical Engineering, University of Minnesota, Minn. 1965.

8 Kenning, D. B. R., "Two-Phase Flow with Nonuniform Surface Tension," *Applied Mechanics Review,* Vol. 21, 1968, p. 1101.

9 Chandrasekhar, S., *Hydrodynamic and Hydromagnetic Stability,* Oxford University Press, Oxford, England, 1961, Chap. 6.

Journal of Heat Transfer

Discussion

Shape of Two-Dimensional Solidification Interface During Directional Solidification by Continuous Casting[1]

T. Jászay, T. Környey, P. Radenkovits.[2] In 1978 the *Journal of Heat Transfer* published this most interesting article on the shape and location of solidus-liquidus interface during continuous casting. Our own investigations led to the conclusion that the findings of this paper regarding the range of validity of the results should be modified according to the following formulation.

The geometry being analysed is shown in Fig. 1. An ingot is being formed by uniform withdrawal at velocity w from an insulated mold. Since the mold is insulated,

$$\frac{\partial \zeta}{\partial \xi} = 0 \qquad (\xi = 1, \quad \eta < 0) \tag{1}$$

Below the mold the surface of the ingot is strongly cooled. The temperature of the coolant, t_∞, and the heat transfer coefficient, α, are constants. The boundary condition is then

$$\frac{\partial \zeta}{\partial \xi} = -\mathrm{B}\zeta \qquad (\xi = 1, \quad \eta > 0) \tag{2}$$

Since, in the center of the ingot, the direction of the withdrawal velocity and that of the heat flux are identical,

$$\frac{\partial \zeta}{\partial \xi} = 0 \quad (\xi = 0) \tag{3}$$

The temperature of the solidified ingot far from the mold and that of the coolant are identical, hence

$$\zeta = 0 \qquad (\eta = \epsilon = \infty) \tag{4}$$

The molten substance, with definite melting point t_s, above the solidification interface is superheated and transfers heat to the interface. It is assumed that there is a uniform heat flux $\dot{q}_1$, to the interface. Since the ingot is being withdrawn at a uniform rate, the latent heat of fusion removed per unit area locally at the interface is $w\rho h dx/ds$ where ds is a differential length along the interface. The sum of the aforementioned two heat fluxes leaves the interface, the $t = t_s$ isothermal surface, by conduction. The boundary condition at the interface is then

$$\left(\frac{\partial \zeta}{\partial \xi}\right)^2 + \left(\frac{\partial \zeta}{\partial \eta}\right)^2 + \mathrm{PS}\frac{\partial \zeta}{\partial \eta}\left(1 + Q\sqrt{1 + \left(\frac{\partial \zeta}{\partial \xi}\right)^2 \Big/ \left(\frac{\partial \zeta}{\partial \eta}\right)^2}\right) = 0 \qquad (\zeta = 1) \tag{5}$$

In the solidified ingot, the energy is transported by movement and conduction. Since it is assumed that the thermal properties are constant, the equation to be solved within the solidified material is as follows.

$$\nabla^2 \zeta - \mathrm{P}\frac{\partial \zeta}{\partial \eta} = 0 \tag{6}$$

Possibilities for Simplification. (1) In region $\eta > 0$ the solution of equation (6) can be written as follows.

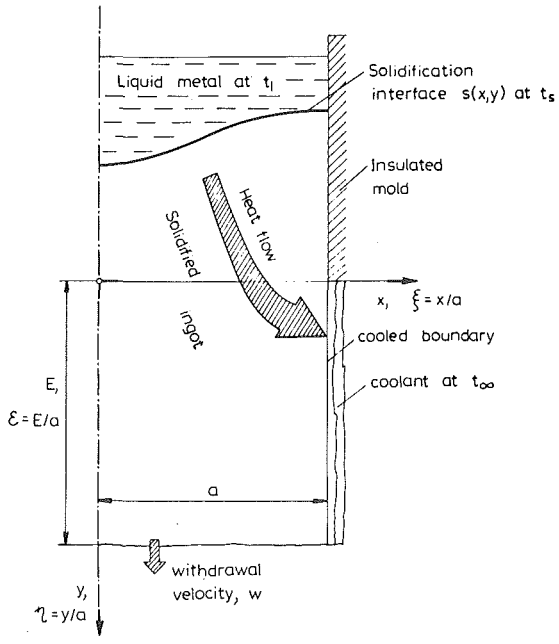

Fig. 1 Ingot geometry

[1] By R. Siegel, published in the 1978 issue of the ASME JOURNAL OF HEAT TRANSFER, Vol. 100, No. 1, pp. 3–10.

[2] Technical University of Budapest, 1111 Budapest, Muegyetem rkp. 3, Hungary.

$$\zeta = \sum_{i=1}^{\infty} \zeta_i, \text{ where } \zeta_i = C_i \varphi(\mu_i \xi) \exp(\nu_i \eta)$$

$$\nu_i = 0.5\mathrm{P}(1 - \sqrt{1 + (2\mu_i/\mathrm{P})^2})$$

The μ_i values ($\mu_1 < \mu_2 < \mu_3 \ldots$) are the positive roots of the following equation.

$$\left.\frac{\partial \varphi(\mu_i \xi)}{\partial \xi}\right|_{\xi=1} = \mathrm{B}\varphi(\mu_i)$$

Should the ingot be a slab with a thickness of $2a$, φ denotes the cosine function. When ingot is a cylinder with a diameter of $2a$, φ stands for the J_0 Bessel function of the first kind of zero order. In case of $\epsilon \gg 0$ it is true that $\zeta \approx \zeta_1$, this is why boundary equation (4) can be substituted by the following.

$$\frac{\partial \zeta}{\partial \eta} = \nu_1 \zeta \qquad (0 \ll \eta = \epsilon \neq \infty) \tag{4a}$$

(2) In the case $Q \approx 0$, the heat transferred from the molten substance to the interface is small as compared to the latent heat of solidification, or

$$\left(\frac{\partial \zeta}{\partial \xi}\right)^2 \Big/ \left(\frac{\partial \zeta}{\partial \eta}\right)^2 \approx 0$$

(the interface is flat), the boundary condition (5) can be written as follows.

$$\left(\frac{\partial \zeta}{\partial \xi}\right)^2 + \left(\frac{\partial \zeta}{\partial \eta}\right)^2 + \mathrm{PS}^* \frac{\partial \zeta}{\partial \eta} = 0 \qquad (\zeta = 1) \tag{5a}$$

where

$$\mathrm{S}(1+Q) \approx \mathrm{S}^* \approx \mathrm{S}\left(1 + Q\sqrt{1 + \left[\left(\frac{\partial \zeta}{\partial \xi}\right) \Big/ \left(\frac{\partial \zeta}{\partial \eta}\right)\right]_a^2}\right)$$

(3) In the case $Q \gg 1$, the heat released during solidification is small as compared to the heat transferred from the molten substance, or

$$\left(\frac{\partial \zeta}{\partial \xi}\right)^2 \Big/ \left(\frac{\partial \zeta}{\partial \eta}\right)^2 \approx 0$$

(the solidus interface is flat), boundary equation (5) can be substituted by the following.

$$\left(\frac{\partial \zeta}{\partial \xi}\right)^2 + \left(\frac{\partial \zeta}{\partial \eta}\right)^2 + \mathrm{PS}^{**} \left(\frac{\partial \zeta}{\partial \eta}\right) \sqrt{1 + \left(\frac{\partial \zeta}{\partial \xi}\right)^2 \Big/ \left(\frac{\partial \zeta}{\partial \eta}\right)^2} = 0 \qquad (\zeta = 1) \tag{5b}$$

$$\mathrm{S}(1+Q) \approx \mathrm{S}^{**} \approx \mathrm{S}\left(Q + 1\Big/\sqrt{1 + \left[\left(\frac{\partial \zeta}{\partial \xi}\right)^2 \Big/ \left(\frac{\partial \zeta}{\partial \eta}\right)^2\right]_a}\right)$$

(4) In the case of small Péclet number, equation (6) can be written

$$\nabla^2 \zeta = 0 \tag{6a}$$

Results

1 Mr. Siegel's paper gives the solution of the model consisting of equations (1–4, 5*b*) and (6*a*) regarding an ingot bounded by two infinite parallel planes, supposing that $B = \infty$.

2 Reference [1] gives the solution of the model consisting of equations (1–4, 5*a*) and (6*a*) regarding an ingot bounded by two infinite parallel planes, supposing that $B = \infty$. The results are the dotted lines of Fig. 2. In this case the parameter is $A \equiv \mathrm{PS}^+$.

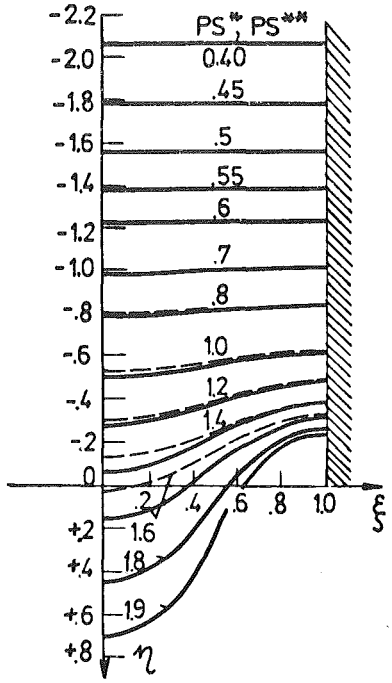

Fig. 2 Shape of solidification interface

3 We have obtained our own results by solving the model consisting of equations (1–3, 4*a*, 5*a*) and (6). The results are those solutions of the system of linear algebraic equations, which system can be derived from equations (1–3, 4*a*) and (6) by using the finite difference scheme, and which solutions satisfy the finite differences form of equation (5*a*) on the line $\zeta = 1$. We have obtained the solutions by successive approximations. In the calculations the $\Delta\xi = \Delta\eta = .05$ and $\epsilon \approx 1.5$ values were used. The results of calculations were considered as correct when, on the solidus line, the error of heat balance was less than 0.2 percent. Our own results on a cylindrical ingot are shown in Figs. 3 and 4.

Analysis

1 The location and shape of the solidification interface are determined, even in the rather idealized above model, by four parameters (PS, P, *Q*, B). In the case of planar solidus-liquidus interface or small superheat of the molten metal, the number of parameters can be reduced to three; for, in this case, PS and *Q* can be united into a single quantity (PS^+). As is shown by Fig. 3, the shape and location of the interface are rather responsive to the alteration of each of the parameters.

2 Figure 2 clearly shows that, in case the interface does not differ considerably from the plane, boundary equations (5*a*) and (5*b*) yield the same result.

Nomenclature

a = half-width of slab ingot, or radius of cylindrical ingot
$\mathrm{B} = \alpha a/\lambda$, Biot number
c = specific heat of solid
h = latent heat of fusion per unit mass of solid
$\mathrm{P} = wa\rho c/\lambda$ Péclet number
$Q = \dot{q}_l/(w\rho h)$, dimensionless
$\dot{q}_l$ = (uniform) heat flux from liquid substance to solidification interface
$\mathrm{S} = h/[c(t_s - t_\infty)]$, reciprocal of the Stefan number
s = distance along interface
t = temperature
w = withdrawal velocity of ingot
x, y = coordinates
α = convective heat transfer coefficient
$\xi = x/a$, $\eta = y/a$, dimensionless coordinates
$\zeta = (t - t_\infty)/(t_s - t_\infty)$ dimensionless temperature
λ = thermal conductivity of solidified metal
ρ = density of solidified metal

Subscripts

a = average
l = liquid metal
s = at solidification temperature
∞ = at temperature of coolant

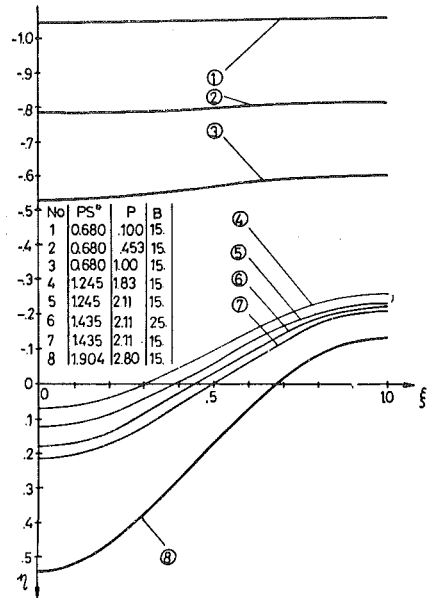

Fig. 3 Location and shape of solidification interface

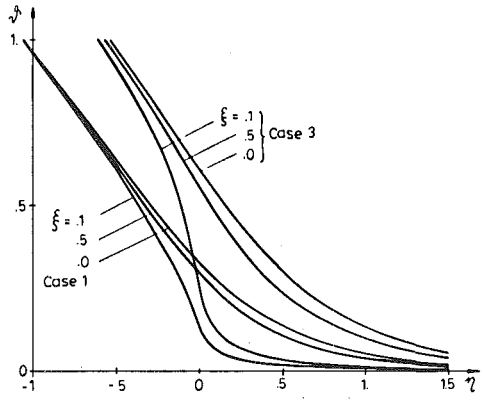

Fig. 4 Temperature distribution in the solidified slab

3 If boundary equation (4*a*) is applied when $\epsilon = \eta = 1.5$, the temperature-distribution $\vartheta(\xi, \eta = 1.5)$ can be approached, by the function $CJ_0(\mu_1\xi)$ with an error less than 1 percent in all the cases shown by Fig. 3; i.e., the application of boundary equation (4*a*) with this value of ϵ does not yield considerable error. The same theory is made probable by Fig. 4, according to which, in case of $\eta > 0.75$, temperatures in function of η seem to diminish exponentially.

4 Curves No. 1, 2 and 3 in Fig. 3, show that the location of the solidus interface depends very strongly on the Péclet number, being its approximate linear function, if the rest of the parameters are considered to be constant.

5 In the case of cylindrical or prismatic ingots the results are the same in quality, although they differ numerically. This is why the statement that Fig. 2. can be applied in case of $P \leqq .5$ should be modified by stating that it is only valid when $P \approx 0$.

Reference

1 Siegel, R., "Analysis of Solidification Interface Shape During Continuous Casting of a Slab," *International Journal of Heat and Mass Transfer*, Vol. 21. No. 11, Nov. 1978, pp. 1421–1430.

A Parametric Analysis of the Performance of Internally Finned Tubes for Heat Exchanger Application[1]

A. Bejan.[2] The Webb and Scott paper focuses on a topic of contemporary importance, namely, the performance of internally finned tubes as a technique for augmenting heat transfer in heat exchangers. The authors recognize in their Introduction that the expression "optimum performance" is a source of controversy in the active field of heat transfer augmentation research. They also state that, in their study, " 'optimum' means to maximize (or minimize) the objective function for minimum tube material content." In fact, this is only the first of three viewpoints adopted by the authors in evaluating the performance of internally finned tubes. The three evaluation criteria are

(A) the ability of internal finning to reduce material volume, while keeping the pumping power and the overall heat transfer coefficient (heat "duty") unchanged,

(B) the ability of internal finning to increase the heat transfer coefficient, while keeping the pumping power and tube length unchanged, and

(C) the ability of internal finning to reduce the pumping power requirement, while keeping the heat transfer coefficient and tube length unchanged.

I can understand the historical reasons for considering only viewpoint (A): There was a time when the single most expensive item in the constitution of a heat exchanger was the material necessary for building the apparatus. Today, we are forced to recognize that heat exchangers *steadily* waste fuel (not "energy," rather, the exergy content of fuel) [1]. As the price of fuel (or bottled exergy) continues to rise, the same cost minimization formula which in the past gave us criterion (A) now suggests a criterion which evaluates the ability of heat exchangers to conserve exergy. This means that one of the designer's jobs is to minimize the production of entropy in the heat exchanger. In the case of internally finned tubes as a design alternative vis-a-vis internally smooth tubes, it is the designer's duty to evaluate the impact of internal finning on the rate of entropy generation in the tube.

Consider now criteria (B) and (C). The ability of internal fins to improve the thermal contact (B) or to reduce the pumping power requirement (C) is tied directly to the ability to reduce the entropy generation rate. We know that the pumping power requirement represents "lost available power" (irreversibility), but the same description applies to the heat exchange between two bodies in imperfect thermal contact (heat transfer across a non-zero temperature difference means lost available power too). Then, why treat as different the two entropy generation contributions (fluid friction, inadequate thermal contact), as the authors do in criteria (B) and (C)? I will offer an explanation for this choice later in this discussion.

Criteria (B) and (C) are philosophically one and the same: The would-be designer is interested in maximizing the ratio R = (heat transfer coefficient)/(pumping power) while keeping the tube length unchanged. Unfortunately, this easy-to-calculate ratio has nothing to do with the important task of improving the thermodynamic performance of a heat exchanger [2]. There exists no consistent relationship between maximizing this ratio and conserving fuel (exergy) in the apparatus. One can show analytically that the dependence between entropy generation and R is *nonmonotonic*, hence, in some heat exchangers increasing R leads to exergy savings, while in others it leads to increased exergy waste [2].

Ouellette and Bejan [3] reached similar conclusions when they studied the same topic as Webb and Scott and calculated the change in entropy generation rate associated solely with using an internally

[1] By R. L. Webb and M. J. Scott, published in the February 1980 issue of the Journal of Heat Transfer, Vol. 102, pp. 38–43.

[2] Assistant Professor, Department of Mechanical Engineering, University of Colorado, Boulder, Colo. 80309

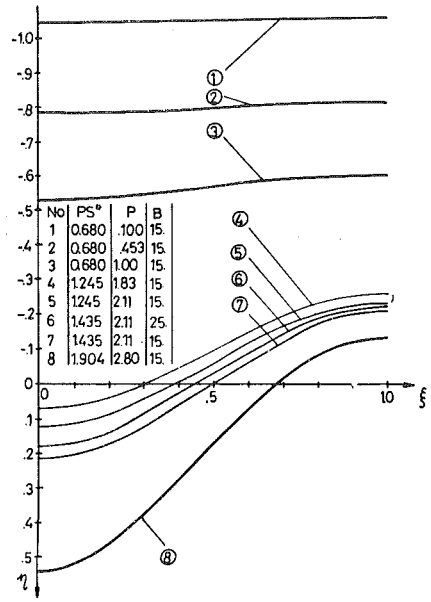

Fig. 3 Location and shape of solidification interface

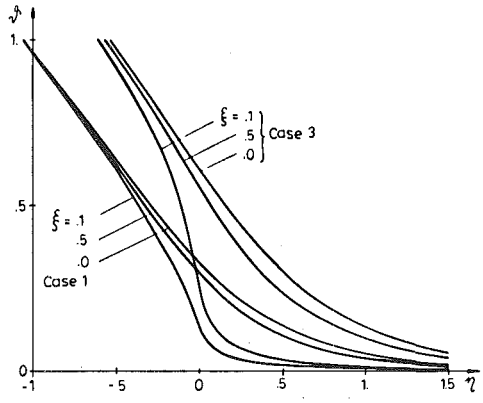

Fig. 4 Temperature distribution in the solidified slab

3 If boundary equation (4*a*) is applied when $\epsilon = \eta = 1.5$, the temperature-distribution $\vartheta(\xi, \eta = 1.5)$ can be approached, by the function $CJ_0(\mu_1\xi)$ with an error less than 1 percent in all the cases shown by Fig. 3; i.e., the application of boundary equation (4*a*) with this value of ϵ does not yield considerable error. The same theory is made probable by Fig. 4, according to which, in case of $\eta > 0.75$, temperatures in function of η seem to diminish exponentially.

4 Curves No. 1, 2 and 3 in Fig. 3, show that the location of the solidus interface depends very strongly on the Péclet number, being its approximate linear function, if the rest of the parameters are considered to be constant.

5 In the case of cylindrical or prismatic ingots the results are the same in quality, although they differ numerically. This is why the statement that Fig. 2. can be applied in case of $P \leqq .5$ should be modified by stating that it is only valid when $P \approx 0$.

Reference

1 Siegel, R., "Analysis of Solidification Interface Shape During Continuous Casting of a Slab," *International Journal of Heat and Mass Transfer*, Vol. 21. No. 11, Nov. 1978, pp. 1421–1430.

A Parametric Analysis of the Performance of Internally Finned Tubes for Heat Exchanger Application[1]

A. Bejan.[2] The Webb and Scott paper focuses on a topic of contemporary importance, namely, the performance of internally finned tubes as a technique for augmenting heat transfer in heat exchangers. The authors recognize in their Introduction that the expression "optimum performance" is a source of controversy in the active field of heat transfer augmentation research. They also state that, in their study, " 'optimum' means to maximize (or minimize) the objective function for minimum tube material content." In fact, this is only the first of three viewpoints adopted by the authors in evaluating the performance of internally finned tubes. The three evaluation criteria are

(A) the ability of internal finning to reduce material volume, while keeping the pumping power and the overall heat transfer coefficient (heat "duty") unchanged,

(B) the ability of internal finning to increase the heat transfer coefficient, while keeping the pumping power and tube length unchanged, and

(C) the ability of internal finning to reduce the pumping power requirement, while keeping the heat transfer coefficient and tube length unchanged.

I can understand the historical reasons for considering only viewpoint (A): There was a time when the single most expensive item in the constitution of a heat exchanger was the material necessary for building the apparatus. Today, we are forced to recognize that heat exchangers *steadily* waste fuel (not "energy," rather, the exergy content of fuel) [1]. As the price of fuel (or bottled exergy) continues to rise, the same cost minimization formula which in the past gave us criterion (A) now suggests a criterion which evaluates the ability of heat exchangers to conserve exergy. This means that one of the designer's jobs is to minimize the production of entropy in the heat exchanger. In the case of internally finned tubes as a design alternative vis-a-vis internally smooth tubes, it is the designer's duty to evaluate the impact of internal finning on the rate of entropy generation in the tube.

Consider now criteria (B) and (C). The ability of internal fins to improve the thermal contact (B) or to reduce the pumping power requirement (C) is tied directly to the ability to reduce the entropy generation rate. We know that the pumping power requirement represents "lost available power" (irreversibility), but the same description applies to the heat exchange between two bodies in imperfect thermal contact (heat transfer across a non-zero temperature difference means lost available power too). Then, why treat as different the two entropy generation contributions (fluid friction, inadequate thermal contact), as the authors do in criteria (B) and (C)? I will offer an explanation for this choice later in this discussion.

Criteria (B) and (C) are philosophically one and the same: The would-be designer is interested in maximizing the ratio R = (heat transfer coefficient)/(pumping power) while keeping the tube length unchanged. Unfortunately, this easy-to-calculate ratio has nothing to do with the important task of improving the thermodynamic performance of a heat exchanger [2]. There exists no consistent relationship between maximizing this ratio and conserving fuel (exergy) in the apparatus. One can show analytically that the dependence between entropy generation and R is *nonmonotonic*, hence, in some heat exchangers increasing R leads to exergy savings, while in others it leads to increased exergy waste [2].

Ouellette and Bejan [3] reached similar conclusions when they studied the same topic as Webb and Scott and calculated the change in entropy generation rate associated solely with using an internally

[1] By R. L. Webb and M. J. Scott, published in the February 1980 issue of the Journal of Heat Transfer, Vol. 102, pp. 38–43.

[2] Assistant Professor, Department of Mechanical Engineering, University of Colorado, Boulder, Colo. 80309

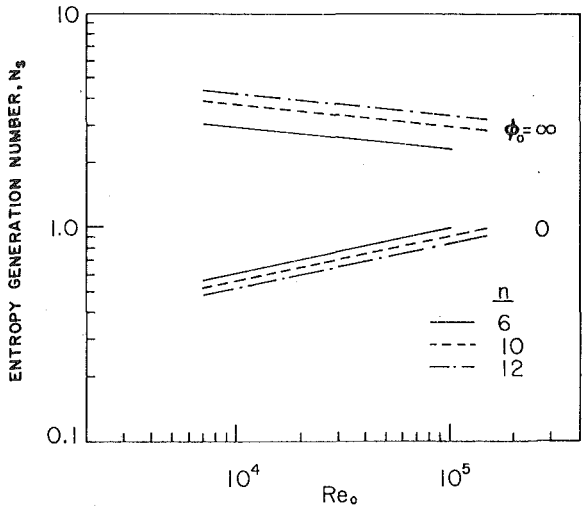

Fig. 1 Entropy generation number N_S associated with using n straight fins on the inside surface of a smooth tube [3]

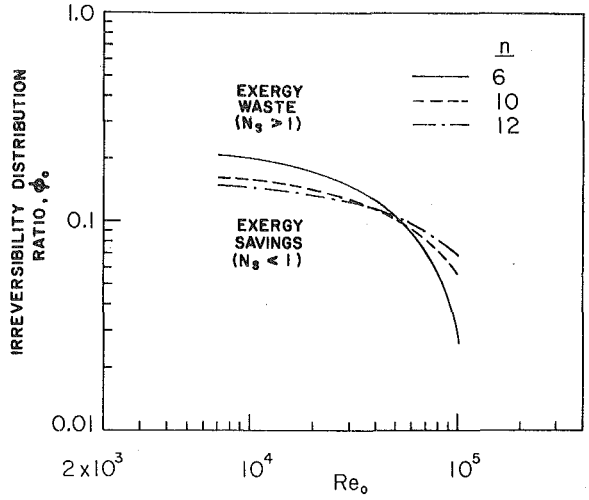

Fig. 2 The irreversibility distribution ratio ϕ_0 (fluid friction irreversibility/inadequate thermal contact irreversibility), showing the operating domain (ϕ_0, Re_0) in which finning leads to exergy savings [3]

finned tube instead of an internally smooth tube. This change can be expressed as an *entropy generation number* N_S defined as

$$N_S = \frac{S_{\text{finned tube}}}{S_{\text{smooth tube}}} \tag{1}$$

where S is the rate of entropy generation per unit tube length. Figure 1 shows the entropy generation number in the case of n internal straight fins with the following dimensions: height = 1.5 mm, width = 1 mm, tube i.d. = 14 mm. The Nusselt number and friction factor data on this group of internally finned tubes are given by Carnavos [4]. The analytical details leading to plotting Fig. 1 are presented in reference [3].

If the number of fins (n) is fixed, the entropy generation number emerges as a function of two parameters which describe the operating mode of the piece of heat exchanger tubing: (1) the Reynolds number Re_0, and (2) the *irreversibility distribution ratio* ϕ_0 defined as

$$\phi_0 = \left(\frac{S_{\text{fluid friction}}}{S_{\text{inadequate thermal contact}}}\right)_{\text{smooth tube.}} \tag{2}$$

Depending on the operating mode of the apparatus (Re_0, ϕ_0), internal finning can either reduce irreversibility ($N_S < 1$) or actually increase the rate of exergy waste ($N_S > 1$). Figure 2 shows the important operating domain (ϕ_0, Re_0) in which finning is thermodynamically advantageous ($N_S < 1$). Plots like Fig. 2 can be constructed for any design change: the plot is the property of the design change. With a particular heat exchanger application (Re_0, ϕ_0) in mind, the designer can use the plots corresponding to Fig. 1 to decide the actual savings in fuel (exergy) consumption. It is important to remember that one cannot evaluate the fuel-saving potential of internally finned tubes without specifying the apparatus in which the finned tubes will be incorporated. Stated differently, one should not evaluate internally finned tubes alone, without considering the larger system of which the finned tubes are only a part.

Related to my previous statement, let me offer an explanation as to why some still regard fluid friction and inadequate thermal contact as two different entities in the process of improving heat exchanger performance. Historically, it has been less expensive and more convenient to optimize heat exchangers *alone* [5], removed from the aggregate (power/refrigeration) system. Removing the heat exchanger from its "nest" means accepting a number of peripheral parameters (pressure drop, inlet-outlet temperature difference, etc.) as *constraints.* When the flow rates through the apparatus are specified, the peripheral constraints assume the form of fixed pumping power, fixed heat transfer rate, etc. Engineers are *erroneously* taught that the job of heat exchangers is to transfer fixed quantities of heat. Such a constraint stems from having isolated the heat exchanger from the bigger picture which includes the aggregate system.

The function of the aggregate system defines also the function of the subsystems. It follows that the function of heat exchangers for power and refrigeration plants is not to "transfer heat," but to duct the working fluid in *the least irreversible manner* the designer can afford [6]. For example, the use of regenerative (counter flow) heat exchangers in a Brayton cycle comes from the need to insulate the warm end of the cycle from the cold end, i.e., the need to minimize the production of entropy in the power/refrigeration plant [7].

In conclusion, if the heat transfer community is to make a lasting contribution to solving the fuel (exergy) problem, we must acquire a clear understanding of the existing connection between heat transfer processes and the unnecessary consumption of fuel (exergy). We must conceptualize the efficiency of a heat transfer device relative to the true function served by this device in the larger (aggregate) system. It is important not to isolate a heat exchange apparatus, but to optimize it *in harmony* with the aggregate system.

If heat transfer is to continue as a viable field, as opposed to an archival one, its emphasis must change as the challenges change. (For a similar conclusion, see Lienhard's letter on the history of heat transfer [8].)

Additional References

1 Cambel, A. B., Editor, *Proceedings of the Second Law of Thermodynamics Workshop,* George Washington University, Washington, D. C., Aug. 14–17, 1979, to appear in *Energy,* Vol. 5, 1980.

2 Bejan, A., "General Criterion for Rating Heat Exchanger Performance," *International Journal of Heat Mass Transfer,* Vol. 21, 1978, p. 655.

3 Ouellette, W. R., and Bejan, A., "Entropy Generation Criterion Applied to Various Heat Transfer Augmentation Techniques," Report CUMER-79-5, Department of Mechanical Engineering, University of Colorado, Boulder, Colorado 80309, Aug. 1979 (copies available upon request).

4 Carnavos, T. C., "Some Recent Developments in Augmented Heat Exchange Elements," *Heat Exchanger Design and Theory Sourcebook,* Afgan, N. H., and Schlunder, E. U., Editors, Scripta, Washington, D. C., 1974, p. 441.

5 Kays, W. M., and London, A. L., *Compact Heat Exchangers,* 2nd Edition, McGraw-Hill, New York, 1964.

6 Bejan, A., "The Concept of Irreversibility in Heat Exchanger Design: Counterflow Heat Exchangers for Gas-to-Gas Applications," ASME JOURNAL OF HEAT TRANSFER, Vol. 99, 1977, p. 374.

7 Bejan, A., "A General Variational Principle for Thermal Insulation System Design," *International Journal of Heat Mass Transfer,* Vol. 22, 1979, p. 219.

8 Lienhard, J. H., ASME Heat Transfer Division Newsletter, Oct. 1978, p. 3; published also in *Heat Transfer Engineering,* Vol. 1, No. 1, 1979.